

University of Strathclyde

Department of Civil and Environmental Engineering

**The architecture and fluid flow properties of shallow
fault systems: implications for environmental
monitoring of subsurface technologies**

Christopher J. McMahon

Doctor of Philosophy (PhD)

2024

Declaration of Authenticity and Author's Rights

This thesis is the result of the author's original research. It has been composed by the author and has not been previously submitted for examination which has led to the award of a degree. The copyright of this thesis belongs to the author under the terms of the United Kingdom Copyright Acts as qualified by the University of Strathclyde Regulations 3.50. Due acknowledgement must always be made of the use of any material contained in, or derived from, this thesis.

Signed: C. McMahon

Date: 07/06/2024

Acknowledgements

Firstly, it is only right to extend a warm thank you to my supervisors Jen Roberts, Zoe Shipton and Gareth Johnson for all their support, advice, encouragement, humour and most of all patience as we all navigated the last five years. Completing a PhD is challenging enough, but their ability to act as role models through various unexpected events, not least a global pandemic, ensured I was able to complete this thesis. You have all facilitated my personal and professional development throughout my PhD, and for that I am forever grateful.

To my external supervisors, Julian Strand and Eric Tenthorey, thank you for supporting two research visits to Australia. Julian, you made me feel welcome and at home, even on the other side of the world. Our academic chats about fault zones and natural hydrogen, and sidetracks about life, music and art, are already a fond memory. Eric, thank you for supporting my studies in multiple locations – Glasgow, London, Canberra and Otway – and for always being up for a chat and a drink. You have both helped me to develop as a researcher and provided me with incredibly useful insights into different working styles and environments, which has been invaluable.

To those who supported my research visits to Australia, too many to name. Notably, staff from CSIRO (Linda, Jeremie, Claudio, Laurent and Lionel) and DMIRS core library staff (you had to shift a lot of rock core, but were always accommodating and supportive). Additionally, staff at Geoscience Australia (GA), particularly Andrew Feitz (and the low carbon geoscience team), for creating a welcoming work environment and social life while on research visits. To the organisations that have supported this research (CSIRO, DMIRS, CO2CRC and GA), thank you providing valuable collaborations that really enhanced this PhD. To other supporters and collaborators, including Mark from the Port Campbell Tourist Information Centre and Stephen Gallagher from the University of Melbourne, thank you for your time and insights.

For the members of the research groups and communities I have been fortunate enough to interact with during my PhD (Faults and Fluid Flow (FaFF) research group, CO₂ research group, Tectonic Studies Group (TSG), UKCCSRC, IEAGHG and others) thank you for providing opportunities to discuss research and develop knowledge, skills and confidence.

Those who have helped me throughout my academic journey cannot go unmentioned. To my undergraduate project supervisors Daniel Koehn and Roderick Brown, your knowledge, insights and teaching styles are memorable. Daniel, thank you for supporting me on my first attempts at academic research, providing useful feedback and supporting amazing opportunities (i.e. a research expedition to Uganda). To my masters supervisor Katriona Edlmann, thank you for developing my research and writing skills and giving me the confidence to pursue a PhD. Your support then and throughout my PhD is appreciated.

Finally, the sappy section... To my peers, teachers, friends and family who have supported me throughout my life – thank you. There are too many people who have positively influenced me to mention each individually. To my mum and dad, thank you for your endless encouragement, kindness and support. Without you both I would not be the person I am. To my aunt, thanks for always being there to lend a hand and helping me when needed, and you never even complained (much). To my brother Aiden, thank you for giving me the time and space back when we shared a room to study, it wasn't always to your liking at the time, but it has helped me progress to now be at the stage where I have completed this PhD thesis. I'd say I'd go back and do it again, but I am sure we both enjoy having our own space. Not to forget, my little fluffy dog Luna – walking together helped to clear my mind and helped my thinking throughout my thesis writing. To end, to my partner Bailey, thank you for being you and helping me be me. Your unwavering support throughout my studies has been a driving force that has kept me going. I love you all and I look forward to continuing the journey ahead, together.

Abstract

Action and solutions to combat the challenges of changing climate is needed. To meet global climate targets, there is an anticipation that there must be a scaling up of existing and emerging subsurface technologies (e.g. geological carbon dioxide (CO₂) storage, energy storage (e.g., hydrogen) and geothermal energy). Many of these emerging technologies involve some element of subsurface fluid injection, storage, and withdrawal. Therefore key to secure and safe operation is robust site selection criteria, appropriate measuring, monitoring, and verification (MMV) systems and remediation procedures. Understanding the architecture of shallow fault zones (<1 km depth in the Earth's crust) and implications for subsurface fluid flow is important to inform these criteria, systems and approaches. Yet, shallow fault zones are less well studied and modelled compared with deeper faulting (i.e. reservoir depths). To enhance current understanding of shallow fault systems, this thesis presents a comprehensive study of two field sites which have injected CO₂ into shallow fault zones: the In-Situ Lab (Harvey, Western Australia) and the Otway International Test Centre (Otway, Victoria). Data collected at the field sites are examined, rock core is observed at different scales and sampled, and fieldwork is undertaken to understand the regional structural setting. By synthesising these data, research findings show that shallow fault zones often do not exhibit "classic" fault architectures, which are based on deformation in the brittle regime, and instead the dominant deformation style in shallower fault zones is particulate flow, which is only observed through using methods of study across a range of scales. The resulting variability in deformation styles influences the hydraulic properties of the rock. Furthermore, fault rock and surrounding host rock can often be weak in shallow fault zones meaning the methods used for analysis need to be suitable for use on lower strength sedimentary rocks. Shallow fault zones present new challenges in effectively designing suitable geological modelling approaches due to increased uncertainties in shallow stress magnitudes and the characteristics of shallow fault architecture – meaning it is not reasonable to use standard fault or stress analysis tools. Separately, a global study of natural hydrogen seepage sites is presented which provides insights into variations in surface seepage expression and controls on the production, consumption and transformation of hydrogen in the subsurface, with implications for environmental monitoring.

Research Summary

PhD Aim: To improve understanding of the architecture of shallow fault systems and their control on subsurface fluid flow.

Fault zones affect fluid movement within the Earth's subsurface at various scales, with a host of implications for performance and measurement, monitoring, and verification (MMV) of subsurface technologies (e.g. geological CO₂ storage, energy storage, geothermal energy, and radioactive waste disposal). However, to date most fault studies have been focused on faults at hydrocarbon reservoir depths (typically >1km), with limited work focusing on shallower faults (<1km depth). Defining fault zones was important to establish consistent terminology. There are therefore five broad categories of faults in the subsurface, defined by fault activity, depth and burial/exhumation history. This categorisation is new and provides important context for studying shallow fault zones. The categories are:

1. Faulting in 'young' rocks or soils that have not been exhumed. The faulting will have been active close to the Earth's surface in materials that are likely to be very poorly consolidated unless there has been very near-surface diagenesis. These fault rocks are currently experiencing the greatest levels of stress in their history and are considered to be underconsolidated in an engineering soil mechanics sense (e.g. Brumbys Fault, see Section 3.2.3).
2. Faulting in rocks that have been exhumed from depths less than 1km, and which may be completely, partially or un-lithified. Because they are at stress levels less than the greatest stress levels they have experienced, they are considered to be over consolidated in an engineering sense (e.g. F10 Fault, see Section 3.1.3).
3. Faults that have been active at greater depths in the Earth's crust (>1km depth) and have since been uplifted to depths shallower than 1km, and overprinted by later faulting at shallower depths.
4. Faults has been active at depth, and been exhumed with no further fault activity during exhumation.
5. A final category are faults which are presently active or inactive at depths >1km and have not been exhumed.

The 1km depth is used as this is a key transition depth where the dominant deformation processes change (see Section 2.3). Faulting and fault zones in category 1 and 2 as referred to as “shallow faulting”, “shallow fault zones” or “shallow fault systems” – these are the focus of this thesis. Category 1 could be described as “near-surface faulting”. Category 2 can be described as “shallowly exhumed”. Category 3, 4 and 5 faults are not the focus of this thesis, these are referred to as “deep faults” and processes as “deeper faulting”.

Understanding shallow fault zone architecture is important to predict how they influence the hydraulic properties and pathways in the overburden and the implications this could have for subsurface containment and effective MMV systems design. This PhD aimed to address this knowledge gap.

Two field test facilities in Australia have injected CO₂ into shallow fault zones: CSIRO’s In-Situ Lab (Perth, Western Australia) and the CO2CRC’s Otway International Test Centre (OITC) Otway, Victoria. Table 0-1 summarises the characteristics of the main faults at these sites, which formed the focus for field research during this study.

Table 0-1– Comparative summary of the two faults studied for this thesis.

Characteristics		In-Situ Lab	Otway International Test Centre
		Harvey, Western Australia	Otway, Victoria
Intersecting wells		Harvey—1, 2, 3,4, In-Situ Lab-OB1	Brumbys-1, -2, -3, -4, Pizo-1, -2,
Fault	Name	F10 Fault	Brumbys Fault
	Host lithology	Siliciclastic	Carbonate
	Interpreted Type	Normal	Strike Slip
	Fault width	~300m	<5m
	Vertical distance from surface to bottom of fault	>1km	~425m

	Vertical Throw	750-1600m	2-4m
	Surface Length	30-40km	~1-1.5km
	Max. Burial Depth	~1-2km	~100-200m
Injection experiment	Injection depth	~340m	~80m
	Quantity of CO₂	38t	10t
	Date	Completed: February 2020	Completed: May 2024

Boreholes intersecting fault zones with core recovered are globally rare, and so these field sites present a unique opportunity – particularly as they are two different lithologies. Both sites are at different stages of their respective shallow release experiments (Table 0-1), with the In-Situ lab having completed in 2020 and the OITC completed in 2024. This then allows “history matching” at the In-Situ Lab for the F10 Fault, as results are published, and forecast at the OITC for the Brumbys Fault experiment, as data are still being collected and analysed. Significant amounts of subsurface data have been collected at both study sites, making them ideal sites to study shallow fault zones.

Through examining data collected at the field sites, observations made from the rock core and sampling, fieldwork to understand the regional structural setting and synthesis of these data, this thesis finds that shallow fault zones are complex. **Shallow fault zones often do not exhibit “classic” fault architecture** often presented in the literature that comprises a fault core of fine-grained material (gouge) and surrounding fractured fault damage zone. Instead, observations from the studied shallow fault zones indicate that their geometry can be asymmetric and have anisotropic deformation patterns. Such **variability in deformation style can influence the hydraulic properties of the rock**, leading to differences in permeability both vertically and laterally. Further, the observable deformation varies at different scales, and so **it is important to use methods of study across a range of scales** (i.e. from ‘macro scale’ field observation to ‘meso scale’ core logging to ‘micro scale’ thin sections and XCT) to allow a comprehensive understanding of the fault zone architecture and deformation processes. This is not necessarily distinct from deeper fault zones, but as **the dominant**

deformation style in shallower fault zones is particulate flow processes it is often difficult to observe deformation or movement indicators at the macro scale besides offset horizons. Moreover, observations from the sites studied indicate that the **fault rock and surrounding host rock can often be weak in shallow fault zones** – both as a function of the fault zone deformation and due to the burial history, which is often limited to shallow depths and prevents lithification. These observations have been found at other sites where there has been drilling through fault zones or low-strength sedimentary rocks. This means the **methods used for analysis need to be suitable for use on lower strength sedimentary rocks** to ensure effective data collection.

Attempts to model the stress regime around shallow fault zone systems indicate that these **shallow fault zones present new challenges in effectively designing suitable geological modelling approaches** to capture their unique architectures and associated uncertainties. One challenge is the increased uncertainty in some important fault and fault-related variables for the mechanical and hydraulic behaviour. For example, understanding the stress regime is important for being able to effectively predict fault reactivation and fracture networks. Yet, **for shallow fault systems the stress magnitude is highly uncertain due to the low vertical stresses nearer to the Earth's surface**. Such uncertainty has resulted in all three possible faulting modes being interpreted at both sites. An additional challenge is the suitability of modelling approaches and tools for shallow fault zone architecture. For example, observations indicate the absence of tectonic fractures at the studied sites – meaning **it is not reasonable to use standard fault or stress analysis tools** (e.g. fault/fracture reactivation potential, fracture stability, slip/dilation tendency analysis) to predict the location and behaviour of fracture networks around the fault zones. **Further work is required to develop and adapt modelling approaches to account for the unique architecture of shallow fault zones** and assess the impact that these architectures could have on the mechanical and hydraulic behaviour of shallow fault zones.

If subsurface fluids migrate through the overburden towards the shallow subsurface, then understanding and predicting the fate of that fluid within the subsurface and any potential pathways to surface is crucial to enable the design of effective MMV systems. To assess subsurface fluid flow pathways and surface expressions of seepage and the role of fault zones (during a period when no fieldwork was possible due COVID

restrictions) a study on natural hydrogen seeps was undertaken - which also compared hydrogen migration and seeps with CO₂ migration and seeps. **Compared with CO₂, hydrogen is more easily consumed or transformed in the subsurface** by biotic or abiotic reactions, and more readily dispersed in air. The **surface expression of hydrogen seepage was also different between sites of hydrogen seepage**, depending on the local geological and hydrogeological conditions, but broadly the same as surface expressions of CO₂ seepage. These findings indicate that while there are transferable knowledge and learnings between CO₂ and hydrogen, it will be necessary to tailor MMV programmes specific to the fluid injected as well as the site characteristics.

Table of Contents

Declaration of Authenticity and Author’s Rights	ii
Acknowledgements	iii
Abstract	v
Research Summary	vi
Table of Contents	xi
Table of Figures	xviii
List of Tables	xxx
Chapter 1 Introduction	32
1.1 Context of study	32
1.2 Summary of main field sites studied in this thesis.....	36
1.3 Research questions and objectives.....	37
1.4 Thesis structure	38
Chapter 2 Literature review: Fault architecture and fluid flow.....	41
2.1 Subsurface storage systems and fluid flow in porous media	41
2.1.1 Porous media and subsurface storage environments.....	41
2.1.2 Fundamentals of fluid flow in porous media	42
2.1.3 Parameters that influence fluid flow in porous media.....	44
2.2 Fault architecture and studying fault systems	53
2.2.1 Introduction to fault zones	53
2.2.2 Studying fault zones: methods and challenges	57
2.3 Fault zone architecture in the shallow subsurface	60
2.3.1 Deformation mechanisms in shallow fault zones.....	61
2.4 Siliciclastic hosted fault zones: controls, processes and fluid flow.....	64
2.4.1 Fault processes and features in siliciclastic fault zones	64
2.4.2 Faulting and fluid flow in siliciclastic fault zones.....	73

2.5	Carbonate hosted fault zones: controls, processes and fluid flow	77
2.5.1	Fault processes, porosity and permeability in carbonate rocks	78
2.5.2	Faulting and fluid flow in carbonate fault rocks	81
2.6	Implications for subsurface technologies and research gaps	82
2.6.1	Fluid flow and leakage	83
2.6.2	Site selection and monitoring.....	83
2.6.3	Research gaps.....	84
Chapter 3	Site overview: In-Situ Lab (WA, Australia) and Otway International Test Centre (VIC, Australia)	86
3.1	In-Situ Lab, Harvey (Western Australia, Australia).....	86
3.1.1	In-Situ Lab: Operation, location, scope and infrastructure	86
3.1.2	Regional geology of the Perth Basin	90
3.1.3	F10 Fault: Background, deformation and fluid flow modelling	100
3.1.4	Key findings and research gaps	109
3.2	Otway International Test Centre, Nirranda (Victoria, Australia).....	114
3.2.1	Otway International Test Centre (OITC): Operation, location, scope and infrastructure	114
3.2.2	Regional geology of the Otway Basin	118
3.2.3	Brumbys Fault.....	122
3.2.4	Key findings and research gaps	126
Chapter 4	Approach, Data and Methods	128
4.1	Fracture logging	129
4.2	Deformation logging	134
4.3	Petrographic analysis	137
4.4	XCT analysis.....	139
4.5	Fieldwork in the Port Campbell Embayment	140
4.5.1	Field observation.....	140

4.5.2	Geochemical analysis	140
Chapter 5	Multiscale characterisation of the fault architecture of the F10 Fault at the In-Situ Lab (Harvey, Western Australia): developing new methods to effectively characterise shallow fault zone architecture	141
5.1	Introduction	141
5.2	Geology of the Harvey-2 and Harvey-3 cores	141
5.3	Fracture logging of the Harvey-2 and Harvey-3 cores	145
5.3.1	Fracture logging: Harvey-2 results	145
5.3.2	Fracture logging: Harvey-3 results	148
5.3.3	Fracture logging: Synthesis and discussion	153
5.4	Deformation logging of the Harvey-2 and Harvey-3 cores	155
5.4.1	Deformation logging: Harvey-2 and Harvey-3 results	155
5.4.2	Bedding dip: Harvey-2 and Harvey-3 results.	161
5.5	Petrography of the Harvey-2 core	163
5.6	Harvey-2 XCT: Results	165
5.7	Synthesis and discussion	166
5.7.1	Harvey-2 Core description: Discussion	166
5.7.2	Comparing the Harvey-2 and Harvey-3 cores	172
5.7.3	The F10 Fault: Implications for fluid flow	173
5.7.4	Limitations	174
5.8	Conclusions and further work	175
Chapter 6	Multiscale characterisation of the fault architecture within the Port Campbell Embayment (Victoria, Australia): implications for subsurface engineering	178
6.1	Introduction	178
6.2	Field area: the Otway Basin	178
6.3	Methods	178
6.3.1	Brumbys-1 Core	179

6.4	Results	179
6.4.1	Observation of Brumbys-1 core.....	179
6.4.2	Field observations	182
6.5	Synthesis and discussion	187
6.5.1	Architecture of faults in the Port Campbell Limestone	187
6.5.2	Deformation, mineralogy and permeability in the Brumbys-1 core.....	188
6.5.3	Faulting mechanisms	190
6.5.4	Limitations	192
6.6	Recommendations and conclusions.....	192
Chapter 7	Modelling shallow fault zones using petroleum-based modelling approaches: challenges and learnings	195
7.1	Overview.....	195
7.2	Method	196
7.2.1	Step 1: Model building	196
7.2.2	Step 2: Fault slip scenarios	198
7.2.3	Step 3: Mechanical properties.....	199
7.3	Results	199
7.3.1	Step 4: Simulation results	199
7.3.2	Step 5: Fracture analysis.....	203
7.4	Discussion.....	203
7.4.1	Fault architecture.....	203
7.4.2	Stress data uncertainty.....	204
7.5	Summary	204
Chapter 8	Natural hydrogen seeps as analogues to inform monitoring of engineered geological hydrogen storage.....	206
8.1	Declaration of Work.....	206
8.2	Abstract.....	206

8.3	Introduction	208
8.3.1	Overview of natural hydrogen production, migration, accumulation, and consumption in the subsurface	209
8.4	Methods	211
8.5	Results	213
8.5.1	Surface expression of hydrogen seeps	213
8.5.2	Dry seepage through soils and unconsolidated sediments	213
8.5.3	Dry seepage from rock fractures	222
8.5.4	Wet seepage through water	222
8.5.5	Hydrogen concentration and seep rates	223
8.6	Discussion	227
8.6.1	Characteristics of hydrogen Seepage Sites	227
8.6.2	Comparing hydrogen seepage to other gas seepage	236
8.6.3	Recommendations for engineered geological hydrogen storage	238
8.6.4	Key research and data gaps	239
8.7	Conclusions.....	244
Chapter 9	Discussion	246
9.1	Defining shallow fault zones	246
9.2	Comparing the F10 Fault and the Brumbys Fault.....	248
9.2.1	The effect of lithology on fault architecture	249
9.2.2	Predicting fluid flow in shallow fault zones	250
9.3	Learnings and knowledge transfer from other subsurface technologies	251
9.3.1	Mont Terri fault injection experiments	252
9.3.2	Nuclear waste storage: lower strength sedimentary rocks	253
9.4	Subsurface fluid flow and environmental monitoring	254
Chapter 10	Conclusions and further work	256

10.1	RQ1: How does the architecture of shallow fault zones affect fault-related fluid flow in the shallow subsurface?	261
10.1.1	RQ1 key findings	261
10.1.2	RQ1 implications	263
10.1.3	RQ1 recommendations for further work.....	265
10.2	RQ2: How important is the scale of analysis when examining shallow fault zones? 267	
10.2.1	RQ2 key findings	267
10.2.2	RQ2 implications	268
10.2.3	RQ2 recommendations for further work:.....	268
10.3	RQ3: How effective are petroleum-based modelling tools in modelling shallow fault zones?.....	269
10.3.1	RQ3 key findings	269
10.3.2	RQ3 recommendations for future work.....	269
10.4	RQ4: How does natural hydrogen seepage present at the surface and how do we effectively monitor seepage?.....	270
10.4.1	RQ4 key findings	270
10.4.2	RQ4 implications	272
10.4.3	RQ4 recommendations for further work.....	272
10.5	Summary	273
	References	274
	Appendix 1 – In-Situ Lab: Fluid flow modelling.....	319
	Assumptions.....	319
	Model design	319
	Reservoir parameters	320
	Results	320
	Appendix 2 – In-Situ Lab: Environmental monitoring.....	321

Monitoring the In-Situ Lab experiment.....	321
Surface gas	321
Groundwater	322
Pressure and temperature	322
Seismic	322
Electrical Resistivity Imaging (ERI)	323
Other monitoring (logging, petrophysical and time-lapse).....	323
Appendix 3 – OITC – Stage 1 and Stage 2 Summaries	324
Progress and results from stages 1-3	324
Stage 1 – Storage of CO ₂ in a Depleted Gas Formation.....	324
Stage 2 – Storage of CO ₂ in a Saline Formation	327
Appendix 4 – Thin section preparation method	330
Appendix 5 – XCT data collection: scan sections, setting and notes	331
Appendix 6 – Modelling Theory	339
Modelling theory	339
Stress analysis	339
Fault Response Modelling (FRM)	339
Appendix 7 – Natural hydrogen seepage data tables.....	341
Appendix 8 – Logging data from the Harvey-2, Harvey-3 and Brumbys-1 cores.....	364

Table of Figures

Figure 2-1– Example of mechanical dispersion in porous media, with multiple pathways (a-d) through the pore network (Afanasyev, 2018). Not all flow pathways would be active at the same time, as flow pathways would not cross each other.	44
Figure 2-2 – Flow in porous medium, showing the real diffusive path length (solid line) and the direct diffusive path length (dashed line) (Kilgallon, 2016).	45
Figure 2-3 – Schematic showing change in porosity and permeability of a porous medium. Both porosity and permeability increase to the right-hand side as the space between the grains is greater and the pore spaces are connected.	46
Figure 2-4 – Schematic of trapping, fluid flow and viscous fingering in geological CO ₂ storage reservoir (Jia and McPherson, 2019).	49
Figure 2-5 – A) Evolution of CO ₂ trapping mechanisms over time. B) Summary of results of various injection experiments showing the type of trapping achieved with time after injection has stopped (from Snæbjörnsdóttir et al., 2020).	49
Figure 2-6 – Schematic of subsurface CO ₂ leakage pathways (Wang et al. 2020).	51
Figure 2-7 – Geometric attributes of a normal fault (Torabi et al., 2019). “Fault length” is the lateral extent of the fault zone. “Fault height” is the vertical extend of the fault zone.	53
Figure 2-8 - Illustration of a normal fault. A) dip-slip normal fault – showing both vertical and horizontal (dextral) displacement. B) Fault appears as a sinistral fault in map view (horizontal section at Level A). C) Profile perpendicular to fault strike showing heave and throw. D) Profile perpendicular to fault strike showing the true displacement (Fossen, 2015).....	54
Figure 2-9 – Fault zone structures. (a) Typical fault damage zone and fault core. (b) multiple fault cores encompassed by a large damage zone (Faulkner et al., 2010).	55
Figure 2-10 – Fault evolution with depth and temperature (Brandes and Tanner, 2019).	56
Figure 2-11 – Deformation mechanisms in unconsolidated sediments (Brandes and Tanner, 2019). Although cataclasis can occur at depths <1km, is not the dominant	

deformation mechanism at these depths – instead particulate flow processes dominate.....	62
Figure 2-12 – Deformation band type in relation to depth and phyllosilicate content. Boundary transitions are gradual (Fossen et al., 2007).	66
Figure 2-13 – Fault rock classification (from Woodcock and Mort, 2008).	67
Figure 2-14 – Types of deformation bands based on their deformation mechanism (Fossen et al., 2007).....	68
Figure 2-15 – Burial and uplift history for a sandstone. During uplift, sandstone enter the tensile region which can result in tension structures forming (Fossen et al., 2007).	69
Figure 2-16– Kinematic classification of deformation bands (Fossen et al., 2007).....	71
Figure 2-17 – Fault permeability structures in soft sediments deformed at shallow depths (Bense et al., 2013).....	72
Figure 2-18 – (a) fault core (red line) is permeable and acts as a fluid flow conduit. (b) fault core and damage zone (black lines) are both permeable and act as a fluid flow conduit. (c) The fault core is impermeable, but the surrounding damage zone is permeable and acts as a fluid flow conduit. (d) heterogenous fault zone systems that leads to a complex multi-strand permeability system (Bond et al., 2017).	75
Figure 3-1 – A) Geological maps showing the location of the Harvey wells (H-1, H-2, H-3, H-4) and surrounding wells (Lake Preston-1 (LP-1), Preston-1 (P-1) and Pinjarra-1). B) Stratigraphy of the Perth Basin (from CSIRO, 2019). Inset shows location of the site within Australia.....	88
Figure 3-2 – Aerial view of the ISL showing the Harvey-2 (Injection well, green) and surrounding groundwater (blue), monitoring (purple) and soil gas wells (beige) (Myers et al., 2020).	89
Figure 3-3 – Divisions of the Perth Basin. The basin can be subdivided into 3 main sections: northern (north of latitude 31°S), central (between latitudes 31°S and 33°S) and southern (south of 33°S). The beige/brown line represents the coastline. The red box indicates the location of the ISL (modified from Crostella and Backhouse, 2000).	92
Figure 3-4 – Subdivision of the Southern Carnarvon and Perth Basins (Mory, 1994).....	93

Figure 3-5 – Geology of the In-Situ Lab site Michael et al., 2019. The four main stratigraphic units are shown: Wonnerup Member, Yalgorup Member, Eneabba Formation and Leederville Formation. Harvey 1, 2, 3 and 4 wells are shown. The F10 Fault is shown in the SE of the In-Situ Lab site. Harvey-2 (injection well) has been backfilled with cement (grey shading) up to a depth of approximately 400 m. The potential CO₂ storage reservoir is the Wonnerup Member.....94

Figure 3-6– Conceptual model of the Harvey-1 and Harvey-3 boreholes at the In-Situ Lab (Stokes et al., 2018). Red box indicates studied zone in Stokes et al., 2018.96

Figure 3-7 – Modelled faults at the top Wonnerup surface. Fault stick azimuths (and range) interpreted on 2D-seismic lines and offset (m) on the top Wonnerup horizon are show. Maximum horizontal stress direction is shown (from Rasouli et al., 2013) (figure adapted from Langhi et al., 2013).99

Figure 3-8 – A) Gamma log of the Harvey-2 well, interpreted geological age based on palynology and stratigraphy. B) 2D seismic cross section, oriented west-east (perpendicular to F10 Fault) showing Harvey-2 well, F10 Fault zone and interpreted horizons/stratigraphy (Michael et al., 2020). 100

Figure 3-9 – A: Regional structural map. B: Structural map of In-Situ Lab/SW Hub area (Langhi et al., 2013; Pevzner et al., 2015; Delle Piane et al., 2018)..... 101

Figure 3-10 – Plot of the intensity of deformation in the Harvey-2 core. A = Disaggregated sands, B = Altered palaeosol, C = Thin isolated zones of disaggregation (less intense deformation) (CSIRO, 2019). Pale yellow zones indicate areas of continuous deformation. 104

Figure 3-11 – A: Red arrows show minor fault surfaces with slickensides in a well consolidated mudstone. B: 400mm of incohesive breccia in sandstone (shown between red dashed lines). C: 150mm cluster of cataclastic deformation bands (between two red arrows) in sandstone (CSIRO, 2019). 105

Figure 3-12 – Seismic line crossing the Harvey-2 borehole and F10 Fault zone. Deformation information is mapped onto the Harvey-2 borehole. A network of conjugate and synthetic faults in the hanging-wall have been interpreted (from Langhi et al., 2023). 106

Figure 3-13 – Compilation of published fault displacement versus fault rock thickness (figure from CSIRO 2019). A) fault rock data. C) fault zones. Nomenclature retained from the original figure (data after Childs et al. (2009); please refer to the original publication for the many references from which this data was compiled). Vertical coloured bars indicate the range of displacements observed in seismic for the F10 Fault, diagonal bars highlight the trend of the data, and the horizontal bars indicate the extrapolation of the intersection of the vertical and diagonal bars extrapolated onto the thickness axis. The fault rock thickness dataset has a median D/T of 50 and the fault zone thickness dataset a median of 2.5.....	108
Figure 3-14 – Updated porosity and permeability plot of the F10 Fault zone, including Harvey-2 data, shown by blue unfilled circles (CSIRO, 2019).	110
Figure 3-15 – Location of the CO2CRC OITC site in Victoria, Australia. CO2 and Natural Gas fields are shown, as well as source, injection, and monitoring wells (Undershultz et al., 2011).	114
Figure 3-16 - CO2CRC Strategic Direction Plan. Top sections indicate the storage projects and the bottom sections indicate the capture projects (CO2CRC, 2020a)...	115
Figure 3-17 - Otway site schematic. Stage 1 and Stage 2 wells are shown, as well as surface and subsurface monitoring equipment (CO2CRC, 2020a). This figure does not consider the shallow stratigraphy in detail and thus the stratigraphic units shown are not named or highly depth accurate.	116
Figure 3-18 – Map of the Otway Basin showing structural features and the field area for this study. Volcanic eruption points are modified after Lesti et al. 2008. Studied region is highlighted (see Chapter 6).	118
Figure 3-19 – Map of Port Campbell Embayment showing the thickness of the Port Campbell Limestone (from Radke et al., 2022). Field locations that were visited during research for this thesis are shown with brown circles, and notable sites are lettered and in bold and described in the text (see Chapter 6). Landmarks not in bold are included for orientation purposes.	119
Figure 3-20 – Schematic of the shallow stratigraphy of the Otway site. Not to scale horizontally. The presence of glauconite markers indicates around 2m of vertical displacement within the PCL (Feitz et al., 2021).	123

Figure 3-21 – Map showing the layout of the Otway International Test Centre (OITC), including Brumbys wells (orange) and monitoring wells (light green). Red line depicts the surface trace of the Brumbys Fault (solid = 3D seismic trace, dashed = regional 2D seismic).	125
Figure 3-22 – Schematic cross section at the OITC showing the Brumbys Fault, the Brumbys 1, 2, 3 and 4 wells, the Piezo wells and the stratigraphy (modified from Tenthorey et al. (2024)).	125
Figure 4-1 – Drilling induced fracture at ~790m depth (Yalgorup Member) in sandstone in the Harvey-2 core.	131
Figure 4-2 – Fractured palaeosol section in the Harvey-2 core. Multiple fracture orientations and angles, likely caused by a mix of drilling-induced fractures and the exploitation of existing sedimentary (pre-tectonic) structures by drilling.	132
Figure 4-3 – Tectonic fracture in coarse sandstone from ~730m depth (Yalgorup Member) in the Harvey-2 core. Any displacement was not able to be estimated, as no markers are offset.....	133
Figure 4-4– Example deformation log interpretation of tray no. 168 at a depth of 666m. The lithology of this tray was entirely sandstone. Top image shows the core tray photo. Bottom image shows the core tray photo with the assigned deformation numbers. ...	135
Figure 4-5 – Example deformation log interpretation of tray no. 277 at a depth of 970m. The lithology of this tray was entirely palaeosol. Top image shows the core tray photo. Bottom image shows the core tray photo with the assigned deformation numbers. ...	136
Figure 4-6 – Image of the Nikon DS Ri2 microscope.	138
Figure 4-7– Siemens medical X-ray CT scanner SOMATOM Definition AS.	140
Figure 4-8 – Control samples. Left to right: Water, Teflon, Gypsum, Quartz and Aluminium.....	140
Figure 5-1– Examples of the variability of the undeformed sandstone in the Harvey-2 core. A: Tray 254 (Start depth = 905.5m, Yalgorup Member) – typical coarse-grained sandstone, some grit. B: Tray 150 (Start depth = 617.4m, Yalgorup Member) - Green coloured sandstone. C: Tray 204 (Start depth = 766.7, Yalgorup Member) – Interbedded	

sandstone, mudstones and palaeosols. D: Tray 378 (Start depth = 1264.1m) – Cross-bedded sandstone of the Wonnerup member.	142
Figure 5-2 – A: Tray 147 (Start depth = 609.4m, Yalgorup Member) – Dark brown/grey/black deformed palaeosol. B: Tray 160 (Start Depth = 644.2m, Yalgorup Member) – Massive brown/red/purple palaeosol with intermixed infilled rootlets/burrows with coarse sand. C: Tray 186 (Start depth = 715.9m, Yalgorup Member) – Interbedded muddy brown/beige/green palaeosol D: Tray 276 (Start depth = 967.6m, Yalgorup Member) – Deformed sandy palaeosol with red/brown oxidation. E: Tray 334 (Start depth = 1132.5m) – Green, yellow, red, brown and purple sandy and muddy palaeosols with roots and/or burrows.....	143
Figure 5-3 – Pie charts showing the percentage of each of the two lithologies in the Harvey-2 and Harvey-3 cores.	144
Figure 5-4 – Total number of fractures for each of the two lithologies in the Harvey-2 core.	145
Figure 5-5 – Harvey-2 fracture intensity with depth (m). The total number of fractures per metre of the sampled intervals are shown, as well as a breakdown by lithology (SST = sandstone, PS = palaeosol). Background colours indicate the units: light blue = Eneabba Formation, orange = Yalgorup Member, yellow = Wonnerup Member.	146
Figure 5-6 – Total number of fractures for each fracture descriptor score in the Harvey-2 core. Increasing fracture descriptor number means a fracture most likely to be tectonic and open to fluid flow (see Section 4.1).	147
Figure 5-7 – Slickensides in palaeosol in the Harvey-2 core.	148
Figure 5-8 – Total number of fractures in each of the two lithologies in the Harvey-3 core.	149
Figure 5-9 – Harvey-3 fracture intensity with depth (m). The total number of fractures per metre of the sampled intervals are shown, as well as a breakdown by lithology (SST = sandstone, PS = palaeosol). Background colours indicate the units: light blue = Eneabba Formation, orange = Yalgorup Member, yellow = Wonnerup Member.	150
Figure 5-10 – Total number of fractures for each fracture descriptor score in the Harvey-3 core. Increasing fracture descriptor number means a fracture most likely to be tectonic and open to fluid flow (see Section 4.1).	151

Figure 5-11 – PS slickensides. Depths are: A) 780.9m, B) 1400.75m. Image C is a comparative example of a large present-day soil slickenside and is used under the creative commons licence and is the original image of John A. Kelley (Kelley, 2010). 152

Figure 5-12 – Depth vs fracture descriptor score in the Harvey-2 and Harvey-3 cores. Fractures with a higher score are more likely to have been formed due to a tectonic process. Dot colour indicates the number of fractures recorded for each score at a particular depth..... 153

Figure 5-13 – Deformation logs of the Harvey-2 core for both sandstone and palaeosol lithologies. Colours indicate the units: light blue = Eneabba Formation, orange = Yalgorup Member, yellow = Wonnerup Member. 156

Figure 5-14 – Deformation logs of the Harvey-3 core separated by for sandstone and palaeosol lithologies. Colours indicate the units: light blue = Eneabba Formation, orange = Yalgorup Member, yellow = Wonnerup Member (see Section 3.1.2 for formation/member descriptions). 157

Figure 5-15 – Total core length (m) for each deformation number descriptor for the two lithologies (SS = sandstone, PS = palaeosol) in the Harvey-2 core. 159

Figure 5-16 – Total core length (m) for each deformation number descriptor for the two lithologies (SS = sandstone, PS = palaeosol) in the Harvey-3 core..... 159

Figure 5-17 – Bedding angle changes against depth (m) in the Harvey-2 and Harvey-3 cores. Less data from Harvey-3 as the bedding was less obvious to measure and there were more cross-bedded sandstones. As such, measurements were only collected when there was a clear lithological contact. 161

Figure 5-18 – Photomicrographs of thin sections taken from the Harvey-2 core. A) Fine-grained sandstone, angular grains up to 200 microns in size, undeformed (Sample 1). B) Small angular grains up to 500 microns in size (medium to coarse grained) sandstone, undeformed (Sample 1). C) Grain crushing, creating of fine material <50 microns in size (Sample 3). D) Grain fracturing and fracture propagation through multiple grains, highlighted by red arrows (Sample 3). E) Grain to grain contact between quartz and feldspar grains, fracturing of grains (Sample 5). 164

Figure 5-19 – XCT images on the bottom and core photographs taken shortly after the core was drilled in 2015 on the top. Some sections of the core have been damaged or

broken during storage, transport and analysis since 2015. A: A 1m section of undeformed core from 862.45-863.4m depth (Tray #238). B: Example of a deformation band in a section from 555-555.3m depth (Tray #127). C: Example of a shear band in a section from 556.15-557.1m depth (Tray #127). 165

Figure 5-20 – Conceptual 2D model of a narrow width F10 Fault zone based on the deformation logs from the Harvey-2 core. Where features intersect the borehole in the figure, they have been observed at that depth in the Harvey-2 core. Other features are interpretation and extrapolation of core and seismic data. The F10 Fault zone is likely comprised of lenses of major deformation (characterised predominately by particulate flow processes, with minor cataclastic components) with sections of minor deformation (fracturing, minor disaggregation) and sections which are entirely undeformed. There are other key deformation indicators, including disrupted, and steepened bedding and the presence of deformation bands. Note the in this model the thickness of the Yalgorup Member in the footwall is >1km, far thicker than expected (700-800m). 170

Figure 5-21 – Conceptual 2D model of a wide width F10 Fault zone based on the deformation logs from the Harvey-2 core. Where features intersect the borehole in the figure, they have been observed at that depth in the Harvey-2 core. Other features are interpretation and extrapolation of core and seismic data. The F10 Fault zone is likely comprised of lenses of major deformation (characterised predominately by particulate flow processes, with minor cataclastic components) with sections of minor deformation (fracturing, minor disaggregation) and sections which are entirely undeformed. This deformation makes distinguishing which unit the deformation is in difficult. There are other key deformation indicators, including disrupted bedding angles and the presence of deformation bands. There is no top Yalgorup boundary in the hangingwall in this model, as the boundary reported by a previous sedimentological study (CSIRO, 2019) is within the fault zone: and as such the boundary is likely to have experienced disruption. In this scenario the footwall thickness of the Yalgorup Member is correct (maximum ~700-800m), and the top Yalgorup is well below the borehole intersection in the hangingwall. 171

Figure 6-1 – Depth (m) and deformation number (0-4), showing the average deformation in each tray of the Brumbys-1 core. Colours indicate units: Brown = Hesse Clay, Light Blue = PCL, Grey = G. Marl..... 180

Figure 6-2 – Thin section of the Port Campbell Limestone showing brecciation of grains at the mm-scale (interpreted by Radke et al., 2021)..... 181

Figure 6-3 – **A)** Reverse fault at the mouth of the Sherbrook River, fault expires into a cave. Offset <1m. **B)** Small ~0.3-0.5m dipping fractures within specific layer of the PCL. **C)** Vertical feature (red) associated with broken rubbly zone along strike – this broken/brecciated material is not observed anywhere else on cliffs in this area. Location: Gibson Beach (-38.669940, 143.113588). **D)** Veining/deformation associated with reverse fault on Gibson Beach (location: -38.666352, 143.106704)..... 183

Figure 6-4 – Images from Timboon Quarry. Both photos show the freshness of the surface. The rubbly nature of the surfaces is because of the quarrying method used and is not a geological feature. A) Cave collapse feature in the PCL. B) Staining of the PCL as minerals are leached from the volcanic rocks that penetrate the PCL sequence. 185

Figure 6-5 – Percentage calcium carbonate (CaCO₃) from the Gibson Steps and Gibson Beach exposures, compared with the percentage calcium carbonate from the Brumbys-1 core. Gibson Beach measurements that are below sea level were acquired by moving laterally along the beach to deeper portions of the section. Figure courtesy of Stephen Gallacher, University of Melbourne..... 186

Figure 6-6 – Graph showing the deformation (0-4, left hand y-axis) and permeability variation with depth (mD, right hand y-axis). Two permeability curves are plotted (high permeability case, Perm1 and low permeability case, Perm2) from Radke et al., 2021. 188

Figure 6-7 – Graph showing mineralogy variations with depth. Mineralogy is shown on the right-hand y-axis (wt % Rietveld) for calcite and aragonite. Two permeability curves are plotted (high permeability case, Perm1 and low permeability case, Perm2) from Radke et al., 2021 on the left-hand y-axis (mD). Purple circles highlight areas of interest – correlating higher % aragonite with drops in permeability. Red zone indicates the extent of the fault zone based on the deformation logs of the core. 189

Figure 6-8 – Graph showing the 27 zones of the Brumbys-1 core. For each zone, the mineralogy (Dolomite) is shown on the right-hand y-axis (wt % Rietveld) and two permeability curves are plotted (high permeability case, Perm1 and low permeability

case, Perm2). Red zone indicates the extent of the fault zone based on the deformation logs of the core. 190

Figure 7-1– Flow diagram showing the fracture analysis part of the modelling workflow. 196

Figure 7-2 – Left image showing the 2D seismic surface showing the Brumbys Fault in the centre. The right-hand image shows the Brumbys Fault in Move, with a satellite image overlain to show the theoretical surface trace of the fault..... 197

Figure 7-3 – Example model results (from Scenario 1) showing the slip magnitude across the Brumbys Fault surface. 202

Figure 8-1 – Location of 60 hydrogen seeps within 13 clusters (letters A-M) that may be analogous of leakage from engineered geological hydrogen stores. The cluster ID (letter – name) is written adjacent and this corresponds to the cluster column in Table A7 - 1, Table A7 - 2 and Table A7 - 3. 214

Figure 8-2 – Hydrogen concentrations (vol %) for each cluster of seepage sites, plotted as (a) a function of seep type and (b) a function of measurement type (i.e. whether measured in the near surface, top ~1m in soils/fractured rock (Group 1) or at the surface in gas vents or bubbles (Group 2)). Coloured boxes represent the sample median (horizontal line), and the first and third quartiles, with the extending lines representing the minimum, the maximum values. Grey dots show the data points, black crosses show outliers. Numbers on/near boxplots correspond to cluster number in Table A7 - 1, Table A7 - 2 and Table A7 - 3 and Figure 8-1. Seep cluster ID F has hydrogen seeping via bedrock fractures and bubbles in water and thus have gas sampled both from the subsurface and the surface. 217

Figure 8-3 – Soil gas profiles of Smith Bay (#9, Zgonnik et al. 2015), Arthur Road Bay (#8, Zgonnik et al. 2015) and Satellite Podovoye (#6, Larin et al. 2015). Distance on the x-axis is normalised so that a value of 1 corresponds to the edge of the depression feature. The allows comparison between features of different sizes. Hydrogen concentrations are normalised where the maximum concentration taken along a transect is = 1. Measurements that were recorded as SAT (= detector saturated) were set to 1. Depression shape, size, orientation and transect orientations are shown for each site. 218

Figure 8-4 – Transects of hydrogen concentration at the edge of the Nikulino (#4, Larin et al. 2015), Yakhroma (#3, Larin et al. 2015) and Jones Lake Bay (#10, Zgonnik et al. 2015) features..... 219

Figure 8-5 – Measured gas concentrations reported from hydrogen seepage sites. Clusters are organised by surface expression of seepage. Cluster 6 is split into 2 sections to represent different surface expression of seepage, either via (a) bedrock fractures or (b) water. Coloured boxes represent the sample median (horizontal line), and the first and third quartiles, with the extending lines representing the minimum, the maximum values. Grey dots show the data points, black crosses show outliers..... 220

Figure 8-6 – Hydrogen concentrations (ppm) of seepage from specific rock types in Oman. Coloured boxes represent the sample median (horizontal line), and the first and third quartiles, with the extending lines representing the minimum, the maximum values. Crosses indicate outliers. The shale outlier reporting 3400ppm is seep #28, where the shales directly overlie Precambrian basement and are below the ophiolite nappe..... 221

Figure 8-7 – Seep area vs reported rate of hydrogen seepage. Numbers (#) are seep numbers (Tables Table A7 - 1, Table A7 - 2, Table A7 - 3 and Table A7 - 4). Markers represent surface expression of seepage: circles represent soils and sediments, and triangles represent bedrock fractures. Error bars represent maximum and minimum leakage rates constrained by uncertainties in assumptions. Seep area is the footprint of the subcircular depression, or the size of the region of leakage. Data from Larin et al. (2015), Zgonnik et al. (2015; 2019) and Moretti et al. (2019a)..... 225

Figure 8-8 – Flux vs leakage rate. Numbers (#) are seep numbers (Tables Table A7 - 1, Table A7 - 2, Table A7 - 3 and Table A7 - 4). Markers represent surface expression of seepage: circles represent soils and sediments, and triangles represent bedrock fractures. 226

Figure 8-9 – Seep type, geological environment and surface expression of hydrogen seepage with example images and cartoons of typologies. (1) Subcircular depressions with three shapes – circular, elliptical and irregular. (2) Fractured rocks with diffusive flows of hydrogen (Zgonnik et al. 2019). (3) Bubbling seepage offshore, New Caledonia (#34). Images in (2) from Zgonnik et al. 2019 and (3) from Vacquand et al. (2018). Satellite photos in (1) from Google Maps..... 232

Figure 8-10 – Potential mechanisms for hydrogen generation and consumption (purple circles), trapping (green circles) and migration (orange circles) in the subsurface and seep expression at the surface (black circles). Adapted from Heinemann et al. (2021).
..... 233

Figure 9-1 – Schematic of 6 types of faulting: 1) Faulting in ‘young’ rocks or soils that have not been exhumed, these are likely to be very poorly consolidated unless there has been very near-surface diagenesis. They are currently experiencing the greatest levels of stress in their history and are considered to be underconsolidated in an engineering soil mechanics sense (e.g. Brumbys Fault, see Section 3.2.3). 2) Faulting in rocks that have been exhumed from depths less than 1km, may be completely, partially or unlithified. Because they are at stress levels less than the greatest stress levels they have experienced, they are considered to be overconsolidated in an engineering sense (e.g. F10 Fault, see Section 3.1.3). 3) Faults that have been active at greater depths in the Earth’s crust (>1km depth), display deep deformation features (e.g. mylonite, s-c fabrics) and have since been uplifted to depths shallower than 1km, and overprinted by later faulting at shallower depths. 4) Faults has been active at depth, display deep deformation features and been exhumed with no further fault activity during exhumation. 5) Faults which are presently active or inactive at depths >1km and have not been exhumed. 6) Buried shallow faults (depths >1km), which could have started as either category 1 or 2. 247

Figure 9-2 – Cross section of the geology around the Mont Terri rock laboratory. Note the “main fault” crosses the laboratory. The fault zone is around 1-6m in width (Nussbaum et al., 2017). 252

List of Tables

Table 0-1– Comparative summary of the two faults studied for this thesis.....	vii
Table 1-1 – Summary of RQ and RO and the relevant chapters in which they are addressed.	37
Table 2-1 – Hydrogen (H ₂) and carbon dioxide (CO ₂) dynamic viscosity, solubility and compressibility.....	46
Table 2-2 – Mechanisms/controls on rock properties in fault zones, key processes and resulting features (adapted from Bense et al., 2013).	64
Table 2-3 – Processes that impact the permeability of poorly lithified fault zones (adapted from Bense et al., 2013).....	73
Table 3-1- The location of each borehole at the In-Situ Lab, and depths that major rock formations were encountered. The formations were dated by palynology and boundaries recognised by breaks on wireline logs (Delle Piane et al., 2018).	89
Table 3-2 – Descriptions of deformation and alteration in Harvey-2 core (data from CSIRO, 2019).....	102
Table 3-3 – Upper stratigraphy of the Port Campbell Embayment.....	120
Table 4-1– Overview of methods used in this thesis and corresponding research questions (RQ) and research objectives (RO).	128
Table 4-2– Four fracture characteristic categories: angle, smoothness, slickensides and mineralisation.	129
Table 4-3 – Fracture interpretation categories.	131
Table 4-4 – Deformation descriptor number (N), deformation classification, and qualitative description for each category based on the core shape and cohesiveness.	134
Table 5-1 – Comparison of the Harvey-3 and Harvey-3 cores in terms of length, lithology and formation depths.	144

Table 5-2 – Summary comparison of deformation in the Harvey-2 and Harvey-3 cores. Core length (m) and % total core are provided for each lithology and a total value for each of the two cores.	160
Table 5-3 – Thin section sample names and depths.....	163
Table 7-1 – Modelling scenarios for each stress regime, with stress magnitudes and horizontal (azimuth) directions.....	198
Table 7-2 – Mechanical properties and the possible ranges based on previous testing (Feitz et al., 2021).	199
Table 7-3 – Model scenarios showing the conditions for each scenario constrained by maximum possible fault burial depth (~200m, assuming a typical pressure gradient of ~1MPa per 100m depth), followed by the slip modelling results in the right hand columns. Results include the maximum possible slip per event, the number of slip events to match the observed slip (150m horizontal, 4m vertical), and slip rate (which is horizontal for strike slip scenarios and vertical for normal/reverse and calculated based on fault movement over a 10Ma period).	201
Table 8-1 – Seep shape, axis orientation, stress orientation (S_{HMAX}) with distance from seep and prevailing wind direction.	230
Table 8-2 – Interpreted sources of hydrogen from the literature. Other locations (e.g. Philippines, Mali, Australia) presented in the results section discuss similar hydrogen sources and generation processes, but also with significant unknowns and uncertainty.	234
Table 9-1 – Comparison between the F10 Fault and the Brumbys Fault and injection experiments at both study sites.....	248
Table 10-1 – Summary of RQ and RO, including the status of each research objective and a summary of the work undertaken.....	257

Chapter 1 Introduction

1.1 Context of study

Climate has changed. We are no longer discussing the idea of climate change, instead we are now living in a time of anthropogenic changing climate. Action and solutions to combat the challenges of changing climate is needed. International agreements, such as the Paris Climate Agreement, which was ratified by 196 countries at COP21, committed to minimising global temperature increases and tackling the main cause of anthropogenic climate change (United Nations, 2015). However, these targets have not been met or are being postponed to the future (UNFCCC, 2023a; UNFCCC; 2023b). To meet global climate targets, there is an anticipation that there must be a scaling up of existing and emerging subsurface technologies (e.g. geological carbon dioxide (CO₂) storage, energy storage (e.g., hydrogen (H₂), compressed air) and geothermal energy), alongside other low-carbon energy sources (e.g. renewable energies, nuclear power), to support the energy transition and a move towards a global net zero future (Climate Change Committee, 2021). Although the climate emergency is urgent – progress thus far deploying some of these solutions has been slow (e.g., Martin-Roberts *et al.*, 2021; Miodic *et al.*, 2023), therefore much has still to be done to meet global targets.

Geoscience as a discipline is well placed to play a key role the energy transition by enhancing our understanding of them through research and development (Gardiner *et al.*, 2023). An understanding of subsurface geological processes is important to ensure the security and safe operation of all subsurface technologies. Many of these emerging technologies involve some element of subsurface fluid injection, storage, and withdrawal. Therefore key to secure and safe operation is robust site selection criteria and appropriate measuring, monitoring, and verification (MMV) and remediation procedures.

One subsurface technology of relevance is geological porous media storage of CO₂, H₂, methane (CH₄) or other fluids. Effective MMV systems will ensure the fate of any injected fluids can be reconciled, so understanding the factors which influence the containment, capacity and injectivity of fluids in the subsurface is important (Ofoegbou *et al.*, 2011; Kampman *et al.*, 2012; Loveless *et al.*, 2014; Rohmer *et al.*, 2015; Ali *et al.*, 2022, Krevor *et al.*, 2023; Miodic *et al.*, 2023). There are varying levels of experience across the

different potential storage fluids, plus each fluids brings its own unique challenges based on fluid properties, but there are learnings that can be shared between technologies (Tarkowski and Uliasz-Misiak, 2021). For example, subsurface storage of “Town Gas”- a mixture of hydrogen and methane – provided insights into the effect of bacteria (e.g. methanogens) on the storage of hydrogen (Panfilov, 2010). Further, the effect of mixing has been investigated and indicate that fluids can react together to form other fluids (e.g. CO₂ and H₂ can react in the reservoir to form CH₄) (Ebigbo *et al.*, 2013; Shi *et al.*, 2020). Fluid mixing and resulting reactions are an important consideration for geological porous media storage, particularly at sites such as depleted hydrocarbon reservoirs where small quantities of legacy hydrocarbons may remain in-situ, or sites where mixtures of gases are used (e.g. using a different gas from the stored gas to act as “cushion gas”) (Heinemann *et al.*, 2021a). Above the reservoir, there is work to assess how the sealing capacity of reservoir caprocks varies with different geological or fluid parameters (Shukla *et al.*, 2010; Espinoza and Santamarina, 2017; Dewhurst *et al.*, 2018). However, there is an emerging understanding of the need to characterise the overburden system of a geological storage site rather than solely the reservoir/caprock system (Roberts *et al.*, 2017), particularly areas where multiple technologies utilise the subsurface – meaning coordinating the use of the subsurface storage capacity is crucial (Bauer *et al.*, 2013; Bartel and Janssen, 2016; Bump and Hovorka, 2023). Consequently, research bodies, government organisations and industry have now explored novel trapping systems (e.g. overburden migration-assisted trapping) rather than conventional reservoir/caprock systems (Bump *et al.*, 2023).

For all storage types, one key factor that can influence the fate of fluids, performance and success of these sites is the presence of geological fault zones. Fault zones and faulting-associated deformation affects fluid movement within the Earth’s subsurface from the microscale to macroscale through different mechanisms (e.g Caine *et al.*, 1996; Dockrill and Shipton, 2010; Bense *et al.*, 2013; Brandes and Tanner, 2019). These mechanisms are sensitive to a range of variables including rock type, diagenesis, burial depth, stress regime, previous deformation, and other factors, which may vary both along and across the fault (e.g. Sibson, 1977; Aydin and Johnson, 1983; Fisher *et al.*, 2003; Shipton and Cowie, 2003; Agosta and Aydin, 2006; Fossen *et al.*, 2007; Michie, 2014; Torabi *et al.* 2019). Deformation processes and subsequent subsurface processes may enhance or reduce permeability and thus, faults can be a barrier to fluid flow,

conduit, or a combination of both specific to a location in the fault zone and surrounds (e.g. Bense and Person, 2006; Miocic *et al.*, 2016; Viswanathan *et al.*, 2022; Fisher *et al.*, 2023). Furthermore, depending on hydrogeological conditions, fluids can both flow laterally across faults and vertically up faults, sometimes along a single fault (Faulkner *et al.*, 2010). Therefore, fault zones have a key role in crustal fluid flow. Much research is underway to better understand the mechanical and hydraulic properties of fault zones, and their implications for geological storage, but also other applications such as managing seismicity risks and groundwater.

To date the majority of fault studies have been focused on faults at reservoir depths (>1km depth) in the context of hydrocarbon extraction or geofluid storage (e.g., Aydin, 2000; Chadwick *et al.*, 2009) as they act as a closure/seal/trap (Sorkhabi and Tsuji, 2005), or as conduits of heat flow for geothermal projects (Barton *et al.*, 1995; Huenges and Ledru, 2011; Loveless *et al.*, 2014). Much subsurface research expands on legacy hydrocarbon research and this pattern is seen in the structural geology and faulting literature. The reason for the focus on hydrocarbon systems is likely due to selection bias and availability bias, which has been proven to reduce the quality of results (Shipton *et al.*, 2020). Studies which are influenced by selection bias can often miss important details. Examples of good practice include research from McCay *et al.*, (2019) – where structural observations were combined with sedimentology to show the importance of sedimentology on controlling fluid flow – rather than only focusing on studying the fractures in the rocks which most would assume to be a primary control on the permeability. Similarly, a study by Roberts *et al.*, (2019b) indicates that a shale unit is more permeable than a sandstone unit, due to the way the shale responds uplift and unloading which enhances its permeability. These studies exemplify the need to consider biases in methodologies, but also both challenge typical preconceptions of geological features and their implications.

Bias in previous research on fault zones is important when considering how transferable our understanding of deeper fault zones is to faults in at shallower depths in the Earth's crust. Faults in the shallow subsurface differ to those at depth (Rawling and Goodwin, 2003; Bense *et al.*, 2013), with consequence for fluid flow. Pressure and temperature vary with depth which has implications for fluid mechanics and pore fluid composition, and in-situ stress can vary with depth (Meixner *et al.*, 2014). The water table may vary

over time at a site as local climates change (e.g. post-glaciation). Other depth specific factors to account for include the effect of surface processes and the effect of diagenesis on rock properties with increasing burial depth. Further, deformation processes and styles change with depth, with a transition from particulate flow dominated processes to cataclastic processes at approximately 1 km below surface as subsurface conditions change (e.g. stress, pressure, and temperature) (Fossen *et al.*, 2007) (see Section 2.3).

Being able to physically observe exposed faults at the Earth's surface would indicate that the fault has either been active at the surface (though could be inactive in the modern day), or the fault has been exhumed to some degree. With increasing depth, fault processes and deformation mechanisms change (see Section 2.3). There are therefore five broad categories of faults in the subsurface, defined by fault activity, depth and burial/exhumation history. This categorisation is new and is presented up front rather than in a later chapter because it is important for the study context. Chapter 2 (Literature Review) finds that no previous authors have attempted to distinguish faults based on depths and history. This is important given the influence that these factors will have on fault mechanics and fluid flow. The categories are:

1. Faulting in 'young' rocks or soils that have not been exhumed. The faulting will have been active close to the Earth's surface in materials that are likely to be very poorly consolidated unless there has been very near-surface diagenesis. These fault rocks are currently experiencing the greatest levels of stress in their history and are considered to be underconsolidated in an engineering soil mechanics sense. (e.g. Brumbys Fault, see Section 3.2.3)
2. Faulting in rocks that have been exhumed from depths less than 1km, and which may be completely, partially or un-lithified. Because they are at stress levels less than the greatest stress levels they have experienced, they are considered to be over consolidated in an engineering sense (e.g. F10 Fault, see Section 3.1.3).
3. Faults that have been active at greater depths in the Earth's crust (>1km depth) and have since been uplifted to depths shallower than 1km, and overprinted by later faulting at shallower depths.
4. Faults has been active at depth, and been exhumed with no further fault activity during exhumation.

5. A final category are faults which are presently active or inactive at depths >1km and have not been exhumed.

The 1km depth is used as this a key transition depth where the dominant deformation processes change (see Section 2.3). Faulting and fault zones in category 1 and 2 as referred to as “shallow faulting”, “shallow fault zones” or “shallow fault systems” – these are the focus of this thesis. Category 1 could be described as “near-surface faulting”. Category 2 can be described as “shallowly exhumed”. Category 3, 4 and 5 faults are not the focus of this thesis, and these faults are referred to as “deep faults” and processes as “deeper faulting”. Shallow faulting is less well studied compared to deeper faulting, particularly from a fluid flow perspective (e.g. Heynekamp *et al.*, 1999; Cashman and Cashman, 2000; Rawling and Goodwin, 2003). Understanding the architecture of shallow fault systems and the way in which shallow fault systems respond to environmental factors, both natural (e.g. tectonic processes, weathering) and anthropogenically induced (e.g. injection of fluids), is important to forecast the effects they will have on the migration of fluids in the shallow subsurface. This is particularly important for emerging geological storage technologies, as it is important to understand the role that shallow fault systems could play as a fluid pathway in the overburden of geological storage sites (see Section 2.1.3). Ultimately, understanding shallow fault architecture and the fluid flow properties of shallow fault systems will aid the design of effective MMV systems. Therefore, further research remains crucial to enable the effective operation of these technologies to facilitate the scaling-up required (Heinemann *et al.*, 2021b; Miocic *et al.*, 2023).

The research undertaken for this thesis aims to assess the architecture and fluid flow properties of shallow fault systems and considers the implications this has for the effective design of MMV systems for subsurface storage technologies. Learnings can be shared, where applicable, for other shallow applications (e.g. groundwater resources, shallow geothermal systems and remediation technologies).

1.2 Summary of main field sites studied in this thesis

Demonstrating the potential of subsurface technologies at field sites is crucial to drive the uptake of these technologies globally (Stephenson *et al.*, 2022), as they provide an opportunity to examine how fluids move and interact in the shallow subsurface and provide useful insights for the scaling-up of these technologies (Roberts and Stalker,

2020). Although useful, field sites are globally rare meaning opportunities for research are typically limited. This thesis uses two field experiments with shallow fault systems as case studies. These sites are both located in Australia. First, CSIRO’s In-Situ Lab located near Perth, Western Australia, where CO₂ injection targets the F10 Fault. Second, the Otway International Test Site operated by CO2CRC and Geoscience Australia in Victoria, where CO₂ injection targets the Brumbys Fault. An overview of activities to date at both sites is presented in Chapter 3. These sites provide an opportunity to examine two shallow fault zones, located in sites that have a host of legacy subsurface data and have an ongoing programme of research and injection experiments. Learnings from the research presented in this thesis can also be compared to field injection test results at these sites.

1.3 Research questions and objectives

The research questions (RQ) and objectives (RO) that form the focus of this thesis are outlined in Table 1-1.

Table 1-1 – Summary of RQ and RO and the relevant chapters in which they are addressed.

	Task	Chapter(s)
RQ1	How does the architecture of shallow fault zones affect fault-related fluid flow in the shallow subsurface?	
RO1	Understand the regional and tectonic setting, and the history of geological activity at both field sites.	3, 5, 6
RO2	Observe, describe and interpret the fault architecture and its heterogeneity in both the F10 and Brumbys Fault zones.	4, 5, 6, 9
RO3	Synthesise observations and features between the two faults and examine implications for fault process, shallow fault systems, fluid flow in the shallow subsurface and MMV.	9
RQ2	How important is the scale of analysis when examining shallow fault zones?	
RO4	Analyse shallow fault zones at different scales.	4, 5, 6
RO5	Compare and assess the effectiveness of methods to study shallow fault zones.	4, 5, 6

RQ3	How effective are petroleum-based modelling tools in modelling shallow fault zones?	
RO6	Create geological models of both fault zones.	7
RO7	Model strain and stress around the fault zones based on fault kinematics.	7
RO8	Understand how stress variations and uncertainty affect fault interpretation.	3, 7
RO9	Benchmark models to the observed fault architecture and model permeability structures (e.g. fractures).	7
RQ4	How does natural hydrogen seepage present at the surface and how do we effectively monitor seepage?	
RO10	Collate a database of hydrogen seepage sites which are analogous to seepage from an engineered geological hydrogen storage site.	8
RO11	Describe and characterise surface expressions of natural hydrogen seepage.	8
RO12	Present implications and recommendations for monitoring of engineered geological hydrogen storage sites.	8, 9

An additional research question (RQ4) was added because of travel restrictions that were introduced in at the start of the COVID-19 pandemic, which is when the Australia fieldwork was originally scheduled (April 2020). Travel restrictions then remained in place until late 2022, allowing fieldwork to commence in March 2023.

1.4 Thesis structure

Chapter 1 provides a high-level introduction to provide context for the research in this thesis. The two field sites are introduced, then the research aims and objectives are outlined. It concludes with the thesis structure.

Chapter 2 contains a literature review of the parameters that are critical for subsurface storage of fluids, as well as processes that influence shallow subsurface fluid flow. It focuses on fault processes and fluid flow pathways in the shallow subsurface and provides context for the research in this project.

Chapter 3 is an overview of the two main field areas investigated, including a summary of the operations and scope of the site, the regional geology, background on the fault of interest and research findings.

Chapter 4 presents an overview of the methods applied to study shallow fault systems in this thesis and links to the research questions and objectives set out in Chapter 1.

Chapter 5 is a study of the architecture and fluid flow properties of the F10 Fault zone, located at the In-Situ Lab in Western Australia, Australia. This chapter demonstrates two new methods of analysing rock core, one of which was specifically designed to capture deformation styles observed in shallow fault zones – using the Harvey-2 core as a case study as it cuts a shallow fault zone (F10 Fault). Petrographic analysis and XCT data are presented to show the variation and style of deformation at different observational scales, and to consider the effectiveness of different analytical techniques for characterising core from shallow fault zones. It concludes by considering implications for fluid flow.

Chapter 6 is a study of the architecture and fluid flow properties of the Brumbys Fault located at the Otway International Test Centre in Victoria, Australia. Similar to Chapter 5, this chapter applies a new methodology for characterising deformation in the Brumbys-1 core, which cuts a shallow fault zone (Brumbys Fault). Deformation logs are combined with fieldwork in the Port Campbell Embayment region to assess faulting kinematics, deformation features and spatial distribution. Additionally, geochemical analysis is used to compare lithological variations inland and at the coast. This chapter concludes by considering the effect the Brumbys Fault may have on subsurface fluid flow and considers regional faulting mechanisms to explain variations in faulting styles.

Chapter 7 is a short chapter discussing the challenges of modelling shallow fault zones, using standard approaches from the hydrocarbon industry. It presents a model workflow designed to model fractures around a fault zone. This chapter explores the challenges of applying hydrocarbon-based reservoir modelling software to the overburden of geological storage sites, with a focus on shallow fault systems and stress tensors.

Chapter 8 presents a published paper on natural hydrogen seepage sites and the insights they can provide for the monitoring of engineered geological hydrogen storage sites. This work was published in a special issue of the Geological Society of London

called “Enabling Secure Subsurface Storage in Future Energy Systems” and is titled “Natural hydrogen seeps as analogues to inform monitoring of engineered geological hydrogen storage” (McMahon, 2023).

The discussion in Chapter 9 brings together overarching themes from the previous chapters. First, faults are categorised based on their depth, activity and burial/exhumations history. Then, there is a comparison and synthesis of the research on the F10 and Brumbys Fault zones. Then, transferable learnings from/to other subsurface technologies or field sites that consider the shallow subsurface are considered. Finally, this chapter concludes by considering subsurface fluid flow and implications for environmental monitoring of subsurface technologies.

Chapter 10 presents conclusions and further work resulting from this PhD.

Chapter 2 Literature review: Fault architecture and fluid flow

This chapter presents a comprehensive review of subsurface storage systems and fluid flow in the subsurface (Section 2.1). Faults and fault zone processes are then examined, including how fault zones are studied, and the inherent bias that results (Section 2.2). Section 2.3 discusses shallow fault zones, with proceeding sections focused on faulting in siliciclastic (Section 2.4) and carbonate (Section 2.5) lithologies. Finally, the implications of fault processes for subsurface technologies and key research gaps are outlined in Section 2.6.

2.1 Subsurface storage systems and fluid flow in porous media

This section explores the fundamentals of fluid flow in porous media. First, it presents an overview of porous media and subsurface storage environments (Section 2.1.1). Next, the fundamental properties of fluid flow are discussed and the parameters that influence them are explored (Section 2.1.2). Aspects of fluid flow within the reservoir and overburden of geological storage sites are considered, with a focus on carbon dioxide (CO₂) or hydrogen (H₂) storage sites (Section 2.1.3). As such, the main fluids considered in this section are CO₂ and H₂, rather than traditional reservoir fluids (e.g. hydrocarbons, brine or water).

2.1.1 Porous media and subsurface storage environments

A porous medium is any material that contains pores (space) within its framework, which can be filled with fluid (e.g. liquid or gas). Porous media are of interest for geological storage as the porosity provides space in which to store fluids (e.g. CO₂, H₂ or other fluids). Understanding how fluids move through porous media is important for designing effective and secure injection, storage, and remediation strategies for subsurface storage technologies.

For subsurface geological porous media storage, the system must contain a suitable reservoir. Reservoir rocks are porous and permeable, meaning fluids can move through and be stored in the pore network of the rock. A reservoir rock is often overlain by a rock with lower porosity and permeability (e.g. clay-rich or salt-rich rock), which allows it to act as a seal and stops the fluid migrating out of the reservoir – often called a caprock or seal rock. Structural seals, or traps, can also aid the containment of fluids by acting as barriers to fluid movement (e.g. anticlinal folds, or low-permeability fault zones). In

classic petroleum geology literature, the overburden would contain the reservoir rock, the sealing caprock and all the overlying geology to the Earth's surface (i.e. all the rock units above the petroleum source rock) (Mahoo and Dow, 1994; Peters *et al.*, 2012). However, for geological porous media storage the terminology used is different. The reservoir and caprock are typically referred to as the "storage complex" and the overburden is more commonly considered to be the rocks above the storage complex (Chadwick *et al.*, 2017; Roberts *et al.*, 2017; Rahman *et al.*, 2022). Although, as discussed in Section 1.1, there is value in characterising the overburden system as well as the storage complex (Roberts *et al.*, 2017; Bump *et al.*, 2023; Bump and Hovorka, 2023).

2.1.2 Fundamentals of fluid flow in porous media

2.1.2.1 Darcy Flow

Darcy's Law explains how a single fluid flows in porous media, showing that water flux (flow rate) is proportional to a hydraulic gradient. How proportional these are is controlled by the hydraulic conductivity, which depends on both the fluid and medium properties (Darcy, 1856; Hubbert, 1940; Liu, 2017). Darcy's Law can be stated as:

$$Q = KA \frac{\Delta h}{L}$$

Q = Volumetric Flow Rate (m³/s)

K = hydraulic Conductivity (m²)

A = cross-sectional Area (m²)

h = head (m)

L = length of Pressure Drop (m)

2.1.2.2 Non-Darcy Flow

Darcy's Law is limited to laminar flow of a single fluid in a homogeneous medium. In geoscience applications, it is more likely there is a heterogenous medium with multiple fluids and potentially non-laminar (turbulent) anisotropic flow. Multiphase flow of fluids is common in geoscience applications such as geological CO₂ storage, here supercritical CO₂ is being injected into a reservoir with formation brine (Jia and

McPherson, 2019). The Navier-Stokes equation is used in these scenarios and considers the density, pressure, temperature and velocity of the fluid, as well as mass transport processes (e.g. diffusion). The equations are not included here as this is a coupled system of equations that can be altered depending on the properties of the system that you intend to investigate, and there is still uncertainty in the consistency of the results produced (see Zawawi *et al.*, 2018; Sheng, 2020).

2.1.2.3 Mass Transport: Advection, Diffusion, Dispersion and Sorption

Mass transport processes also govern how fluids flow and interact in a porous medium. Advection represents the transport of a fluid due to its bulk motion. Advection is calculated using the average linear velocity (from Darcy's Law). If there are deviations from the average linear velocity, then hydrodynamic dispersion is occurring (a combination of molecular diffusion and mechanical dispersion).

Molecular diffusion is described by Fick's laws and represents the intermingling of particles due to their kinetic energy of random motion, associated with temperature, viscosity and particle mass (Lyman, 1982; Domenico and Schwartz, 1990). The porosity, tortuosity and reactivity of the media with the fluid determines the diffusion (McDermott, 1999). Particles tend to diffuse from areas of higher concentration to areas of lower concentration. Molecular diffusion of CO₂ is an important controlling factor of dissolution kinetics in a reservoir (Iglauer, 2011).

Mechanical dispersion (Figure 2-1) is controlled by the dispersivity (both longitudinal and transverse) and represents fluids moving at rates faster and slower than the average linear velocity as it moves through the tortuous pore network (McDermott, 1999).

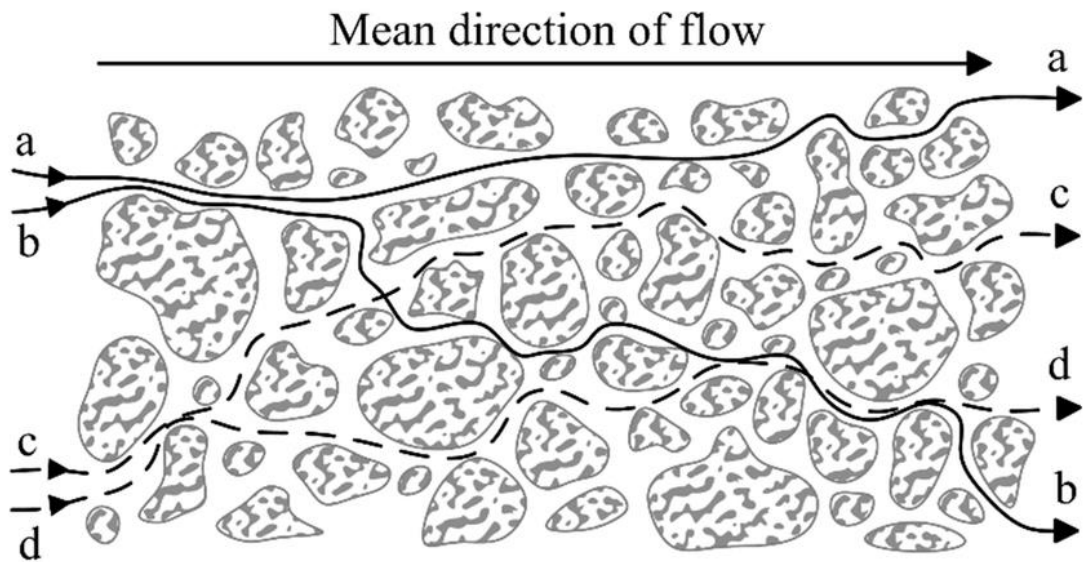


Figure 2-1– Example of mechanical dispersion in porous media, with multiple pathways (a-d) through the pore network (Afanasyev, 2018). Not all flow pathways would be active at the same time, as flow pathways would not cross each other.

Sorption (reactions with the rock matrix) can occur when fluids contain reactive components.

2.1.3 Parameters that influence fluid flow in porous media

This section outlines the material (rock) and fluid parameters that influence fluid flow in the subsurface, as well as dynamic parameters that consider the interaction of rock and fluids.

2.1.3.1 Material parameters

Porosity is simply the empty space within a rock matrix, measured as:

$$n = \frac{V_v}{V_t}$$

n = porosity (%)

V_v = volume of void space

V_t = volume of matrix

Rock porosity varies depending on rock type, depositional environment, and diagenetic history (cementation, compaction and dissolution) of the rock. These factors affect the size, type, shape, packing and orientation of grains and ultimately the space (porosity) between grains. Primary porosity is the original rock porosity upon deposition,

secondary porosity relates to porosity as a result of modifications (e.g. diagenesis, fractures) after initial deposition. Effective porosity is often used as this represents the interconnected porosity, which is the porosity available for fluid flow. The complexity of the interconnected pore network can be defined by its tortuosity (Carman, 1956; Grathwohl, 1998).

Tortuosity considers the ratio of the real diffusive path length (l_e) to the direct diffusive path length (l) (Figure 2-2) – giving the tortuosity factor (τ_f).

$$\tau_f = \frac{l_e}{l}$$

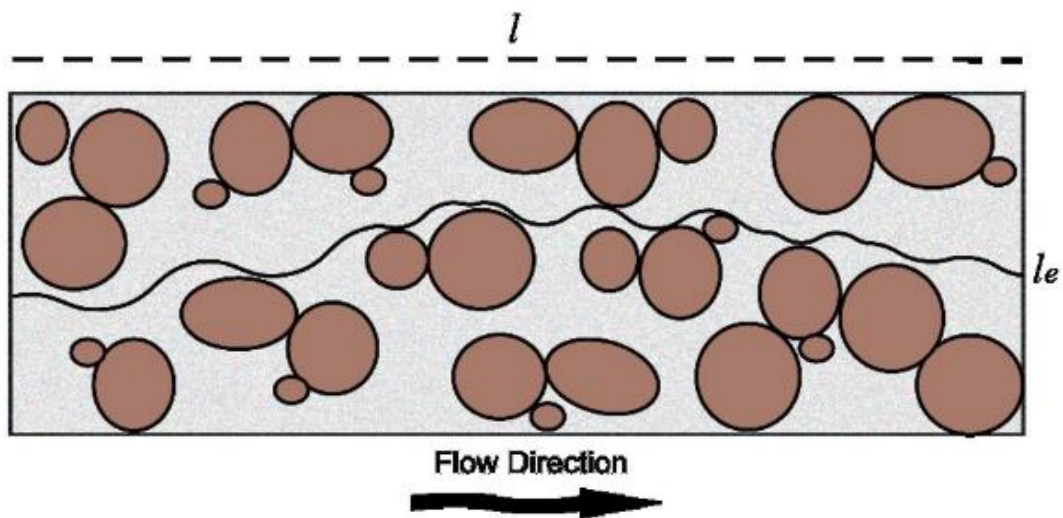


Figure 2-2 – Flow in porous medium, showing the real diffusive path length (solid line) and the direct diffusive path length (dashed line) (Kilgallon, 2016).

As porosity increases, tortuosity decreases (Grathwohl, 2012). Permeability depends on the effective porosity of the matrix. It explains the ease of flow of a fluid through a system.

Porosity and permeability are the two fundamental rock (material) properties that control how fluids flow in the subsurface (Figure 2-3).

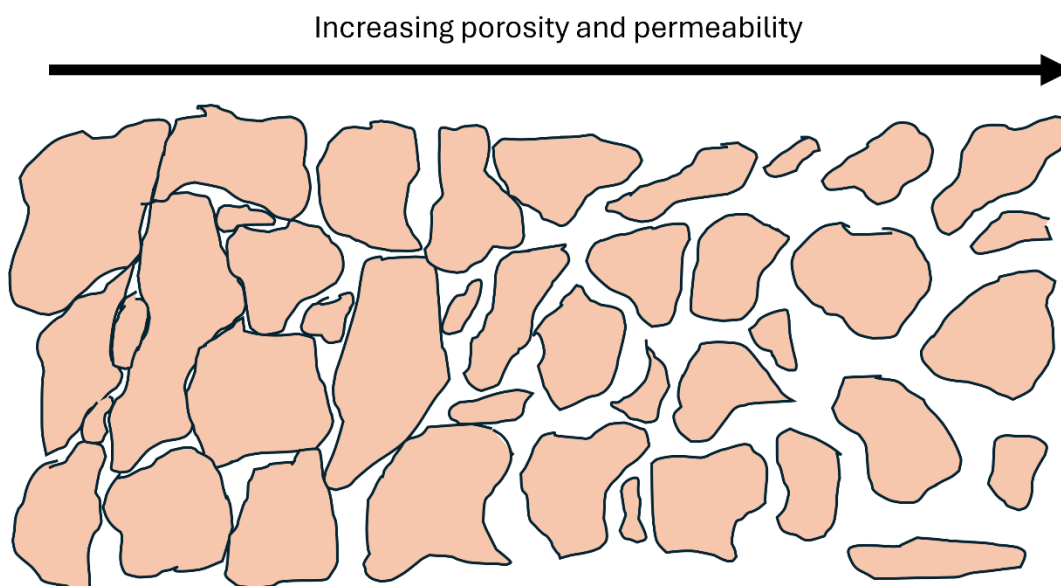


Figure 2-3 – Schematic showing change in porosity and permeability of a porous medium. Both porosity and permeability increase to the right-hand side as the space between the grains is greater and the pore spaces are connected.

2.1.3.2 Fluid parameters

The parameters of geofluids like CO₂ are better understood than geofluids associated with emerging subsurface technologies (e.g. H₂). Fluids have specific properties, and these vary with subsurface conditions including temperature and pressure, with key parameters often being viscosity (how easily a fluid flows), solubility (how easily a fluid will dissolve into water/brine) and compressibility (change in fluid volume due to pressure change), among many others (Table 2-1).

Table 2-1 – Hydrogen (H₂) and carbon dioxide (CO₂) dynamic viscosity, solubility and compressibility.

Properties	Hydrogen (H ₂)	Carbon Dioxide (CO ₂)
Dynamic viscosity (10 ⁻⁵ Pa s) at 20°C	0.88	1.47
Solubility (in water) at 20°C	0.0016	1.7
Compressibility (Z) at 20°C and 1MPa	1.0021	0.9454

Understanding how fluid parameters change with depth in the subsurface is important to predict how the behaviour of the fluid may change during injection, storage or withdrawal. Furthermore, understanding how fluids react in the subsurface, with each

other or with the surrounding rocks, is important for effective storage of fluids (see Section 1.1).

2.1.3.3 *Dynamic parameters*

Wettability describes the tendency of a fluid to adhere to the matrix surface when two or more immiscible fluids are present and depends on the contact angle of the rock type (Jia and McPherson, 2019). This concept is relevant in all porous media where there are fluids such as oil, gas, brine, or water present. Fluids that preferentially ‘wet’ a surface will replace existing fluids on the rock surface. This wettability depends on a combination of the rock and fluid properties (e.g. pressure, salinity, presence of other fluids) (Jun and Wan, 2012).

Wettability controls the capillary pressure and the relative permeability of a reservoir. Capillary pressure is the pressure differential between two immiscible fluids in a porous medium (Tiab and Donaldson, 2016) and is inversely proportional to the pore size (Slatt, 2013). Where multiple fluids are present, the effective permeability (the ability of that fluid or phase to flow in the presence of another fluid or phase) is used. The relative permeability of a rock to a fluid is the ratio of the effective permeability (of the fluid) and the absolute permeability (of the rock) (Satter and Iqbal, 2016). In geological CO₂ storage studies, it has been shown that when CO₂ migrates into a water-wet system that the CO₂ migration is slowed, whereas in a CO₂-wet system CO₂ migration is increased (Al-Khdheawi *et al.*, 2017). Wettability has implications for CO₂ containment and trapping within the reservoir (Iglauer *et al.*, 2015; Yekeen *et al.*, 2020). Consideration should also be given to CO₂ migration into fault systems that may be water-wet – as this could slow or stop the migration of CO₂ within a fault zone.

For H₂ there has been little work to assess the effect of hydrogen on wettability (Edlmann *et al.*, 2019; Miocic *et al.*, 2023). Studies have shown that CO₂ and CH₄ can alter the wettability of rocks and this further work is required to understand the effect H₂ may have on rock wettability and how different subsurface conditions (i.e. pressure, temperature) would affect H₂ wettability (Edlmann *et al.*, 2019; Miocic *et al.*, 2023).

2.1.3.4 *Fluid trapping and migration in CO₂ and H₂ reservoirs*

Storage fluids (e.g. CO₂, H₂ and CH₄) are lighter than pore-filling brines (Miocic *et al.*, 2019b) and consequently migrate upwards towards the Earth’s surface due to their

buoyancy effect after injection. These fluids can be stopped by fluid barriers (e.g., impermeable rocks or faults) where they will accumulate (Bachu and Bennion, 2008; Miocic *et al.*, 2019b; Karolytė *et al.*, 2020). This is known as structural trapping.

Intra-reservoir fluid flow occurs during the injection and withdrawal of fluids, due to the change induced in the pressure gradient. For geological CO₂ storage, injected CO₂ will be injected in supercritical phase and will displace and dissolve into the reservoir fluid (e.g. brine) (Jia and McPherson, 2019). Supercritical CO₂ displays “viscous fingering”, a process resulting in solubility trapping via dissolution (Figure 2-4) (Waggoner *et al.*, 1992). Models suggest most CO₂ is not trapped by solubility trapping and instead remains in supercritical phase, with trapping of this remaining CO₂ via residual trapping and structural trapping within the reservoir (Jia and McPherson, 2019) (Figure 2-5). Structural trapping relies on the CO₂ remaining in the reservoir due to an overlying caprock/seal (e.g. low permeability rock unit). Residual trapping is when the CO₂ is held in place by surface tension (Doughty and Pruess; Flett *et al.*, 2014), which is controlled by the wettability. Over time, trapping of CO₂ via mineralisation can occur as the CO₂ reacts with the reservoir rocks (e.g. Snæbjörnsdóttir *et al.*, 2020). Observations from field studies in basaltic rocks indicate that most trapping is solubility trapping in the first year, before moving on to mineral trapping.

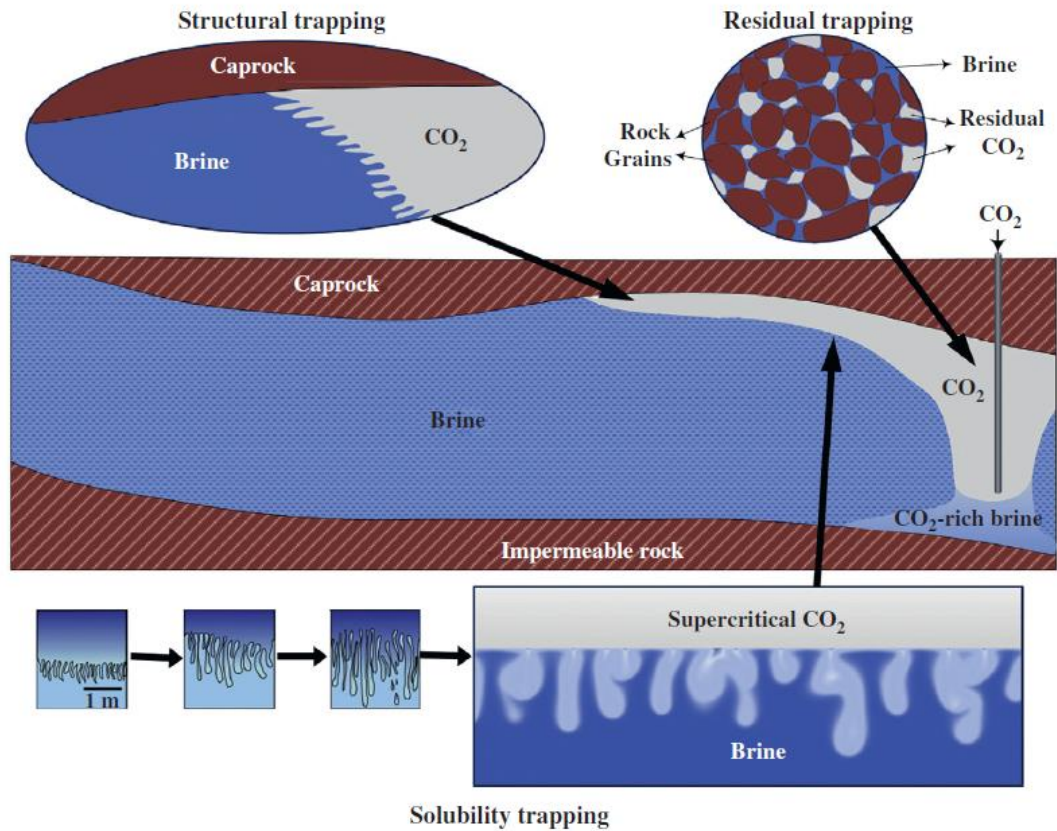


Figure 2-4 – Schematic of trapping, fluid flow and viscous fingering in geological CO₂ storage reservoir (Jia and McPherson, 2019).

Over time the CO₂ trapping will evolve and become more secure (Figure 2-5).

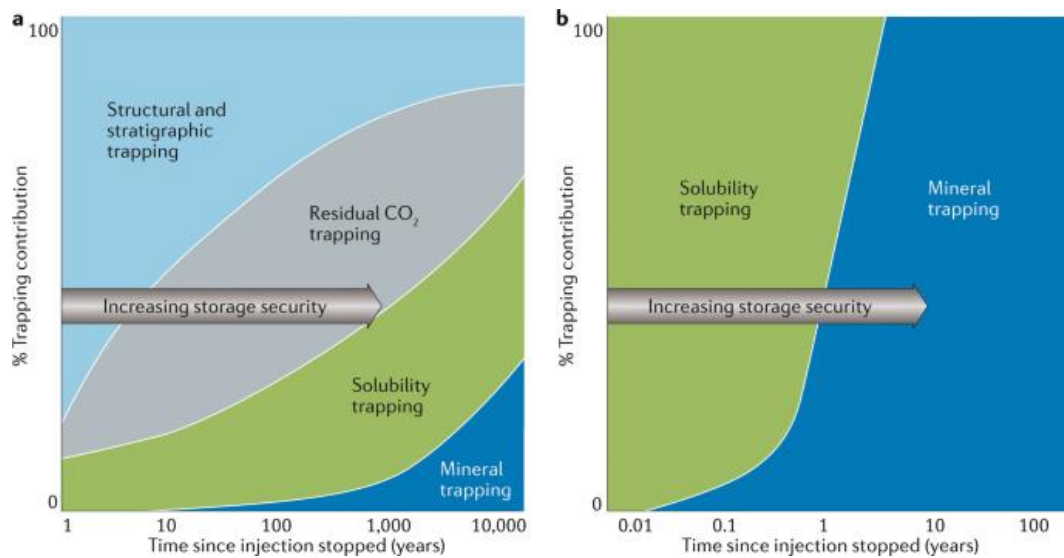


Figure 2-5 – A) Evolution of CO₂ trapping mechanisms over time. B) Summary of results of various injection experiments showing the type of trapping achieved with time after injection has stopped (from Snæbjörnsdóttir et al., 2020).

For geological H₂ storage, there are additional pressure changes in the well compared to CO₂ storage as there will be repeated cycles of injection and withdrawal. Experiments from injection and withdrawal of CO₂ have shown this cyclicity can influence the relative permeability of the fluid system (Edlmann *et al.*, 2019), so this requires further work to understand this effect on H₂ storage systems (Miocic *et al.*, 2023).

2.1.3.5 Leakage from reservoirs and fluid flow in the overburden

Leakage occurs when a stored fluid migrates and escapes from the reservoir. Although porous media storage is designed to be secure, leakage can occur in various ways (Gholami *et al.*, 2021; Miocic *et al.*, 2021). Common leakage pathways include:

- **Caprock:** Diffusion rates through caprocks are incredibly slow (Lu *et al.*, 2009) and therefore negligible in terms of overall leakage. Capillary leakage of fluids through the caprock is usually an incredibly slow process and does not account for significant amounts of leakage over short timescales (e.g. years). However, there is potential for leakage over time due to pressure and temperature changes which can mechanically weaken the caprock and develop fractures or reactivate existing fractures – creating enhanced permeability (Green and Ennis-King, 2010; Naylor *et al.*, 2011; Renard *et al.*, 2012; Gheibi *et al.*, 2017; Miocic *et al.*, 2019b; Gholami *et al.*, 2021).
- **Faults:** Fault zones and fault-associated deformation can create leakage pathways. Changing stress and pressure can result in reactivation of fault zones and deformation features (e.g. fractures). Fault zones can be both conduits or barriers to fluid flow depending on the geological properties and setting (Viswanathan *et al.*, 2022; Fisher *et al.*, 2023) (see Section 2.4 and 2.5).
- **Engineered pathways (e.g. wells):** Can provide fluids with a pathway from the reservoir through the overburden and to the Earth's surface. During the installation, operation or abandonment of wells there can be construction or degradation issues that could create permeable fluid pathways (Zhang and Bachu, 2011; Ringrose, 2020; Gholami *et al.*, 2021).

These pathways are of interest for all subsurface fluid storage (e.g. CO₂, H₂ and CH₄), but some fluids pose different or greater challenges due to their properties. For example, H₂ leakage risk is greater than that of CH₄ or CO₂ due to its physical properties (e.g. low interfacial tension) which increases the rate of diffusion of hydrogen through a caprock

due to lower capillary entry pressure (Ugarte and Salehi, 2022). Conversely, for CH₄ storage there is high interfacial tension, higher capillary entry pressure and less likelihood of capillary leakage (Ugarte and Salehi, 2022). The fluid behaviour is dependent on the pressure and temperature (i.e. depth). Therefore, consideration should be given to the properties of the fluid being stored in the subsurface and the depth of storage when assessing leakage mechanisms and risk.

Figure 2-6 outlines some common leakage pathways for CO₂.

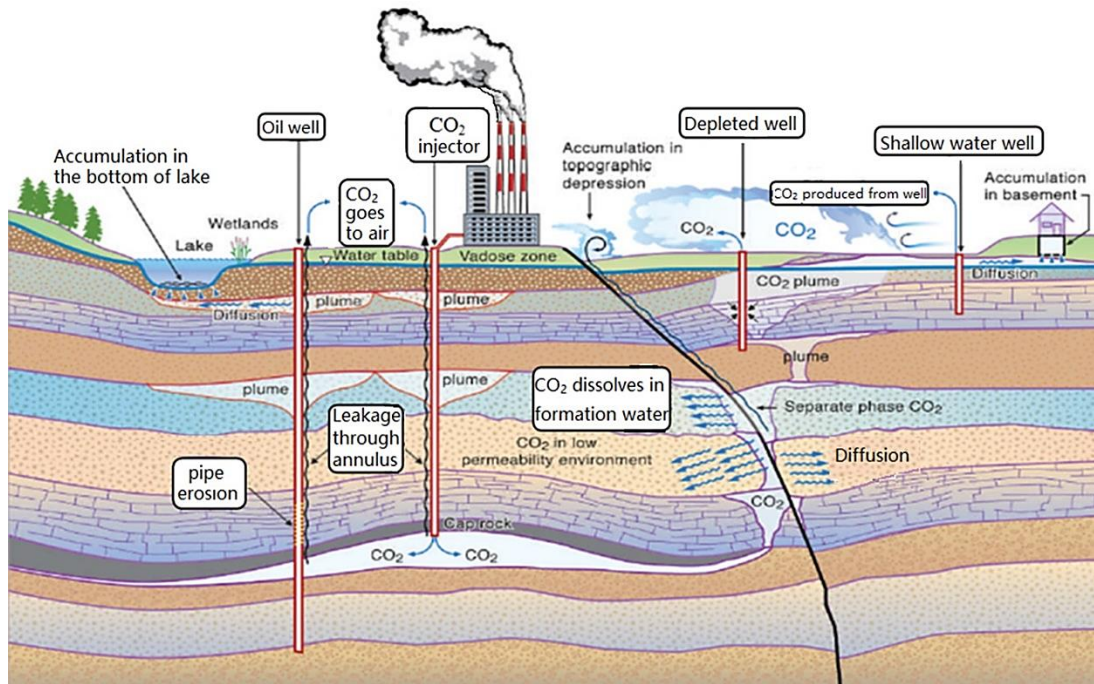


Figure 2-6 – Schematic of subsurface CO₂ leakage pathways (Wang *et al.* 2020).

Natural analogue studies of natural CO₂ sites have highlighted the importance of fluid overpressure above reservoir overburdens creating a pressure seal, which can successfully act to retain CO₂ in the subsurface (Roberts *et al.*, 2017). However, it was noted that in sites where a pressure seal was present, CO₂ still leaked to surface, likely via extensional fault systems where the damage zone could act as a fluid conduit (Roberts *et al.*, 2017). These fault systems do not need to be directly connected to the reservoir to act as efficient fluid pathways (Roberts *et al.*, 2017). Bond *et al.*, (2017) note that natural CO₂ seeps highlight the importance of fault related fracture permeability for subsurface storage integrity.

Once a fluid has migrated from a reservoir, there is the potential for this fluid to migrate through the overburden and towards the Earth's surface.

2.1.3.6 *Near surface fluid flow and seepage*

If fluids leak from the reservoir, then they can migrate into the overburden of the storage site. During this migration, fluids may be trapped or baffled in overlying rocks which are suitable reservoirs/caprocks (Roberts *et al.*, 2017). Additionally, the changing depth (and pressure/temperature) will result in a phase change of some fluids – e.g. CO₂ will move out of the supercritical phase to gas phase at depths <1km.

If fluids make their way to the near surface, this can lead to enhanced concentrations of fluids in shallow groundwater aquifers (as fluids dissolve). For CO₂, the change out of supercritical phase and into gas phase will result in an increased buoyancy compared to groundwater – meaning CO₂ may settle above the water table (phreatic zone) (Roberts *et al.*, 2017). This CO₂ will be denser than surrounding soil gases in the vadose zone (unsaturated zone), so may disperse laterally as fluid concentration increases in the soil (Annunziatellis *et al.*, 2008; Kirk, 2011; Roberts *et al.*, 2017; Wang *et al.*, 2020).

Seepage occurs when a fluid migrates through the entire overburden and reaches the Earth's surface. Natural seepage of fluids has been documented globally for common storage fluids – CO₂ (Roberts *et al.*, 2014; 2015; 2016; 2019a; 2019b; Miocic *et al.*, 2016), H₂ (Zgonnik *et al.*, 2020; Frery *et al.* 2021; Stalker *et al.*, 2022; McMahon *et al.*, 2023; Langhi and Strand, 2023) and CH₄ (Etiopie *et al.*, 2015). In addition, studies of engineered seepage have provided important learnings for MMV at subsurface porous media storage sites (Roberts and Stalker, 2020). Further work studying natural hydrogen seepage is discussed in Chapter 8.

Fluid leakage or seepage in unconsolidated sediments (often found in the near surface), can cause subsurface sediment remobilisation. The cohesiveness of the sediment controls its deformation style – low cohesion sediments will deform by fluidisation whereas high cohesion sediments will deform by fracturing and folding. Subsurface sediment remobilisation is caused by changing pressure (e.g. due to fluid injection) and deformation creates enhanced permeability pathways (May *et al.*, 2019).

2.2 Fault architecture and studying fault systems

This section outlines fault zones and their architecture (Section 2.2.1) and how fault zones are studied, with a focus on the methods used and challenges fault studies present (Section 2.2.2).

2.2.1 Introduction to fault zones

Faults are widespread in the Earth's lithosphere, often occurring in clusters and creating complex heterogeneous subsurface structures with implications for multiple geoscience sub-disciplines (Brandes and Tanner, 2019). Fault zones (Figure 2-7) encompass the volume of rock deformed when two rock units move in relation to each other, due to lithospheric stress (Loveless *et al.*, 2011).

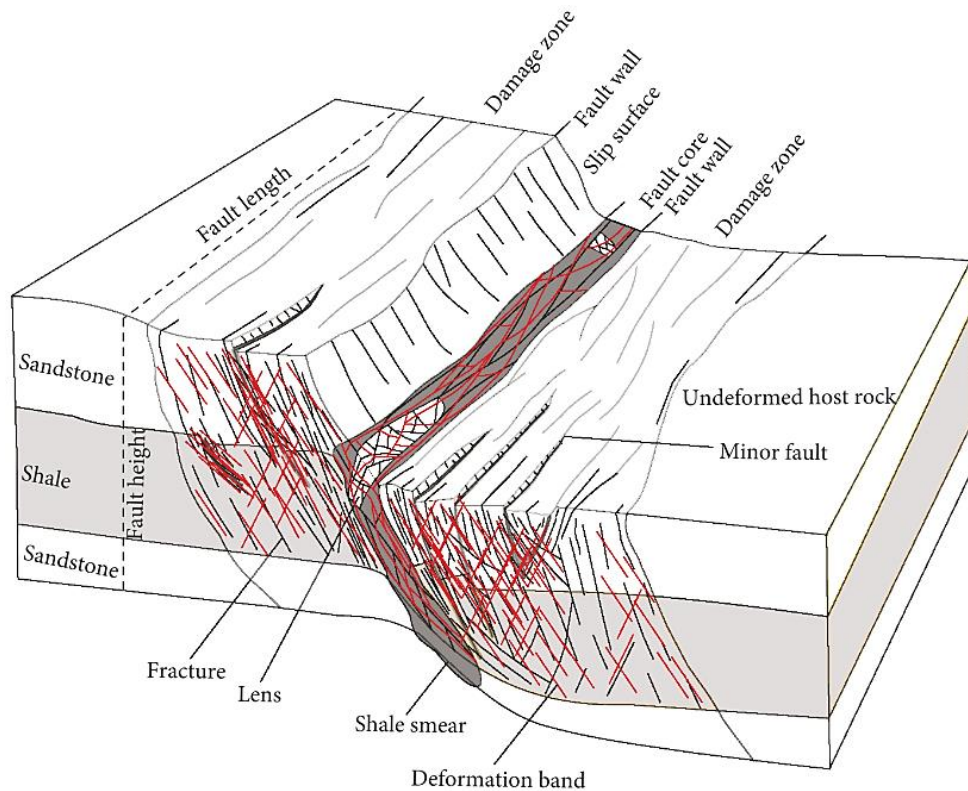


Figure 2-7 – Geometric attributes of a normal fault (Torabi *et al.*, 2019). “Fault length” is the lateral extent of the fault zone. “Fault height” is the vertical extent of the fault zone.

There are three main types of faults, often characterised by the kinematics and the angle:

- Normal faults – occur in extensional environments where one side of the fault (hanging-wall) has moved downward relative to the other (footwall). Typically dipping $\sim 60^\circ$.
- Reverse faults – occur in compressional environments where one side of the fault block (hanging-wall) has moved up and over the other block (footwall). Typically dipping $\sim 30^\circ$.
- Strike-slip faults – the two blocks slide past each other – with either a dextral component (movement to the right) or a sinistral component (movement to the left). Typically vertical, so dipping $\sim 90^\circ$.

The amount of displacement on these faults vertically is referred to as “throw”. The amount of displacement horizontally is referred to as “heave”. The total slip on a fault is the combination of both the throw and heave (Figure 2-8).

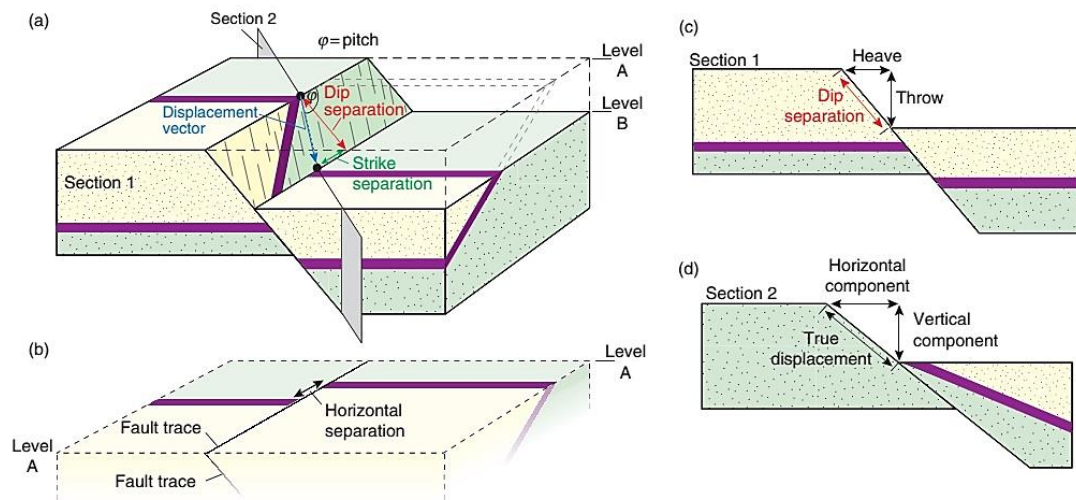


Figure 2-8 - Illustration of a normal fault. A) dip-slip normal fault – showing both vertical and horizontal (dextral) displacement. B) Fault appears as a sinistral fault in map view (horizontal section at Level A). C) Profile perpendicular to fault strike showing heave and throw. D) Profile perpendicular to fault strike showing the true displacement (Fossen, 2015)

Fault zone architecture is often characterised by two main zones: a high-strain fault core and a low-strain fault damage zone (see Figure 2-7). Most of the fault displacement is accommodated in the fault core, which often contains a fine-grained gouge or smear surface (Sibson, 1977; Caine *et al.*, 1996). The fault damage zone surrounds the fault core. It can include subsidiary faults or fracture networks and contains structural elements related to the growth of the fault (Sibson, 1977; Caine *et al.*, 1996; Loveless *et*

al., 2011). Fault zones can contain multiple fault cores in one damage zone when there is high strain material (Figure 2-9).

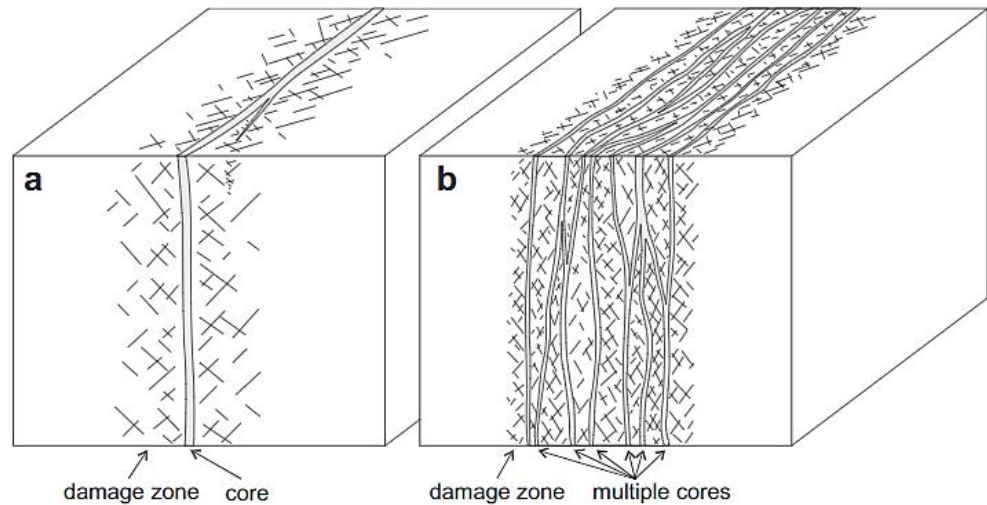


Figure 2-9 – Fault zone structures. (a) Typical fault damage zone and fault core. (b) multiple fault cores encompassed by a large damage zone (Faulkner *et al.*, 2010).

Faults can link together and grow by propagation to form multiple strands or segments (Walsh and Waterson, 1991). An example of “soft” fault linkage, where a zone of high strain occurs between two fault strands, is a relay ramp. Relay ramps are characterised by rotated bedding and folding, and can occur at a variety of scales (Suppe and Medwedeff, 1990; Stewart and Hancock, 1991; Peacock and Sanderson, 1994; Huggins *et al.*, 1995; Childs *et al.*, 2009).

2.2.1.1 The control of faulting depth on fault architecture

Fault architecture varies with the depth of fault activity, due to different mechanical processes, lithologies and fault zone structural styles (Brandes and Tanner, 2019), resulting in fault zones displaying different properties as you move from the Earth’s surface to different depths within the Earth’s subsurface.

At the Earth’s surface, faults are sometimes visible as a fault scarp. This is where there has been a discrete rupture at the Earth’s surface due to fault movement. Different fault kinematics will produce different types of fault scarp (Stewart and Hancock, 1990):

- Normal faults: High-angle step-like vertical offset in ground surface. Easiest to observe.

- Reverse faults: Lower-angle vertical offset, where the hanging-wall block has come over the footwall.
- Strike-slip faults: Horizontal offset, can only be easily observed when the ground slopes (e.g. a valley) making them the most difficult to observe.

Fault scarps are often visible in active fault zones, as over time these features can be eroded. If a fault moves in the subsurface and does not rupture the surface, a fold scarp can be formed where the Earth's surface is deformed due to the underlying fault movement. If a fault is not visible at the Earth's surface, the motion on the fault plane must have ended before the surface, or the fault scarp has been eroded or buried.

In the subsurface, there are three depth zones in which different types of deformation occurs: (i) brittle; (ii) the transition zone between, and (iii) plastic and (ii) the transition zone between, shown in Figure 2-10.

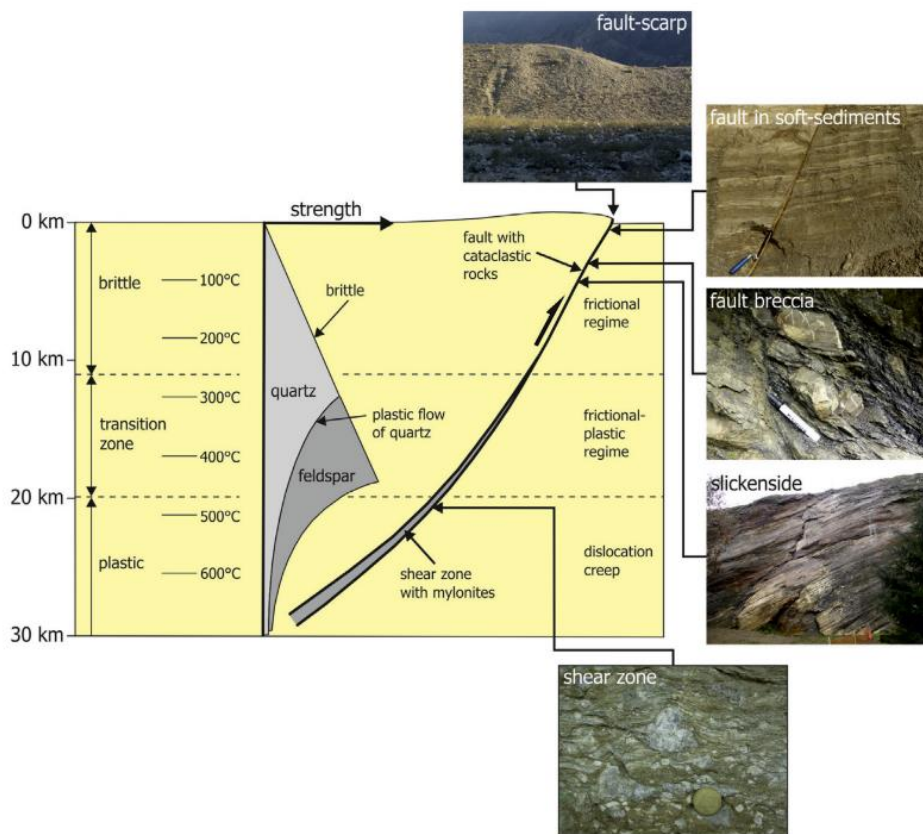


Figure 2-10 – Fault evolution with depth and temperature (Brandes and Tanner, 2019).

The top 10km depth of the lithosphere is dominated by brittle deformation processes (Brandes and Tanner, 2019). At the lithospheric scale, these deformation processes are controlled by the material properties of the lithosphere (i.e. by the rocks and minerals

which make up the lithosphere). This means that for each fault zone, the material properties of the host rock will influence the deformation processes. At the base of the brittle deformation zone (~10km depth), there is an intermediate transition zone between brittle and ductile (plastic) deformation behaviour, occurring from anywhere from 10km to 20km in depth, depending on geothermal gradient, and lithology. Below 20km depth, and temperatures >480°C, deformation is fully ductile. Dislocation creep is the primary deformation mechanism and features such as mylonites can develop (Brandes and Tanner, 2019).

Importantly, brittle and ductile deformation is not exclusive to particular depths; strain-rate dependent deformation behaviour (e.g., earthquakes) can result in brittle deformation at depths which typically are dominated by ductile deformation processes (Frost *et al.*, 2011; Inbal *et al.*, 2015; Brandes *et al.*, 2019). Additionally, deformation mechanisms such as fault related folding can occur in the upper lithosphere as a far-field effect of fault movement (Brandes and Tanner, 2014).

2.2.2 Studying fault zones: methods and challenges

Studying fault zones presents challenges as we are limited in the data which are able to be collected. Where faults are exposed at the Earth's surface, it may be possible to conduct fieldwork and collect data on the fault zone. However, most fault zones are not exposed at the surface. So, we must rely on using methods which allow us to image and measure the fault properties remotely in the subsurface.

The most common method used to image fault zones in the subsurface is geophysical methods (e.g. seismic imaging) (Tanner *et al.*, 2019). This involves using a source (either natural or engineered) to generate sound waves which pass through and are reflected by the rock. An array of receivers processes the reflected signals and the time taken for the waves to reach the receiver can be used to estimate geological boundaries, structural features and rock type. Other geophysical methods can also be used to study fault zones. For example, ground penetrating radar (GPR) could be used to collect information on shallower structures in the subsurface as the depth this can penetrate to is limited (<50m). With all geophysical methods, there are uncertainties in the collected data and the resolution is limited by the method used and the geological setting. One of the main limitations to the quantity of data collected is the cost. Seismic imaging of the subsurface is expensive, particularly offshore. Therefore, to date most seismic data

collected has been for petroleum exploration and extraction. Seismic data are therefore biased towards reservoir depths. Consequently, most images of faults in seismic are from petroleum basins where the survey is designed to maximise resolution at reservoir depths.

Features at sub-seismic scales (or below the resolution of other geophysical methods) will not be imaged, meaning features such as smaller fault zones or fault-related deformation (e.g. fractures) will not be detected (Bond *et al.*, 2017). Fractures are an important control on fluid flow in the subsurface (see Section 2.4.1.2), even where appropriate caprocks/seals are present (e.g., Bond *et al.*, 2017). This highlights the importance scale and resolution when choosing a method for fault analysis.

Within-fault variability is an important parameter to consider. Most fault studies focus on down-dip sections of fault to examine relationships between fault properties and stratigraphy (De Rosa *et al.*, 2018). However, studies have shown that the size and location of relatively high permeability fault rocks exert the strongest influence on hydraulic behaviour, rather than the mean low permeability fault core thickness (Heynekamp *et al.*, 1999; Lunn *et al.*, 2008; Caine and Minor, 2009; De Rosa *et al.*, 2018). Therefore, it is important to investigate the along strike variations at different scales to assess the probability of higher permeability areas in a low permeability fault zone (De Rosa *et al.*, 2018). These higher permeability areas could provide routes for fluid flow.

In addition to field studies and fault imaging, there are other methods used to collect data on fault properties and behaviour. 3D geological models of fault zones are used to assess fault kinematics and assess the impact of changing variables (e.g. stress, fluid pressure, temperature, rock properties). These models can then be used to assess various scenarios and consider implications for fault reactivation or fracture development. Chapter 7 discusses fault modelling in further detail.

Where it is possible to get samples from fault zones, either in the field or from rock core recovered from the subsurface – it is possible to conduct experiments to assess the fault rock properties (e.g. mechanical and hydraulic). These methods can provide useful quantification of key parameters for geological modelling. Other common methods applied to rock core include fracture logging (Kulander *et al.*, 1990). This involves logging the location and properties of fractures along a cored section. Focus is given to if the fracture is naturally occurring (i.e. formed in the subsurface due to tectonic processes)

or induced (i.e. due to the drilling, extraction, handling, or storage of the core). The location, type and formation mechanism of the fracture are important to predict the influence these may have on the mechanical or hydraulic properties of the rock. Fractures and fracture logging are discussed further in Sections 2.3, 2.4.1.2, 4.1 and 5.3. Other experiments assessing fault zone kinematics and properties include sandbox experiments (e.g. Buchanan and McClay, 1991; Bernard *et al.*, 2007; Herbert *et al.*, 2015) and field experiments (see Chapter 3).

Additionally, being aware of bias is important in any geoscience discipline. Shipton *et al.*, (2020) used fault zone studies as an example to highlight bias in data collection (i.e., which outcrops/analogues are studied), geologists themselves (how they operate and their interests) and the use and communication of data. This is something to consider as it is important that we try to be conscious of potential biases in data and ensure that this does not adversely influence research.

Having examined fault architecture and how we study faults, and some of the key limitations and considerations, the next section considers fault architecture in shallow fault zones (Section 2.3).

2.3 Fault zone architecture in the shallow subsurface

For the purposes of this study the “shallow subsurface” is considered <1km depth. As such, faulting that takes place in the shallow subsurface is referred to as “shallow faulting” and the resulting fault zones as “shallow fault zones” or “shallow fault systems” (see Section 1.1). Faulting that has taken place at “deeper depths” (>1km) is referred to as “deeper faulting” and faults at these depths as “deep faults”. Where there has been deeper faulting and later the fault zone has been uplifted or exhumed to depths <1km, these fault zones are referred to as “exhumed faults”. The focus of this section is on shallow faulting and shallow fault zone processes.

Shallow fault studies are not as common as studies of deeper faults, as most fault studies have focused on faulting in deeper consolidated rocks (Brandes and Tenner, 2019) as these rocks are the focus of most subsurface research (i.e. petroleum and mining industries). At these deeper depths, the consolidation states of rocks tend to increase due to increasing pressure, diagenetic processes, and other at depth processes. The resulting grain compaction leads to a loss of porosity (e.g., Bethke and Corbet, 1988) and a reduction in permeability (Bense and Person, 2006), which ultimately decreases permeability.

Studies indicate that the architecture of faults that form in the shallow subsurface varies compared to deeper faulting. In the shallow subsurface, fault zones are exposed to contrasting rheological properties and confining pressures (Balsamo *et al.*, 2008; Loveless *et al.*, 2011), resulting in significant architectural differences compared to faulting at deeper depths (Heynekamp *et al.*, 1999; Caine and Minor, 2009). In shallow fault zones, there are three sections of fault architecture that have been observed: i) fault core, ii) fault damage zone, ii) mixed zone.

In shallow fault zones, the fault core is often reported as a deformation band shear zone (see Section 2.4.1.3) (Heynekamp *et al.*, 1999; Rawling and Goodwin, 2003; 2006; Minor and Hudson, 2006) or a continuous clay smear (see Section 2.4.1.4) (Heynekamp *et al.*, 1999; Rawling, *et al.*, 2001; Bense *et al.*, 2003; Caine and Minor, 2009). These types of fault core have low permeability.

The damage zone of faults in poorly lithified siliciclastic sediments often contains shear deformation bands, rather than fracture networks (Heynekamp *et al.*, 1999; Rawling and

Goodwin, 2003; 2006; Minor and Hudson, 2006) – leading to a reduction in fault zone permeability (Rawling *et al.*, 2001). However, at shallow depths (<1km) disaggregation bands are common (see Section 2.4.1.3).

Faults in poorly lithified sediments often have a third architectural zone – the mixed zone. This zone separates the fault core and fault damage zone (Mozley and Goodwin, 1995; Rawling and Goodwin, 2006). It contains variably deformed, entrained, and attenuated beds that are rotated parallel to the fault zone with a continuous displacement geometry (Lindsay *et al.*, 1993; Bense and Person, 2006; Loveless *et al.*, 2011). As displacement increases, initial sedimentary characteristics (e.g., bedding) are progressively modified. If fault displacement exceeds bed thickness, these features can be lost entirely which creates a homogeneous zone of mixed beds at the grain scale (Mozeley and Goodwin, 1995; Heynekamp *et al.*, 1999; Rawling and Goodwin, 2006). Mixed zone can contain units (e.g., blocks or lenses) of undeformed sediment which are often separated from the mixed zone by localised shear zones or deformation band shear zones (Rawling and Goodwin, 2006; Caine and Minor, 2009)

The mixed zone terminology has resulted in confusion in the literature (e.g., Evans and Bradbury, 2004), meaning when possible, the two main zones (fault core and fault damage zone) should be used. Additionally, some have suggested that the mixed zone simply contains multiple features, not whether the components are chaotic or ordered – which is an issue of terminology bias (Shipton *et al.*, 2020).

It is important to note that the shallow subsurface is not exclusively comprised of younger rocks that are weak and unconsolidated. There are areas where older rocks have been exhumed to these depths and thus their mechanical properties are reflective of their burial and uplift history. The following section outlines the deformation mechanisms that occur in shallow fault zones (Section 2.3.1).

2.3.1 Deformation mechanisms in shallow fault zones

Rock porosity and depth are the primary controls on deformation mechanisms of near surface unconsolidated sediments (Figure 2-11).

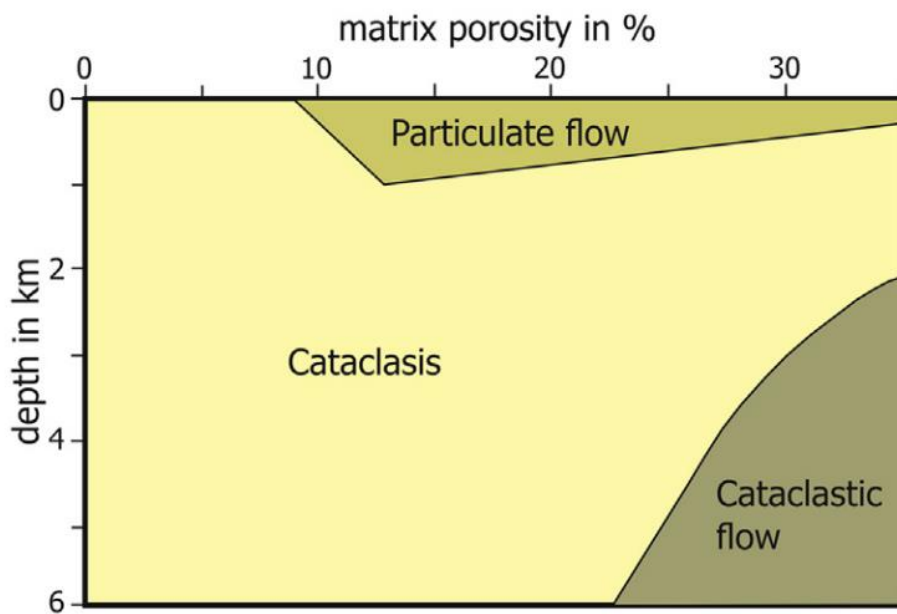


Figure 2-11 – Deformation mechanisms in unconsolidated sediments (Brandes and Tanner, 2019). Although cataclasis can occur at depths <1km, is not the dominant deformation mechanism at these depths – instead particulate flow processes dominate.

In the shallow subsurface, particulate flow is the dominant deformation mechanism. Here, any unlithified (or soft) sediments display a non-linear stress strain relationship, meaning elastic deformation induces particulate flow processes such as grain sliding/rolling, a disaggregation of grain fabric and pore dilation that cannot be restored (Jones, 1994, Bense *et al.*, 2003). The crushing of grains (cataclasis) is possible at deeper depths, in conjunction with particulate flow (Bense *et al.*, 2003). Faulting at deeper depths is often characterised by cataclastic processes resulting in the presence of fault breccia and/or gouge.

The change from particulate flow to cataclastic processes at ~1km depth likely occurs gradually, with a transition zone where, for example, small or weaker grains break under pressure conditions but larger, and stronger, grains continue to deform by particulate flow (Bense *et al.*, 2003), sometimes called facilitated or dependant particulate flow (Borradaile, 1981; Rawling and Goodwin, 2003). Therefore, multiple deformation processes and deformation features can operate simultaneously in mixed zones and deformation processes should not be assumed to operate in isolation at these depths. Furthermore, major seismic events (e.g., earthquakes) that cause surface ruptures can result in cataclastic processes occurring at shallow depths (Cashman, *et al.*, 2007; Doan and Gary, 2009; Balsamo and Storti, 2011). Conversely, fluid overpressure where

sediments are rapidly subsiding can reduce rock strength and cause particulate flow processes to occur at depths >1km.

As faults can be several kilometres in length, and comprise of varying rock units, it is possible for different sections of faults to undergo different styles of deformation due to the mechanical and material properties of the host rock. The lithology present will depend on the geological history and current environment and surface processes. Therefore, different geological environments promote different structural features - which can affect the permeability of the fault, which influences fluid flow both across the fault and up-dip. To consider the effect of different geological environment, the proceeding sections present an overview of faulting and fluid flow in siliciclastic rocks (Section 2.4) and carbonate rocks (Section 2.5).

2.4 Siliciclastic hosted fault zones: controls, processes and fluid flow

Siliciclastic rocks are sedimentary rocks dominated by silicate minerals (e.g. quartz, feldspar, micas etc), with common types including sandstone, shale and conglomerate. The following subsections outline deformation features and alteration processes that occur in siliciclastic rocks, with an emphasis on shallow fault zone processes (Section 2.4.1). The impacts these features have on fluid flow is synthesised in Section 2.4.2.

2.4.1 Fault processes and features in siliciclastic fault zones

Both particulate flow and cataclastic processes produce particular and different deformation features. The deformation regime can be deduced from observation of these features. Particulate flow is the dominant deformation mechanism in poorly consolidated sediments, which are often found in the shallow subsurface, and produces key structural features, outlined in Section 2.4.1.1. Cataclastic processes are outlined in Section 2.4.1.2. Deformation bands are discussed in Section 2.4.1.3, as these can have both a particulate flow or cataclastic component. Other features, not related to deformation, which can influence the rock properties are presented in Section 2.4.1.4. Table 2-2 summarises the main mechanisms and controls on rock properties in fault zones and which processes they are associated with, with proceeding sections and figures outlining these processes in detail.

Table 2-2 – Mechanisms/controls on rock properties in fault zones, key processes and resulting features (adapted from Bense et al., 2013).

Mechanism/Control	Process	Features
Particulate flow	Grain rolling, sliding	Bands (e.g. Disaggregation bands, dilation bands, sand smear)
		Sediment mixing and dilation
Cataclasis	Fracturing, brecciation, grain crushing	Shear fractures, joints
		Breccias

		Cataclastic deformation bands
Lithology (% clay)	Phyllosilicate smearing	Phyllosilicate bands or clay smear
Diagenesis	Fluid flow controlled dissolution and cementation	Veins, concretions and localised precipitation
Fault movement/reactivation	Fault growth	Relay ramp, segment boundaries, asperities, juxtaposition of lithologies at fault zone.

2.4.1.1 Particulate flow

Disaggregation zones have been defined as a zone in which faulting occurs and there is no grain size reduction (low effective stress), with throws on the millimetre to centimetre scale (Sperrevik *et al.*, 2002). Therefore, there remains a homogeneous structure which is like that of the host sediment. Disaggregation zones usually do not create barriers to fluid flow (Sperrevik *et al.*, 2002).

In disaggregation zones, deformation likely occurred because of particulate flow (Borradaile, 1981). Particulate flow has been suggested as the dominant deformation mechanism of faults at shallow depths, particularly depths <1km. At these depths, particulate flow is the dominant deformation mechanism compared to cataclasis (Bense *et al.*, 2003).

Disaggregation zones typically occur in clean (low clay-content, <10%) sandstones (Figure 2-12) with high porosity, where the grains roll past each other (without crushing, or cataclasis) and cause a pore dilation (opening) and disaggregation of grain fabrics (Fulljames *et al.*, 1997). This is because these zones do not contain enough phyllosilicates (e.g., micas) to induce porosity reduction either by induced mixing or pressure solution (Fisher and Knipe, 1998). Therefore, particulate flow faults are not typically seen as impermeable structures (Fulljames *et al.*, 1997) as the fault gouge has

properties similar to the surrounding matrix. Conversely, cataclastic processes typically result in a fault gouge with a reduced hydraulic conductivity (Bense *et al.*, 2003).

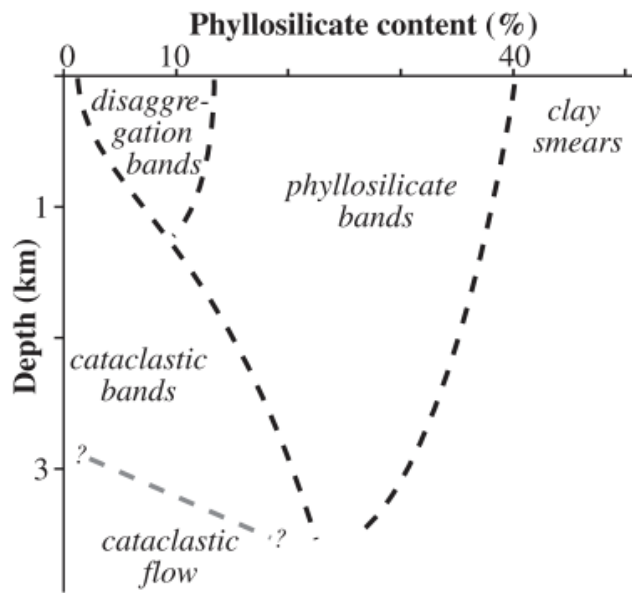


Figure 2-12– Deformation band type in relation to depth and phyllosilicate content. Boundary transitions are gradual (Fossen *et al.*, 2007).

There are examples of particulate flow in New Mexico (Rawling *et al.*, 2001; Rawling and Goodwin, 2003) and Greece (Loveless *et al.*, 2011), as well as sandbox experiments that show grain deformation via particulate flow in ring shear experiments (Mandl *et al.*, 1977) and in normal faulting experiments (McClay and Ellis, 1987).

2.4.1.2 Cataclasis

Cataclasis is the processes by which a rock is deformed by fracturing or crushing (Sibson, 1977), resulting in cataclastic rocks (e.g. cataclastite, breccia, gouge). This occurs when there is high strain during fault zone movement or can occur due to impact events (e.g. meteorites) (Blenkinsop, 2000; Ruzucka *et al.*, 2005; Pittarello *et al.*, 2015).

There are multiple classifications of cataclastic fault rock types, based on the original work of Sibson (1977). Figure 2-13 shows a common classification matrix.

		Non-foliated	Foliated	
>30% large clasts (>2 mm)	75 to 100% large clasts (>2 mm)	Crackle breccia		
	60 to 75% large clasts (>2 mm)	Mosaic breccia		
	30 to 60% large clasts (>2 mm)	Chaotic breccia		
<30% large clasts (>2 mm)	Incohesive		Fault Gouge	
	Cohesive	Glass or devitrified glass	Pseudotachylyte	
		0 to 50% matrix (<0.1 mm)	Protocataclasite	protomylonite
		50 to 90% matrix (<0.1 mm)	(meso)cataclasite	(meso)mylonite
		90 to 100% matrix (<0.1 mm)	Ultrocataclasite	Ultramylonite
		Pronounced graub growth		blastomylonite

Figure 2-13 – Fault rock classification (from Woodcock and Mort, 2008).

2.4.1.3 Deformation bands

There are four main types of deformation bands (Figure 2-14). The depth at which deformation bands form, as well as the rock type and geochemical processes will control which type of deformation bands form.

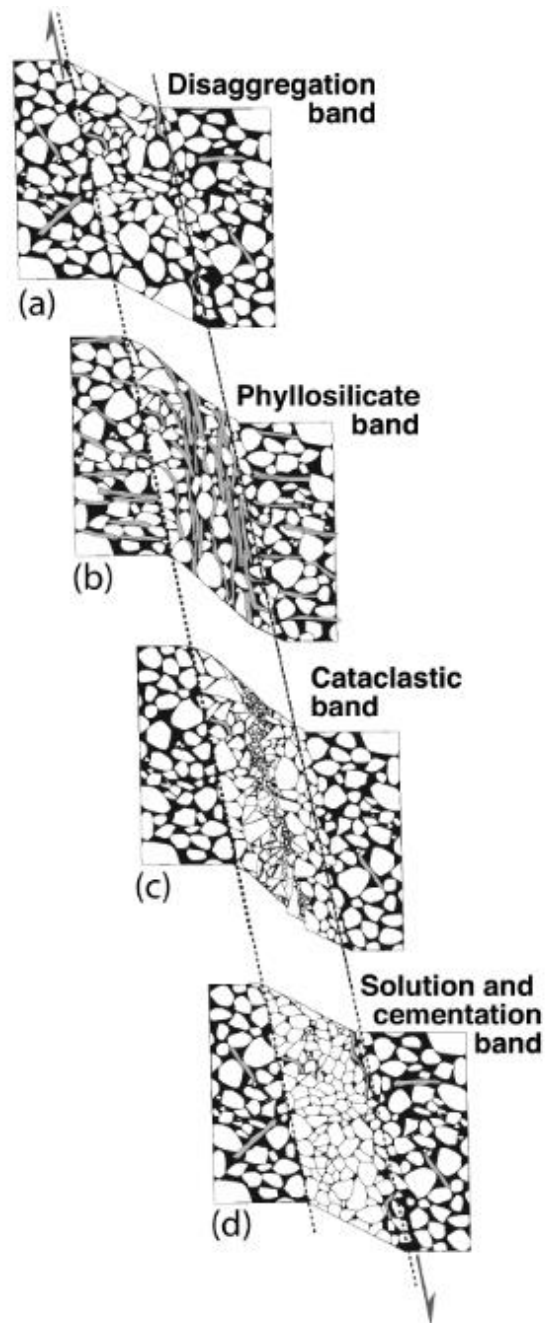


Figure 2-14 – Types of deformation bands based on their deformation mechanism (Fossen et al., 2007).

Furthermore, the burial and uplift history (Figure 2-15) of the rock can influence rock properties (e.g., permeability).

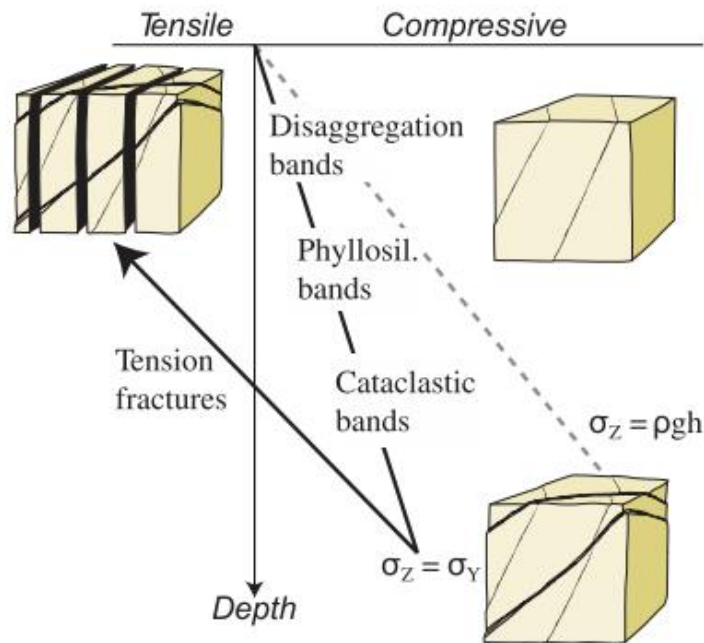


Figure 2-15 – Burial and uplift history for a sandstone. During uplift, sandstone enter the tensile region which can result in tension structures forming (Fossen *et al.*, 2007).

This means deformation bands can occur due to both particulate flow and cataclasis. Disaggregation bands are near surface deformation bands, which can result in a porosity change (either increase or decrease) depending on the dominant component (Fossen *et al.*, 2007), either dilational (increased porosity) or compactional (decreased porosity). In most cases, the permeability and porosity contrasts are low and fluid flow is not greatly influenced (Fossen *et al.*, 2007), however disaggregation bands can focus fluid flow (Bense *et al.*, 2003; Balsamo *et al.*, 2008). However, when particulate flow processes (e.g., disaggregation bands) cause mixing of different types of unlithified sediments, at both the bed and grain scale, this results in a more poorly sorted sediment mixture compared to any individual sediment bed (Bense *et al.*, 2013). Tectonic mixing of sediment in fault zones typically causes permeability reduction due to increasing heterogeneity (Heynekamp *et al.*, 1999; Faereth, 2006; Rawling and Goodwin, 2006; Balsamo and Storti, 2011). Heynekamp *et al.*, (1999) examined mixing in the Sand Hill fault zone (New Mexico, USA) and record a permeability reduction of up to six orders of magnitude. Permeability anisotropy can occur in fault zones due to rotation of sediment grains (e.g., due to alignment with fault dip). This causes increased tortuosity of fluid flow paths (see Section 2.1.2 and 2.1.3) and a reduction in permeability across the fault

of up to two orders of magnitude compared to along fault fluid flow (Arch and Maltman, 1990).

At deeper depths, deformation bands (e.g., shear deformation bands) can form cataclastic bands (crushed material, e.g., fault gouge) often with a lower porosity and a reduced hydraulic conductivity (Bense *et al.*, 2003). Although these typically occur at depths >1km, there have been some cases where these processes have been found to occur within the shallow subsurface (Cashman and Cashman, 2000; Rawling and Goodwin, 2003; 2006; Caine and Minor; Balsamo and Storti, 2010). This shows the variability of deformation bands and highlights that a simple linear model of deformation band evolution cannot always be assumed. Furthermore, in examples of shallow depth cataclastic bands these would lower porosity and thus would have an impact on fluid flow. The influence of cataclastic deformation bands has been analysed through sub-core scale studies which have shown that cataclastic deformation bands reduce both porosity and permeability – meaning they can act as fluid barriers in the subsurface (Romano *et al.*, 2020).

At deeper depths, deformation bands can develop both in the damage zone of faults (Shipton and Cowie, 2001; 2003; Fossen *et al.*, 2007) and in the process zones (Ballas *et al.*, 2015) meaning they can affect fluid flow by lowering permeability. In cases where dilational porosity increase later undergoes cementation (e.g., Du Bernard *et al.*, 2002) or in phyllosilicate bearing sandstones (e.g., Fisher and Knipe, 2001), the porosity and permeability can decrease sufficiently from the host rock and result in reduced fluid flow. Different types of deformation bands can have varying effects on fluid flow, so efforts to characterise the type of band and kinematics are important (Figure 2-16).

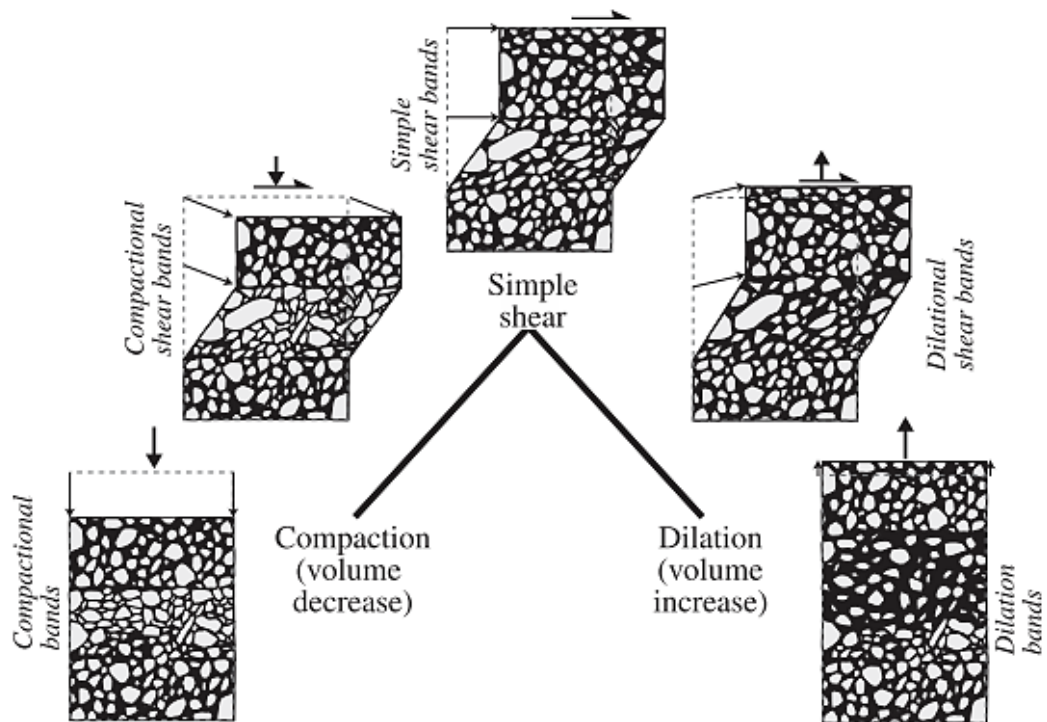


Figure 2-16– Kinematic classification of deformation bands (Fossen *et al.*, 2007).

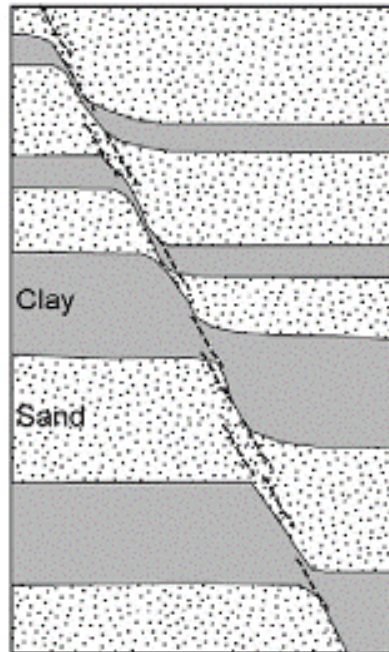
2.4.1.4 Other features influencing rock properties in siliciclastic fault zones

Clay smearing occurs where clay or shale layers are present in a fault zone. During deformation, these layers can be dragged along a fault plan resulting in a smear (Smith, 1980; Fulljames *et al.*, 1997; Bense *et al.*, 2003). This is common in sandstones with a clay percentage that is >40% (Weber *et al.*, 1978). This can occur in shallow fault zones but is not limited to them.

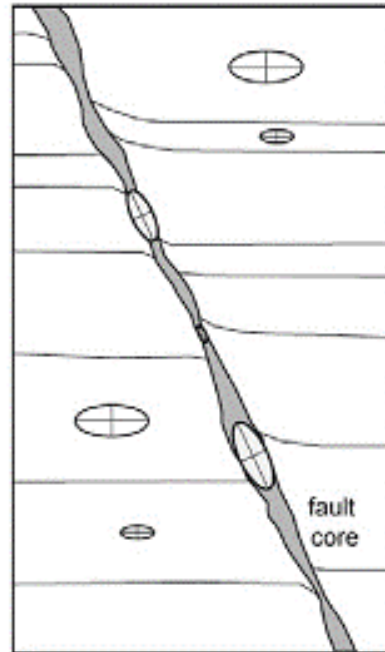
Where clay or shale smearing occurs, this typically results in a strong reduction in effective hydraulic conductivity of a fault zone (Bense *et al.*, 2003). Clay smearing has been extensively studied as it can provide an effective fluid seal (Yielding *et al.*, 1997) and block across fault fluid flow (Bense and Van Balen, 2004), which can cause reservoir/aquifer compartmentalisation (Bense *et al.*, 2013). As fault displacement increases clay and sand smear develop a layered structure (Figure 2-17) which develops a strongly anisotropic fault core (Bense and Person, 2006).

Unlithified siliciclastic rock

Fault zone architecture



Permeability structure



 permeability ellipse

 Dissaggregation zones and phyllo-silicate framework bands

Figure 2-17 – Fault permeability structures in soft sediments deformed at shallow depths (Bense *et al.*, 2013).

In these examples, the sand seams will have greater permeability than clay smear meaning the anisotropic nature of the fault will create a combined conduit-barrier system (Loveless *et al.*, 2011; Bense *et al.*, 2013). Flow parallel to the fault dip is much greater, due to the disruption of the sedimentary layering, compared to flow laterally across the fault core and disaggregated sediments. There are examples in which shale becomes entrained in the fault core, e.g., Colorado Plateau (Davatzes and Aydin, 2005; Shipton *et al.*, 2006), accompanied by complex deformation band networks which likely create an effective fluid barrier (Rawling *et al.*, 2001).

Diagenetic processes vary with depth, and the distinction between surface processes and diagenesis (at the near surface) and diagenetic processes and metamorphism are unclear, but it is generally agreed that diagenetic processes occur from 0-250°C and from up to 250MPa (c). Diagenetic processes vary with geological setting and lithology, but processes such as mineral precipitation can cause cementation of fault planes which consequently results in a partial or complete loss of porosity (Knipe, 1993;

Leveille *et al.*, 1997). Cementation also increases rock strength, encouraging more cataclastic deformation processes compared to particulate flow deformation processes. Examples of diagenetic effects on fault rocks include the Moab fault Zone (Utah, USA) where multiple precipitation episodes are recorded (Chan *et al.*, 2000). Rocks that have been buried to deeper depths are more likely to have seen multiple stages of diagenesis as temperature and pressure have increased (Montañez and Crossey, 2018). Therefore, diagenetic processes would have a more profound influence on the mechanical and hydraulic properties of deep faults, due to the time these faults would have spent in the subsurface at different pressure and temperature conditions.

2.4.2 Faulting and fluid flow in siliciclastic fault zones

The porosity of the host rock influences the deformation mechanisms. For example, fine-grained low porosity sediments such as silt and clay tend to deform via discrete fault surfaces whereas more porous materials (e.g., sands) would deform via tabular deformation bands. In high porosity sediments (e.g., gravels), faults are typically diffuse, occasionally showing a preferred orientation indicating the fault trace (Kim *et al.*, 2004; Brandes and Tanner, 2019).

Juxtaposed units of different hydraulic conductivity can result in barriers to fluid flow through the fault zone. Deformation processes (e.g., clay smearing or grain scale mixing between different sediments like clay or sand) can also reduce the overall hydraulic conductivity (Heynekamp *et al.*, 1999; Bense *et al.*, 2003). Therefore, the deformation processes that occur will lead to an enhanced fault zone permeability or a reduced permeability (Table 2-3).

Table 2-3 – Processes that impact the permeability of poorly lithified fault zones (adapted from Bense *et al.*, 2013).

Process	Feature	Permeability	Reference
Particulate flow	Disaggregation bands, dilation bands, sand smear	Enhanced	Du Bernard <i>et al.</i> , (2002), Bense <i>et al.</i> , (2003), Exner and Graseman (2010)

Particulate flow	Sediment mixing and dilation	Reduced	Heynekam <i>et al.</i> , (1999), Rawling and Goodwin (2006)
Fracturing	Shear fractures, joints	Enhanced	Balsamo <i>et al.</i> , (2010)
Brecciation	Breccias	Enhanced	Caine and Minor (2009)
Phyllosilicate smearing	Phyllosilicate bands or clay smear	Reduced	Fulljames <i>et al.</i> , (1997)
Cataclasis	Cataclastic deformation bands	Reduced	Sigda <i>et al.</i> , (1999), Sigda and Wilson (2003), Cashman and Cashman (2000)
Fluid flow controlled dissolution and cementation	Veins, concretions and localise precipitation	Enhanced or reduced	Mozley and Goodwin (1995), Balsamo <i>et al.</i> , (2013)
Fault growth	Relay ramp, segment boundaries, asperities, juxtaposition of lithologies at fault zone.	Enhanced or reduced	Rawling and Goodwin (2006), Loveless <i>et al.</i> , (2011)

In general, particulate flow (shallow) deformation processes usually do not create barriers to fluid flow (Sperrevik *et al.*, 2002). This is because these zones do not typically contain enough phyllosilicates (e.g., micas) to induce porosity reduction either by induced mixing or pressure solution (Fisher and Knipe, 1998). Therefore, shallow fault zones in well sorted clean sediments are typically dominated by particulate flow deformation processes and are not considered to be impermeable structures because the fault core has properties similar to the surrounding matrix (Fulljames *et al.*, 1997; Pei, *et al.*, 2015).

The overall effect on fluid flow around near surface fault rocks will depend on the porosity and permeability changes induced by fault processes, which themselves governed by a combination of fault depth, local geology, sediment lithification/compaction state and the dominant deformation processes acting within the fault zone. Of these factors, geology exerts the most control on fluid flow as the geology (e.g., the phyllosilicate content of sandstones) controls the features that develop (e.g., phyllosilicate deformation bands, clay, and shale smear), as well as the stress conditions at time of faulting and the maximum temperature reached in the fault zone after faulting (Yielding *et al.*, 2010). Both the host rock properties and geological deformation processes influence the permeability structure and thickness of fault zones, consequently controlling fluid flow parallel to and lateral to fault dip (Bense *et al.*, 2013).

The typical conceptual model for fluid flow in fault zones in siliciclastic rocks suggests that the fault core and fault damage zones will have contrasting mechanical and hydraulic properties (Faulkner *et al.*, 2010). The fault core typically has low permeability, due to the increased phyllosilicate content and smearing processes, whereas the fault damage zone has higher permeability (than the host rock) due to open rock fractures, if not cemented (Caine *et al.*, 1996; Faulkner and Rutter, 2001; Guglielmi *et al.*, 2008; Cappa, 2009). Figure 2-18 shows hypothetical fault zone permeability models.

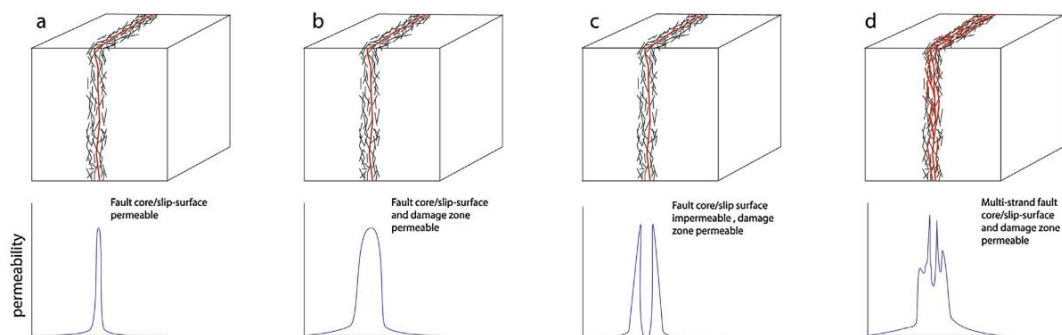


Figure 2-18 – (a) fault core (red line) is permeable and acts as a fluid flow conduit. (b) fault core and damage zone (black lines) are both permeable and act as a fluid flow conduit. (c) The fault core is impermeable, but the surrounding damage zone is permeable and acts as a fluid flow conduit. (d) heterogenous fault zone systems that leads to a complex multi-strand permeability system (Bond *et al.*, 2017).

Vertical (fault-parallel) fluid migration relies primarily on fracture permeability in the surrounding damage zone, which can provide fluid pathways even in otherwise impermeable units (Eichhubl *et al.*, 2009; Dockrill and Shipton, 2010). However,

diagenetic processes (e.g., cementation) can result in decreased permeability around the fault zone by infilling fractures (Bense *et al.*, 2003; Davatzes and Aydin, 2005) and consequently lower vertical fluid migration. In poorly consolidated shallow sediments, the fault damage zone often contains disaggregation bands which replace fracture networks.

The overall impact of a fault on lateral fluid flow can be described by considering any juxtaposed units across a fault zone (Haneberg, 1995; Yielding *et al.*, 1997; Mailloux *et al.*, 1999) as well as the permeability and continuity of fault rock in the fault core, which is dependent on the host rock composition, shear strain and faulting mechanisms (e.g., deformation bands, clay smearing and processes occurring in the mixed zone) (Miocic *et al.*, 2020).

At shallow depths (<1km) geological processes impact hydrogeological processes more than hydrogeological processes impact geological processes – meaning that at shallow depths hydrogeological processes can be predicted from structural geologic data (Bense *et al.*, 2013).

2.5 Carbonate hosted fault zones: controls, processes and fluid flow

Carbonate rocks are sedimentary rocks dominated by carbonate minerals (e.g. calcite, aragonite, dolomite), with common types including limestone and dolostone. The following subsections outline fault processes that occur in carbonate rocks, with an emphasis on shallow fault zone processes (Section 2.5.1). The impacts these features have on fluid flow is synthesised in Section 2.5.2.

The models and understanding of porosity, permeability and fluid flow presented thus far have focused on clastic rocks. This understanding is not directly transferable to carbonate hosted fault rocks due to their deformation mechanisms (Willemse *et al.*, 1997; Kelly *et al.*, 1998; Mollema and Antonellini, 1999; Salvini *et al.*, 1999; Graham *et al.*, 2003; Agosta and Aydin, 2006; Tondi *et al.*, 2006) and pore types (e.g., vugs, molds, fractures and channels) (Wang 1997; Lucia 1999; Agosta *et al.*, 2007). Furthermore, there has been a lack of petrophysical data for carbonate fault rocks (Agosta *et al.*, 2007) and only since 2010 has research progressed significantly in this field.

The fault zone architecture model of a fault core surrounded by a fault damage zone has been shown to be broadly applicable to carbonate fault zones (Agosta and Kirschner, 2003; Storti *et al.*, 2003; Micarelli *et al.*, 2006). Fault damage zones in carbonates contain small faults, veins, fractures cleavage and folds, like siliciclastic rocks (Caine *et al.*, 1996). The fault core can be either a single, or multiple, slip surface(s) with a variety of lithologies (e.g., carbonate breccias, carbonate cataclasites, carbonate and shale gouges, secondary calcite cements, veins, and host rock lenses (Chester and Logan, 1987; Sibson, 1997; Mitchell and Faulkner, 2009; Bastesen and Braathen, 2010; Haines *et al.*, 2016).

Carbonate hosted-fault zones have additional structural elements. Examples include:

- faults cores with discontinuous lenses of fault rock, with various fabrics and petrophysical properties (Michie and Haines, 2016),
- fault zones that host a fracture splay zone, where fractures and subsidiary slip surfaces are generated at a point of strain accumulation. This relates to the mechanical stratigraphy imposed by lithofacies with different mechanical properties being juxtaposed (Michie *et al.*, 2014).

- fault zones with permeable deformation features (e.g., fracturing, fault breccia) which allow both horizontal (along) fault and vertical (up) fault fluid flow (Lee *et al.*, 1997; Matonti *et al.*, 2012)
- two further damage zone elements (Micarelli *et al.*, (2016):
 1. intensely deformed damage zone (IDDSZ), a dense connected fractures network
 2. weakly deformed damage zone (WDDZ), less frequent sub-vertical fractures

The architecture of carbonate hosted fault rocks controls how fault rocks form and are distributed. The architecture of carbonate fault zones, like siliciclastic fault zones, will vary between settings and not all architectural or structural elements will always be present (Michie *et al.*, 2014). Understanding how these features are generated in the host rock and the fault kinematics at play is important to predict the influence these features will have on fluid flow (Cooke *et al.*, 2018).

2.5.1 Fault processes, porosity and permeability in carbonate rocks

Fault processes in carbonate rocks differs from those observed in siliciclastic rocks due to the ability of carbonate minerals to undergo deformation by physio-chemical and crystal-plasticity processes (Cooke, 2019). The deformation mechanisms mostly commonly documented in carbonates include grain crushing, rotation and translation, cementation, pressure solution, peloid disintegration and smearing (Tondi *et al.*, 2006; Rath *et al.*, 2011; Cilona *et al.*, 2012; Antonellini *et al.*, 2014; Rotevatn *et al.*, 2016; Kaminskaite *et al.*, 2019). These deformation mechanisms influence the porosity and permeability of carbonate hosted fault rocks. The primary deformation mechanisms in carbonates rocks are controlled by the lithology of the host rock (Cilona *et al.*, 2019), therefore this deformation is dependent on the host rock texture, porosity, and pore connectivity. Other factors such as the mineralogy, grain size, burial depth, fault properties, diagenesis and fluid histories also influence deformation in carbonate rocks (Cooke, 2019). This makes it clear that a good understanding of the host rock lithology is crucial for understanding how the porosity and permeability will be affected by faulting, this allowing a prediction of the effect faulting will have on fluid flow.

2.5.1.1 *Fault processes in lower porosity carbonates*

Fault rocks in low porosity carbonates are the most well documented. In tight carbonate rocks which are well cemented (low porosity), deformation typically is focused on localised fractures (Dunn *et al.*, 1972; Rutter and Hadzadeh, 1991). This is because on a macro scale the rock deforms in a brittle manner due to the cementation of the grains (Cello *et al.*, 2001; Ghisetti *et al.*, 2001; Rawling *et al.*, 2001; Agosta and Kirschner, 2003; Agosta *et al.*, 2008; Kim and Sanderson, 2010; Molli *et al.*, 2010). Localised dilatational features such as joints, veins and stylolites form (Agosta *et al.*, 2009; Agosta *et al.*, 2015). Fluids can play an important role in the deformation process both chemically (solution transfer at grain scale) and physically (reduced rock strength, raised pore pressure) (Fitz-Diaz *et al.*, 2011).

The petrophysical properties of fault rocks that originate in low porosity carbonates is highly dependant on the degree of diagenesis. Porosity and permeability both display and increase when the fault rock is uncemented, but when cemented the permeability could be reduced relative to the host rock (Agosta *et al.*, 2007; Cooke, 2019). The porosity and permeability values in lower porosity carbonates tend to increase as you move from the host rock into the fault zone, until you reach the fault core where there is a decrease in the inner fault core around the principal slip surface (Agosta *et al.*, 2007; Michie *et al.*, 2020). This decreased permeability in the inner fault core is often like that of the host rock (Michie *et al.*, 2020). Michie *et al.*, (2018) noted that in some instances fault core permeability does increase, highlighting the highly variable nature of faulting in carbonate rocks.

2.5.1.2 *Fault processes in higher porosity carbonates*

In poorly cemented carbonate rocks, the grains have few inter-granular contacts favouring granular-relatively-low-cohesive behaviour of rocks. Faulting in these rock types results in a porosity reduction (typically via compaction, but also by dilation, or shear-enhanced compaction) due to the strain being accommodated by the pore space. Processes such as pressure solution (Rutter, 1983; Groshong, 1988), pore collapse, grain rotation and grain fracturing can all occur because of compaction (Cooke, 2019).

Granular carbonate rocks favour the formation of deformation bands (Tondi *et al.*, 2006; Rath *et al.*, 2011; Tondi *et al.*, 2012; Cilona *et al.*, 2014; Rotevatn *et al.*, 2016). Like in

siliciclastic rocks, carbonate rocks exhibit different types of deformation bands (Tondi, 2007; Antonellini *et al.*, 2014; Rotevatn *et al.*, 2016; Kaminskaite *et al.*, 2019). Dilation bands form when rocks with low cohesive strength deform via granular flow (sediment disaggregation) under tensile stress (Du Bernard *et al.*, 2002). When this process is accompanied with compaction, compaction bands can form. When shear stress is applied, grains will begin to move past each other (offset) and cataclasis often occurs forming dilatant shear bands (Fossen *et al.*, 2007; Cooke, 2019).

In highly porous carbonates, where throws are larger than the deformation band scale, the mechanisms of deformation are less well documented (Cooke *et al.*, 2018; Michie *et al.*, 2020).

2.5.1.3 Permeability in carbonate fault zones

Carbonates exhibit highly variable (by several orders of magnitude) fault rock permeability, even over small areas along fault strike (Miche and Haines, 2016; Cooke *et al.*, 2019). Michie *et al.*, (2020) observed that intrinsic factors (e.g., host rock texture and porosity) are the primary control on fault rock development and deformation style, thus controlling the fault rock permeability. Additionally, although they note that burial depths at the time of faulting can influence how the rock deforms, this is not seen to be a major contributing factor in faults with displacements >1m (Michie *et al.*, 2020).

Carbonate faults, especially in heterogeneous facies, are structurally complex and exhibit variable deformation along strike. Michie *et al.*, (2021) documented the variation in permeability along-strike of carbonate hosted fault rocks and found that the heterogeneity of the displaced rocks and juxtaposition type were the overriding controls on fault permeability. This is expected as bulk fault permeability is generally a function of structural complexity (Cooke, 2019). Consequently, faults in carbonates with juxtaposed rock types with similar properties are less likely to be of low permeability, compared to juxtaposed heterogeneous units (Cooke, 2019). Shallowly buried carbonate rocks tend to have the most amount of complexity (Matonti *et al.*, 2012; Cooke *et al.*, 2019).

The permeability of fault rocks in carbonates will determine the ability for fault zones to act as seals or conduits to fluid flow. Solum and Huisman (2017) assessed the fault seal potential in carbonate rocks. They presented multiple examples of both static and

dynamic fault seals in carbonate reservoirs and aquifers and outlined the mechanisms of how fault rocks seals occur in carbonate rocks (e.g., cataclasis, cementation, incorporation of clays or anhydrites, dynamic recrystallisation and pressure solution). They concluded that there was much more work to be done to understand the commonality of each of these mechanisms (Solum and Huisman, 2017).

2.5.2 Faulting and fluid flow in carbonate fault rocks

Like in siliciclastic rocks, knowing the host rock properties allows a better prediction of fault processes and consequently their effect on porosity and permeability (Bense *et al.*, 2013; Cilona *et al.*, 2019). However, to date, there is a surprising limitation on the available data in which the porosity and permeability of carbonate rocks have been quantified (Michie *et al.*, 2020). This makes predicting fluid flow patterns challenging and an area which requires further research in respect to carbonate hosted fault zones.

2.6 Implications for subsurface technologies and research gaps

Shallow fault zones have been studied in the Gulf of Corinth (Loveless *et al.*, 2011) the Lower Rhine Embayment (Bense *et al.*, 2003), the Rio Grande Rift basin (Heynekamp *et al.*, 1999; Caine and Minor, 2009), southern Italy (Balsamo and Storti, 2010), and Austria (Exner and Grasemann, 2010). Studies have found shallow fault zones in poorly consolidated sediments that cut aquifers can act as hydraulic barriers which prevent fluid flow across faults (Grauch *et al.*, 2001; Minor and Hudson, 2006), leading to aquifer compartmentalisation (Loveless *et al.*, 2011). However, others (e.g., Rawling *et al.*, 2001; Bense *et al.*, 2003; Caine and Minor, 2009) suggest that shallow fault zones may act as preferential fluid conduits allowing fluid flow along faults, which is supported by flow tracers, numerical groundwater modelling and hydrogeological data (Bredehoeft *et al.*, 1982; Person *et al.*, 2000; Heffner and Fairley, 2006; Bense and Person, 2006; Bense *et al.* 2008). These studies provide useful insights into shallow fault zone processes for groundwater flow and learnings should be transferable to subsurface storage technologies and the design of effective MMV systems.

There are also multiple fault studies in shallow fault zones in the paleoseismological literature. These studies typically do not focus on the hydraulic properties of the fault zone and instead consider the location, timing, and size of past earthquakes (e.g. McCalpin and Nelson, 2009). Fault zone structures are mainly mapped to identify sedimentary packages that can be dated to bracket surface rupturing events.

For geological porous media storage, there have been numerous studies indicating that faults play a key role in the migration of geofluids (e.g., CO₂) in the subsurface (see Section 2.1.3 and sections within). Fault parallel migration of CO₂ has been observed in fault damage zones (e.g., Annunziatellis *et al.*, 2008; Gilfillan *et al.*, 2011, Kampman *et al.*, 2012, Burnside *et al.*, 2013, Bond *et al.*, 2017, Miocic *et al.*, 2019a). Cases of across fault migration have also been recorded (e.g., Shipton *et al.*, 2004; Dockrill and Shipton, 2010). Furthermore, natural analogue studies of natural CO₂ reservoirs indicate that leakage of CO₂ reservoirs is usually due to fault related leakage (Miocic *et al.*, 2016; Roberts *et al.*, 2017; Miocic *et al.*, 2020). However, most studies to date have focused on deeper faulting, within the storage complex or in the overburden (e.g. Burnside *et al.*, 2013).

2.6.1 *Fluid flow and leakage*

Key to ensuring retention of materials in the subsurface is the storage security of the reservoir or store in which the materials reside. Faults in the shallow subsurface (<1km) in poorly consolidated or unlithified clean siliciclastic sediments can act as baffles or conduits to geofluids (e.g., hydrocarbons, CO₂, H₂) as the deformation processes associated with this type of geology at these depths favours the retention, or enhancement of host rock permeability.

Examples in Italy of faults acting as effective fluid conduits for CO₂, even when not directly connected to the subsurface reservoir, highlight the importance of near surface faults that have permeability (either from host rock or from fault processes that enhance permeability) (e.g., Ascione *et al.*, 2014; Roberts *et al.*, 2014; Roberts *et al.*, 2017). Where near surface fault rocks either retain host rock permeability or have enhanced permeability due to deformation processes (e.g., particulate flow, disaggregation, dissolution, or fracturing), they could act as fluid conduits to the surface. Therefore, it should not be assumed that near surface fault systems are potential fluid migration baffles in the overburden of a geological storage site.

Understanding the fluid flow processes and any role of shallow fault systems acting either as a barrier or conduit to fluid flow (and potentially surface leakage) should consider near surface geological processes and fault rock types. This will require some characterisation of the near surface geology (Roberts *et al.*, 2014; Roberts *et al.*, 2019b).

2.6.2 *Site selection and monitoring*

Site selection processes should involve a characterisation of the geology and structural features of the near surface (upper 1km), as well as traditional characterisation of the structure and characteristics of the reservoir at depth (Roberts *et al.*, 2017). This has already been suggested to inform monitoring programmes from analogue studies of natural CO₂ seeps, as the near surface geology is important for seep location and expression (Roberts *et al.*, 2014) which determines which monitoring tools are appropriate at the site, and where monitoring programmes should target.

Near surface site characterisation will ensure that any near surface faults can be recorded, characterised, and assessed for their potential to act as fluid pathways. Crucial to this characterisation is an understanding of the host rock lithology and fault

rock types, as these will influence the dominant geological processes. In turn, this will influence the dominant hydrogeological processes which occur, as at shallow depths this is predominantly controlled by geology (Bense *et al.*, 2013).

Many of the features that create fluid conduits (e.g., fracture networks in fault damage zones) are below seismic resolution. Therefore, the methods used to detect faults may not accurately represent the subsurface features that pose a leakage risk (e.g., Bond *et al.*, 2017). Roberts *et al.*, (2019a) used a geospatial approach to analyse crustal fluid flow and found that although macrocrustal fluid flow is controlled by deep extensional and compressional feature, near surface (shallow) fluid flow is governed by smaller scale features and hydrogeological factors. This highlights the need to have an appropriately designed programme of surface characterisation and surface monitoring for subsurface storage sites, as different processes control fluid flow compared to regional scale.

Near surface faults that have been characterised to be permeable, particularly those with a vertical (fault parallel) permeability (e.g., permeable damage zone), should be monitored at the surface as potential leakage outlets. These more permeable pathways will likely be the first natural indication of leakage from the storage site that can be measured at the surface. Furthermore, this would allow an estimate of the leakage rate and an assessment could be carried out to determine if this leakage is acceptable for the purpose of the store. However, impermeable fault zones are also important for fluid flow, as they will also channel fluid flow - but differently. Regardless of the mechanism of migration from the storage system, and regardless that shallow fault zones might not intersect the storage complex at all, shallow fault zones could channel fluids (whether as conduits or barriers) and therefore could influence fluid distribution.

2.6.3 Research gaps

This literature review shows that fault zones are important for subsurface fluid flow, as they act as both barriers and conduits to fluids. Evidence from the literature shows that there have been fewer studies on shallow fault zones with further research required to understand shallow fault zone process and the effect these have on rock properties. Understanding of shallow fault zone processes varies with lithology: siliciclastic rocks are better understood compared to carbonate rocks, but there remains significant scope for further work for both in determining how fault zone processes vary with depth, lithology, and the influence of subsurface and surface processes. As subsurface

technologies (e.g. porous media storage) scale-up there is a need to expand and utilise all available subsurface storage sites – which means characterising the overburden of storage sites and understanding how shallow fault zones effect fluid flow will be crucial to deploy effective MMV strategies.

This thesis contributes to further understanding of these key research gaps, and opens up new questions for future research.

Chapter 3 Site overview: In-Situ Lab (WA, Australia) and Otway International Test Centre (VIC, Australia)

This chapter presents an overview of the two field experiments studied in this thesis: the In-Situ Lab (Western Australia, Australia) (Section 3.1) and the CO₂RC Otway International Test Centre (OITC) (Victoria, Australia) (Section 3.2). Both have, as part of their experimental design, cored through a shallow fault zone to observe the interactions between injected CO₂ and the fault zone. Neither site investigation has so-far included a detailed study of the deformation across either fault zone, which is why the operators were supportive in collaborating in this PhD research.

For each site, the scope, objectives and set-up are first explained, before the regional geology and details of the fault of interest are described. Results and discussion are presented, with areas for further work highlighted.

3.1 In-Situ Lab, Harvey (Western Australia, Australia)

3.1.1 *In-Situ Lab: Operation, location, scope and infrastructure*

The In-Situ Laboratory (In-Situ Lab) is a research site located near Harvey, a town around 125km south of Perth, Western Australia. The site aims to de-risk the commercial deployment of CCS in Australia. The Commonwealth Scientific and Industrial Research Organisation (CSIRO) developed In-Situ Lab between 2016-2019, using the resources and information gathered during the South West Hub CCS Project (2011-2015) (Figure 3-1). The South West Hub was originally set up to focus on assessing the CO₂ storage potential of the region, with the In-Situ Lab expanding the scope to include monitoring, experimental analysis and modelling. Partner institutions include the University of Western Australia, Curtin University, regional government department Western Australia (WA) Department of Mines, Industry Regulation and Safety (DMIRS) and federal government Department of Industry, Innovation and Science (DIIS). As such, this is a collaborative project bringing together teams from different industries to develop this field site.

The In-Situ Lab aimed to successfully instrument an existing well and demonstrate CO₂ injection. The purpose of releasing CO₂ into the F10 Fault was to understand how CO₂

migration is affected by fault zones in the shallow subsurface (Michael *et al.*, 2019; 2020).

The In-Situ Lab utilises four vertical wells: (Harvey-1 (drilled 2012) and Harvey-2, Harvey-3 and Harvey-4 (drilled 2015) and seismic data collected through both 2D and 3D surveys between 2010 and 2015 (Figure 3-1). The four boreholes cut four major rock formations, shown in Table 3-1. The Harvey-1 well cuts a fifth deeper horizon. There are additional monitoring and sampling wells around the Harvey-2 borehole at the In-Situ Lab site (e.g. ISL OB-1, ISL OB-2) (Figure 3-2), and nearby petroleum wells (e.g. Pinjarra-1). These monitoring wells were used to monitor the CO₂ injected into Harvey-2, with behind casing instrumentation (including geophones, electrodes, fibre-optic sensors for acoustics and temperature and pressure/temperature gauges). Another groundwater well near the fault zone was used for fluid sampling.

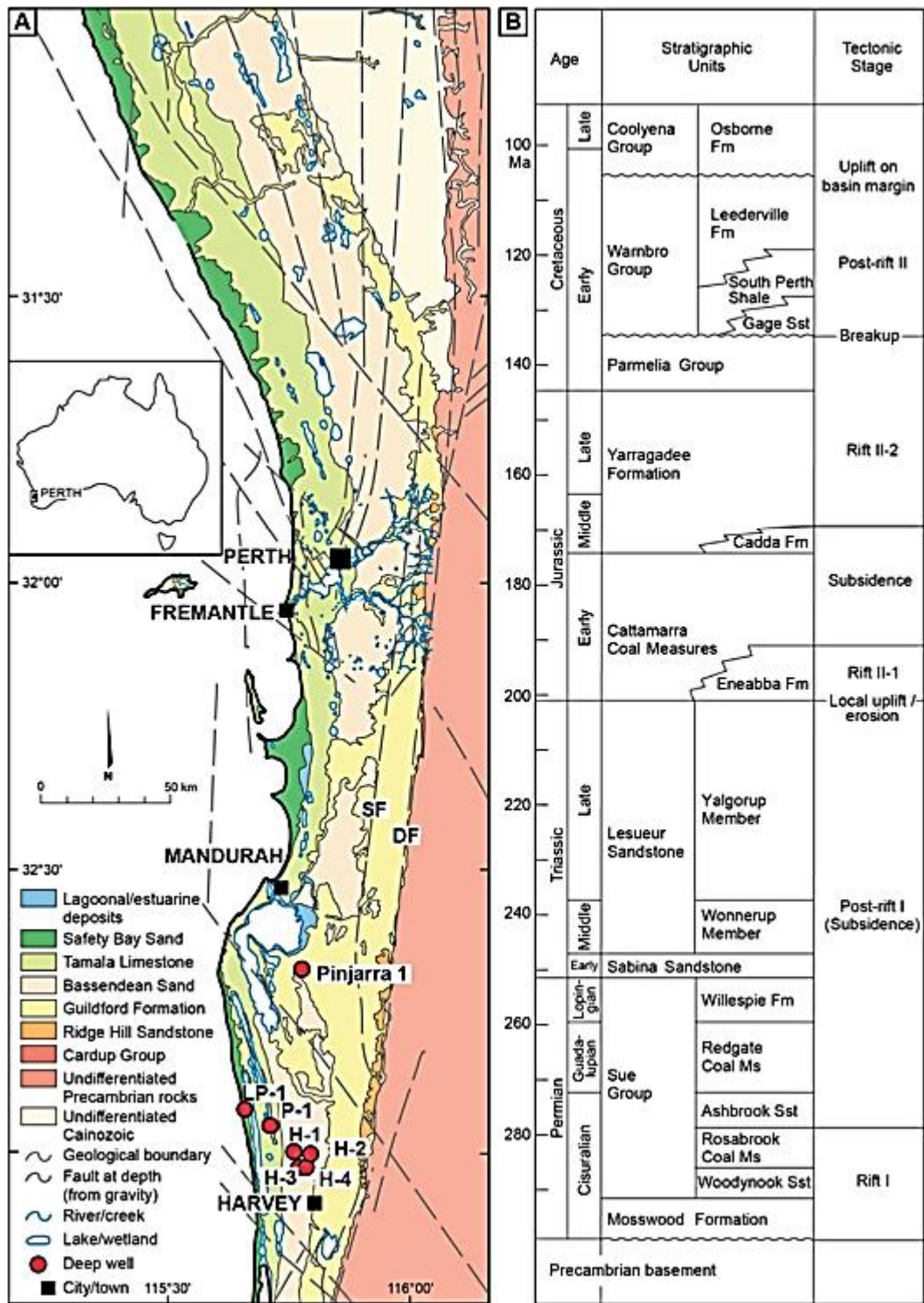


Figure 3-1 – A) Geological maps showing the location of the Harvey wells (H-1, H-2, H-3, H-4) and surrounding wells (Lake Preston-1 (LP-1), Preston-1 (P-1) and Pinjarra-1). B) Stratigraphy of the Perth Basin (from CSIRO, 2019). Inset shows location of the site within Australia.

Table 3-1- The location of each borehole at the In-Situ Lab, and depths that major rock formations were encountered. The formations were dated by palynology and boundaries recognised by breaks on wireline logs (Delle Piane et al., 2018).

	Age	Harvey 1	Harvey 2	Harvey 3	Harvey 4
Location E		385502.04	392052.65	387392.34	389946.08
Location N		6348947.56	6347141.74	6343895.95	6343842.51
Ground level datum (m)		19.1	15.4	20.2	15.9
Depth below ground level (m)					
Eneabba	E. Jurass.	250	135	245	165
Lesueur	L.-M. Triass.	704	419	741	1020
Yalgorup	L. Triass.	704	419	741	1020
Wonnerup	M. Triass.	1380	1245	1418	1579
Sabina	E. Triass.	2895			
	Total depth	2945	1350	1550	1802



Figure 3-2 – Aerial view of the ISL showing the Harvey-2 (Injection well, green) and surrounding groundwater (blue), monitoring (purple) and soil gas wells (beige) (Myers et al., 2020).

The Harvey-2 borehole was initially drilled as part of the South West Hub activities to constrain the depths of the Yalgorup and Wonnerup members, but later became the CO₂ injection well for the In-Situ Lab.

Research in Chapter 5 of this thesis focuses primarily on core from Harvey-2 and Harvey-3 wells. These wells offer a comparison of the same units and lithologies in each well (Table 3-1), but only the Harvey-2 well cuts the F10 Fault, and Harvey-3 does not (Figure 3-5 and Figure 3-6).

In February 2019, CSIRO injected 38t of CO₂ at ~340m depth into the Harvey-2 well which intersects the F10 Fault zone to assess how the CO₂ would interact with the fault zone and to test various MMV technologies (Michael *et al.*, 2019). Although the scope of the In-Situ Lab project changed through the project scoping phase due to logistical issues, the experiment was deemed to be successful. The experiment used a combination of approaches, including utilising the previous South-West Hub data, borehole and core characterisation, surface and subsurface monitoring and various modelling approaches. This has allowed the site to continue to be in operation and further experiments are being designed and planned. In early 2024, additional boreholes were drilled as part of future planned experiments, but data from these are still being processed at the time of completing this thesis.

The following sections explain the regional geology at the site (Section 3.1.2), with a focus on the F10 Fault zone (Section 3.1.3). Findings from the 2019 CO₂ injection experiment are summarised and areas for further work highlighted (Section 3.1.4). Details on the monitoring techniques deployed at the In-Situ Lab are summarised in Appendix 1.

3.1.2 Regional geology of the Perth Basin

The ISL is located in the Perth Basin (Figure 3-3), which extends 1300km north-south along the south-west margin of Australia (Olierook *et al.*, 2014a) and covers an area of around 100,000km²; 45,000km² onshore and 55,000km² offshore (Playford *et al.*, 1976).

The Perth Basin formed due to oblique rifting during multiple periods (Permian, Late Triassic to Early Jurassic and Middle Jurassic to Early Cretaceous) as part of the East Gondwana rift system (Playford *et al.*, 1976; Crostella and Backhouse, 2000) during the breakup of Australia and Greater India (Song and Cawood, 1999).

Southern parts of the basin saw deposition and rifting throughout the Cretaceous (Playford *et al.*, 1976; Marshall *et al.*, 1989; Spring and Newell, 1993, Quaofe *et al.*, 1994; Mory and lasky, 1996) – with inversion, erosion, strike-slip tectonics, and volcanism. Consequently, the Perth Basin has a complex structural architecture with multiple structural units that are the result of the later strike slip motion during Cretaceous rifting (Harris 1994).

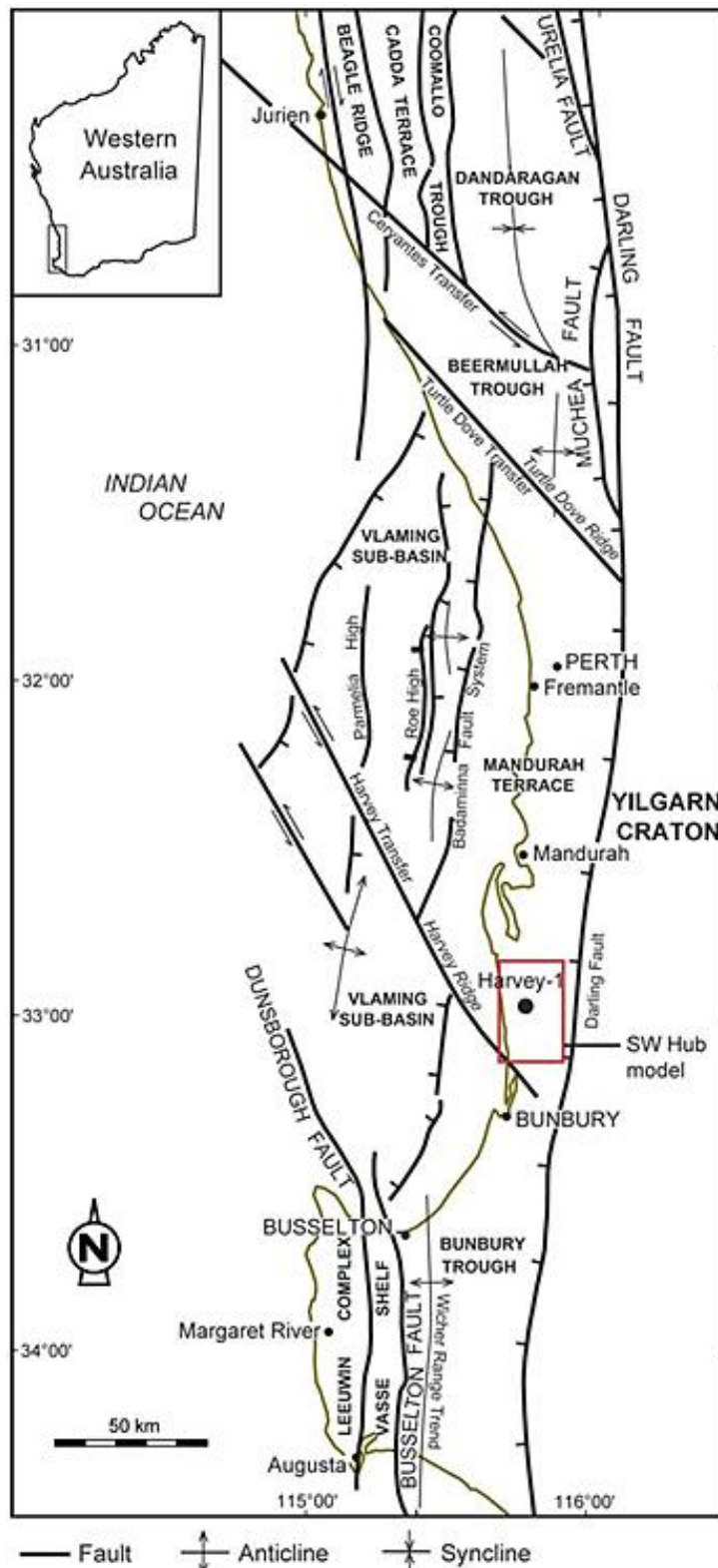


Figure 3-3 – Divisions of the Perth Basin. The basin can be subdivided into 3 main sections: northern (north of latitude 31°S), central (between latitudes 31°S and 33°S) and southern (south of 33°S). The beige/brown line represents the coastline. The red box indicates the location of the ISL (modified from Crostella and Backhouse, 2000).

The central and southern parts of the Perth Basin can be further divided into five structural units (Figure 3-3): Vlaming Sub-Basin (offshore), Mandurah Terrace (onshore and offshore), Berrmullah and Bunbury Troughs (onshore) and the Vasse Shelf (onshore). These structural units are separated from the Yilgarn Craton to the west by the north-south trending Darling Fault.

The In-Situ Lab sits in the southern Perth Basin, located on the southern end of the Mandurah Terrace, east of the offshore Vlaming Sub-Basin (Langhi et al., 2013; Delle Piane et al., 2018). The In-Situ Lab sits on the Harvey Ridge (Figure 3-3 and Figure 3-4), a north-west to south-east trending basement high (Crostellla and Backhouse, 2000) marked by the presence of the Harvey Transfer Zone (Delle Piane et al., 2018).

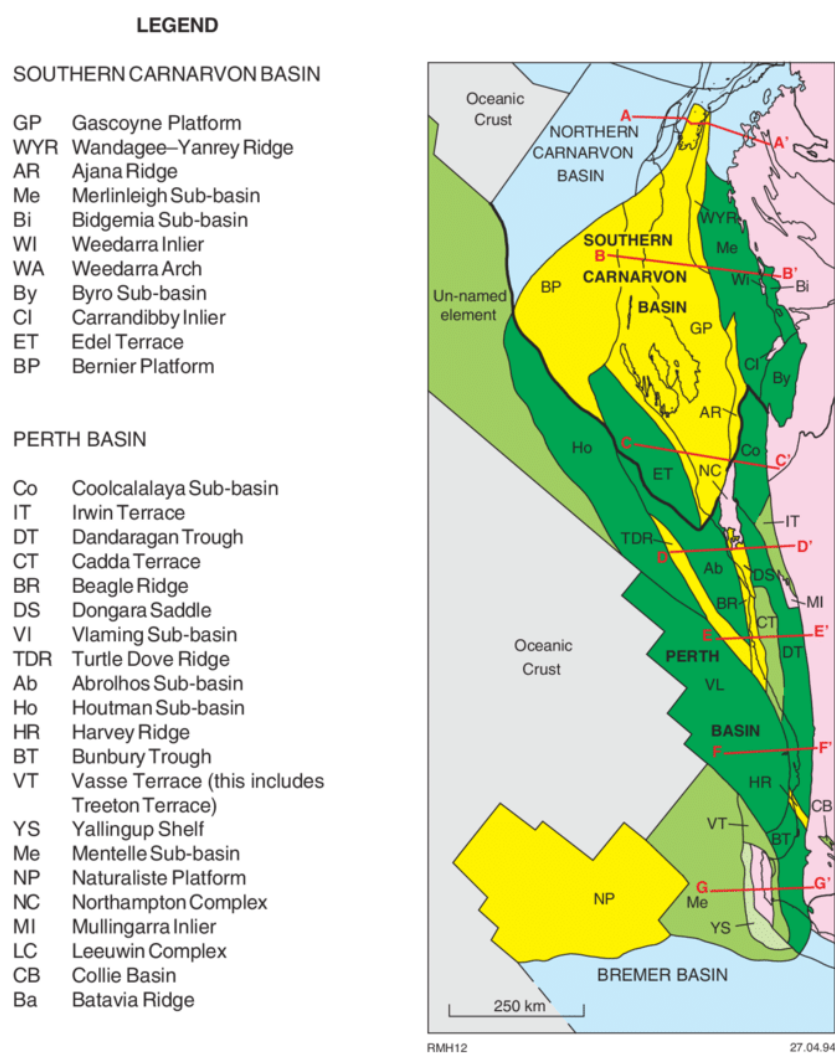


Figure 3-4 – Subdivision of the Southern Carnarvon and Perth Basins (Mory, 1994).

3.1.2.1 Stratigraphy of the In-Situ Lab area

The subsurface geology (Figure 3-5) of the In-Situ Lab site is comprised predominately of post-Permian continental clastic rocks (Delle Piane et al., 2018), with Triassic and Jurassic sediments unconformably overlain by a Cretaceous to Quaternary sequence (Figure 3-5).

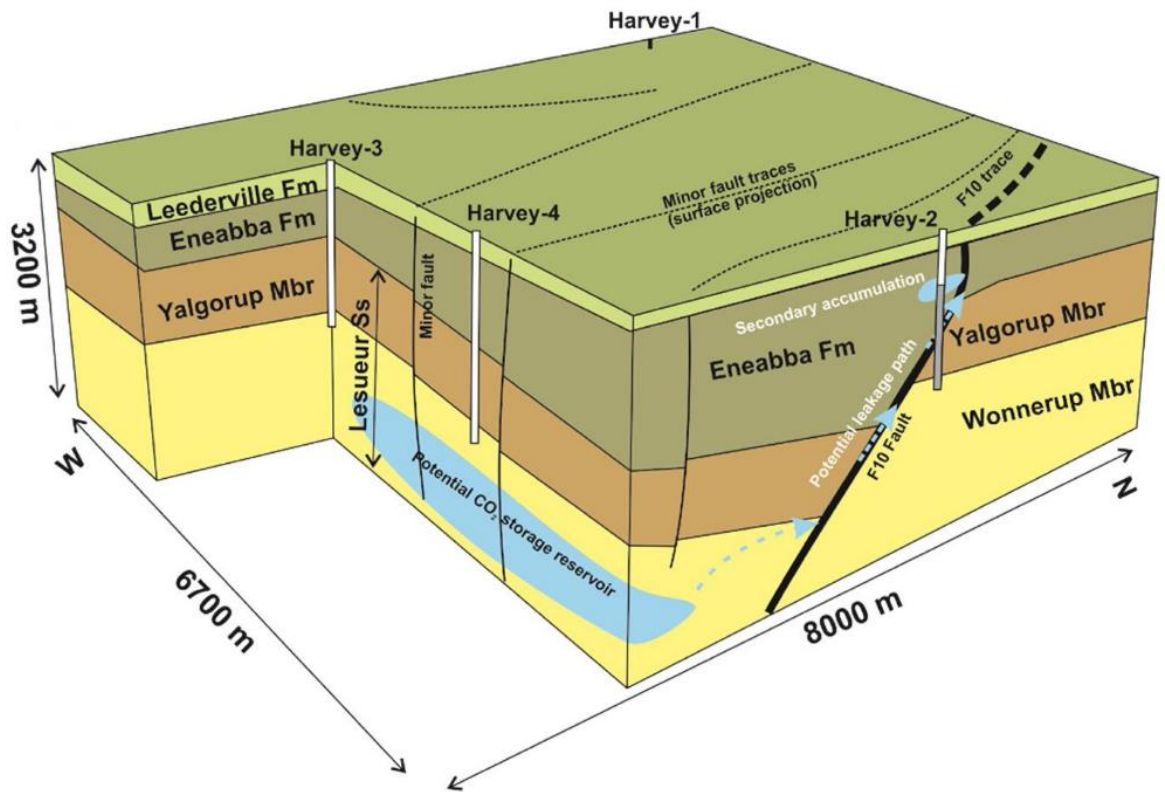


Figure 3-5 – Geology of the In-Situ Lab site Michael et al., 2019. The four main stratigraphic units are shown: Wonnerup Member, Yalgorup Member, Eneabba Formation and Leederville Formation. Harvey 1, 2, 3 and 4 wells are shown. The F10 Fault is shown in the SE of the In-Situ Lab site. Harvey-2 (injection well) has been backfilled with cement (grey shading) up to a depth of approximately 400 m. The potential CO₂ storage reservoir is the Wonnerup Member.

The oldest sedimentary unit at the ISL is the Early Triassic Sabina Sandstone, a poorly consolidated green to grey micaceous sandstone, interbedded with grey shale and siltstone (Playford et al., 1976). This is only cut by the Harvey-1 well (Table 3-1 and Figure 3-6). The overlying Lesueur Sandstone has been extensively studied in the Harvey-1 borehole (Timms et al., 2012; Delle Piane et al., 2013; Olierook et al., 2014a; Timms et al., 2015). The Lesueur Sandstone contains two distinct members: the Middle Triassic Wonnerup Member and the upper Triassic Yalgorup Member. The Wonnerup Member is a sequence of medium to granule sized moderately to poorly sorted arkose and quartzose sandstones. The Yalgorup Member is more variable, containing sandstone,

siltstone and claystones (Playford *et al.*, 1976) as well as palaeosols (Lim *et al.*, 2017). These units are overlain by the Early Jurassic Eneabba Formation, which is a feldspathic sandstone, with interbeds of conglomerate (minor), claystone (of various colours), siltstone and minor coal (Mory, 1995). Given their similarities, the boundary between the Eneabba Formation and the underlying Yalgorup member is not clear at the ISL. The depositional environment from the Eneabba Formation and Yalgorup Member is likely an anastomosing river (CSIRO, 2019). These units have an average bedding dip of around 20° to the east.

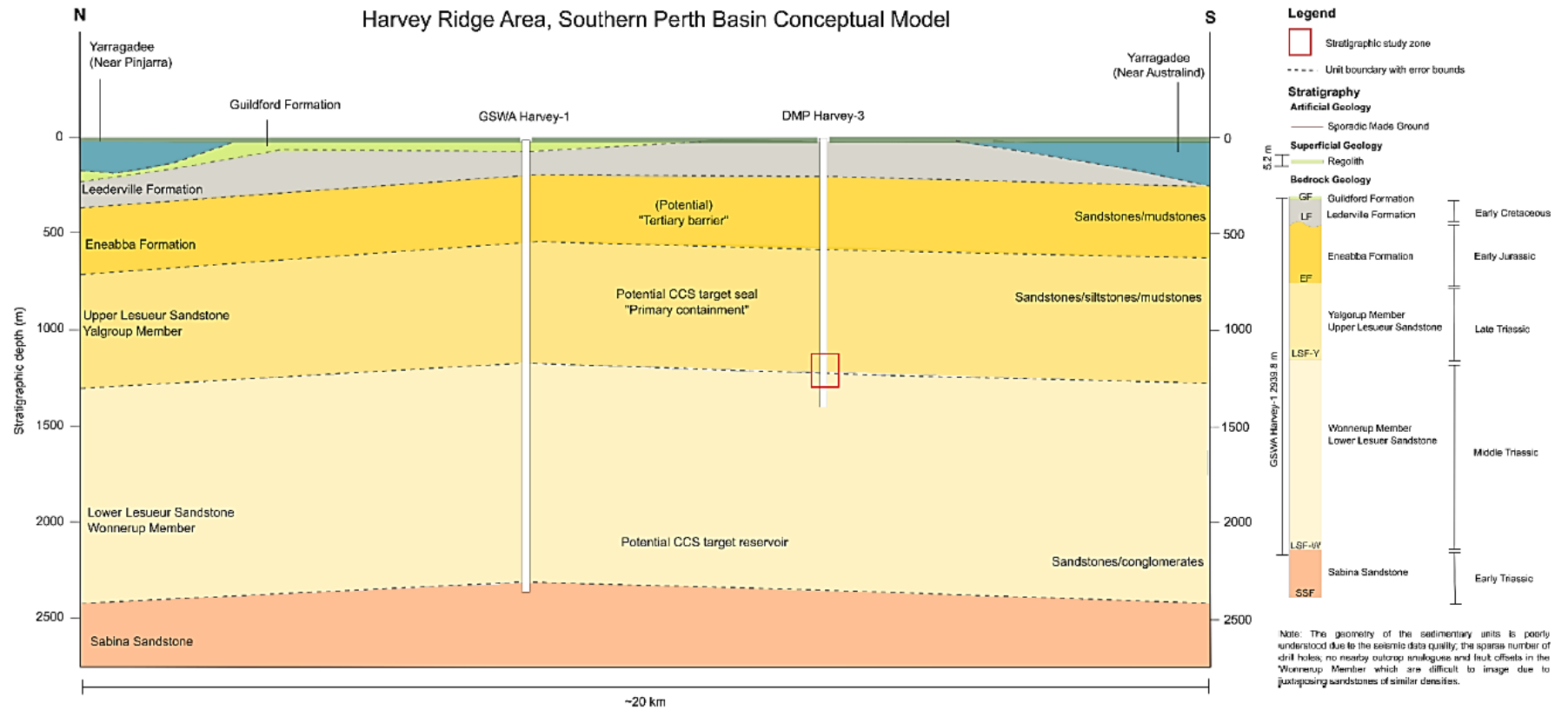


Figure 3-6– Conceptual model of the Harvey-1 and Harvey-3 boreholes at the In-Situ Lab (Stokes et al., 2018). Red box indicates studied zone in Stokes et al., 2018.

The unconformity between the Eneabba formation and the overlying Cretaceous Leaderville formation is at 135-250m depth across the Harvey region. The Leaderville Formation is around 100m thick, comprising horizontally bedded, poorly consolidated, fine to coarse grained sandstone. This is interbedded with black carbonaceous shale, glauconitic shale and lignite seams (Playford *et al.*, 1976). Disconformably overlying is the Pleistocene Guildford Formation which comprises of alluvial sands and clays, with a local basal conglomerate. This formation lies directly below the surficial sediment cover (Low, 1971).

The diagenetic history of the Lesueur Sandstone (Yalgorup and Wonnerup Members) is well documented. The Lesueur Sandstone has been diagenetically altered by feldspar dissolution, pore-occluding kaolinite formation, quartz overgrowths, and chemical compaction. These diagenetic alterations result in an overall decrease in reservoir quality with depth (Delle Piane *et al.*, 2018). This was not expected to affect the In-Situ Lab shallow release experiment as these features were not observed in the target formation (Eneabba formation) at ~340m depth).

3.1.2.2 Regional stress and fault regime

The current stress regime at the southern Perth Basin is interpreted to be a transitional reverse to strike slip regime, although there is potential for a normal regime to be interpreted at depths >400m (King *et al.*, 2008; Michael *et al.*, 2019). At 400m depth, the minimum horizontal stress was estimated to be 7.4 MPa from leak off tests. The maximum horizontal stress orientation is between 84°-106° (King *et al.*, 2008; Rasouli *et al.*, 2013). King *et al.*, (2008) used the relationship between minimum and maximum horizontal stress to calculate a maximum horizontal stress of 8.7 MPa at 400m – although stress magnitudes are reported incorrectly in some CSIRO reports. The increase in vertical stress with increased overburden means that the stress regime will change with depth, from a strike slip/reverse regime near the surface to a normal regime at depth.

The literature on faulting in the Perth Basin is limited (Olierook *et al.*, 2014b). As there are no outcrops, the understanding of fault distribution, geometry and timing are based on geophysical methods (Delle Piane *et al.*, 2018). The geophysical data available in the Perth Basin (primarily seismic) is of poor quality resulting in poor stratigraphic constraints (Delle Piane *et al.*, 2018). This means that only major faults that appear on

the seismic (e.g. with throw tens of meters) have enough data available to be able to resolve their activity, re-activation potential or importance for basin compartmentalisation (Lasky *et al.*, 1991; Lasky, 1993). Furthermore, as there is a lack of data on key fault properties, the burial history of the faults are uncertain and poorly constrained – which has implications for interpreting faulting and deformation processes.

Langhi *et al.*, (2013) identified and named the fault subtypes in the In-Situ Lab area (Figure 3-7). A series of relatively small faults (F2, F4, F5, F6, F11-F15) which trend broadly WNW, NW and NNW; which are bound by two main larger faults (F1 and F10). The F1 fault trends NS to NNW and the F10 trends north-west to north north-west.

The following section provides an overview of the F10 Fault. These sections present work conducted prior to this PhD. Background information is provided, before focusing on previous work to characterise deformation (Section 3.1.3.1) and fluid flow (Section 3.1.3.2) in the F10 Fault zone. Finally, key findings and main research gaps (Section 3.1.4).

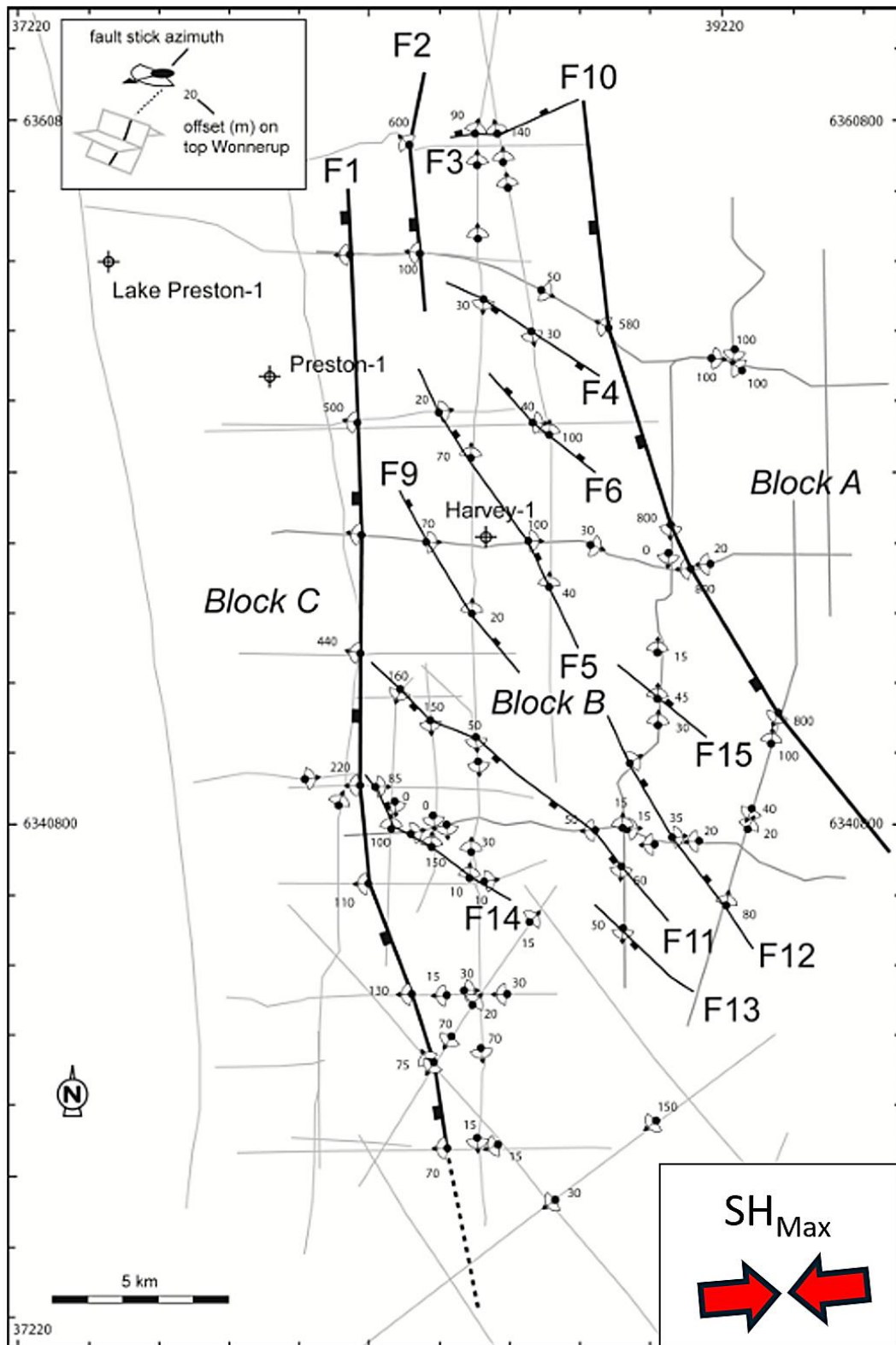


Figure 3-7 – Modelled faults at the top Wonnerup surface. Fault stick azimuths (and range) interpreted on 2D-seismic lines and offset (m) on the top Wonnerup horizon are shown. Maximum horizontal stress direction is shown (from Rasouli et al., 2013) (figure adapted from Langhi et al., 2013).

3.1.3 F10 Fault: Background, deformation and fluid flow modelling

The F10 Fault is the largest structural feature in the Harvey area and splits the In-Situ Lab site into two structural blocks: the hanging wall containing the Harvey-1, Harvey-3 and Harvey-4 wells and the footwall block which Harvey-2 spuds into (Figure 3-9) (CSIRO, 2019). The F10 Fault is >30km long, strikes north north-west to south south-east (~330°) and dips between 60-70° towards the south-west (Michael *et al.*, 2019; 2020) (Figure 3-8).

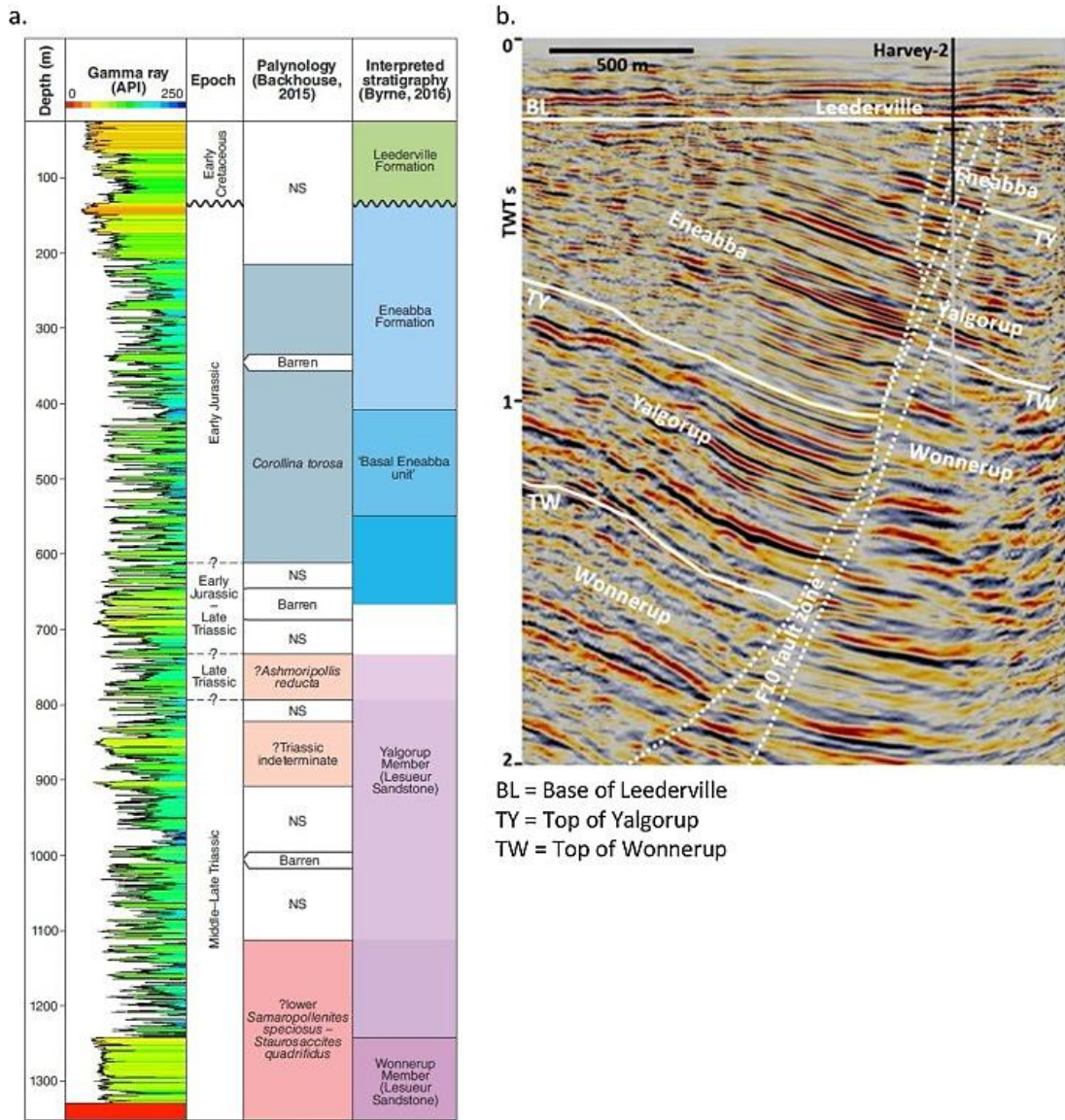


Figure 3-8 – A) Gamma log of the Harvey-2 well, interpreted geological age based on palynology and stratigraphy. B) 2D seismic cross section, oriented west-east (perpendicular to F10 Fault) showing Harvey-2 well, F10 Fault zone and interpreted horizons/stratigraphy (Michael *et al.*, 2020).

The F10 Fault has been interpreted to be a normal fault based on the angle of dip and the observed horizontal offset on seismic sections (Langhi *et al.*, 2013; CSIRO, 2019). The throw of the F10 Fault varies with depth: displacement is estimated to be 1600m at the top of the Sabina Sandstone (~2900m depth), 1,000m at the top of the Wonnerup Member (~1250 depth in Harvey-2 well), and 750m at the top of the Yalgorup member (~420m depth in Harvey-2 well) (CSIRO, 2019). This upward displacement gradient is common for normal faults (Walsh and Watterson, 1989). The F10 Fault does not extend past the unconformity (base of Leederville Formation, ~200m depth), so it is not exposed at the Earth's surface. The absence of clear seismic reflectors in the upper formations (e.g. Eneabba) mean there are difficulties in constraining or interpreting the structures present (CSIRO, 2019).

As the F10 Fault is orientated $>90^\circ$ from the modern-day maximum horizontal stress direction it is not optimally orientated for reactivation via normal or strike slip motion.

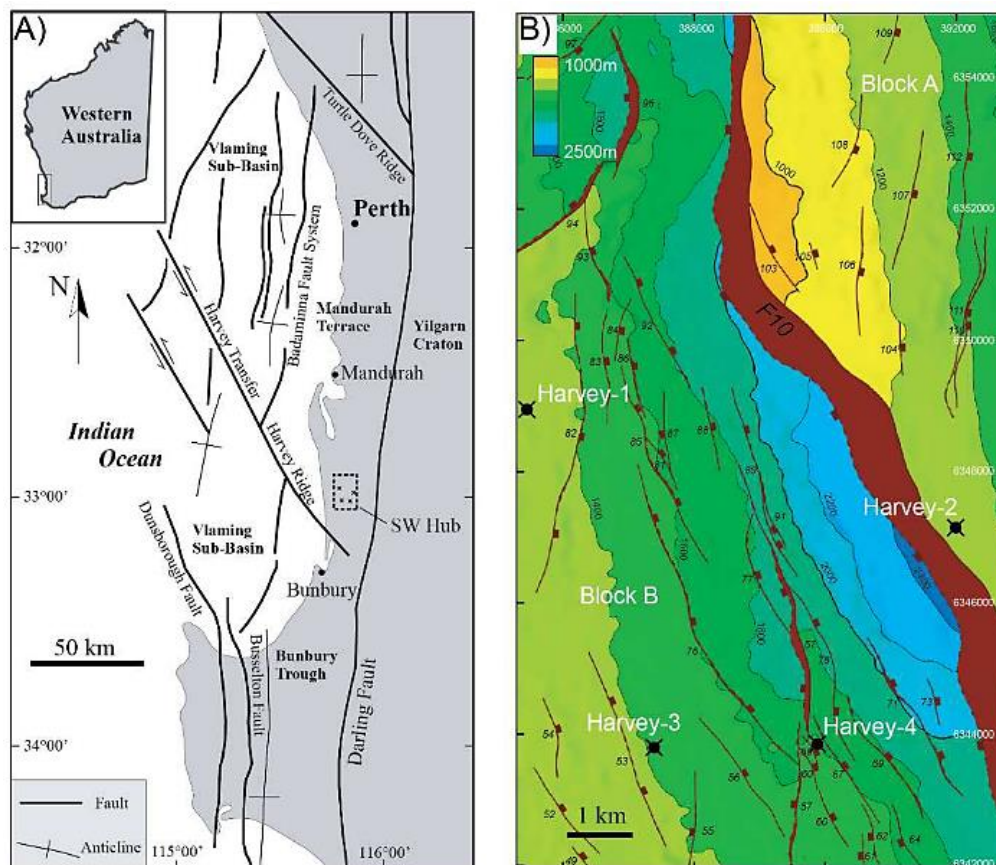


Figure 3-9 – A: Regional structural map. B: Structural map of In-Situ Lab/SW Hub area (Langhi *et al.*, 2013; Pevzner *et al.*, 2015; Delle Piane *et al.*, 2018)

3.1.3.1 F10 Fault: Deformation

The Harvey-2 well penetrates the F10 Fault zone. Core recovery in Harvey-2 starts at 207.7m depth in the Eneabba Formation, close to the unconformity with the overlying Leaderville formation which is estimated to be around 200m below surface (Rockwater, 2015). From 207.7m to 1350.2 (1142.5m length), the core has almost 100% recovery.

In the Harvey-2 core, fractures, disaggregation and particulate flow are the dominant deformation mechanisms (CSIRO, 2019). Only 14.7m of undeformed rock is observed from the top of the core at 222.4m (measured depth). This is followed by several sections of core which show deformation features – disaggregation between lenses of less deformed lithologies (Table 3-2).

Table 3-2 – Descriptions of deformation and alteration in Harvey-2 core (data from CSIRO, 2019).

Measured Depth (m)	Zone of Deformation (m)	Rock Unit	Features
222.4 – 246	23.6	Eneabba Formation	Altered disaggregated sand with palaeosol intervals, of which some appear less deformed and altered
272.5 – 293.8	21.3	Eneabba Formation	Deformed/altered core, predominately palaeosol (which is unusual as deformation etc. is usually focused in the sands)
334.7 – 419.2	84.5	Eneabba Formation	Disaggregated sands with zones of altered palaeosols (some patches of 5-7m of undisturbed lithology)

455 – 462.7	7.7	Yalgorup Member	Disaggregated sands
527 – 531.8	4.8	Yalgorup Member	Disaggregated sands
598.3 – 610.4	12.1	Yalgorup Member	Disaggregated sands
650 – 696.2	46.2	Yalgorup Member	Disaggregated sands
844.9 – 857.2	12.3	Yalgorup Member	Disaggregated sands

The disaggregated zones are focused in the sandstone, oxidised hardpans, silty palaeosols and silts, which are all the more competent lithologies present. In addition to the deformation outlined in Table 3-2, there are some notable multi-meter thick (<10m) sections of disaggregation between 598.2 and 857.2m (CSIRO, 2019) (Table 3-2). After 860.5m, all deformation is interpreted as pre-F10 deformation (CSIRO, 2019). Almost 225m of disaggregation zones have been observed in the Harvey-2 core, although CSIRO, 2019 noted that this interpretation is highly subjective and not comprehensive as the data were not collect systematically and instead only random observations were made. Therefore, there was a clear need to systematically characterise the deformation in the Harvey-2 core for the entire core length.

The primary zones of deformation mapped by CSIRO, 2019 are illustrated in Figure 3-10.

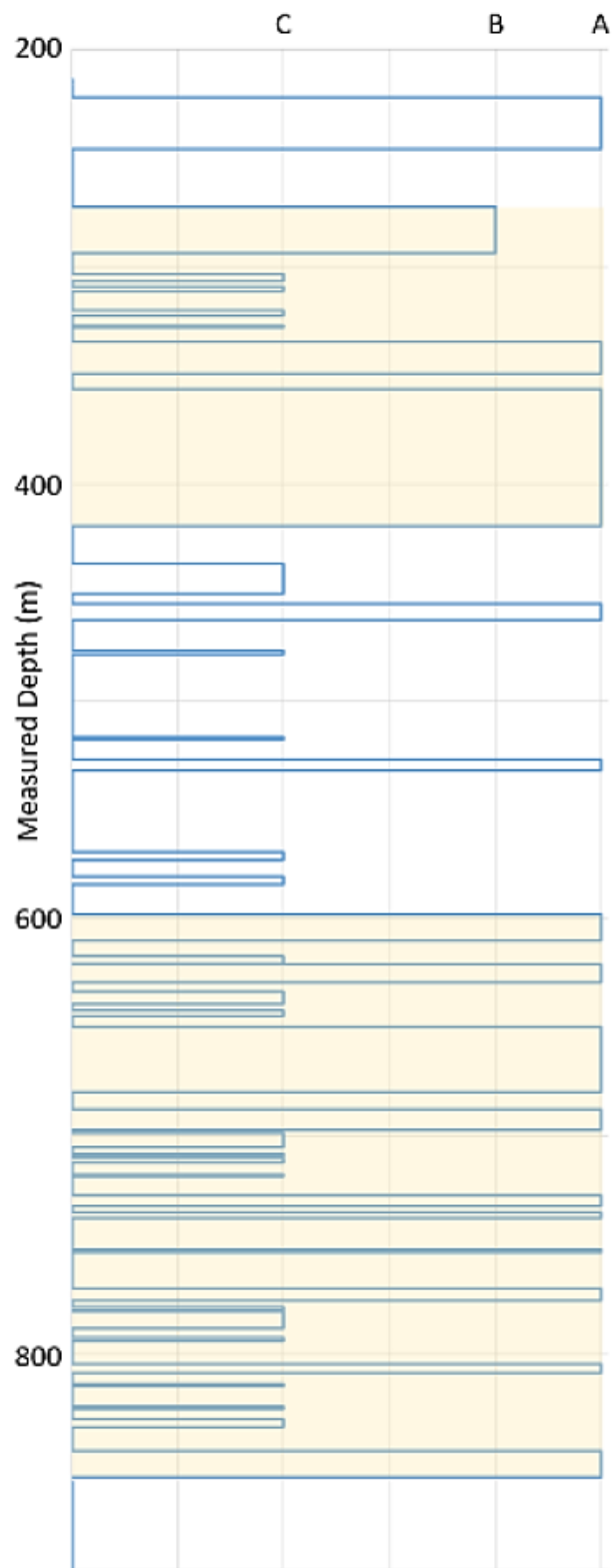


Figure 3-10 – Plot of the intensity of deformation in the Harvey-2 core. A = Disaggregated sands, B = Altered palaeosol, C = Thin isolated zones of disaggregation (less intense deformation) (CSIRO, 2019). Pale yellow zones indicate areas of continuous deformation.

Small faults were noted by Rockwater (2015) in the Harvey-2 Detailed Lithological Log at depths of 507.7, 674.5, 877.6 and 1333.75m depth (all in sandstones). A fault zone was noted between 77.295 and 773.70m in conglomerate with displaced bedding and a shear zone (with slickenlines) was noted in a well consolidated mudstone between 808.8-811.35m (Rockwater, 2015; CSIRO, 2019). CSIRO (2019) suggest that some of the disaggregated zones notes in the Harvey-2 core correlate with some of the minor faults with surround the Harvey site (see Figure 3-7), suggesting that the F2 fault and F5 faults intersect the Harvey-2 borehole at 350-405m and 230-250m.

Other fault-related features are observed with the Yalgorup Member, including slickensides on minor fault planes (Figure 3-11A), incohesive breccias (Figure 3-11B) and cataclastic bands in sandstones (Figure 3-11C).

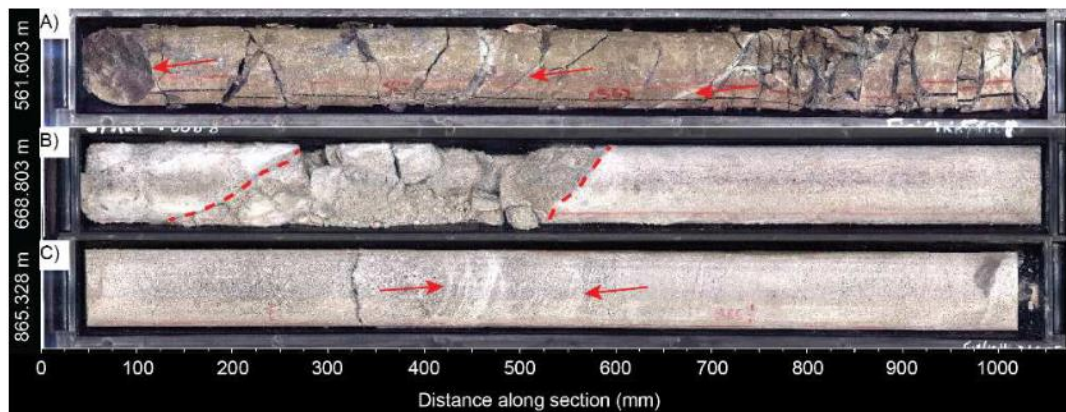


Figure 3-11 – A: Red arrows show minor fault surfaces with slickensides in a well consolidated mudstone. B: 400mm of incohesive breccia in sandstone (shown between red dashed lines). C: 150mm cluster of cataclastic deformation bands (between two red arrows) in sandstone (CSIRO, 2019).

The deformed zone is primarily in the Eneabba Formation and Yalgorup Member, with the Yalgorup Member showing minimal signs of deformation (small mm-scale displacement deformation bands) below 860.5m measured depth (CSIRO, 2019). A schematic interpretation of the deformation logs and data (Figure 3-10 and Table 3-2) is shown on a seismic line in Figure 3-12.

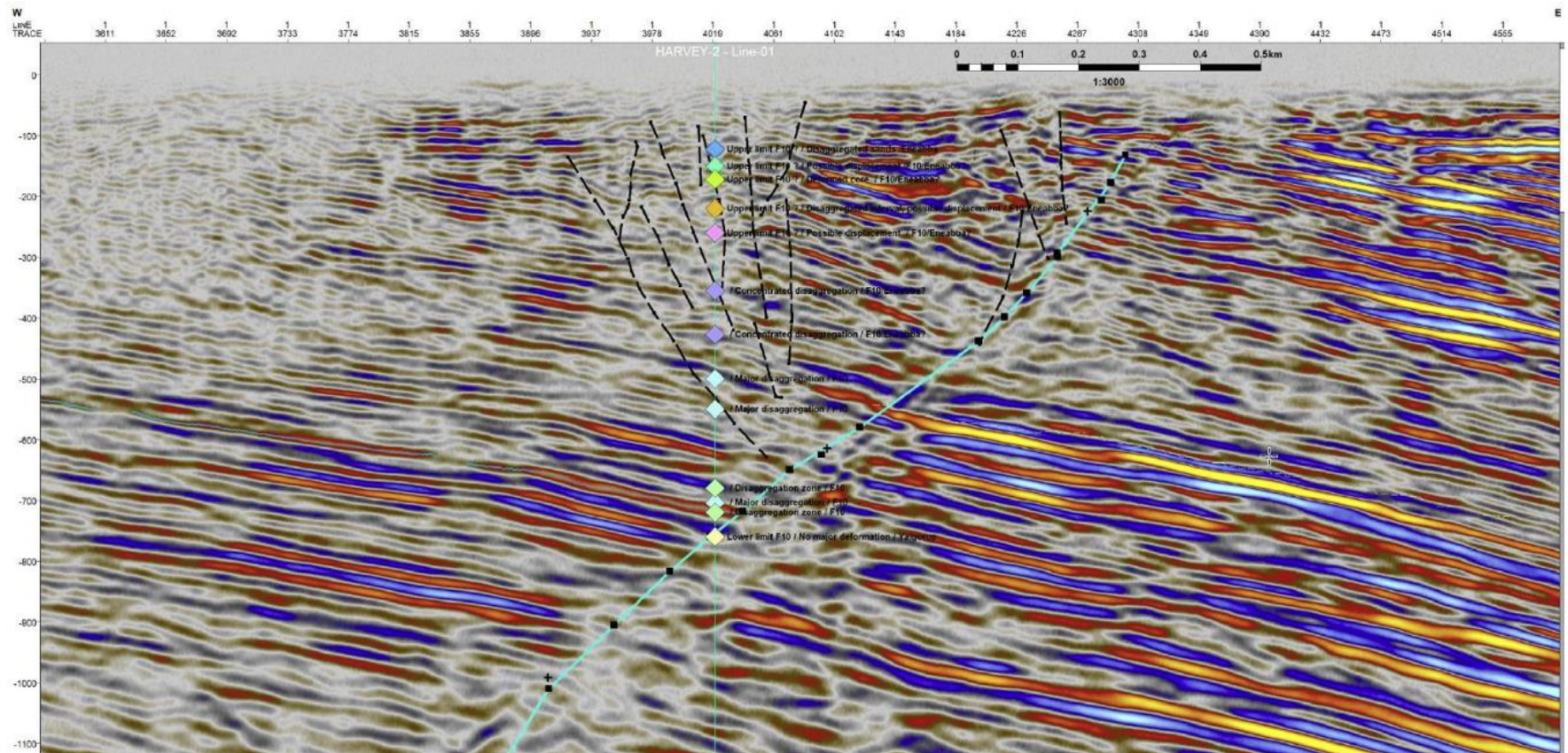


Figure 3-12 – Seismic line crossing the Harvey-2 borehole and F10 Fault zone. Deformation information is mapped onto the Harvey-2 borehole. A network of conjugate and synthetic faults in the hanging-wall have been interpreted (from Langhi et al., 2023).

The change in deformation intensity at ~860m depth has been interpreted as the footwall bounding surface of the F10 Fault (CSIRO, 2019). The upper hanging wall bounding surface is not well defined, and it is not clear if it has even been cored as there is evidence of deformation 14m from the start of coring at 224m (CSIRO, 2019). The lack of detailed data on the type of deformation and the intensity of deformed areas means there was significant scope for more detailed analysis of the F10 Fault zone in the Harvey-2 core.

Cataclastic deformation bands in the porous sandstones of the Harvey-2 core (e.g., Figure 3-11C) are reported as features which indicate a damage zone (CSIRO, 2019). These features tend to induce porosity loss and pore size reduction in the host rock. This could impact fluid flow by decreasing porosity and hydraulic conductivity and creating barriers or baffles to fluid flow in the areas in which they are present (Pittman 1981; Hardmann and Booth, 1991; Fossen *et al.*, 2007). However, the vertical and lateral distributions of these deformation bands would need to be extensive to be the cause of any impermeability. Alternatively, areas of disaggregated sands have been noted to result in higher permeabilities (e.g., Fisher and Knipe, 1998, Sperrevik *et al.*, 2002; Bense *et al.*, 2013). This could result in preferential fluid flow pathways through these zones (see Section 2.4). Therefore, there was scope for further work required to assess how the deformation style may influence fluid flow in and around the F10 Fault zone.

The thickness of the fault rock and fault zone have been estimated by CSIRO (2019) using fault displacement/thickness relationships (Childs *et al.*, 2009) (Figure 3-13). Assuming a fault dip of around 70° and ~750m minimum displacement (at the top of the Yalgorup member), this scaling relationship would indicate a true fault rock thickness between 1-~1-100m and a fault zone thickness of ~300-800mm. Based on the data published by Childs *et al.*, (2009), the observed fault rock thickness by CSIRO (2019) when examining the in the Harvey-2 core is at the lower end of the range of possible fault rock/fault zone thicknesses for a fault with the displacement of the F10 Fault. Therefore, there is further scope to confirm possible fault rock thickness based on more accurate deformation information.

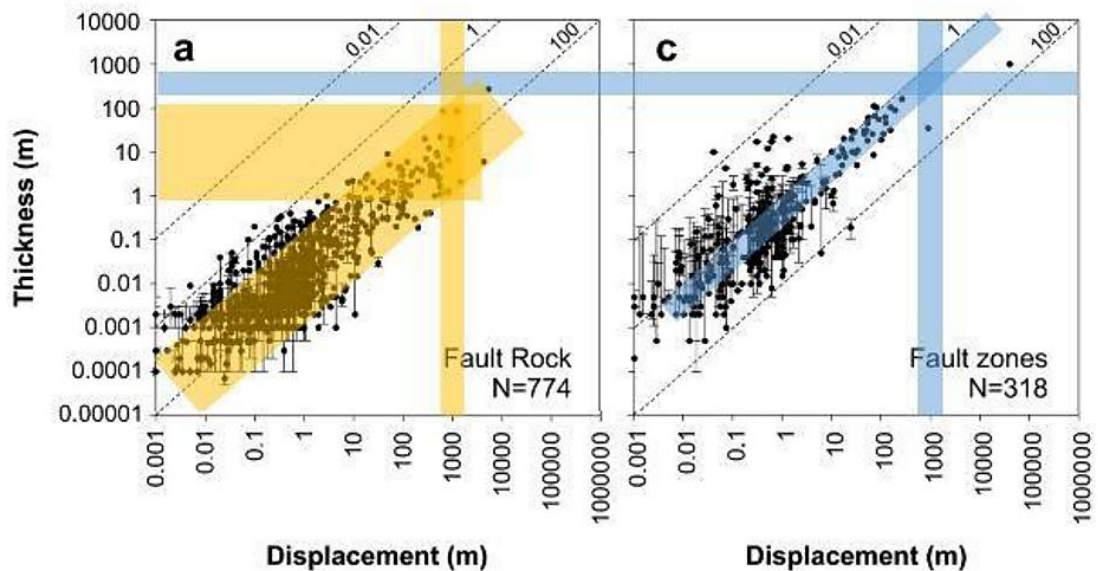


Figure 3-13 – Compilation of published fault displacement versus fault rock thickness (figure from CSIRO 2019). A) fault rock data. C) fault zones. Nomenclature retained from the original figure (data after Childs et al. (2009); please refer to the original publication for the many references from which this data was compiled). Vertical coloured bars indicate the range of displacements observed in seismic for the F10 Fault, diagonal bars highlight the trend of the data, and the horizontal bars indicate the extrapolation of the intersection of the vertical and diagonal bars extrapolated onto the thickness axis. The fault rock thickness dataset has a median D/T of 50 and the fault zone thickness dataset a median of 2.5.

3.1.3.2 F10 Fault: Fluid flow modelling

CSIRO (2019) conducted modelling of potential flow pathways in the F10 Fault zone using reservoir flow simulation models (Tempest-MORE) to inform CO₂ injection strategies to deploy for the field experiment. Detailed information on model assumptions, design, results and implications are presented in Appendix 1. A summary is presented in this section.

Results from modelling indicated that the injected CO₂ may be affected by the fault and by the dip of the formation. The plume should rise vertically both syn-injection and post-injection. Key limitations to the modelling data include a lack of porosity and permeability data collected for the Eneabba formation, instead using analogous information from similar facies. Some values were calculated (e.g., relative permeability and capillary pressure) based on core analysis from Harvey-1, Harvey-3 and Harvey-4, but not Harvey-2. CSIRO (2019) suggest future work could better characterise the porosity and permeability of the Eneabba formation within the Harvey-2 borehole itself where possible. Additionally, there was limited investigation of rock-fluid interactions and limited investigation of reservoir volume (CSIRO, 2019). CSIRO (2019) concluded

that because so little is known about the properties of the F10 Fault zone, constraining the length of the fault zone, fault displacement, characteristics, and the implications this has for fluid flow would help inform better models and ultimately better future injection strategies. This challenge was taken on in this thesis and Chapter 5 explores these areas in further detail.

3.1.4 *Key findings and research gaps*

This section summarises the injection experiment, key findings from the In-Situ Lab research and research gaps. Further work is ongoing at the In-Situ Lab, but this remains in the preliminary stages and data are not yet available at the time of writing this thesis.

The results of the injection experiment were not as expected from initial site characterisation and modelling of the stratigraphy and the fault zone (Michael *et al.*, 2020). Several geological and engineering challenges were encountered during the experiment (summarised in Stalker *et al.*, 2021), including:

- Drilling issues (e.g. drilling in poorly consolidated rock)
- Wellbore stability and leakage
- Permeability uncertainties
- Fault zone uncertainty

Ultimately, the experiment resulted in leakage of formation water and CO₂ up the well and the experiment was stopped (Stalker *et al.*, 2021). The injection test resulted in lower-than-expected injectivity and low vertical hydraulic connectivity (Michael *et al.*, 2020), evidenced by the challenges in injecting the CO₂ and the lack of any vertical migration. Previous studies by Stalker and Roberts (2020) show that at CO₂ field sites the process of drilling and installing the well can often alter rock properties and influence the results of experiments. Therefore, there is scope to reevaluate the fault architecture and hydraulic connectivity at this site to understand if the engineering or the geology is the most likely explanation for the results differing from predictions.

After the shallow release experiment, it was possible to update several of the models allowing assumptions to be checked and clarified where appropriate. This combines data acquired throughout the full process, from pre-injection through to post-injection, utilising existing data alongside new petrophysical, modelling and monitoring data

acquired. The F10 Fault zone porosity and permeability values can be updated to include Harvey-2 data acquired for and during the processes of the experiment (Figure 3-14).

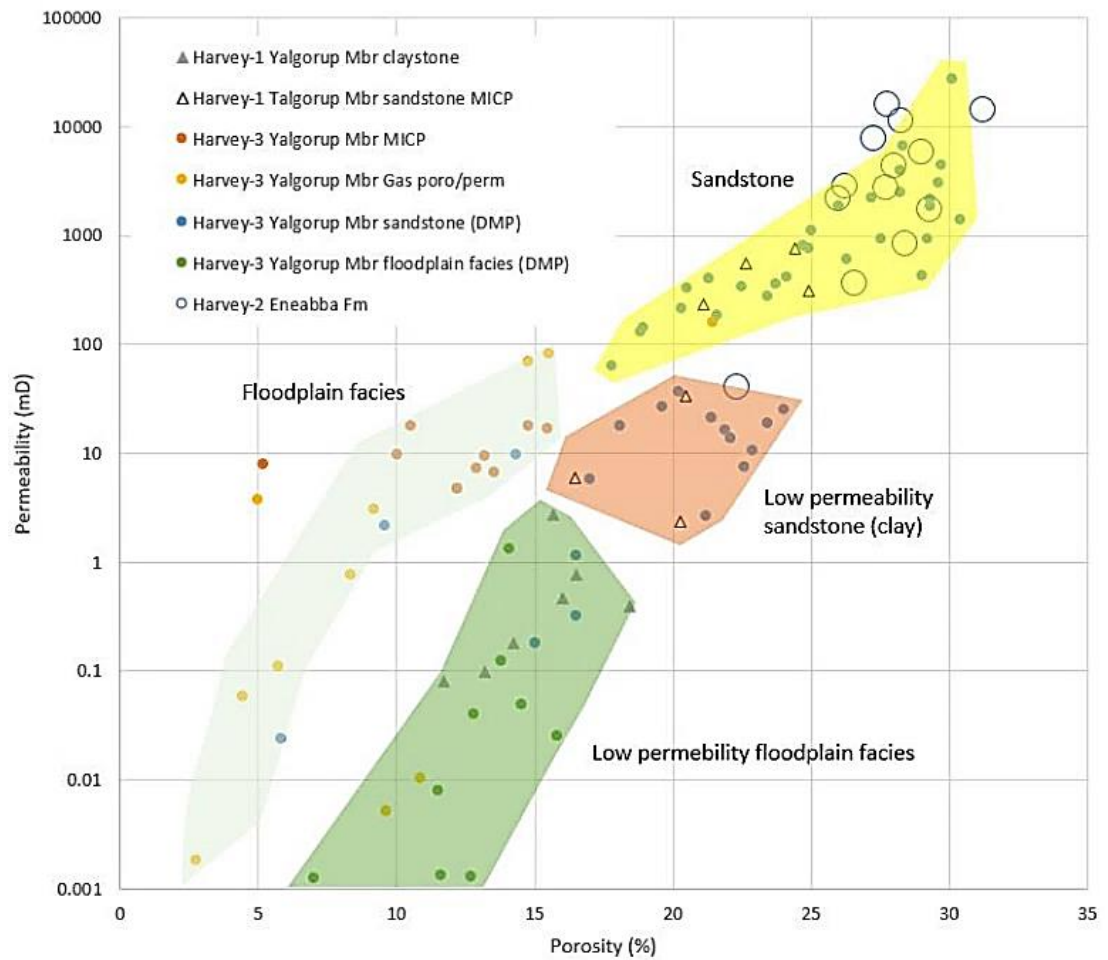


Figure 3-14 – Updated porosity and permeability plot of the F10 Fault zone, including Harvey-2 data, shown by blue unfilled circles (CSIRO, 2019).

These data were then used by CSIRO (2019) to better inform the 3D geological model used prior to injection to try to create a new model by way of history matching (see Appendix 2). The numerical models were updated to run simulations of the release experiment using data collected during the experiment. These models draw on all the available data from previous geophysical and geological interpretation, including past modelling. However, despite the input of this data the model remains inconsistent with observations, forecasting CO₂ breakthrough significantly earlier (after only 1 day) than reality. These updated models are in the preliminary stage and if improved can help to inform future experiments (CSIRO, 2019).

Although much of the data presented were incorporated in improved and updated models after the shallow release experiment in February 2019, CSIRO identified that there remains significant scope for further work in several areas including fault characterisation (Section 3.1.4.1), numerical modelling (Section 3.1.4.2) and MMV (Section 3.1.4.3), among others (Stalker *et al.*, 2021).

3.1.4.1 Further characterising and analysis of the F10 Fault zone

Although there has been significant work on the In-Situ Lab to date, questions remain to be answered – particularly surrounding Harvey-2 core material and the F10 Fault zone. It has been noted that there is alteration in the core above around 860m in the Harvey-2 core and this has been interpreted as an indication of the bottom edge of the F10 Fault zone (CSIRO, 2019). However, there was no/relatively little experimental testing and sampling on the Harvey-2 core material. This lack of testing and analysis is a result of the poorly consolidated (weak) nature of the core, particularly at shallower depths, which limited the available testing opportunities due to achievability and cost. Therefore, there was significant scope for non-destructive or alternative experimental testing that accommodates the weakness of the core material and provides more detailed and accurate quantifiable information that can be used for future models or injection experiments. The fact that the F10 Fault does not outcrop and is only crosscut by the Harvey-2 well, means that there is little information regarding the style of deformation, or any heterogeneity which could affect fluid flow. This implies that there is significant uncertainty in the fault zone permeability, how anisotropic this permeability may be and the overall hydraulic behaviour of the fault zone and surrounding host rock. The uncertainties associated with the F10 Fault are the motivation for conducting the research in this research and examining deformation and faulting at the In-Situ Lab. These research gaps are explored in Chapter 5.

3.1.4.2 Further numerical modelling

The hydraulic properties of the F10 Fault zone have not been well constrained via observations or testing. The creation of flow models with updated and better quantifiable data could allow a better understanding of how this shallow fault zone may affect fluid flow. The reservoir models would also benefit from additional data. Particularly data derived from the Harvey-2 borehole or core material where possible (e.g. deformation style and intensity, hydraulic properties and mechanical properties).

They would also benefit from better characterisation of the F10 Fault zone, as outlined in Section 3.1.4.1.

Improved numerical simulations (e.g., isothermal simulations, black-oil simulations) would increase the model confidence. Additionally, the consideration of very low permeability scenarios or any possible lack of injectivity would provide further data.

To increase the usefulness of future attempts to history match models, CSIRO (2019) suggest that reservoir properties and aquifer support constraints could be derived from a pressure transient analysis of the downhole pressure dataset from Harvey-2. Additionally, a framework for history matching would allow more parameters to be investigated (CSIRO, 2019).

3.1.4.3 Additional monitoring of the In-Situ Lab site

Surface monitoring started only one month prior to the injection experiment, due to the re-scoping. This does not account for potential seasonal variations in in-situ soil CO₂ levels and does not provide an adequate baseline dataset for comparison.

Active seismic techniques used to collect the 2D and 3D seismic surveys (collected between 2010-2015) generated data that was of poor quality, so future seismic acquisitions would benefit from different seismic techniques or approaches to reduce noise in data. This would allow better detection of the velocity of anomalies from injected CO₂ (CSIRO, 2019). The noise was primarily from injection related operations. Therefore, noise reduction could be achieved by scheduling injection breaks for active seismic monitoring. Alternatively, an additional observation well could be used (CSIRO, 2019). This could provide options for downhole seismic techniques, for example reverse 4D seismic. Passive seismic techniques would benefit from additional sensors (more elements in the array) to allow a more coherent energy package to be distinguished with more confidence (CSIRO, 2019). Generally, the seismic data is difficult to interpret and correlate with any geological features in the subsurface. This means any seismic data interpretation has high uncertainty (CSIRO, 2019).

Electrical resistivity imaging would benefit from finer electrode spacing (current was 3m) to allow for more detailed imaging of the CO₂ plume migration. As it was mostly unsuccessful during this injection experiment, it should be reviewed and improved to ensure better results in future experiments.

Overall, more research to improve the detectability of leakage pathways through more targeted monitoring is important to ensure the safe injection and storage of CO₂ in the subsurface. CSIRO (2019) state that this could be aided by better fault zone coverage (i.e. additional wells with better instrumentation).

Chapter 5 explores these research gaps in further detail, with a focus on characterising the architecture of the F10 Fault and considering implications for fluid flow, environmental monitoring, and future injection experiments. Chapter 7 considers modelling of shallow fault zones.

3.2 Otway International Test Centre, Nirranda (Victoria, Australia)

3.2.1 Otway International Test Centre (OITC): Operation, location, scope and infrastructure

Established in 2004, the Cooperative Research Centre for Greenhouse Gas Technologies (CO2CRC) is a research organisation in Australia that aims to reduce greenhouse gas emissions through research in CCS. CO2CRC established the Otway International Test Centre (OITC) (Figure 3-15) in the Otway Basin (Victoria). The OITC is located around 300km south-west of the city of Melbourne, between the towns of Port Campbell and Warrnambool in an area typically used for dairy farming (Undershultz *et al.*, 2011, Dance, 2013). There have been several phases of R&D activities at the OITC, utilising CO₂ from the nearby Buttress-1 field.

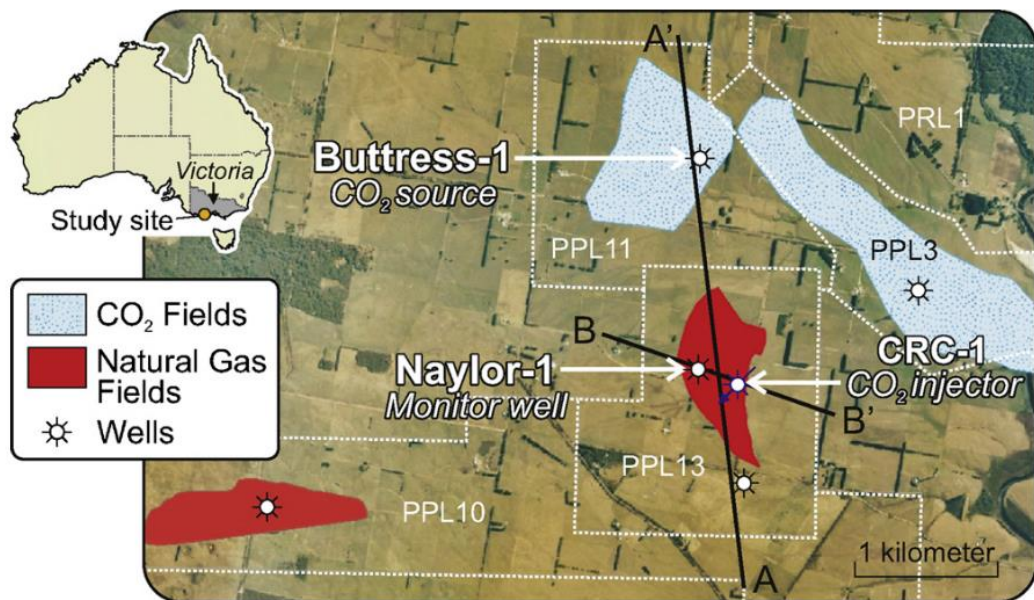


Figure 3-15 – Location of the CO₂CRC OITC site in Victoria, Australia. CO₂ and Natural Gas fields are shown, as well as source, injection, and monitoring wells (Undershultz *et al.*, 2011).

CO₂CRC's operations demonstrate CO₂ storage end to end, from developing capture technologies to storage monitoring solutions. CO₂CRC have a long-term strategic plan for both the storage and capture aspects (Figure 3-16). The focus here is the storage project, which is split into three stages:

1. Stage 1: Concept stage aiming to successfully transport, inject and store CO₂ in a depleted gas formation (2004-2009).

2. Stage 2: Risk reduction stage aiming to successfully inject and monitor CO₂ in a saline formation (2009-2019).
3. Stage 3: Cost reduction stage aiming to demonstrate safe and reliable subsurface CO₂ monitoring at a cost-effective price (2016-2026).

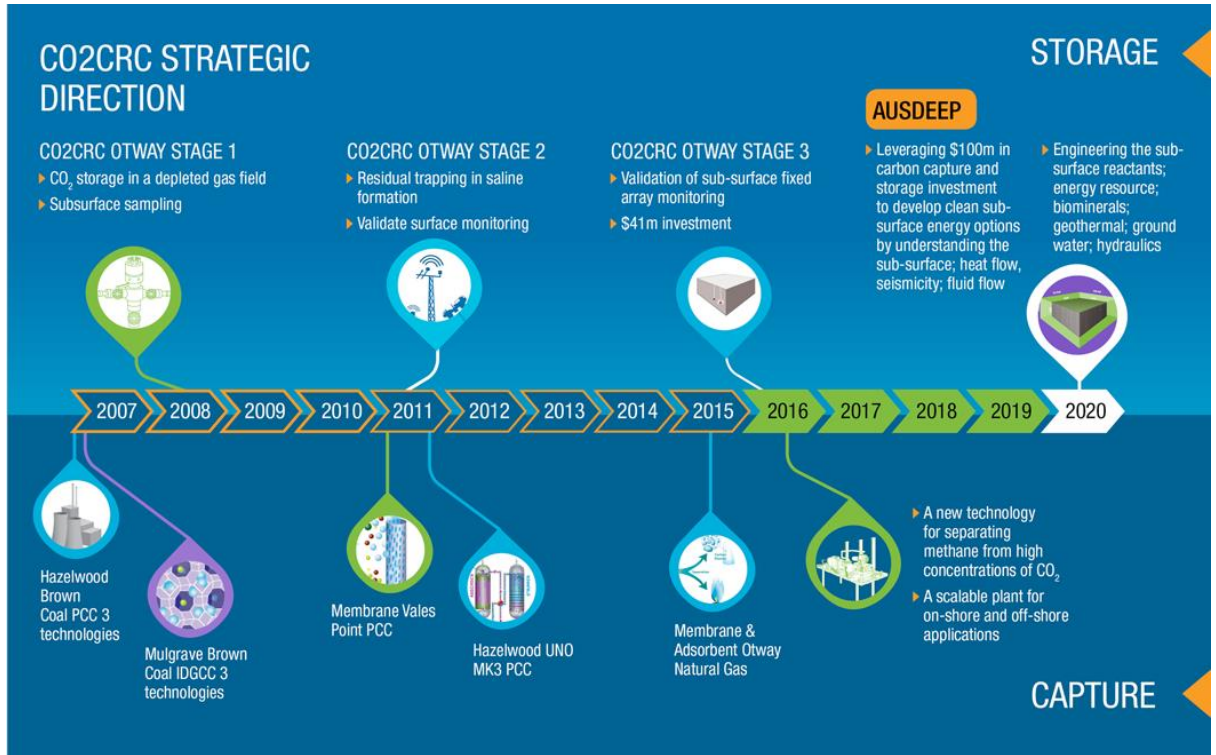


Figure 3-16 - CO2CRC Strategic Direction Plan. Top sections indicate the storage projects and the bottom sections indicate the capture projects (CO2CRC, 2020a).

Figure 3-17 shows a cross sectional overview of the Otway site.

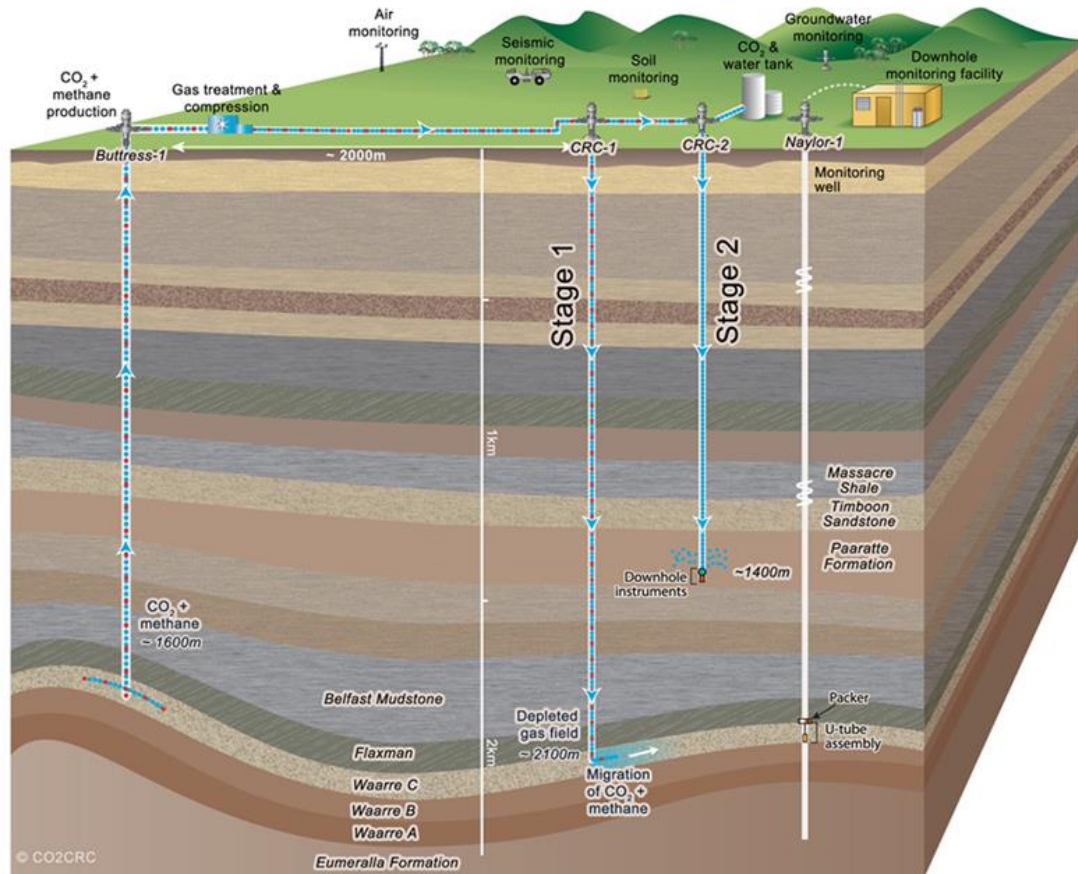


Figure 3-17 - Otway site schematic. Stage 1 and Stage 2 wells are shown, as well as surface and subsurface monitoring equipment (CO2CRC, 2020a). This figure does not consider the shallow stratigraphy in detail and thus the stratigraphic units shown are not named or highly depth accurate.

Stage 1 and Stage 2 projects successfully demonstrated the injection and storage of CO₂ in both a depleted gas reservoir and a saline aquifer (see Appendix 3). Consequently, the deeper subsurface >1km is well characterised in terms of reservoir geology at the OITC. However, as previous work has been at deeper depths, there was a lack of data for the shallow subsurface at the OITC (Bailey *et al.*, 2017).

Stage 3 of the Otway project is currently ongoing at the time of writing this thesis. Stage 3 aims to develop a monitoring programme that primarily utilises subsurface (downhole) equipment in wellbores (Jenkins *et al.*, 2017). Between July and September 2019, four new wells were drilled to support the development and validation of CO₂ monitoring technologies throughout Stage 3 and across various subprojects (CO2CRC, 2019).

The focus for this thesis is Stage 3 operations and experiments – specifically the “Otway Fault Project” which investigates a shallow fault zone. This project aims to understand the design, execution and monitoring of a CO₂ release experiment. Bailey *et al.*, (2017)

noted multiple faults were present in the near surface Port Campbell Limestone (PCL) unit at the OITC. Brumbys Fault, the chosen site for the release experiment, is one such shallow fault zone. The project started in January 2016 and has three phases:

1. Phase 1 (2016-2017): Near-surface site characterisation and the identification of a suitable fault for injection
2. Phase 2 (2018-2020): Subsurface sampling and experiment site appraisal
3. Phase 3 (2023-2024): Drill additional wells and conduct controlled release experiment

The controlled release experiment targets the Brumbys Fault, aiming to understand how faults can influence the migration of injected CO₂. These processes will subsequently affect the monitoring strategies that should be suitable to ensure safe and effective storage.

Phase 1 and 2 of the project were completed between 2016 and 2017. These phases involved geophysical surveys and groundwater permeability assessments (Feitz *et al.*, 2018b) including: 3D seismic surveys, electrical resistivity surveys, ground penetrating radar, groundwater slug tests, nuclear magnetic resonance logging and LIDAR and aerial imagery for elevation studies (CO2CRC, 2019). Phase 2 also focused on updating existing geological models, exploring potential monitoring methods (e.g., VSP surveys) and building a strong case to proceed with the release experiment (Phase 3) to understand potential leakage pathways due to the presence of the Brumbys Fault (CO2CRC, 2019). Phase 2 recommended that the injection was focused on a (non-fractured) marl rich layer of the Port Campbell Limestone to ensure the injection CO₂ reaches the targeted fault zone (CO2CRC, 2019). Phase 3 of the Otway Fault Project was successfully completed in April 2024. It involved the injection of a small amount of CO₂ (16.5 tonnes) into the shallow subsurface over a period of around 8 days. The data and analysis from this stage are ongoing at the time of writing this thesis.

The following sections present the data relevant for the Otway Fault Project including the regional geology at the site (Section 3.2.2) and background on the Brumbys Fault (Section 3.2.3). Finally, progress and areas for further work identified by CO2CRC are summarised in Section 3.2.4, these research gaps are then explored in Chapter 6.

3.2.2 Regional geology of the Otway Basin

The Otway Basin (Figure 1) covers an area around 60,000km² in southeast Australia (Holdgate and Gallagher, 2003). The basin is bound to the east (Otway Ranges) and to the west and north by structural highs (Dance, 2013), with the southern part of the basin extending offshore and limited by the present continental slope (Holdgate and Gallagher, 2003). The onshore portion of the basin accounts for over half of the total area. The basin has been subdivided into a series of intra-basinal structural embayments, troughs and highs (ranges) (Figure 3-18). These structures were formed during faulting and rifting events in the Mesozoic, which have influenced the thickness and facies of some of the Late Cretaceous and Tertiary lithofacies (Holdgate and Gallagher, 2003).

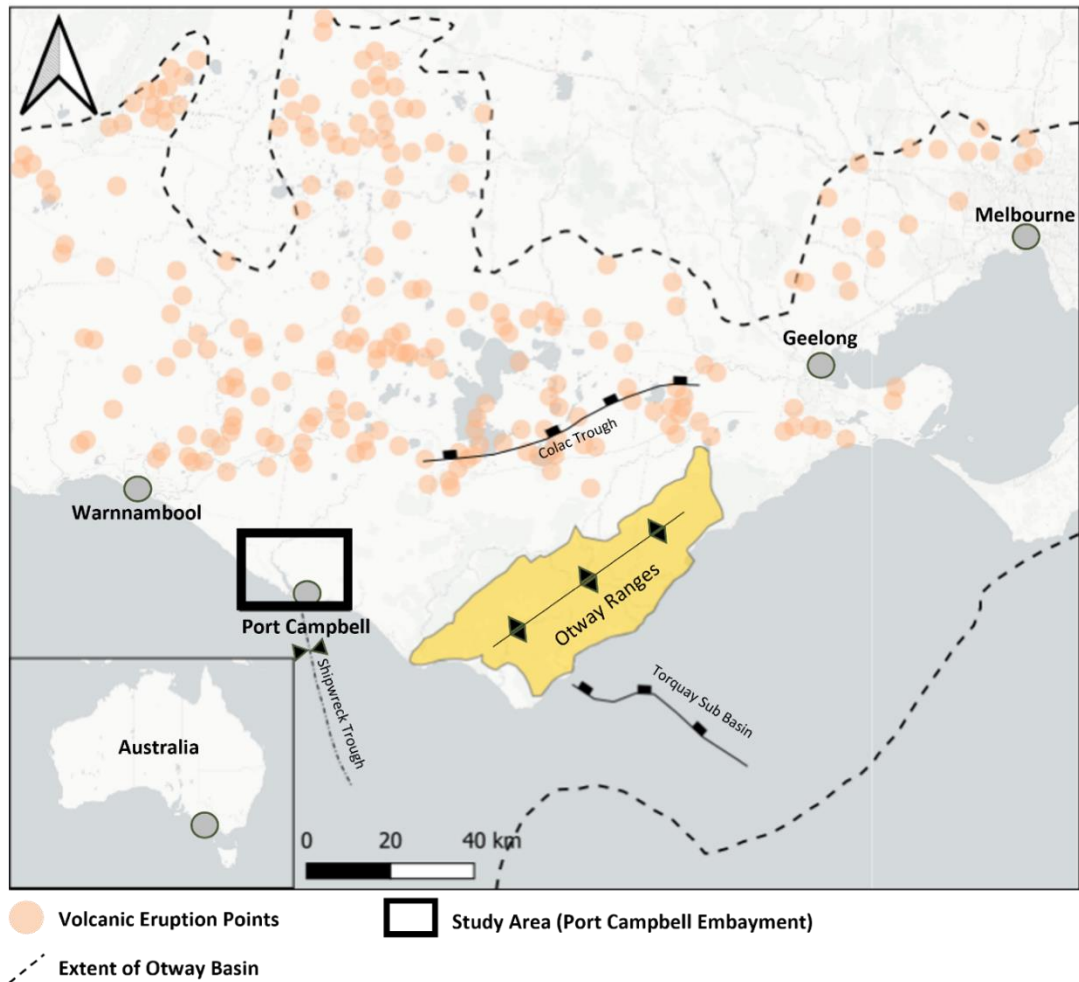


Figure 3-18 – Map of the Otway Basin showing structural features and the field area for this study. Volcanic eruption points are modified after Lesti et al. 2008. Studied region is highlighted (see Chapter 6).

The formation of the Otway Basin was contemporaneous with the breakup of eastern Gondwana along the Australian Southern Margin and subsequent seafloor spreading in the Tasman Sea in the east (Hill and Durrand, 1993; Woodlands and Wong, 2001, Krassay *et al.*, 2004, Dance, 2013). The basin contains multiple depocenters which trend west to north-west (Dance, 2019) and are characterised by a series of half-graben structures. Multiple episodes of faulting and inversion during rifting, sagging and compressional phases resulted in compartmentalisation and the formation of anticlinal structures (Jenkins *et al.*, 2012). This provided reservoirs and seals suitable for hydrocarbon accumulations to form.

The OITC sits within the Port Campbell Embayment, a subdivision of the Otway Basin. The Port Campbell Embayment (Figure 3-19) is located on the eastern section of the Otway Basin (Dance, 2014; Tassone *et al.*, 2017). The block is bound to the north and south by the Naylor South Fault and the Buttress and Boggy Creek Complexes, respectively (Dance, 2019).

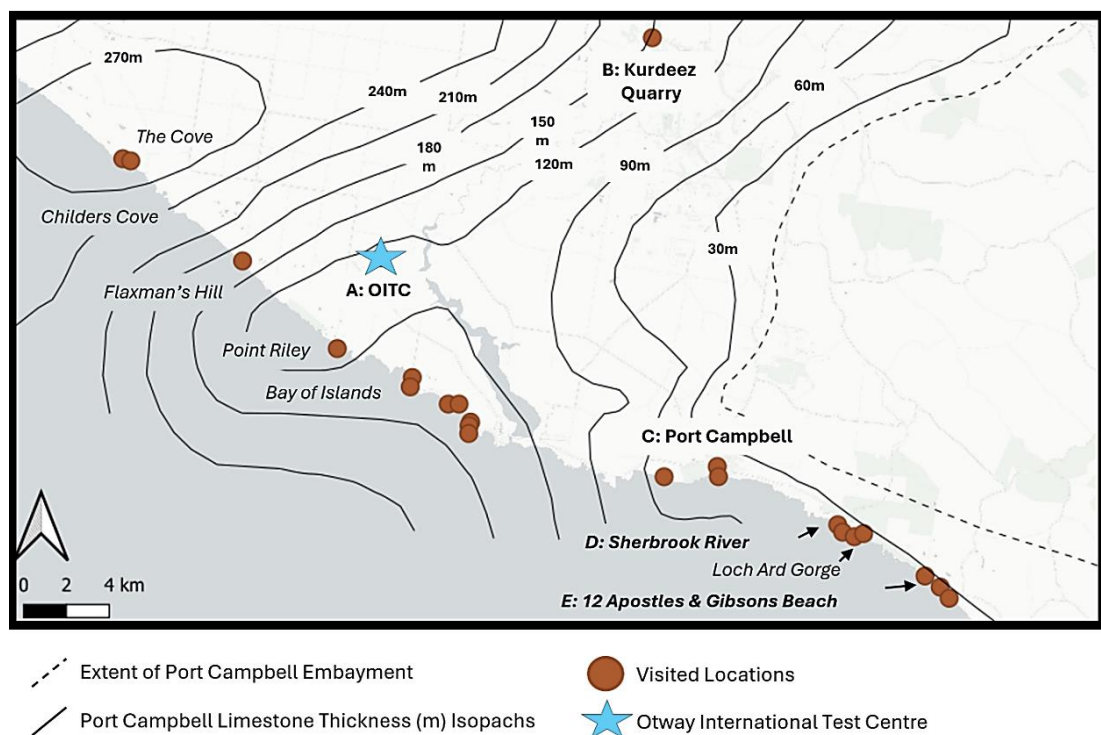


Figure 3-19 – Map of Port Campbell Embayment showing the thickness of the Port Campbell Limestone (from Radke *et al.*, 2022). Field locations that were visited during research for this thesis are shown with brown circles, and notable sites are lettered and in bold and described in the text (see Chapter 6). Landmarks not in bold are included for orientation purposes.

3.2.2.1 Stratigraphy of the OITC area

The main units exposed in the Port Campbell Embayment are the stratified and karstified Miocene Port Campbell Limestone (PCL), which is overlain at the surface by a thin layer of Hesse Clay. These units are underlain by the relatively impermeable Miocene Gellibrand Marl (Table 3-3).

Table 3-3 – Upper stratigraphy of the Port Campbell Embayment.

Unit	Description	Age	Thickness (m)
Hesse Clay	Impermeable	Pliocene	3-5
Port Campbell Limestone (PCL)	The PCL is a series of laterally continuous intercalated limestone, marl, and marly limestones.	Miocene	121
Gellibrand Marl	Impermeable and homogeneous.	Miocene	335m

The Port Campbell Limestone Port Campbell Limestone (PCL) is a grey poorly consolidated heterogeneous carbonate rock (Feitz *et al.*, 2021; Radke *et al.*, 2022). This unit is significantly heterogeneous, but is typically a light grey, fined grained, friable calcarenite, with abundant fossils (Caritat *et al.*, 2013). The mineralogy of the PCL is predominately calcite, with some aragonite in the lower permeability/muddier facies. In highly permeable intervals, dolomite is present as a component of cements (Feitz *et al.*, 2021). The non-carbonate mineralogy is low (between 3-10%) and is predominately quartz and minor amounts of clay, feldspar and mica (Feitz *et al.*, 2021). The PCL contains both intergranular and fracture porosity, giving an anisotropic hydraulic conductivity (Leonard, 1983). It typically outcrops along (southern) coastal cliffs in the Port Campbell Embayment and it thins towards the north (Duran, 1986). The PCL was deposited approximately between 15-6Ma (Radke *et al.*, 2022) in a shallow marine environment. It is a regionally extensive unit which has undergone post-breakup faulting and folding since the mid-Eocene (Holdford *et al.*, 2011). It was deposited during a time of active volcanism in the Otway Basin with multiple volcanic centres identified in the north of the basin (see Figure 3-18). Due to the young age of the PCL, it has never been buried to any significant depth, with an estimated maximum burial of ~200m (Radke *et*

al., 2021). Consequently, the PCL is weak and unconsolidated, which is evidenced in coastal exposures by the way it is easily eroded.

Diagenetic alteration in the PCL has resulted in changes to the mineralogy, leaving only minor amounts of aragonite associated with lower-permeability, muddy horizons (Radke *et al.*, 2022). Dolomite is found associated with cements in higher-permeability horizons of the PCL. Overall, between 3-15% of the sequence is non-carbonate material (Radke *et al.*, 2022). Well log data analysis indicated that the effective porosity of the PCL is 0.177-0.585, with a permeability range of 2-2285mD (Feitz *et al.*, 2021).

Following deposition, exposure of the PCL due largely to sea level fall exposed the PCL to surface weathering processes. Present day, coastal exposures of the PCL are cliffs that are up to 70m tall in places and exhibit karst features (Edwards and Tickell, 1996).

The Hesse Clay is thought to be coeval with or younger than the Newer Volcanics and postdates the Hanson Plain Sand (Radke *et al.* 2022). Analysis of the Hesse Clay by Mercury Injection Capillary Pressure indicated that the Hesse Clay would provide a suitable top sealing unit (Feitz *et al.*, 2021).

According to Radke *et al.*, (2022), the upper portion of the Gellibrand Marl and Port Campbell Limestone section were deposited between 15 and 10.5 Ma, based on the foraminiferal data from the Brumbys-1 core. The blanketing Hesse Clay (seemingly unfaulted) is believed to be derived from the Newer Volcanics which were deposited between 4.6 Ma and 5000 years BP (Boyce, 2013). Most of the clay appears to have been deposited between 3.0 and 1.8 Ma (van den Hove *et al.*, 2017).

3.2.2.2 Regional stress and fault regime

All fault types have been observed in the Otway Basin (normal faulting, strike slip faulting and reverse faulting) (King *et al.*, 2015, Bailey *et al.*, 2017, Tassone *et al.*, 2017). Two fault types have been observed at the OITC: normal faulting at depths of 1-3km (Tenthorey *et al.*, 2010; King *et al.*, 2015) and strike slip faulting in the shallow subsurface (depth <1km) (Bailey *et al.*, 2017; Tenthorey *et al.*, 2019; Feitz *et al.*, 2022). A third type of faulting is found along the coast, 30km from the OITC, where reverse faults have been observed (DSE, 2011; Bailey *et al.*, 2017). Consequently, there are different interpretations of the stress regime in the region.

Some studies suggest the shallow neotectonic regime is a reverse faulting regime (e.g. Tassone *et al.*, 2017). However, studies from deeper depths have interpreted normal and strike slip stress regimes (Berard *et al.*, 2008; Vidal-Gilbert, *et al.*, 2010, Tenthorey *et al.*, 2010). These different interpretations of the stress regime are due to the studied depth and method used. Stress variations are not surprising, as multiple studies have shown that there is often contemporary stress variation within basins (Bell, 1996; Tingay *et al.*, 2006; Heidbach *et al.*, 2007; 2010). However, these variations highlight the uncertainty in the stress tensor, mainly due to variations in the magnitude of the principal stresses. This uncertainty is amplified in the shallow subsurface, as vertical stress and rock densification generally reduces with proximity to the Earth's surface. Significant uncertainty therefore exists regarding the stress tensor.

There is a broad agreement that the maximum horizontal stress direction is $\sim 142^\circ$ (Tenthorey *et al.*, 2010; 2013, Tassone *et al.*, 2017), however magnitudes vary from 16-38 MPa. These magnitudes ultimately require clarification as the range in magnitudes allows for different stress regimes to be interpreted.

3.2.3 *Brumbys Fault*

The Brumbys Fault (Figure 3-20) is NNW-SSE trending sub vertical fault (dipping 80°) which reaches a depth of $\sim 450\text{m}$ and has a length of $\sim 1.2\text{km}$ (Feitz *et al.*, 2017; 2018a; 2020). The fault has a small $\sim 2\text{m}$ throw, confirmed by the presence of glauconite units which are offset (Feitz *et al.*, 2021), and uncertain lateral offset (Figure 3-20). The fault zone is between 6-10m in width and the fault is observed up to 3.3m below the surface (Feitz *et al.*, 2021). The fault strikes at $\sim 170^\circ$, which is 28° from the maximum horizontal stress direction of 142° (Peng and Johnson, 1972; Reches and Lockner, 1994; Tenthorey and Cox, 2006; Cunnimham and Mann, 2007; Feitz *et al.*, 2018b). Furthermore, it features jogs, bends and en-echelon fold sets (linear features perpendicular to the maximum horizontal stress, which have been observed in seismic at OITC) which are typical of strike slip faulting systems (Kim *et al.*, 2004; Cunningham and Mann, 2007). Therefore, it has been interpreted as a strike slip fault.

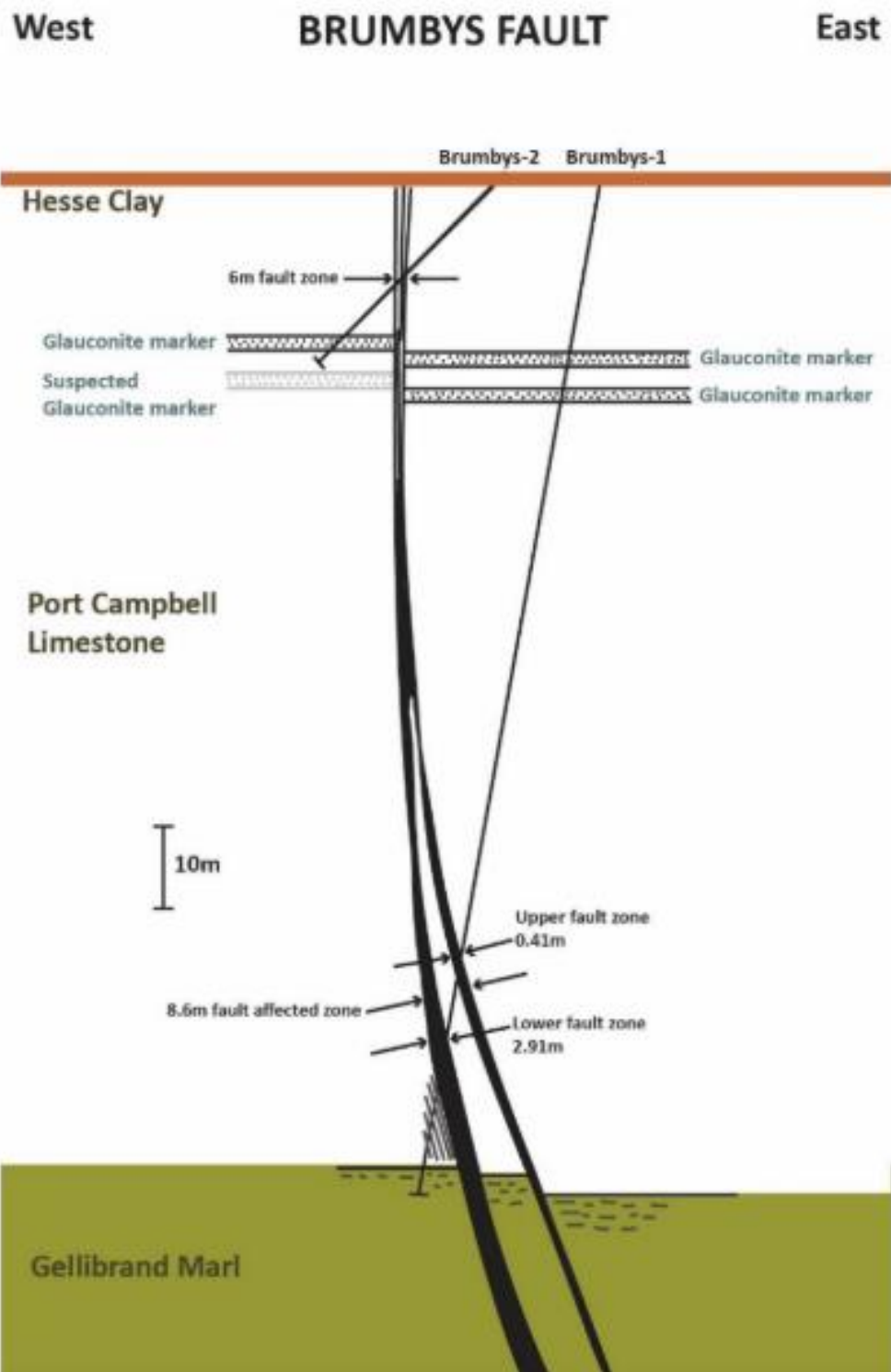


Figure 3-20– Schematic of the shallow stratigraphy of the Otway site. Not to scale horizontally. The presence of glauconite markers indicates around 2m of vertical displacement within the PCL (Feitz et al., 2021).

Estimating the fault displacement from fault length is challenging due to a lack of horizontal fault offset markers (Feitz et al., 2018b). An offset dune system can be seen to the south of the OITC, which is roughly coincident with the strike of the Brumbys Fault

however, the dextral offset on the dunes does not appear to be consistent with the presumed sinistral fault kinematics. Furthermore, there is an apparent absence of other nearby strike slip faults that precludes comparison with other faults. Only ~250m of the fault trace is “visible” in the seismic data, with the full extent unknown (Feitz *et al.*, 2018b). Using an estimate of between 250m-500m, the fault displacement can be estimated (using methods by Kim and Sanderson, 2006) to be 20m. Then applying the fault displacement-thickness relationship developed by Childs *et al.*, (2009), the thickness of the fault can be estimated to be 6-10m (Feitz *et al.*, 2018a).

Two deviated wells intersect the Brumbys Fault (see Figure 3-20, Figure 3-21 and Figure 3-22): Brumbys-1 drilled at 80° intersect at a depth of 126m and Brumbys-2 drilled at 45° intersects at 36m (Figure 3-20). These wells were drilled in 2019 using sonic drilling and were fully cored. The core was not orientated. Sonic drilling of these wells allowed maximum core recovery and limited contamination by drilling fluids. The recovered core was the core taken from the PCL and it was used for petrophysical analysis, geomechanical testing and fluid-rock testing to evaluate contamination potential from CO₂ (CO2CRC, 2019). The wells were instrumented with equipment such as hybrid fibre optic sensing cables with geophones and heating capabilities (for a high-resolution 3D VSP survey and fault characterisation using DTS).

Two further wells were drilled at the OITC in early 2023 in preparation for the shallow injection experiment (Brumbys-3 and Brumbys-4). These wells were not fully cored; only a small section from Brumbys-3 was cored from 23-28m depth to confirm the presence of the glauconitic marker observed in Brumbys-1. Brumbys-3 was used as a source well to conduct a reverse 4D vertical seismic profile (VSP) survey. Groundwater table information was collected via two vertical groundwater piezometers (CO2CRC, 2019; Feitz *et al.*, 2021).

Additionally, a series of baseline monitoring surveys were conducted, specifically for soil gas and soil flux measurements, across the Brumbys Fault.



Figure 3-21 – Map showing the layout of the Otway International Test Centre (OITC), including Brumbys wells (orange) and monitoring wells (light green). Red line depicts the surface trace of the Brumbys Fault (solid = 3D seismic trace, dashed = regional 2D seismic). Satellite image from Google Maps ©2024 Airbus, CNES/Airbus Maxar technologies, Map Data ©2024.

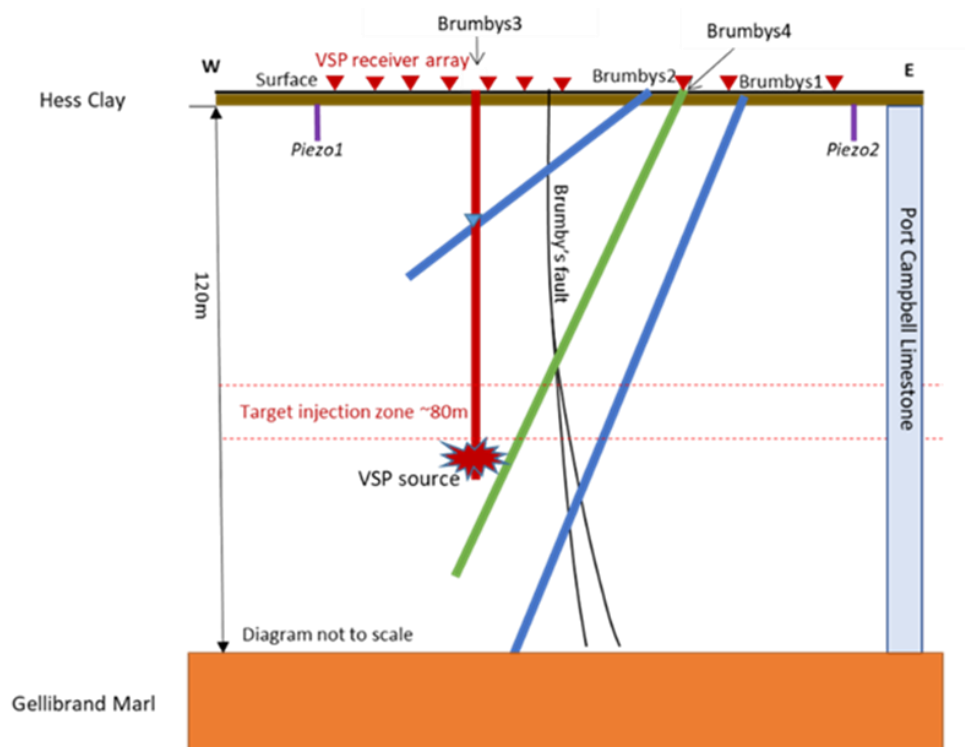


Figure 3-22 – Schematic cross section at the OITC showing the Brumbys Fault, the Brumbys 1, 2, 3 and 4 wells, the Piezo wells and the stratigraphy (modified from Tenthoey et al. (2024)).

Data from seismic shows broad zones of lower primary (P)-wave velocity orientated parallel to the maximum horizontal stress, interpreted as dilatant cracking and joint sets (Feitz *et al.*, 2018b). These features have encouraged carbonate dissolution, resulting in enhanced permeability and porosity, and the development of karst features in the limestone sequence (Feitz *et al.*, 2018b). These karst zones have been inferred to have higher permeability compared to surrounding non-karst zones. Additionally, dilational bends and jogs in high strain zones, were also considered as possible targets of the shallow release experiment (Feitz *et al.*, 2018b).

There are still uncertainties regarding the Brumbys Fault. The latest that faulting could have occurred would be immediately after the deposition of the PCL, which was 10.5Ma-6Ma. The most recent fault movement could be anywhere up to 1Ma. Studies by van den Hove *et al.*, (2017) indicate most of the Hesse Clay appears to have been deposited between 3.0 and 1.8 Ma, meaning ~1.8 Ma might be the lower bound for the last fault movement. Sandiford (2003) uses evidence of reverse faulting in the Neogene to infer that the most recent faulting would have been between 2 and 1 Ma. This means there is around 9-10 million years when faulting could have been active.

The fact that the Brumbys Fault does not outcrop and was only crosscut by two wells, means that there is little information regarding the style of deformation, or any heterogeneity which could affect fluid flow. This implies that there is significant uncertainty in the fault zone permeability, how anisotropic this permeability may be and the overall hydraulic behaviour of the fault zone and surrounding host rock. The uncertainties associated with the Brumbys Fault kinematics and properties is the motivation for conducting this research and examining deformation and faulting at the OITC, and in the Port Campbell Embayment more generally given that there are so few previous studies in the area.

3.2.4 Key findings and research gaps

The findings from the Otway Fault Project are not yet publicly available at the time of writing this thesis as data collection, analysis and interpretation are still underway.

However, there are still some clear research gaps and areas which require further research including:

- Deformation in the Brumbys-1 core (style and intensity)

- Fault kinematics (type of faulting, particularly given the uncertainties in the stress magnitudes at shallow depths)
- Implications for shallow subsurface fluid flow at the OITC

Chapter 6 explores these research gaps in further detail, with a focus on characterising the architecture of the Brumbys Fault and considering implications for fluid flow, environmental monitoring, and future injection experiments. Chapter 7 considers modelling of shallow fault zones, using the Brumbys Fault as an example case study.

Chapter 4 Approach, Data and Methods

This chapter presents an overview of the main methods used in this thesis. Some of the methods used were particular to the site studied, others were used across multiple sites or were specific to the research aims, as summarised in Table 4-1.

Table 4-1– Overview of methods used in this thesis and corresponding research questions (RQ) and research objectives (RO).

		In-Situ Lab (F10 Fault)	OITC (Brumbys Fault)	RQ	RO
Literature review		Y	Y	1	1, 10
Core observations	Geology	Y	Y	1	1, 2
	Fracture logging	Y	N	1, 2	2, 3, 4
	Deformation logging	Y	Y	1, 2	2, 3, 4
	Dip	Y	N	1	2, 3
	Petrographic Analysis	Y	N	1, 2	2, 3, 4
	XCT	Y	N	1,2	2, 3, 4
Fieldwork	Study fault analogue sites	N	Y	1	2, 3, 4
Geochemistry	Geochemical analysis	N	Y	1, 2	2, 3, 4
Modelling	Create 3D model	N	Partially	3	6, 7, 8, 9
Secondary data	Other data available from collaborators or literature	Core photographs, seismic lines	Core photographs	1, 2	1, 4

Data synthesis	Bring together literature with observations and interpretations			1, 2, 3, 4	3, 5, 10, 12
-----------------------	---	--	--	---------------	--------------------

Two of the main methods use needed to be devised specifically for this study as conventional fault analysis methods and data could not be collected due to the nature of the fault zones. These methods are outlined in the following two sections – fracture logging (Section 4.1) and deformation logging (Section 4.2).

4.1 Fracture logging

To evaluate any fracturing associated with the F10 Fault zone, new fracture logs were collected in April 2023 for sub-sections of the Harvey-2 core. This method was subsequently applied to the Harvey-3 core in March 2024.

Due to time constraints it was not possible to collect a fracture log of the entire core length. Therefore, data were collected at regular evenly spaced intervals for a total of 25% of the core length: fracture logs were taken for 5 trays (15m), no logs were taken for the next 15 trays (45m), then the process was repeated (study 5 trays, skip 15 trays). Collecting data at regular intervals removed sampling bias in the data collection. There was significant core loss in the first 10 trays of the Harvey-2 core, so fracture data collection started from Tray 10 (depth 223.2m).

To log the fractures, a “fracture descriptor number” was assigned based on four categories outlined in Table 4-2.

Table 4-2– Four fracture characteristic categories: angle, smoothness, slickensides and mineralisation.

Fracture Descriptor Number	Angle °	Description
0	0-20	Fracture angle between 0-20°
1	20-40	Fracture angle between 20-40°
2	75-90	Fracture angle between 75-90°
3	40-75	Fracture angle between 40-75°

Fracture Descriptor Number	Surface Roughness	Description
0	Rough/Undulating	Surface is rough and/or undulating
1	Mostly smooth	Surface is almost planar, with some small undulations
2	Flat, planar	Flat, smooth, planar surface
Fracture Descriptor Number	Slickensides	Description
0	No slickensides	No slickensides visible
1	Minor slickensides	Some slickensides/slight shine on surface
2	Major slickensides	Clear slickensides, shine on surface
Fracture Descriptor Number	Mineralised	Description
0	Yes	Mineralisation visible on or around fracture
1	No	No mineralisation visible on or around fracture

A cumulative “fracture descriptor score” was then calculated by adding the “fracture descriptor number” from each category. High scores indicate a fracture that is more likely to be formed tectonically and be open to fluid flow. Low scores indicate fractures that are more likely to be associated with drilling or depositional features and closed to fluid flow. This specific approach was designed with shallow fault zones and processes in mind; however, it is important consider all possible cementing histories and likely fracture types based on the geological history of the study site.

The cumulative score system allowed easy filtering of the fractures. To give examples: a fracture with a smooth planar fracture with an angle of 60°, showing slickensides and not mineralised, would score an 8 overall. In comparison, a fracture that has an angle of 10°, no slickensides and a rough surface would score somewhere between 0-2 overall.

Data were also collected on the colour of any mineralisation present, as well as the rock type in which the fractures were located.

Separately, the interpretation of the type of fracture was recorded. It was important to capture this information at the time of observation to sense-check that this method was appropriate and to avoid having to retrospectively interpret each fracture (Table 4-3X)

Table 4-3 – Fracture interpretation categories.

Fracture Interpretation Number	Fracture Interpretation Type	Description
0	Drilling	Drilling induced fracture
1	Pre-Tectonic (e.g. bedding)	Fracture along existing bedding plane or other sedimentological features
2	Tectonic	Fracture caused by tectonic process (i.e. faulting or deformation)

Figure 4-1, Figure 4-2 and Figure 4-3 show examples of each type of fracture.



Figure 4-1 – Drilling induced fracture at ~790m depth (Yalgorup Member) in sandstone in the Harvey-2 core.



Figure 4-2 – Fractured palaeosol section in the Harvey-2 core. Multiple fracture orientations and angles, likely caused by a mix of drilling-induced fractures and the exploitation of existing sedimentary (pre-tectonic) structures by drilling.



Figure 4-3 – Tectonic fracture in coarse sandstone from ~730m depth (Yalgorup Member) in the Harvey-2 core. Any displacement was not able to be estimated, as no markers are offset.

The fracture logging method outlined in this section does not necessarily capture all deformation features in the core, only fracturing. Therefore, an additional methodology was developed to capture the other types of deformation.

4.2 Deformation logging

To enhance understanding of the location and deformation intensity of the F10 Fault zone within the Harvey-2 core, a more detailed deformation log was collected compared to previous logs recorded at the site (see Section 3.1.3). The fault is not at all clear in the Harvey-2 borehole, not least because the degree of deformation means the core is very broken up (see Section 3.1.3). To establish if this core deformation is fault-related, or drilling-related a new methodology to log the core was developed. This methodology was designed to be efficient: partly due to time constraints, but also because when characterising geological storage sites resources are not often spent on core logging. The In-Situ Lab was a good site to develop this new methodology because it can be validated against the known position of the fault from 2D and 3D seismic data.

The method of deformation logging was designed to capture additional deformation types that are common in shallow fault zones (e.g. disaggregated zones), and to be applicable across different lithologies. Logging was undertaken at the Geological Survey of Western Australia (GSWA) Perth Core Library in Carlisle, Perth (Australia) over 7 days in February and March 2023.

Due to the length of the core (~1.15km) and the limited time available to view the core, an appropriate method of collecting useful data had to be created. The key objective was to understand where the F10 zone was present in the Harvey-2 core and to characterise what the fault zone looked like in terms of style of deformation. Therefore, a description matrix was designed that allowed the characterisation of each 1m section of the core based on the amount of deformation (Table 4-4).

Table 4-4 – Deformation descriptor number (N), deformation classification, and qualitative description for each category based on the core shape and cohesiveness.

N	Deformation	Description
0	Undeformed	Circular core, no sediment/fragments
1	Minor Deformation	Circular core, minor sediment/fragments
2	Moderate Deformation	Subcircular core, minor sediment/fragments

3	Deformed	Some subcircular/broken core, sediment/large fragments
4	Major Deformation	Incohesive core, significant sediment/significant small fragments
5	Core Loss	No core/sediment/fragments

Two examples of the interpretation, one from each lithology, are shown in Figure 4-4 and Figure 4-5.

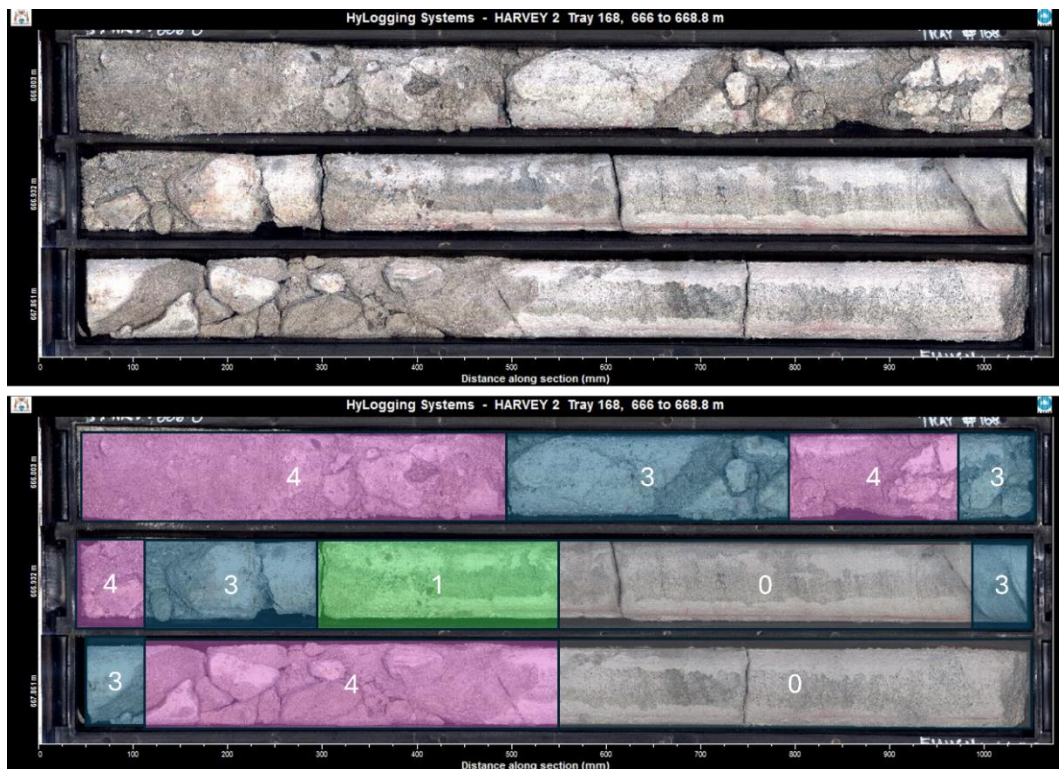


Figure 4-4– Example deformation log interpretation of tray no. 168 at a depth of 666m. The lithology of this tray was entirely sandstone. Top image shows the core tray photo. Bottom image shows the core tray photo with the assigned deformation numbers.

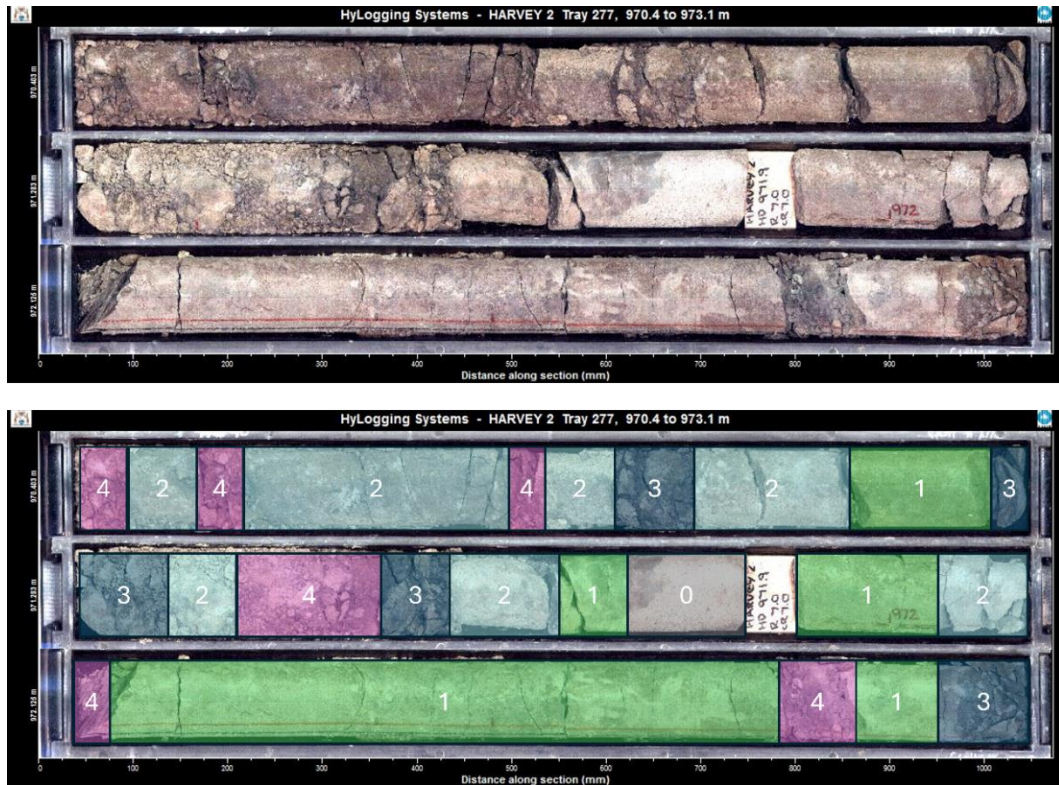


Figure 4-5 – Example deformation log interpretation of tray no. 277 at a depth of 970m. The lithology of this tray was entirely palaeosol. Top image shows the core tray photo. Bottom image shows the core tray photo with the assigned deformation numbers.

To capture sections of the core where core was not recovered this was categorised separately as “5”. These areas were then compared with drilling logs and notes to ascertain if this core loss was more likely to be associated with drilling-related difficulties or associated with the rock properties. Any areas of the core that suffered losses for engineering reasons were filtered out of the dataset to ensure only core loss that was present due to geological controls was counted.

When describing the core, two geologists stood at opposite ends of the core tray to eliminate any parallax error due to the observation position. The 1m section of core would then first be characterised by lithology (i.e., what percentage of that 1m section is which lithology, out of 100%). For example, a tray with 50% sandstone and 50% palaeosol would be recorded as such. Then, the 1m section would be further characterised using the “deformation descriptor number” (Table 4-4), with each deformation descriptor number assigned to a percentage of the tray section and the total adding to 100%.

For example, a 1m section of core that is entirely sandstone and has 50% undeformed and 50% deformed would receive the characterisation of: 100% sandstone, 50% number descriptor “0” and 50% number descriptor “3”, with each of the remaining number descriptors receiving 0%. This would give an “average deformation number” of 1.5 for that section of core.

For a tray which has multiple lithologies in the same 1m section, for example 50% palaeosol and 50% sandstone, the deformation would be recorded for each lithology. So, if the sandstone portion of this tray was half undeformed and half majorly deformed, it would receive 25% “0” and 25% “4” – which means of the 50% of the tray which is sandstone, half is deformed and half is majorly deformed. This section would receive an average deformation number of 2. The palaeosol deformation would be recorded separately, meaning both average deformation numbers for each lithology could be combined to give an average deformation number for that 1m section of core.

Other observations such as deformation features and bedding indication (angle from the core axis) were also noted while assessing the deformation in the core. This was to see if there were any anomalous bedding values which could indicate the horizons have been displaced or deformed.

All depths recorded are measured depth along the core and have not been corrected for any possible inclination.

The Harvey-2 and Harvey-3 cores had different diameters. The Harvey-2 core is ~80 mm in diameter, versus the Harvey-3 core having a larger 120 mm diameter.

This method was carried out independently from the fracture logging method outlined in Section 4.1 and without consultation of any existing published logging data to remove any confirmation bias.

This method was designed on the Harvey-2 core, and then later applied to the Brumbys-1 core in April 2023 and Harvey-3 core in March 2024.

4.3 Petrographic analysis

As the Harvey-2 core is generally a weak core, particularly the sections from shallower depths, traditional sampling approaches (e.g. core plug drilling, core flood tests, sample cutting) have been limited in their success (CSIRO, 2019).

Thin sections were prepared using a dry polishing method that was designed to produce the best possible results given that the samples were weak (Appendix 4). Thin sections were viewed using a Nikon DS Ri2 microscope (Figure 4-6), with a 360° rotating stage and different lenses for different magnifications. Images were captured for photomicrographs using NIS-Elements software.

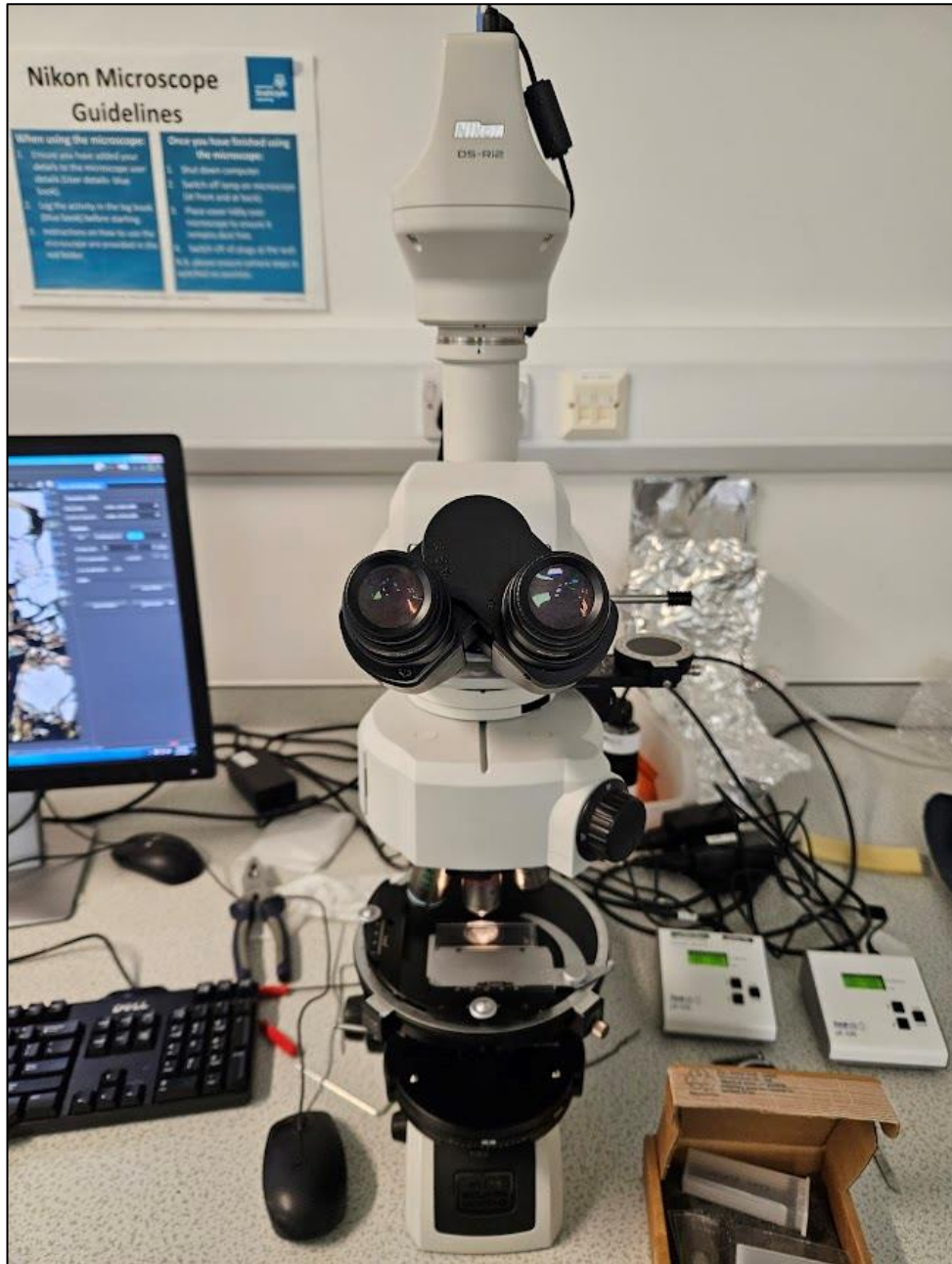


Figure 4-6 – Image of the Nikon DS Ri2 microscope.

4.4 XCT analysis

Due to the weak nature of the Harvey-2 core, X-ray computed tomography (XCT) was used to non-destructively scan to view the core in 3D and assess any deformation features.

Where possible, sections of the core were removed from the core tray and placed on the XCT scanning table. Some sections of core were simply too fragile to be able to remove them from the core trays without damaging the core and could not be scanned. The details of the scanned sections are summarised in Appendix 5. The best voxel resolution on the highest energy settings is $\sim 0.1 \text{ mm}^3$.

XCT scanning took place at the Australian Resources Research Centre (ARRC) which is where the CSIRO Kensington office is based in Western Australia. The XCT scanning took place over several days from 20th-23rd March 2023. The scanner was a Siemens medical XCT scanner SOMATOM Definition AS (Figure 4-7).



Figure 4-7– Siemens medical X-ray CT scanner SOMATOM Definition AS.

The settings for each scan are recorded in Appendix 5. Alongside each scan five control samples with known properties (e.g. mass, density were also scanned) to allow calibration of the scanned images (Figure 4-8).

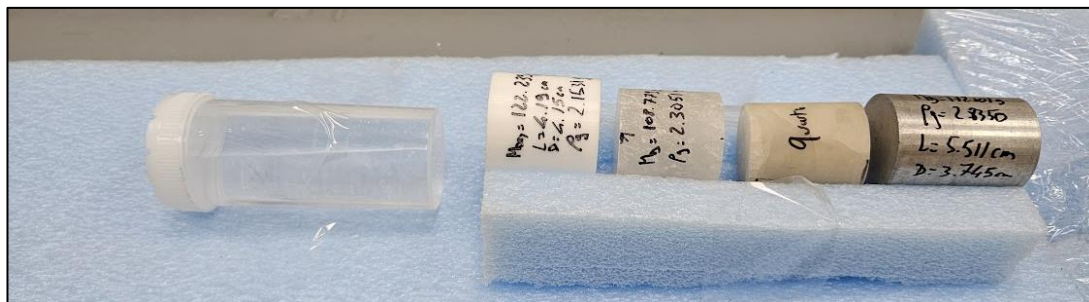


Figure 4-8 – Control samples. Left to right: Water, Teflon, Gypsum, Quartz and Aluminium.

4.5 Fieldwork in the Port Campbell Embayment

4.5.1 Field observation

Given the limited inland exposure of any rocks in Port Campbell Embayment area, fieldwork focused on the coastal cliffs, from Childers Cove in the west (38.489101, 142.672736) to Gibson Beach in the east (-38.674070, 143.117769) - approximately ~45km of coastline - except for one accessible inland location: Kurdeez Quarry an open pit limestone quarry (Figure 3-19, Location B).

At the coastal cliffs, access to the cliff faces is limited due to the lack of access points, tides, and safety. This precluded the collection of detailed field data, and as the site is a national park it was not possible to collect any hand specimens or samples. Instead, field observations were made from adjacent cliffs and viewpoints, some of which are tourist lookout spots.

4.5.2 Geochemical analysis

A portable XRF analyser (a non-destructive method) was used to determine the percentage carbonate content of 178 sample points at the exposed PCL at Gibson Steps and Gibson Beach coastal exposures (see Figure 3-19, Location E) using the volumetric technique of Wallace et al. (2002).

Chapter 5 Multiscale characterisation of the fault architecture of the F10 Fault at the In-Situ Lab (Harvey, Western Australia): developing new methods to effectively characterise shallow fault zone architecture

5.1 Introduction

This chapter presents analysis of the F10 Fault found at CSIRO's CO₂ field experiment facility, the In-Situ Laboratory (In-Situ Lab) (Section 3.1). There are no outcrops of the F10 Fault, or analogues, but the Harvey-2 well cuts across the fault (see Section 3.1.1 and 3.1.2). The Harvey-2 core was therefore studied to characterise the fault and understand its architecture following the two new methodologies (described in Section 4.1 and 4.2) designed to characterise fractures and deformation. To allow comparison between deformed and undeformed core, and therefore to validate these methods, the Harvey-3 core was also analysed. These wells are ~5.6km apart. Both cores contain the same geological units and lithologies (see Section 3.1.1), but the Harvey-2 core crosscuts the F10 Fault whereas the Harvey-3 core does not, and seismic surveys show no evidence of any other major faults (i.e. at the same scale as the F10) being present in the Harvey-3 core. This does not rule out smaller fault zones crosscutting either well that are at the sub-seismic resolution. This chapter therefore presents analysis of the Harvey-2 and Harvey-3 cores.

A research paper on this work "Multiscale characterisation of the fault architecture of the F10 Fault at the In-Situ Lab (Harvey, Western Australia): developing new methods to effectively characterise shallow fault zone architecture" is in preparation for publication.

5.2 Geology of the Harvey-2 and Harvey-3 cores

The Harvey-2 and Harvey-3 cores contain similar lithologies and units, with the primary lithologies being sandstone and palaeosol of the Eneabba Formation, Yalgorup Member and Wonnerup Member (see Section 3.1.2 and 3.1.3). As the core is ~1.2km in length, it was not in the scope of this project to fully characterise the sedimentology of the core due to time constraints, but high-level observations show key variations. Sandstones vary in colour and grain size, but commonly they are medium to coarse grain size and

occasionally interbedded with muddier horizons/palaeosols (Figure 5-1). Some sections display very coarse grain sizes (i.e. grit). The Eneabba Formation and Yalgorup Member display similar characteristics and are not easily distinguished at the core scale, however the Wonnerup Member is easily distinguished by the presence of cross-beds.



Figure 5-1– Examples of the variability of the undeformed sandstone in the Harvey-2 core. A: Tray 254 (Start depth = 905.5m, Yalgorup Member) – typical coarse-grained sandstone, some grit. B: Tray 150 (Start depth = 617.4m, Yalgorup Member) - Green coloured sandstone. C: Tray 204 (Start depth = 766.7, Yalgorup Member) – Interbedded sandstone, mudstones and palaeosols. D: Tray 378 (Start depth = 1264.1m) – Cross-bedded sandstone of the Wonnerup member.

The palaeosol is highly variable, displaying variations in colour, textures, deformation and interbedding (Figure 5-2).



Figure 5-2 – A: Tray 147 (Start depth = 609.4m, Yalgorup Member) – Dark brown/grey/black deformed palaeosol. B: Tray 160 (Start Depth = 644.2m, Yalgorup Member) – Massive brown/red/purple palaeosol with intermixed infilled rootlets/burrows with coarse sand. C: Tray 186 (Start depth = 715.9m, Yalgorup Member) – Interbedded muddy brown/beige/green palaeosol. D: Tray 276 (Start depth = 967.6m, Yalgorup Member) – Deformed sandy palaeosol with red/brown oxidation. E: Tray 334 (Start depth = 1132.5m) – Green, yellow, red, brown and purple sandy and muddy palaeosols with roots and/or burrows.

CSIRO (2019) have interpreted types of palaeosols within the Harvey cores, such as the red/oxidised sandier palaeosol being an “aridisol” and the muddier horizons as “vertisols”, however this interpretation is not complete and does not account for all possible variations. The specific characterisation of palaeosols was out of the scope of this study, and so all types are referred to simply as palaeosols. Palaeosols are also known to display features such as slickensides, which form as part of a soil process rather than a tectonic or deformation related process.

The percentage of each lithology in each core is shown in Figure 5-3. The stratigraphy can be seen in logs and cross-sections in Figure 3-5, Figure 3-6 and Figure 3-8 and Table 3-1 in Chapter 3. Overall, there is a similar percentage split in the two boreholes. There is 4% less sandstone and 4% more palaeosol in the Harvey-3 borehole compared to the Harvey-2 borehole.



Figure 5-3 – Pie charts showing the percentage of each of the two lithologies in the Harvey-2 and Harvey-3 cores.

Table 5-1 – Comparison of the Harvey-2 and Harvey-3 cores in terms of length, lithology and formation depths.

	Harvey-2	Harvey-3
Start Depth (m)	207.7	668.4
End Depth (m)	1350	1550
Total Cored Length (m)	~1150	~890
% Sandstone (Total Core Length (m))	46 (~529)	42 (~373.8)
% Palaeosol (Total Core Length (m))	54 (~621)	58 (~516.2)
Eneabba Formation Start Depth (m)	135	245
Yalgorup Formation Start Depth (m)	419	741
Wonnerup Formation Start Depth (m)	1245	1418

5.3 Fracture logging of the Harvey-2 and Harvey-3 cores

This section presents results from fracture logging of the Harvey-2 and Harvey-3 cores following the method outlined in Section 4.1. The fracture logging method was ultimately deemed to be ineffective for analysing deformation in shallow fault zones. Better insight was obtained via deformation logging presented in Section 5.4.

5.3.1 Fracture logging: Harvey-2 results

In total, 1266 fractures were recorded in the sections of the Harvey-2 core which were sampled (which comprised 25% of the core across its total length). 373 (29%) were in sandstone and 893 (71%) were in palaeosol (Figure 5-4).

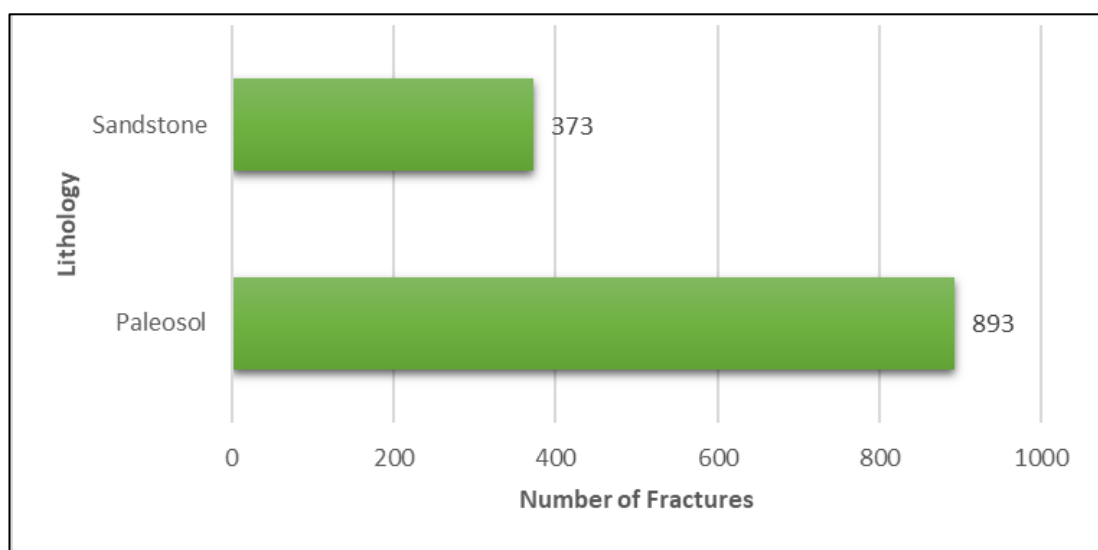


Figure 5-4 – Total number of fractures for each of the two lithologies in the Harvey-2 core.

The fracture intensity with depth is shown in Figure 5-5.

Harvey-2: Fracture Intensity

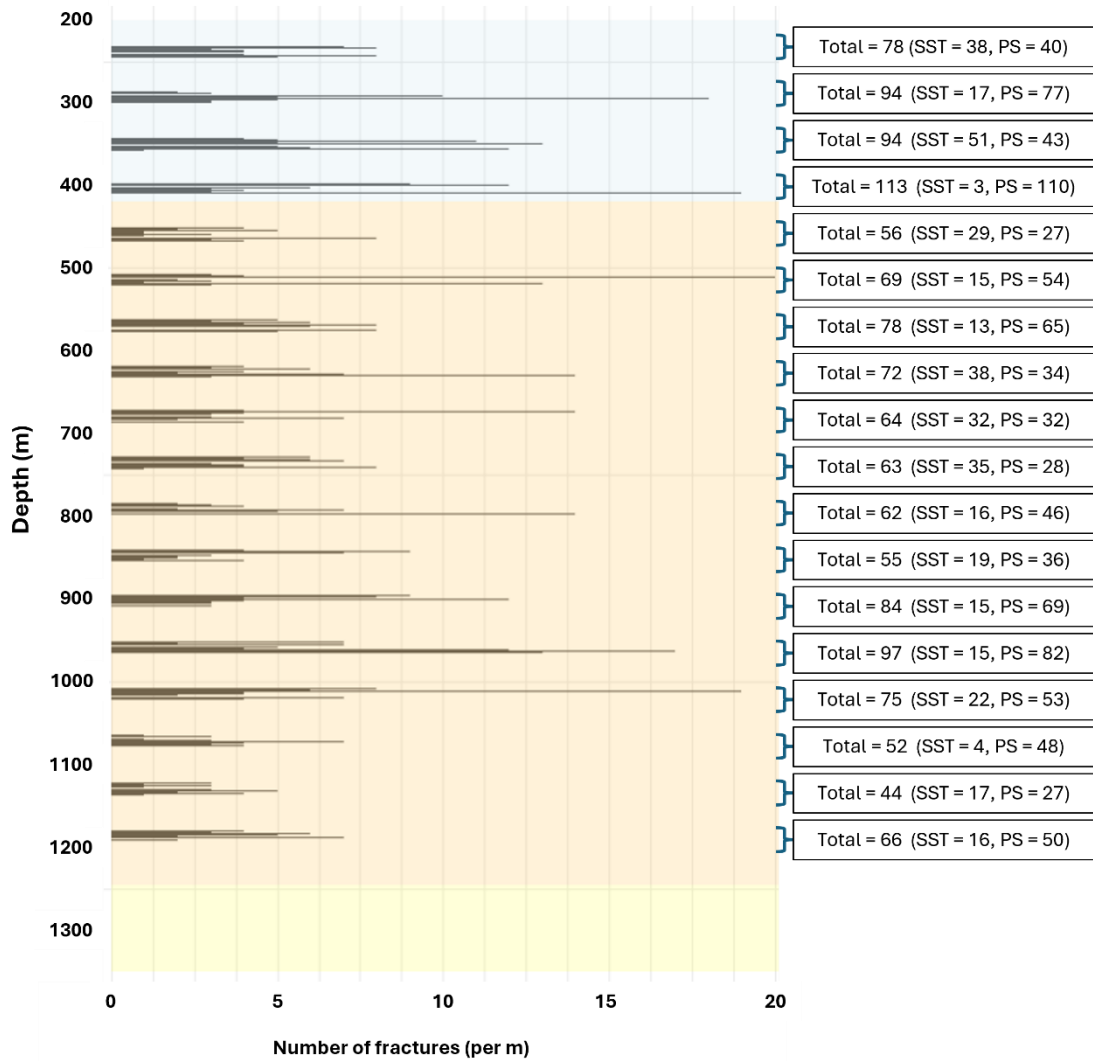


Figure 5-5 – Harvey-2 fracture intensity with depth (m). The total number of fractures per metre of the sampled intervals are shown, as well as a breakdown by lithology (SST = sandstone, PS = palaeosol). Background colours indicate the units: light blue = Eneabba Formation, orange = Yalgorup Member, yellow = Wonnerup Member.

Each fracture was assigned a fracture descriptor number (Figure 5-6).

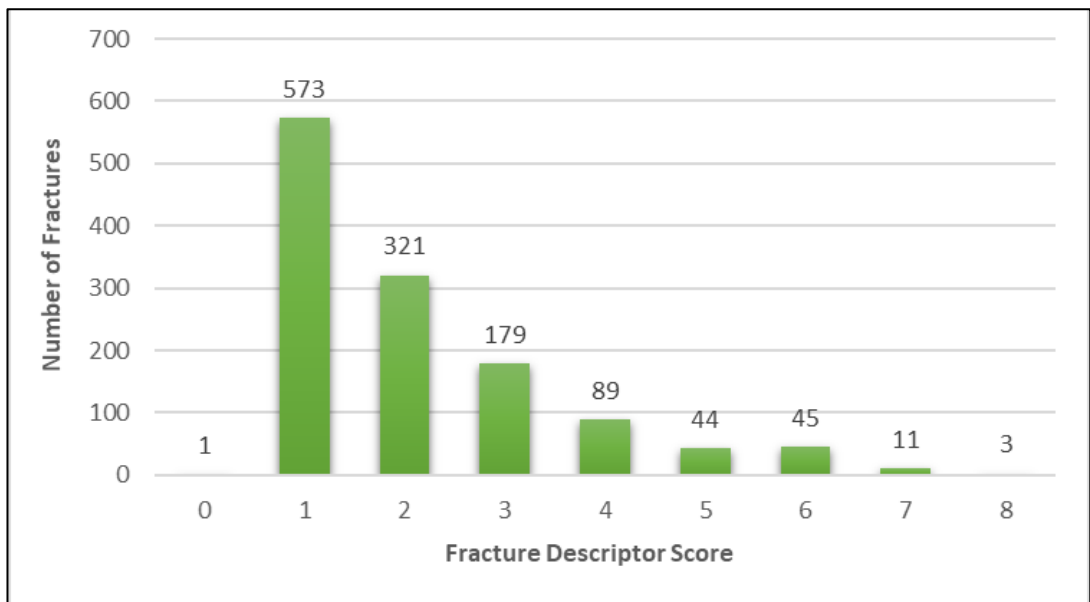


Figure 5-6 – Total number of fractures for each fracture descriptor score in the Harvey-2 core. Increasing fracture descriptor number means a fracture most likely to be tectonic and open to fluid flow (see Section 4.1).

Fractures were then plotted with depth to show how fracturing varies throughout the length of the Harvey-2 core (Figure 5-12).

Observations of the Harvey-2 core showed three distinct fracture types: drilling related fractures, pre-tectonic fractures (i.e. fractures occurring along bedding planes or other sedimentological features), and tectonic or deformation related fractures (see Section 4.1 for examples of each fracture type).

Fractures in the palaeosol were observed of all three categories. High-angle fractures with slickensides were observed in multiple sections of the palaeosol (Figure 5-7).



Figure 5-7 – Slickensides in palaeosol in the Harvey-2 core.

5.3.2 Fracture logging: Harvey-3 results

In total, 1033 fractures were recorded in the sections of the Harvey-3 core which were sampled. 324 (31%) were found in sandstone and 709 (69%) were found in palaeosol (Figure 5-8).

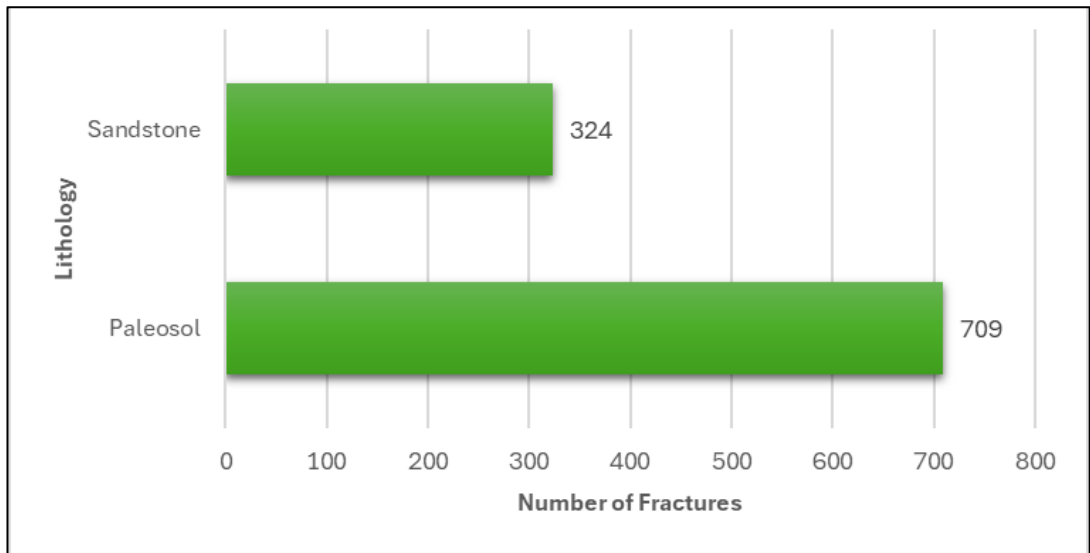


Figure 5-8 – Total number of fractures in each of the two lithologies in the Harvey-3 core.

The fracture intensity with depth is shown in Figure 5-9.

Harvey-3: Fracture Intensity

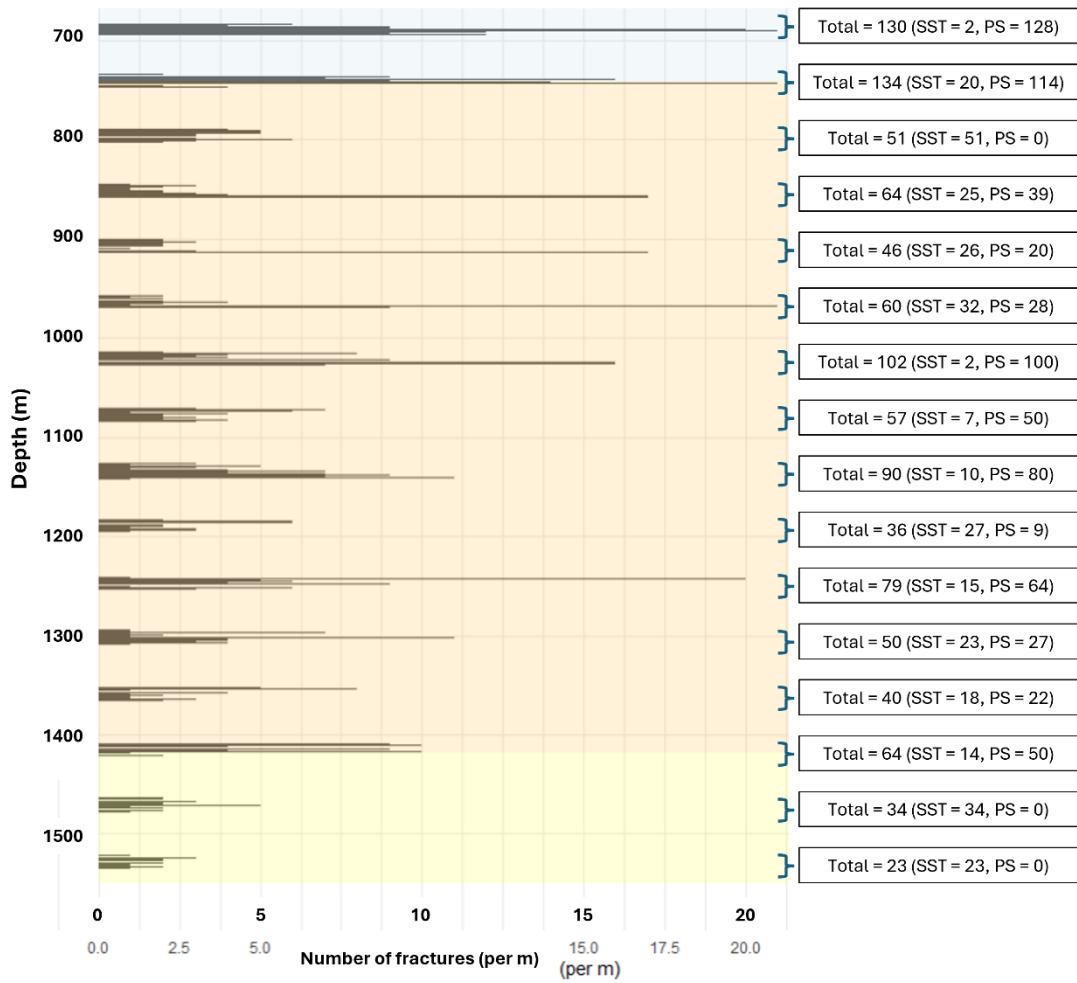


Figure 5-9 – Harvey-3 fracture intensity with depth (m). The total number of fractures per metre of the sampled intervals are shown, as well as a breakdown by lithology (SST = sandstone, PS = palaeosol). Background colours indicate the units: light blue = Eneabba Formation, orange = Yalgorup Member, yellow = Wonnerup Member.

For each fracture, a fracture descriptor score was determined based on the fracture characteristics (Figure 5-10).

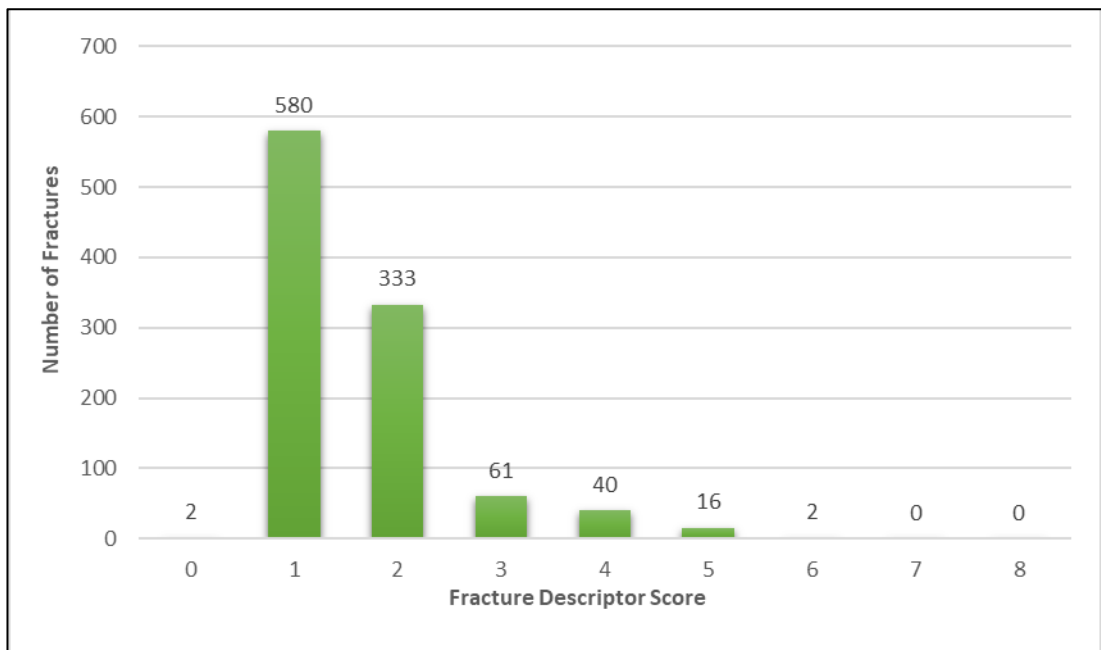


Figure 5-10 – Total number of fractures for each fracture descriptor score in the Harvey-3 core. Increasing fracture descriptor number means a fracture most likely to be tectonic and open to fluid flow (see Section 4.1).

Fractures were then plotted with depth to show how the type of fracturing varies throughout the length of the Harvey-3 core (Figure 5-12).

Like observations made in the palaeosols of the Harvey-2 core, the Harvey-3 palaeosols also show slickensides (Figure 5-11).



Figure 5-11 – PS slickensides. Depths are: A) 780.9m, B) 1400.75m. Image C is a comparative example of a large present-day soil slickenside and is used under the creative commons licence and is the original image of John A. Kelley (Kelley, 2010).

5.3.3 Fracture logging: Synthesis and discussion

Figure 5-12 compares the fracture number scores in the Harvey-2 and Harvey-3 cores.

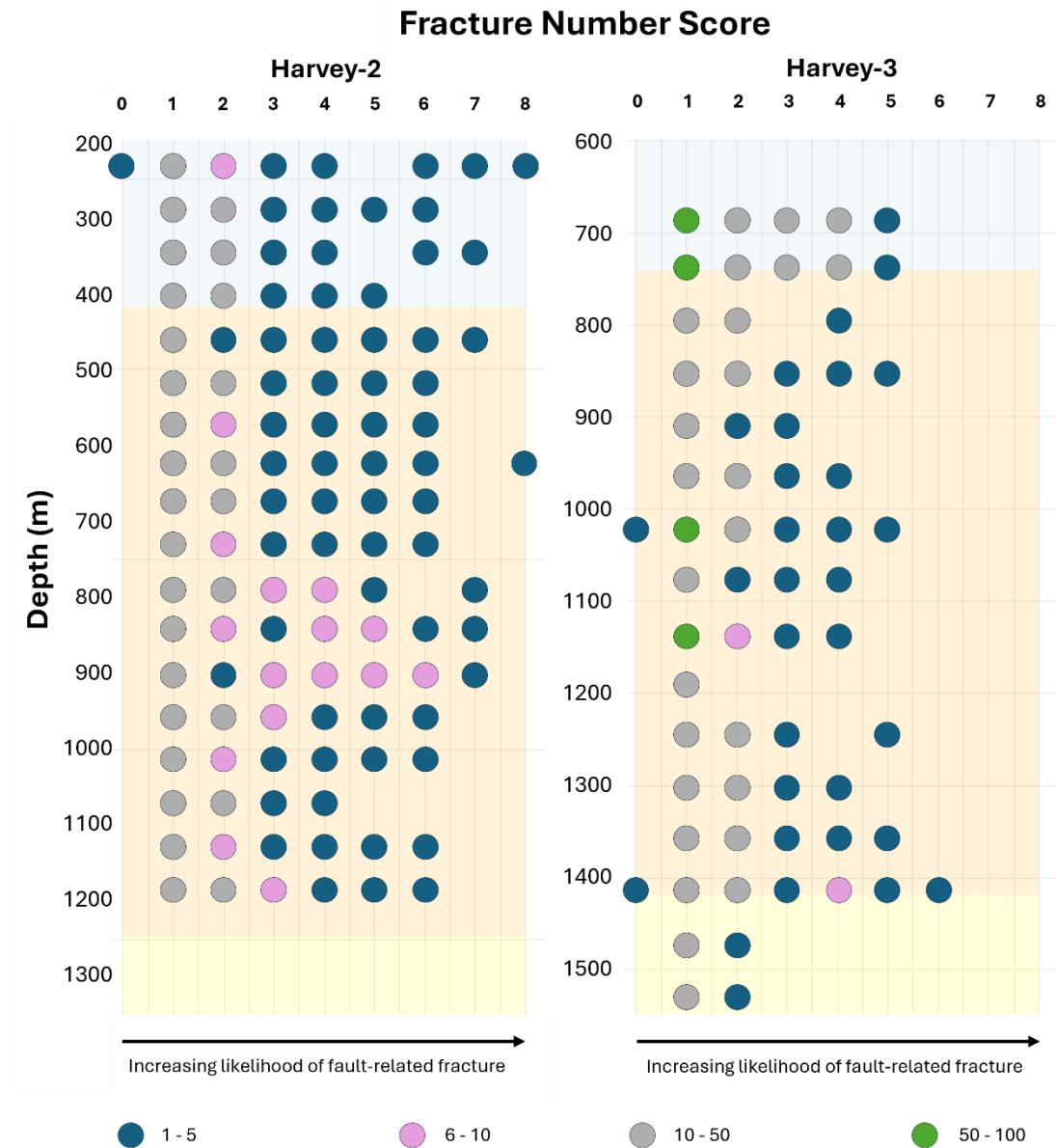


Figure 5-12 – Depth vs fracture descriptor score in the Harvey-2 and Harvey-3 cores. Fractures with a higher score are more likely to have been formed due to a tectonic process. Dot colour indicates the number of fractures recorded for each score at a particular depth.

Fracture logging of both cores produces a broadly similar number of fractures for the length of the core studied. In Harvey-2, fractures with a fracture number score of zero to five are evenly distributed throughout the length of the core. Fractures with the highest fracture number scores (6-8) are not common, with only 20 out of 1266 (1.5%) in the full sampled section. These higher fracture scores are found only between depths of 200-

950m (Figure 5-12). In Harvey-3, observations match Harvey-2 with fractures with a fracture number score of zero to five being evenly distributed throughout the length of the core. Fractures with the highest fracture number scores (6-8) are not common, with only two out of 1033 (0.2%) in the full sampled section. These higher fracture scores are found at a depth of ~1410m (Figure 5-12).

The results from the fracture logging indicate that the fracturing in the Harvey-2 and Harvey-3 cores is mostly from non-tectonic sources such as engineered drilling during core recovery or due to opening along existing sedimentary structures (e.g. bedding planes, soil structures). This is indicated by the low number of fractures with a high fracture descriptor score. There are more tectonic related fractures in the Harvey-2 core, which is likely due to the presence of the F10 Fault.

The data captured by the fracture logging method was not always useful. For example, slickensides would typically be a good indicator of a tectonic fracture, but in this core where palaeosols were present, this was not useful. There was no way to determine slickensides formed via soil processes or via tectonic processes. If applying this method to another core, careful care should be taken to assess the importance of each fracture property recorded and a weighting could be applied to each property depending on how useful that data is, depending on the lithology or fracture types being studied. Research in this thesis shows that fracture properties such as angle and roughness were useful, as these could be easily measured and related to tectonic deformation. However, other data such as fracture mineralisation provided very little useful data due to lack of data points (few mineralised fractures) and slickensides were problematic due to the uncertain nature of their formation.

The fracture logging method did not suitably capture all types of deformation present, such as zones of disaggregation. Consequently, a new method was developed to capture and characterise the deformation in both cores. This method is explained in Section 4.2 and the results are presented in the next section.

5.4 Deformation logging of the Harvey-2 and Harvey-3 cores

This section presents results of deformation logging on the Harvey-2 and Harvey-3 cores from the method outlined in Section 4.2.

5.4.1 *Deformation logging: Harvey-2 and Harvey-3 results*

The style of deformation in the core samples varies between the sandstone and palaeosol:

- Majorly deformed sandstone presents as sediment in the core trays – with a loss of any structure or core shape. The less deformed sections of the sandstone present as circular and coherent core in the core trays, with no sediment or loss of core shape. Less deformed sections of sandstone often contain clasts that are cobble/boulder size.
- Deformed palaeosol is more brittle, with the majorly deformed sections presenting as broken angular clasts of varying sizes in the core trays, with the smaller clast sizes typically collocated with zones of highest deformation.

Figure 5-13 and Figure 5-14 show deformation logs of the Harvey-2 and Harvey-3 cores.

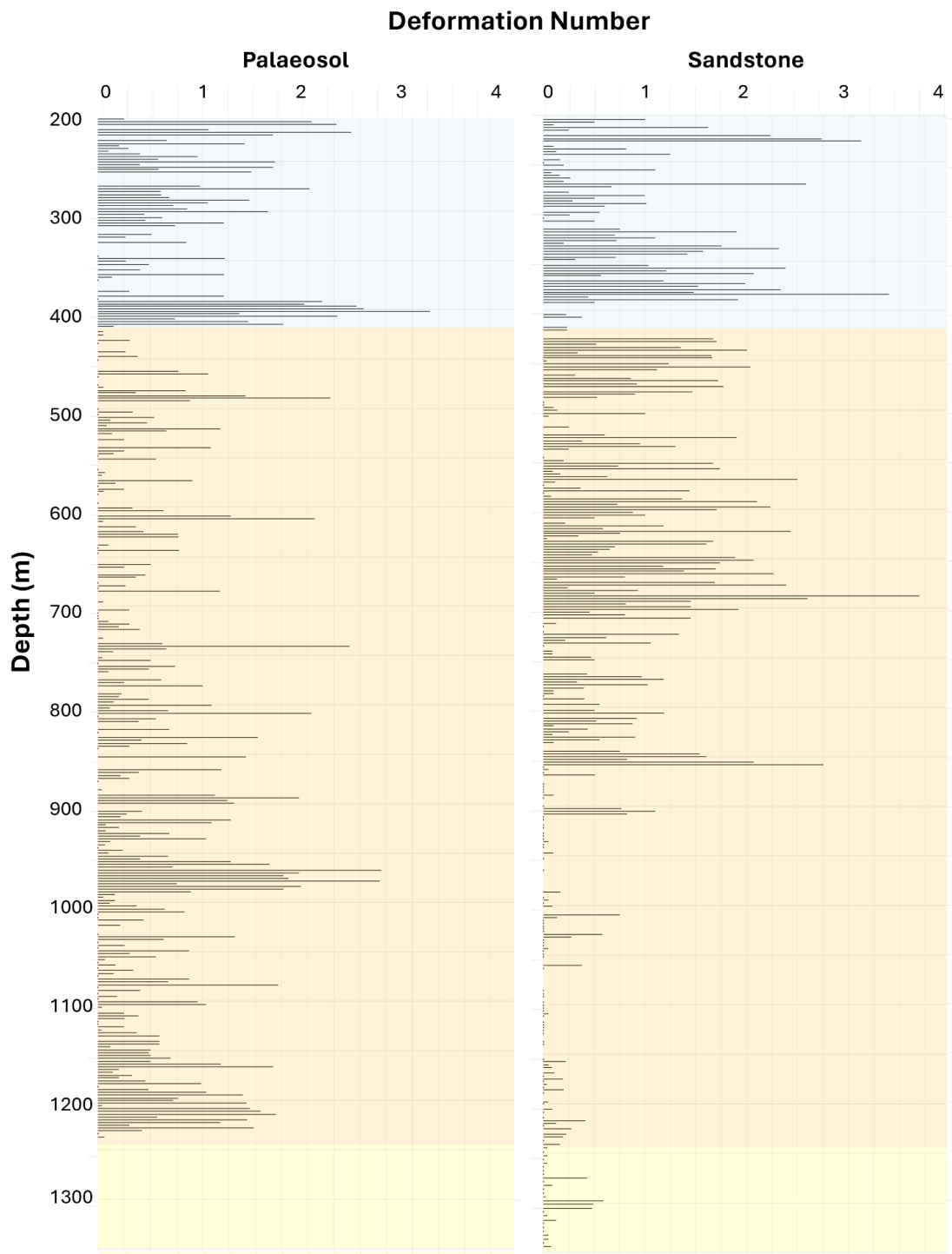


Figure 5-13 – Deformation logs of the Harvey-2 core for both sandstone and palaeosol lithologies. Colours indicate the units: light blue = Eneabba Formation, orange = Yalgorup Member, yellow = Wonnerup Member.

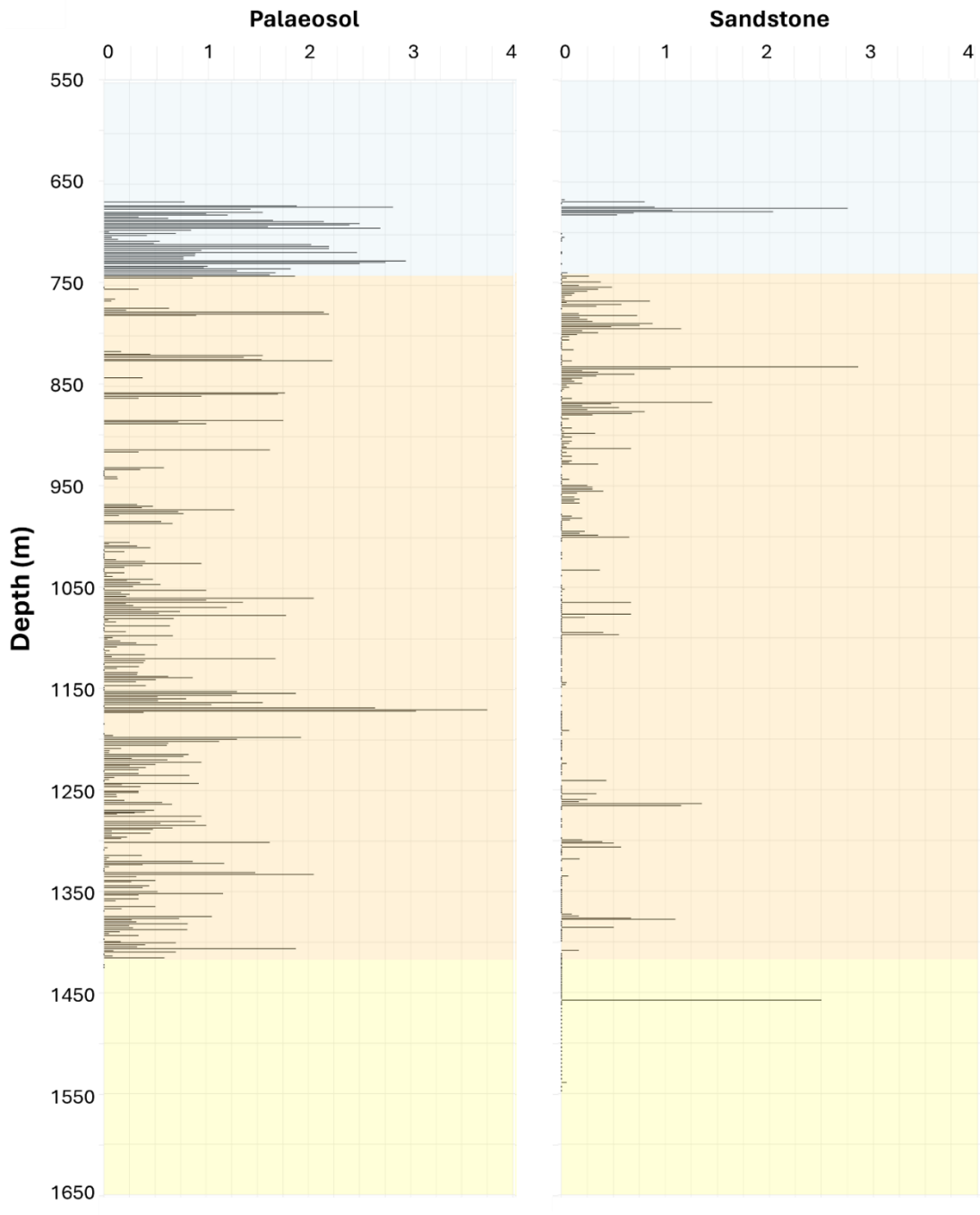


Figure 5-14 – Deformation logs of the Harvey-3 core separated by for sandstone and palaeosol lithologies. Colours indicate the units: light blue = Eneabba Formation, orange = Yalgorup Member, yellow = Wonnerup Member (see Section 3.1.2 for formation/member descriptions).

The Harvey-2 core contains more deformation than the Harvey-3 core. We find that deformation in the Harvey-2 core is distinctly different between the two lithologies. Deformation in the palaeosols varies through the core, but does not seem to be significantly affected by the F10 Fault zone. There are zones which show enhanced deformation (e.g. ~200m, ~400m and ~975m). Similarly, deformation in the sandstones varies with depth, with zones of enhanced deformation at ~225m, ~400m, ~700m and ~850m. However, the sandstone deformation is concentrated at shallower depths, with minor to major deformation until 860m depth. After 860m depth, the core is essentially undeformed. Both lithologies show concentrated areas of deformation around 200-225m and 370-430m, although there are typically less palaeosols in the most deformed section of the fault zone (~600-800m).

Some sections of the sandstone within these higher deformation zones could be highly altered palaeosol. The sand-rich palaeosol (aridisol) may have been altered due to the faulting and disaggregation, allowing fluids to move through these units and flush out the characteristic iron oxide staining – leaving behind sand with a clean appearance

Figure 5-15, Figure 5-16 and Table 5-2 provide summary information on the total length of the Harvey-2 and Harvey-3 cores assigned to each descriptor number for each of the two lithologies.

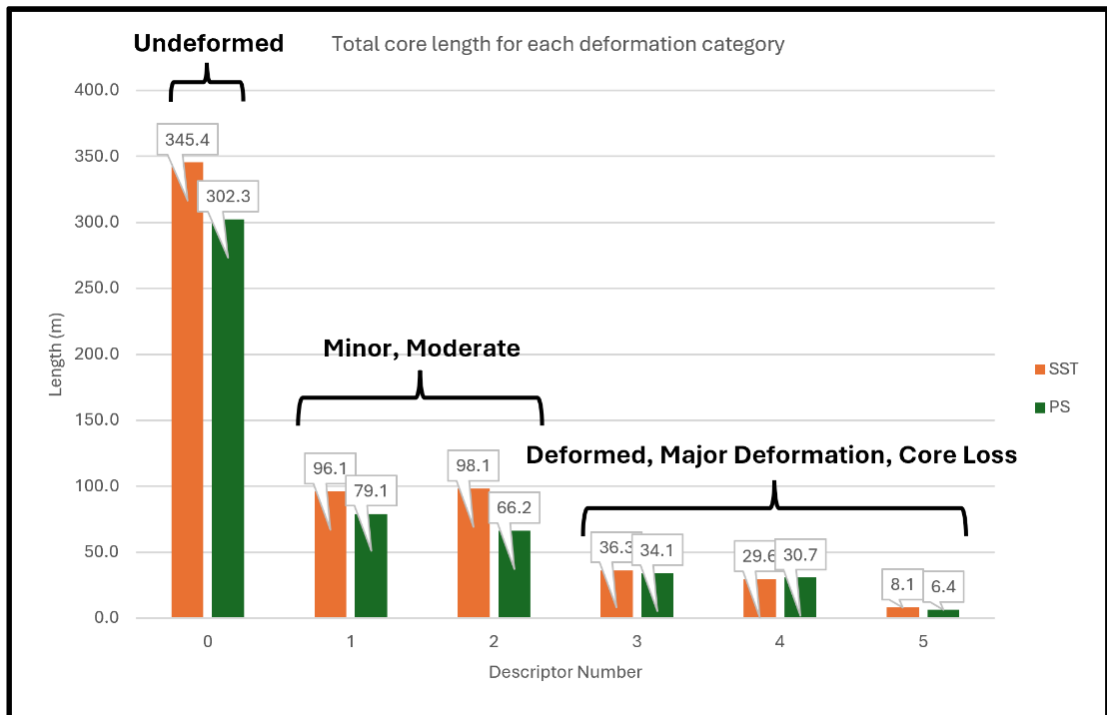


Figure 5-15 – Total core length (m) for each deformation number descriptor for the two lithologies SS = sandstone, PS = palaeosol) in the Harvey-2 core.

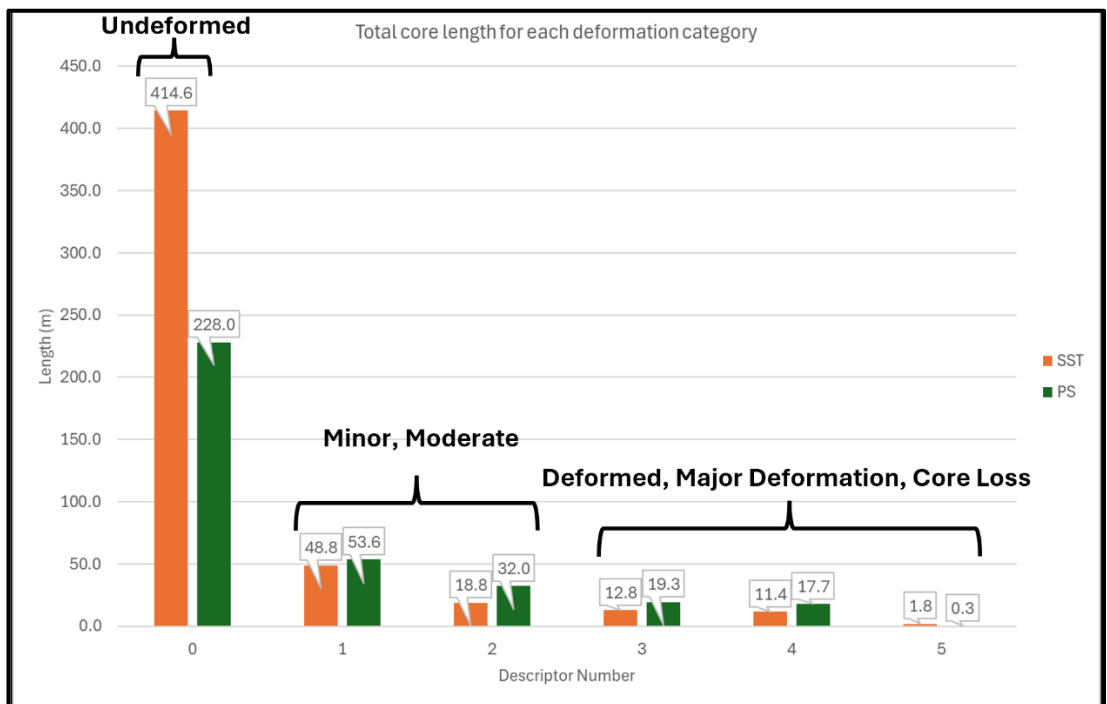


Figure 5-16 – Total core length (m) for each deformation number descriptor for the two lithologies SS = sandstone, PS = palaeosol) in the Harvey-3 core.

Table 5-2 – Summary comparison of deformation in the Harvey-2 and Harvey-3 cores. Core length (m) and % total core are provided for each lithology and a total value for each of the two cores.

	Harvey-2 (~1150m total core length)			Harvey-3 (~860m total core length)		
	SST (m)	PS (m)	Total (m)	SST (m)	PS (m)	Total (m)
Undeformed	345.4 (30%)	302.3 (26%)	648m (56%)	414.6 (48%)	228 (27%)	644m (75%)
Minor/Moderate	194.2 (17%)	145.3 (12%)	340m (29%)	67.6 (8%)	75.6 (10%)	154m (18%)
Deformed, Majorly Deformed or Core Loss	74 (8%)	71.2 (7%)	172m (15%)	26 (3%)	37.3 (4%)	63m (7%)

5.4.2 Bedding dip: Harvey-2 and Harvey-3 results.

Where it was possible to distinguish bedding, the angle of the bedding was measured (see Section 4.2). The core from Harvey 2 and 3 are not oriented and so the strike could not be measured. Figure 5-17 presents variation in bedding angles with depth in the Harvey-2 and Harvey-3 cores.

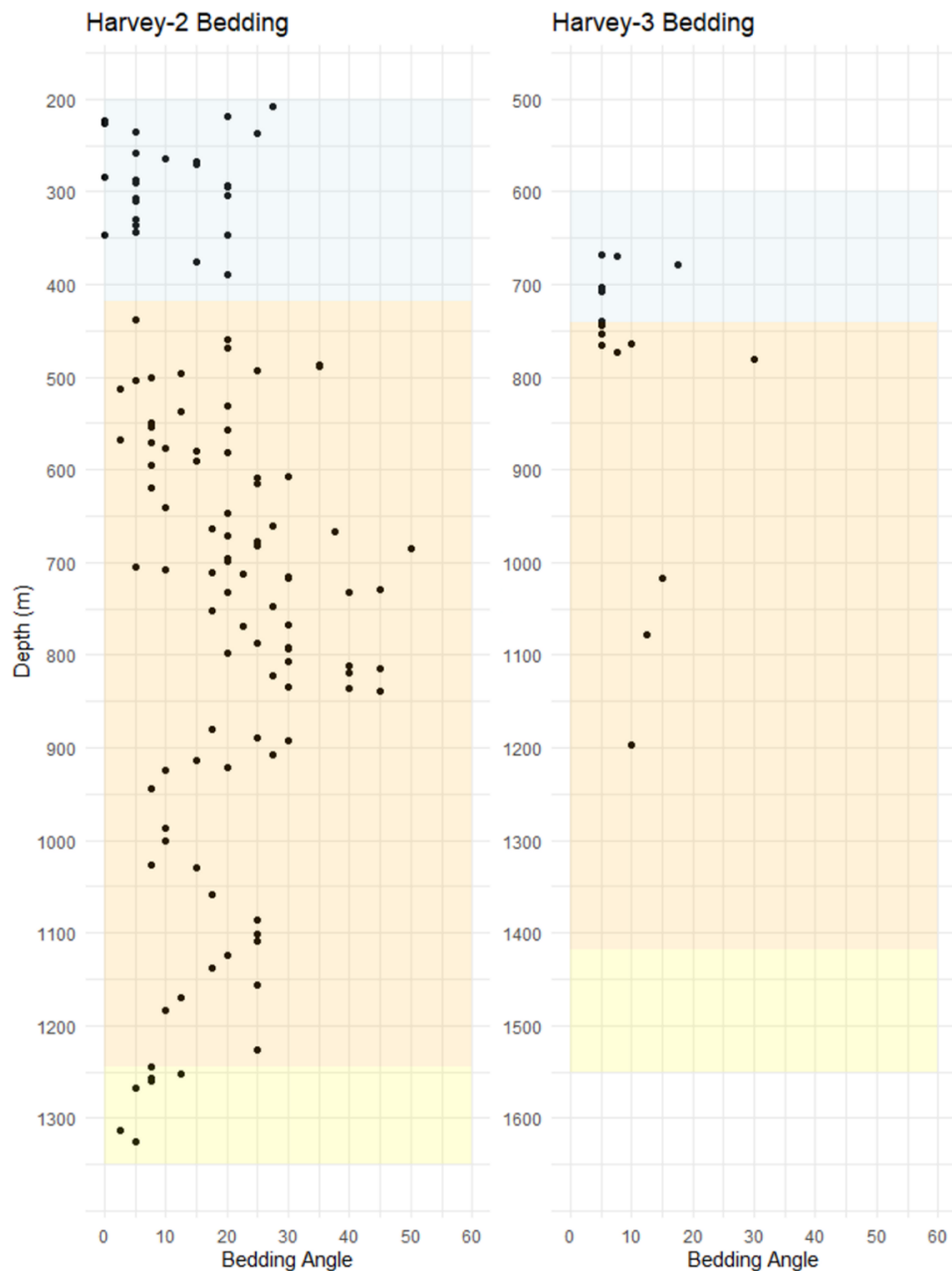


Figure 5-17 – Bedding angle changes against depth (m) in the Harvey-2 and Harvey-3 cores. Less data from Harvey-3 as the bedding was less obvious to measure and there were more cross-bedded sandstones. As such, measurements were only collected when there was a clear lithological contact.

The bedding in the Eneabba Formation, Yalgorup Member and Wonnerup Member is typically 20° or less (see Section 3.2). Dip data collected through much of the Harvey 2 core are in line with these values, except for depths between 500-900m which have bedding angles >25° and up to 45°. In Harvey-3, all but one bedding value is below 20°. The higher bedding angles in Harvey-2 are likely indicators of tectonic movement and deformation due to the presence of the F10 Fault, which has disrupted the bedding angle.

5.5 Petrography of the Harvey-2 core

This section presents results from the samples collected and prepared as thin sections for petrographic analysis (see Section 4.3 for method and equipment).

For this study, samples from Harvey-2 were collected for further analysis, with a focus on collecting samples from depths previously unsampled by CSIRO and the aim of finding evidence of faulting or deformation at the micro-scale. From these samples, six thin sections were created (Table 5-3).

Table 5-3 – Thin section sample names and depths.

Thin Section No.	Sample Number	Formation	Lithology	Start Depth (m)
612883-1	1	Eneabba	Sandstone	207.7
612883-2	2	Eneabba	Sandstone	207.7
612884-1	3	Eneabba	Sandstone	293.9
612884-2	4	Eneabba	Sandstone	296.4
612887	5	Yalgorup	Sandstone	422.4
612889	6	Yalgorup	Palaeosol	932.4

Harvey-2 Petrography: Results

Photomicrographs of select thin sections are shown in Figure 5-18.

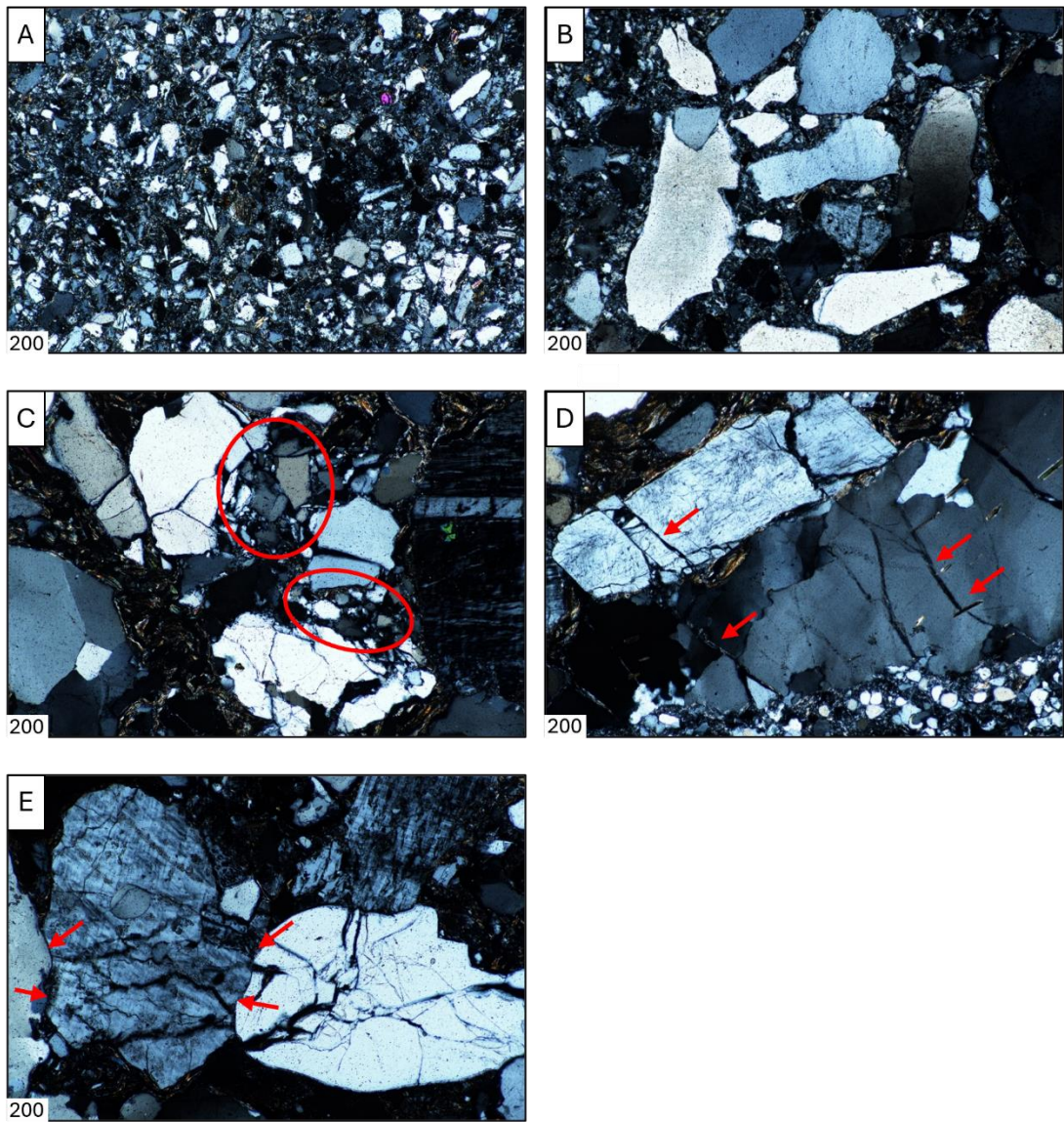


Figure 5-18 – Photomicrographs of thin sections taken from the Harvey-2 core. A) Fine-grained sandstone, angular grains up to 200 microns in size, undeformed (Sample 1). B) Small angular grains up to 500 microns in size (medium to coarse grained) sandstone, undeformed (Sample 1). C) Grain crushing, creating of fine material <50 microns in size (Sample 3). D) Grain fracturing and fracture propagation through multiple grains, highlighted by red arrows (Sample 3). E) Grain to grain contact between quartz and feldspar grains, fracturing of grains (Sample 5).

There is evidence of brittle cataclastic deformation present in the samples taken between 293-423m depth from the Harvey-2 core, characterised by fracturing of grains, fractures cross cutting multiple grains, grain-to-grain contact and crushing of grain edges. This type of deformation is not visible at the core scale and provides an insight into the micro-scale deformation mechanisms in the Harvey-2 core and the F10 Fault zone.

5.6 Harvey-2 XCT: Results

The aim was to scan a section of core from 844.8m - 863.4m depth, as well as select trays that displayed deformation features (e.g. deformation/disaggregation bands). The decision to scan these sections was informed by the results of the deformation logging outlined in Section 5.4. Figure 5-19 shows examples of some of the XCT images showing undeformed and deformed sections of the Harvey-2 core. All the XCT data are not presented here as there is limited analytical options due to the data resolution and the scope/time-constraints of this PhD project.

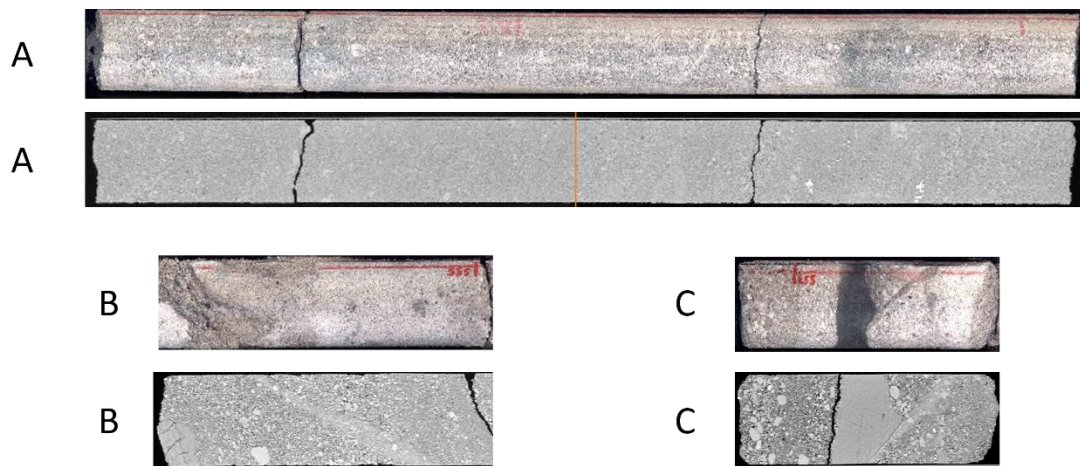


Figure 5-19 – XCT images on the bottom and core photographs taken shortly after the core was drilled in 2015 on the top. Some sections of the core have been damaged or broken during storage, transport and analysis since 2015. A: A 1m section of undeformed core from 862.45-863.4m depth (Tray #238). B: Example of a deformation band in a section from 555-555.3m depth (Tray #127). C: Example of a shear band in a section from 556.15-557.1m depth (Tray #127).

XCT images of the Harvey-2 core show two types of bands: deformation bands and shear bands, typically at angles around 40-60° from horizontal. Shear bands typically occur in the sandstone horizons when they are adjacent to a more clay rich horizon (e.g. example C in Figure 5-19). Compactional or disaggregated bands are when grains have moved and rotated (e.g. example B in Figure 5-19). These features are visible in other scanned sections.

It is not possible to give the orientation of the bands as the core is not orientated. Importantly, the deformation bands observed in XCT are not always obvious to see when viewing the core at hand specimen scale, which means it is challenging to confidently estimate the frequency of the bands within the core.

Quantitative analysis from the XCT data is also problematic to acquire. Due to the scale of the scanning, by using a medical grade XCT scanner, the quality of the data does not allow for grain scale analysis of pore networks, porosity calculations or other similar numerical analysis relevant to fluid flow.

5.7 Synthesis and discussion

This discussion summarises the observations of the Harvey-2 and Harvey-3 cores and presents the limitations and recommendations from this work.

5.7.1 *Harvey-2 Core description: Discussion*

This section explores the various methods used to analyse the Harvey-2 core and summarises key observations and implications.

Deformation logs in the Harvey-2 core show that the primary area of deformation is between 207m-860m (207m is the top of the cored section, and so deformation could continue to shallower depths, but not to surface). Deformation is most prominent in the sandstone of both the Eneabba formation and the Yalgorup formation. There is no evidence of any significant deformation in the Wonnerup member which is found below 860m. The Wonnerup member may be likely less prone to deformation as it has been buried and compacted more than the overlying Yalgorup and Eneabba units due to its position at the bottom of these stratigraphic units. The main zone of deformation identified through deformation logging presented in this thesis also corresponds to a change in the angle of bedding observed within the core (between 500-900m), which could be inferred to indicate faulting or associated deformation (see Section 2.2).

The fractures throughout the core are predominately related to drilling or pre-tectonic structures (related to soil processes in the palaeosols), hence most fractures have fracture descriptor score of 5 or less. Those fractures which have higher fracture descriptor scores (6-8) are those most likely to be tectonic. There are some fractures with a fracture descriptor score of 6-8 in the Harvey-2 core, these are predominately located within the main zone of deformation outlined by the deformation logs (i.e. below ~900m depth). By comparison, there are no fractures with a fracture descriptor score of 6-8 in the Harvey-3 core (which does not cut the F10 fault).

Other challenges when studying fractures in palaeosols include differentiating features associated with deformation or movement and features associated with soil processes. As the palaeosols contain swelling clays, paedogenic slickensides can form (e.g. Figures Figure 5-7 and Figure 5-11 in sections 5.3.1 and 5.3.2). Paedogenic slickensides are a result of soil processes (Gray and Nickelsen, 1989; Coulombe *et al.*, 1996; Kovda and Mermut, 2018), not tectonic processes, and thus it is important not to interpret them as tectonic.

Photomicrographs of samples taken from within the deformation zone in Harvey-2 (~500-900m) show clear evidence of both disaggregation and cataclastic deformation processes (see Figure 5-18). These include evidence of grains moving, rolling, or sliding past and into each other resulting in the fracturing of grains, brecciation of grains and the creation of finer material as a result of this contact and crushing. There is no evidence of similar deformation features in Harvey-3.

XCT scanning revealed features in the core that were not always visible at the hand-specimen scale. Deformation bands, specifically disaggregation bands and shear bands were observed in the scanned sections from within the deformation zone. The presence of shear deformation bands would suggest that these sections of the lithologies have been buried to deeper depths and then exhumed – as these microstructures form typically at depths >1km (see Section 2.4). Deformation bands have been recorded in Harvey-3 and Harvey-4 at depths >1.4km (Delle Piane *et al.*, 2018), and they are observed in Harvey-2 at depths 500-1200m. In Harvey-2, since deformation bands have been recorded at depths both within and outwith the F10 deformation zone, for improved understanding of the burial and uplift history of the F10 Fault further work is needed to understand the formation process, timing and spatial distribution of deformation bands.

Observations of the Harvey-2 core indicate there is around 75m of deformed sandstone (see Section 5.4). This is the minimum estimate assuming adding the length of core characterised as “deformed”, “majorly deformed” and “core loss”. Sections categorised as “minor deformation” are not included. On a 1:10 or 1:20 ratio of damage zone width to slip (e.g. Childs *et al.*, 2009), this would mean an estimated slip of around 750-1500m. This correlates well to previous interpretations of slip from seismic, which are from 750m-1600m (see Section 3.1).

Based on the evidence from the core logs, photomicrographs and XCT images, the fault zone and fault-associated deformation in the Harvey-2 core is interpreted to be located between 207-860m depth (207m is the top of the cored section, and so deformation could continue to shallower depths, but not to surface), with the F10 Fault zone deformation focused between ~600-860m.

Two conceptual 2D models of the fault zone - narrow fault or a wide fault - are shown in Figure 5-20 and Figure 5-21. The narrow model (Figure 5-20) is based on the seismic shown in Figure 3-12, but this interpretation does not work kinematically with the expected offset on the F10 Fault as the boundary between the Eneabba and Yalgorup on either side of the fault does not match with observations of the thickness of these units (see Table 3-1). The Eneabba/Yalgorup boundary on the west side of the fault would need to be ~700m deeper, in which case this would not then correlate with the boundary in the Harvey-2 core at 419m depth. Alternatively, the Eneabba/Yalgorup boundary on the east side would have to be at a shallower level, in which case it must have been eroded and replaced with the unconformably overlying Leaderville Formation.

The wider fault scenario (Figure 5-21) is kinematically more likely, fitting better with the known thickness of the units. The wider fault scenario has a fault zone width of ~500m, which is within the range of widths expected (~300-800m) based on fault displacement/thickness relationships (see Figure 3-13 and Section 3.1.3). Furthermore, the wider fault scenario suggests that there is no hanging wall in the Harvey-2 core, which would explain why deformation is so high at the start of the core as core recovery started within the F10 Fault zone. However, there are significant uncertainties that remain regarding the unit boundary between the Eneabba Formation and Yalgorup Member.

Well and seismic data are not useful for determining the boundary between the Eneabba and Yalgorup units; these are lithologically similar and so there are no obvious wireline logging data or seismic reflectors to help distinguish the boundary. Therefore, defining the Eneabba - Yalgorup boundary is difficult (Core Lab, 2016). There has been no confirmation of any interpreted boundaries by other methods (e.g. additional coring), other than palynology analysis from the cores taken at the In-Situ Lab.

Palynology was used to help determine the relative ages of samples (Backhouse, 2015). The Backhouse (2015) is an unpublished report, but the data are shown in Figure 3-8.

The Eneabba Formation is Jurassic, whereas the Yalgorup Member is late Triassic – meaning the ages of the palynology samples could be used to help identify the units and their boundary. The palynology analysis places the bottom Eneabba boundary at 419m in the Harvey-2 core (Backhouse, 2015) (Table 3-1). There is uncertainty in the unit boundaries due to the spacing of the palynology samples (J. Strand, pers. comm.). The next sample point is 300m deeper in the core, and so there is ~300m of possible uncertainty on the unit boundary (J. Strand, pers. comm.), meaning 419m should be considered the minimum base Eneabba. Furthermore, the top Yalgorup boundary is between 610-730m (Delle Piane *et al.*, 2018) – meaning there is another ~100m of uncertainty on the Eneabba/Yalgorup boundary.

The palynology samples used to determine the unit boundaries in the other Harvey wells (1, 2, 4) are likely to be more accurate compared to Harvey-2 as these wells contain a continuous (unfaulted) sequence (see Section 5.7.2). However, there will still be uncertainty on these boundaries based on sampling intervals and uncertainties related to lithology and palynology.

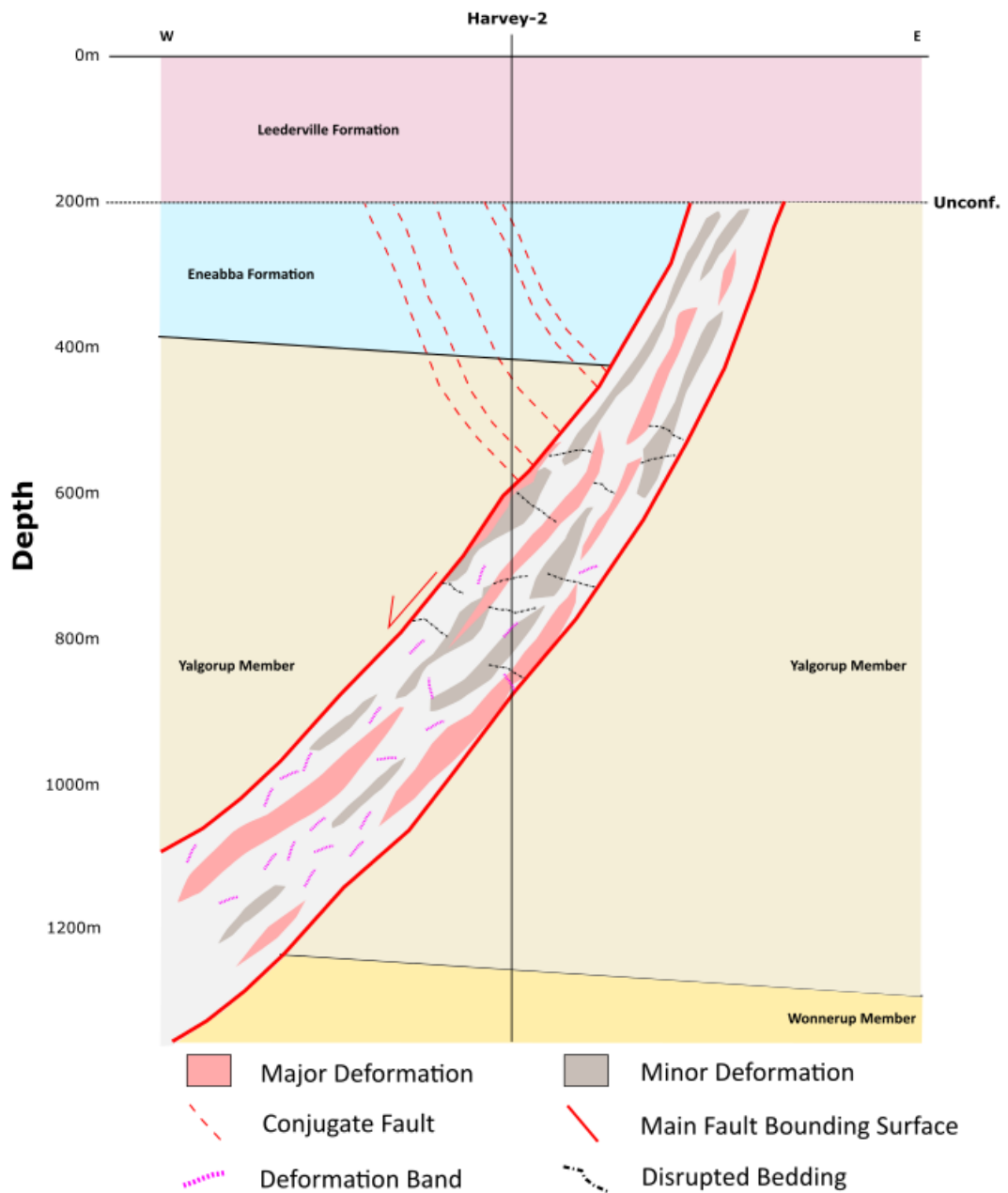


Figure 5-20 – Conceptual 2D model of a narrow width F10 Fault zone based on the deformation logs from the Harvey-2 core. Where features intersect the borehole in the figure, they have been observed at that depth in the Harvey-2 core. Other features are interpretation and extrapolation of core and seismic data. The F10 Fault zone is likely comprised of lenses of major deformation (characterised predominately by particulate flow processes, with minor cataclastic components) with sections of minor deformation (fracturing, minor disaggregation) and sections which are entirely undeformed. There are other key deformation indicators, including disrupted, and steepened bedding and the presence of deformation bands. Note the in this model the thickness of the Yalgorup Member in the footwall is >1km, far thicker than expected (700-800m).

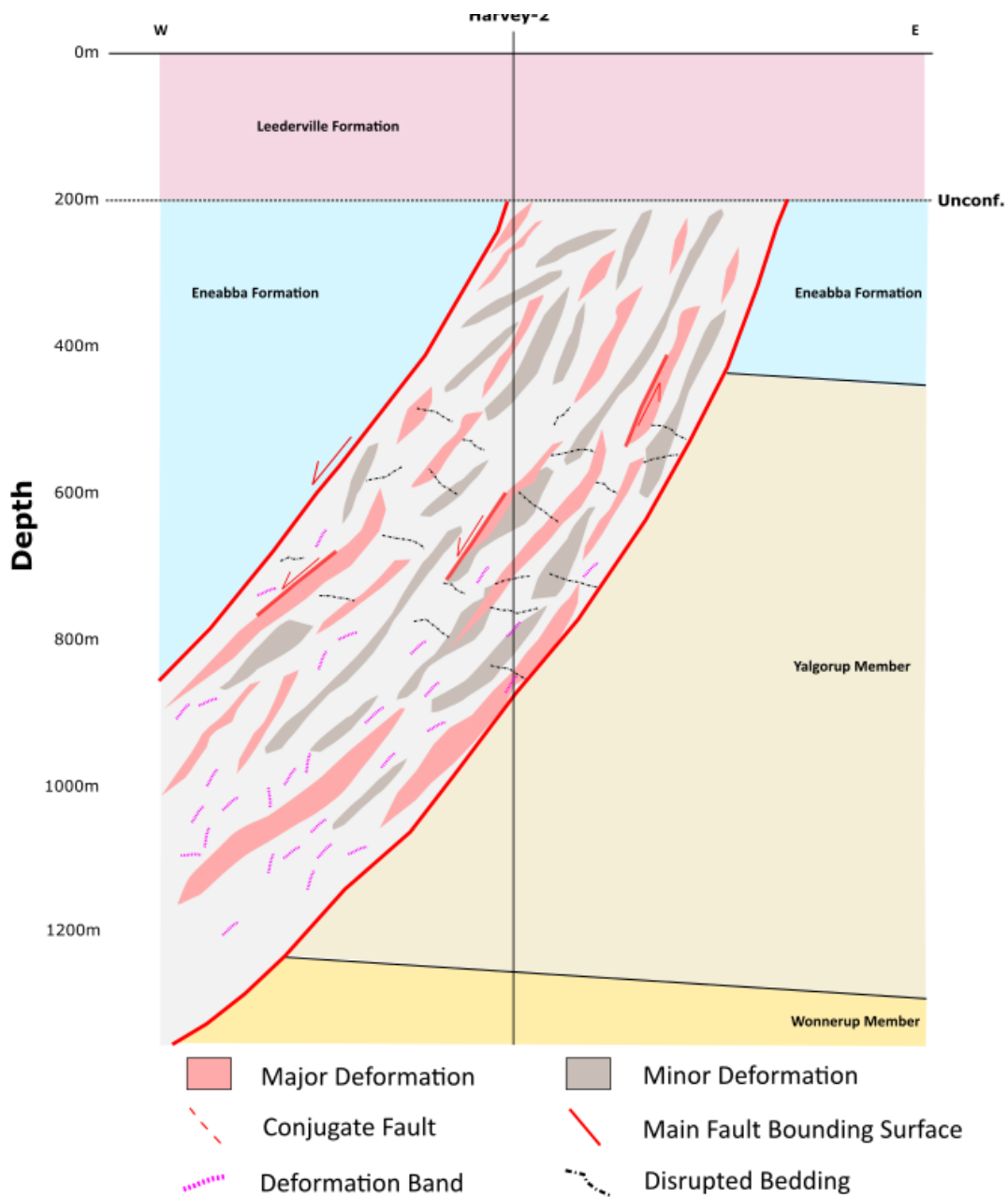


Figure 5-21 – Conceptual 2D model of a wide width F10 Fault zone based on the deformation logs from the Harvey-2 core. Where features intersect the borehole in the figure, they have been observed at that depth in the Harvey-2 core. Other features are interpretation and extrapolation of core and seismic data. The F10 Fault zone is likely comprised of lenses of major deformation (characterised predominately by particulate flow processes, with minor cataclastic components) with sections of minor deformation (fracturing, minor disaggregation) and sections which are entirely undeformed. This deformation makes distinguishing which unit the deformation is in difficult. There are other key deformation indicators, including disrupted bedding angles and the presence of deformation bands. There is no top Yalgorup boundary in the hangingwall in this model, as the boundary reported by a previous sedimentological study (CSIRO, 2019) is within the fault zone: and as such the boundary is likely to have experienced disruption. In this scenario the footwall thickness of the Yalgorup Member is correct (maximum ~700-800m), and the top Yalgorup is well below the borehole intersection in the hangingwall.

5.7.2 Comparing the Harvey-2 and Harvey-3 cores

When comparing the observations from the Harvey-2 and Harvey-3 cores, there are clear similarities and differences.

- **Formations:** Proportion of sandstone and palaeosol
- **Fractures:** Fracture logging of both cores produces a broadly similar number of fractures for the length of the core studied. However, fracture logging shows that there are clearly more fractures which could be related to tectonic deformation in the Harvey-2 core when compared to the Harvey-3 core.
- **Deformation:** Deformation logging of both cores finds the Harvey-2 borehole is significantly more deformed when compared to the Harvey-3 borehole. The deformation in the Harvey-2 borehole is higher in a clearly defined zone, which has been interpreted to represent the F10 Fault zone within the core.

Both logging methods (fracture logging and deformation logging) have identified the F10 Fault zone in Harvey-2, though the fault is much clearer through deformation logging compared to fracture logging. Deformation logging should identify the fault more clearly than fracture logging because the deformation logging method was specifically designed to capture deformation types that you would expect to find in a fault zone deformed in the shallow subsurface. In contrast, fracture logging is biased towards deformation types that that you would expect to find in a fault zone deformed in the deep subsurface (i.e. brittle deformation) (see Section 2.3).

As expected, lithology plays a clear role in controlling the deformation type, severity, and location (see Section 2.4 and 2.5). The sandstone in Harvey-2 is deformed at depths <860m, but in Harvey-3 the sandstone shows no systematic or large-scale patterns of deformation. By contrast, the palaeosol in both Harvey-2 and Harvey-3 are deformed throughout the core length in a similar style (i.e. fracturing). These results support the interpretation that the sandstone is a better indicator of fault related deformation.

Results indicate the Harvey-3 well does not intersect a large fault zone, which aligns well with the regional data (see Section 3.1). There are smaller zones of more deformed lithology, or deformation related features (e.g. deformation bands), but not at the same scale as in Harvey-2. Comparing observations between the Harvey-2 and Harvey-3 wells has helped to validate the deformation logging method as an approach to characterise

deformation in shallow fault zones because the results identify a fault in Harvey-2 and not in Harvey-3. However, the success of the method relies on consideration of the lithologies being assessed.

5.7.3 The F10 Fault: Implications for fluid flow

Fault processes can affect subsurface fluid flow (Section 2.4, 2.5 and 2.6). In the F10 Fault zone, both particle flow processes (e.g. disaggregation, disaggregation bands, grain rotation and movement) and cataclastic processes (e.g. grain collisions, grain crushing, brecciation of grains) are observed at varying scales. These features can either enhance or reduce permeability. For example, disaggregation bands and brecciation/fracturing can be dilational processes that can create enhanced permeability. Conversely, cataclastic processes can generate fine material which can reduce the permeability of the rock. As processes which both enhance and reduce permeability are present at different scales in the F10 Fault, there will likely be increased anisotropy in permeability in the fault zone creating both lateral and vertical heterogeneity. This highlights the challenges around effectively designing ways to collect data that account for and capture these heterogeneities.

Due to the limited number of tectonic fractures, it is not expected that these fractures would have any significant impact on fluid flow in the subsurface pre-, syn- or post-injection. However, drilling induced fractures and the opening of pre-existing sedimentary structures could in theory play a role in enhancing near-wellbore fluid flow during any future injection experiments. This has been observed in other CO₂ release experiments (Roberts and Stalker, 2020), but this was not the case at the In-Situ Lab release experiment. Due to the complications in the In-Situ Lab injection experiment, it is unclear if this is due to a geological or engineering reason, so it does not provide any useful insight. Therefore, based on evidence from other CO₂ experiments it can be argued that understanding the connectivity of the fractures observed in the Harvey-2 core would be crucial to estimate any effect they may have on fluid flow. Further work is required to analyse fracture properties (e.g. orientations, length etc.). This was not possible for the Harvey-2 or Harvey-3 cores as the core sample does not allow a measurement of length and the core was not orientated.

The deformation bands observed can influence fluid flow by either reducing or enhancing permeability. It was not possible to estimate the effect of these bands from

the XCT data collected due to the low-resolution nature of the medical XCT scanner used (see Section 4.4). Further work would be required to fully characterise the extent to which these types of bands were present through the deformation zone and the effect they had on porosity and permeability. The spatial distribution and lateral extent of these features would ideally be examined to assess any effect they could have on fluid flow – however this might prove challenging: while pore network models would be possible from higher resolution XCT imaging, this relies on sampling the core to get smaller core plug, which has been challenging and costly in previous attempts due to the weak nature of the core (see Section 3.1.4).

Some sections of the sandstone within the fault zone which have been deformed could also be highly altered palaeosol. The sand-rich palaeosol (aridisol) may have been altered due to the faulting and disaggregation, allowing fluids to move through these units and flush out the characteristic iron oxide staining – leaving behind sand with a clean appearance. This could explain why there are typically less palaeosols in the most deformed section of the fault zone (~600-800m) (see Section 5.4.1).

The injection of fluids (either drilling fluids or injected fluids for experiments) could have encouraged swelling of clays in the palaeosols, thereby reducing permeability. Furthermore, any transport of these clays to other horizons due to fault movement, or in the process of injection, could result in the pore networks becoming smaller or blocked entirely. This could possibly be a geological reason that would explain why the injection experiment showed no CO₂ migration via the F10 Fault zone (see Section 3.1.4).

5.7.4 Limitations

This study uses data from two cores presented in this chapter, alongside seismic data and other regional structural data (see Section 3.1). Although these cores are extensive in their length, they still do only provide a small sample of the subsurface. As with all core studies, there is still much more we do not know about the subsurface geology and caution should be taken extrapolating the observations made at these cores laterally.

The deformation style and intensity changes through the deformed section. Lithology affects deformation, but there is a lack of detailed studies conducted on the lithology and sedimentological variations of the Harvey cores, particularly for the palaeosol. Therefore, assessing the effect these variations could have on the deformation intensity

or style is difficult. A full detailed sedimentological study was outwith the scope of this PhD due to the time available to view and study the core.

As the Harvey cores are generally weak, the options for further analysis on core material is limited by what can be sampled. This means analysis of core material to provide information on the mechanical and hydraulic properties of the rocks is challenging, time-consuming and expensive. Thus, there has been limited work on this core since the injection experiment in February 2019 and there remains significant challenges in conducting further analysis. Thin sections have been shown to be an effective way to sample and analyse the rock at the micro-scale (see Section 5.5), however a greater number of thin sections would be required to quantify the effects of the micro-scale deformation processes. Methods that are non-destructive (e.g. XCT scanning) have been shown to be effective ways to characterise the rock at the “meso” scale (see Section 5.6). Characterising the “micro” scale via XCT would require more detailed scans of smaller sections of the Harvey-2 core – which again presents challenges in taking samples for this analysis. Additionally, these methods are also expensive and time-consuming, particularly considering the thickness of deformation in the F10 Fault and the quantity of core available for analysis.

5.8 Conclusions and further work

Multiscale analysis of the Harvey-2 core has provided a greater constraint on the architecture of the F10 Fault zone. Previous studies lacked detail on the deformation intensity at various scales (see Section 3.1.3 and 3.1.4). New core logging methods combined with grain analysis and XCT data has given an enhanced insight into the spatial variation and type of deformation mechanisms present within the core. Deformation is observed through the entire length of the Harvey-2 core, with deformation highest in the zone interpreted to represent the Harvey-2 fault zone (207m – 860m). Deformation systematically varies with depth and with lithology: sandstones are deformed only in the fault zone, with palaeosols deformed for the entire length of the core. Deformation processes are controlled by depth and lithology: deformation in the sandstones is related to the fault zone, whereas deformation in the palaeosol is primarily related to the mechanical rock properties and fault-related deformation was minimal. Studying the Harvey-3 core has helped to verify the deformation logging methodology and to confirm the control that lithology has on deformation type and

intensity, as the palaeosols in the Harvey-3 core were also deformed even without the presence of a major fault zone. Further, while fracture logging is a traditional core logging technique, not only is fracture logging challenging when working with larger core lengths and limited study time, but also does not provide useful data on the extent or type of deformation expected from shallow fault zone processes. Had the only method of analysis been fracturing logging, the results of this study would have been different - processes that reduce and enhance permeability would not have been identified and the fault characteristics (e.g. geometry, deformation intensity and style) would be no more certain than from previous data. Therefore, future studies of shallow fault zones should not focus on fracture logging and should instead consider other methods to capture the deformation in the core, such as the deformation logging method developed and applied in this thesis.

Evidence from thin sections shows that the dominant deformation processes in the core are disaggregation related processes such as grain crushing, grain rolling and grain-to-grain contact resulting in fracturing and brecciation of grains. Evidence from XCT scanning revealed the presence of both shear and disaggregation bands throughout the scanned sections of Harvey-2 core which were not always observable in hand specimen. These observations indicate that the fault processes could result in either locally enhanced or reduced permeabilities. The variability in porosity and permeability means the likely flow pathways around the F10 Fault zone will be heterogeneous in nature, with potentially anisotropic flow pathways and increased tortuosity. Fluid flow pathways around the F10 Fault will therefore be influenced by these by this hydraulic anisotropy and tortuosity (see Section 2.1). The variability in fault deformation can be expected from shallow fault zone deformation styles and processes (see Section 2.4). The previous modelling of the F10 Fault zone did not consider the fault properties in this much detail (see Section 3.1.4 and Appendix 1).

Finally, the results from this study have shown that there is significant scope for further work in key areas:

- **Fracturing:** Analysis of fracture properties (e.g. orientations, length etc.) and their spatial distribution and extent around the F10 Fault zone.
- **Deformation bands:** Analysis of spatial distribution and lateral extend to fully assess the effect they have on subsurface fluid flow pathways.

- **Lithology:** Additional study to characterise the variation in their properties. The sandstone and palaeosol character vary throughout the Harvey-2 and Harvey-3 cores. Understanding these variations and the implications they may have for the way the rock behaves mechanically or hydraulically is important to fully understand the way the rock deforms and any influences on subsurface fluid flow. As the palaeosols contain swelling clays, further work should assess the effect any injection of fluids (either drilling fluids or injected fluids for experiments) could have on encouraging swelling. Any additional swelling of these clays could either enhance or reduce permeability (by creating fractures or blocking pore network). Furthermore, any transport of these clays to other horizons could result in similar processes in typically clay-poor stratigraphic horizons.
- **Scale:** Further micro-scale analysis could provide quantification of the effects of different deformation processes on the porosity and permeability of the F10 Fault zone.

The learnings from this project and the suggested further work are important contributions in the design and planning of future injection experiments at the In-Situ Lab. This work has shown the style and extent of deformation in the Harvey-2 core, assessed the extent of the F10 Fault zone and considered implications for subsurface fluid flow. Future injection experiments, and any associated studies (e.g. modelling, monitoring) should consider this more detailed understanding of the F10 Fault deformation styles and heterogeneity and the potential anisotropic permeability distribution in the subsurface caused by the F10 Fault zone. The suggested further work would enhance this understanding and would provide better data for future injection experiments and fault and fluid flow modelling. Furthermore, as Eneabba Formation and Yalgorup Member were deposited in an anastomosing river setting (see Section 3.1.2), the findings from these rocks are likely applicable to other shallow basin settings where these depositional settings are common.

The following chapter focuses on a different fault, the Brumbys Fault, located at the CO2CRC OITC.

Chapter 6 Multiscale characterisation of the fault architecture within the Port Campbell Embayment (Victoria, Australia): implications for subsurface engineering

6.1 Introduction

This chapter presents a multiscale study of the fault architecture in the Port Campbell Embayment. This work was stimulated by uncertainties regarding fault architecture at the OITC and the potential benefits of characterising and incorporating data from similar faults in the region. This chapter presents results from core logging and fieldwork, as well as synthesis of results with existing geochemical datasets to postulate on faulting mechanisms. It concludes by comparing faults observed in coastal outcrops to that described at the OITC, and assesses how regional variations in faulting patterns may lead to erroneous interpretation.

A research paper on this work “Multiscale characterisation of the fault architecture within the Port Campbell Embayment (Victoria, Australia): implications for subsurface engineering” is in preparation for publication.

6.2 Field area: the Otway Basin

To investigate the impact of shallow faulting on fluid flow, we studied the Port Campbell Embayment within the Otway Basin (Victoria, Australia) (see Section, 3.2.1, 3.2.2 and 3.2.3). This was specifically of interest due to the Otway Shallow Fault project and injection experiment (see Section 3.2.4).

6.3 Methods

A multiscale approach was used to characterise the fault architecture in the Port Campbell Embayment. Observations started at the centimetre scale by assessing the style and intensity of deformation in the Brumbys-1 core (as per Section 4.2). Geochemical data were also collected at the centimetre scale from the coast (see Section 4.5). Then, larger scale exposures of the PCL were studied in the field at the “meso” scale (multi-meter to tens of meter scale), both at the coast and inland, to assess variations in faulting patterns within the Port Campbell Embayment (see Section 4.5). Finally, observations of deformation are reconciled with observations of faulting

trends with the regional geology of the Otway Basin (see Section 6.5). Fracture logging of the Brumbys-1 core was deemed to be not useful, because the core lacked evidence of fracturing and the methodology did not capture the observed deformation styles (see Section 5.3.3) – therefore fracture logging was not undertaken at this site.

6.3.1 *Brumbys-1 Core*

The Brumbys-1 core is the only core in the region that has recovered substantial core from the shallow subsurface. There are small amounts of core from the Brumbys-2 and -3 wells, however this is only 35m in Brumbys-2 and 6m in Brumbys-3 (see Section 3.2). Therefore, the Brumbys-1 core was used as the main primary data source as this is the most fully cored section of the PCL in the region. Seismic surveys also suggested that the Brumbys-1 well would intersect Brumbys-1 fault at depth, near the planned CO₂ injection horizon. A deformation log was constructed in April 2023 to systematically examine deformation across Brumbys Fault as captured within Brumbys-1 core (see Section 4.2).

6.4 Results

Results are presented from analysis of the Brumbys-1 core (Section 6.4.1) and field observations in the Port Campbell Embayment (Section 6.4.2).

6.4.1 *Observation of Brumbys-1 core*

Deformation logging (Figure 6-1) shows that deformation varies systematically with lithology and depth:

- The shallowest unit, the Hesse Clay, is entirely undeformed.
- The PCL has variable deformation, generally increasing with depth with the most deformed zone occurring from 97-101 m depth, correlating with the fault zone interval observed by Radke *et al.*, (2022). The deformation does not increase linearly with depth, but there is an increase in deformation from 5-50 m, before a zone of lower deformation between ~55-75 m and finally the highest deformation is observed between 80-120m.
- The deepest unit, the Gellibrand Marl is undeformed starting at 122m.

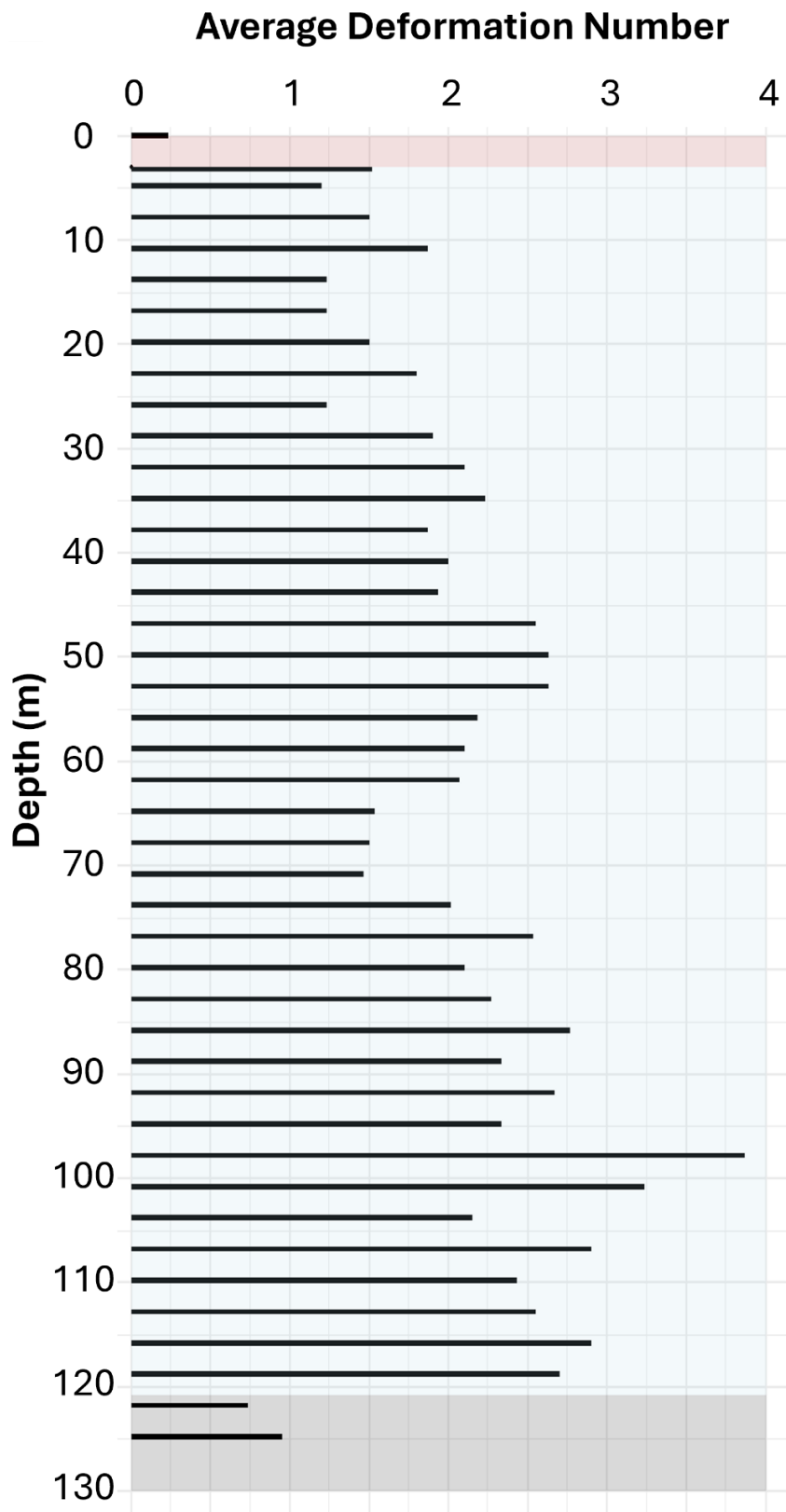


Figure 6-1 – Depth (m) and deformation number (0-4), showing the average deformation in each tray of the Brumbys-1 core. Colours indicate units: Brown = Hesse Clay, Light Blue = PCL, Grey = G. Marl.

At depths where the Brumbys-1 core was deformed with an average deformation number above 3.5, brittle deformation processes such as small scale (mm) fracturing and brecciation were observed. These features were constrained to sections where the PCL was well cemented. Similar brecciation has been observed in previous studies of the PCL (e.g. Radke *et al.*, 2021, Figure 6-2).

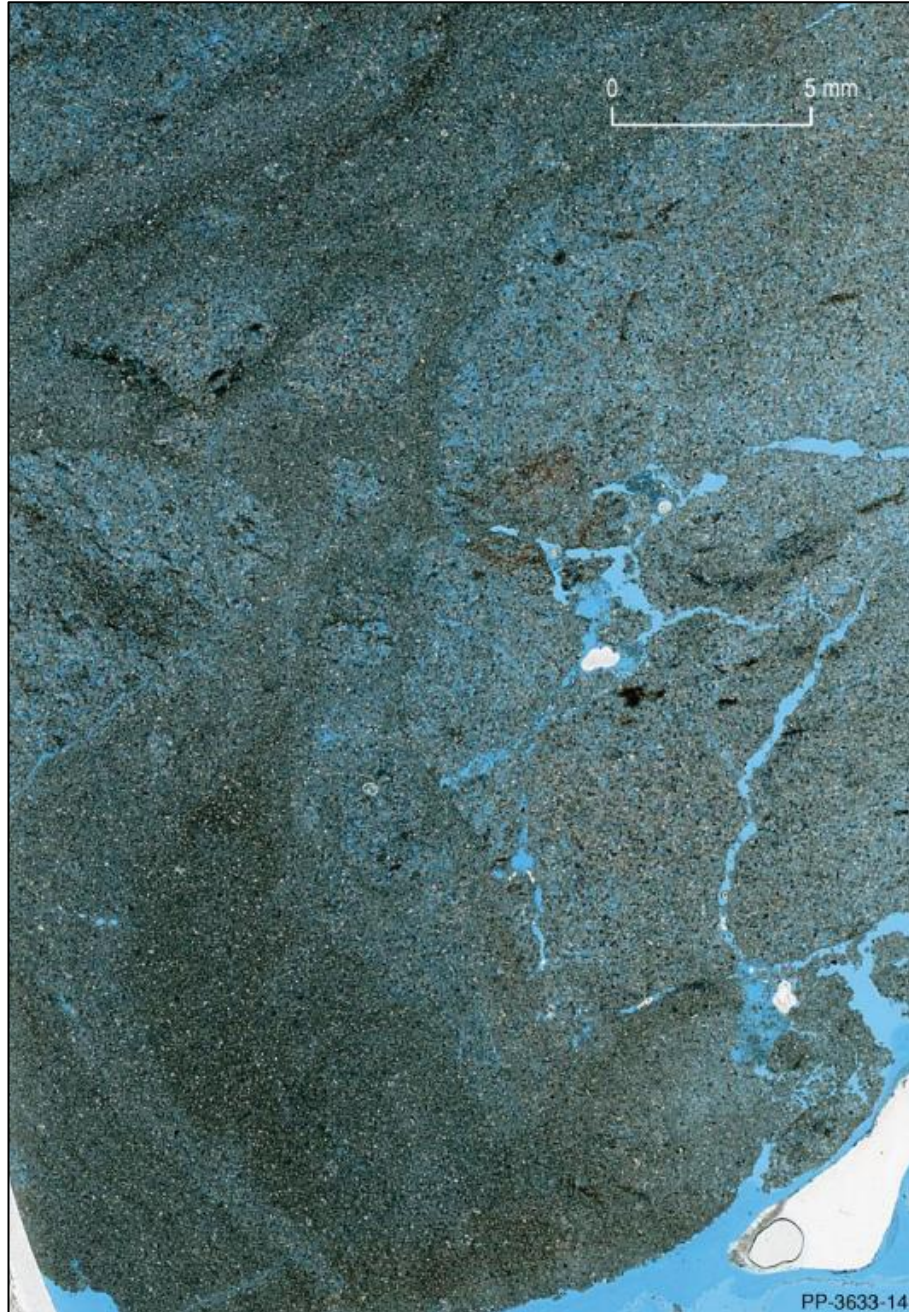


Figure 6-2 – Thin section of the Port Campbell Limestone showing brecciation of grains at the mm-scale (interpreted by Radke *et al.*, 2021).

Combining our observation and deformation log data, it is reasonable to interpret that the fault zone intersects the Brumbys-1 core between 96-102m due to the amount of deformation recorded and the features observed in the core consistent with fault zones processes (e.g. fracturing, brecciation) at this depth. This correlates within 1m to the interpretation made through sedimentary logging of the core (Radke *et al.*, 2022) which was not consulted beforehand.

6.4.2 *Field observations*

6.4.2.1 *Coastal Outcrops*

At the coast, the outer surface of the PCL has been weathered due to coastal erosion. Beneath the outer weathered surface, the rocks have a chalky texture, exhibiting similar characteristics to the PCL core observed in the Brumbys cores and at the Kurdeez Quarry. As it is not possible to take samples at the coast, we assume the rocks would display similar strength profiles to those measured from the PCL in the Brumbys-1 core (see Tenthorey *et al.*, 2022).

Reverse faults with 0.5-2m throw are observed at coastal outcrops (Figure 3-19, Locations D & E) and sometimes correlate with caves in the PCL (e.g. Sherbrook River) (Figure 3-19, Image A). Reverse faulting was observed to the east of the town of Port Campbell, whereas no faults were observed to the west of the town. Strike measurements could not be deduced from the 2D coastline outcrops.

At outcrops where it was possible to observe the fault zones up close (Figure 3-19, Location D & E), the faults did not clearly exhibit a fault core/damage zone architecture, meaning that no cataclastic deformation was observed. One exception was a broken/rubbly zone associated with a large vertical fracture – although it is not possible to say how linked these features are (Figure 6-3, Image C). Smaller, more localized vertical and sub-vertical fractures are confined to individual layers within the PCL (Figure 6-3, Image B).

The slip surfaces of the reverse faults were not planar or obvious, with the surface geometry usually undulating. Fault zones were occasionally associated with 5-20mm wide calcite veins (Figure 6-3, Image D), typically orientated in the same direction as the fault dip.

Figure 6-3 shows the faults and features observed.

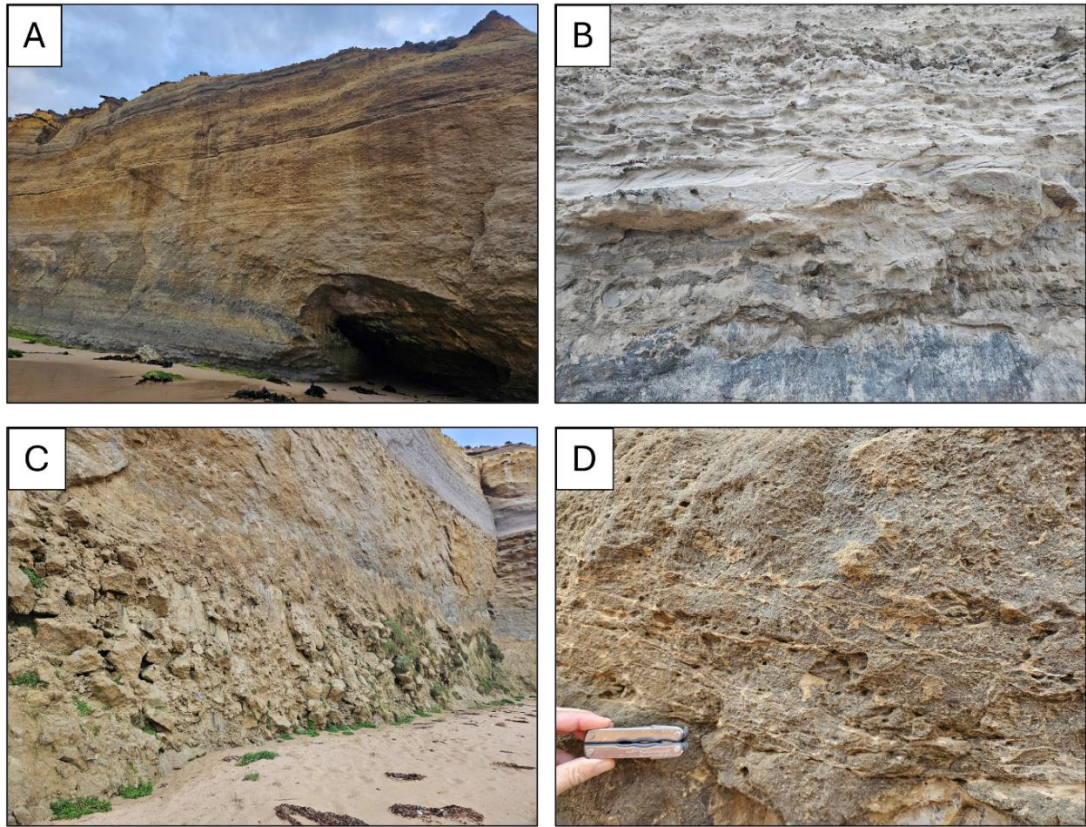


Figure 6-3 – A) Reverse fault at the mouth of the Sherbrook River, fault expires into a cave. Offset <1m. B) Small ~0.3-0.5m dipping fractures within specific layer of the PCL. C) Vertical feature associated with broken rubbly zone along strike – this broken/brecciated material is not observed anywhere else on cliffs in this area. Location: Gibson Beach (-38.669940, 143.113588). D) Veining/deformation associated with reverse fault on Gibson Beach (location: -38.666352, 143.106704).

6.4.2.2 Inland Outcrop

At Kurdeez Mineral Quarry, located 5km north of Timboon, the character of the PCL was more easily visible due to freshness of the surfaces. Due to the fresh and unweathered surfaces, the rocks in the quarry were largely unconsolidated and chalky in texture, showing similar characteristics to the rock core recovered from the Brumbys-1, 2 and 3 wells.

Interestingly, the quarry outcrops exhibited volcanic features that were not observed at the coast. Here, the internal stratigraphy of the PCL is penetrated with large clasts of volcanic material, which is typically vesicular in nature, with a dark black/green colour on fresher sections and more brown/grey colour on weathered and oxidised surfaces. Leaching of minerals from these clasts results in staining of the PCL surface (Figure 6-4, Image B).

There were several examples of karst features that had been infilled by volcanic material. One example was a large cave-like feature >10m deep and 10-15m wide that had been infilled with large amounts of volcanic material, which is locally called “coffee rock”. Another example is a slumped zone where there is a section of the PCL surrounded by dark brown material (Figure 6-4, Image A). Closer inspection revealed a rock that was finely laminated with alterations of layers that were light brown, cream and dark brown. Excavators removed a highly crystallised calcite boulder from this zone.



Figure 6-4 – Images from Timboon Quarry. Both photos show the freshness of the surface. The rubbly nature of the surfaces is because of the quarrying method used and is not a geological feature. A) Cave collapse feature in the PCL. B) Staining of the PCL as minerals are leached from the volcanic rocks that penetrate the PCL sequence.

6.4.2.3 CaCO_3 content of the Port Campbell Limestone

Results of the Gibson Steps and Gibson Beach are shown in Figure 6-5. These data are compared to percentage carbonate data which was collected from the Brumbys-1 well. The results show that there are no significant differences in CaCO_3 content between both sites. This suggests that there is not a lithological variation between the PCL measured inland at the OITC boreholes and the exposed PCL at the costal cliffs.

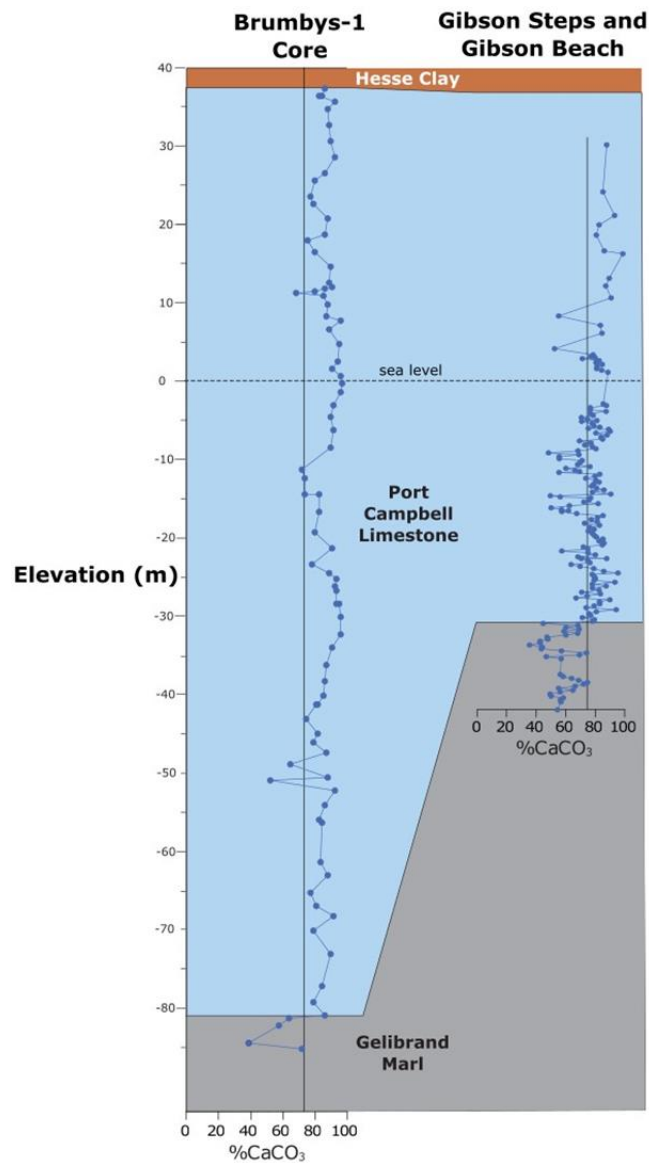


Figure 6-5 – Percentage calcium carbonate (CaCO_3) from the Gibson Steps and Gibson Beach exposures, compared with the percentage calcium carbonate from the Brumbys-1 core. Gibson Beach measurements that are below sea level were acquired by moving laterally along the beach to deeper portions of the section. Figure courtesy of Stephen Gallacher, University of Melbourne.

6.5 Synthesis and discussion

Field observations from ~45km of coastline indicates spatially variable faulting. Reverse faulting is observed to the east of the town of Port Campbell (Figure 2, Location C), whereas no other faulting was observed to the west of the town. Several vertical features were observed along the coast, however it was not possible to see exposures in 3D and therefore no potential offset could be observed – therefore it is not clear if these are possible faults, vertical fractures or other deformation features. The faulting observed at the coast is different from the interpreted fault kinematics of the Brumbys Fault at the OITC. Observations of the Brumbys Fault inland suggests a strike slip fault, with around 2-4m of vertical offset and an uncertain horizontal offset.

6.5.1 *Architecture of faults in the Port Campbell Limestone*

Observations of deformation from the Brumbys Fault zone and from coastal exposures indicate that faulting in the Port Campbell Limestone does not exhibit “archetypal” fault zone architecture such as fine-grained fault core and surrounding damage zone (e.g. Caine *et al.*, 1996; Wibberley *et al.*, 2008; Choi *et al.*, 2016; Torabi *et al.*, 2020). In the Brumbys-1 core, deformation in the interpreted fault zone is dominated by disaggregation and smaller-scale (mm) brecciation of the PCL. This is similar observation to that made by Radke *et al.*, (2022) who observed grain-scale brecciation. In higher porosity carbonate rocks, strain can be accommodated by the pore space during deformation meaning grains compact and dilate leading to pressure solution, grain fracturing/rotation and pore collapse (e.g. Cooke, 2019). Such deformation would normally result in a decrease in porosity and permeability. However, in the areas of highest deformation in the Brumbys-1 core (i.e. the fault zone) the grains are more cemented (based on higher dolomite values), which likely explains why observations indicate evidence of brecciation and fracturing as the rock can more easily deform in a brittle manner. Brittle deformation would allow an enhancement to the permeability as space opens due to fracturing and dilation. Overall, the dominant deformation process within the PCL is a brittle particulate flow process. This is expected, as this type of deformation typically occurs at shallow depths (<1km) in the Earth’s crust (Heynekamp *et al.*, 1999; Caine and Minor, 2009), and so our observations are consistent with the depositional and burial history of the PCL over the last 15Ma (see Radke *et al.*, 2022 and Section 3.2.2).

6.5.2 Deformation, mineralogy and permeability in the Brumbys-1 core

To understand the effect of any faulting and associated deformation on fluid flow within the PCL, estimated permeability curves (from Radke *et al.*, 2021) were compared with the newly collected deformation log of the Brumbys-1 core (Figure 6-6). Permeability and mineralogy curves from Radke *et al.*, (2021) were also compared (Figure 6-7 and Figure 6-8).

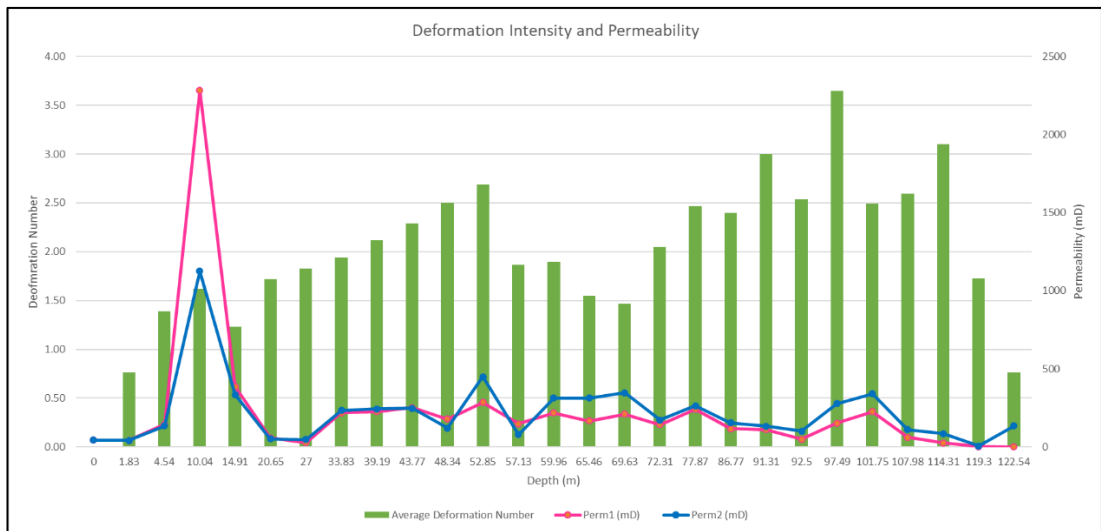


Figure 6-6 – Graph showing the deformation (0-4, left hand y-axis) and permeability variation with depth (mD, right hand y-axis). Two permeability curves are plotted (high permeability case, Perm1 and low permeability case, Perm2) from Radke *et al.*, 2021.

There is no clear link between deformation and permeability. There are some small correlations at some depths (e.g. 4m-20m), but in other zones there is no obvious correlation. In contrast, there is a strong link between mineralogy and permeability.

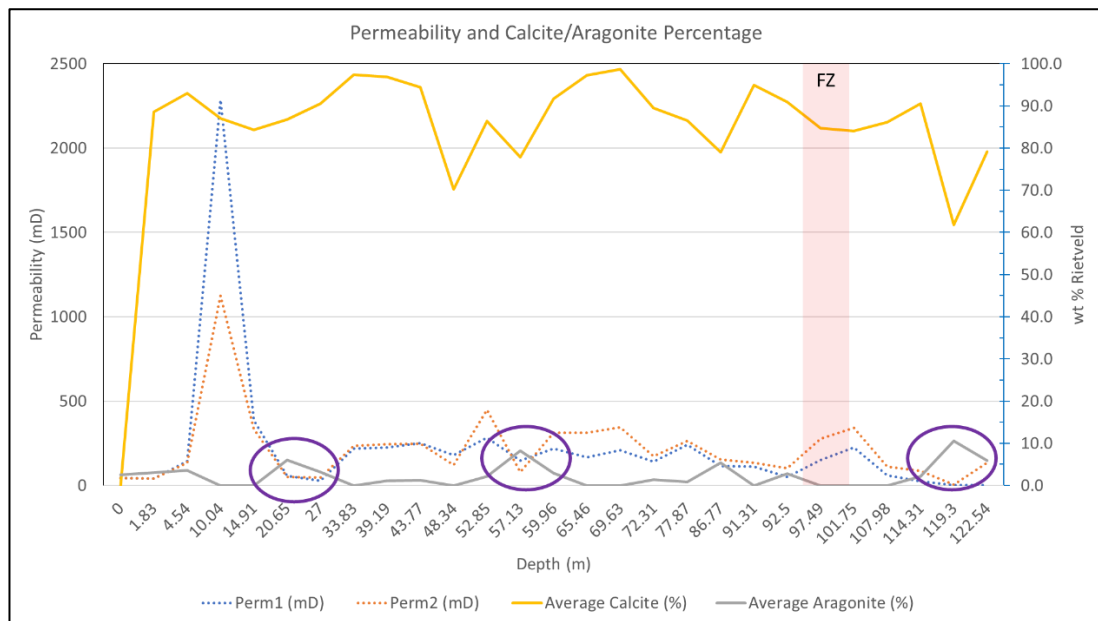


Figure 6-7 – Graph showing mineralogy variations with depth. Mineralogy is shown on the right-hand y-axis (wt % Rietveld) for calcite and aragonite. Two permeability curves are plotted (high permeability case, Perm1 and low permeability case, Perm2) from Radke et al., 2021 on the left-hand y-axis (mD). Purple circles highlight areas of interest – correlating higher % aragonite with drops in permeability. Red zone indicates the extent of the fault zone based on the deformation logs of the core.

Depths with higher aragonite percentage typically correlate to depths that have drops in permeability, which is expected because aragonite is typically easily replaced during diagenesis by calcite as fluids circulate through the sedimentary sequence. These aragonite rich areas should therefore be viewed as low flow, or no flow areas – i.e., seals or baffles in the PCL sequence. Furthermore, areas where there are mineralogical changes do not necessarily mean there will be increased permeability, as the reprecipitation of minerals can lead to pore blocking in other sections of the stratigraphy.

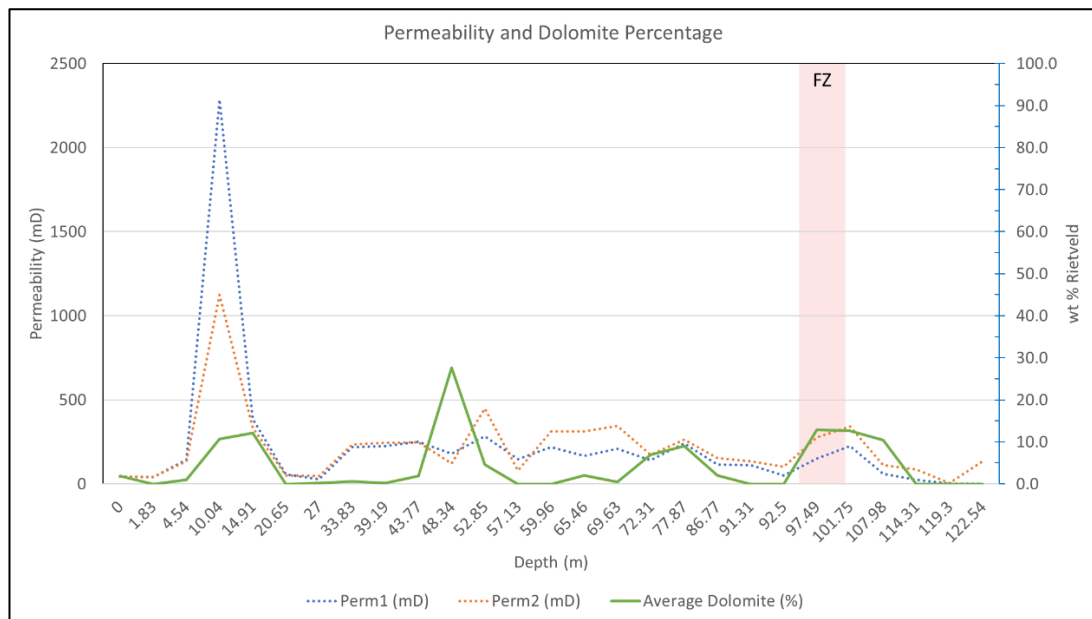


Figure 6-8 – Graph showing the 27 zones of the Brumbys-1 core. For each zone, the mineralogy (Dolomite) is shown on the right-hand y-axis (wt % Rietveld) and two permeability curves are plotted (high permeability case, Perm1 and low permeability case, Perm2). Red zone indicates the extent of the fault zone based on the deformation logs of the core.

Contrary to aragonite, when there is high dolomite percentage, there is an increase in permeability. This makes sense as dolomite can form in multiple ways, for example due to the evaporation of water in sabkhas or due to brine influx in shallow zones beneath the seafloor. These zones have therefore experienced some movement of fluids post-deposition, likely in the shallow seafloor. These zones can therefore be likely seen as zones of higher flow.

It seems that the dominant control on permeability at the core scale will be largely controlled by mineralogical differences within the strata. In zones of highest deformation, the effect of the deformation processes would likely influence the permeability of the PCL, but as a secondary control.

6.5.3 Faulting mechanisms

Our results indicate a spatial variation in faulting within the PCL between the strike slip fault observed inland (Brumbys Fault) and reverse faulting observed at the coast. There are several mechanisms that could cause this variation. This difference cannot be caused by variations in stress tensors across the basin, as multiple sources in the literature report similar stress orientations (see Section 3.2.2). Geochemical evidence suggests that there is not a large difference in mineralogy in the PCL between the coast

and inland, which rules out the difference in faulting being down to mechanical strength variations (see Section 6.4.2.3). At both sites, the PCL has not been buried more than 200m, so different burial histories are not a likely explanation of the variations observed (see Section 3.2.2). Similarly, the PCL is a young rock (~10Ma) and has therefore not had an extensive diagenetic alteration and there is no evidence to suggest that this would dramatically vary between the coast and inland.

The likely variation in faulting between the coast and inland is possibly due to larger regional structures or events. At the coast, the PCL thins towards the south-east (see Figure 3-19) and has shallow angle folding in line with larger offshore fold structures (e.g. Shipwreck Trough syncline). This thinning and folding makes the PCL more susceptible to deformation and consequently the development of faults. Such fold-induced faulting has been observed in other carbonate sequences (e.g. Leader *et al.*, 2010) and fault-fold relationships are well documented in the literature (e.g. Mitra, 2002; Moustafa *et al.*, 2013; Brandes and Tanner, 2014; Coleman *et al.*, 2019, and others) (see Section 2.2).

It is possible that the Brumby's Fault may be related to or influenced by basement structures, or by nearby volcanic activity. The striking observation of volcanic clasts in the PCL at the Kurdeez Quarry (see Figure 6-4, Image B) suggests that nearby volcanic activity during the Pliocene and Quaternary may influence fault kinematics in the area. The presence of volcanic clasts in the PCL indicates that the PCL was in the process of being deposited when the volcanic clasts were ejected. This observation is somewhat contradictory to the current understanding of the depositional timelines of these units as the PCL was deposited between 15-6Ma (Radke *et al.*, 2021) (see Section 3.2.2). The Newer Volcanics were deposited 4.6Ma to 5000 years before present (Gill, 1964; Singleton and Joyce, 1969; Gill, 1971; Thomas, 1976; Johnson *et al.*, 1989; Rosengren; 1994; Oostingh *et al.*, 2017). There is no overlap in deposition between these units, but yet there are volcanics observed within the PCL sequence at Kurdeez quarry meaning the dates in the literature do not seem to correlate with observations made.

There are a number of examples where soft-sediments have been deformed in the region of seismically active volcanic regions (e.g. Mills, 1983; Loon, 2009; Owen *et al.*, 2011; Ko *et al.*, 2017). Shallow faulting observed at the OITC may have been influenced by nearby volcanic activity and the deformation observed is related to soft-sediment style

deformation. This is particularly relevant if the timing of the deposition of the PCL and volcanics is uncertain and possibly coeval.

6.5.4 Limitations

There were several limitations of this study, namely restrictions on sampling and accessibility. Due to the protected nature of the Port Campbell Embayment coastal area, it is not possible to collect samples. Additionally, the accessibility of the coastal exposures is limited due to the rural area, lack of access points and safety issues (i.e. cliff stability).

The Brumbys-1 core was drilled using sonic drilling which results in the core being surrounded in a muddy layer. This disturbs the core and must be scraped off to view a clean surface. Additionally, there was a delay to studying this core due to the COVID-19 pandemic, meaning the core has now been stored for several years and this has resulted in the core drying out significantly. These processes now affect how the core looks visually. Error that this could cause was limited by referring to core photographs taken immediately after the core was drilled to look for obvious signs of deterioration or desiccation that may have affected our observations during deformation logging.

Data availability in the near surface, particularly for things like stress magnitudes is difficult to measure and thus these data are not readily available which creates additional uncertainty in stress regimes and potential faulting types. The uncertainty in faulting type adds uncertainty to any interpretation of how a fault may influence fluid flow, as there are hydraulic and mechanical differences between faults of different types (e.g. strike slip fault vs normal fault).

6.6 Recommendations and conclusions

This study aimed to better understand shallow fault zone architecture in the Port Campbell Embayment to provide additional context to the Brumbys Fault at the OITC, given the field injection tests at the site. Field observations show that where faults are present, the architecture differs spatially across the embayment. In addition to differences in fault type (coastal outcrops show reverse faulting, whereas inland faulting is strike slip), heterogeneity within the PCL is observed – such as different weathering styles, karst features and volcanic deposits. Several factors could cause the observed variation in faulting types, results have shown that these variations are not likely to be

caused by variations in stress tensors, different burial or diagenetic histories, or differences in mechanical strength, but instead are likely caused by regional controls such as larger regional structures, basement structures or the influence of nearby volcanic centres.

Results show that although local fault exposures are useful, there are often regional variations in fault architecture and understanding how smaller-scale observations fit within a regional structural framework is crucial to making informed interpretations.

Observations show that the deformation in the faulted region of the PCL in the Brumbys-1 core is dominated by dilational disaggregation and minor cataclastic processes which will likely enhance permeability. This means that areas within the Brumbys Fault will likely act as vertically enhanced fluid pathways. However, this deformation will not be uniform with depth and will be influenced by the mineralogy of each of the horizons within the PCL. Therefore, it is likely that sections of the fault with higher amounts of deformation may act as a better fluid pathway compared to lower deformation areas. Prior fault and fluid flow models have assumed the Brumbys Fault to have one permeability value for its entire length (e.g. Feitz *et al.*, 2021), but this is likely an oversimplification of the anisotropic nature of the fault zone deformation and permeability. It is much more likely that the fault zone will have varying permeability with depth, with the primary control on the permeability being the host rock properties for each horizon within the PCL. For example, layers where there are increased aragonite concentrations are likely to act as baffles to vertical fluid flow due to their lower permeability.

Generally, there are still limitations in data availability and understanding of shallow faulting processes, particularly in carbonate rocks, which present challenges in effectively predicting fluid flow in shallow fault zones. This creates uncertainty in fluid flow pathways and inhibits target monitoring based on geoscience knowledge and instead means a blanket monitoring approach is often required. Further work is recommended on:

- **Regional faulting mechanisms:** Further work is required to ascertain the influence and timing of the potential faulting mechanisms outlined in Section 6.5.3 and how they may have influenced the development of the Brumbys Fault. Analysis of regional seismic datasets could provide insights into larger

subsurface structures that may have influenced the development of faults with different kinematics in the shallow subsurface.

- **Shallow subsurface characterisation:** Further characterisation of the shallow subsurface in carbonate lithologies to understanding controls on deformation processes and the influence deformation features have on hydraulic properties and fluid flow. This information will allow the design of targeted monitoring approaches which monitor the most likely pathways to surface. Targeted monitoring has been shown to be the most effective approach for monitoring seepage from natural CO₂ and H₂ seeps (e.g. Roberts *et al.*, 2017; Prinzhofer *et al.* 2019; Myagkiy *et al.* 2020a, 2020b; Frery *et al.* 2021 Moretti *et al.* 2021a, 2021b; McMahon *et al.*, 2023), but this requires an understanding of the processes (e.g. faulting) that take place in the shallow subsurface that can influence fluids and flow pathways.

The following chapter considers the challenges of modelling of shallow fault zones using petroleum-based modelling approaches.

Chapter 7 Modelling shallow fault zones using petroleum-based modelling approaches: challenges and learnings

7.1 Overview

This chapter presents work completed during COVID-19 pandemic. This work was some of the first work completed as part of this PhD project after field visits were cancelled due to the COVID-19 pandemic.

This chapter initially aimed to model the Brumbys Fault zone, prior to fieldwork to examine the site (Chapter 6), with two main research questions:

1. What influence did the type of stress regime have on the likely location, distribution, and geometry of deformation (i.e. fractures)?
2. How would any deformation/fractures likely influence fluid flow around the Brumbys Fault zone?

The modelling set up and workflow were completed prior to having access to the Brumbys-1 core (as international travel to Australia was not possible during the COVID-19 pandemic) and therefore this was designed prior to primary data collection. The workflow was based on typical modelling workflows which are designed and biased towards the deeper subsurface (e.g. hydrocarbon applications).

It became clear after visiting the Brumbys-1 core in April 2023 that the core was not tectonically fractured and that attempting to characterise fractures in the core would not be useful research task. Although core photographs were available prior to defining the modelling, these did not clearly show the deformation features due to the image resolution and the coating of the core in a layer of carbonate drilling mud (see Section 3.2.3). Therefore, it became clear that the proposed modelling approaches which relied on analysing fractures were unsuitable for the type of fault and lithology. As such, this chapter presents preliminary results from the modelling work and goes on to discuss some of the challenges of applying these more classic fault analysis and modelling approaches to shallow fault zones. The modelling theory is provided in Appendix 6. This chapter will first present the summary geological data needed, before discussing how

the models were built. It will then go on to present different modelling scenarios, fault slip scenarios and then discuss the usefulness of the results.

7.2 Method

A modelling workflow was developed with 5 stages:

1. Build conceptual geological model (fault and observation surfaces)
2. Input/calculate expected slip on the fault surface (including slip types and vectors)
3. Assign mechanical properties to the fault and observation surface
4. Run simulations + create fracture networks.
5. Analyse results (e.g. fracture analysis)

Figure 7-1 shows the fracture analysis workflow.

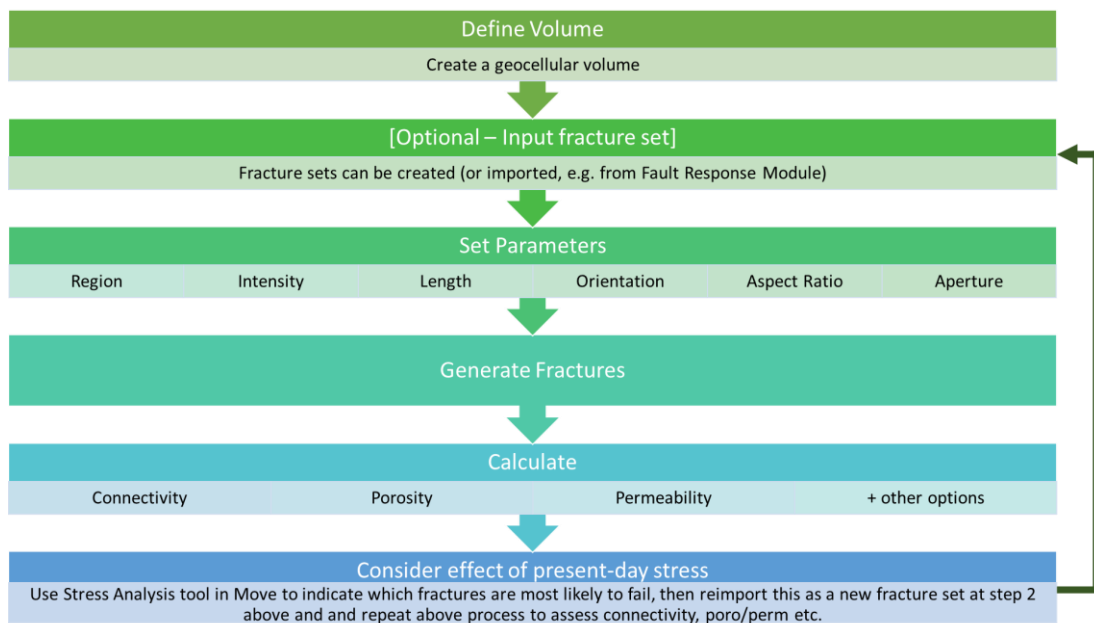


Figure 7-1– Flow diagram showing the fracture analysis part of the modelling workflow.

7.2.1 Step 1: Model building

The model was designed by integrating different data sets (e.g. LIDAR, geophysical surveys, seismic, rock cores, hydrogeological surveys) (Radke et al., 2017). The base geological model used for this analysis is based on version two of the static 3D geological model created in Schlumberger Petrel by CO2CRC and partners (Feitz et al.,

2017). The model consists of 27 layers, from the surface (46.45m above MSL) to the bottom of the PCL (-84.12m above MSL). 25 of these layers are internal zones of the PCL. The remaining two are the top of the Hesse Clay, above the PCL, and the top of the Marl below the PCL. In addition to the stratigraphy, there is a fault surface that represents the Brumbys Fault. The structural surfaces of the layers and the Brumbys Fault were interpreted from cross line-65 of the Otway mini-3D seismic cube in depth domain (Wang *et al.*, 2020). CO2CRC interpreted the fault geometry using the Schlumberger Petrel ant-tracking workflow, which uses a signal tracking algorithm to find the best connectivity for fault related features (see Radke *et al.*, 2017 for full workflow).

The stratigraphic layers and the Brumbys Fault surface were imported into Move as EarthVisionGrid surfaces using the “depth” option in the import wizard in Move. In Move, the stratigraphic surfaces were edited to be split into two sections by the Brumbys Fault, giving a footwall and hangingwall section of each surface. Any edge effects were removed by filtering the edge of the surfaces. The fault surface was extended, as the fault is known to extend outwith the area of the 3D seismic survey with a total minimum length of ~1.2km (see Section 3.2.3). The fault mesh was then resampled using the adaptive sampling tool in Move to retain the geometry of the original surface whilst creating a more uniform mesh surface to allow the algorithms to run as intended (Figure 7-2).

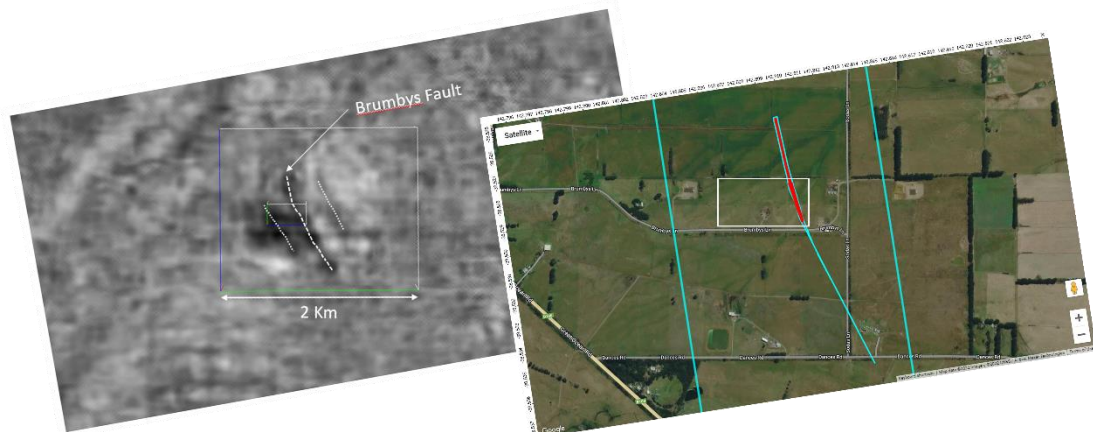


Figure 7-2 – Left image showing the 2D seismic surface showing the Brumbys Fault in the centre. The right-hand image shows the Brumbys Fault in Move, with a satellite image overlain to show the theoretical surface trace of the fault.

Various well data for the Brumbys-1 borehole (see Wang *et al.*, 2020) were added to the model as the Brumbys-1 well imported using the “depth” function in the import wizard.

Once imported, the well log data (e.g. clay volume, porosity, permeability) were added along the well track.

7.2.2 Step 2: Fault slip scenarios

From observations at the Otway site, the fault has a vertical offset of 4m and a horizontal offset of 150m. Rather than input these values as the slip and have the fault move in one large movement, the “remote loading” option in Move was used. This allows you to load a fault with a remote pressure. Additionally, “slip zone modelling” and “regional stress” options were used to apply a far field stress to the fault zone and allow interaction between the triangular elements of the model. Based on the input stress field, the model calculates the slip required to cause this stress across the fault plane. This allows the modelling of different stress fields and consequently the distance the fault would have to move to create/accommodate such stresses can be estimated.

To account for the uncertainty in the stress regime and magnitudes, eight scenarios were set up to act as end member scenarios for each possible permutation of stresses (Table 7-1). Depth of the fault acts as limit on the vertical stress magnitude. A maximum fault burial depth of 200m was assumed, given the geological history of the area (see Section 3.2.2). Maximum and minimum stress gradient were set as 20MPa/km and 10MPa/km based on previous studies of deeper stresses and average stress gradients with depth. This then provides an upper and lower limit for the vertical stress of 2MPa (maximum) and 1MPa (minimum) respectively based on the gradients and depth of fault burial. The fault was modelled as cohesionless (0MPa).

Table 7-1 – Modelling scenarios for each stress regime, with stress magnitudes and horizontal (azimuth) directions.

Scenario No.	Stress Regime	σ_1 (MPa)	σ_2 (MPa)	σ_3 (MPa)	σ_1 (°)	σ_2 (°)	σ_3 (°)
1	Strike Slip	2.1	2	0.6	142	0	232
2		6.5	2	1.9			
3		1.1	1	0.3			
4		3	1	0.9			
5	Normal	2	1.9	0.6	0	165	255
6		1	0.9	0.3			
7	Reverse	7	2.1	2	255	165	0
8		3.5	1.1	1			

7.2.3 Step 3: Mechanical properties

Table 7-2 summarises the mechanical properties that were used as data inputs for the model.

Table 7-2 – Mechanical properties and the possible ranges based on previous testing (Feitz et al., 2021).

Parameter	Value
Poisson's Ratio	0.13-0.28
Young's Modulus	190-600 (MPa)
Friction Coefficient	0.65-0.70
Cohesion	~1-10 MPa

Varying the properties within the ranges shown did not have any significant effect on the results. This shows that the mechanical properties are not a primary control on the outputs in these scenarios.

7.3 Results

7.3.1 Step 4: Simulation results

Table 7-3 summarises the results from the eight scenarios presented in Table 7-1. These scenarios provide an estimate of the number of slip events that would take place for the given stress regime and an estimate of the slip rate per year given the estimated horizontal (~150m) and vertical (~4m) displacements of the Brumbys Fault (e.g. Figure 7-3). The purpose of these scenarios was to estimate strain and stress fields around the Brumbys Fault for different stress regime scenarios. Strain and stress fields can be used to predict the behaviour of any fractures (i.e. if the fractures are open, or prone to reactivation). A fracture network could be created based on the most likely orientations and this network could then be analysed using fracture analysis tools in different stress regimes to understand how fractures may respond to different possible present-day stress scenarios, or any changes in stress due to injection of fluids.

The results range from slip rates of 0.015mm per year for a strike slip fault and 0.0004mm per year for normal or reverse faults – which are not significant enough to cause any notable seismic events. Expectedly, higher stress magnitudes resulted in higher maximum displacement for all scenarios (47mm for strike slip, 9mm for normal and 85mm for reverse). This means the fault would move less often, but when it did move

the displacement would be greater. Overall these results are not surprising and are in line with the expected fault kinematics from a fault with this displacement and geometry.

Table 7-3 – Model scenarios showing the conditions for each scenario constrained by maximum possible fault burial depth (~200m, assuming a typical pressure gradient of ~1MPa per 100m depth), followed by the slip modelling results in the right hand columns. Results include the maximum possible slip per event, the number of slip events to match the observed slip (150m horizontal, 4m vertical), and slip rate (which is horizontal for strike slip scenarios and vertical for normal/reverse and calculated based on fault movement over a 10Ma period).

Scenario No.	Stress Regime	σ_1 (MPa)	σ_2 (MPa)	σ_3 (MPa)	σ_1	σ_2	σ_3	Model Max Slip (mm)	No. of Slip Events	Slip Rate (mm/yr)
					Azimuth (°)	Azimuth (°)	Azimuth (°)			
1	Strike Slip	2.1	2	0.6	142	0	232	15	10,000	0.015
2		6.5	2	1.9				47	3,192	
3		1.1	1	0.3				8	18,750	
4		3	1	0.9				22	6,818	
5	Normal	2	1.9	0.6	0	165	255	9	444	0.00004
6		1	0.9	0.3				4.4	909	
7	Reverse	7	2.1	2	255	165	0	85	47	0.00004
8		3.5	1.1	1				42	96	

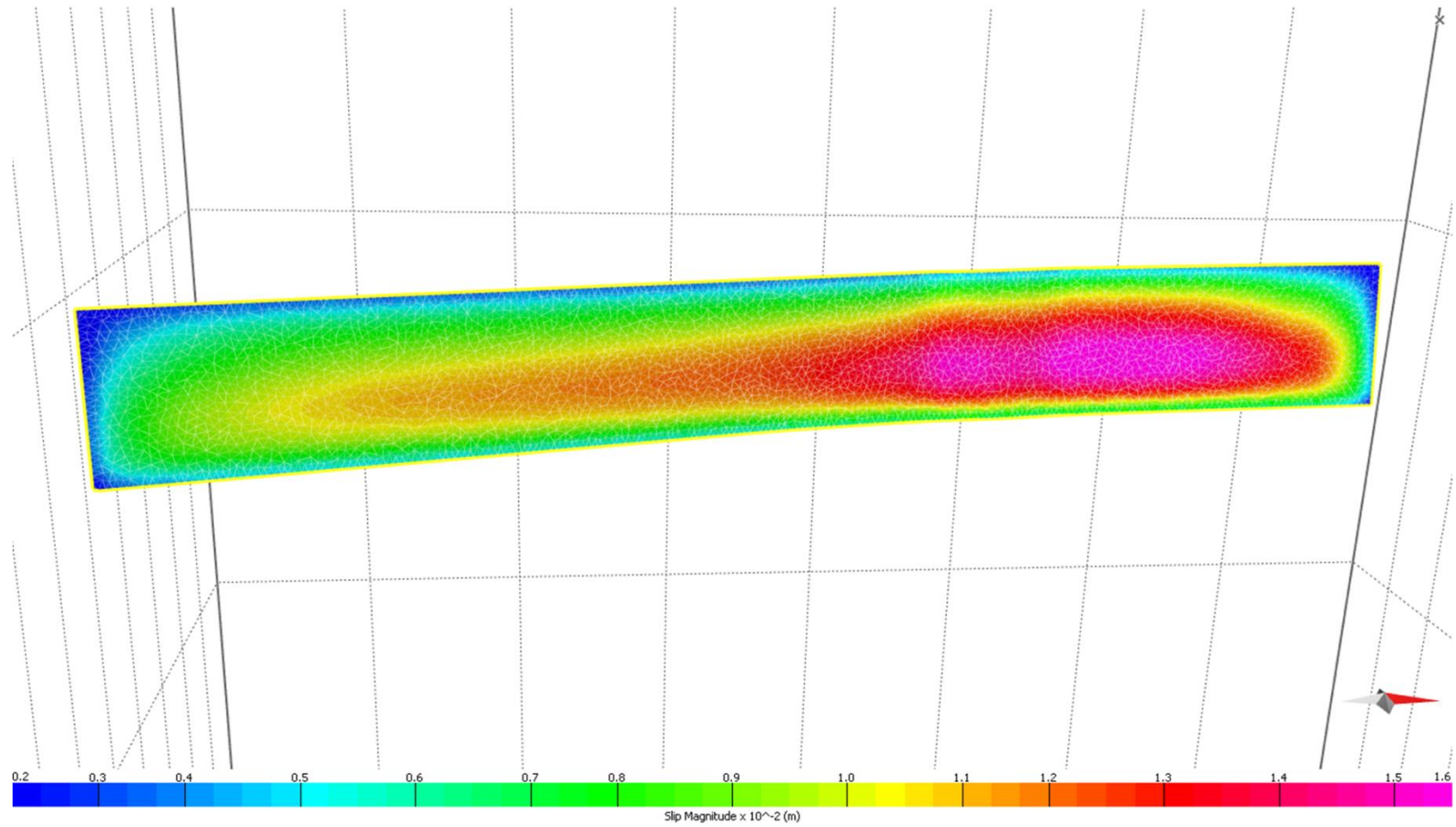


Figure 7-3 – Example model results (from Scenario 1) showing the slip magnitude across the Brumbys Fault surface.

7.3.2 Step 5: Fracture analysis

At this stage, the final step would have been to create fracture models to populate a discrete fracture network for flow modelling. The output from the simulations of the fault response module (step 4) would have allowed an analysis of the stability of these fractures for each of the possible stress fields or allow analysis of the fractures in later (i.e. present-day stress fields). However, the post-pandemic visits to the core store showed that there were no fractures observed in the Brumbys-1 core or the Port Campbell Limestone more generally as evidenced by deformation logs from Brumbys-1 (Section 6.4.1) and similar observations in the Harvey-2 core (Section 5.3, 5.4 and 5.7.4). Deformation features are not typically tectonic fractures and therefore it made sense to not to proceed with this workflow as it was not going to be able to effectively capture or quantify the types of deformation that were observed. In short, the approaches typically used to create fracture networks around fault zones and explore the fracture characteristics and their implications are not appropriate for shallow fault systems.

Upon realising the modelling would not accommodate the deformation features observed in shallow fault systems (and given the available data from the Harvey-2 core prior to fieldwork) no attempt was made to create a similar model for the F10 Fault. Had fieldwork not been delayed by 2 years due to the covid pandemic this would have been realised much sooner in the workflow and alternative modelling approaches could have been investigated or developed.

7.4 Discussion

7.4.1 Fault architecture

The geometry of the Brumbys Fault has been estimated from seismic data and the fault surface was picked using the ANT tracking algorithm in Petrel by Wang *et al.*, (2020). The final geometry of the fault surface contains some jogs and bends, which would be expected from a strike slip fault. These jogs and bends created the areas which had some of the highest stress due to the geometry. In a “classic” fault zone with a fractured damage zone these zones with highest stress would be potential areas that could focus fluid flow, as fractures could be propped open. However, with the understanding of the lithology and deformation styles in the Port Campbell Limestone (see Section 6.4 and Section 6.5), there are no fractures in this unit and therefore highly unlikely that there are

any fractures which could act as fluid pathways, regardless of the stress magnitude or orientation.

7.4.2 Stress data uncertainty

There is significant uncertainty in the present-day stress regime in the literature (see Section 3.2.2.2). To capture this, ten high and low stress scenarios were modelled across each of the three possible faulting types (Table 7-3). Furthermore, there is additional uncertainty in how the stress regime has evolved over time and how that compares to the present-day stress in the region. Due to this uncertainty in the stress data, the modelling outputs can provide drastically different scenarios for the slip rate of the fault over time. As the uncertainty in the stresses is so large, it is not possible to make any reasonable conclusions from these data. These challenges around stress magnitudes also present in Chapter 6 when trying to reconcile the fault kinematics of the Brumbys Fault, with regional variability in fault type and an uncertain regional stress regime. Further work is required to assess how best to estimate or measure stress data in the shallow subsurface, accounting for possible variations and uncertainties, to ultimately provide realistic values that can be used to inform structural modelling.

7.5 Summary

Modelling of shallow fault zones using “classic” structural geology or petroleum-based modelling tools is possible to do, but the results are likely not useful due to the uncertainties in the input data and the bias in the model design towards processes relevant to deeper fault zones. To model shallow fault zones and the influence of shallow fault deformation on fluid flow, modelling approaches should account for the fundamental differences and additional uncertainties that are present when working with shallow fault zones. For the Brumbys Fault, these modelling approaches were not suitable or useful due to the uncertainties in the stress regime and the type of deformation observed in the lithology. This is also true for the F10 Fault.

Firstly, shallow fault zones tend to have different deformation styles compared to those faults at deeper depths (see Chapter 2, Chapter 5 and Chapter 6). This means that applying classic fracture-based modelling approaches may not be suitable as the deformation style, particular in weaker and more unconsolidated materials, is more

likely to favour deformation via processes such as particulate flow processes and disaggregation rather than fracturing.

Secondly, the uncertainty in the magnitude of the stress regime matters more when studying faults that are nearer to the surface. This is because the stresses are typically lower (particularly the vertical stress as a vertical rock mass is decreased), allowing interpretations of different stress regimes (see Section 3.2.2). As the stresses are lower, the margin to move from one stress regime to another is greatly decreased and can even be within the error range expected on a stress magnitude. This makes interpreting which stress regime is dominant difficult. This has a host of implications for the type of faulting, the style of deformation and for predicting potential fluid flow pathways. It also means that stress conditions on a fault varies with depth. As such, for faults that extend from shallow to deep subsurface conditions, fluid flow may change both due to properties of the fluid itself (Section 2.1.3.2) and changes in fault properties due to stress change with depth.

These differences in shallow fault zone architecture and the uncertainties associated with working in the shallow subsurface mean that great care should be taken when applying classic fault analysis tools or workflows to ensure that the resulted collected are meaningful and realistic. There are some advantages to working in the shallow subsurface, such as the ability to collect higher resolution data, but there are equally other challenges such as the greater uncertainties in the stress regime.

Chapter 8 Natural hydrogen seeps as analogues to inform monitoring of engineered geological hydrogen storage

8.1 Declaration of Work

Chapter 8 has been published in the special issue of the Geological Society of London titled “Enabling Secure Subsurface Storage in Future Energy Systems”. The initial discussion and planning of this paper was undertaken by CJM, JJR, GJ and KE. The paper was prepared by CJM, with contributions from all other authors.

Full citation: McMahon, C.J., Roberts, J.J., Johnson, G., Edlmann, K., Flude, S. and Shipton, Z.K., 2023. Natural hydrogen seeps as analogues to inform monitoring of engineered geological hydrogen storage.

DOI: <https://doi-org.proxy.lib.strath.ac.uk/10.1144/SP528-2022-59>

Supplementary material: <https://doi-org.proxy.lib.strath.ac.uk/10.15129/89bae037-9174-4556-883b-86e6c3216590>

8.2 Abstract

Engineered geological porous media hydrogen storage must be designed to ensure secure storage, and use appropriate monitoring, measurement, and verification tools. Here, we identify and characterise 60 natural hydrogen seeps as analogues for potential leakage from engineered storage reservoirs to consider implications for monitoring. We report and compare the geological and environmental setting; seepage mode (dry gas/associated with water); co-released gases; seep rates and areal fluxes; temporal variation; seep structure; gas source, and composition. Seep characteristics are determined by local geological and hydrological conditions, specifically whether hydrogen gas is seeping through soils and unconsolidated sediments, fractured bedrock, or into water. Hydrogen is typically co-emitted with other gases (CO₂, CH₄, N₂) with CH₄ the most common co-emitted gas. The structural controls on seep location and characteristics are similar between hydrogen and CO₂ seeps. However, compared to CO₂, hydrogen is more readily dispersed when mixing with air and hydrogen is more prone to being consumed or transformed via biotic or abiotic reactions, and so the quantity of leaked hydrogen can be greatly attenuated before seeping. Monitoring

approaches should therefore be tailored to the local geology and hydrological conditions, and monitoring approaches to detect hydrogen and associated gases would be appropriate.

8.3 Introduction

Hydrogen is proposed to aid the diversification and decarbonisation of multiple energy sectors, including heat, transport, power, and industry (Hanley *et al.* 2018; Lazarou *et al.* 2018) and provide energy storage to support the expansion of renewable energy. A hydrogen economy could require large-scale hydrogen storage (Heinemann *et al.* 2021), and it is estimated that geological storage of hydrogen could provide giga-watts (GW) of stored energy capacity (IEA 2013; Mouli-Castillo *et al.* 2021). Options for geological hydrogen storage include salt caverns, or porous rocks such as saline aquifers or depleted hydrocarbon reservoirs (Tarkowski 2019), situated onshore or offshore (Heinemann *et al.* 2018; Mouli-Castillo *et al.* 2021). Currently, hydrogen is stored in onshore salt caverns as feedstock for petrochemical processes, with examples in Teesside (UK) and Texas (USA) (Panfilov 2016). To date there has been no industrial storage of 100% hydrogen in porous rock, but some experience was gained during the commercial storage of ‘town gas’ containing ~50% hydrogen in saline aquifers in France, Germany and the Czech Republic during the 1960’s and 1970’s (Carden and Paterson 1979).

Engineered geological hydrogen stores must ensure safe and secure storage (Heinemann *et al.* 2021). Leakage from engineered hydrogen stores could have a cascade of environmental, social, and economic risks (Heinemann *et al.* 2021; Stalker *et al.* 2022). Understanding how hydrogen might leak out of the geological store, and potentially to the surface, is fundamental to constrain risk in any future geological storage sites. Potential geofluid leakage pathways from the subsurface to the surface have been well documented by decades of research to understand hydrocarbon retention and migration and to ensure containment for the geological storage of CO₂ and radioactive waste. However, differences in the physicochemical properties of hydrogen, and the selection and cyclic operation of storage sites, bring unique scientific challenges (Heinemann *et al.* 2021).

Growing interest in prospecting for natural hydrogen accumulations has led to the identification of several surface occurrences of gas that contains native/molecular hydrogen (H₂) (Prinzhofer *et al.* 2018; Vacquand *et al.* 2018; Zgonnik 2020; Cathles and Prinzhofer, 2020). Over 300 occurrences of natural hydrogen are documented worldwide (Zgonnik 2020), some of which are interpreted as seeps of a hydrogen-bearing

gas that is leaking from a reservoir at depth. Sites of CO₂ and CH₄ seepage have previously provided useful insights for the engineered geological storage of gases in the subsurface, particularly for evaluating measuring, monitoring and verification (MMV) methods. Native hydrogen is physically different to CO₂ and CH₄, being a small molecule, with a lower density, making it mobile and buoyant. It is highly flammable, but overall, not highly reactive, and has a low solubility in water, meaning it often concentrates in the gas phase. The atmospheric concentration of hydrogen is 0.000531 vol % (Novelli *et al.* 1999), or 0.531 ppm, lower than both CO₂ and CH₄. The low atmospheric concentration of hydrogen enables relatively easy detection of hydrogen seeps in amounts over this value. These different physico-chemical properties mean hydrogen seeps may be different to CO₂ and CH₄ seeps, and it is important to know what these differences are and consequently how MMV for engineered geological hydrogen storage may need to be adapted accordingly. In this paper, we examine a global inventory of hydrogen seepage sites to understand the factors that control their location and characteristics (surface expression, seep rate), leakage mechanisms and implications for the monitoring of geologically engineered hydrogen stores.

8.3.1 Overview of natural hydrogen production, migration, accumulation, and consumption in the subsurface

Abiotic and biotic subsurface hydrogen generation and consumption mechanisms are well understood (Sherwood Lollar *et al.* 2014; Panfilov 2016; Gregory *et al.* 2019). Hydrogen is naturally produced in the geological subsurface abiotically through various water-rock interactions and via radiolysis of water during naturally occurring radioactive decay in rocks (Sherwood Lollar *et al.* 2014). Shallow biotic sources of hydrogen include microbes found in soil and as part of insect microbiomes (Conrad and Seiler 1980; Zimmerman *et al.* 1982; Sugimoto *et al.* 1998).

Factors that influence hydrogen flux between source or reservoir and surface include biological activity, temperature, atmospheric pressure, Earth tides, and seismic activity (Sugisaki *et al.* 1983; Sato *et al.* 1986; Voitov *et al.* 1995; Cathles and Prinzhofer 2020; Zgonnik 2020), like natural CO₂ seeps (Miocic *et al.* 2016, Roberts *et al.* 2019a). However, for hydrogen no studies have yet shown the link between deeper hydrogen reservoirs and surface hydrogen seepage sites.

While conventional oil and gas knowledge may indicate that deep, geologically produced hydrogen is too small and mobile to form economic accumulations, the presence of hydrogen-bearing seeps implies that subsurface accumulations of hydrogen do indeed exist, and significant concentrations of hydrogen have been discovered in a small number of gas reservoirs (Coveney *et al.* 1987; Prinzhofer *et al.* 2018).

In the subsurface, hydrogen may be consumed by methanogen microorganisms, to produce organic molecules, the most common being CH₄. Such biological conversion of hydrogen to CH₄ has been observed in both in subsurface 'town gas' storage sites (Buzek *et al.* 1994) and in deep mines where drilling introduces microbes that convert geologically produced hydrogen into methane (Warr *et al.* 2021). Hydrogen may also be consumed during abiotic polymerisation reactions to produce methane and higher alkanes via processes such as Fischer-Tropsch type reactions (Etiope and Sherwood Lollar 2013). Temporally these reaction rates will vary, with microbial consumption of hydrogen likely to be faster compared to larger-scale geological process reactions.

8.4 Methods

First, we expand the Zgonnik (2020) global dataset (n=333) to include newly identified hydrogen seeps (n=4) that have information published since Zgonnik (2020), and prior to February 2022. For the purpose of this study, we refer to all of these published sites as seeps, regardless of whether the original studies convincingly rule out shallow or surface sources of hydrogen (artificial or biotic). We consider sites of seepage to be either surface vents (where gases escape to the atmosphere, e.g. via rock fractures), high concentrations of hydrogen in shallow subsurface boreholes (~1m in soil/rock) and where hydrogen seeps through water as bubbles at the water surface. We then filter the dataset to identify hydrogen seeps that fit two criteria:

1. *Geological and physical environment*: we select seeps that are in geological and physical environments representative of environments analogous to engineered geological hydrogen storage in porous media (e.g. saline aquifers or depleted oil/gas reservoirs) or that show key hydrogen seep processes (e.g. in ophiolites). Thus, we do not consider hydrogen occurrences or seeps associated with mid-ocean ridge zones, gases associated with drilling of super-deep wells, drilling muds and mining, volcanic gases, high temperature geothermal systems and hydrogen gas in microscopic fluid inclusions or absorbed on mineral surfaces in various rock types and geological settings.

2. *Source*: We do not consider occurrences of hydrogen that are generated by geochemical or biological processes at surface or in the shallow subsurface (e.g. in soil).

Thus, we consider only the 60 out of the total 337 seeps that are analogous to potential engineered hydrogen storage in porous media. For hydrogen seeps that meet these conditions we draw on published information to determine: the geological and environmental setting; whether seepage is as a dry gas or dissolved; co-released gases; seep rates (rate of emission) and fluxes (rate of emission per unit area) and how these were measured or derived; duration of seepage and temporal variation; physical aspects such as the area and shape of seepage; concentration and source of hydrogen. Seeps are numbered (#) and are referred to by the assigned number throughout.

We harmonise units, and report hydrogen concentrations as a percentage (vol %) of relative gas composition. We report seep rate in g(hydrogen)/day, like Roberts *et al.*

(2018) and Roberts and Stalker (2020), who report data on CO₂ flux from natural CO₂ seepage sites, field experiments and industry in g/m²/day. When converting from m³/day, we take hydrogen density to be 0.0827kg/m³ equivalent to standard temperature (0°C) and pressure (100kPa).

Where seep rates and/or fluxes are not explicitly reported, we derive these, where possible, from available information. For example, if the area of seepage is reported or can be derived from dimensions or images, and the seep rate is known, gas flux can be calculated. For these calculations, where seep rate is reported as a range, we use the median value to derive the flux (flux = seep rate/area).

8.5 Results

Our screening results in 60 seeps in 13 geographic clusters (Figure 8-1). Summary information about each seep is detailed in Tables Table A7 - 1, Table A7 - 2, Table A7 - 3 and Table A7 - 4 in Appendix 7, with further detail in the supplementary information.

8.5.1 *Surface expression of hydrogen seeps*

The surface expression of natural hydrogen emanations can be either ‘dry’ (n=33), where hydrogen seeps to atmosphere from rock or soil, or ‘wet’ (n=27), where hydrogen bearing gases bubble through water. Wet seeps include those on land associated with rivers and springs (n=26) or on the seabed in the near offshore (continental shelf) (n=1).

The surface expression of dry seeps is governed by outcropping geology and sedimentary cover. Where there is soil or unconsolidated sediments (e.g. sand) hydrogen seeps form circular/subcircular features that are visually prominent (n=18). In contrast, where bedrock crops out, hydrogen seeps form no physical expression, and is spatially constrained, typically to a fracture or several fractures (n=14).

8.5.2 *Dry seepage through soils and unconsolidated sediments*

We report 19 hydrogen seeps through soils and unconsolidated sediments. 18 sites are circular or oval shaped features with located in six regions USA (#8-12), Brazil (#14-15), Russia (#1-7), Mali (#13) and Australia (#16-18)) (Table A7 - 1). These typically manifest as depressions, with changes in vegetation or vegetation loss, and in some cases water collects in them to form permanent or ephemeral lakes. These physical features are sometimes referred to as “fairy circles”, but as this term is a specific ecological characterisation (Getzin *et al.* 2021), we refer to them as subcircular depressions based on their shape and characteristics and caution against using the term “fairy circles”. One site (#19) has no detailed data on the physical expression of seepage.

In the 18 cases of subcircular depressions (#1-18), soils and poorly consolidated modern and quaternary sediments obscure the bedrock geology. In all these cases the bedrock geology comprises sedimentary rock units overlying metamorphic or igneous basement rocks, typically stable intracratonic basin crust that is Archean to Proterozoic in age (Moretti *et al.* 2021b). For one case (#19), soils overlie metamorphic ophiolitic bedrock directly with no sedimentary cover (Yuce *et al.* 2014).

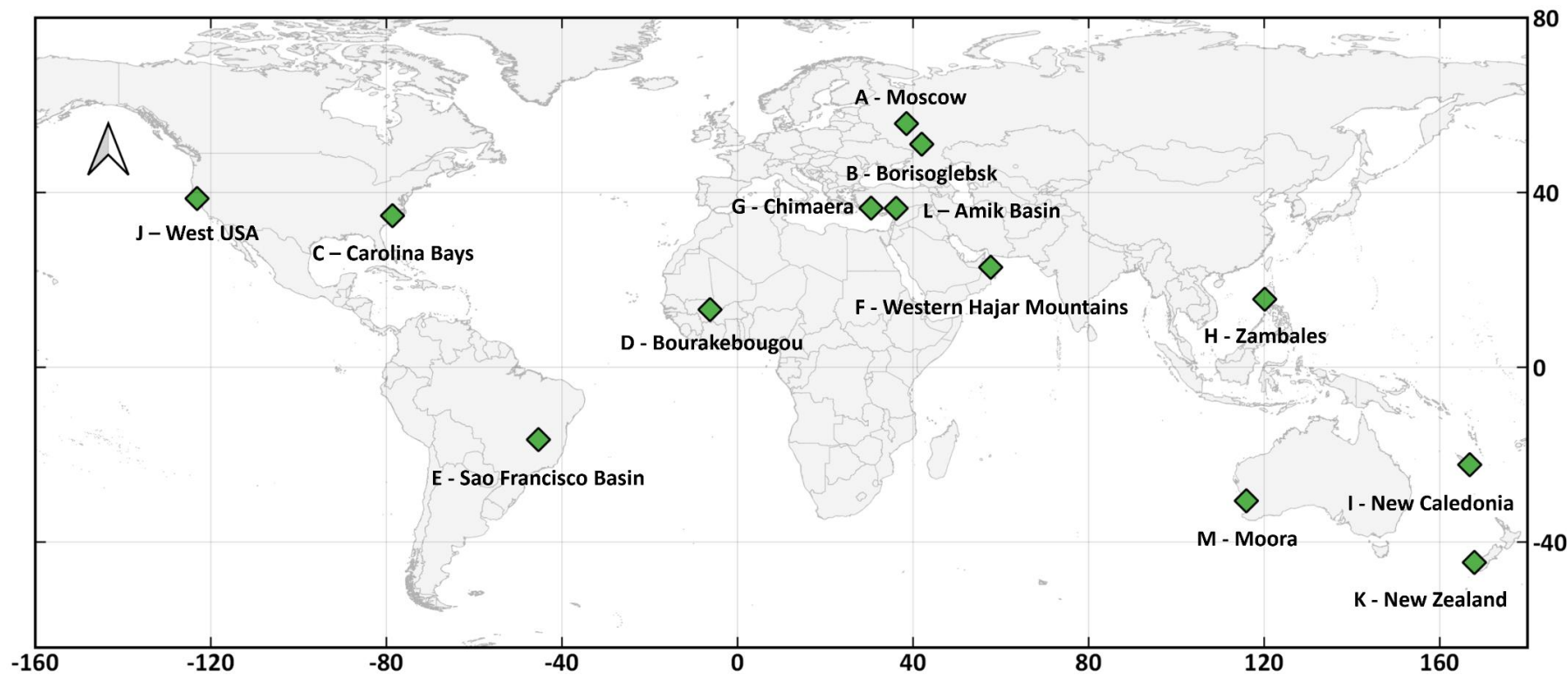


Figure 8-1 – Location of 60 hydrogen seeps within 13 clusters (letters A-M) that may be analogous of leakage from engineered geological hydrogen stores. The cluster ID (letter – name) is written adjacent and this corresponds to the cluster column in Table A7 - 1, Table A7 - 2 and Table A7 - 3.

In many cases, these subcircular depressions form clusters of depressions spanning areas that are thousands of square kilometres; 17 of the entries in our database are in such depression-clusters, covering areas of $\sim 1,000 \text{ km}^2$ (Brazil), $3,300 \text{ km}^2$ (Russia), and $15,000 \text{ km}^2$ (USA). The remaining two (#13 and #19) are reported as individual depressions, but it is clear from satellite images that other structures do exist in the case of #13. Satellite images for location #19 are less clear and show no obvious features. Individual seep shapes can be circular (#1-7, Larin *et al.* 2015), elliptical (#8-10, #12, Zgonnik *et al.* 2015), and irregular (#14-18, Moretti *et al.* 2021b; Frery *et al.* 2021) – therefore we refer to them collectively as subcircular. There is little published information about the shape, area or size of sites of hydrogen seepage in Mali, although the one depression documented by Prinzhofer (2018) (#13) is large, oval-shaped, with a diameter of $\sim 1.5 \text{ km}$.

Subcircular features associated with hydrogen seepage have been observed to appear and establish over short timeframes (1-2 years). For example, time-lapse satellite images track the formation of the Elektrostal seep (#1) over a two-year period between 2002 and 2004 (Larin *et al.* 2015), and the formation of the Jones Lake Bay seep (#10) over a one-year period (Zgonnik *et al.* 2015). In both cases, the onset of feature formation and hydrogen seepage is documented at these sites, and seepage is ongoing (or seep cessation is not yet reported). Subcircular features in the Carolina region have been shown to exist for tens of thousands of years using optically-stimulated luminescence, LiDAR and other data (Moore *et al.* 2016; Piovan and Hodgson, 2017). Moretti *et al.* (2021b) found that in agricultural areas in Brazil, archive images show the reappearance of features following disturbance by ploughing, however they also note that the appearance/disappearance of new structures is often not observed or reported.

A change in vegetation or vegetation loss is often associated with these features (Larin *et al.* 2015; Zgonnik *et al.* 2015; Prinzhofer *et al.* 2019; Frery *et al.* 2021). When depressions have a shallow water table often a lake or wetlands form in the sunken centre as the land subsides. Frery *et al.* (2021) note that new trees have become established on the external ring of two actively seeping depressions in Australia. Furthermore, Frery *et al.* (2021) note that vegetation distribution and disturbance is not uniform between sites in the same location with active hydrogen seepage.

The diameter of subcircular features varies between sites; ranging from tens of meters (#3) to kilometres (#2) (Larin *et al.* 2015; Zgonnik *et al.* 2015). Moretti *et al.* (2021b) found an average diameter of hydrogen seep depressions between 200-300m from the sites they collated from Brazil, Russia, and Australia. Larin *et al.* (2015) studied depressions in Russia and Australia (many of them not sampled for hydrogen) and found a sub-exponential relationship between size and frequency for depressions (with a diameter <1,000m); i.e., smaller depressions are more common than larger depressions.

The maximum depth (amplitude) is only explicitly quantified for 4 out of the 18 subcircular depression sites (#5, #8, #9, #14) and ranges from ~1m to ~8 m. Two of these seeps (#8 and #9) have an outer raised rim of ~3m rather than an internal depression. The cross-sectional depth profile is rounded (i.e., plate shaped) rather than cone or bowl shaped (#5, #8, #9, #14).

Hydrogen concentrations are reported for all 19 dry, soil and sediment hosted seeps (Figure 8-2). There are 18 seeps (#1-18) using soil gas sampling methods, and while the measurement depth is not consistent between studies, from 0.10 m to ~1.2 m (Larin *et al.* 2015, Zgonnik *et al.* 2015; Prinzhofer *et al.* 2019), there is no clear correlation between sampling depth and hydrogen concentration. Sampling depths are not reported at seep #13 (Prinzhofer *et al.* 2018). Reported hydrogen concentrations range from 0.0001%-99% (Figure 8-2).

Soil gas sampling at seeps #1-12, #16-18, report hydrogen concentrations that are spatially variable within depressions (Figure 8-3 and Figure 8-4), but typically highest nearer the edge (or rim) of larger subcircular depressions (Zgonnik *et al.* 2015; Larin *et al.* 2015; Frery *et al.* 2021; Moretti *et al.* 2021b). These higher concentrations of hydrogen have been observed to correspond with soils or sediments of higher permeabilities (e.g. sand) (Zgonnik *et al.* 2015). Some features in seeps #1-12 have hydrogen emissions outside the subcircular depression (Figure 8-4), whereas in seeps #13-14 this is not the case (Moretti *et al.* 2021b). Features that are filled with water have not been measured for hydrogen concentration due to the measurement technique (soil gas sampling) not being suitable.

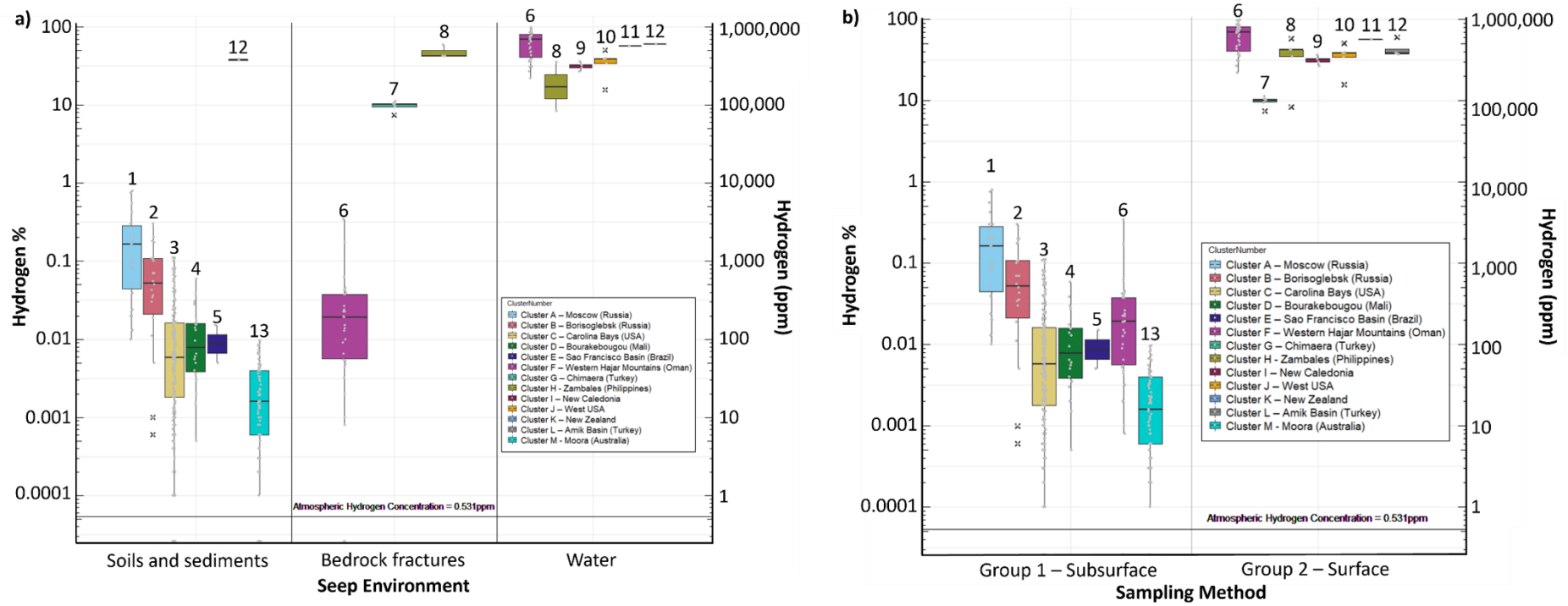


Figure 8-2 – Hydrogen concentrations (vol %) for each cluster of seepage sites, plotted as (a) a function of seep type and (b) a function of measurement type (i.e. whether measured in the near surface, top ~1m in soils/fractured rock (Group 1) or at the surface in gas vents or bubbles (Group 2)). Coloured boxes represent the sample median (horizontal line), and the first and third quartiles, with the extending lines representing the minimum, the maximum values. Grey dots show the data points, black crosses show outliers. Numbers on/near boxplots correspond to cluster number in Table A7- 1, Table A7- 2 and Table A7- 3 and Figure 8-1. Seep cluster ID F has hydrogen seeping via bedrock fractures and bubbles in water and thus have gas sampled both from the subsurface and the surface.

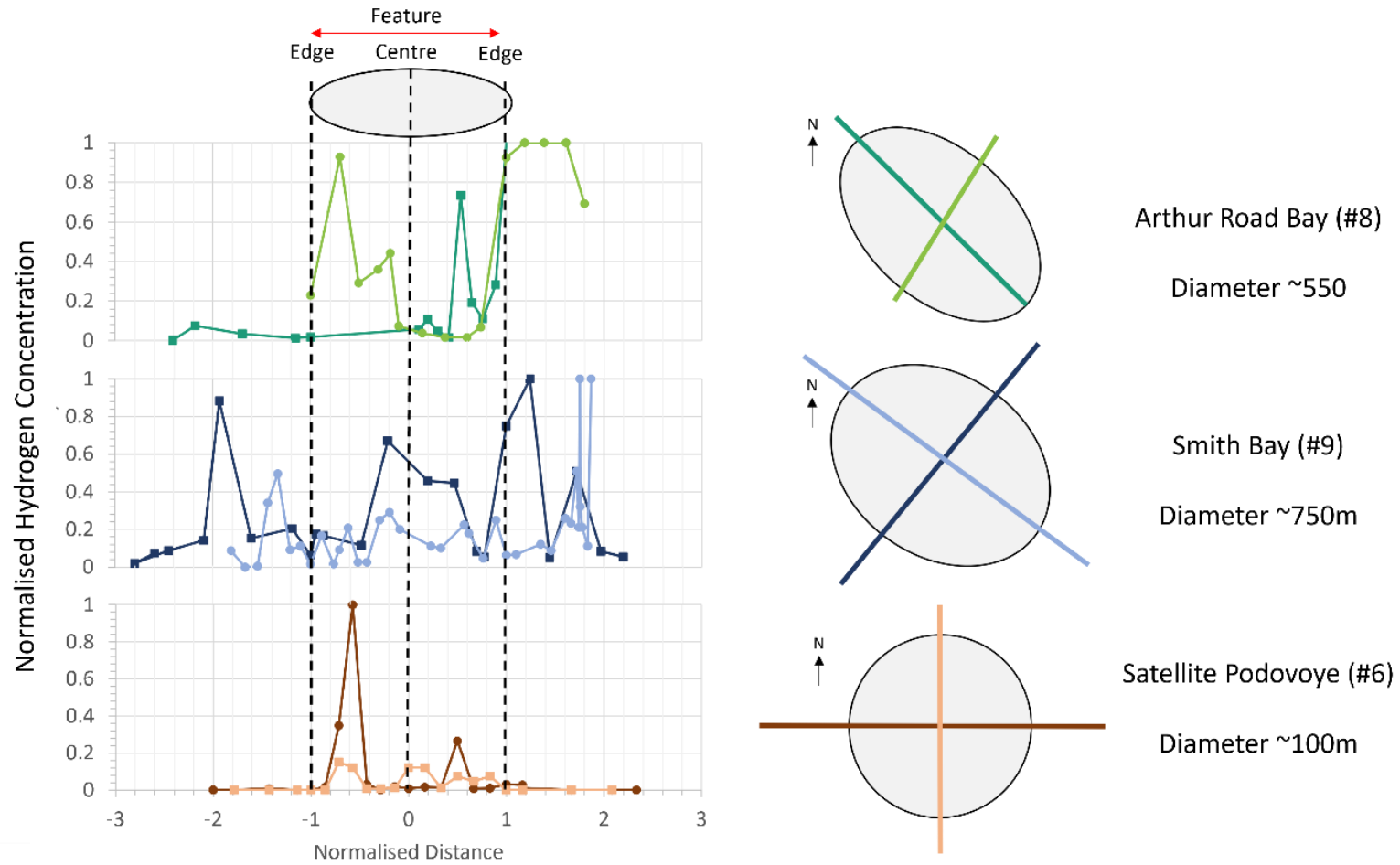


Figure 8-3 – Soil gas profiles of Smith Bay (#9, Zgonnik et al. 2015), Arthur Road Bay (#8, Zgonnik et al. 2015) and Satellite Podovoye (#6, Larin et al. 2015). Distance on the x-axis is normalised so that a value of 1 corresponds to the edge of the depression feature. This allows comparison between features of different sizes. Hydrogen concentrations are normalised where the maximum concentration taken along a transect is = 1. Measurements that were recorded as SAT (= detector saturated) were set to 1. Depression shape, size, orientation and transect orientations are shown for each site.

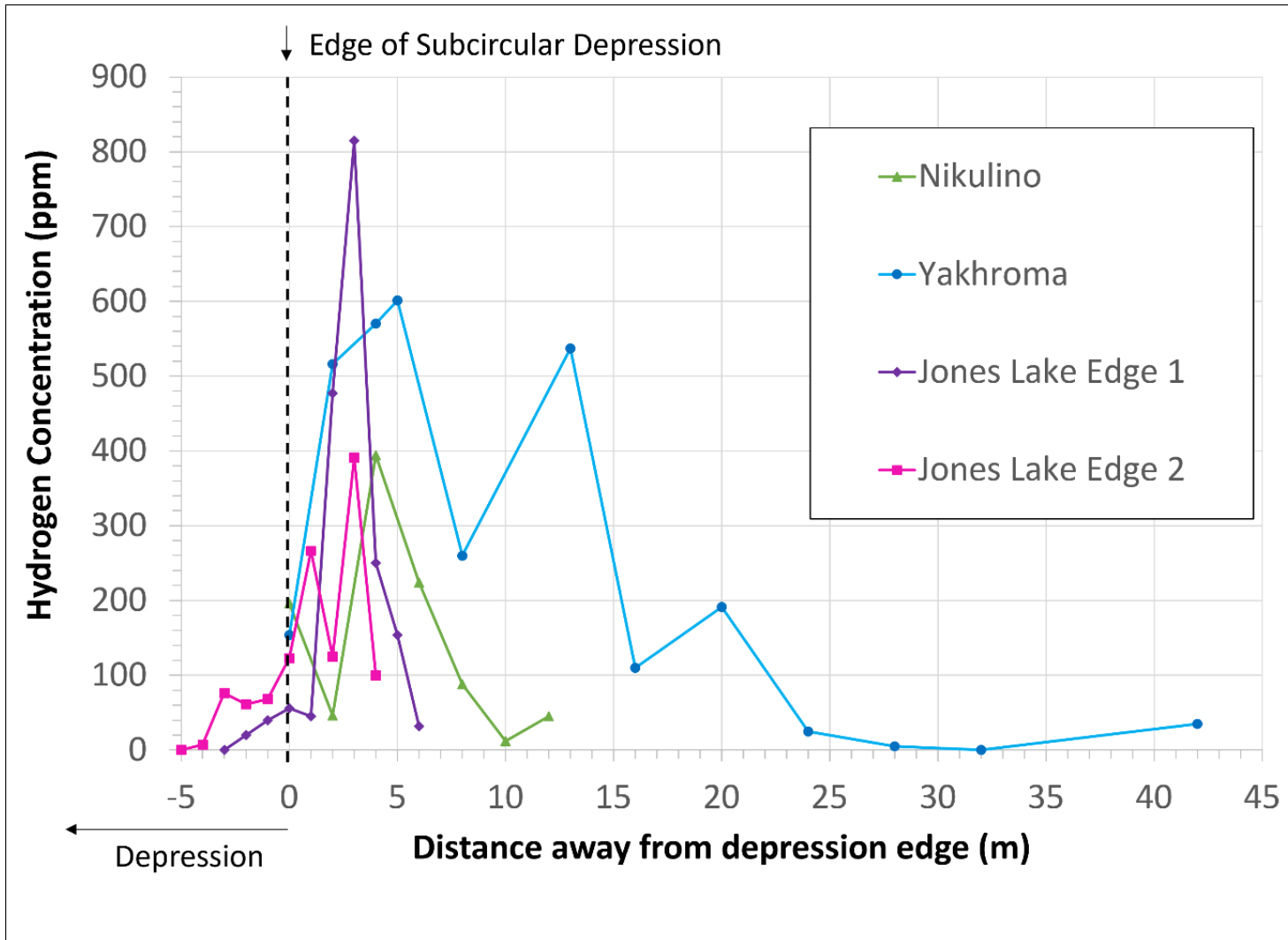


Figure 8-4 – Transects of hydrogen concentration at the edge of the Nikulino (#4, Larin et al. 2015), Yakhroma (#3, Larin et al. 2015) and Jones Lake Bay (#10, Zgonnik et al. 2015) features.

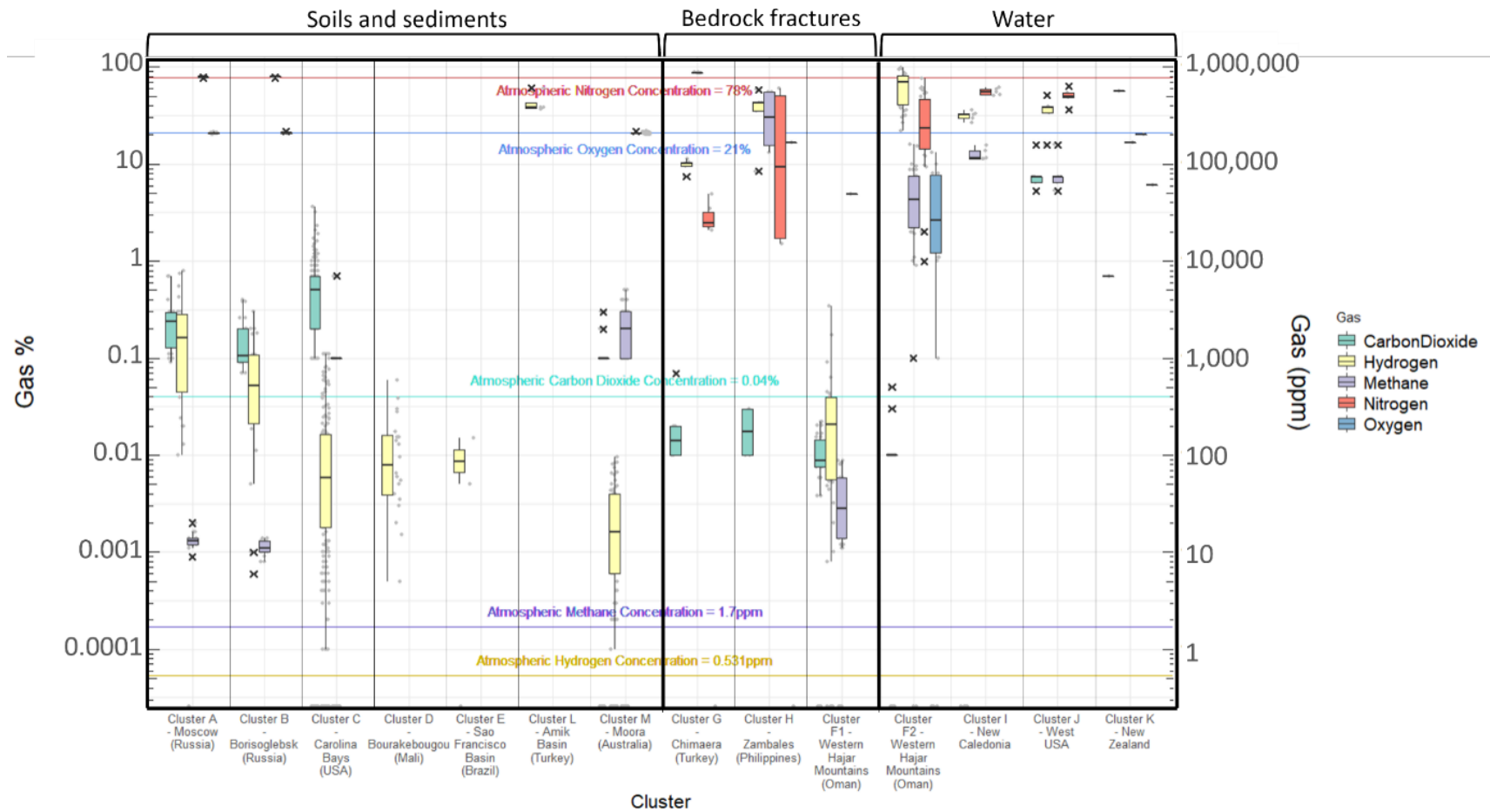


Figure 8-5 – Measured gas concentrations reported from hydrogen seepage sites. Clusters are organised by surface expression of seepage. Cluster 6 is split into 2 sections to represent different surface expression of seepage, either via (a) bedrock fractures or (b) water. Coloured boxes represent the sample median (horizontal line), and the first and third quartiles, with the extending lines representing the minimum, the maximum values. Grey dots show the data points, black crosses show outliers.

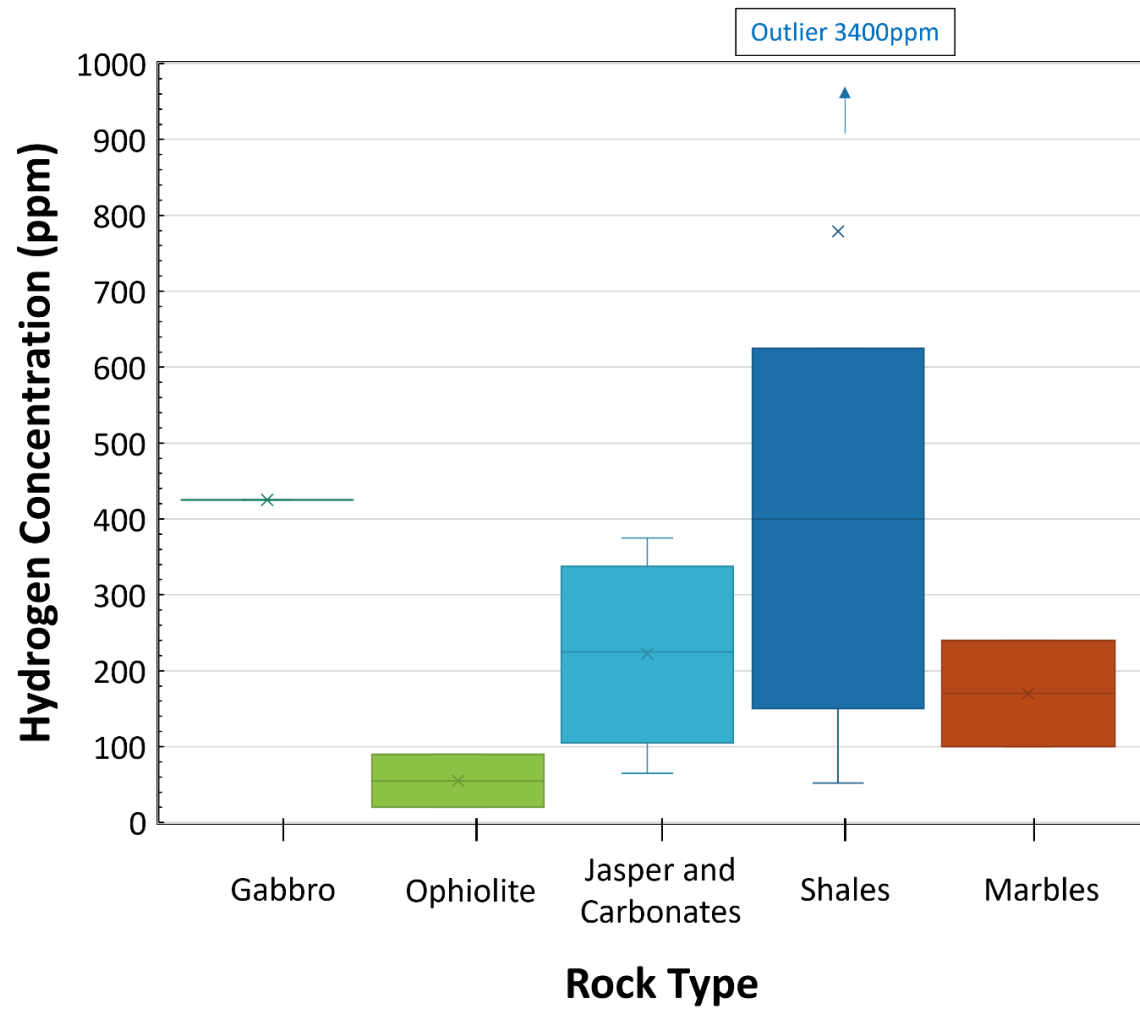


Figure 8-6 – Hydrogen concentrations (ppm) of seepage from specific rock types in Oman. Coloured boxes represent the sample median (horizontal line), and the first and third quartiles, with the extending lines representing the minimum, the maximum values. Crosses indicate outliers. The shale outlier reporting 3400ppm is seep #28, where the shales directly overlie Precambrian basement and are below the ophiolite nappe.

In seeps #1-13 and #16-18, other gases associated with hydrogen are reported (Figure 8-5). While these samples are collected from atmosphere, not soil gas wells, the concentration of methane and carbon dioxide are above their respective atmospheric levels alongside hydrogen. In seeps #8-12, CH₄ concentrations vary from 0.0011-27.5%, however in #11, Zgonnik *et al.* (2015) observe gas bubbling in stagnant pools that contains no hydrogen despite its presence in soil gas at the same location. Instead, the gas bubbling from the pools consists of 35% N₂, 53% CH₄ and 9% CO₂ (Zgonnik *et al.* 2015).

8.5.3 *Dry seepage from rock fractures*

There are 14 cases of hydrogen emitted directly from the bedrock, without overlying soil or sediments. Of these, 3 cases manifest as hydrogen-bearing gas actively venting from bedrock fractures (#31-33) and 11 cases are of high concentrations of hydrogen gas measured in-situ within subsurface fractures (#20-30) (Table A7 - 2). All the fracture seeps (Oman, Turkey, and the Philippines) have a common geological setting: ophiolitic or subduction complexes (compression zones). These types of emissions have been referred to in the literature as reduced gas seepages, due to their composition (H₂, CH₄, N₂) and interpreted formation processes (Vacquand *et al.* 2018).

Field measurements of hydrogen concentrations (ppm) are reported for 11 of the 14 sites – all from seeps in Oman (Figure 8-6). Concentrations of hydrogen range from 20ppm to 3400ppm. Hydrogen is co-released with N₂, CO₂ and CH₄ (Figure 8-5) and minor components of other gases (e.g. noble gases and/or hydrocarbons). There is no relationship between the exposed rock type and the hydrogen concentration for the dry seeps in Oman (Figure 8-6).

Two of the 14 sites (#31-32), in Turkey and the Philippines) are seeps that are dominantly composed of CH₄, with subsidiary hydrogen (7-42% H₂). These seeps are famous for long-lived flames which emanate from rock fractures and ignite spontaneously (Hosgörmez *et al.* 2008; Vacquand *et al.* 2018). The Los-Fuegos Eternos seeps (#32, Table A7 - 3) have been burning for over 2500 years (Hosgörmez *et al.* 2008).

8.5.4 *Wet seepage through water*

We found 27 ‘wet’ seeps where hydrogen bearing gases bubble through water, either on land at springs (n=26) or to seabed in the near offshore (continental shelf) (n=1) (Table

A7 - 3). These are located in 6 regions: Oman (n=20), New Caledonia (n=2), Philippines (n=2), Turkey (n=1), USA (n=1) and New Zealand (1). Within Oman, the springs form sub-clusters within the Western Hajar mountains.

In all cases, hydrogen is seeping from ophiolitic and subduction related rocks, such as peridotites. The springs are ultrabasic (hyperalkaline) systems that locally precipitate carbonate (Neal and Stranger, 1983; Deville and Prinzhofer, 2016; Vacquand *et al.* 2018).

For 'wet' hydrogen seeps, hydrogen concentrations vary from 8.4% to 99% of the total gas volume (Figure 8-2a). Hydrogen is the major gas at 17 sites (15 of which are in Oman). When hydrogen is a major gas, it comprises 43% or greater and up to 99% (#50), and commonly associated with CH₄, N₂, or CO₂, each typically below 10% (Figure 8-4 and Figure 8-5). N₂ is the dominant gas at 9 sites all in New Caledonia or the Philippines, whereas at Bahla, Oman, (#38), N₂ and hydrogen are in equal proportion and both dominant. For 12 seeps, there are multiple measurements within the same spring and hydrogen concentrations can vary considerably between samples (e.g. #47, hydrogen concentration range 43-97%).

Oman is the only cluster of hydrogen seeps that have two distinct types of seepage – both 'wet' seeps from springs and 'dry' seeps from fractured rock, both of which are in peridotites.

8.5.5 Hydrogen concentration and seep rates

Hydrogen concentrations can be split into 2 distinct groups (Figure 8-2b). Group 1 with concentrations below 1% include all subcircular depression seeps and all the bedrock fracture seepage sites in Oman. At these sites concentration measurements are collected after creating a borehole in soils or rock. Group 2 with concentrations above ~7-10% include all seepage through water, plus the bedrock fracture and soil seepage sites in Turkey and the Philippines. These measurements were all collected in containers (from rock fractures or bubbling springs) and then analysed in a lab via gas chromatography.

Hydrogen seep rates are reported in the literature for 10 of the seeps associated with subcircular depression features (Table A7 - 4), and for 2 rock units in Oman associated with dry fractured bedrock type seeps. Where a range of seep rates are reported for a site, authors note this is due to uncertainty in the assumptions made in the calculation

(e.g. different values for soil porosity (Zgonnik *et al.* 2015), or the area chosen to represent seepage), rather than temporal variability. Where seep rate is reported in the literature, we take an average (median) value of this seepage rate range, and thus the rate has some uncertainty.

Seep rate (Figure 8-7) ranges between locations from 0.002 tonnes hydrogen per day (0.78 tonnes per year, #12 (Table A7 - 4), through to 2 tonnes per day (700 tonnes per year, #7). There is no relationship between seep rate and spatial location. Seepage sites with larger spatial extent have higher total seep rate, but this could simply reflect the calculation method.

Seep flux (Figure 8-8) is reported for 4 seeps (#8-10, 12) and calculated for the remaining 8 seeps. Flux tends to be on the order of 0.002 tonnes hydrogen per day (0.73 tonnes per year) to 5 tonnes hydrogen per day (1825 tonnes per year). Similar to seep rates, we observe no relationship between flux rate and spatial location. Further, there is no relationship between flux and the size of the seep, though there are relatively few data points.

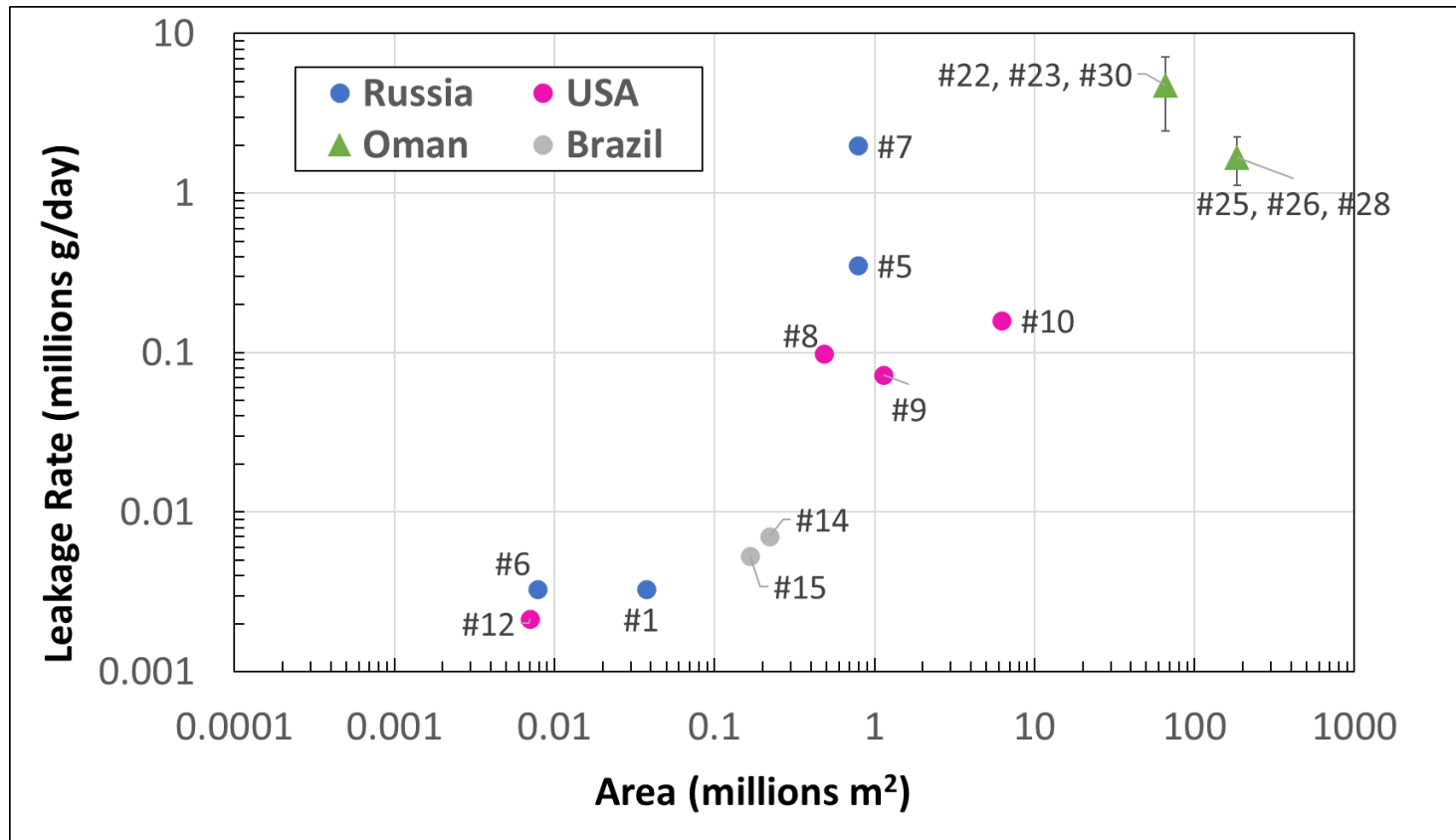


Figure 8-7 – Seep area vs reported rate of hydrogen seepage. Numbers (#) are seep numbers (Tables Table A7 - 1, Table A7 - 2, Table A7 - 3 and Table A7 - 4). Markers represent surface expression of seepage: circles represent soils and sediments, and triangles represent bedrock fractures. Error bars represent maximum and minimum leakage rates constrained by uncertainties in assumptions. Seep area is the footprint of the subcircular depression, or the size of the region of leakage. Data from Larin et al. (2015), Zgonnik et al. (2015; 2019) and Moretti et al. (2019a).

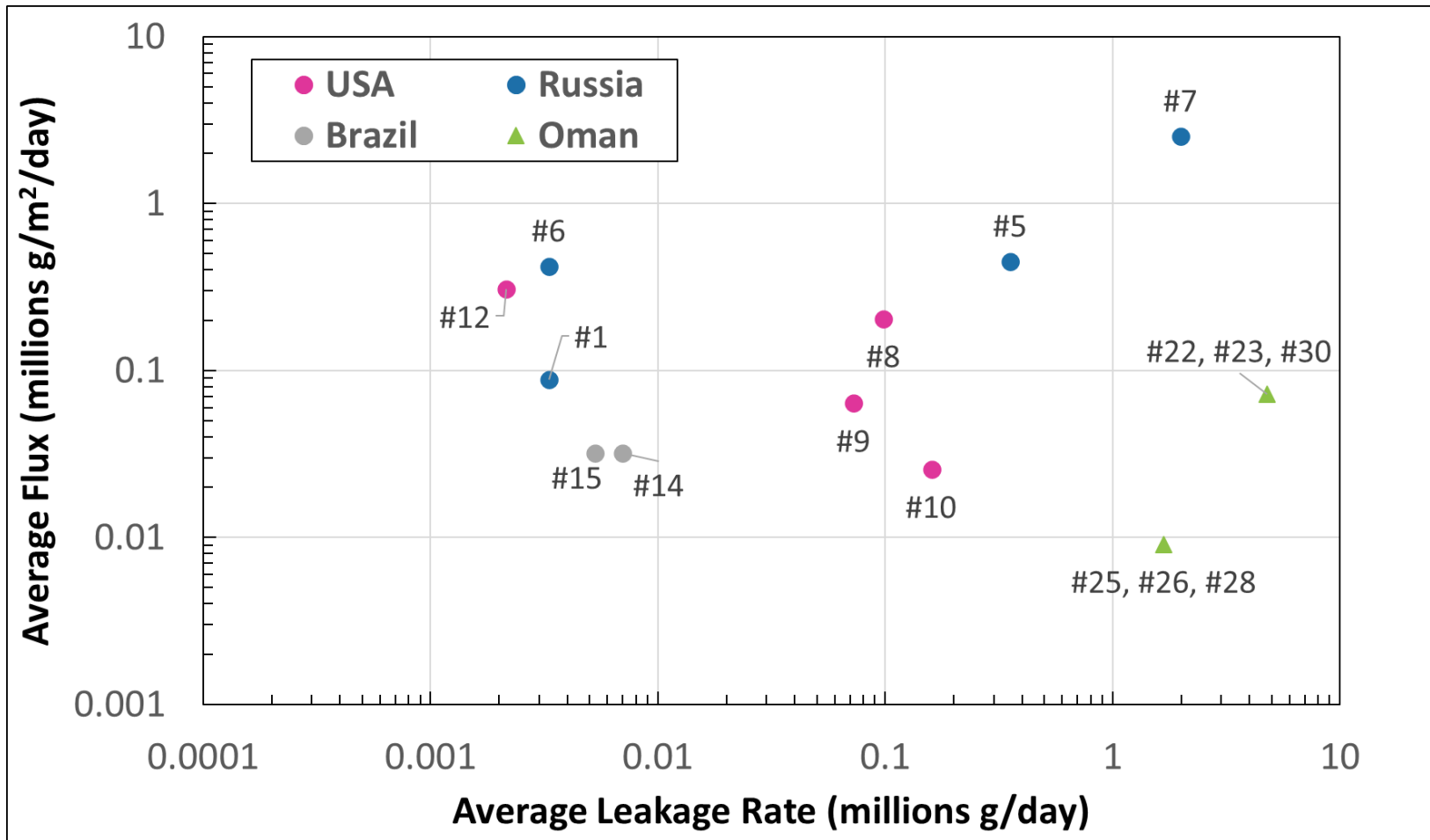


Figure 8-8 – Flux vs leakage rate. Numbers (#) are seep numbers (Tables Table A7- 1, Table A7- 2, Table A7- 3 and Table A7- 4). Markers represent surface expression of seepage: circles represent soils and sediments, and triangles represent bedrock fractures.

8.6 Discussion

8.6.1 Characteristics of hydrogen Seepage Sites

Whilst the physical and geological environment controls the surface expression of hydrogen seepage, variability is observed between seep characteristics and rate of emission within similar environments.

8.6.1.1 Seepage controls on measured hydrogen concentration

We see two distinct groups in the hydrogen concentration data (Figure 8-2b). This could be explained as gases bubbling through water are likely to have higher concentrations compared to soil gas as the gas from depth is less diluted by air. Also, when gas bubbles through water, the more soluble co-existing gases will dissolve out faster than hydrogen, which means hydrogen concentrations in the gas phase will increase. However, more work may be required to ensure that the split in data is not due to sampling artefacts in the data collected as there is a split between those samples collected in shallow boreholes (e.g. soil gas wells, and in fractured rocks to ~1m depth) (Group 1, <1% hydrogen) and those collected directly from bubbling springs or gas vents (Group 2, >7% hydrogen) (Figure 8-2b).

Pulses and daily cycles of seepage are observed at natural hydrogen seeps where seepage occurs through soils and unconsolidated sediments (Prinzhofer *et al.* 2019; Moretti *et al.* 2021a). Continuous monitoring of hydrogen concentrations over 1-8 months at 2 seeps in Brazil located ~1.5 km from each other (#14, #15) found that hydrogen emissions varied with time (Prinzhofer *et al.* 2019; Moretti *et al.* 2021a). These studies used sensors spaced tens of meters apart and found two types of temporal variability: daily diurnal cycles and apparently random short-lived increased emission events which cause greater variation. Spatial variability was observed across the depression as sensors recorded different reading of hydrogen concentrations, even during “pulse” events (Moretti *et al.* 2021b). The distribution of concentrations was patchy, including areas of no measurable hydrogen. Further, transects across these features in Russia and the USA (#1-12) indicate that hydrogen seepage is spatially variable, but often higher at or near the depression edge (Figure 8-3 and Figure 8-4), indicating localised preferential migration pathways of hydrogen in the near surface. These preferential pathways likely focus in higher permeability soils and sediments

(Myagkiy *et al.* 2020b). Moretti *et al.* (2021b) note that even around the rim the emission rates were spatially different. The daily cycle of emissions can be seen across multiple sensors; however, the short-lived increased emission events were limited to specific monitoring locations and did not manifest across the whole seep area. These two studies concluded that the observed spatial variability in hydrogen concentrations indicate that different preferential seepage pathways must exist, influenced by soil characteristics (e.g. permeability) and heterogeneity, and that these pathways can have an effect temporally on when hydrogen reaches the surface from the subsurface source or point of leakage (Moretti *et al.* 2021b). However, neither study effectively ruled out the possibility of a biological or microbial source of the measured hydrogen, and it is possible that the observed spatial and temporal variability represents biological action rather than gas seepage.

Our compilation suggests that where seepage occurs through soils and unconsolidated sediments, the seep rate is roughly proportional to seep area (Figure 8-7). However, there are very few data points (seep rate is calculated for only 10 of the 60 identified seeps in this study), and this inferred relationship might be an artefact of the assumptions and uncertainties within seep flux and seep rate calculations. Firstly, flux is very sensitive to estimates of the seep area (Prinzhofer *et al.* 2019). Secondly, flux calculations assumed consistent flux, and did not account for variations with space and time as has been observed at natural hydrogen seeps where seepage occurs through soils and unconsolidated sediments (Prinzhofer *et al.* 2019; Moretti *et al.* 2021a). The calculations also typically do not account for any diffusive flux around seep hotspots (e.g. Zgonnik *et al.* 2019; Prinzhofer *et al.* 2019). Where emission rates are reported, they are derived by the rate of accumulation into soil gas sampling wells. This methodology uses a pump, resulting in a disturbance of both advective and diffusive gas flow in the soils, meaning that gas emission rates are likely to be over-estimated. Recent models by Myagkiy *et al.* (2021b) do not consider this effect. While measurement of hydrogen fluxes in nature is known to be difficult (Meridith *et al.* 2014), more robust measurement methods and techniques, such as use of closed-system soil gas chambers, should be used to measure hydrogen flux measurements more accurately. Current flux and seepage rate data are therefore problematic and these large uncertainties may explain the lack of relationship between seep rate and flux (Figure 8-8). There is currently not

enough data to draw comparisons of seep rate and flux between different measured hydrogen concentrations or surface expressions of seepage.

8.6.1.2 Physical and structural features of hydrogen seeps

Documented hydrogen seeps are associated with structural and physical manifestations at the surface. If hydrogen were to leak from an engineered reservoir and reach the surface, we might therefore expect the leak to manifest in a similar way. Physical features of hydrogen seepage thus have the potential to be a useful tool in monitoring engineered geological hydrogen storage sites. The three types of seepage we have identified have some unique physical characteristics (Figure 8-9).

Springs can have some physical features caused by processes not directly related to hydrogen seepage (carbonate precipitation), whilst seepage from bedrock fractures have minimal physical characteristics – there are examples of gases spontaneously igniting at surface (Vacquand *et al.* 2018). Of the three types, seepage through sediments and soils is the only type of seepage that we identify to have broadly consistent visible physical features: subcircular depressions.

The physical origin of the observed subcircular features has yet to be resolved. Some studies from the subcircular depressions in Russia, USA, Mali, and Brazil conclude that hydrogen-bearing gas seepage from depth results in localised rock alteration and subsidence or collapse (Zgonnik *et al.* 2015; Donzé *et al.* 2020), similar to offshore pockmark formation (Gay *et al.* 2019). Other authors have suggested that the depressions are not a result of hydrogen seepage, but caused by other environmental factors, and their presence provides a preferential flow for seeping hydrogen. For example, Moore *et al.* (2016) argue that the depressions located in the Carolina Bays (#8-12) have migrated hundreds of meters over time (hundreds to thousands of years), likely in correlation to the prevailing wind direction, suggesting that these features are mobile, and otherwise unrelated to the presence of hydrogen. Similarly, the subcircular depressions in Brazil (#14, #15) are documented on geological maps as karstic lakes often with economic clay and spongillite sedimentary fill. Detailed studies of the sedimentation within some of these lakes (Almeida *et al.* 2010) have not yet identified any features associate with gas seepage, such as carbonate lenses or chimney structures, suggesting that they are not the result of gas seepage.

Previous work has suggested that large fault systems control hydrogen seep locations in Brazil (#14, 15, Coelho *et al.* 2008) and Australia (#16-18, Frery *et al.* 2021), either providing a conduit for deep seated hydrogen to reach the surface, or to accumulate in subsurface reservoirs (Romero-Silva and Zalán, 2005; Donzé *et al.* 2020). If the depressions are large formed by karstic processes, fault systems present may control the location of some karstic lakes by enhancing subsurface fluid flow, and also provide a migration pathway. In Oman, there are fault systems which have been proposed as a migration pathway for hydrogen (Neal and Stranger, 1983).

Previous authors have speculated that the location, alignment, and axes of the subcircular shape of depressions are a result of structural features, such as basement faults or local stress regimes (Larin *et al.* 2015; Zgonnik *et al.* 2015; Cathles and Prinzhofer, 2020; Donzé *et al.* 2020; Frery *et al.* 2021). This has been observed previously at CO₂ vents (Bonini, 2012). To explore this, we used World Stress Map (WSM) data (Heidbach *et al.* 2016) to compare the local stress regime with alignment of the orientation of subcircular hydrogen seeps (Table 8-1).

Table 8-1 – Seep shape, axis orientation, stress orientation (S_{HMAX}) with distance from seep and prevailing wind direction.

Location	Depression shape (axis orientation)	Stress orientation (S_{HMAX}) (distance from depression)	Prevailing wind direction
USA (Carolina Bays) (#8-12)	Elongate (30° to 45°, NNE-NE)	10° to ~65° (160-515km)	30-60° (NNE-ENE)
Russia (#1-7)	Circular	No data within 700km of depressions	WSW-SSW
Australia (#16-18)	Some elongation (N-NW)	110° (~50km)	East
Brazil (#13-14)	Some elongation (~120°, SE)	52-92° (155-250km)	WNW-WSW

We find little compelling evidence that depression shape is controlled by stress orientation, but note that stress data is sparse. While there is some indication that the shape and orientation of depressions in USA, Russia, and Brazil (#1-14) might be influenced by lacustrine and aeolian processes (Almeida *et al.* 2010; Zgonnik *et al.* 2015; Moore *et al.* 2016) particularly over long timescales, this does not explain the initial formation mechanism.

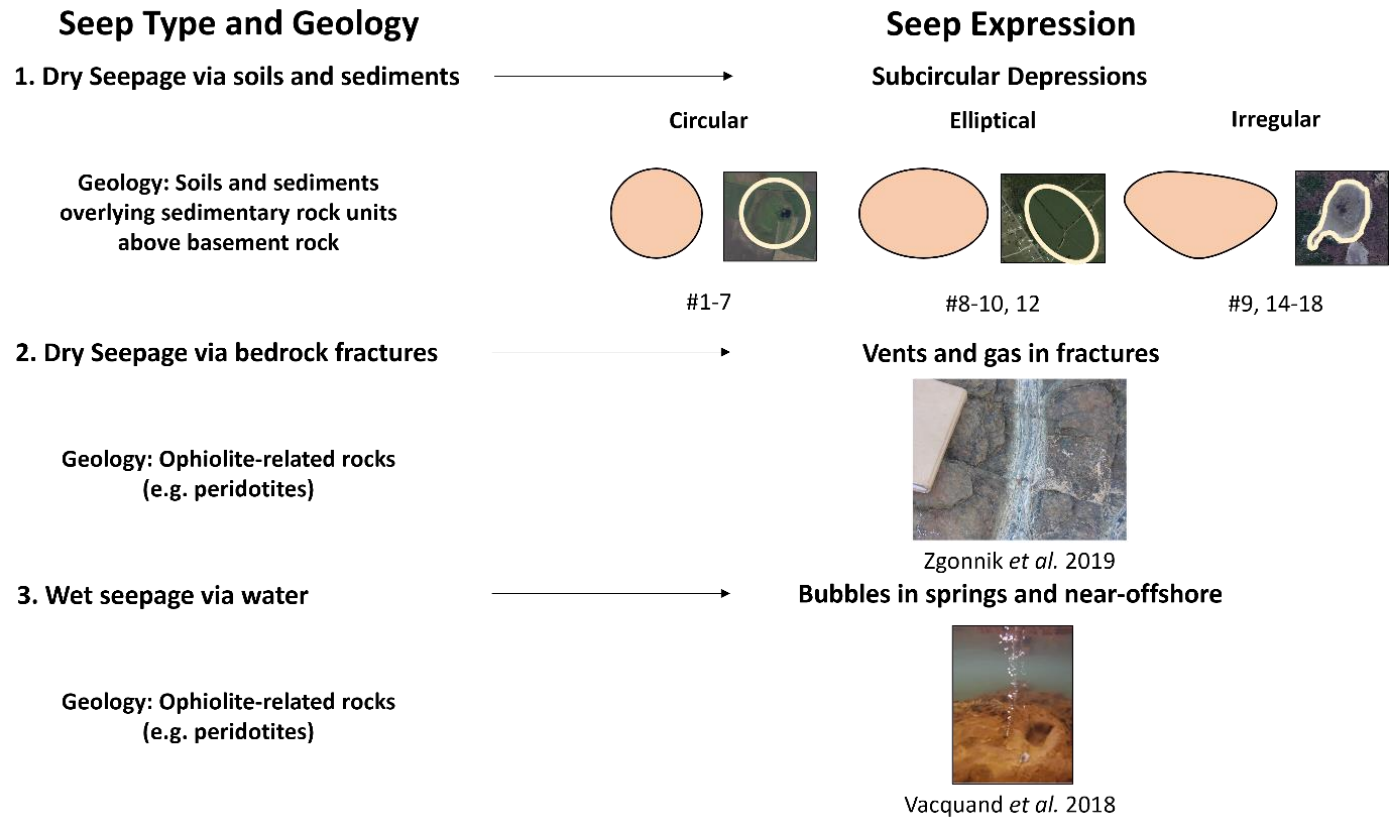


Figure 8-9 – Seep type, geological environment and surface expression of hydrogen seepage with example images and cartoons of typologies. (1) Subcircular depressions with three shapes – circular, elliptical and irregular. (2) Fractured rocks with diffusive flows of hydrogen (Zgonnik *et al.* 2019). (3) Bubbling seepage offshore, New Caledonia (#34). Images in (2) from Zgonnik *et al.* 2019 and (3) from Vacquand *et al.* (2018). Satellite photos in (1) from Google Maps.

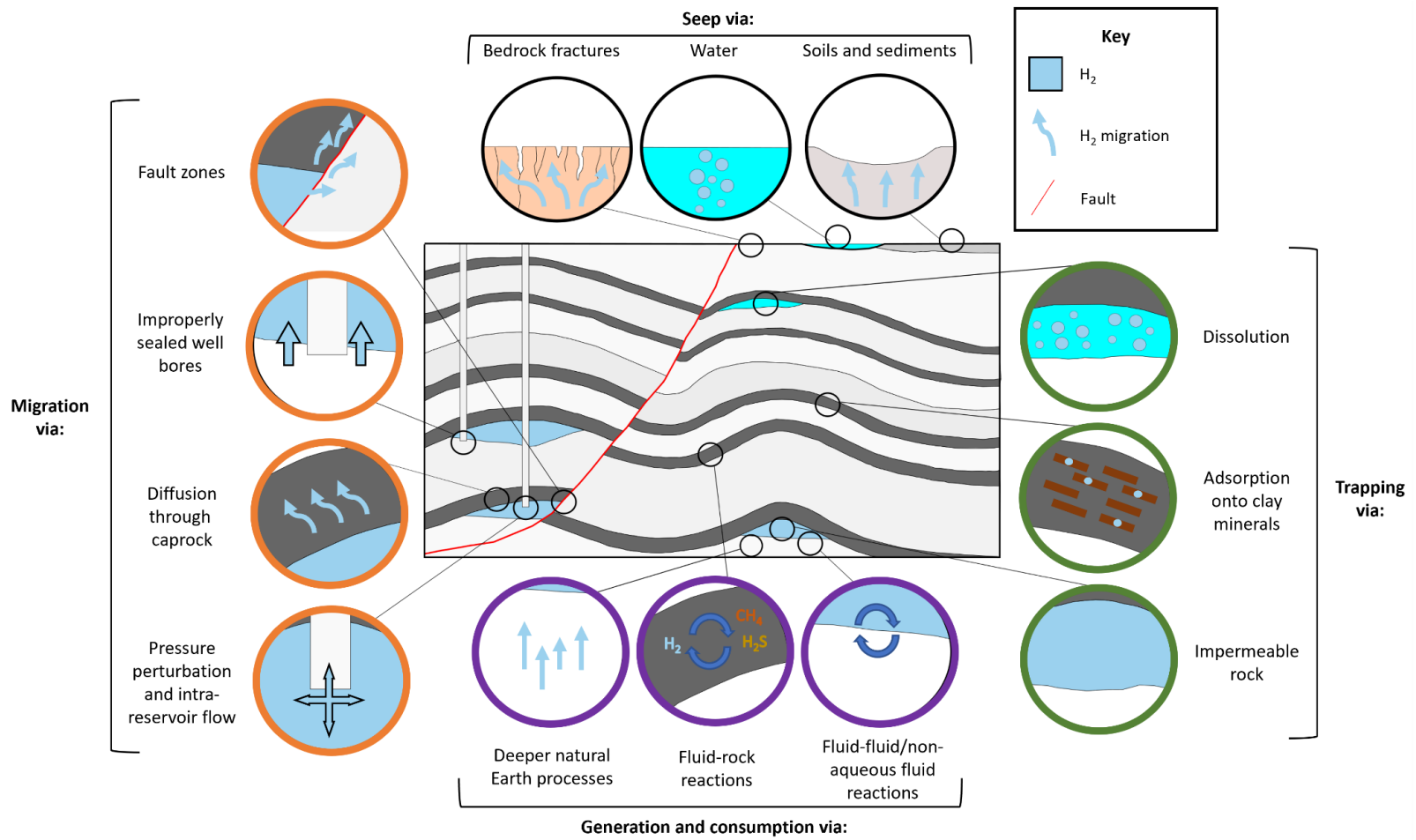


Figure 8-10 – Potential mechanisms for hydrogen generation and consumption (purple circles), trapping (green circles) and migration (orange circles) in the subsurface and seep expression at the surface (black circles). Adapted from Heinemann et al. (2021).

8.6.1.3 Hydrogen source, transformation and associated gases

Any robust monitoring program needs to understand how leaked fluids may be modified as they migrate, react, and accumulate in the subsurface at geological storage site, and how they seep (Figure 8-10).

Although hydrogen generation and consumption mechanisms in the subsurface are generally well understood (Sherwood Lollar *et al.* 2014; Panfilov, 2016; Gregory *et al.* 2019), there is no clear agreement on the source(s) of hydrogen at the documented seeps (Larin *et al.* 2015; Zgonnik *et al.* 2015, 2019; Prinzhofer *et al.* 2018, 2019; Vacquand *et al.* 2018) (Table 8-2). Zgonnik *et al.* (2015) note that there must be a large-scale process that can generate and sustain significant quantities of hydrogen over time.

Table 8-2 – Interpreted sources of hydrogen from the literature. Other locations (e.g. Philippines, Mali, Australia) presented in the results section discuss similar hydrogen sources and generation processes, but also with significant unknowns and uncertainty.

Location	Interpreted Source	Reference
Russia (#1-7)	Unknown (discussed multiple options)	Larin <i>et al.</i> 2015
USA (Carolina) (#8-12)	Deep geochemical processes	Zgonnik <i>et al.</i> 2015
Oman (#19-29, #36-55)	Deep subsurface source (water interactions with Fe-rich minerals or serpentinization of mantle rock)	Zgonnik <i>et al.</i> 2019
Turkey (#31, #58)	Serpentinization (CH ₄ is produced from the H ₂ reacting in presence of CO ₂ , Fischer-Tropsch type reactions)	Hosgörmez <i>et al.</i> 2008

New Caledonia (#34, #35)	Serpentinization and deeper earth processes	Deville and Prinzhofer 2016; Vacquand <i>et al.</i> 2018
--------------------------	---	--

As bubbling gas seeps are found in ophiolitic settings, many authors have proposed serpentinization processes to be a key contributor to the production of hydrogen at these locations (Vacquand *et al.* 2018; Zgonnik *et al.* 2019; Zgonnik, 2020). Based on major gas concentrations, stable isotopes, and noble gas geochemistry, Vacquand *et al.* (2018) conclude that, while low temperature, shallow serpentinization is a dominant source of hydrogen in ophiolite systems, hydrogen associated with higher proportions of N₂ and CH₄ likely derives from a deeper, hotter source; this source is likely related to geothermal activity and mantle gases and indicates that deep hydrogen sources are a component of many ophiolite-hosted seeps. Figure 8-6 illustrates that the highest measured hydrogen concentration in a seep occurred in rock units that are not directly overlying ophiolitic rocks (where serpentinization takes place). This seep in Oman occurs in shales directly overlying Precambrian crust, which is a major source of hydrogen generated by water-rock interaction and radiolysis (Sherwood Lollar *et al.* 2014). This supports the hypothesis that shallow serpentinization is not the sole source of hydrogen in many ophiolite hosted seeps. Therefore, multiple sources of hydrogen can exist at the same seep location, where gases mix and consequently increasing complexity in source attribution.

As hydrogen migrates from source to surface, hydrogen can react both abiotically and biotically. 45 of the seeps presented in this paper have hydrogen occurring with methane, with examples #31, #31 #32 (Table A7 - 2), where methane is the dominant seeping gas. Methane can be formed by both abiotic and biotic processes that consume or transform hydrogen (Panfilov, 2016; Gregory *et al.* 2019). Abiotic reactions include transformation to methane and other hydrocarbons at higher temperatures (>600°C) and at lower temperatures (e.g. Fischer–Tropsch-type synthesis, as low as 50°C, Sherwood Lollar *et al.* 2002, 2006, 2008). Recent studies at a geothermal field in Italy conclude that hydrogen produced at deeper levels of the crust is abiotically consumed at high temperatures to form CH₄ (Leila *et al.* 2021). Hydrogen can be biotically transformed to methane via methanogenesis. Hydrogenotrophic methanogen bacteria

oxidise hydrogen in the presence of CO₂ to form CH₄ and H₂O in Sabatier's reaction (Panfilov, 2016). Hydrogen can also be consumed in other biotic reactions, examples include: H₂S (sulphate reduction), acetate (acetogenesis), Fe²⁺ (iron-reduction) and H₂O (aerobic hydrogen oxidation) (Panfilov, 2016; Gregory *et al.*, 2019; Thaysen *et al.* 2021; Muhammed *et al.*, 2022). Closer to surface, microbial communities in soils can act as a hydrogen consumer (Conrad and Seiler, 1981; Myagkiy *et al.* 2020a) and also produce hydrogen (Sugimoto *et al.* 1998).

For the studied seeps, the understanding of the hydrogen generation and reactions processes in ophiolite settings is broadly well understood and detailed (Vacquand *et al.* 2018). These seeps have mixed gases that can be traced to different sources of hydrogen production in the subsurface and show transformation of hydrogen as it migrates from depth to surface. Figure 8-5 highlights the variability of gas mixtures that are reported for the seepage sites presented. These surface compositions do not necessarily reflect the original deep gas composition in the subsurface. The data that exists to make these assumptions for the seeps based in ophiolitic geology does not currently exist for seepage through soils and sediments that form subcircular depressions. This data is required to understand the source and migration of hydrogen from depth to surface – although this is difficult to collect due to the dilute and diffuse nature of the seeps.

The gas composition generated in the subsurface may differ to what reaches the surface – with implications for monitoring at engineered geological hydrogen storage sites. Controlled release experiments could be one option to study how well gas signatures are preserved as they migrate in the subsurface. Additionally, engineered hydrogen storage sites will likely have a purer quality of hydrogen than naturally produced, meaning pure hydrogen migration (no co-gases) could differ compared to hydrogen alongside other gases (CO₂, CH₄, N₂). However, mixtures at engineered storage sites could vary depending on the type of cushion gas used and this should be considered in any monitoring strategy.

8.6.2 Comparing hydrogen seepage to other gas seepage

The differences in hydrogen behaviour compared to other gases have implications for the monitoring of engineered geological hydrogen storage sites.

Hydrogen seeps share some characteristics with CO₂ and CH₄ seeps. CO₂ seeps are known to form in circular depressions (Roberts *et al.* 2015) and CH₄ seepage offshore leaves pockmarks (circular depressions) in seafloor sediments (e.g. Räss *et al.* 2018). CH₄ and CO₂ seeps migrate along faults and fractures, like hydrogen seeps (Zgonnik *et al.* 2019). Both hydrogen and CO₂ seeps (e.g. Roberts *et al.* 2019a; 2019b) have been found to occur as bubbles in spring waters. This distribution of these features at surface can then influence the spatial distribution of seepage (e.g. fracture controlled distribution in Oman, Zgonnik *et al.* 2019).

Hydrogen has a low solubility in water: at 20°C the solubility of hydrogen is 0.0016 g/kg water. At the same temperature CO₂ is around 1.4 g/kg water. Hydrogen is less soluble than CO₂ in both mole fraction and mass fraction terms (Ennis-King, 2021). This explains why hydrogen is likely found bubbling in water at the surface, as hydrogen is less soluble than other gases, so in the presence of water hydrogen concentration may be elevated compared to other gases. However, hydrogen can be found dissolved in shallow low-salinity aquifers. Frery *et al.* (2021) note that the high geothermal gradient in their study region in Australia (40°C/km), coupled with the low salinity of the groundwater systems, means increased hydrogen solubility would result in high concentrations of aqueous phase hydrogen at shallower depths (<1km). Thus, hydrogen can migrate in both gaseous (via major faults) and aqueous phase (shallow-depth low salinity aquifers). Seasonal changes in water table or groundwater conditions could alter these hydrogen migration pathways, as at sites of CO₂ seepage (Roberts *et al.*, 2015), and clearly structures (e.g. faults, fractures) effect fluid flow in both hydrogen and CO₂ seeps (e.g. Roberts *et al.* 2017, 2019a).

Hydrogen seepage sites do share some characteristics with other gas seeps; however, there are notable differences. Hydrogen may pose a different risk compared to CO₂ or CH₄ seepage. Unlike CO₂, which is denser than air, hydrogen will not accumulate at high concentrations in topographic depressions, posing less of a safety risk. However, hydrogen seepage sites are often associated with vegetation loss and decay of organic matter (Sukhanova *et al.* 2013), meaning there may be other hazards from hydrogen seepage. Some hydrogen seepage sites are associated with spontaneously igniting gases that can burn for 1000s of years. These sites are dominated by methane which is the primary source for the ignition. Mostly notably, sites of hydrogen seepage differ from

sites of CO₂ seepage in that hydrogen can be transformed before reaching surface due to subsurface reactions (see Section 8.6.1.3).

8.6.3 Recommendations for engineered geological hydrogen storage

Our findings on natural hydrogen analogues have implications for monitoring of engineered hydrogen stores.

For engineered stores, the pressure conditions of a storage site will likely change during injection and withdrawal cycles (Heinemann *et al.* 2021), therefore a cyclic emission style might be expected. In addition, hydrogen seepage from engineered stores will vary both predictably (atmospheric and diurnal changes) and perhaps less predictably, such as when biological communities establish – with implications for effective monitoring of engineered geological hydrogen storage sites. If a leak from engineered storage was to be established and reach the surface, manifesting as a diffuse seep, the observations from many of the studied natural seeps suggest that short term (diurnal, seasonal) and long-term variation in hydrogen seepage is to be expected (Prinzhofer *et al.* 2019; Myagkiy *et al.* 2020a, 2020b; Frery *et al.* 2021 Moretti *et al.* 2021a, 2021b). This means that background monitoring over an extended time (several weeks to capture diurnal cycles, but up to 2 years to capture seasonal variation) should be established prior to hydrogen storage. Other useful data could include weather data (e.g. temperature, humidity, air pressure) and consider aspects such as tides.

The surface expression of hydrogen seepage varies depending on the geology and sediment cover. The type of hydrogen seepage and the surface expression (if any), and therefore appropriate monitoring approaches, will be controlled to an extent by the exposed bedrock and superficial deposits. Our findings suggest that, where seepage occurs through soils and unconsolidated sediments, a physical expression will establish, assisting the identification of leakage, and thus monitoring approaches such as remote sensing image analysis could be appropriate. Monitoring in subcircular depressions should note that hydrogen concentrations are spatially variable (Figure 8-3 and Figure 8-4), and hydrogen flux may occur outside the boundaries of the subcircular depression. Within ophiolitic or subduction complexes, where there is no soil or sediment cover, seepage is via fractured rocks and springs. Different monitoring approaches will be required, but, as with natural CO₂ seeps (Roberts *et al.* 2019b), monitoring approaches might target springs and water courses, or topographic lows.

Springs could be used to locate monitoring equipment and monitor gases. Seepage may be detected by periodic groundwater (aquifer) sampling and analysis (e.g. Etiope *et al.* 2017), by measuring molecular composition of dissolved gases, as well as water properties (e.g. pH and Eh).

Owing to the mobility, reactivity, and consumption of hydrogen in the subsurface, both abiotically and biotically, challenges for monitoring hydrogen are different compared to other more developed geological gas storage technologies (e.g. CO₂, CH₄ storage). Thus far, we have considered monitoring of gas leaving the reservoir due to buoyancy forces. However, hydrogen could also be lost from the reservoir via transformation into different gases (e.g. CH₄) by reducing fluid or rock reactions and microbial action. Hydrogen can also be trapped on mineral surfaces (e.g. clay minerals) (Truche *et al.* 2018) and consumed by soil bacteria if a leak were to reach the surface (Conrad and Seiler, 1981; Myagkiy *et al.* 2020a). These reactions could result in hydrogen leakage from a reservoir being difficult to detect at the surface. Consequently, subsurface (direct) monitoring techniques (e.g. monitoring of the reservoir integrity and subsurface borehole monitoring techniques) will likely be crucial to detect any hydrogen leakage early and with a higher degree of certainty. Highly sensitive monitoring approaches may be required to detect hydrogen seepage, although hydrogen has a low atmospheric concentration, the highly mobile and buoyant nature of hydrogen means that hydrogen dispersal will be high. Hydrogen plume dispersal studies will be important to understand how hydrogen may behave if released at surface and how to appropriately measure and monitor for this. Monitoring for common transformation gases (e.g. CH₄) and analysing the isotopic composition could be appropriate in environments where hydrogen is able to be transformed to other compounds.

8.6.4 Key research and data gaps

Natural analogues of CO₂ seepage and storage have been used for decades to provide information on seep rate, flux, subsurface geometries, CO₂ migration and trapping, and more (Irwin and Barnes, 1980; Pearce *et al.* 1996; Pearce *et al.* 2004; Holloway *et al.* 2007; Miocic *et al.* 2013; Roberts *et al.* 2017, 2019a; 2019b). This information has been used to make robust recommendations for effective MMV strategies. For sites of hydrogen seepage and accumulation, we are limited in the data available and by the data reported. There are: (a) a general lack of reported data for natural hydrogen seepage

and accumulation. This is related to, (b) broader issues around the field data collection methodologies (e.g. drilling, measurements from only one point in time) and (c) uncertainty is introduced by simplifying and estimating values (e.g. area, porosity) for calculating hydrogen fluxes from seep rates and concentrations. Finally, (d) studies must consider and rule out biological sources of hydrogen.

There are a combination of reasons regarding a lack of reported data on hydrogen seepage and accumulations. Firstly, hydrogen has different physiochemical properties when compared to other gases meaning the overall risk and hazard differs and is perhaps reduced – which may explain a general lack of reported sites of seepage. Secondly, the lack of any global exploration programme for natural hydrogen means that there may be seepage sites or accumulations that exist that have not yet been discovered. This could be because they may occur in different locations to conventional hydrocarbon resources, both geographically and in terms of depth in the subsurface. Many of the examples of hydrogen seeps presented in this paper suggest a deep-seated source of hydrogen, and the Precambrian crust has been established as a significant reservoir of hydrogen (Sherwood Lollar *et al.* 2014). Only in the late 2010s and early 2020s have both academia and industry started to pursue natural hydrogen as a possible low-carbon energy resource, however there is a rapid increase in interest in this area. New companies, e.g. Natural Hydrogen Energy LLC (NH2E, 2022), have been created that are dedicated to prospecting and drilling for natural hydrogen accumulations in the subsurface, while existing well-established companies are expanding from other operations to consider subsurface hydrogen storage and natural hydrogen. Further, governments are now permitting for natural hydrogen exploration (e.g. Government of South Australia, 2022). Thirdly, we have discussed the multiple ways in which hydrogen can react in the subsurface before reaching the surface – potentially leading to its transformation or consumption. Finally, the highly mobile nature of hydrogen and the restricted range of conditions that are likely to cause its accumulation in subsurface reservoirs might simply mean that there are very few hydrogen-bearing gas seeps.

Hydrogen concentration has been observed to vary throughout the day (Prinzhofer *et al.* 2019; Moretti *et al.* 2021a) and these temporal variations introduce significant

uncertainty in estimating seep and flux rates. Further, detailed information is missing at many sites around the rate of emission.

Many of the reported seeps measured hydrogen in soil gas wells produced by drilling. Hydrogen may be produced during drilling due to cracking of organic matter (Halas *et al.* 2021) and/or water (Kita *et al.* 1982). A circular depression in South Gironde, France was initially thought to be a hydrogen seep, based on early drilling studies, but was ruled out after it was found that hydrogen could be artificially generated in the soil during drilling (Halas *et al.* 2021). Halas *et al.* (2021) highlight the importance of developing a robust sampling method and note that studies of natural hydrogen seepage should avoid drilling in the sampling process. Of the studies discussed in this paper, only Zgonnik *et al.* (2015) and Zgonnik *et al.* (2019) specifically address this issue and state that significant flushing time was allowed between measurements to ensure that any hydrogen was not associated with drilling. Zgonnik *et al.* (2019) argue that drilling is not responsible for the hydrogen measured in their study due to the lack of hydrogen in drilled borehole samples from unfractured rocks in the area, but this conclusion does not account for potential variation in water and organic matter content that may act as a source of drilling induced hydrogen. Other papers are unclear regarding the potential for results to be affected by drilling induced hydrogen. Consequently, we recommend a standardised and effective methodology for the collection of field data, that accounts for the need to measure differently depending on the style of seepage and rules out hydrogen production via sampling methodology. Recent more detailed studies have made progress in this respect, for example studies in Brazil have conducted detailed analysis of hydrogen seepage. These explore the meaning of pulsed emissions (Cathles and Prinzhofer, 2020) and longer-term monitoring of a depression (Moretti *et al.* 2021a). These monitoring programmes use multiple sensors, deployed over a time interval to get an idea of the spatial and temporal variation in seepage. This methodology is more effective than measurements from one point in time that are spatially constrained. Thus, we recommend that sufficient sensors are deployed to elucidate the spatial variation in seepage (the actual number will depend on the seep characteristics and size, but as a rule of thumb we recommend a spacing of no more than tens of metres between sensors, e.g. Moretti *et al.* (2021a)) and that these are deployed over a period (i.e. months at a minimum, but ideally one or two years) to appropriately capture diurnal and seasonal temporal variation in seepage. Additionally, results from Larin *et al.* (2015) and

Zgonnik et al. (2015) analyse soil gas using pumped measurement protocols, but instead flux chamber methods should be deployed to quantify hydrogen flux rates more accurately. Lastly, drilling should be avoided to ensure that no hydrogen is produced by this method as evidenced by Kita et al. (1982) and Halas et al. (2021), which would subsequently influence measured hydrogen concentrations.

There is an additional problem of consistency in the data reported in the published literature. This can make comparisons between different datasets, and identifying contributions of biologically produced hydrogen, problematic. Often data are averaged (e.g. concentrations) and assumptions are made (e.g. area, porosity), which introduces uncertainty into the final flux estimates (e.g. Cathles and Prinzhofer, 2020; Donzé *et al.* 2020). Therefore, we recommend consistency in the reporting of data, as well as analysis of the spatial and temporal evolution of hydrogen seepage. For each seepage site, the spatial area of seepage should be quantified (e.g. for subcircular depressions the radius/diameter of the depression) as well as the cross sectional profile of the seepage area or profiles for non-circular seeps. Data such as the surface geology and type and quantity of gases present should be recorded. Where possible, gas fluxes should be recorded and any information about the source of hydrogen and the temporal evolution of seepage (e.g. time of onset of seepage) should be recorded. Additionally, the methodology used should be described in enough detail to allow understanding of the conditions in which samples (e.g. gas concentrations) were collected. This includes whether samples were taken at the surface (in air), in the subsurface (in soils or rock) or in/near water. Subsurface samples should note the depth at which they were taken and the means to reach this depth (i.e. drilling or otherwise). Samples near or from water (e.g. springs) should collect basic data on the water properties (at a minimum temperature, pH and Eh should be recorded). Other data such as the time samples were collected, the season in which samples were collected and the weather at the time of sampling should be noted. Other environmental factors which might influence the collected data should be noted (e.g. vegetation, land use). Further work is needed to understand the formation of surface subcircular depressions, controls on their size and shape as well as how any orientation relates to subsurface structural features.

Studies of CO₂ seeps in Daylesford (Australia) have highlighted the importance of different spatial scales of analysis, as well as the importance of surface processes in

controlling seepage locations and rates (Roberts *et al.* 2019a). This highlights the importance of understanding surface processes that can influence how fluids seep and how they may influence surface seep expression, ensuring that the focus is not fully on the migration from the deep subsurface. This is an area to consider in further studies.

Although there is a good understanding of natural methods of hydrogen production in the subsurface, the discussions highlight that there are still many unknowns regarding the source of the hydrogen in many of the examples presented. From source to surface, the migration of hydrogen can be baffled by several processes that can transform or trap hydrogen. Understanding migration pathways to surface, as well as potential baffles is important in assessing the risk of hydrogen both exiting the storage reservoir and reaching the surface. There is only one published example of a natural hydrogen accumulation in Mali. While there is a documented seep in Mali (#13, Table A7 - 1) (Prinzhofer *et al.* 2018), it is located 218 km away from the production well). The lack of documented seeps directly above or close to this accumulation suggests that the accumulation must have an appropriate seal that is stopping hydrogen migrating to the Earth's surface. The lack of examples of natural hydrogen storage means this one analogue in the literature of natural hydrogen storage (Prinzhofer *et al.* 2018) is likely not analogous for all future engineered hydrogen storage sites, or indeed any other natural hydrogen accumulations. This is similar to the findings of Roberts *et al.* (2017) who note that natural CO₂ reservoirs are not direct analogues of CO₂ storage sites due to the differences in processes and operation, but do provide valuable learnings for MMV. Prospecting for new natural hydrogen seepage and accumulations could help to develop understanding of seepage pathways and barriers. This will be important for the effective site selection and monitoring of engineered geological hydrogen storage. However, in all cases, the source of natural hydrogen and the migration pathways are poorly understood, and so robust implications for site selection of hydrogen stores cannot be made.

8.7 Conclusions

To date natural hydrogen seepage sites have been largely unreported and understudied. Furthermore, sites of hydrogen seepage at the surface have only been studied by those primarily interested in prospecting for natural hydrogen accumulations in the subsurface. However, natural hydrogen seepage and accumulation can inform appropriate monitoring approaches for engineered geological hydrogen storage.

We know from hydrogen seepage that seep characteristics are determined by local geological and hydrological conditions, specifically whether hydrogen gas is seeping through soils and unconsolidated sediments, fractured bedrock, or water (e.g. springs). Where hydrogen seeps through soils and sediments, seeps manifest as sub-circular depressions with patchy flux, and the spatial extent of the seep controls the seep rate. Where hydrogen seeps through bedrock fractures or into springs, gas emissions are highly localised, with small spatial footprint of seepage. In the studied seeps, hydrogen seepage is known to seep to the surface over extended periods of time (years, as a minimum).

Monitoring approaches for engineered hydrogen stores should therefore be tailored according to the exposed geology and hydrological conditions. We find similarities in the controls on seep location and characteristics between hydrogen seeps and CO₂ seeps, which have been more widely studied to inform geological CO₂ storage. However, compared to CO₂, hydrogen is more readily dispersed because of its high mobility (due to small size and low density), and so maximum concentrations of hydrogen in gas streams that reach the surface are typically lower than CO₂ concentrations at CO₂ seeps.

In all cases, hydrogen is typically co-emitted with other naturally occurring gases such as CO₂, CH₄, and small amounts of trace hydrocarbons or noble gases, with CH₄ the most dominant co-emitted gas in most cases presented here. Hydrogen can be consumed or transformed in the subsurface, and so the quantity of leaked hydrogen might be greatly attenuated before it reaches the Earth surface. As such, subsurface monitoring approaches to detect hydrogen, or tools that also monitoring for co-gases could be appropriate in environments that promote the transformation of hydrogen to other compounds.

In all cases, the source of hydrogen and the migration pathways are uncertain, and so robust implications for site selection of hydrogen stores cannot be made. We recommend: 1) a standardised and effective methodology for the collection of field data, that accounts for the need to measure differently depending on the style of seepage, 2) consistency in the reporting of data, analysis of the spatial and temporal evolution of hydrogen seepage and consideration of how surface processes may influence surface seep expression, 3) further work to understand the initial formation of surface subcircular depressions, controls on their size and shape as well as how any orientation relates to subsurface structural features, 4) further work to detail and mitigate hydrogen seepage risks.

Chapter 9 Discussion

This chapter links together common themes discussed throughout this thesis. First, Section 9.1 defines shallow fault systems and categorises the F10 and Brumbys Fault zones. Section 9.2 compares and synthesises findings from the F10 and Brumbys Faults. Section 9.3 presents learnings from other technologies relevant to shallow fault zones and studying rocks in the shallow subsurface. Finally, Section 9.4 considers implications for subsurface fluid flow and environmental monitoring.

9.1 Defining shallow fault zones

Five types of faulting were defined in Section 1.1. Figure 9-1 presents a schematic of these fault types and argues for a sixth fault type.

In the categorisation outlined in Section 1.1, the Brumbys Fault is a category 1 fault: a fault that was active at shallow depths and which has not been exhumed since it was active. The F10 Fault is a category 2 fault, as it has been partially exhumed, though it still has sections which remain unconsolidated. These two fault zones are compared in Section 9.2.

Deeper faults can be both active during exhumation, resulting in the overprinting of deeper structures by shallower structures (category 3) or inactive, resulting in the preservation of deeper structures during exhumation (category 4). Category 5 faults are faults which were active, or inactive, at depths >1km, and which have since been exhumed.

Category 6 faults are those which were formed in the shallow subsurface and then buried to depths >1km, these have been observed in the literature (Antonellini *et al.*, 1994; Fossen *et al.*, 2007). These have shallow deformation features (e.g. disaggregation bands which are cut by cataclastic deformation bands at depth (Antonellini *et al.*, 1994; Fossen *et al.*, 2007). Therefore, there are important considerations when examining shallow faults which have been buried, meaning fluid flow may be influenced by both older shallow deformation features and overprinting deeper deformation features and diagenesis. Therefore, the research and methods developed in this thesis are relevant not only for studying faults in shallow subsurface, but potentially also for buried shallow fault systems.

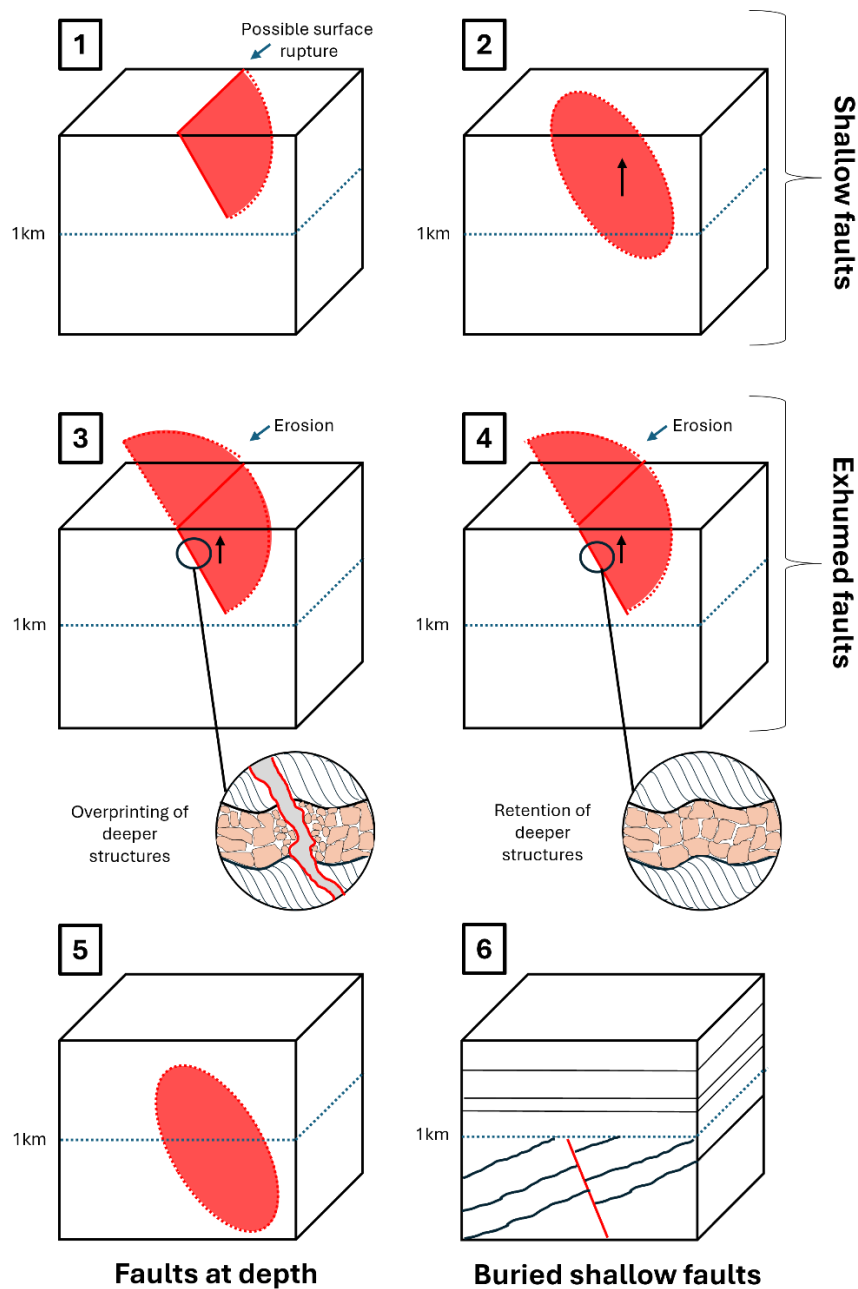


Figure 9-1 – Schematic of 6 types of faulting: 1) Faulting in ‘young’ rocks or soils that have not been exhumed, these are likely to be very poorly consolidated unless there has been very near-surface diagenesis. They are currently experiencing the greatest levels of stress in their history and are considered to be underconsolidated in an engineering soil mechanics sense (e.g. Brumbys Fault, see Section 3.2.3). 2) Faulting in rocks that have been exhumed from depths less than 1km, may be completely, partially or unlithified. Because they are at stress levels less than the greatest stress levels they have experienced, they are considered to be overconsolidated in an engineering sense (e.g. F10 Fault, see Section 3.1.3). 3) Faults that have been active at greater depths in the Earth’s crust (>1km depth), display deep deformation features (e.g. mylonite, s-c fabrics) and have since been uplifted to depths shallower than 1km, and overprinted by later faulting at shallower depths. 4) Faults has been active at depth, display deep deformation features and been exhumed with no further fault activity during exhumation. 5) Faults which are presently active or inactive at depths >1km and have not been exhumed. 6) Buried shallow faults (depths >1km), which could have started as either category 1 or 2.

9.2 Comparing the F10 Fault and the Brumbys Fault

Although both shallow faults, the F10 Fault and Brumbys Fault represent two very different fault zones in terms of the type of faulting, the differences in fault zone scale and the differences in the host rock lithology (Table 9-1).

Table 9-1 – Comparison between the F10 Fault and the Brumbys Fault and injection experiments at both study sites.

Characteristics		In-Situ Lab Harvey, Western Australia	Otway International Test Centre Otway, Victoria
Intersecting wells		Harvey—1, 2, 3,4, In-Situ Lab-OB1	Brumbys-1, -2, -3, -4, Pizo-1, -2,
Fault	Name	F10 Fault	Brumbys Fault
	Host lithology	Siliciclastic	Carbonate
	Interpreted Type	Normal	Strike Slip
	Fault width	~300m	<5m
	Vertical distance from surface to bottom of fault	>1km	~425m
	Vertical Throw	750-1600m	2-4m
	Surface Length	30-40km	~1-1.5km
	Max. Burial Depth	~1-2km	~100-200m
Injection experiment	Injection depth	~340m	~80m
	Quantity of CO₂	38t	10t
	Date	Completed: February 2020	Completed: May 2024

There are obvious differences between both fault zones. The F10 Fault represents a large normal fault in siliciclastic rock, whereas the Brumbys Fault is a smaller strike slip fault

hosted in a carbonate sequence. These differences provided the opportunity to assess some of the commonalities and differences between each of the sites in contrasting lithologies – this is discussed in the following section.

9.2.1 The effect of lithology on fault architecture

The lithological differences between each of the two fault zones highlight some of the challenges that can be faced when considering local geological heterogeneities and variable diagenetic histories. Both fault zones were hosted in weak and poorly lithified rocks, and the host rocks had never been buried to any great depth. Both fault zones displayed common faulting and deformation features despite the difference in host rock type. The fault zones did not display “classic” fault zone architecture (see Section 2.2.1) and the deformation at both sites was dominated by particle flow processes, with minor elements of brittle and cataclastic deformation (see Section 5.7.1 and Section 6.5.1). However, local lithological heterogeneities were observed that influenced the deformation style and overall interpretation of faulting.

At the F10 Fault, the difference in the deformation intensity within the different units (i.e. sandstone being deformed only inside the fault zone, whereas the palaeosol was deformed both within and outside the fault zone) was an important factor in characterising the extent and style of faulting. The deformation in the palaeosol is not primarily controlled by the presence of the fault zone, but instead seems to be controlled by the variations in the strength of the palaeosol – which is dependent on the type of palaeosol present. The palaeosols displayed slickensides features that could initially be assumed to be an indication of tectonic activity. However, in this lithology slickensides can develop due to soil processes and cannot be assumed to be indicators of tectonic activity. This is an important observation which highlights the importance of understanding the local geological heterogeneities to interpret fault deformation processes. Further work is required to clearly identify and distinguish features in these types of lithologies that are the result of sedimentary or soil processes, or those caused by later deformation associated with fault processes, to allow more accurate determination of the extent of fault related deformation features and their implications. Further work to characterise each of the types of palaeosol would be beneficial to understand how these different types may deform and the effect they would have on either fluid flow pathways or barriers.

At the In-Situ Lab, the CO₂ injected did not migrate vertically (see Section 3.1.4) – possibly due to the palaeosol acting as a sealing horizon, and therefore it may well be that the In-Situ Lab experiment would have never been able to investigate how the CO₂ would have interacted with the fault zone.

At the Brumbys Fault, it was clear that the lithological variability in the units contained within the Port Campbell Limestone were influencing the porosity and permeability of different horizons. Deformation in carbonate rocks is partly controlled by the porosity of the host rock: it is important to capture any variations in porosity and permeability as this will influence the style of deformation and faulting. Therefore, in sequences where there are large variations in porosity (this sequence has between 17-58% porosity) it should be expected that there are also variations in deformation style. Higher porosity sections will deform via compaction and shearing, whereas lower porosity sections may tend to have more brittle styles of deformation. However, this assumes that the rocks are cohesive enough to deform in these styles. Observations laid out in Chapter 6 would suggest that the rocks within and around the Brumbys Fault were not cohesive enough to deform in a brittle manner at macroscopic scale, with only minor brecciation being observed in some of the lower porosity sections that were highly cemented. Further work is required to understand how deformation is accommodated in low cohesion carbonate rocks of different porosities and what effect that will have on the hydraulic properties of the fault zone after deformation has occurred (see Section 2.5.2 and 6.6).

9.2.2 *Predicting fluid flow in shallow fault zones*

Fluid flow processes in response to deformation features in siliciclastic sequences are relatively well understood (see Section 2.4 and Section 5.7.3). Key parameters which control fluid flow are lithology, porosity, permeability and the effect of diagenetic alteration, and overall fault architecture (Lunn *et al.*, 2008). There is a relative paucity of studies on the architecture of shallow fault zones compared to deeper faulting (see Section 2.2.2), and it is important not to assume rock properties at depth are transferable to shallow subsurface settings (e.g. Roberts *et al.*, 2019b). Furthermore, shallow fault processes are different compared to deeper faulting (see Section 2.3, 2.4 and 2.5). Evidence from the In-Situ Lab results suggests that other geological or engineering parameters may influence fluid flow more than the fault zone or fault-associated deformation (Section 3.1.4, Section 5.7.3, e.g. Stalker *et al.*, 2021). Previous

studies have highlighted the importance of sedimentological work alongside structural studies (e.g. McCay *et al.*, 2019), and “seal bypass systems” are widely recognised as systems that enable fluid flow via cross-stratal fluid migration (Brunside *et al.*, 2013; Cartwright *et al.*, 2017). Further studies to assess the primary control on fluid flow is required to assess how important shallow fault zones processes are compared to the other possible features which can influence shallow subsurface fluid flow pathways.

Predicting fluid flow in shallow carbonate rocks remains challenging and significant amounts of uncertainty remains. To predict fluid flow effectively in carbonate rocks there needs to be further work to understand variations in the hydraulic properties of carbonate fault rocks, specifically the porosity and permeability. When considering shallow faulting in carbonate rocks, the style of deformation will be largely controlled by the host rock properties – including the mechanical strength of the rock, the hydraulic properties (e.g. porosity) and any diagenetic alteration, as like siliciclastic rocks. There remains a lack of studies that that have quantified these properties and thus it remains a challenge to then predict expected fault architecture accurately in these types of lithologies. In this thesis, our observations of one shallow fault zone in a carbonate sequence are present and implications for fluid flow are considered, however further work is required to understand how widespread these observations and features are in other shallow fault systems in these lithologies. Further studies would allow a broader understanding of shallow carbonate rocks, their deformation styles and the effect different deformation styles would have on fluid flow in shallow carbonate fault zones. Additional work to understand how these features develop with time, due to either further diagenetic alteration or near-surface weathering will be important to consider the evolution of these systems over longer time periods. This further work would aid the effective design of environmental monitoring technologies which account for the heterogeneities present in these complex systems.

9.3 Learnings and knowledge transfer from other subsurface technologies

This project has focused on two main study sites and has explored the movement of fluids within the shallow subsurface and seepage to surface, primarily considering CO₂ and H₂ as the main fluids. However, there other sites, experiments, technologies, and fluids can provide useful insights and learnings on shallow subsurface fluid flow which are relevant for shallow faulting. This section explores some of these connections.

9.3.1 Mont Terri fault injection experiments

The Mont Terri laboratory in north-east Switzerland investigates hydrogeological, geochemical, and geotechnical behaviour of the Opalinus Clay unit (Figure 9-2). There have been numerous experiments over the operation of this laboratory (see Bossart *et al.*, 2017 for summary). Here, the focus is on the results from the fault experiments and consideration of any transferable learnings from studies of a different fault type (in this case a reverse thrust fault) and different lithology (clay).

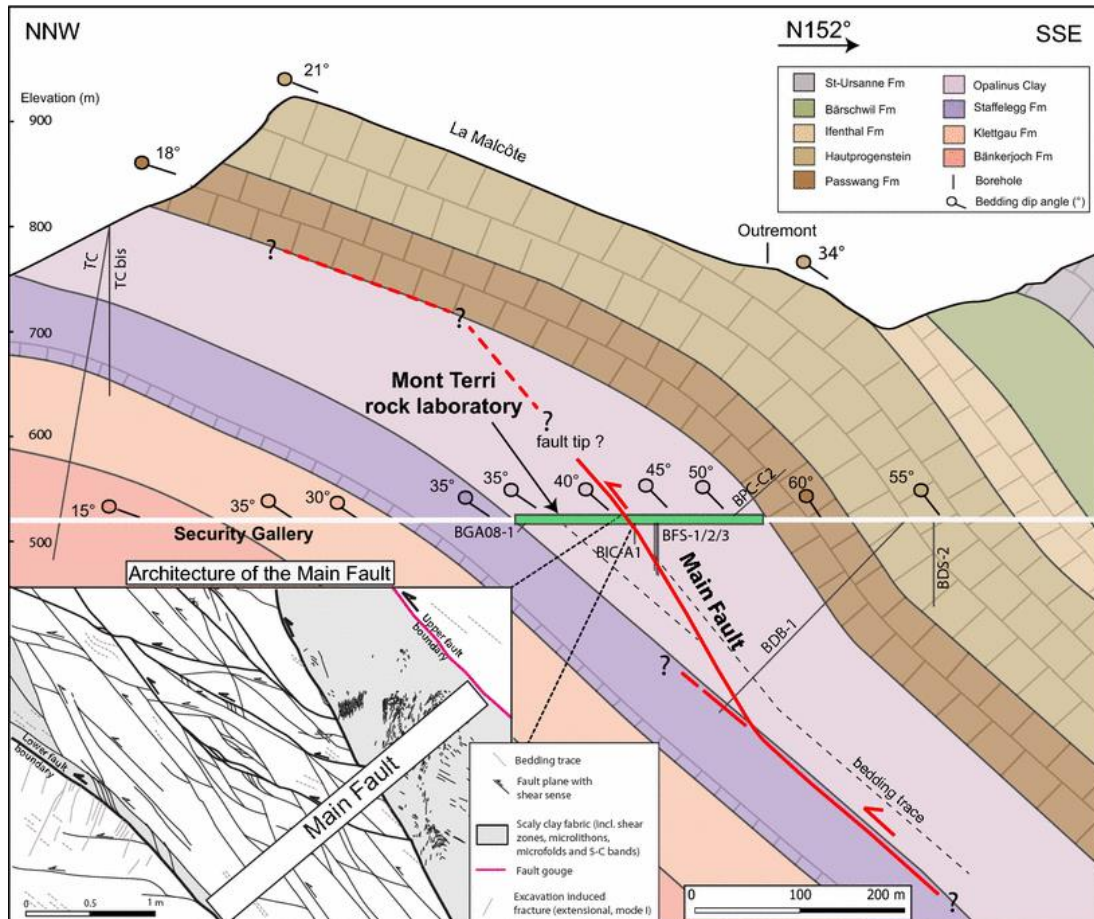


Figure 9-2 – Cross section of the geology around the Mont Terri rock laboratory. Note the “main fault” crosses the laboratory. The fault zone is around 1-6m in width (Nussbaum *et al.*, 2017).

The experiments have focused on the “main fault”, a thrust fault dipping 40-45°, with a thickness ~1-4.5m (Jaeggi *et al.*, 2017). Here, they have mapped the fault zone, conducted microscopic analysis (Laurich *et al.*, 2014; Laurich, 2015) and ultrasonic seismic characterisation (Schuster *et al.*, 2017).

Results from the experiments indicate that the deformation in the clay is highly variable, with 5 main structural elements at the outcrop scale, and laterally these elements are

difficult to correlate (Jaeggi *et al.*, 2017). Interestingly, they conclude that fault zones in clay rocks (with low stiffness and pronounced bedding anisotropy) are discontinuous with multiple fault strands with variable internal structures (Laurich *et al.*, 2017; Jaeggi *et al.*, 2017).

These findings could have implications for the types of deformation that would be expected in the clay-rich palaeosols in the Harvey-2 and Harvey-3 cores at the microstructural scale. Further work to study the palaeosols from the Harvey core, first to identify the clay-rich horizons and then to characterise them at the microstructural scale would allow an interesting comparison to the observations made at the Mont Terri rock laboratory. This would allow a better understanding of the types of deformation in these units, the timing of tectonic events and the effect these units may have on fault zone permeability.

9.3.2 Nuclear waste storage: lower strength sedimentary rocks

In the nuclear waste storage literature, there are similar challenges presented of managing lower strength sedimentary rocks (LSSR). These rocks are defined as mechanically weak, fine-grained sedimentary rocks, usually with high clay/mud content meaning the rock has low permeability and open fractures are not able to be sustained (Radioactive Waste Management, 2016a; Waters *et al.*, 2018). These rocks are seen as beneficial for nuclear waste storage, as they act as an effect seal, do not sustain open fractures, and consequently do not allow groundwater flow (Nuclear Waste Services, 2022). Much research is being undertaken to understanding the properties of LSSR and assess which are suitable for nuclear waste storage sites, as not all LSSR are necessarily impermeable. Other geological controls such as faulting or folding could make them unsuitable seals (Nuclear Waste Storage, 2022).

There are similarities between the LSSR described in the nuclear waste storage literature, those studied at the Mont Terri site and those muddier and more clay rich palaeosol horizons studied in the Harvey-2 core and the muddier horizons observed in the Brumbys-1 core. Clearly, there are opportunities to share learnings from these different end uses to improve overall understanding of fluid flow in these types of lithologies.

9.4 Subsurface fluid flow and environmental monitoring

Generally, shallow fault zones will influence fluid flow in the subsurface. Understanding the host rock properties, the fault zone architecture, and the influence of any alteration (e.g. diagenesis or weathering) at each site will be crucial to establish the likely effect of the fault zone. Crucially, it should be assessed on a site-by-site basis how much the presence of a shallow fault zone matters. For some sites, it may be that there are other geological or engineering characteristics that dominate fluid flow, and that shallow faulting will have a secondary role to play. These characteristics will affect the design of MMV systems (see Section 2.6). Fluid flow focused via a geological fault zone may result in fluid seepage at surface as a point source, which would require targeted monitoring focused on the area where the fault reaches the surface. Where faults do not reach the surface (e.g. F10 and Brumbys), they may play a role in channelling fluids to the top of the fault zone – then the overlying geology will control the fate of the fluid. By contrast, fluid migration and seepage to the surface via multiple reservoir and overburden systems may be more diffuse and require monitoring of features over a larger area. Not all sites require surface monitoring - only where (a) monitoring is for assurance or regulatory (b) a leak or migration or issue is expected and therefore a monitoring programme designed. Where monitoring is required, a targeted environmental monitoring programme should be designed, informed by geological understanding. Understanding and characterising seepage locations at the surface and developing effective methods to gather data on these features (e.g. hydrogen seepage sites) will be crucial to develop MMV systems for different subsurface technologies and geofluids.

Ultimately, characterising the shallow subsurface (i.e. overburden systems) is important, and evidence from this thesis has highlighted the of the complex nature of two parts of this system – shallow fault zones and surface seepage sites. For shallow fault zones, understanding the differences in deformation types at different scales, spatial heterogeneity in deformation style and effect and anisotropic nature of permeability in shallow fault zones is important to assess the effect shallow faulting has on fluid flow. For seepage sites, understanding and characterising seepage locations at the surface and developing effective methods to gather data on these features (e.g. hydrogen seepage sites) will be crucial to develop MMV systems for different subsurface technologies and geofluids. Together, these studies have contributed to our

understanding of fluid flow in the shallow subsurface and the design of effective environmental monitoring for subsurface technologies.

Chapter 10 Conclusions and further work

This thesis presents an analysis of the architecture of two shallow fault zones and their influence on fluid flow in the subsurface. Five categories of fault zones are outlined in Section 1.1. The research in this thesis has focussed on two categories collectively referred to as “shallow faulting”, “shallow fault systems” or “shallow fault zones”:

Category 1: Faulting in ‘young’ rocks or soils that have not been exhumed. The faulting will have been active close to the Earth’s surface in materials that are likely to be very poorly consolidated unless there has been very near-surface diagenesis. These fault rocks are currently experiencing the greatest levels of stress in their history and are considered to be underconsolidated in an engineering soil mechanics sense. (e.g. Brumbys Fault, see Section 3.2.3)

Category 2: Faulting in rocks that have been exhumed from depths less than 1km, and which may be completely, partially or un-lithified. Because they are at stress levels less than the greatest stress levels they have experienced, they are considered to be over consolidated in an engineering sense (e.g. F10 Fault, see Section 3.1.3).

Shallow fault zones are globally under studied. At the time of writing, there are only two field sites in the world that have conducted CO₂ injection experiments that were specifically focussed on understanding how fault zones influence CO₂ fluid flow. Both field sites are located in Australia: the In-Situ Lab (Western Australia) and the Otway International Test Centre (Victoria). Neither site specifically intended to study shallow fault systems (fault categories 1 or 2). Research presented in this thesis has identified that the fault zones present at these sites can be classified as shallow fault systems, rather than the more conventional faults that would be expected within a storage complex (reservoir/caprock). As such, these two field sites are used in this thesis as case studies to assess the fault architecture and fluid flow properties of the shallow fault systems (see Section 3.1 and 3.2). A combination of deformation logging, petrographic analysis (via thin sections and XCT) and fieldwork were used to assess shallow fault zone architecture at several scales (see Chapter 4).

This PhD set out to address four research questions (see Section 1.3). A summary table of the RQ and RO is included to explain the status of each research objective.

Table 10-1 – Summary of RQ and RO, including the status of each research objective and a summary of the work undertaken.

RQ / RO	Task	Status	Summary
RQ1	How does the architecture of shallow fault zones affect fault-related fluid flow in the shallow subsurface?		
RO1	Understand the regional and tectonic setting, and the history of geological activity at both field sites.	Achieved	Achieved by thorough review of relevant academic sources, government, and industry sources (see Section 3.1 and Section 3.2). Since there was no previous synthesis of these data at either the F10 or Brumbys Fault, this is the first time that this information was synthesised for the purpose of understanding the fault and history.
RO2	Observe, describe and interpret the fault architecture and its heterogeneity in both the F10 and Brumbys Fault zones.	Achieved	Achieved by applying and developing new methods to rapidly characterise very long sections of core, which describe the architecture of shallow fault zones, outlined in Chapter 4 (core logging, various petrographic analysis, and fieldwork) to the Harvey-2, Harvey-3 and Brumbys-1 cores. Observations, including the detailed description of deformation in the cores, allowed a better understanding and interpretation of the fault architecture and deformation processes, and the factors influencing their development (e.g. lithology) (see Section 5.3, Section 5.4, Section 5.5, Section 5.6 and Section 6.4). Typical core logging approaches would not have been effective in capturing this level of detail on the types of

			deformation present. Furthermore, the core material was weak which prevented sampling and analysis via conventional processes (Section 5.7.4).
RO3	Synthesise observations and features between the two faults and examine implications for fault process, shallow fault systems, fluid flow in the shallow subsurface and MMV.	Achieved	Achieved by integrating RO1 and RO2, assessing implications and highlighting areas which would benefit from further work (see Section 10.1.2).
RQ2	How important is the scale of analysis when examining shallow fault zones?		
RO4	Analyse shallow fault zones at different scales.	Achieved	Achieved by analysing fault architecture at multiple scales across the different faults studied, e.g. fieldwork at “macro” scale in the Port Campbell Embayment (see Section 6.4.2 and Section 6.5.1), rock core at “meso” scale (see Section 5.3, Section 5.4 and Section 6.4.1) and thin sections at “micro” scale (see Section 5.5).
RO5	Compare and assess the effectiveness of methods to study shallow fault zones.	Achieved	Achieved by using multiple methodologies to analyse shallow fault systems (see Section 5.7, Section 6.5, Section 7.4 and Section 7.5), it was possible to make recommendations on which methods were most

			effective (see Section 10.2.1). Methods could also be compared to those used to study similar rock types (see Section 9.2).
RQ3	How effective are petroleum-based modelling tools in modelling shallow fault zones?		
RO6	Create geological models of both fault zones.	Partially achieved	A model was created of the Brumbys Fault. When it became clear that the modelling workflow was not suitable, no attempt to model the F10 Fault was made (see Section 7.2).
RO7	Model strain and stress around the fault zones based on fault kinematics.	Achieved	Achieved by modelling various fault kinematics based on data from the literature (see Section 7.3).
RO8	Understand how stress variations and uncertainty affect fault interpretation.	Achieved	Achieved by modelling various possible stress regimes around the Brumbys Fault, based on fault kinematics, regional fault observations and regional stress data (see Section 7.4).
RO9	Benchmark models to the observed fault architecture and model permeability structures (e.g. fractures).	Not achieved	Not achieved due to the data available (i.e. uncertain stress magnitudes) and limitations/unsuitability of applying hydrocarbon workflows to shallow fault zones (see Section 7.4 and 7.5).

RQ4	How does natural hydrogen seepage present at the surface and how do we effectively monitor seepage?		
RO10	Collate a database of hydrogen seepage sites which are analogous to seepage from an engineered geological hydrogen storage site.	Achieved	Achieved through a systematic literature review (see Section 8.4). Seepage sites were scoped in depending on their characteristics and the source of hydrogen.
RO11	Describe and characterise surface expressions of natural hydrogen seepage.	Achieved	Achieved by combining observations of hydrogen seepage sites from the literature (see Section 8.6.1 and Section 8.6.2).
RO12	Present implications and recommendations for monitoring of engineered geological hydrogen storage sites.	Achieved	Achieved by considering the global database of hydrogen seepage sites, their characteristics and subsurface processes that could influence seepage, and then presenting recommendations for monitoring engineered geological hydrogen storage sites (See Section 8.6.3).

In the remainder of this chapter, each research question (RQ) is outlined in turn, together with relevant key findings, new research contribution, recommendations and further work.

10.1 RQ1: How does the architecture of shallow fault zones affect fault-related fluid flow in the shallow subsurface?

10.1.1 RQ1 key findings

Key findings and contributions to knowledge from RQ1 include:

- **Shallow fault systems:** Two types of shallow fault systems are defined and distinguished from exhumed faults that may be observed at the surface or in the near surface (see Section 1.1 and 9.1, Figure 9-1):
 - **Category 1:** Faulting in ‘young’ rocks or soils that have not been buried, these are likely to be very poorly consolidated unless there has been very near-surface diagenesis. They are currently experiencing the greatest levels of stress in their history, and are considered to be underconsolidated in an engineering soil mechanics sense. (e.g. Brumbys Fault, see Section 3.2.3)
 - **Category 2:** Faulting in rocks that have been exhumed from depths less than 1km, may be completely, partially or unlithified. Because they are at stress levels less than the greatest stress levels they have experienced, they are considered to be overconsolidated in an engineering sense (e.g. F10 Fault, see Section 3.1.3).

These fault categories are new: previous authors have not attempted to delineate these different processes which could be important for understanding implications for the mechanical and hydraulic fault mechanical properties.

- **Shallow fault zone architecture:** The shallow fault zones in this study do not exhibit “classic” fault zone architecture of a fine-grained fault core surround by a fractured damage zone. Instead, the geometry of the shallow fault zones studied is non-planar and there is not a clear fault core or damage zone – highlighting the need to not oversimplify faults, particularly when considering the effect they may have on subsurface fluid flow. In both studied fault zones, and as commonly observed by previous authors, lithology has a control on deformation type and intensity. However, there are specific variations in rock properties of shallow fault systems due to the subsurface conditions (e.g.

consolidation state, stress, surface processes, diagenesis) which has been evidenced in the observations made on the two fault zones studied in this thesis.

- **F10 Fault deformation:** Deformation is observed through the entire length of the Harvey-2 core, with deformation highest in the zone interpreted to represent the F10 Fault zone and fault-associated deformation (207m – 860m). If the interpreted fault zone depths are aligned with the previous interpretation from (low quality) seismic images, this results in unlikely offsets on the fault. Given the uncertainties in the picks for the formation tops in both the core (based on palynology) and seismic (little to no difference in seismic character between the units), a far wider fault zone makes more kinematic sense. A focused zone with sections of major deformation is observed between ~600-860m depth. Deformation systematically varies with depth and with lithology: sandstones are only deformed in the fault zone; whereas palaeosols are deformed for the entire length of the core. Deformation in the sandstones is related to the F10 Fault zone, whereas deformation in the palaeosol is likely related to the mechanical rock properties and fault-related deformation was a secondary control. Evidence from thin sections of the sandstone shows that the dominant deformation processes in the core are disaggregation related processes such as grain crushing, grain rolling and grain-to-grain contact resulting in fracturing and brecciation of grains. Evidence from XCT scanning revealed the presence of both shear and disaggregation bands throughout the scanned sections of sandstone in the Harvey-2 core. Deformation bands have been recorded at depths both within and outwith the interpreted deformation zone.
- **F10 Fault lithology:** The injection of fluids (either drilling fluids or injected fluids for experiments) could have encouraged swelling of clays in the palaeosols, thereby reducing permeability. Furthermore, any transport of these clays to other horizons due to fault movement, or in the process of injection, could result in the pore networks becoming smaller or blocked entirely. This could possibly be a geological reason that would explain why the injection experiment showed no CO₂ migration via the F10 Fault zone
- **Brumbys Fault deformation:** Observations have provided new insights into the deformation style in the faulted PCL in the Brumbys-1 core. Deformation is dominated by dilational disaggregation and minor cataclastic processes. Deformation is not uniform with depth within the PCL.

- **Brumbys regional significance:** Field observations show that where faults are present, the architecture differs spatially across the Port Campbell Embayment. In addition to differences in fault type (coastal outcrops show reverse faulting, whereas inland faulting is strike slip), other heterogeneity is observed within the PCL such as variations in weathering style, karst features and volcanic deposits (some of which infill karst). Several factors could cause the observed variation in faulting types: these variations are not likely to be caused by variations in stress tensors, different burial or diagenetic histories, or differences in mechanical strength. Instead, they are likely caused by regional controls such as larger regional structures, basement structures or the influence of nearby volcanic centres. Therefore, although local fault exposures are useful, there are often regional variations in fault architecture and understanding how smaller-scale observations fit within a regional structural framework is crucial to making informed interpretations.
- Shallow fault zones can act as both a barrier or a conduit to fluid flow depending on the dominant deformation processes. An important control on the deformation style is the properties of the host rock, particularly the mineralogy, porosity, and any secondary diagenetic, or weathering, features. In both fault zones other lithological controls might have more significant effect on fluid flow than the fault zone itself (e.g. lithology). Given that the contrast between fault zone flow properties and host rock flow properties is not likely to be as large in shallow faults as in deeper faults, shallow fault zones may not influence subsurface fluid flow significantly in some geological settings, and it should not be assumed that they will be the primary control on fluid flow.

10.1.2 RQ1 implications

- **F10 Fault implications for fault fluid flow:** The observed deformation style could result in either locally enhanced or reduced permeabilities. The variability in porosity means the flow pathways around the F10 Fault zone will be heterogeneous in nature, with potentially anisotropic flow pathways and increased tortuosity compared to undeformed sections (see Section 2.1). The variability in fault deformation can be expected from shallow fault zone deformation styles and processes (see Section 2.4). Previous fluid flow modelling by CSIRO (2019) of the F10 Fault zone did not consider the fault properties in this much detail (see Section 3.1.4 and Appendix 1). Due to the issues with the injection experiment, the findings are inconclusive about

how well the experimental results matched the modelling predictions, but the observations indicate that the CO₂ did not behave as modelled (i.e. the CO₂ exploited a thin horizon rather than spreading out as larger mass). The observations of shallow faulting presented in this thesis could be used to design informed geological models that reflect the architecture of shallow fault zones, which in turn would provide more realistic modelling results on the influence of the fault zone on fluid flow.

- **Brumbys Fault implications for fluid flow:** Deformation in Brumbys-1 due to the Brumbys Fault will likely enhance permeability. Areas within the Brumbys Fault that are most deformed will likely act as vertically enhanced fluid pathways, whereas lower deformation areas are more likely to have lower permeability. However, the primary control on the permeability of this fault zone will be the host rock properties for each horizon within the PCL. For example, mineralogy will control fluid flow in areas with increased aragonite concentrations, as these zones have lower permeability.
- How much the presence of a shallow fault zone matters must therefore be assessed on a site-by-site basis. For some sites, it may be that there are other geological or engineering issues that govern fluid flow, and that shallow faulting will have a secondary role to play. This will affect the design of MMV systems.
- Fluid flow focused via a geological fault zone may result in fluid seepage at surface as a point source, which would require targeted monitoring focused on the area where the fault reaches the surface. Where faults do not reach the surface (e.g. F10 and Brumbys), they may play a role in channelling fluids to the top of the fault zone – then the overlying geology will control the fate of the fluid. By contrast, fluid migration and seepage to the surface via multiple reservoir and overburden systems may be more diffuse and require monitoring of features over a larger area. Not all sites require surface monitoring - only where (a) monitoring is for assurance or regulatory (b) a leak or migration or issue is expected and therefore a monitoring programme designed. Where monitoring is required, a targeted environmental monitoring programme should be designed, informed by geological understanding, as studies have shown that the seepage can vary both spatially and temporally over geological timescales (e.g. Burnside *et al.*, 2013; Roberts *et al.*, 2019a; 2019b).

Understanding and characterising seepage locations at the surface and developing effective methods to gather data on these features (e.g. hydrogen seepage sites) will be crucial to develop MMV systems for different subsurface technologies and geofluids (McMahon *et al.*, 2023).

- Future injection experiments, and any associated studies (e.g. modelling, monitoring) should consider this more detailed understanding of shallow fault zone processes and deformation styles, as well as their heterogeneity and the potential anisotropic permeability distribution in the subsurface caused by the shallow fault zones.

10.1.3 RQ1 recommendations for further work

In this thesis, observations from two shallow fault zones are presented and implications considered. Further work is required to understand how widespread these observations and features are in other shallow fault systems in different geological settings and lithologies, including how shallow fault systems change with increasing depth.

There is significant scope for further work in key areas. For the F10 Fault at the In-Situ Lab:

- **Fracturing:** Future analysis of fracture properties would require orientated core or downhole imaging to allow measurement of fracture orientations. These tools would help to better understand their frequency and spatial distribution around the F10 Fault zone.
- **Deformation bands:** To better understand the burial and uplift history of the F10 Fault, further work on the deformation bands is required to elucidate the formation process, timing and their spatial distribution. Analysis of the lateral extent of these sub-seismic features is important to fully assess the effect they may have on subsurface fluid flow pathways.
- **Lithology:** Additional study to characterise the variation in lithological properties. The sandstone and palaeosol character vary throughout the Harvey-2 and Harvey-3 cores. Understanding these variations and the implications they may have for the way the rock behaves mechanically or hydraulically is important to enable the design and implementation of suitable MMV for subsurface fluids. As the palaeosols contain swelling clays, further work should

assess the effect any injection of fluids (either drilling fluids or injected fluids for experiments) could have on encouraging swelling. Any additional swelling of these clays could reduce permeability. Furthermore, any transport of these clays to other horizons, or smearing within fault rocks, could result in the pore networks becoming smaller or blocked entirely.

Research findings at Brumbys Fault highlights the need for the following further research at and around the site:

- **Regional faulting mechanisms:** Ascertain the influence and timing of the potential faulting mechanisms outlined in Section 6.5.3 and how they may have influenced the development of the Brumbys Fault. Analysis of regional seismic datasets could provide insights into larger subsurface structures that may have influenced the development of faults with different kinematics in the shallow subsurface.

More generally, work on the Brumbys Fault has highlighted areas for further work in carbonate lithologies:

- **Lithology:** Further studies to quantify the porosity and permeability variations of carbonate rocks in the shallow subsurface, as this controls the style of deformation.
- **Shallow subsurface characterisation:** Characterisation of the shallow subsurface in carbonate lithologies to understanding controls on deformation processes and the influence deformation features have on hydraulic properties and fluid flow. This information will allow the design of targeted monitoring approaches which monitor the most likely pathways to surface. Targeted monitoring has been shown to be the most effective approach for monitoring seepage from natural CO₂ and H₂ seeps (see Section 6.6).

More generally, there is opportunity for further studies of shallow fault zones in different lithologies to examine the major controls on deformation processes across different lithologies and geological contexts. For example, further work on shallow fault zones in clay rich rocks.

Furthermore, the synthesis of the data in this study from the two field sites demonstrates the usefulness of sharing learning between sites. In future, it would be advantageous to consider transferable knowledge and learnings to enable the effective design of site

experiments, geological modelling, and monitoring approaches (e.g. Stalker *et al.*, 2021).

10.2 RQ2: How important is the scale of analysis when examining shallow fault zones?

10.2.1 RQ2 key findings

Key findings and contributions to knowledge from RQ2 include:

- Deformation styles and processes vary at different scales (e.g. “micro” scale observations of the Harvey-2 core material indicated grain crushing and fracturing processes that were not visible at the “meso” core scale) (Section 5.5). This is in line with previous work (see Sections 2.3, 2.4 and 2.5).
- Traditional structural analysis of rock core (i.e. fracture logging) does not provide useful data on the extent or type of deformation expected from shallow fault zone processes (see Section 5.3.3). Had the only method of analysis been fracture logging, the results of this study would have been different - processes that reduce and enhance permeability would not have been identified and the fault characteristics (e.g. geometry, deformation intensity and style) would be no more certain than from previous data. This is an important contribution from this thesis.
- Comparing results from the Harvey-2 and Harvey-3 cores helped to verify the effectiveness of the deformation logging methodology in rapidly and effectively capturing the deformation styles (e.g. disaggregation) exhibited by shallow faulting in a very long run of core (see Section 5.7.2). More detailed logging that captured, fractures, deformation and disaggregation zones, particularly in oriented core, would have been more useful, but not likely feasible (or cost effective) in over 1km of core.
- Evidence from XCT scanning revealed the presence of both shear and disaggregation bands throughout the scanned sections of Harvey-2 core which were not always observable in hand specimen (see Section 5.6). This highlights the difficulty of picking out subtle features in shallow cores where core preservation is not always very good. The XCT results could not provide information at the micro scale due to the resolution limitation of equipment used and the sampling challenges.

- Analytical methods which require sampling of shallow fault zones are not always possible, straightforward, or efficient (in time required or financially) as often the material can be weak and that means you are limited in what can be sampled and which methods can be used (Section 5.7.4). This is not necessarily unique to shallow fault zones, but is an increased challenge compared to deeper faults as shallow fault zones and surrounding lithology are often unconsolidated or mechanically weak.

10.2.2 RQ2 implications

- Studies of shallow fault zones should not focus on fracture logging and should instead consider other methods to capture the deformation in the core, such as the deformation logging method developed and applied in this thesis.
- Consideration should be given to the value of applying a particular methodology or analytical technique based on the quality of data able to be collected and the cost both time and financial (especially in commercial projects). Not all methods are useful, and this will vary between study site based on the site objectives, geological setting and data availability.
- New approaches are needed when examining shallow fault zones. Findings from this PhD have shown that traditional methods of fault analysis are not necessarily applicable or useful for shallow fault zones as they do not provide the insights needed to develop geologically realistic interpretations or models.

10.2.3 RQ2 recommendations for further work:

There is scope for further work in key areas:

- Fracture logging methods need to be tested on different lithologies and structural settings to understand how well this captures all types of fractures and their characteristics.
- Development of tools to integrate the results from fracture logging and deformation logging into structural models for examining fault properties – such as their mechanical or hydraulic behaviour (see Section 10.3).

- Micro-scale analysis (e.g. micro-XCT) could provide quantification of the effects of different deformation processes (e.g. deformation band type) on the porosity and permeability of the F10 Fault zone.

10.3 RQ3: How effective are petroleum-based modelling tools in modelling shallow fault zones?

10.3.1 RQ3 key findings

Key findings and contributions to knowledge from RQ3 include:

- Modelling of shallow fault zones using “classic” structural geology or petroleum-based modelling tools is possible to do, but the results are likely not useful due to the uncertainties in the input datasets and the bias in the model design towards deeper fault zones. Current models for the sites do not account for the complexity of shallow fault zones and incorrectly assume the fault architecture is the same as deeper faults. For the Brumbys Fault, these modelling approaches were not suitable or useful due to the uncertainties in the stress regime and the type of deformation observed in the lithology. The same can be said for the F10 Fault.
- Uncertainty in stress tensor magnitude is enhanced as you work with faults that are nearer to the surface. This is because the stresses are typically lower (particularly the vertical stress as a vertical rock mass is decreased), the allowing interpretations of different stress regimes (see Section 3.2.2). As the stresses are lower, the margin to move from one stress regime to another is greatly decreased and can even be within the error range expected on a stress magnitude. This makes interpreting which stress regime is dominant difficult. It also means that stress conditions on a fault varies with depth. As such, for faults that extend from shallow to deep subsurface conditions, fluid flow may change both due to properties of the fluid itself (Section 2.1.3.2) and changes in fault properties due to stress change with depth. These challenges around stress magnitudes also present in Chapter 6 when trying to reconcile the fault kinematics of the Brumbys Fault, with regional variability in fault type and an uncertain regional stress regime.

10.3.2 RQ3 recommendations for future work

There is scope for further work in key areas:

- Converting the deformation data collected as part of the deformation logs into a useful data source as a modelling input to ultimately capture permeability variations with depth/proximity to a fault zone and how this can change up/down/across fault zones.
- Future modelling of shallow fault zones should adapt traditional modelling approaches to account for the fundamental differences in the fault architecture and additional uncertainties that are present when working in the shallow subsurface (e.g. stress tensor uncertainties and variability). This needs to be underpinned by more studies of shallow fault zone processes so that those models are underpinned by a physics-based process understanding.
- Assessment of how best to estimate or measure stress data in the shallow subsurface, accounting for possible variations and uncertainties, to ultimately provide more realistic values that can be used to inform structural modelling.
- Modelling the interactions between depth, fluid flow and fault properties. Whilst fault zones may play a role in channelling fluids towards the near surface, there are other influences that may control fluid flow and distribution in the very near surface. Considering the effect of surface processes and systems (e.g. weathering, water table and groundwater influences, engineering) on fluid flow are important and interesting areas for further work. Insights from this further work would assist the development of effective environmental monitoring systems where needed and would help to focus studies on the most important parameters influencing fluid flow both at different depths and in different geological settings.

10.4 RQ4: How does natural hydrogen seepage present at the surface and how do we effectively monitor seepage?

10.4.1 RQ4 key findings

Key findings and contributions to knowledge from RQ4 are presented below:

- Seep characteristics are determined by local geological and hydrological conditions, specifically whether hydrogen gas is seeping through soils and unconsolidated sediments, fractured bedrock, or water (e.g. springs). Where hydrogen seeps through soils and sediments, seeps manifest as sub-circular

depressions with patchy flux, and the spatial extent of the seep controls the seep rate. Where hydrogen seeps through bedrock fractures or into springs, gas emissions are highly localised, with small spatial footprint of seepage. In the studied seeps, hydrogen seepage is known to seep to the surface over extended periods of time (years, as a minimum).

- There are similarities in the controls on seep location and characteristics between hydrogen seeps and CO₂ seeps, which have been more widely studied to inform geological CO₂ storage. However, compared to CO₂, hydrogen is more readily dispersed because of its high mobility (due to small size and low density), and so maximum concentrations of hydrogen in gas streams that reach the surface are typically lower than CO₂ concentrations at CO₂ seeps.
- Hydrogen is typically co-emitted with other naturally occurring gases such as CO₂, CH₄, and small amounts of trace hydrocarbons or noble gases, with CH₄ the most dominant co-emitted gas in most cases presented here.
- Hydrogen can be consumed or transformed in the subsurface, and so the quantity of leaked hydrogen might be greatly attenuated before it reaches the Earth surface.
- For sites of hydrogen seepage and accumulation, we are limited in the data available and by the data reported. There are:
 - a general lack of reported data for natural hydrogen seepage and accumulation.
 - issues around the field data collection methodologies (e.g. drilling, measurements from only one point in time).
 - uncertainty introduced by simplifying and estimating values (e.g. area, porosity) for calculating hydrogen fluxes from seep rates and concentrations.
- The following recommendations are made for future work reporting on hydrogen seeps:
 - a standardised and effective methodology for the collection of field data, that accounts for the need to measure differently depending on the style of seepage.

- consistency in the reporting of data, analysis of the spatial and temporal evolution of hydrogen seepage and consideration of how surface processes may influence surface seep expression.

10.4.2 RQ4 implications

- Monitoring approaches for engineered hydrogen stores should be tailored according to the exposed geology and hydrological conditions.
- Subsurface monitoring approaches to detect hydrogen, or tools that also monitoring for co-gases, could be appropriate in environments that promote the transformation of hydrogen to other compounds.

10.4.3 RQ4 recommendations for further work

There is significant scope for further work in key areas:

- To understand the initial formation of surface subcircular depressions, controls on their size and shape as well as how any orientation relates to subsurface structural features and/or in-situ stress. Crucially, studies should look to ascertain the role of hydrogen in the development of these systems – does hydrogen seepage cause these systems to form, or does hydrogen simply exploit these features as they are more permeable pathways to surface. Studies could look at feature evolution over time (e.g. using satellite imagery).
- Detailing and mitigating risks associated with hydrogen seepage. For example, controlled release experiments (similar to those conducted with CO₂ as the primary fluid) would provide more information on how hydrogen behaved and interacted in the shallow subsurface and at the Earth's surface.
- Consideration of how to rule out biological sources of hydrogen seepage (e.g. isotopic testing hydrogen seepage gases to determine possible sources)

10.5 Summary

Shallow fault zones are typically understudied compared to deeper fault zones, from the categorisation of different types of shallow faulting, through to methods of collecting and analysing data from shallow fault systems and through to the implications for subsurface fluid flow. Access to data and materials on faults is globally rare, and perhaps even more for shallow fault systems due to bias in fault studies. This PhD thesis presents a new study, providing new insights into shallow fault zone architecture and processes, as well as developing new methods of capturing shallow fault zone data.

References

- Abrajano, T.A., Sturchio, N.C., Bohlke, J.K., Lyon, G.L., Poreda, R.J., Stevens, C.M. 1988. Methane-hydrogen gas seeps, Zambales Ophiolite, Philippines: Deep or shallow origin?. *Chemical Geology*, Vol. 71, Iss. 1-3, pp. 211-222. [https://doi.org/10.1016/0009-2541\(88\)90116-7](https://doi.org/10.1016/0009-2541(88)90116-7).
- Afanasyev, A., 2018, November. Numerical modelling of solute flow dispersion in porous media using simulator MUFITS. In *Journal of Physics: Conference Series* (Vol. 1129, p. 012002). IOP Publishing.
- Agosta, F. and Aydin, A., 2006. Architecture and deformation mechanism of a basin-bounding normal fault in Mesozoic platform carbonates, central Italy. *Journal of Structural Geology*, 28(8), pp.1445-1467.
- Agosta, F., Alessandrini, M., Tondi, E., Aydin, A. 2010. Oblique normal faulting along the northern edge of the Majella anticline, central Italy: Inferences on hydrocarbon migration and accumulation. *Journal of Structural Geology*, Vol. 32, Iss. 9, pp. 1317-1333.
- Agosta, F., Kirschner, D.L. 2003. Fluid conduits in carbonate-hosted seismogenic normal faults of central Italy. *Journal of Geophysical Research: Solid Earth*, Vol 108, Iss. B4.
- Agosta, F., Mulch, A., Chamberlain, P., Aydin, A. 2008. Geochemical traces of CO₂-rich fluid flow along normal faults in central Italy. *Geophysical Journal International*, Vol. 174, Iss. 2, pp. 758-770.
- Agosta, F., Prasad, M., Aydin, A. 2007. Physical properties of carbonate fault rocks, fucino basin (Central Italy): implications for fault seal in platform carbonates. *Geofluids*, Vol. 7, pp.19-32.
- Agosta, F., Wilson, C., Aydin, A. 2015. The role of mechanical stratigraphy on normal fault growth across a Cretaceous carbonate multi-layer, central Texas (USA). *Italian Journal of Geosciences*, Vol. 134, Iss. 3, pp. 423-441.

- Ali, M., Jha, N.K., Pal, N., Keshavarz, A., Hoteit, H. and Sarmadivaleh, M., 2022. Recent advances in carbon dioxide geological storage, experimental procedures, influencing parameters, and future outlook. *Earth-Science Reviews*, 225, p.103895.
- Al-Khdheawi, E.A., Vialle, S., Barifcani, A., Sarmadivaleh, M. and Iglauer, S., 2017. Influence of rock wettability on CO₂ migration and storage capacity in deep saline aquifers. *Energy Procedia*, 114, pp.4357-4365.
- Almeida, A.C.S., Varajão, A.F.D.C., Gomes, N.S., Varajão, C.A.C., Volkmer-Ribeiro, C. 2010. Characterization and origin of spongillite-hosting sediment from João Pinheiro, Minas Gerais, Brazil. *Journal of South American Earth Sciences*, 29, 439–453, <https://doi.org/10.1016/j.jsames.2009.09.006>.
- Annunziatellis, A., Beaubien, S.E., Bigi, S., Ciotoli, G., Coltella, M. and Lombardi, S., 2008. Gas migration along fault systems and through the vadose zone in the Latera caldera (central Italy): Implications for CO₂ geological storage. *International journal of greenhouse gas control*, 2(3), pp.353-372.
- Antonellini, M.A., Aydin, A. & Pollard, D.D. 1994. Microstructure of deformation bands in porous sandstones at Arches National Park, Utah. *Journal of Structural Geology* , 16, 941–959.
- Antonellini, M., Petracchini, L., Billi, A. & Scrocca, D. 2014. First reported occurrence of deformation bands in a platform limestone, the Jurassic Calcare Massiccio Fm., northern Apennines, Italy. *Tectonophysics*, Vol. 628, pp. 85–104.
- Arch, J., Maltman, A. 1990. Anisotropic permeability and tortuosity in deformed wet sediments. *Journal of Geophysical Research*. Vol. 95 (B6), pp. 9035–9045.
- Ascione, A., Bigi, S., Ciotoli, G., Corradetti, A., Etiope, G., Ruggiero, L., Sacco, P., Tartarello, C., Tavani, S. and Valente, E. (2014). The southern Matese active fault system: New geochemical and geomorphological evidence. *Atti 33 Convegno Nazionale GNGTS 25-27 November 2014, Bologna, Italy. Tema 1: Geodinamica*, pp. 11-19.
- Aydin, A. 2000. Fractures, faults, and hydrocarbon entrapment, migration and flow. *Marine Petroleum Geology*. Vol. 17, Iss. 7, pp. 797–814.
- Aydin, A. and Johnson, A.M., 1983. Analysis of faulting in porous sandstones. *Journal of structural Geology*, 5(1), pp.19-31.

- Bachu, S., Bennion, B. 2008. Effects of In-Situ conditions on relative permeability characteristics of CO₂-brine systems. *Environmental Geology*, Vol 54, pp. 1707–1722.
- Backhouse J. 2015. GSWA Harvey 2 Palynology Report: Backhouse Biostrat Pty Ltd, Report for Geological Survey of Western Australia, Report BB490. Unpublished.
- Bailey, A.H.E., Pevzner, R., Urosevic, M., Popik, D. and Feitz, A.J., 2017. Shallow geology of the CO₂CRC Otway Site: Evidence for previously undetected neotectonic features?. *Energy Procedia*, 114, pp.4424-4435.
- Ballas, G., Fossen, H., Soliva, R. 2015. Factors controlling permeability of cataclastic deformation bands and faults in porous sandstone reservoirs. *Journal of Structural Geology*. Vol 76, pp. 1-21.
- Balsamo, F., Bezerra, F.H.R., Vieira, M.M., Storti, F. 2013. Structural control on the formation of iron-oxide concretions and Liesegang bands in faulted, poorly lithified Cenozoic sandstones of the Paraíba Basin, Brazil. *Geological Society of America Bulletin*. Vol. 125, Iss. 5/6, pp. 913–931.
- Balsamo, F., Storti, F. 2010. Grain size and permeability evolution of soft-sediment extensional sub-seismic and seismic fault zones in high-porosity sediments from the Croton basin, Southern Apennines, Italy. *Marine and Petroleum Geology*, Vol. 27, pp. 822-837.
- Balsamo, F., Storti, F. 2011. Size-dependent comminution, tectonic mixing, and sealing behaviour of a “structurally oversimplified” fault zone in poorly lithified sands: evidence for a coseismic rupture? *Geological Society of America Bulletin*. Vol. 123, Iss. 3/4, pp. 601–619.
- Balsamo, F., Storti, F., Piovano, B., Salvini, F., Cifelli, F., Lima, C. 2008. Time dependent structural architecture of subsidiary fracturing and stress pattern in the tip region of an extensional growth fault system, Tarquinia basin, Italy. *Tectonophysics*, Vol. 454, pp. 54-69.
- Bartel, S. and Janssen, G. 2016. Underground spatial planning–Perspectives and current research in Germany. *Tunnelling and Underground Space Technology*, 55, pp.112-117.
- Barton, C.A., Zoback, M.D., Moos, D. 1995. Fluid flow along potentially active faults in crystalline rock. *Geology*. Vol. 23, pp. 683-686.

- Bastesen, E., Braathen, A. 2010. Extensional faults in fine grained carbonates—analysis of fault core lithology and thickness–displacement relationships. *Journal of Structural Geology*, Vol. 32, Iss. 11, pp. 1609-1628.
- Bauer, S., Beyer, C., Dethlefsen, F., Dietrich, P., Duttmann, R., Ebert, M., Feeser, V., Görke, U., Köber, R., Kolditz, O. and Rabbel, W. 2013. Impacts of the use of the geological subsurface for energy storage: an investigation concept. *Environmental earth sciences*, 70, pp.3935-3943.
- Bell, J.S. 1996. In-Situ stresses in sedimentary rocks (part 2): Applications of stress measurements. *Geoscience Canada*, Vol. 23, pp. 135-153.
- Bense, V.F. and Person, M.A., 2006. Faults as conduit-barrier systems to fluid flow in siliciclastic sedimentary aquifers. *Water Resources Research*, 42(5).
- Bense, V.F., Gleeson, T., Loveless, S.E., Bour, O. and Scibek, J., 2013. Fault zone hydrogeology. *Earth-Science Reviews*, 127, pp.171-192.
- Bense, V.F., Person, M.A., Chaudhary, K., You, Y., Cremer, N., Simon, S. 2008. Thermal anomalies indicate preferential flow along faults in unconsolidated sedimentary aquifers. *Geophysical Research Letters*, Vol. 35, L24406.
- Bense, V.F., Van Balen, R.T. (2004). The effect of fault relay and clay smearing on groundwater flow patterns in the Lower Rhine Embayment. *Basin Research*. Vol. 16, pp. 397–411.
- Bense, V.F., Van den Berg, E.H., Van Balen, R.T. 2003. Deformation mechanisms and hydraulic properties of fault zones in unconsolidated sediments; the Roer Valley Rift System, The Netherlands. *Hydrogeology Journal*, Vol. 11, Iss. 3, pp.319-332.
- Berard, T., Sinha, B.K., Van Ruth, P., Dance, T., John, Z. and Tan, C. 2008, October. Stress estimation at the Otway CO₂ storage site, Australia. In *SPE Asia Pacific Oil and Gas Conference and Exhibition* (pp. SPE-116422). SPE.
- Bernard, S., Avouac, J.P., Dominguez, S. and Simoes, M. 2007. Kinematics of fault-related folding derived from a sandbox experiment. *Journal of Geophysical Research: Solid Earth*, 112(B3).

- Bethke, C.M., Corbet, T. 1988. Linear and non-linear solutions for one-dimensional compaction flow in sedimentary basins. *Water Resources Research*. Vol. 24, pp. 461–467.
- Bilham, R., King, G. 1989. The morphology of strike slip faults: examples from the San Andreas fault, California. *J. Geophys. Res.* 94, 10204–10226
- Blenkinsop, T., 2000. From Microstructures to Mountains: Deformation Microstructures, Mechanisms and Tectonics. *Deformation Microstructures and Mechanisms in Minerals and Rocks*, pp.90-105.
- Bond, C.E., Kremer, Y., Johnson, G., Hicks, N., Lister, R., Jones, D.G., Haszeldine, R.S., Saunders, I., Gilfillan, S.M., Shipton, Z.K. and Pearce, J. 2017. The physical characteristics of a CO₂ seeping fault: The implications of fracture permeability for carbon capture and storage integrity. *International Journal of Greenhouse Gas Control*, Vol. 61, pp. 49-60.
- Bonini, M. 2012. Mud volcanoes: indicators of stress orientation and tectonic controls. *Earth science Reviews*, 115, 121-152, <https://doi.org/10.1016/j.earscirev.2012.09.002>.
- Boreham, C., Underschultz, J., Stalker, L., Kirste, D., Freifeld, B., Jenkins, C., Ennis-King, J. 2011. Monitoring of CO₂ storage in a depleted natural gas reservoir: Gas geochemistry from the CO₂CRC Otway Project, Australia. *International Journal of Greenhouse Gas Control*, Vol. 5, Iss. 4, pp. 1039-1054.
- Börner, J. H., Herdegen, V., Repke, J.-U., Spitzer, K. 2013. The impact of CO₂ on the electrical properties of water bearing porous media – laboratory experiments with respect to carbon capture and storage, *Geophysical Prospecting*, Vol. 61, pp. 446–460
- Borradaile, G.J., Tarling, D.H. 1981. The influence of deformation mechanisms on magnetic fabrics in weakly deformed rocks. *Tectonophysics*, Vol. 77, Iss. 1-2, pp. 151-168.
- Bossart, Paul, Frédéric Bernier, Jens Birkholzer, Christophe Bruggeman, Peter Connolly, Sarah Dewonck, Masaaki Fukaya. 2018. "Mont Terri rock laboratory, 20 years of research: introduction, site characteristics and overview of experiments." *Mont Terri Rock Laboratory, 20 years: Two decades of research and experimentation on claystones for geological disposal of radioactive waste (2018)*: 3-22.

Bourdet, J., Sarout, J., Strand, J., Delle Piane, C., Vialle, S., Langhi, L., Harris, B., Lebedev, M., Teo, B., Esteban, L., Godel, B., Dautriat, J., Emelyanova, I., Pervukhina, M., Glubokovskikh, S., Noble, R., Saeedi, A. 2019. Assessment of multi- barrier systems for CO₂ containment in the Yalgorup Member of the Lesueur Sandstone, South West Hub. CSIRO Report Number EP19286.

Brandes, C., Plenefisch, T., Tanner, D.C., Gestermann, N., Steffen, H. 2019. Evaluation of deep crustal earthquakes in northern Germany – possible tectonic causes. *Terra Nova*. Vol. 31, pp. 83-93.

Brandes, C., Tanner, D. 2019. Introduction, in *Understanding Faults: Detecting, Dating, and Modelling*, pp. 1-10

Brandes, C., Tanner, D.C. 2014. Fault-related folding: a review of kinematic models and their application. *Earth Science Review*. Vol. 138, pp. 352-370.

Bredehoeft, J.D., Belitz, K., Sharp-Hansen, S. 1992. The hydrodynamics of the Big Horn Basin: a study of the role of faults. *AAPG Bulletin*, Vol. 76, Iss. 4, pp. 530-546.

Bretan, P., Yielding, G. and Jones, H. 2003. Using calibrated shale gouge ratio to estimate hydrocarbon column heights. *AAPG bulletin*, Vol. 87, Iss. 3, pp. 397-413.

Buchanan, P.G. and McClay, K.R., 1991. Sandbox experiments of inverted listric and planar fault systems. *Tectonophysics*, 188(1-2), pp.97-115.

Bump, A.P. and Hovorka, S.D. 2023. Fetch-trap Pairs: Exploring definition of carbon storage prospects to increase capacity and flexibility in areas with competing uses. *International Journal of Greenhouse Gas Control*, 122, p.103817.

Bump, A.P., Bakhshian, S., Ni, H., Hovorka, S.D., Olariu, M.I., Dunlap, D., Hosseini, S.A. and Meckel, T.A. 2023. Composite confining systems: Rethinking geologic seals for permanent CO₂ sequestration. *International Journal of Greenhouse Gas Control*, 126, p.103908.

Bunch, M.A. 2013 Gauging geological characterisation for CO₂ storage: the Australasian experience so far..., *Australian Journal of Earth Sciences*, Vol. 60, pp. 5-21.

Burke, M., Van Gent, D. and Stalker, L. 2014. Creating Community Links for Carbon Capture and Storage. *Energy Procedia*, 63, pp.7053-7060.

Burnside, N.M., Shipton, Z.K., Dockrill, B. and Ellam, R.M. 2013. Man-made versus natural CO₂ leakage: A 400 ky history of an analogue for engineered geological storage of CO₂. *Geology*, Vol. 41, Iss. 4, pp. 471-474.

Buzek, F., Onderka, V., Vančura, P., Wolf, I. 1994. Carbon isotope study of methane production in a town gas storage reservoir, *Fuel*, Vol 73, Iss. 4, pp. 747-752, [https://doi.org/10.1016/0016-2361\(94\)90019-1](https://doi.org/10.1016/0016-2361(94)90019-1).

Caine, J.S., Evans, J.P. and Forster, C.B. 1996. Fault zone architecture and permeability structure. *Geology*, 24(11), pp.1025-1028.

Caine, J.S., Minor, S.A. 2009. Structural and geochemical characteristics of faulted sediments and inferences on the role of water in deformation, Rio Grande Rift, New Mexico. *GSA Bulletin*, Vol. 121 Iss. 9-10, pp. 1325-1340

Caine, J.S., Minor, S.A., Grauch, V.J.S., Budahn, J.R. and Keren, T.T. 2017. A comprehensive survey of faults, breccias, and fractures in and flanking the eastern Española Basin, Rio Grande rift, New Mexico. *Geosphere*, 13(5), pp.1566-1609.

Cappa, F. 2009. Modelling fluid transfer and slip in a fault zone when integrating heterogeneous hydromechanical characteristics in its internal structure, *Geophysical Journal International*. Vol. 178, pp. 1357–1362

Carden, P.O. and Paterson, L. 1979. Physical, chemical and energy aspects of underground hydrogen storage. *International Journal of Hydrogen Energy*, 4(6), pp.559-569. [https://doi.org/10.1016/0360-3199\(79\)90083-1](https://doi.org/10.1016/0360-3199(79)90083-1).

Carman, P. C. 1956. *Flow of gases through porous media*, London, Butterworths Scientific Publications.

Cartwright, J., Huuse, M. and Aplin, A. 2007. Seal bypass systems. *AAPG bulletin*, 91(8), pp.1141-1166.

Cashman, S. and Cashman, K. 2000. Cataclasis and deformation-band formation in unconsolidated marine terrace sand, Humboldt County, California. *Geology*, 28(2), pp.111-114.

Cathles, L. and Prinzhofer, A. 2020. What Pulsating H₂ Emissions Suggest about the H₂ Resource in the Sao Francisco Basin of Brazil. *Geosciences*, Vol. 10, Iss. 4, p. 149 <https://doi.org/10.3390/geosciences10040149>.

Cello, G., Tondi, E., Micarelli, L., Invernizzi, C. 2001. Fault zone fabrics and geofluid properties as indicators of rock deformation modes. *Journal of Geodynamics*, Vol. 32, Iss. 4-5, pp. 543-565.

Chadwick, R.A., Noy, D.J., Holloway, S. 2009. Flow processes and pressure evolution in aquifers during the injection of supercritical CO₂ as a greenhouse gas mitigation measure. *Petroleum Geoscience*, Vol. 15, pp. 59-73

Chadwick, R.A., Williams, G.A. and Noy, D.J. 2017. CO₂ storage: Setting a simple bound on potential leakage through the overburden in the North Sea Basin. *Energy Procedia*, 114, pp.4411-4423.

Champ, P. 2010. Building a Robust Groundwater Model for the Southern Perth Basin, WA: 3D Visualization and Modelling of Geology Using Petrel™. *Groundwater*, Canberra.

Chan, M.A., Parry, W.T., Bowman, J.R. 2000. Diagenetic hematite and manganese oxides and fault-related fluid flow in Jurassic sandstones, southeastern Utah. *AAPG Bulletin*, Vol. 84, pp. 1281–1310.

Chang, Y.-B., Coats, B.K., Nolen, J.S. 1996. A Compositional Model for CO₂ Floods Including CO₂ Solubility in Water. *Society of Petroleum Engineers*.

Chester, F.M., Logan, J.M. 1986. Implications for mechanical properties of brittle faults from observations of the Punchbowl fault zone, California. *Pure and Applied Geophysics*, Vol. 124, Iss. 1-2, pp. 79-106.

Childs, C., Manzocchi, T., Walsh, J.J., Bonson, C.G., Nicol, A., Schöpfer, M.P. 2009. A geometric model of fault zone and fault rock thickness variations. *Journal of Structural Geology*, Vol. 31, Iss. 2, pp. 117-127.

Choi, J.H., Edwards, P., Ko, K. and Kim, Y.S. 2016. Definition and classification of fault damage zones: A review and a new methodological approach. *Earth-Science Reviews*, 152, pp.70-87.

Cilona, A., Baud, P., Tondi, E., Agosta, F., Vinciguerra, S., Rustichelli, A. and Spiers, C.J. 2012. Deformation bands in porous carbonate grainstones: Field and laboratory observations. *Journal of Structural Geology*, Vol. 45, pp. 137–157.

Cilona, A., Solum, J.G., Lucca, A., Storti, F., Balsamo, F., Taberner, C. 2019. Evolution of Pore Types and Petrophysical Properties of Fault Rocks in Low-Porosity Carbonates. *SEPM (Society for Sedimentary Geology)*, Vol. 18, Iss. 2, pp. 94-107.

Climate Change Committee. 2021. Independent Assessment: The UK's Net Zero Strategy

CO2CRC. 2019. Annual Report 2018-2019.

CO2CRC. 2020a. About Us, via <http://www.co2crc.com.au/about-us-2/> [Accessed 1/6/2020].

CO2CRC. 2020b. Latest research results, via <http://www.co2crc.com.au/latest-research-results/> [Accessed 9/6/2020]

Coelho, J.C.C.; Martins-Neto, M.A.; Marinho, M.S. 2008. Estilos estruturais e evolução tectônica da porção mineira da bacia proterozóica do São Francisco. *Rev. Bras. Geociências*, 38 (Suppl. S2), 149–165. DOI: 10.25249/0375-7536.2008382S149165

Coleman, A.J., Duffy, O.B. and Jackson, C.A.L. 2019. Growth folds above propagating normal faults. *Earth-science reviews*, 196, p.102885.

Comninou, M. and Dundurs, J. 1975. The angular dislocation in a half space. *Journal of Elasticity*, 5, pp.203-216.

Conrad, R. and Seiler, W. 1980. Contribution of hydrogen production by biological nitrogen fixation to the global hydrogen budget. *Journal of Geophysical Research*, 85, 5493, <https://doi.org/10.1029/JC085iC10p05493>.

Conrad, R. and Seiler, W. 1981. Decomposition of atmospheric hydrogen by soil microorganisms and soil enzymes. *Soil Biology and Biochemistry*, Vol. 13, pp. 43-49. [https://doi.org/10.1016/0038-0717\(81\)90101-2](https://doi.org/10.1016/0038-0717(81)90101-2).

Cook, P.J. 2013. The CO2CRC Otway Project In Australia, in Gluyas, J., Mathias, S., (Editors). *Geological Storage of Carbon Dioxide (CO2)*, pp. 251-274

- Cooke, A.P. 2019. The impact of faults on fluid flow in porous carbonate rocks. PhD Thesis. University of Leeds.
- Cooke, A.P., Fisher, Q.J., Michie, E.A. and Yielding, G. 2020. Permeability of carbonate fault rocks: a case study from Malta. *Petroleum Geoscience*, Vol. 26, Iss. 3, pp.418-433.
- Cooke, A.P., Fisher, Q.J., Michie, E.A., Yielding, G. 2018. Investigating the controls on fault rock distribution in normal faulted shallow burial limestones, Malta, and the implications for fluid flow. *Journal of Structural Geology*, Vol. 114, pp. 22-42.
- Core Lab. 2016. Routine Core Analysis Report. Harvey-2. West Australia. PRP-15-005.
- Coulombe, C.E., Wilding, L.P. and Dixon, J.B. 1996. Overview of Vertisols: characteristics and impacts on society. *Advances in agronomy*, 57, pp.289-375.
- Coveney, R.M., Goebel, E.D., Zeller, E.J., Dreschhoff, G.A.M., Angino, E.E. 1987. Serpentinization and the Origin of Hydrogen Gas in Kansas. *AAPG Bulletin*, 71, <https://doi.org/10.1306/94886D3F-1704-11D7-8645000102C1865D>.
- Crostella, A., Backhouse, J. 2000. Geology and Petroleum Exploration of the Central and Southern Perth Basin, Western Australia. GSWA Report 57. Geological Survey of Western Australia.
- CSIRO. 2019. CSIRO In-Situ Laboratory to De-Risk Deployment of Carbon Storage, Final Report.
- Cunningham, W.D., Mann, P. 2007. Tectonics of strike-slip restraining and releasing bends. *Geological Society, London, Special Publications*, Vol. 290, pp. 1-12.
- Daley, T.M., Sharma, S., Dzunic, A., Urosevic, M., Kepic, A., Sherlock, D. 2009. Borehole seismic monitoring at Otway using the Naylor-1 instrument string (No. LBNL-2337E). Lawrence Berkeley National Lab (LBNL), Berkeley, CA (United States).
- Dance, T. 2013. Assessment and geological characterisation of the CO2CRC Otway Project CO2 storage demonstration site: From prefeasibility to injection. *Marine and Petroleum Geology*, Vol. 46, pp. 251-269.
- Dance, T. 2014. Characterising the storage site, in Cook, P. (Editor). *Geologically Storing Carbon: Learning from the Otway Project Experience*. CSIRO Publishing

Dance, T. 2019. Geological characterisation of Australia's first carbon dioxide storage site. The Australian School of Petroleum, The University of Adelaide, PhD Thesis

Dance, T. and Paterson, L. 2016. Observations of carbon dioxide saturation distribution and residual trapping using core analysis and repeat pulsed-neutron logging at the CO2CRC Otway site. *International Journal of Greenhouse Gas Control*, Vol. 47, pp. 210-220.

Dance, T., Spencer, L., Xu, J-Q. 2009. Geological characterisation of the Otway project pilot site: What a difference a well makes. *Energy Procedia*, Vol. 1, pp. 2971-2878

Davatzes, N. C. and Aydin, A. 2005. Distribution and nature of fault architecture in a layered sandstone and shale sequence: An example from the Moab fault, Utah, *AAPG Memoir*. Vol. 85, pp. 153–180.

De Rosa, S.S., Shipton, Z.K., Lunn, R.J., Kremer, Y. and Murray, T. 2018. Along-strike fault core thickness variations of a fault in poorly lithified sediments, Miri (Malaysia). *Journal of Structural Geology*, Vol. 116, pp. 189-206.

Delaney, P., Pollard, D. 1981. Deformation of Host Rocks and Flow of Magma During Growth of Minette Dikes and Breccia-Bearing Intrusions Near Ship Rock, New Mexico. *U.S. Geological Survey Professional Paper 1202*, 61p

Delle Piane, C., Bourdet, J., Dautriat, J., Esteban, L., Kager, S., Lebedev, M., Maney, B., Nourifard, N., Rezagholilou, A., Sarmadivaleh, M., Sarout, J., Skea, C., Yurikov, A. 2018. The Lesueur: Deposition, Rocks, Facies, Properties. Project 7-0115-0240, Final Report. *CSIRO Report Number EP181193*.

Delle Piane, C., Olierook, H.K., Timms, N.E., Saeedi, A., Esteban, L., Rezaee, R., Mikhaltsevitch, V., Iglauer, S. and Lebedev, M. 2013. Facies-based rock properties distribution along the Harvey 1 stratigraphic well. Australian National Low Emissions Coal (ANLEC) Research & Development, *CSIRO Report Number EP133710*.

Deville, E., Prinzhofer, A. 2016. The origin of N₂-H₂-CH₄-rich natural gas seepages in ophiolitic context: A major and noble gases study of fluid seepages in New Caledonia. *Chemical Geology*, Vol. 440, pp. 139-147. <https://doi.org/10.1016/j.chemgeo.2016.06.011>.

- Dockrill, B. and Shipton, Z.K., 2010. Structural controls on leakage from a natural CO₂ geologic storage site: Central Utah, USA. *Journal of Structural Geology*, 32(11), pp.1768-1782..
- Donzé, F.V., Truche, L., Shekari Namin, P., Lefeuvre, N., Bazarkina, E.F. 2020. Migration of natural hydrogen from deep-seated sources in the São Francisco Basin, Brazil. *Geosciences*, 10(9), p.346. <https://doi.org/10.3390/geosciences10090346>.
- DSE, 2011. Review of land stability at Sturgess Point, Port Campbell. Department of Sustainability and Environment. Report # 514/01/11.
- Du Bernard, X., Eichbuhl, P., Aydin, A. 2002. Dilation bands: a new form of localized failure in granular media. *Geophysical Research Letters*, Vol. 29, Iss. 4, 2176.
- Dunn, D.E., LaFountain, L.J., Jackson, R.E. 1973. Porosity dependence and mechanism of brittle fracture in sandstones. *Journal of Geophysical Research*, Vol. 78, Iss. 14, pp. 2403-2417.
- Duran, J. 1986. Geology, Hydrogeology and Groundwater Modelling of the Port Campbell Hydrogeological Sub-Basin, Otway Basin, SW Victoria. Geological Survey of Victoria, Unpublished Report, 1986/24
- Ebigbo et al. 2013 – Ebigbo, a., Golfier, F. and Quintard, M. 2013. a Coupled, Pore-scale Model for Methanogenic Microbial Activity in Underground Hydrogen Storage. *Advances in Water Resources* 61, pp. 74–85.
- Edlmann, K., Hinchliffe, S., Heinemann, N., Johnson, G., Ennis-King, J. and McDermott, C.I. 2019. Cyclic CO₂-H₂O injection and residual trapping: implications for CO₂ injection efficiency and storage security. *International Journal of Greenhouse Gas Control*, 80, pp.1-9.
- Edwards, J., Tickell, S. J., Willcocks, A. J., Eaton, A. R., Cramer, M. L., King, R. L., & Bourton, S. M. 1996. Colac 1:250 000 geological map. Geological Survey of Victoria.
- Ennis-King, J. 2021. Underground storage of hydrogen: mapping out the options for Australia (RP1.1-04).

Ennis-King, J., Wu, G. 2005. Simulation of Geological Storage of Carbon Dioxide in the Onshore Perth Basin. Cooperative Research Centre for Greenhouse Gas Technologies (CO2CRC). Report No: RPT05-0087.

Etioppe, G. and Sherwood Lollar, B. 2013. Abiotic methane on Earth. *Reviews of Geophysics*, 51(2), pp.276-299. <https://doi.org/10.1002/rog.20011>.

Etioppe, G., 2015. Natural gas seepage. *The Earth's hydrocarbon degassing*, p.199.

Etioppe, G., Samardžić, N., Grassa, F., Hrvatović, H., Miošić, N., Skopljak, F. 2017. Methane and hydrogen in hyperalkaline groundwaters of the serpentinized Dinaride ophiolite belt, Bosnia and Herzegovina. *Applied Geochemistry*, 84, pp.286-296. <https://doi.org/10.1016/j.apgeochem.2017.07.006>.

Exner, U., Grasemann, B. 2010. Deformation bands in gravels: displacement gradients and heterogeneous strain. *Journal of the Geological Society*. Vol. 167, Iss. 5, pp. 905–913.

Faereth, R.B. 2006. Shale smear along large faults: continuity of smear and the fault seal capacity. *Journal Geological Society of London*. Vol. 163, pp. 741–751.

Faulkner, D. R. and Rutter, E. H. 2001. Can the maintenance of overpressured fluids in large strike-slip fault zones explain their apparent weakness?, *Geology*, Vol. 29, pp. 503–506.

Faulkner, D.R., Jackson, C.A.L., Lunn, R.J., Schlische, R.W., Shipton, Z.K., Wibberley, C.A.J., Withjack, M.O. 2010. A review of recent developments concerning the structure, mechanics and fluid flow properties of fault zones. *Journal of Structural Geology*. Vol. 32, pp. 1557–1575.

Feitz, A., Pevzner, R., Harris, B., Schaa, R., Tertysnikov, K., Ziramov, S., Gunning, M., Ransley, T. R., Lai, E., Bailey, A. H., Schacht, U., Fomin, T., Urosevic, M. 2017. The CO2CRC Otway Shallow CO2 Controlled Release Experiment: Site Suitability Assessment, *Energy Procedia*. *Energy Procedia*. 114, 3671-3678.

Feitz, A., Radke, B., Chan, K.S., Ricard, L., Kalinowski, A., Wang, L., Tenthorey, E., Schaa, R., Tertysnikov, K., Glubokovskikh, S. and Schacht, U. 2021. The CO2CRC Otway shallow CO2 controlled release experiment: Fault characterization and leakage

scenarios. 15th International Conference on Greenhouse Gas Control Technologies GHGT-15, 15th -18th March 2021, Abu Dhabi, UAE, pp. 1-10

Feitz, A., Radke, B., Ricard, L., Glubokovskikh, S., Kalinowski, A., Wang, L., Tenthorey, E., Schaa, R., Tertyshnikov, K., Schacht, U. and Chan, K. 2022. The CO2CRC Otway shallow CO2 controlled release experiment: Fault characterization and geophysical monitoring design. *International Journal of Greenhouse Gas Control*, 118, p.103667.

Feitz, A., Radke, B., Schaa, R., Pethick, A., Ziramov, S., Urosevic, M., Tenthorey, E., Pan, Z., Ennis-King, J., Wang, L., Gunning, M.E. 2018a, October. The CO2CRC Otway shallow CO2 controlled release experiment: Geological model and CO2 migration simulations. In 14th Greenhouse Gas Control Technologies Conference Melbourne (pp. 21-26).

Feitz, A., Ricard, L., Radke, B., Chan, K., Glubokovskikh, S., Tenthorey, E., Pevzner, R., Tertyshnikov, K., Urosevic, M., Lebedev, M., Ennis-King, J., Schacht, U., Vialle, S., Harris, B., Wang, L., Coene, E., Green, C., Kalinowski, A., Sidenko, E., Credoz, A. 2020. SRD3.3 Science Case for Phase 3. CO2CRC Publication Number RPT20-6218. CO2CRC Ltd.

Feitz, A., Tertyshnikov, K., Pevzner, R., Ricard, L., Harris, B., Schaa, R., Schacht, U., Kalinowski, A., Vialle, S., Glubokovskikh, S., Lebedev, M. 2018b. The CO2CRC Otway shallow CO2 controlled release experiment: Preparation for Phase 2. *Energy Procedia*, Vol. 154, pp. 145-150.

Feitz, A.J., Pevzner, R., Harris, B., Schaa, R., Tertyshnikov, K., Ziramov, S., Gunning, M., Ransley, T.R., Lai, E., Bailey, A.H., Schacht, U. 2017. The CO2CRC Otway shallow CO2 controlled release experiment: Site suitability assessment. *Energy Procedia*, Vol. 114, pp. 3671-3678.

Fisher, Q.J., Casey, M., Harris, S.D. and Knipe, R.J., 2003. Fluid-flow properties of faults in sandstone: the importance of temperature history. *Geology*, 31(11), pp.965-968.

Fisher, Q.J., Knipe, R. 1998. Fault sealing processes in siliciclastic sediments. Geological Society, London, Special Publications, Vol. 147, pp. 117-134.

Fitz-Diaz, E., Hudleston, P., Siebenaller, L., Kirschner, D., Camprubí, A., Tolson, G. & Pi Puig, T. 2011. Insights into fluid flow and water-rock interaction during deformation of carbonate sequences in the Mexican fold-thrust belt. *Journal of Structural Geology*, Vol. 33, pp. 1237-1253.

Fossen, H., Schultz, R.A., Shipton, Z.K. and Mair, K. 2007. Deformation bands in sandstone: a review. *Journal of the Geological Society*, 164(4), pp.755-769.

Frery, E., Langhi, L., Maison, M., Moretti, I. 2021. Natural hydrogen seeps identified in the North Perth Basin, Western Australia. *International Journal of Hydrogen Energy*, 46(61), pp.31158-31173. <https://doi.org/10.1016/j.ijhydene.2021.07.023>.

Frost, E., Dolan, J., Ratschbacher, L., Hacker, B., Seward, G. 2011. Direct observation of fault zone structure at the brittle-ductile transition along the Salzach-Ennstal-Mariazell-Puchberg fault system, Austrian Alps. *Journal of Geophysical Research*. Vol. 116, B02411.

Fulljames, J.R., Zijerveld, L.J.J., Franssen, R.C.M.W., Møller-Pedersen, P., Koestler, A.G. 1997. Fault seal processes: systematic analysis of fault seals over geological and production time scales. *Norwegian Petroleum Society Special Publications*, Vol.7, Iss. 7, pp. 51-59.

Gay, A., Lopez, M., Potdevin, J.-L., Vidal, V., Varas, G., Favier, A., Tribovillard, N. 2019. 3D morphology and timing of the giant fossil pockmark of Beauvoisin, SE Basin of France. *Journal of the Geological Society*, 176, 61–77, <https://doi.org/10.1144/jgs2018-064>.

Getzin, S., Yizhaq, H. and Tschinkel, W.R. 2021. Definition of “fairy circles” and how they differ from other common vegetation gaps and plant rings. *Journal of Vegetation Science*, 32(6), p.e13092. <https://doi.org/10.1111/jvs.13092>.

Gheibi, S., Holt, R.M. and Vilarrasa, V. 2017. Effect of faults on stress path evolution during reservoir pressurization. *International Journal of Greenhouse Gas Control*, 63, pp.412-430.

Ghisetti, F., Kirschner, D.L., Vezzani, L., Agosta, F. 2001. Stable isotope evidence for contrasting paleofluid circulation in thrust faults and normal faults of the central Apennines, Italy. *Journal of Geophysical Research: Solid Earth*, Vol. 106, Iss. B5, pp. 8811-8825.

Gholami, R., Raza, A. and Iglaue, S. 2021. Leakage risk assessment of a CO₂ storage site: A review. *Earth-Science Reviews*, 223, p.103849.

Gill, E.D. 1964. Rocks contiguous with the basaltic cuirass of western Victoria. *Proceedings of the Royal Society of Victoria*, 77(2), pp.331-355.

Gill, E.D. 1971. Applications of radiocarbon dating in Victoria, Australia.

Government of South Australia. 2022. Gold Hydrogen natural hydrogen exploration. <https://www.energymining.sa.gov.au/industry/energy-resources/regulation/projects-of-public-interest/gold-hydrogen-natural-hydrogen-exploration#summary> [Accessed 16/06/22].

Graham, B., Antonellini, M., Aydin, A. 2003. Formation and growth of normal faults in carbonates within a compressive environment. *Geology*, Vol. 31, pp. 11-14.

Grathwohl, P. 1998. Diffusion in natural porous media: contaminant transport, sorption, desorption and dissolution kinetics, Dordrecht, Kluwer Academic Publishers.

Grauch, V.J., Hudson, M.R., Minor, S.A. 2001. Aeromagnetic expression of faults that offset basin fill, Albuquerque basin, New Mexico. *Geophysics*, Vol. 66, Iss. 3, pp. 707-720.

Gray, M.B. and Nickelsen, R.P. 1989. Pedogenic slickensides, indicators of strain and deformation processes in redbed sequences of the Appalachian foreland. *Geology*, 17(1), pp.72-75

Green, C.P. and Ennis-King, J. 2010. Effect of vertical heterogeneity on long-term migration of CO₂ in saline formations. *Transport in porous media*, 82, pp.31-47.

Gregory, S.P., Barnett, M.J., Field, L.P., Milodowski, A.E. 2019. Subsurface Microbial Hydrogen Cycling: Natural Occurrence and Implications for Industry, *Microorganisms*, Vol. 7, Iss. 53, pp. 1-27. <https://doi.org/10.3390/microorganisms7020053>.

Groshong Jr, R.H. 1988. Low-temperature deformation mechanisms and their interpretation. *Geological Society of America Bulletin*, Vol. 100, Iss. 9, pp. 1329-1360.

Guglielmi, Y., Cappa, F., and Amitrano, D. 2008. High-definition analysis of fluid-induced seismicity related to the mesoscale hydromechanical properties of a fault zone, *Geophysical Research Letters*, Vol. 35, L06306.

- Haines, T.J., Michie, E.A., Neilson, J.E., Healy, D. 2016. Permeability evolution across carbonate hosted normal fault zones. *Marine and Petroleum Geology*, Vol. 72, pp. 62-82.
- Halas, P., Dupuy, A., Franceschi, M., Bordmann, V., Fleury, J.M., Duclerc, D. 2021. Hydrogen gas in circular depressions in South Gironde, France: Flux, stock, or artefact?. *Applied Geochemistry*, 127, p.104928. <https://doi.org/10.1016/j.apgeochem.2021.104928>.
- Haneberg, W.C. 1995. Steady-state groundwater-flow across idealized faults. *Water Resources Research*, Vol. 31, Iss. 7, pp. 1815-1820.
- Hanley, E.S., Deane, J.P., Gallachóir, B.Ó. 2018. The role of hydrogen in low carbon energy futures—A review of existing perspectives. *Renewable and Sustainable Energy Reviews*, 82, pp.3027-3045. <https://doi.org/10.1016/j.rser.2017.10.034>.
- Hardman, R.F.P., Booth, J.E. 1991. The significance of normal faults in the exploration and production of North Sea hydrocarbons. Geological Society, London, Special Publications. Vol. 56, pp. 1-13.
- Harris, L.B. 1994. Structural and tectonic synthesis for the Perth Basin, Western Australia. *Journal of Petroleum Geology*, Vol. 17, pp. 129-156.
- Heffner, J., Fairley, J. 2006. Using surface characteristics to infer the permeability structure of an active fault zone. *Sedimentary Geology*, Vol. 184, Iss. 3-4, pp. 255-265
- Heidbach, O., Rajabi, M., Reiter, K., Ziegler, M. 2016, World Stress Map Database Release 2016. V. 1.1. GFZ Data Services. <http://doi.org/10.5880/WSM.2016.001>.
- Heidbach, O., Reinecker, J., Tingay, M., Müller, B., Sperner, B., Fuchs, K. and Wenzel, F. 2007. Plate boundary forces are not enough: Second-and third-order stress patterns highlighted in the World Stress Map database. *Tectonics*, Vol. 26, Iss. 6.
- Heidbach, O., Tingay, M., Barth, A., Reinecker, J., Kurfeß, D. and Müller, B. 2010. Global crustal stress pattern based on the World Stress Map database release 2008. *Tectonophysics*, Vol. 482, Iss. 1-4, pp. 3-15.
- Heinemann, N., Alcalde, J., Miocic, J.M., Hangx, S.J., Kallmeyer, J., Ostertag-Henning, C., Hassanpouryouzband, A., Thaysen, E.M., Strobel, G.J., Schmidt-Hattenberger, C.

and Edlmann, K. 2021b. Enabling large-scale hydrogen storage in porous media—the scientific challenges. *Energy & Environmental Science*, 14(2), pp.853-864.

Heinemann, N., Booth, M.G., Haszeldine, R.S., Wilkinson, M., Scafidi, J., Edlmann, K. 2018. Hydrogen storage in porous geological formations—onshore play opportunities in the midland valley (Scotland, UK). *International Journal of Hydrogen Energy*, 43(45), pp.20861-20874. <https://doi.org/10.1016/j.ijhydene.2018.09.149>.

Heinemann, N., Scafidi, J., Pickup, G., Thaysen, E.M., Hassanpouryouzband, A., Wilkinson, M., Satterley, A.K., Booth, M.G., Edlmann, K. and Haszeldine, R.S. 2021a. Hydrogen storage in saline aquifers: The role of cushion gas for injection and production. *International journal of hydrogen energy*, 46(79), pp.39284-39296.

Herbert, J.W., Cooke, M.L., Souloumiac, P., Madden, E.H., Mary, B.C. and Maillot, B. 2015. The work of fault growth in laboratory sandbox experiments. *Earth and Planetary Science Letters*, 432, pp.95-102.

Heynekamp, M.R., Goodwin, L.B., Mozley, P.S. and Haneberg, W.C. 1999. Controls on fault-zone architecture in poorly lithified sediments, Rio Grande Rift, New Mexico: Implications for fault-zone permeability and fluid flow. *Geophysical Monograph Series*, 113, pp.27-49.

Hill, K.C., Durrand, C. 1993. The western Otway Basin: an overview of the rift and drift history using serial composite seismic profiles. *PESA Journal*, Vol. 21, pp. 67-78.

Holdgate, G.R., Gallagher, S.J. 2003. Chapter 10: Tertiary, in Birch W. D. (Editor). *Geology of Victoria*. Geological Society of Australia Special Publication 23. Geological Society of Australia (Victoria Division).

Holford, S., Hillis, R., Duddy, I., Green, P., Stoker, M., Tuitt, A., Backé, G., Tassone, D., MacDonald, J. 2011. Cenozoic post-breakup compressional deformation and exhumation of the southern Australian margin. *The APPEA Journal*, Vol. 51, pp. 613-638.

Holloway, S., Pearce, J.M., Hards, V.L., Ohsumi, T., Gale, J. 2007. Natural emissions of CO₂ from the geosphere and their bearing on the geological storage of carbon dioxide. *Energy*, 32(7), pp.1194-1201. <https://doi.org/10.1016/j.energy.2006.09.001>.

Hooke, R. 1978. *De Potentia Restitutiva, or of Spring. Explaining the Power of Springing Bodies*, London

Hosgörmez, H., Etiope, G., Yalçın, M.N. 2008. New evidence for a mixed inorganic and organic origin of the Olympic Chimaera fire (Turkey): a large onshore seepage of abiogenic gas. *Geofluids*, Vol. 8, Iss. 4, pp. 263-273. <https://doi.org/10.1111/j.1468-8123.2008.00226.x>.

Huenges, E., Ledru, P. 2011. *Geothermal Energy Systems: Exploration, Development, and Utilization*. John Wiley & Sons, p. 486pp.

Huggins, P., Watterson, J., Walsh, J.J. and Childs, C. 1995. Relay zone geometry and displacement transfer between normal faults recorded in coal-mine plans. *Journal of Structural Geology*, 17(12), pp.1741-1755.

Iasky R. P. 1993. A structural study of the southern Perth Basin, Western Australia. *Geological Survey of Western Australia*, No. 31, p. 56

Iasky R. P., Young R. A., Middleton M. F. 1991. Structural study of the southern Perth Basin by geophysical methods. *Exploration Geophysics*, Vol. 22, pp. 199–206.

IEA. 2013. *Energy Technology Roadmap Hydrogen and Fuel Cells*, JRC Scientific Policy Report

Iglauer, S., Pentland, C.H. and Busch, A. 2015. CO₂ wettability of seal and reservoir rocks and the implications for carbon geo-sequestration. *Water Resources Research*, 51(1), pp.729-774.

Inbal, A., Ampuero, J.P., Clayton, R.W. 2016. Localized seismic deformation in the upper mantle revealed by dense seismic arrays. *Science*. Vol. 354, 88-92.

Irwin, W.P. and Barnes, I. 1980. Tectonic relations of carbon dioxide discharges and earthquakes. *Journal of Geophysical Research*, 85, 3115-3121. <https://doi.org/10.1029/JB085iB06p03115>.

Jaeggi, David, Ben Laurich, Christophe Nussbaum, Kristof Schuster, and Peter Connolly. 2018. "Tectonic structure of the "main fault" in the Opalinus Clay, Mont Terri rock laboratory (Switzerland)." *Mont Terri Rock Laboratory, 20 Years: Two Decades of Research and Experimentation on Claystones for Geological Disposal of Radioactive Waste* (2018): 69-86.

Jenkins, C., Marshall, S., Dance, T., Ennis-King, J., Glubokovskikh, S., Gurevich, B., La Force, T., Paterson, L., Pevzner, R., Tenthorey, E., Watson, M. 2017. Validating Subsurface Monitoring as an Alternative Option to Surface M&V-The CO2CRC's Otway Stage 3 Injection. *Energy Procedia*, Vol. 114, pp. 3374-3384.

Jenkins, C.R., Cook, P.J., Ennis-King, J., Undershultz, J., Boreham, C., Dance, T., de Caritat, P., Etheridge, D.M., Freifeld, B.M., Hortle, A., Kirste, D. 2012. Safe storage and effective monitoring of CO2 in depleted gas fields. *Proceedings of the National Academy of Sciences*, Vol. 109, Iss. 2, pp. E35-E41.

Johnson R W, Knutson J, Taylor S R (eds). 1989. *Intraplate Volcanism in Eastern Australia and New Zealand*. Cambridge, England: Cambridge Univ Press, 408 p.

Jones, M. 1994. Mechanical principles of sediment deformation. In: Maltman, A. (Ed.), *The Geological Deformation of Sediments*. Chapman and Hall, pp. 37-72.

Kaminskaite, I., Fisher, Q.J. & Michie, E.A.H. 2019. Microstructure and petrophysical properties of deformation bands in high porosity carbonates. *Journal of Structural Geology*, Vol. 119, pp. 61–80.

Kampman, N., Burnside, N.M., Shipton, Z.K., Chapman, H.J., Nicholl, J.A., Ellam, R.M., Bickle, M.J. 2012. Pulses of carbon dioxide emissions from intracrustal faults following climatic warming. *Nature Geoscience*. Vol. 5, pp. 352–358.

Kelley, J.A. 2010. Soil Science: Image of soil slickenside. From: <https://www.flickr.com/photos/soilscience/5097597864>.

Kelly, P.G., Sanderson, D.J., Peacock, D.C.P. 1998. Linkage and evolution of conjugate strike-slip fault zones in limestones of Somerset and Northumbria. *Journal of Structural Geology*, Vol. 20, Iss. 11, pp. 1477-1493.

Kim, Y.S. and Sanderson, D.J. 2005. The relationship between displacement and length of faults: a review. *Earth-Science Reviews*, Vol. 68, Iss. 3-4, pp. 317-334.

Kim, Y.S., Peacock, D.C., Sanderson, D.J. 2004. Fault damage zones. *Journal of Structural Geology*, Vol. 26, Iss. 3, pp. 503-517.

- Kim, Y.S., Sanderson, D.J. 2010. Inferred fluid flow through fault damage zones based on the observation of stalactites in carbonate caves. *Journal of Structural Geology*, Vol. 32, Iss. 9, pp.1305-1316.
- King, R.C., S.P. Holford, R.R. Hillis, A. Tuitt, E. Swierczek, G. Backe, D. Tassone, M. Tingay. 2012. Reassessing the In-Situ stress regimes of Australia's petroleum basins. *The APPEA Journal* 52, 415-426.
- Kirk, K. 2011. Natural CO₂ flux literature review for the QICS project. British Geological Survey Commissioned Report: *Comptes Rendus Geoscience*, 11(005), p.38.
- Kita, I., Matsuo, S., Wakita, H. 1982. H₂ generation by reaction between H₂O and crushed rock: An experimental study on H₂ degassing from the active fault zone. *Journal of Geophysical Research: Solid Earth*, 87, 10789–10795, <https://doi.org/10.1029/JB087iB13p10789>.
- Knipe, R.J. 1993. The influence of fault zone processes and diagenesis on fluid flow. in: Horbury, A.D., Robinson, A.G. (eds.) *Diagenesis and basin development*. AAPG Studies in Geology, Vol. 36, pp. 135–148.
- Ko, K., Kim, S.W., Lee, H.J., Hwang, I.G., Kim, B.C., Kee, W.S., Kim, Y.S. and Gihm, Y.S. 2017. Soft sediment deformation structures in a lacustrine sedimentary succession induced by volcano-tectonic activities: an example from the Cretaceous Beolgeumri Formation, Wido Volcanics, Korea. *Sedimentary Geology*, 358, pp.197-209.
- Kovda, I. and Mermut, A.R. 2018. Vertic features. In *Interpretation of micromorphological features of soils and regoliths* (pp. 605-632). Elsevier.
- Krassay, A.A., Cathro, D.L., Ryan, D.J. 2004. A regional tectonostratigraphic framework for the Otway Basin. In: *PESA Eastern Australasian Basins Symposium*, vol. 2, pp. 97-116.
- Krevor, S., De Coninck, H., Gasda, S.E., Ghaleigh, N.S., de Gooyert, V., Hajibeygi, H., Juanes, R., Neufeld, J., Roberts, J.J. and Swennenhuis, F. 2023. Subsurface carbon dioxide and hydrogen storage for a sustainable energy future. *Nature Reviews Earth & Environment*, 4(2), pp.102-118.

Kulander, B.R., Dean, S.L. and Ward, B.J. 1990. Fractured core analysis: interpretation, logging, and use of natural and induced fractures in core. American Association of Petroleum Geologists

Langhi, L. and Strand, J. 2023. Exploring natural hydrogen hotspots: a review and soil-gas survey design for identifying seepage. *Geoenergy*, 1(1).

Langhi, L., Ciftci, B., Strand, J. 2013. Fault seal first-order analysis–SW Hub. CSIRO report EP13879, pp. 50

Langhi, L., Ricard, L. and Strand, J. 2019. Reservoir flow modelling to constrain CO₂ plume-fault interaction. South West Hub Carbon Capture and Storage Project, WA. ASEG Extended Abstracts, pp.1-4.

Larin, N., Zgonnik, V., Rodina, S., Deville, E., Prinzhofer, A., Larin, V.N. 2015. Natural molecular hydrogen seepage associated with surficial, rounded depressions on the European craton in Russia. *Natural Resources Research*, Vol. 24, Iss. 3, pp. 369-383. <https://doi.org/10.1007/s11053-014-9257-5>.

Laurich, B. 2015. Evolution of microstructure and porosity in faulted Opalinus Clay. PhD thesis, RWTH Aachen University, Aachen, Germany

Laurich, B., Urai, J.L. and Nussbaum, C. 2017. Microstructures and deformation mechanisms in Opalinus Clay: Insights from scaly clay from the Main Fault in the Mont Terri Rock Laboratory (CH). *Solid Earth*, 8(1), pp.27-44.

Laurich, Ben, Janos L. Urai, Guillaume Desbois, Christian Vollmer, and Christophe Nussbaum. 2014. "Microstructural evolution of an incipient fault zone in Opalinus Clay: Insights from an optical and electron microscopic study of ion-beam polished samples from the Main Fault in the Mt-Terri Underground Research Laboratory." *Journal of Structural Geology* 67 (2014): 107-128.

Lazarou, S., Vita, V., Diamantaki, M., Karanikolou-Karra, D., Fragoyiannis, G., Makridis, S., Ekonomou, L. 2018. A simulated roadmap of hydrogen technology contribution to climate change mitigation based on Representative Concentration Pathways considerations. *Energy Science & Engineering*, 6(3), pp.116-125. <https://doi.org/10.1002/ese3.194>.

Lee, Y.J., Wiltschko, D.V., Grossman, E.L., Morse, J.W., Lamb, W.M. 1997. Sequential vein growth with fault displacement: An example from the Austin Chalk Formation, Texas. *Journal of Geophysical Research: Solid Earth*, Vol. 102, Iss. B10, pp. 22611-22628.

Leila, M., Lévy, D., Battani, A., Piccardi, L., Šegvić, B., Badurina, L., Pasquet, G., Combaudon, V., Moretti, I. 2021. Origin of continuous hydrogen flux in gas manifestations at the Larderello geothermal field, Central Italy. *Chemical Geology*, 585, p.120564. <https://doi.org/10.1016/j.chemgeo.2021.120564>.

Leonard, G.J. 1983. Hydrogeological Assessment of Lower Tertiary Aquifers in the Childers Cove – Curdie Vale Area, Western Victoria. Geological Survey. Victoria, Unpublished Report, 1983/79.

Lesti, C., Giordano, G., Salvini, F. and Cas, R. 2008. Volcano tectonic setting of the intraplate, Pliocene-Holocene, Newer Volcanic Province (southeast Australia): Role of crustal fracture zones. *Journal of Geophysical Research: Solid Earth*, 113(B7).

Leveille, G.P., Knipe, R., More, C., Ellis, D., Dudley, G., Jones, G., Fisher, Q.J., Allinson, G. 1997. Compartmentalization of Rotliegende gas reservoirs by sealing fault, Jupiter Fields area, southern North Sea. in: Ziegler, K., Turner, P., Daines, S. (eds.) *Petroleum geology of the southern North Sea: future potential*. Geological Society Special Publication, Vol. 123, pp. 87–104.

Lie, K.A., Krogstad, S., Ligaarden, I., Natvig, J., Nilsen, H., Skaflestad, B. 2012. Open-source MATLAB implementation of consistent discretisations on complex grids. *Computational Geosciences*. Vol. 16, pp. 297- 322.

Lim, D., Strachan G., van Gent D., Sharma S. 2017. Underground storage of carbon dioxide in the Harvey area, south-west Western Australia. *The APPEA Journal*, Vol. 57, pp. 177–210.

Lindsay, N.G., Murphy, F.C., Walsh, J.J., Watterson, J. 1993. Outcrop studies of shale smears on fault surfaces. In: Fint, S.S., Bryant, I.D. (eds.), *The Geological Modelling of Hydrocarbon Reservoirs and Outcrop Analogues*, Vol. 15. Blackwell Scientific Publications, Oxford, pp. 11-123.

- Lollar, B.S., Lacrampe-Couloume, G., Slater, G.F., Ward, J., Moser, D.P., Gihring, T.M., Lin, L.H., Onstott, T.C. 2006. Unravelling abiogenic and biogenic sources of methane in the Earth's deep subsurface. *Chemical Geology*, 226(3-4), pp.328-339. <https://doi.org/10.1016/j.chemgeo.2005.09.027>.
- Loon, A.J. 2009. Soft-sediment deformation structures in siliciclastic sediments: an overview. *Geologos*, 15(1), pp.3-55.
- Loveless, S., Bense, V., Turner, J. 2011. Fault architecture and deformation processes within poorly lithified rift sediments, Central Greece. *Journal of Structural Geology*, Vol. 33, Iss. 11, pp. 1554-1568.
- Loveless, S., Pluymaekers, M., Lagrou, D., De Boever, E., Doornenbal, H., Laenen, B. (2014). Mapping the geothermal potential of fault zones in the Belgium-Netherlands border region. *Energy Procedia*. Vol. 59, pp. 351-358.
- Low, G.H. 1971. Definition of two Quaternary formations in the Perth Basin. *Geological Survey of Western Australia. Annual Report, 1970*, pp. 33-34.
- Lu, J.M., Wilkinson, M., Haszeldine, R.S., Fallick, A. E. 2009. Long-term performance of a mudrock seal in natural CO₂ storage. *Geology*, Vol. 37, pp. 35–38.
- Lucia, F.J. 2007. *Carbonate reservoir characterization: An integrated approach*. Springer Science & Business Media.
- Lunn, R.J., Shipton, Z.K. and Bright, A.M. 2008. How can we improve estimates of bulk fault zone hydraulic properties?. *Geological Society, London, Special Publications*, Vol. 299, pp. 231-237.
- Maerten, F., Maerten, L. and Pollard, D.D. 2014. iBem3D, a three-dimensional iterative boundary element method using angular dislocations for modeling geologic structures. *Computers & Geosciences*, 72, pp.1-17.
- Maerten, L., Maerten, F., Lejri, M. and Gillespie, P. 2016. Geomechanical paleostress inversion using fracture data. *Journal of structural Geology*, 89, pp.197-213.
- Magoon, L.B. and Dow, W.G. 1994. *The Petroleum system-from source to trap*. AAPG Memoir 60. American Association of Petroleum Geologist, Tulsa, pp.25-49.

- Mailloux, B.J., Person, M., Kelley, S., Dunbar, N., Cather, S., Strayer, L., Hundleston, P. 1999. Tectonic controls on the hydrogeology of the Rio Grande rift, New Mexico. *Water Resources Research*, Vol. 35, pp. 2641-2659.
- Mandl, G., De Jong, L.N.J., Maltha, A. 1977. Shear zones in granular material. *Rock mechanics*, Vol. 9, Iss. 2-3, pp. 95-144.
- Martin-Roberts, E., Scott, V., Flude, S., Johnson, G., Haszeldine, R.S. and Gilfillan, S. 2021. Carbon capture and storage at the end of a lost decade. *One Earth*. Vol. 4, Iss. 11, pp. 1569-1584.
- Matonti, C., Lamarche, J., Guglielmi, Y. and Marié, L. 2012. Structural and petrophysical characterization of mixed conduit/seal fault zones in carbonates: Example from the Castellans fault (SE France). *Journal of Structural Geology*, Vol. 39, pp. 103-121.
- Mavko, G. 1982. Fault interaction near Hoolister, California. *J. Geophys. Res.* 87, 7807–7816
- May, F., Warsitzka, M. and Kukowski, N. 2019. Analogue modelling of leakage processes in unconsolidated sediments. *International Journal of Greenhouse Gas Control*, 90, p.102805.
- McCalpin, J.P. and Nelson, A.R. 2009. Introduction to paleoseismology. *International Geophysics*, 95, pp.1-27.
- McCay, A.T., Shipton, Z.K., Lunn, R.J. and Gale, J.F. 2019. Mini thief zones: Subcentimeter sedimentary features enhance fracture connectivity in shales. *AAPG Bulletin*, 103(4), pp.951-971.
- McClay, K.R., Ellis, P.G. 1987. Geometries of extensional fault systems developed in model experiments. *Geology*, Vol. 15, Iss. 4, pp. 341-344.
- McGuire, J.J. and Segall, P. 2003. Imaging of aseismic fault slip transients recorded by dense geodetic networks. *Geophysical Journal International*, 155(3), pp.778-788.
- McMahon, C.J., Roberts, J.J., Johnson, G., Edlmann, K., Flude, S. and Shipton, Z.K. 2023. Natural hydrogen seeps as analogues to inform monitoring of engineered geological hydrogen storage.

- Meade, B.J. 2007. Algorithms for the calculation of exact displacements, strains, and stresses for triangular dislocation elements in a uniform elastic half space. *Computers & geosciences*, 33(8), pp.1064-1075.
- Meixner, J., Schill, E., Gaucher, E. and Kohl, T. 2014. Inferring the In-Situ stress regime in deep sediments: an example from the Bruchsal geothermal site. *Geothermal Energy*, 2, pp.1-17.
- Meredith, L.K., Commane, R., Munger, J.W., Dunn, A., Tang, J., Wofsy, S.C., Prinn, R.G. 2014. Ecosystem fluxes of hydrogen: a comparison of flux-gradient methods. *Atmospheric Measurement Techniques*, 7, 2787–2805, <https://doi.org/10.5194/amt-7-2787-2014>.
- Micarelli, L., Benedicto, A., Wibberley, C.A.J. 2006. Structural evolution and permeability of normal fault zones in highly porous carbonate rocks. *Journal of Structural Geology*, Vol. 28, Iss. 7, pp. 1214-1227.
- Michael, K., Avijegon, A., Ricard*, L., Myers, M., Tertyshnikov, K., Pevzner, R., Strand, J., Freifeld, B., Woitt, M., Pervukhina, M., Feitz, A. 2019. In-Situ Laboratory for CO₂ controlled-release experiments and monitoring in a fault zone in Western Australia. *ASEG Extended Abstracts*, 2019(1), pp.1-3.
- Michael, K., Avijegon, A., Ricard, L., Myers, M., Tertyshnikov, K., Pevzner, R., Strand, J., Hortle, A., Stalker, L., Pervukhina, M., Harris, B. 2020. A controlled CO₂ release experiment in a fault zone at the In-Situ Laboratory in Western Australia. *International Journal of Greenhouse Gas Control*, 99, p.103100.
- Michie, E.A.H., Haines, T.J. 2016. Variability and heterogeneity of the petrophysical properties of extensional carbonate fault rocks, Malta. *Petroleum Geoscience*, Vol. 22, Iss. 2, pp. 136-152.
- Michie, E.A.H., Haines, T.J., Healy, D., Neilson, J.E., Timms, N.E. and Wibberley, C.A.J. 2014. Influence of carbonate facies on fault zone architecture. *Journal of Structural Geology*, 65, pp.82-99.
- Michie, E.A.H., Yielding, G. and Fisher, Q.J. 2018. Predicting transmissibilities of carbonate-hosted fault zones. *Geological Society, London, Special Publications*, Vol. 459, pp.121-137.

Mills, P.C. 1983. Genesis and diagnostic value of soft-sediment deformation structures—a review. *Sedimentary Geology*, 35(2), pp.83-104.

Minor, S.A., Hudson, M.R. 2006. Regional Survey of structural properties and cementation patterns of fault zones in the Northern part of the Albuquerque basin, New Mexico - Implications for Ground-water Flow U.S. Geological Survey Professional Paper 1719

Miocic, J., Heinemann, N., Edlmann, K., Scafidi, J., Molaei, F. and Alcalde, J. 2023. Underground hydrogen storage: a review.

Miocic, J., Johnson, G. and Bond, C.E. 2019b. Uncertainty in fault seal parameters: implications for CO₂ column height retention and storage capacity in geological CO₂ storage projects. *Solid Earth*. Vol. 10, pp. 951-967.

Miocic, J.M., Gilfillan, S.M., Frank, N., Schroeder-Ritzrau, A., Burnside, N.M. and Haszeldine, R.S. 2019a. 420,000 year assessment of fault leakage rates shows geological carbon storage is secure. *Scientific Reports*, Vol. 9, pp. 1-9.

Miocic, J.M., Gilfillan, S.M., McDermott, C., Haszeldine, R.S. 2013. Mechanisms for CO₂ leakage prevention—A global dataset of natural analogues. *Energy Procedia*, 40, pp.320-328. <https://doi.org/10.1016/j.egypro.2013.08.037>.

Miocic, J.M., Gilfillan, S.M., Roberts, J.J., Edlmann, K., McDermott, C.I., Haszeldine, R.S. 2016. Controls on CO₂ storage security in natural reservoirs and implications for CO₂ storage site selection. *International Journal of Greenhouse Gas Control*, 51, pp.118-125. <https://doi.org/10.1016/j.ijggc.2016.05.019>.

Miocic, J.M., Gilfillan, S.M., Roberts, J.J., Edlmann, K., McDermott, C.I. and Haszeldine, R.S. 2016. Controls on CO₂ storage security in natural reservoirs and implications for CO₂ storage site selection. *International Journal of Greenhouse Gas Control*, Vol. 51, pp. 118-125.

Miocic, J.M., Johnson, G. and Gilfillan, S. 2020. Stress field orientation controls on fault leakage at a natural CO₂ reservoir. *Solid Earth*, Vol. 11, Iss. 4, pp. 1361-1374.

Miocic, J.M., Johnson, G. and Gilfillan, S.M. 2014. Fault seal analysis of a natural CO₂ reservoir in the Southern North Sea. *Energy Procedia*, 63, pp.3364-3370.

Mitchell, T.M., Faulkner, D.R. 2009. The nature and origin of off-fault damage surrounding strike-slip fault zones with a wide range of displacements: A field study from the Atacama fault system, northern Chile. *Journal of Structural Geology*, Vol. 31, Iss. 8, pp. 802-816.

Mitra, S. 2002. Fold-accommodation faults. *AAPG bulletin*, 86(4), pp.671-693.

Mollema, P.N., Antonellini, M. 1999. Development of strike-slip faults in the dolomites of the Sella Group, Northern Italy. *Journal of Structural Geology*, Vol. 21, Iss. 3, pp. 273-292.

Molli, G., Cortecchi, G., Vaselli, L., Ottria, G., Cortopassi, A., Dinelli, E., Mussi, M., Barbieri, M. 2010. Fault zone structure and fluid–rock interaction of a high angle normal fault in Carrara marble (NW Tuscany, Italy). *Journal of Structural Geology*, Vol. 32, Iss. 9, pp. 1334-1348.

Montañez, I.P., Crossey, L.J. 2018. Diagenesis. In: White, W.M. (eds) *Encyclopedia of Geochemistry*. *Encyclopedia of Earth Sciences Series*. Springer, Cham. https://doi-org.proxy.lib.strath.ac.uk/10.1007/978-3-319-39312-4_35

Moore, C.R., Brooks, M.J., Mallinson, D.J., Parham, D.R., Ivester, A.H., Feathers, J.K. 2016. The quaternary evolution of herndon bay, a carolina bay on the coastal plain of north carolina (usa): implications for paleoclimate and oriented lake genesis, *Southeastern Geology*, Vol. 51

Moretti, I., Brouilly, E., Loiseau, K., Prinzhofer, A., Deville, E. 2021b. Hydrogen Emanations in Intracratonic Areas: New Guide Lines for Early Exploration Basin Screening. *Geosciences*, 11(3), p.145. <https://doi.org/10.3390/geosciences11030145>.

Moretti, I., Prinzhofer, A., Françolin, J., Pacheco, C., Rosanne, M., Rupin, F., Mertens, J. 2021a. Long-term monitoring of natural hydrogen superficial emissions in a brazilian cratonic environment. Sporadic large pulses versus daily periodic emissions. *International Journal of Hydrogen Energy*, 46(5), pp.3615-3628. <https://doi.org/10.1016/j.ijhydene.2020.11.026>.

Morrill, P.L., Kuenen, J.G., Johnson, O.J., Suzuki, S., Rietze, A., Sessions, A.L., Fogel, M.L., Nealson, K.H. 2013. *Geochemistry and geobiology of a present-day*

serpentinization site in California: The Cedars. *Geochimica et Cosmochimica Acta*, Vol. 109, pp.222-240. <https://doi.org/10.1016/j.gca.2013.01.043>.

Mory, A.J. 1995. Geology of the Wedge Island 1:100 000 Sheet, Geological Survey of Western Australia. Explanatory Notes, p. 19

Mory, A.J., 1994. Subdivisions of Western Australian Neoproterozoic and Phanerozoic sedimentary basins. Department of Minerals and Energy.

Mouli-Castillo, J., Heinemann, N., Edlmann, K. 2021. Mapping geological hydrogen storage capacity and regional heating demands: An applied UK case study. *Applied Energy*, 283, p.116348. <https://doi.org/10.1016/j.apenergy.2020.116348>.

Moustafa, A.R. 2013. Fold-related faults in the Syrian Arc belt of northern Egypt. *Marine and Petroleum Geology*, 48, pp.441-454.

Mozley, P.S., Goodwin, L.B. 1995. Patterns of cementation along a Cenozoic normal fault: a record of paleoflow orientations. *Geology*, Vol. 23, Iss. 6, pp. 539-542.

Muhammed, N.S., Haq, B., Al Shehri, D., Al-Ahmed, A., Rahman, M.M., Zaman, E. 2022. A review on underground hydrogen storage: Insight into geological sites, influencing factors and future outlook. *Energy Reports*, 8, pp. 461-499. <https://doi.org/10.1016/j.egyr.2021.12.002>.

Myagkiy, A., Brunet, F., Popov, C., Krüger, R., Guimarães, H., Sousa, R.S., Charlet, L., Moretti, I. 2020a. H₂ dynamics in the soil of a H₂-emitting zone (São Francisco Basin, Brazil): Microbial uptake quantification and reactive transport modelling. *Applied Geochemistry*, 112, p.104474. <https://doi.org/10.1016/j.apgeochem.2019.104474>.

Myagkiy, A., Moretti, I., Brunet, F. 2020b. Space and time distribution of subsurface H₂ concentration in so-called “fairy circles”: Insight from a conceptual 2-D transport model. *BSGF-Earth Sciences Bulletin*, 191(1), p.13. <https://doi.org/10.1051/bsgf/2020010>.

Myers, M., White, C., Pejcic, B., Feitz, A., Roberts, J., Oh, Y.Y., Xu, L., Ricard, L., Michael, K., Avijegon, A. and Rachakonda, P.K. 2020. CSIRO In-Situ Lab: A multi-pronged approach to surface gas and groundwater monitoring at geological CO₂ storage sites. *Chemical Geology*, 545, p.119642.

- Naylor, M., Wilkinson, M. and Haszeldine, R.S. 2011. Calculation of CO₂ column heights in depleted gas fields from known pre-production gas column heights. *Marine and Petroleum Geology*, Vol.28. Iss. 5, pp. 1083-109
- Neal, C., Stanger, G. 1983. Hydrogen generation from mantle source rocks in Oman. *Earth and Planetary Science Letters*, Vol. 66, pp. 315-320. [https://doi.org/10.1016/0012-821X\(83\)90144-9](https://doi.org/10.1016/0012-821X(83)90144-9).
- Nelson, E., Hillis, R., Sandiford, M., Reynolds, S. and Mildren, S. 2006. Present-day state-of-stress of southeast Australia. *The APPEA Journal*, Vol. 46, pp.283-306.
- NH2E. 2022. Natural Hydrogen Energy LLC. <http://nh2e.com/> [Accessed 16/06/22].
- Novelli, P.C., Lang, P.M., Masarie, K.A., Hurst, D.F., Myers, R., Elkins, J.W. 1999. Molecular hydrogen in the troposphere: Global distribution and budget, *Journal of Geophysical Research*, Vol. 104, pp. 30427. doi:10.1029/1999JD900788.
- Nuclear Waste Storage. 2022. Low Strength Sedimentary Rocks (LSSR) – 2022. <https://www.youtube.com/watch?v=d1WJT1F6aMU>
- Nussbaum, C., Kloppenburg, A., Caër, T. and Bossart, P. 2017. Tectonic evolution around the Mont Terri rock laboratory, northwestern Swiss Jura: constraints from kinematic forward modelling, *Swiss J. Geosci.*, 110, 39–66.
- Ofoegbou, G.I., Painter, S., Chen, R., Randall, W.F., Ferril, D.A. 2001. Geomechanical and thermal effects on moisture flow at the proposed Yucca mountain nuclear waste repository. *Nuclear Technology*. Vol. 134, pp. 241–262.
- Olierook, H.K., Delle Piane, C., Timms, N.E., Esteban, L., Rezaee, R., Mory, A.J., Hancock, L. 2014a. Facies-based rock properties characterization for CO₂ sequestration: GSWA Harvey 1 well, Western Australia. *Marine and Petroleum Geology*, Vol. 50, pp. 83-102.
- Olierook, H.K., Timms, N.E., Hamilton, P.J. 2014b. Mechanisms for permeability modification in the damage zone of a normal fault, northern Perth Basin, Western Australia. *Marine and Petroleum Geology*, Vol. 50, pp. 130-147.
- Olson, J., Pollard, D. 1989. Inferring paleostresses from natural fracture patterns: a new method. *Geology* 17, 345–348.

- Olson, J., Pollard, D. 1991. The initiation and growth of en echelon veins. *J. Struct. Geol.* 13 (5), 595–608
- Oostingh, K.F., Jourdan, F., Matchan, E.L. and Phillips, D. 2017. $^{40}\text{Ar}/^{39}\text{Ar}$ geochronology reveals rapid change from plume-assisted to stress-dependent volcanism in the Newer Volcanic Province, SE Australia. *Geochemistry, Geophysics, Geosystems*, 18(3), pp.1065-1089.
- Owen, G., Moretti, M. and Alfaro, P. 2011. Recognising triggers for soft-sediment deformation: current understanding and future directions. *Sedimentary Geology*, 235(3-4), pp.133-140.
- Panfilov, M. 2010. Underground storage of Hydrogen: In-Situ self-organisation and Methane Generation. *Transport in Porous Media* 85(3), pp. 841–865.
- Panfilov, M. 2016. Underground and pipeline hydrogen storage, in Gupta, R., Basile, A., Nejat T. *Compendium of Hydrogen Energy – Hydrogen Storage, Transportation and Infrastructure*, Woodhead Publishing Series in Energy, Vol 2, pp. 91-115.
- Paterson, L., Boreham, C., Bunch, M., Dance, T., Ennis-King, J., Freifeld, B., Haese, R., Jenkins, C., LaForce, T., Raab, M., Singh, R. 2013. Overview of the CO₂CRC Otway residual saturation and dissolution test. *Energy Procedia*, Vol. 37, pp. 6140-6148.
- Peacock, D.C. and Sanderson, D.J. 1994. Geometry and development of relay ramps in normal fault systems. *AAPG bulletin*, 78(2), pp.147-165.
- Pearce, J., Czernichowski-Lauriol, I., Lombardi, S., Brune, S., Nador, A., Baker, J., Pauwels, H., Hatziyannis, G., Beaubien, S., Faber, E. 2004. A review of natural CO₂ accumulations in Europe as analogues for geological sequestration. Geological Society, London, Special Publications, 233(1), pp.29-41. <https://doi.org/10.1144/GSL.SP.2004.233.01.04>.
- Pearce, J.M., Holloway, S., Wacker, H., Nelis, M.K., Rochelle, C., Bateman, K. 1996. Natural occurrences as analogues for the geological disposal of carbon dioxide. *Energy Conversion and Management*, 37(6-8), pp.1123-1128. [https://doi.org/10.1016/0196-8904\(95\)00309-6](https://doi.org/10.1016/0196-8904(95)00309-6).
- Pei, Y., Paton, D.A., Knipe, R.J. and Wu, K. 2015. A review of fault sealing behaviour and its evaluation in siliciclastic rocks. *Earth-Science Reviews*, Vol. 150, pp. 121-138.

Peng, S., Johnson, A.M. 1972, January. Crack growth and faulting in cylindrical specimens of Chelmsford granite. In *International Journal of Rock Mechanics and Mining Sciences & Geomechanics Abstracts*, Vol. 9, No. 1, pp. 37-86.

Person, M., Goodwin, L.B., Rawling, G., Connell, S. 2000. The evolution of fault-zone permeability and groundwater flow patterns within the Albuquerque Basin of the Rio Grande Rift, NM. *Journal of Geochemical Exploration*, Vol. 69-70, pp. 565-568.

Peters, K.E., Curry, D.J. and Kacwicz, M. 2012. An overview of basin and petroleum system modeling: Definitions and concepts.

Pevzner, R., Langhi, L., Shragge, J., Ziramov, S., Strand, J., Potter, T., Tertysnikov, K., Bona, A., Urosevic, M. 2015, *Advanced Processing and Analysis of South West Hub 3D Seismic Data*. ANLEC R&D Project 7-0314- 0231, p. 137.

Pevzner, R., Urosevic, M., Popik, D., Shulakova, V., Tertysnikov, K., Caspari, E., Correa, J., Dance, T., Kepic, A., Glubokovskikh, S., Ziramov, S. 2017. 4D surface seismic tracks small supercritical CO₂ injection into the subsurface: CO₂CRC Otway Project. *International Journal of Greenhouse Gas Control*, Vol. 63, pp. 150-157.

Pevzner, R., Urosevic, M., Tertysnikov, K., AlNasser, H., Caspari, E., Correa, J., Daley, T., Dance, T., Freifeld, B., Glubokovskikh, S., Greenwood, A. 2020. Active surface and borehole seismic monitoring of a small supercritical CO₂ injection into the subsurface: experience from the CO₂CRC Otway Project. In *Active Geophysical Monitoring* (pp. 497-522). Elsevier.

Piovan, S.E., Hodgson, M.E. 2017. How many Carolina bays? An analysis of Carolina bays from USGS topographic maps at different scales. *Cartography and Geographic Information Science*, Vol. 44, Iss. 4, pp. 310-326. <https://doi.org/10.1080/15230406.2016.1162670>.

Pittarello, L., Nestola, F., Viti, C., Crósta, A.P. and Koeberl, C. 2015. Melting and cataclastic features in shatter cones in basalt from the Vista Alegre impact structure, Brazil. *Meteoritics & Planetary Science*, 50(7), pp.1228-1243.

Pittman, E.D. 1981. Effect of fault-related granulation on porosity and permeability of quartz sandstones, Simpson Group (Ordovician) Oklahoma. *AAPG Bulletin*. Vol. 65, pp. 2381–2387.

Playford, P.E., Cockbain, A.E., Low, G.H. 1976. Geology of the Perth Basin, Western Australia. Geological Survey of Western Australia, Perth.

Prinzhofer, A., Cissé, C.S.T., Diallo, A.B. 2018. Discovery of a large accumulation of natural hydrogen in Bourakebougou (Mali). *International Journal of Hydrogen Energy*, Vol. 43, pp. 19315-19326.

Prinzhofer, A., Moretti, I., Francolin, J., Pacheco, C., d'Agostino, A., Werly, J., Rupin, F. 2019. Natural hydrogen continuous emission from sedimentary basins: The example of a Brazilian H₂-emitting structure. *International Journal of Hydrogen Energy*, Vol. 44, Iss. 12, pp. 5676-5685. <https://doi.org/10.1016/j.ijhydene.2018.08.193>.

Radioactive Waste Management. 2016a. National Geological Screening Guidance: Implementing Geological Disposal: Providing information on geology.

Radke, B., Champion, D.C., Gallagher, S.J., Wang, L., De Vleeschouwer, D., Kalinowski, A., Tenthorey, E., Urosevic, M. and Feitz, A. 2022. Geology, geochemistry and depositional history of the Port Campbell Limestone on the eastern flank of the Otway Basin, southeastern Australia. *Australian Journal of Earth Sciences*, 69(4), pp.509-538.

Rahman, M.J., Fawad, M., Choi, J.C. and Mondol, N.H. 2022. Effect of overburden spatial variability on field-scale geomechanical modeling of potential CO₂ storage site Smeaheia, offshore Norway. *Journal of Natural Gas Science and Engineering*, 99, p.104453.

Räss, L., Simon, N.S., Podladchikov, Y.Y. 2018. Spontaneous formation of fluid escape pipes from subsurface reservoirs. *Scientific Reports*, Vol. 8, pp. 1-11. <https://doi.org/10.1038/s41598-018-29485-5>.

Rath, A., Exner, U., Tschegg, C., Grasemann, B., Laner, R., Draganits, E. 2011. Diagenetic control of deformation mechanisms in deformation bands in a carbonate grainstone. *AAPG bulletin*, Vol. 95, Iss. 8, pp. 1369-1381.

Rawling, G.C. and Goodwin, L.B. 2003. Cataclasis and particulate flow in faulted, poorly lithified sediments. *Journal of Structural Geology*, 25(3), pp.317-331.

Rawling, G.C., Goodwin, L.B. 2006. Structural record of the mechanical evolution of mixed zones in poorly lithified sediments, Rio Grande rift, New Mexico, USA. *Journal of Structural Geology*, Vol. 28 Iss. 9, pp. 1623-1639

Rawling, G.C., Goodwin, L.B., Wilson, J.L. 2001. Internal architecture, permeability structure, and hydrologic significance of contrasting fault-zone types. *Geology*, Vol. 29, pp. 43-46.

Reches, Z.E., Lockner, D.A. 1994. Nucleation and growth of faults in brittle rocks. *Journal of Geophysical Research: Solid Earth*, Vol. 99, pp. 18159-18173.

Renard, F., Mair, K. and Gundersen, O. 2012. Surface roughness evolution on experimentally simulated faults. *Journal of Structural Geology*, 45, pp.101-112.

Ringrose, P. 2020. How to store CO₂ underground: Insights from early-mover CCS projects.

Roberts, J.J. and Stalker, L. 2020. What have we learnt about CO₂ leakage from CO₂ release field experiments, and what are the gaps for the future?. *Earth-Science Reviews*, 209, p.102939. <https://doi.org/10.1016/j.earscirev.2019.102939>.

Roberts, J.J., Bell, A.F., Wood, R.A. and Haszeldine, R.S. 2019a. Geospatial statistics elucidate competing geological controls on natural CO₂ seeps in Italy. *Geofluids*, Vol. 2019.

Roberts, J.J., Leplastrier, A., Feitz, A.J., Shipton, Z.K., Bell, A.F., Karolytè, R. 2019b. Structural controls on the location and distribution of CO₂ emission at a natural CO₂ spring in Daylesford, Australia. *International Journal of Greenhouse Gas Control*, Vol. 84, pp. 36-46. <https://doi.org/10.1016/j.ijggc.2019.03.003>.

Roberts, J.J., Stalker, L., Shipton, Z. and Burnside, N. 2018, October. What have we learnt about CO₂ leakage in the context of commercial-scale CCS?. In 14th Greenhouse Gas Control Technologies Conference Melbourne (pp. 21-26).

Roberts, J.J., Wilkinson, M., Naylor, M., Shipton, Z.K., Wood, R.A. and Haszeldine, R.S. 2017. Natural CO₂ sites in Italy show the importance of overburden geopressure, fractures and faults for CO₂ storage performance and risk management. Geological Society, London, Special Publications, Vol. 458, pp.181-211.

Roberts, J.J., Wood, R.A., Wilkinson, M. and Haszeldine, S. 2014. Surface controls on the characteristics of natural CO₂ seeps: implications for engineered CO₂ stores. *Geofluids*, Vol. 15, Iss. 3, pp. 453-463.

Rockwater Pty Ltd. 2015. Detailed Lithological Log, Southwest Hub Geosequestration, Harvey 2.

Rogers, C., van Ruth, P.J. and Hillis, R.R. 2008. Fault reactivation in the Port Campbell Embayment with respect to carbon dioxide sequestration, Otway Basin, Australia. Geological Society, London, Special Publications, Vol. 306, pp. 201-214.

Rohmer, J., Nguyen, T.K. and Torabi, A. 2015. Off-fault shear failure potential enhanced by high-stiff/low-permeable damage zone during fluid injection in porous reservoirs. Geophysical Journal International, 202(3), pp.1566-1580.

Romano, C.R., Zahasky, C., Garing, C., Minto, J.M., Benson, S.M., Shipton, Z.K. and Lunn, R.J. 2020. Subcore scale fluid flow behaviour in a sandstone with cataclastic deformation bands. Water Resources Research, Vol. 56. Iss. 4, p. e2019WR026715.

Romeiro-Silva, P. C., Zalán, P.V. 2005. Contribuição da sísmica de reflexão na determinação do limite oeste do cráton do são francisco. In: simpósio sobre o cráton do são francisco, 3., 2005, salvador. Anais. Salvador: sociedade brasileira de geologia. pp. 44-47.

Rotevatn, A., Thorsheim, E., Bastesen, E., Fossmark, H.S., Torabi, A., Sælen, G. 2016. Sequential growth of deformation bands in carbonate grainstones in the hangingwall of an active growth fault: Implications for deformation mechanisms in different tectonic regimes. Journal of Structural Geology, Vol. 90, pp. 27-47.

Rutter, E.H. 1983. Pressure solution in nature, theory and experiment. Journal of the Geological Society, Vol. 140, Iss. 5, pp. 725-740.

Rutter, E.H., Hadizadeh, J. 1991. On the influence of porosity on the low-temperature brittle—ductile transition in siliciclastic rocks. Journal of Structural Geology, Vol. 13, Iss. 5, pp. 609-614.

Ruzicka, A., Killgore, M., Mittlefehldt, D.W. and Fries, M.D. 2005. Portales Valley: Petrology of a metallic-melt meteorite breccia. Meteoritics & Planetary Science, 40(2), pp.261-295.

Salvini, F., Billi, A., Wise, D.U. 1999. Strike-slip fault-propagation cleavage in carbonate rocks: the Mattinata Fault Zone, Southern Apennines, Italy. Journal of Structural Geology, Vol. 21, Iss. 12, pp. 1731-1749.

Sato, M., Sutton, A.J., McGee, K.A., Russell-Robinson, S. 1986. Monitoring of hydrogen along the San Andreas and Calaveras faults in central California in 1980–1984. *Journal of Geophysical Research: Solid Earth*, Vol. 91, pp. 12315-12326. <https://doi.org/10.1029/JB091iB12p12315>.

Schuster, K., Amann, F., Yong, S., Bossart, P. and Connolly, P. 2018. High-resolution mini-seismic methods applied in the Mont Terri rock laboratory (Switzerland). *Mont Terri Rock Laboratory, 20 Years: Two Decades of Research and Experimentation on Claystones for Geological Disposal of Radioactive Waste*, pp.215-233.

Sempere, J., Mac Donald, K. 1986. Overlapping spreading centers: implications from crack growth simulation by the displacement discontinuity method. *Tectonics* 5, 151–163

Serno, S., Johnson, G., LaForce, T.C., Ennis-King, J., Haese, R.R., Boreham, C.J., Paterson, L., Freifeld, B.M., Cook, P.J., Kirste, D., Haszeldine, R.S. 2016. Using oxygen isotopes to quantitatively assess residual CO₂ saturation during the CO₂CRC Otway Stage 2B Extension residual saturation test. *International Journal of Greenhouse Gas Control*, Vol. 52, pp. 73-83.

Sheng, W. 2020. A revisit of Navier–Stokes equation. *European Journal of Mechanics-B/Fluids*, 80, pp.60-71.

Sherwood Lollar, B., Lacrampe-Couloume, G., Voglesonger, K., Onstott, T.C., Pratt, L.M., Slater, G.F. 2008. Isotopic signatures of CH₄ and higher hydrocarbon gases from Precambrian Shield sites: A model for abiogenic polymerization of hydrocarbons. *Geochimica et Cosmochimica Acta*, 72, 4778–4795, <https://doi.org/10.1016/j.gca.2008.07.004>.

Sherwood Lollar, B., Onstott, T.C., Lacrampe-Couloume, G., Ballentine, C.J. 2014. The contribution of the Precambrian continental lithosphere to global H₂ production. *Nature*, 516(7531), pp.379-382. <https://doi.org/10.1038/nature14017>.

Sherwood Lollar, B., Westgate, T.D., Ward, J.A., Slater, G.F., Lacrampe-Couloume, G. 2002. Abiogenic formation of alkanes in the Earth’s crust as a minor source for global hydrocarbon reservoirs. *Nature*, 416, 522–524, <https://doi.org/10.1038/416522a>.

Shi, Z., Jessen, K. and Tsotsis, T.T. 2020. Impacts of the subsurface storage of natural gas and hydrogen mixtures. *International Journal of Hydrogen Energy*, 45(15), pp.8757-8773.

Shipton, Z.K., Soden, A.M., Kirkpatrick, J.D., Bright, A.M. and Lunn, R.J. 2006. How thick is a fault? Fault displacement-thickness scaling revisited. In Abercrombie, R. (Eds) *Earthquakes: Radiated Energy and the Physics of Faulting*, pages pp. 193-198. AGU (2006)

Shipton, Z., Evans, J., Kirchner, D., Kolesar, P., Williams, A., Heath, J. 2004. Analysis of CO₂ leakage through low-permeability faults from natural reservoirs in the Colorado Plateau, southern Utah. In: Baines, S., Worden, R. (Eds.), *Geological Storage of Carbon Dioxide*. Vol. 233 of Special Publications. Geological Society, London, pp. 43–58.

Shipton, Z.K. and Cowie, P.A. 2003. A conceptual model for the origin of fault damage zone structures in high-porosity sandstone. *Journal of Structural Geology*, 25(3), pp.333-344.

Shipton, Z.K., Cowie, P.A. 2001. Damage zone and slip-surface evolution over mm to km scales in high-porosity Navajo sandstone, Utah. *Journal of Structural Geology*. Vol. 23, pp. 1825-1844.

Shipton, Z.K., Roberts, J.J., Comrie, E.L., Kremer, Y., Lunn, R.J. and Caine, J.S. 2020. Fault fictions: systematic biases in the conceptualization of fault-zone architecture. *Geological Society, London, Special Publications*, Vol. 496, pp. 125-143.

Sibson, R.H., 1977. Fault rocks and fault mechanisms. *Journal of the Geological Society*, 133(3), pp.191-213.

Sigda, J.M., Goodwin, L.B., Mozley, P.S., Wilson, J. 1999. Permeability alteration in small-displacement faults in poorly lithified sediments: Rio Grande Rift, central New Mexico. In: Haneberg, W.C., Mozley, P.S., Casey Moore, J., Goodwin, L.B. (Eds.), *Faults and Subsurface Fluid Flow in the Shallow Crust*, Vol. 113. American Geophysical Union, Washington D. C., pp. 51–68.

Sigda, J.M., Wilson, J.L. 2003. Are faults preferential flow paths through semiarid and arid vadose zones? *Water Resources Research*. Vol. 39. Iss. 8, 1225.

Singleton O P, Joyce E B, 1969. Cainozoic volcanicity in Victoria. Geol Soc Aust Spec Pub, 2: 145-154.

Smith, D.A. 1980. Sealing and non-sealing faults in Louisiana Gulf Coast basins. AAPG Bulletin, Vol. 64, pp. 145–172.

Snæbjörnsdóttir, S.Ó., Sigfússon, B., Marieni, C., Goldberg, D., Gislason, S.R. and Oelkers, E.H. 2020. Carbon dioxide storage through mineral carbonation. Nature Reviews Earth & Environment, 1(2), pp.90-102.

Solum, J.G. and Huisman, B.A.H. 2017. Toward the creation of models to predict static and dynamic fault-seal potential in carbonates. Petroleum Geoscience, Vol. 23, pp.70-91.

Song, T., Cawood, P.A. 1999. Multistage deformation of linked fault systems in extensional regions: an example from the northern Perth Basin, Western Australia. Australian Journal of Earth Sciences, Vol. 46, Iss. 6, pp. 897-903.

Sorkhabi, R., Tsuji, Y. 2005. Faults, Fluid Flow & Petroleum Traps. Vol. 85 of AAPG Memoir. American Association of Petroleum Geologists.

Span, R., Wagner, W. 1996. A New Equation of State for Carbon Dioxide Covering the Fluid Region from the Triple-Point Temperature to 1100 K at Pressures up to 800 MPa, J. Phys. Chem. Ref. Data, Vol. 25, No. 6.

Sperrevik, S., Gillespie, P.A., Fisher, Q.J., Halvorsen, T., Knipe, R.J. 2002. Empirical estimation of fault rock properties, Norwegian Petroleum Society Special Publications, Vol. 11, pp. 109-125.

Stalker, L., Boreham, C., Unterschultz, J., Freifeld, B., Perkins, E., Schacht, U., Sharma, S. 2009. Geochemical monitoring at the CO2CRC Otway Project: tracer injection and reservoir fluid acquisition. Energy Procedia, Vol. 1, pp. 2119-2125.

Stalker, L., Myers, J., Michael, K., Hortle, A., Avijegon, A., Ricard, L., Myers, M., Tertysnikov, K., Pevzner, R., Strand, J. and Pervukhina, M. 2021. Lessons learned: the first In-Situ laboratory fault injection test.

Stalker, L., Roberts, J., Mabon, L., Hartley, P.G. 2022. Communicating leakage risk in the hydrogen economy: lessons already learned from geoenery industries. *Frontiers in Energy Research*.

Stalker, L., Talukder, A., Strand, J., Josh, M., Faiz, M. 2022. Gold (hydrogen) rush: risks and uncertainties in exploring for naturally occurring hydrogen. *The APPEA Journal*, 62(1), pp.361-380.

Stephenson, M.H., Manning, D.A., Spence, M.J., Stalker, L., Shipton, Z.K. and Monaghan, A.A. 2022. Role of subsurface geo-energy pilot and demonstration sites in delivering net zero. *Earth Science, Systems and Society*, 2, p.10045.

Stewart, I.S. and Hancock, P.L. 1990. What is a fault scarp?. *Episodes Journal of International Geoscience*, 13(4), pp.256-263.

Stewart, I.S. and Hancock, P.L., 1991. Scales of structural heterogeneity within neotectonic normal fault zones in the Aegean region. *Journal of Structural Geology*, 13(2), pp.191-204.

Stokes, J., Noble, R., Hill, J., and Olierook, H. 2018. Differentiating domains for CO₂ sequestration at Harvey-3 via integration of geochemistry, spectral mineralogy, facies modelling and wavelet tessellation analysis. Final Report. EP189682.

Storti, F., Billi, A. Salvini, F. 2003. Particle size distributions in natural carbonate fault rocks: insights for non-self-similar cataclasis. *Earth and Planetary Science Letters*, Vol. 206, Iss. 1-2, pp. 173-186.

Sugimoto, A., Inoue, T., Tayasu, I., Miller, L., Takeichi, S. and Abe, T. 1998. Methane and hydrogen production in a termite-symbiont system. *Ecological Research*, 13, 241–257, <https://doi.org/10.1046/j.1440-1703.1998.00262.x>.

Sugisaki, R., Ido, M., Takeda, H., Isobe, Y., Hayashi, Y., Nakamura, N., Satake, H., Mizutani, Y. 1983. Origin of hydrogen and carbon dioxide in fault gases and its relation to fault activity. *Geology*, Vol. 91, Iss. 3, pp. 239-258. <https://doi.org/10.1086/628769>.

Sukhanova, N.I., Trofimov, S.Y., Polyanskaya, L.M., Larin, N.V., Larin, V.N. 2013. Changes in the humus status and the structure of the microbial biomass in hydrogen exhalation places. *Eurasian Soil Science*, Vol. 46, Iss. 2, pp. 135-144. <https://doi.org/10.1134/S1064229313020142>.

- Suppe, J. and Medwedeff, D.A. 1990. Geometry and kinematics of fault-propagation folding. *Eclogae Geologicae Helvetiae*, 83(3), pp.409-454
- Tanner, D.C., Brandes, C. 2020. Introduction in Tanner, D.C., Brandes, C. (ed.). *Understanding Faults: Detecting, Dating and Modelling*. pp. 366.
- Tarkowski, R. 2019. Underground hydrogen storage: Characteristics and prospects, *Renewable and Sustainable Energy Reviews*, Vol. 105, pp. 86-94. <https://doi.org/10.1016/j.rser.2019.01.051>.
- Tarkowski, R. and Uliasz-Misiak, B. 2021. Use of underground space for the storage of selected gases (CH₄, H₂, and CO₂)—possible conflicts of interest. *gospodarka surowcami mineralnymi*, 37(1).
- Tassone, D.R., Holford, S.P., King, R., Tingay, M.R. and Hillis, R.R. 2017. Contemporary stress and neotectonics in the Otway Basin, southeastern Australia. *Geological Society, London, Special Publications*, Vol. 458, pp.49-88.
- Tenthorey, E., A. Feitz, A. Credo, M. Lavina, E. Coene, A. Idiart, and S. Jordana. 2019. "The CO₂CRC Otway Controlled CO₂ Release Experiment in a Fault: Geomechanical Characterisation Pre-Injection." In *Fifth International Conference on Fault and Top Seals*, vol. 2019, no. 1, pp. 1-5. European Association of Geoscientists & Engineers, 2019.
- Tenthorey, E., Cox, S.F. 2006. Cohesive strengthening of fault zones during the interseismic period: An experimental study. *Journal of Geophysical Research: Solid Earth*, Vol. 111(B9).
- Tenthorey, E., Dance, T., Cinar, Y., Ennis-King, J., Strand, J. 2014. Fault modelling and geomechanical integrity associated with the CO₂CRC Otway 2C injection experiment. *International Journal of Greenhouse Gas Control*, Vol. 30, pp. 72-85.
- Tenthorey, E., Feitz, A., Knackstedt, M., Dewhurst, D.N., Watson, M. 2022, October. The Otway CCS Fault Injection Experiment: Fault Analysis. In *Proceedings of the 16th Greenhouse Gas Control Technologies Conference (GHGT-16)* (pp. 23-24).
- Tenthorey, E., John, Z., & Nguyen, D. 2010. CRC-2 Extended Leak-Off and Mini-Frac Tests: Results and Implications. Report RPT10-2228: Cooperative Research Centre for Greenhouse Gas Technologies.

Tenthorey, E., Vidal-Gilbert, S., Backé, G., Puspitasari, R., Pallikathekathil, Z.J., Maney, B., Dewhurst, D.N. 2013. Modelling the geomechanics of gas storage: A case study from the Iona gas field, Australia, *International Journal of Greenhouse Gas Control*, 13, 138-148.

Thaysen, E.M., McMahon, S., Strobel, G.J., Butler, I.B., Ngwenya, B.T., Heinemann, N., Wilkinson, M., Hassanpouryouzband, A., McDermott, C.I., Edlmann, K. 2021. Estimating microbial growth and hydrogen consumption in hydrogen storage in porous media. *Renewable and Sustainable Energy Reviews*, 151, p.111481. <https://doi.org/10.1016/j.rser.2021.111481>.

Thomas, L. 1976. Geothermal resources in Australia. In: *Proc 2nd United Nations Symp Devel Use Geotherm Resour*, San Francisco, Washington D C: U S Government Printing Office, 1: 273-274.

Timms, N.E., Corbel, S., Olierook, H., Wilkes, P., Delle Piane, C., Sheldon, H., Alix, R., Horowitz, F., Wilson, M., Evans, K.A., Griffiths, C., Stütenbecker, L., Israni, S., Hamilton, P.J., Esteban, L., Cope, P., Evans, C., Pimienta, C., Dyt, C., Huang, X., Hopkins, J., Champion, D. 2012. Project 2: Geomodel. CSIRO Report. WA Geothermal Centre of Excellence, p. 188

Timms, N.E., Olierook, H.K., Wilson, M.E., Delle Piane, C., Hamilton, P.J., Cope, P. and Stütenbecker, L. 2015. Sedimentary facies analysis, mineralogy and diagenesis of the Mesozoic aquifers of the central Perth Basin, Western Australia. *Marine and Petroleum Geology*, Vol. 60, pp. 54-78.

Tingay, M., Muller, B., Reinecker, J. and Heidbach, O. 2006. State and origin of the present-day stress field in sedimentary basins: New results from the World Stress Map Project. In *Golden Rocks 2006, The 41st US Symposium on Rock Mechanics (USRMS)*.

Tondi, E. 2007. Nucleation, development and petrophysical properties of faults in carbonate grainstones: Evidence from the San Vito Lo Capo peninsula (Sicily, Italy). *Journal of Structural Geology*, Vol. 29, pp. 614–628,

Tondi, E., Antonellini, M., Aydin, A., Marchegiani, L., Cello, G. 2006. The role of deformation bands, stylolites and sheared stylolites in fault development in carbonate

grainstones of Majella Mountain, Italy. *Journal of Structural Geology*, Vol. 28, Iss. 3, pp. 376-391.

Tondi, E., Cilona, A., Agosta, F., Aydin, A., Rustichelli, A., Renda, P., Giunta, G. 2012. Growth processes, dimensional parameters and scaling relationships of two conjugate sets of compactive shear bands in porous carbonate grainstones, Favignana Island, Italy. *Journal of Structural Geology*, Vol. 37, pp. 53-64.

Torabi, A., Ellingsen, T.S.S., Johannessen, M.U., Alaei, B., Rotevatn, A. and Chiarella, D. 2020. Fault zone architecture and its scaling laws: where does the damage zone start and stop?. *Geological Society, London, Special Publications*, 496(1), pp.99-124.

Torabi, A., Johannessen, M.U. and Ellingsen, T.S.S. 2019. Fault core thickness: Insights from siliciclastic and carbonate rocks. *Geofluids*, Vol. 2019

Truche, L., Joubert, G., Dargent, M., Martz, P., Cathelineau, M., Rigaudier, T., Quirt, D. 2018. Clay minerals trap hydrogen in the Earth's crust: evidence from the Cigar Lake uranium deposit, Athabasca. *Earth and Planetary Science Letters*, 493, pp. 186-197. <https://doi.org/10.1016/j.epsl.2018.04.038>.

Tueckmantel, C., Fisher, Q.J., Manocchi, T., Skachkov, S., Grattoni, C.A. 2012. Two-phase fluid flow properties of cataclastic fault rocks: implications for CO₂ storage in saline aquifers. *Geology*. Vol. 40, pp. 39–42.

Ugarte, E.R. and Salehi, S. 2022. A review on well integrity issues for underground hydrogen storage. *Journal of Energy Resources Technology*, 144(4), p.042001.

Underschultz, J., Boreham, C., Dance, T., Stalker, L., Freifeld, B., Kirste, D., Ennis-King, J. 2011. CO₂ storage in a depleted gas field: An overview of the CO₂CRC Otway Project and initial results. *International Journal of Greenhouse Gas Control*, Vol. 5, Iss. 4, pp. 922-932.

UNFCCC. 2023a. Nationally determined contributions under the Paris Agreement-Synthesis report by the secretariat. In *Proceedings of the Conference of the Parties serving as the meeting of the Parties to the Paris Agreement (CMA)*. FCCC/PA/CMA/2023/12

UNFCCC. 2023b. Long-term low-emission development strategies. Synthesis report by the secretariat. In Proceedings of the Conference of the Parties serving as the meeting of the Parties to the Paris Agreement Third (CMA). FCCC/PA/CMA/2023/10

United Nations. 2015. Paris Agreement.

Vacquand, C., Deville, E., Beaumont, V., Guyot, F., Sissmann, O., Pillot, D., Arcilla, C. Prinzhofer, A. 2018. Reduced gas seepages in ophiolitic complexes: evidences for multiple origins of the H₂-CH₄-N₂ gas mixtures. *Geochimica et Cosmochimica Acta*, Vol. 223, pp. 437-461. <https://doi.org/10.1016/j.gca.2017.12.018>.

Vidal-Gilbert, S., Tenthorey, E., Dewhurst, D., Ennis-King, J., Van Ruth, P. and Hillis, R. 2010. Geomechanical analysis of the Naylor Field, Otway Basin, Australia: Implications for CO₂ injection and storage. *International Journal of Greenhouse Gas Control*, 4(5), pp.827-839.

Voitov, G.I., Nikolaev, I.N., Utochkin, Yu.A., Rudakov, V.P., Ishankuliev, D.I. 1995. On the flow of hydrogen into the surface troposphere in geodynamically different geostructural zones of the Earth. In *Dokl. RAS*, Vol. 344, pp. 110-114.

Wallace, M.W., Holdgate, G.R., Daniels, J., Gallagher, S.J., Smith, A. 2002. Sonic velocity, submarine canyons, and burial diagenesis in Oligocene-Holocene cool-water carbonates, Gippsland Basin Southeast Australia. *AAPG Bull.* 86, 1593–1607.

Walsh, J.J., Waterson, J. 1989. Displacement gradients on fault surfaces, *Journal of Structural Geology*, Vol. 11, Iss. 3, pp. 307-316

Wang, L., Green, C., Radke, B., Tenthorey, E., Ennis-King, J. and Feitz, A. 2020. SRD3. 3 Prediction and verification of shallow CO₂ migration Phase 2: Static model version 2 and CO₂ migration simulations. CO₂CRC Report No. RPT20-6181.

Wang, Z., Palaz, I., Marfurt, K.J. 1997. Seismic properties of carbonate rocks. *Carbonate Seismology*, Vol. 6, pp. 29-52.

Warr, O., Young, E.D., Giunta, T., Kohl, I.E., Ash, J.L., Lollar, B.S. 2021. High-resolution, long-term isotopic and isotopologue variation identifies the sources and sinks of methane in a deep subsurface carbon cycle. *Geochimica et Cosmochimica Acta*, 294, pp.315-334. <https://doi.org/10.1016/j.gca.2020.12.002>

- Waters, C., Schofield, D., Evans, D.E., Millward, D., Haslam, R., O Dochartaigh, B., Bloomfield, J.P., Lee, J.R., Baptie, B., Shaw, R.P., Bide, T. 2018. National geological screening: Northern England region.
- Watson, M.N., Boreham, C.J., Tingate, P.R. 2004. Carbon dioxide and carbonate cements in the Otway Basin: implications for geological storage of carbon dioxide. *The APPEA Journal*, Vol. 44, pp. 703-720.
- Weber, K.J., Mandl, G.J., Pilaar, W.F., Lehner, B.V.F. and Precious, R.G. 1978. The role of faults in hydrocarbon migration and trapping in Nigerian growth fault structures. *Offshore Technology Conference*, 8-11 May, Huston.
- Wibberley, C.A., Yielding, G. and Di Toro, G. 2008. Recent advances in the understanding of fault zone internal structure: a review. *Geological Society, London, Special Publications*, 299(1), pp.5-33.
- Willemsse, E.J., Peacock, D.C., Aydin, A. 1997. Nucleation and growth of strike-slip faults in limestones from Somerset, UK. *Journal of Structural Geology*, Vol. 19, Iss. 12, pp. 1461-1477.
- Wood, B.L. 1972. Metamorphosed ultramafites and associated formations near Milford Sound, New Zealand. *New Zealand Journal of Geology and Geophysics*, Vol. 15, pp. 88-128. <https://doi.org/10.1080/00288306.1972.10423948>.
- Woodcock, N.H. and Mort, K. 2008. Classification of fault breccias and related fault rocks. *Geological Magazine*, 145(3), pp.435-440.
- Woollands, M.A., Wong, D. (Eds.). 2001. *Petroleum Atlas of Victoria*. Victorian Department of Natural Resources and Environment.
- Wu, H., Pollard, D. 1995. An experimental study of the relationships between joint spacing and layer thickness. *J. Struct. Geol.* 16 (6), 887–905
- Yekeen, N., Padmanabhan, E., Thenesh, A., Sevoo, L., Kamalarasan, A., Kanesen, L. and Okunade, O.A. 2020. Wettability of rock/CO₂/brine systems: A critical review of influencing parameters and recent advances. *Journal of Industrial and Engineering Chemistry*, 88, pp.1-28.

- Yielding, G., Freeman, B., Needham, D.T. 1997. Quantitative fault seal prediction. *American Association of Petroleum Geologists Bulletin*. Vol. 81, Iss. 6, pp. 897–917.
- Yielding, G.P.B.S., Bretan, P. and Freeman, B. 2010. Fault seal calibration: a brief review. *Geological Society, London, Special Publications*, Vol. 347, pp. 243-255.
- Yuce, G., Italiano, F., D'Alessandro, W., Yalcin, T.H., Yasin, D.U., Gulbay, A.H., Ozyurt, N.N., Rojay, B., Karabacak, V.O.L.K.A.N., Bellomo, S., Brusca, L. 2014. Origin and interactions of fluids circulating over the Amik Basin (Hatay, Turkey) and relationships with the hydrologic, geologic and tectonic settings. *Chemical Geology*, Vol. 388, pp. 23-39. <https://doi.org/10.1016/j.chemgeo.2014.09.006>.
- Zawawi, M.H., Saleha, A., Salwa, A., Hassan, N.H., Zahari, N.M., Ramli, M.Z. and Muda, Z.C. 2018, November. A review: Fundamentals of computational fluid dynamics (CFD). In *AIP conference proceedings* (Vol. 2030, No. 1). AIP Publishing.
- Zgonnik, V. 2020. The occurrence and geoscience of natural hydrogen: A comprehensive review. *Earth-Science Reviews*, 203, p.103140.
- Zgonnik, V., Beaumont, V., Deville, E., Larin, N., Pillot, D. and Farrell, K.M. 2015. Evidence for natural molecular hydrogen seepage associated with Carolina bays (surficial, ovoid depressions on the Atlantic Coastal Plain, Province of the USA). *Progress in Earth and Planetary Science*, Vol. 2, pp. 1-31. <https://doi.org/10.1186/s40645-015-0062-5>.
- Zgonnik, V., Beaumont, V., Larin, N., Pillot, D., Deville, E. 2019. Diffused flow of molecular hydrogen through the Western Hajar mountains, Northern Oman. *Arabian Journal of Geosciences*, Vol. 12, Iss. 3, pp. 1-10. <https://doi.org/10.1007/s12517-019-4242-2>.
- Zhang, M. and Bachu, S. 2011. Review of integrity of existing wells in relation to CO₂ geological storage: What do we know?. *International Journal of Greenhouse Gas Control*, 5(4), pp.826-840.
- Zimmerman, P.R., Greenberg, J.P., Wandiga, S.O., Crutzen, P.J. 1982. Termites: A Potentially Large Source of Atmospheric Methane, Carbon Dioxide, and Molecular Hydrogen. *Science*, 218, 563–565, <https://doi.org/10.1126/science.218.4572.563>

Appendix 1 – In-Situ Lab: Fluid flow modelling

Assumptions

Geological modelling of the subsurface at the Harvey-2 borehole indicates that there are many (~19) equally possible subsurface geological scenarios for the hydraulic properties of the fault zone and surrounding lithologies. These scenarios were created based on available data (e.g., porosity and permeability, fault displacement, fault properties). Porosity and permeability data for the Yalgorup Member were taken from data collected from the Harvey (Harvey-1 and Harvey-3) and Pinjarra-1 borehole (Bourdet *et al.*, 2019; Langhi *et al.*, 2019) which show well developed similarities in porosity and permeability. There are no measurements of porosity or permeability in the Eneabba sandstones at the injection depth (~340m). Bourdet *et al.*, (2019) suggested that the Eneabba sandstones share similar properties to the Yalgorup Member sandstones, as both are interpreted to be point bar sandstones, and as a result the Eneabba sandstones were assumed to have similar hydraulic properties (CSIRO, 2019). The fault displacement was estimated to be 100m or less at the injection depth due to the decreasing displacement gradient with depth (see Section 3.1.3), however much of its characteristic and properties were not well defined and there was no defined hanging-wall bounding surface (CSIRO, 2019).

Model design

The flow simulation models had a central column representing the Harvey-2 lithology that remains unchanged. The modelled facies consisted of a sandstone, sand palaeosol (with moderate permeability), vertisol (low permeability silty-muddy layers) and silty-muddy Leederville Formation (CSIRO, 2019). Multiple slip surfaces (faults) were incorporated into the model in the areas with more disrupted rock layers.

Different fault displacement scenarios were modelled to account for the variability in the fault displacement down-dip (ranging from ~50m-1600m) (CSIRO, 2019). Fault permeabilities were modelled for high and low permeability scenarios to incorporate uncertainty in the fault properties.

Reservoir parameters

The reservoir model was created using Tempest-MORE set up of black oil with CO₂ dissolution in formation water (CSIRO, 2019). CO₂ properties were derived from Span and Wagner (1996) and a solubility model from Chang *et al.* (1998). Values for CO₂ properties at the relevant injection depth was calculated using the National Institute of Standards and Technology database. Here it was noted that the CO₂ would be in gas phase, buoyant and therefore in the viscosity range which favours viscous fingering (CSIRO, 2019). The trapping style of the CO₂ is assumed to be initially by dissolution, followed by residual trapping with increasing time since injection. Full details of parameters, including extensive plots, can be viewed in the In-Situ Lab Final Report (CSIRO, 2019).

Results

Results were analysed using Tempest-View, the Matlab Reservoir Visualisation Toolbox 2017b (Lie *et al.*, 2012) and CSIRO's own post-processing and visualisation algorithms (CSIRO, 2019).

Three simulations were modelled for each of the 19 geological scenarios, each with varying injection strategies:

1. Injection Rate: 1 tonne per day Total injected CO₂ = 10 tonnes
2. Injection Rate: 5 tonnes per day. Total injected CO₂ = 50 tonnes
3. Injection Rate: 10 tonnes per day: Total injected CO₂ = 100 tonnes

In all cases injection was for 10 days and monitoring was for 60 days. All scenarios showed similar trends in results.

The models used simple numerical simulations (e.g., isothermal simulations, black-oil simulations) and do not consider very low permeability scenarios or lack of injectivity (CSIRO, 2019). CSIRO (2019) reported that many of these limitations are due to time constraints due to changes in the scope of the project.

Appendix 2 – In-Situ Lab: Environmental monitoring

Monitoring the In-Situ Lab experiment

The In-Situ Lab project had several monitoring programmes covering both surface and subsurface activities. The monitoring programme had some key aims, which primarily focused on detecting contamination from operational activities or the CO₂ injection experiment itself, to ensure that there were no unwanted negative environmental effects. The monitoring was also used to collect data to assess the migration of CO₂ syn- and post-injection in the subsurface (CSIRO, 2019).

Surface gas

There was an extensive surface gas monitoring programme undertaken at the In-Situ Lab site (Figure A2. 1).

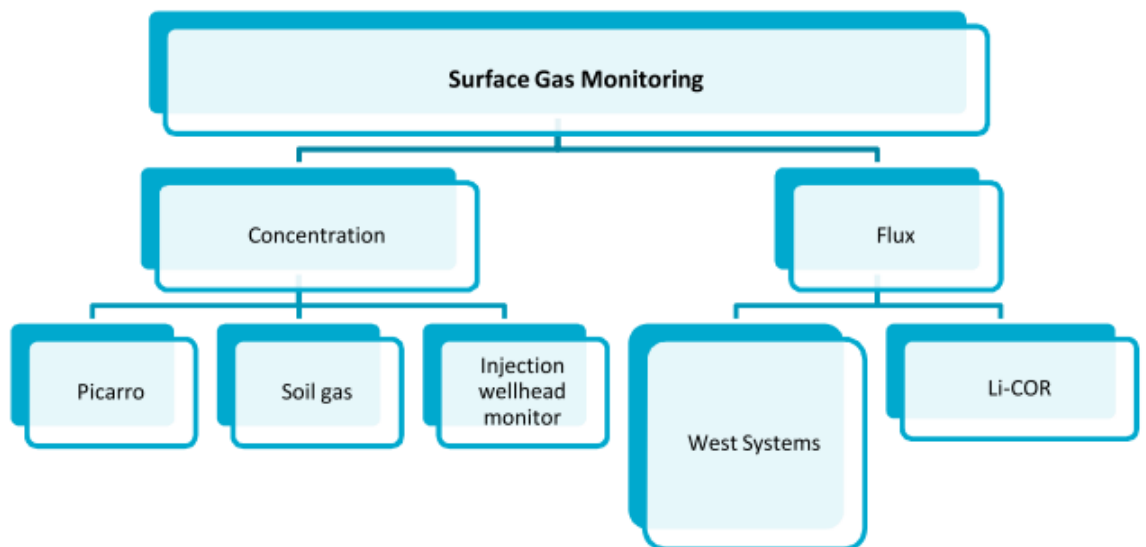


Figure A2. 1 – Monitoring techniques used and corresponding equipment (CSIRO, 2019).

This monitoring programme started around three weeks prior to injection to establish baseline conditions around the Harvery-2 site. Besides one documented well leakage incident, there was no notable leakage of CO₂. CO₂ levels remained close to measured baseline levels (CSIRO, 2019).

Groundwater

Groundwater monitoring was conducted from the groundwater well, stock bore, the injection well and the observation well (In-Situ Lab OB-1). This monitoring included water level and electrical conductivity monitoring. Samples were analysed for anions, cations, alkalinity, dissolved CO₂, carbon isotopic composition, total inorganic carbon (TIC), total carbon (TC) and total organic carbon (TOC)

Groundwater monitoring indicates that the aquifers in the vicinity of the In-Situ Lab site are not potable. When groundwater observations and analysis were compared to regional data this indicated that there were no impacts on groundwater levels or any negative environmental effects from CO₂ injection activities (CSIRO, 2019).

Pressure and temperature

Pressure and temperature equipment were installed in all three wells (injection, groundwater and monitoring well).

Pressure and temperature monitoring equipment was used to identify CO₂ breakthrough time. This equipment also helped to characterise the minor leakage event which occurred. Overall, this equipment was noted to have performed beyond expectation and helped to quantify the CO₂ plume migration in terms of timing and distance travelled (CSIRO, 2019)

The pressure and temperature observations highlight that the CO₂ injection caused no unexpected environmental effects.

Seismic

Active seismic techniques were used for characterisation and monitoring surveys. The characterisation survey was a 3D vertical seismic profile (VSP) which aimed to constrain formation depths and fault geometry, to inform potential migration of injected CO₂. The seismic monitoring allowed the detection of the CO₂ during injection and tracking of its migration in the subsurface through time-lapse seismic data.

Three passive autonomous continuous seismic recorders were also installed at the Harvey site. These monitored injection related seismicity and any other relevant seismic activity (CSIRO, 2019). The passive seismic array also recorded the active seismic

activities and were additionally validated using far-field earthquakes which were also detected.

Electrical Resistivity Imaging (ERI)

The electrode array installed in the Harvey-2 well measured apparent resistivity in the injection well. It is known that the injection of CO₂ changes rock resistivity (Börner *et al.*, 2013). The ERI survey conducted at the Harvey-2 site was concluded as not sufficient to image differences between pre- and post-injection images. This is postulated to be due to the small CO₂ plume volume and the migration of the plume through narrower layers than expected (CSIRO, 2019).

Other monitoring (logging, petrophysical and time-lapse)

Open hole logging operations included ATV image logs, density logs, neutron-laterlog-deviation-temperature logs, pulsed neutron logs, borehole magnetic resonance, multi finger calliper, positive resistivity logs, full-wave sonic logs and single-arm calliper logs (CSIRO, 2019). Not all logs were run the full well length of the monitoring well In-Situ Lab OB-1.

These logs allowed petrophysical analysis (e.g., porosity and permeability data) to be compared to the Harvey-2 laboratory measurements and core samples to create a more complete and accurate quantification of characteristics.

Much of the logging has variable results, full details are in CISRO In-Situ Lab Final Report (2019).

Appendix 3 – OITC – Stage 1 and Stage 2 Summaries

Progress and results from stages 1-3

Stage 1 – Storage of CO₂ in a Depleted Gas Formation

Stage 1 focused on extracting natural CO₂ gas, transporting it, and storing it in a depleted gas reservoir.

Background and planning of Stage 1 operations

The Otway Basin has several natural gas (methane) and natural CO₂ fields (Figure A3. 1; Dance, 2013). The main gas bearing reservoir in the onshore of the Otway Basin is the Waarre Formation (Jenkins *et al.*, 2012). CO2CRC utilised the Buttress CO₂ field as a source of natural CO₂. The Naylor gas field is a depleted natural gas reservoir. This means the CO2CRC site is ideally placed, with the ability to exploit both a CO₂ source (Buttress) and a CO₂ store (Naylor) adjacent to each other.

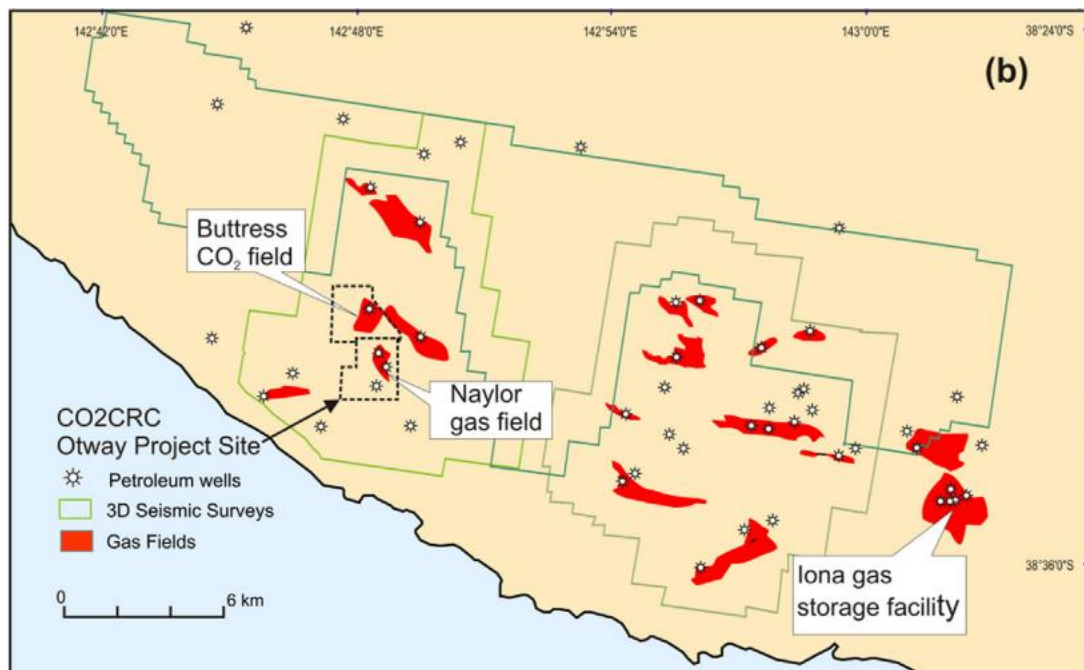


Figure A3. 1 – Petroleum wells and gas fields in the vicinity of the CO2CRC Otway Project site. 3D seismic surveys conducted as part of the site research are also shown (Dance, 2013).

The Buttress CO₂ field had around 75% CO₂, 2% CH₄ and 4% other components, which were primarily heavy hydrocarbons (Cook, 2013). The CO₂ is of volcanic origin, shown by the isotopic composition (Boreham *et al.*, 2011). It has been estimated that the CO₂ influx occurred during the Pleistocene, with an age range of between 2Ma to up to 5,000

years ago (Watson *et al.*, 2004). The high CO₂ content led to the methane gas being unproduced (Boreham *et al.*, 2011).

The Naylor field was depleted between June 2002 and October 2003 (Jenkins *et al.*, 2012), with production stopping after the well started producing water (Dance, 2014) and the well became economically unviable. The use of the Naylor provided benefits as there was additional data from its operations (Jenkins *et al.*, 2012). The original Naylor-1 exploratory well was repurposed and used as a monitoring well for the injected CO₂.

Prior to any operational phases of Stage 1, there was a significant programme of geological site characterisation, coupled with storage system simulations (Dance *et al.*, 2009; Underschultz *et al.*, 2011).

A new well CRC-1 was drilled down one flank of the Naylor geological trapping structure (Bunch *et al.*, 2013), as part of the first stage of the project. This was completed in April 2007 and provided a suitable injection well for the storage experiment. The target formation was the late Cretaceous Waarre C Formation at around 2055m depth (Underschultz *et al.*, 2011; Jenkins *et al.*, 2012). This formation is fault bounded on three sides against the over 300m thick Belfast Mudstone (Jenkins *et al.*, 2012), which forms a structural trap. The reservoir sandstone unit is between 25-30m thick, which is overlain by low-permeability units of the Flaxmans Formation and the Belfast Mudstone (Figure A3. 2 and A3. 3; Jenkins *et al.*, 2012).

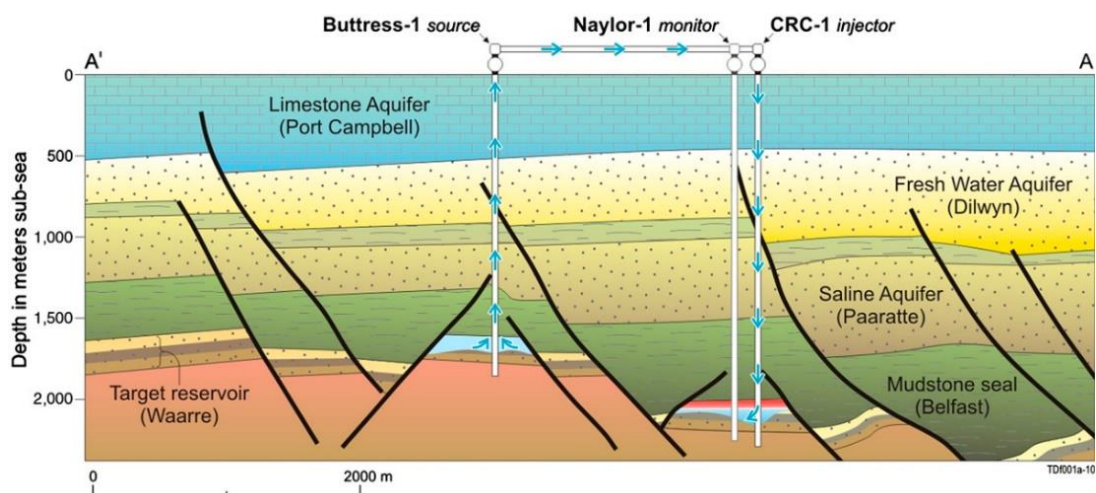


Figure A3. 2 – Cross section showing the Waarre C target storage reservoir and the Belfast Mudstone which acts as a regional seal. Black lines show faults (Underschultz *et al.*, 2011; Jenkins *et al.*, 2012).

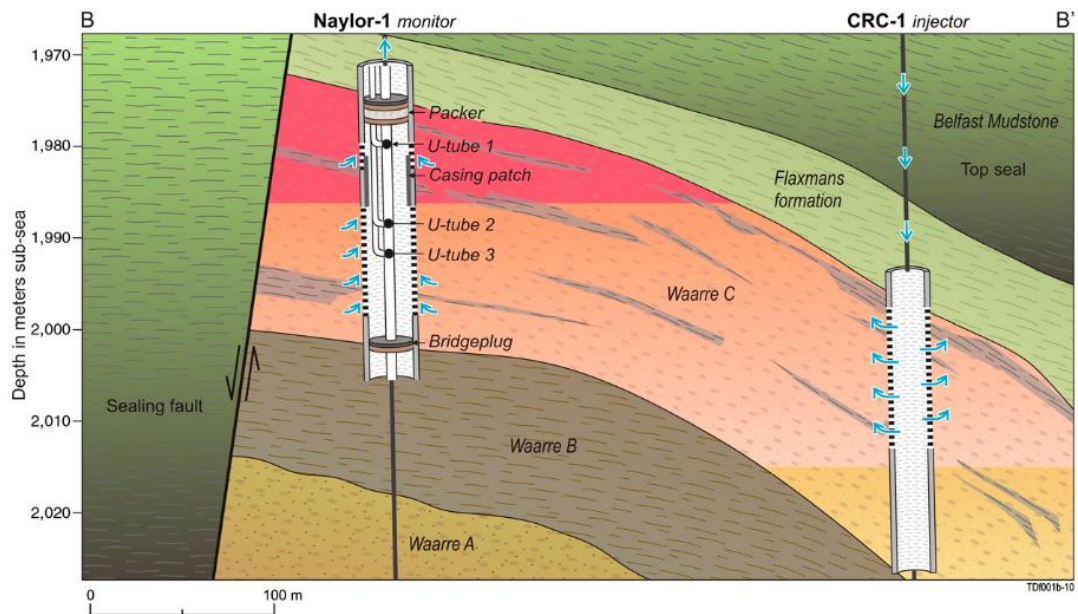


Figure A3. 3 – Injection (CRC-1) and monitoring (Naylor-1) wells (Underschultz *et al.*, 2011).

Injected CO₂ was first extracted from the Buttress field (Buttress-1), where it was dried and compressed before being transported around 2.25km to CRC-1 for injection (Boreham *et al.*, 2011; Bunch, 2013).

Monitoring was performed both pre- and post-CO₂ injection to allow a comparison of the results. Monitoring closest to the reservoir included time-lapse seismic to monitor the CO₂ plume, however it was noted that due to the residual methane in the reservoir, any changes would likely be subtle or unnoticeable (Jenkins *et al.*, 2012). The seismic would however be capable of detecting breaches of the seal and the migration of the CO₂ into overlying formations. The primary assurance monitoring techniques used included using groundwater, soil, gas and atmospheric monitoring to detect leakage further from the reservoir (Jenkins *et al.*, 2012).

The direct measurement of fluid samples from the reservoir (via Naylor-1) was the primary method of assessing the containment of the injected CO₂ (Jenkins *et al.*, 2012). This was possible due to the U-tube fluid sampling equipment installed on the Naylor-1 well (Figure A3. 2 and A3. 3) and the use of tracers to enhance detection methods (Stalker *et al.*, 2009). Naylor-1 well also housed geophysical seismic monitoring equipment (Daley *et al.*, 2009).

Results from Stage 1

The injection of CO₂ via CRC-1 into the Waarre formation lasted around 16 months and around 65,000 tonnes of CO₂ were injected (Underschultz *et al.*, 2011; Bunch *et al.*, 2013). The injection was stopped at this stage as the project goals had been achieved and it had been successfully demonstrated that the CO₂ had accumulated without any indications of issues (Underschultz *et al.* 2011). The monitoring programme indicated that there was no effect on soil, groundwater, or the atmosphere due to the CO₂ injection (Jenkins *et al.*, 2012). The success of the first stage of the Otway project was also attributed to a good working relationship with the local community and government (Jenkins *et al.*, 2012).

Stage 2 – Storage of CO₂ in a Saline Formation

As Stage 1 of the Otway project demonstrated storage of CO₂ in a depleted gas reservoir, Stage 2 focused on storing CO₂ in the Paaratte Formation (a saline aquifer). This project aims to demonstrate non-structural trapping mechanisms (Dance and Paterson, 2016).

Background and planning of Stage 2 operations

Stage 2 of the project had three key phases:

- Phase 2A: Drilling and characterisation of a new injection well (CRC-2)
- Phase 2B: Developing an understanding of residual and dissolution trapping in saline formations, as well as the interactions with impurities. Well testing refinement.
- Phase 2C: Monitor injected CO₂ in a saline formation

Phases 2A and 2B are primarily appraisal phases to facilitate the injection and monitoring of CO₂ in phase 2C.

The Late Cretaceous Paaratte Formation (Figure A3. 2) is at a depth of around 1400m (600m shallower than the gas bearing Waarre Formation targeted in Stage 1). This aquifer has no structural closure and is lithologically heterogeneous (Paterson *et al.*, 2013). The formation thickness varies, but it is typically 400m thick and contains a complex interbedded series of high permeability sandstones and thin mud-rich lithologies (Paterson *et al.*, 2013; Tenthorey *et al.*, 2014; Dance and Paterson, 2016). It is

this reservoir heterogeneity that aims to be exploited for safe CO₂ storage (Dance and Paterson, 2016).

In 2009, a new injection well (CRC-2) was drilled into the Paaratte Formation (Cook *et al.*, 2013). This completed phase 2A of the project (Figure A3. 3). Phase 2B involved conducting a residual saturation and dissolution test. This test was conducted in 2011, lasting 10 days (Figure A3. 4 and A3. 5).

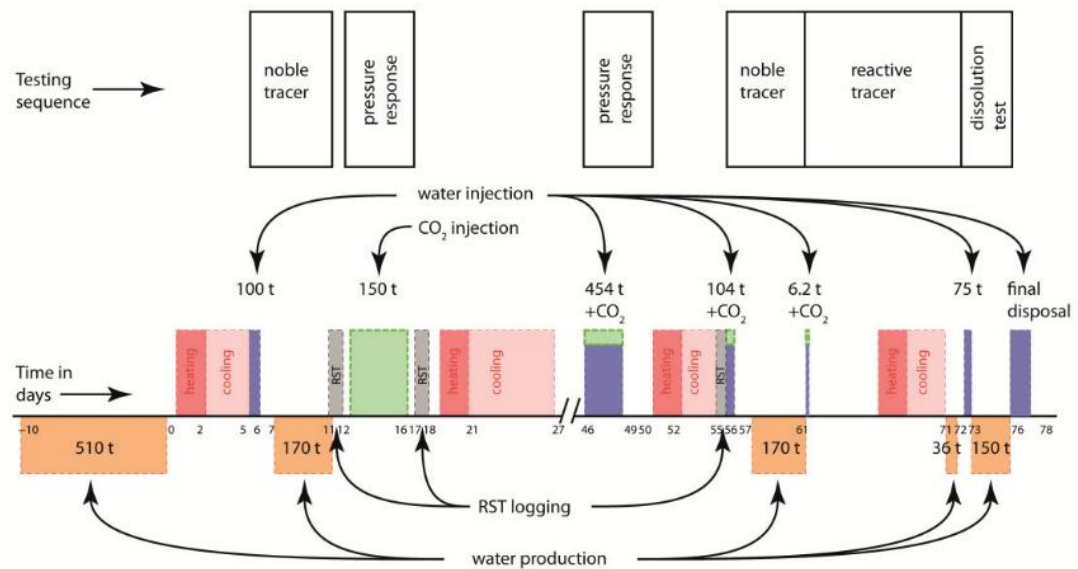


Figure A3.4 – Residual saturation and dissolution test sequence.

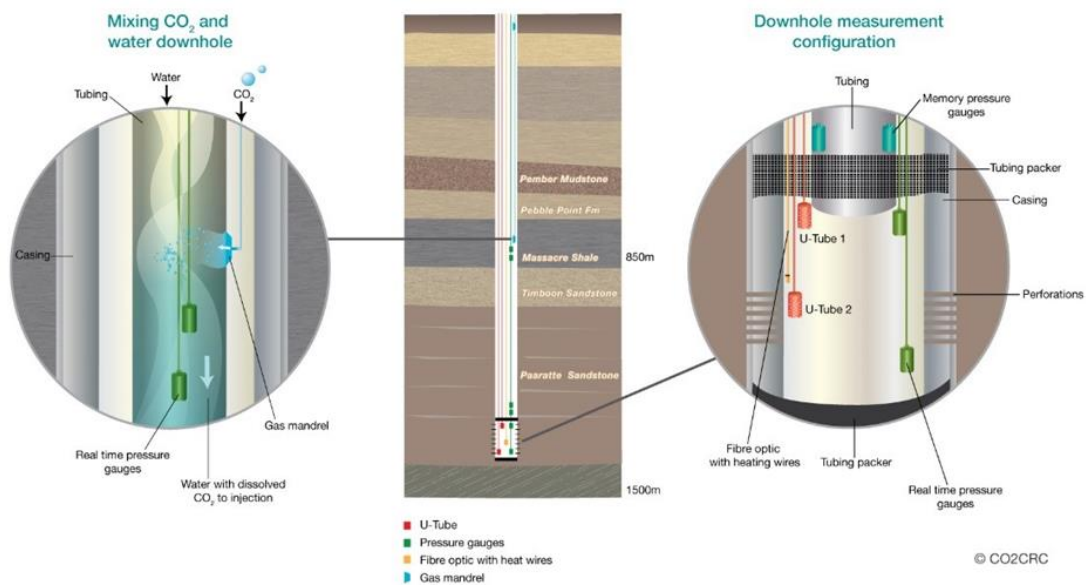


Figure A3.5 – Residual gas saturation test experiments in the CRC-2 well (CO2CRC, 2020b).

Phase 2C of the Stage 2 project focused on using geophysical methods to monitor around 15,000 tonnes of CO₂ injected into the Paaratte Formation via CRC-2 (Tenthorey *et al.*, 2014). The monitoring was primarily done using borehole 4D vertical seismic profile (VSP) and 3D surface time-lapse seismic techniques to confirm plume stabilisation (Tenthorey *et al.*, 2014). In 2015, a buried receiver geophone array was installed (Pevzner *et al.*, 2017; 2020). The last time-lapse survey was undertaken in 2019 and it served as a baseline survey for the Stage 3 operations.

Multiple faults crosscut the Paaratte Formation and it was noted that these could potentially play a role in CO₂ migration within different layers of the formation (Tenthorey *et al.*, 2014). However, Tenthorey *et al.*, (2014) concluded that the faults were unlikely to be reactivated or be a fluid pathway for CO₂ migration, meaning they were likely a sufficient seal preventing CO₂ migration.

Results from Stage 2

The Stage 2 experiments successfully demonstrated the injection of CO₂ into a saline aquifer (Tenthorey *et al.*, 2014). The storage of CO₂ by residual saturation trapping was successful (Paterson *et al.*, 2013). The monitoring of the injected CO₂ was successful and the use of 4D VSP techniques clearly show the plume signature (Pevzner *et al.*, 2020), meaning borehole based seismic techniques could be largely used in areas where conventional 3D surface seismic is not practical. Additionally, using a buried seismic array reduced disruption for landowners outwith the initial installation (Pevzner *et al.*, 2020). Further extensions of the Stage 2 project (e.g., Stage 2B Extension, Serno *et al.*, 2016) demonstrated further experimental approaches to assess residual CO₂ saturation using isotopic methods. Furthermore, it was confirmed that impurities in injected CO₂ did not affect the storage capacity or formation fluids (CO₂CRC, 2020b).

Appendix 4 – Thin section preparation method

Thin section preparation - dry polishing method

1. Sample was vacuum impregnated with epoxy resin (Metprep EpoFlo) and cured at 40 degrees for 3 hours.
2. Excess resin was removed using p80 silicon carbide paper (dry), to expose the surface of the sample.
3. The sample surface was lapped using a Logitech PM6 with 600 grit silicon carbide abrasive mixed with ethylene glycol until planar.
4. Sample was cleaned using an ultrasonic bath with isopropyl alcohol and the surface was dried using compressed air.
5. Sample was bonded to glass using Epo-Thin epoxy resin and cured at 30 degrees for 3 hours.
6. Excess sample was cut off and ground to 150 microns thick using a Petro-Thin.
7. The sample was then lapped on the PM6 to around 40 microns.
8. The sample was ground by hand (dry), on p2500, until 30 micron thickness was achieved (checked in optical microscope).
9. The sample was ground using p4000 silicon carbide paper, dry.
10. Samples were polished using aluminium oxide-based abrasives mixed with ethylene glycol, however this created too much relief (regularly checked on reflected light microscope).
11. p4000 stage was repeated to remove relief then finished with a polishing pad which had been charged with 1 micron diamond solution and left to dry.

Appendix 5 – XCT data collection: scan sections, setting and notes

Table A5-1 – XCT scan runs. Table indicates the sample information (well, tray number, start and end depths) and XCT scanner settings.

Sample No.	Date	Well	Tray	Start Depth (m)	End Depth (m)	Scan Number	Scan Name	kV	mAs	Slice spacing (mm)	FoV	Pitch	Notes
1	21/03/2023	Harvey-2	238	863.4	862.45	4040	T238_1	140	500	0.1	100 (Core), 300 Box	0	
2	21/03/2023	Harvey-2	238	862.45	861.5	4040	T238_2	140	500	0.1	101 (Core), 300 Box	0	
3	21/03/2023	Harvey-2	238	861.5	860.5	4040	T238_3	140	500	0.1	102 (Core), 300 Box	0	
4	21/03/2023	Harvey-2	237	860.05	859.1	4041	T237_2	140	500	0.1	100 (Core), 300 Box	0	Section 1 and 3 of tray too fragile

														to remove - not scanned. See image.
5	21/03/2023	Harvey-2	236	858.2	857.5	4042	T236_1	140	500	0.1	100 (Core), 300 Box	0	Some sections fragile. See image.	
6	21/03/2023	Harvey-2	236	857.5	856.6	4042	T236_2	140	500	0.1	100 (Core), 300 Box	0	Some sections fragile. See image.	

7	21/03/2023	Harvey-2	236	856.6	855.7	4042	T236_3	140	500	0.1	100 (Core), 300 Box	0	
8	22/03/2023	Harvey-2	235	855.7	854.8	4043	T235_1	140	500	0.1	100 (Core), 300 Box	0	
9	22/03/2023	Harvey-2	235	854.8	853.95	4043	T235_2	140	500	0.1	100 (Core), 300 Box	0	Only some core able to be scanned. See image.
10	22/03/2023	Harvey-2	235	853.95	853.3	4043	T235_3	140	500	0.1	100 (Core), 300 Box	0	Only some core able to be scanned.

													d. See image. T235_3 B is empty space.
11	22/03/2023	Harvey-2	234	853.3	852.4	4044	T234_1	140	500	0.1	100 (Core), 300 Box	0	Fragile core.
12	22/03/2023	Harvey-2	234	852.4	851.45	4044	T234_2	140	500	0.1	100 (Core), 300 Box	0	Fragile core.
13	22/03/2023	Harvey-2	234	851.45	850.5	4045	T234_3	140	500	0.1	100 (Core), 300 Box	0	Fragile core.
14	22/03/2023	Harvey-2	233	850.5	849.5	4046	T233_1	140	500	0.1	100 (Core), 300 Box	0	

15	22/03/2023	Harvey-2	233	849.5	848.65	4047	T233_2	140	500	0.1	100 (Core), 300 Box	0	Some sections not able to be scanned. See image.
16	22/03/2023	Harvey-2	233	848.65	847.6	4048	T233_3	140	500	0.1	100 (Core), 300 Box	0	
17	22/03/2023	Harvey-2	232	847.6	846.7	4049	T232_1	140	500	0.1	100 (Core), 300 Box	0	Nice features - shear bands?
18	22/03/2023	Harvey-2	232	846.7	845.75	4050	T232_2	140	500	0.1	100 (Core), 300 Box	0	Nice features -

													shear bands?
19	22/03/2023	Harvey-2	232	845.75	844.8	4051	T232_3	140	500	0.1	100 (Core), 300 Box	0	Nice features - shear bands?
20	23/03/2023	Harvey-2	33	296.5	296.2	4052	T033_2	140	500	0.1	100 (Core), 300 Box	0	Deformation band/compaction band/shear band
21	23/03/2023	Harvey-2	310	1064.5	1065.5	4053	T310_2	140	500	0.1	100 (Core), 300 Box	0	Burrow in PS

22	23/03/2023	Harvey-2	310	1065.4	1066.3	4054	T310_1	140	500	0.1	100 (Core), 300 Box	0	"Undefined" sand from outside fault zone.
23	23/03/2023	Harvey-2	127	557.1	556.15	4054	T127_1	140	500	0.1	100 (Core), 300 Box	0	Clay/silty layer/s mear
24	23/03/2023	Harvey-2	171	676	675.7	4055	T171_1 T	140	500	0.1	100 (Core), 300 Box	0	Def Band
25	23/03/2023	Harvey-2	171	676.3	676	4055	T171_2 B	140	500	0.1	100 (Core), 300 Box	0	Def Band
26	23/03/2023	Harvey-2	172	679.9	678.9	4056	T172_1	140	500	0.1	100 (Core), 300 Box	0	Def Band

27	23/03/2023	Harvey-2	247	889.1	888.1	4057	T247_1	140	500	0.1	100 (Core), 300 Box	0	Def band/p ermeab le bands
----	------------	----------	-----	-------	-------	------	--------	-----	-----	-----	------------------------	---	--

Appendix 6 – Modelling Theory

Modelling theory

To model the Brumbys Fault zone, a 3D model was created using Petroleum Experts (Petex) Move. This section outlines the background theory and algorithms used in each of the two modelling modules used in Move – the Stress Analysis and Fault Response Modelling modules.

Stress analysis

The Stress Analysis module is used to analyse the behaviour of fault and fracture systems under a 3D stress state. It allows the calculation of various parameters (e.g. Slip Tendency, Fracture Stability etc.) and from these parameters can allow analysis of stability, permeability, and leakage. These tools can be used alongside the “Fracture Analysis” tool in move to assess fracture network connectivity, permeability etc. These tools have been successfully used in the past to estimate fault and fracture leakage/seal potential (e.g. Miocic *et al.*, 2013).

Fault Response Modelling (FRM)

The fault response modelling (FRM) module simulates faulting using a boundary element method with triangular elastic dislocations, while considering the mechanical properties of the surrounding rock unit, underneath a horizontal “free” surface that represents the topography. The “free” surface acts as a top boundary to the model.

Boundary element methods have been widely used in the literature for decades to model fault behaviour, as well as spreading centres, igneous dyke emplacement, joint set growth and stress inversion (Mavko, 1982; Bilham and King, 1989; Sempere and MacDonald, 1986; Delaney and Pollard, 1981; Olson and Pollard, 1989; Wu and Pollard, 1995; Olson and Pollard, 1991; Maerten *et al.*, 2014; Maerten *et al.*, 2016).

Elastic dislocation models are based on angular dislocation theory (Comninou & Dundurs, 1975) which has been used to calculate the displacement, strains and stresses from faulting due to earthquake ruptures (e.g. McGuire and Segall, 2003). The FRM module in Move uses triangular dislocation elements (see Meade, 2007 for theory and algorithms). Each of the dislocation elements represent a slip vector on the meshed

fault surface. An observation mesh is used to observe the displacement induced by the fault surface moving. The amount of movement depends on the mechanical properties of the rock (observation surface), slip type (normal/reverse/strike slip) and slip magnitude (amount of displacement on the fault surface).

By adding the total displacement and strain from each triangular dislocation element the total displacement and strain on the fault surface is calculated. From the strain, the magnitude and distribution of fault induced stresses can be calculated using Hooke's Law (Hooke, 1678). From the stresses, known shear-normal stress relationships (e.g. Coulomb stress) can be calculated in the surrounding rock mass. Fracture orientations can be calculated based on the coulomb stress, allowing fractures to be orientated optimally for shear failure (assuming a homogenous medium). Joints can also be modelled.

Appendix 7 – Natural hydrogen seepage data tables

This appendix contains the data tables from Chapter 8.

Table A7 - 1 – Features of natural hydrogen leakage associated with Dry seepage through soils and unconsolidated sediments. All measurements of hydrogen concentration (ppm) are taken in the field using soil gas samples. SAT = sensor saturated; detection limit (of 1100ppm) reached. NR = not reported.

S	Cluster	Site/Sam	Location	Lat/Lon	Geolog	Exposure/S	Sam	Gases	% H₂	N₂	CH₄	CO	O₂	Key
e	Number	ple		g	ical	urface	ple	Present		%	%	₂ %	%	Refere
p	- Name	Name(s)			Setting	Geology	Meth							nce(s)
#							od							
1	A - Moscow	Elektrostal	South Moscow, SW Russia	55.7732 87, 38.5082 2	Contin ental Platfor m	Unconsolida ted granular sediments	Soil Gas (in field)	H ₂ , N ₂ , CH ₄ , CO ₂ , O ₂	0.01 3	NR	NR	NR	NR	
2	B - Borisogl ebsk	South Oktyabr'sk oe	South Moscow, SW Russia	51.0523 83, 41.9987 33	Contin ental Platfor m	Unconsolida ted granular sediments	Soil Gas (in field)	H ₂ , N ₂ , CH ₄ , CO ₂ , O ₂	0.03- 0.05 5	78. 74- 78. 86	0.00 11- 0.00 13	0.1 0- 0.1 1	21. 03- 21. 13	Larin et <i>al.</i> (2015)
3	A - Moscow	Yakhroma	South Moscow,	56.2878 06,	Contin ental	Unconsolida ted granular sediments	Soil Gas	H ₂ , N ₂ , CH ₄ , CO ₂ ,	0.02 39-	77. 9-	NR	0.3 - 0.4	21. 2-	

			SW Russia	37.5268 89	Platfor m		(in field)	O ₂	0.05 08	78. 9			21. 7
4	B - Moscow	Nikulino	South Moscow, SW Russia	56.2271 24, 37.7032 46	Contin ental Platfor m	Unconsolida ted granular sediments	Soil Gas (in field)	H ₂ , N ₂ , CH ₄ , CO ₂ , O ₂	0.03 9	78. 3	NR	0.7	20. 9
5	B - Borisogl ebsk	Ozero Podovoye	South Moscow, SW Russia	51.2298 , 42.0362	Contin ental Platfor m	Unconsolida ted granular sediments	Soil Gas (in field)	H ₂ , N ₂ , CH ₄ , CO ₂ , O ₂	0.00 06- 0.2	78. 77- 79. 00	0.00 10- 0.00 14	0.0 9- 0.3 8	20. 52- 21. 15
6	B - Borisogl ebsk	Satellite Podovoye	South Moscow, SW Russia	51.2298 67, 43.0351 6	Contin ental Platfor m	Unconsolida ted granular sediments	Soil Gas (in field)	H ₂ , N ₂ , CH ₄ , CO ₂ , O ₂	0.00 05- 0.3	78. 86- 79. 07	0.00 08- 0.00 13	0.0 7- 0.2 0	20. 72- 20. 99
7	B - Moscow	Verevskoy e	South Moscow,	56.0640 17,	Contin ental	Unconsolida ted granular sediments	Soil Gas	H ₂ , N ₂ , CH ₄ , CO ₂ ,	0.1- 0.8	78. 63- 09-	0.00		

			SW Russia	37.2676 33	Platfor m		(in field)	O ₂		79. 37	0.00 20			
8	C - Carolina Bays	Arthur Road Bay	Carolina Bays, USA	34.7915 , - 79.2268	Coasta l Plain	Unconsolida ted lacustrine sediments	Soil Gas (in field)	H ₂ , N ₂ , CH ₄ , CO ₂ , O ₂	0.05 86	79. 3	0.00 11	0.6 2	20. 05	Zgonnik <i>et al.</i> (2015)
9	C - Carolina Bays	Smith Bay	Carolina Bays, USA	34.6791 , - 78.5818	Coasta l Plain	Unconsolida ted lacustrine sediments	Soil Gas (in field)	H ₂ , N ₂ , CH ₄ , CO ₂ , O ₂	0.05 74- 0.07 15	79. 15- 79. 40	0.00 11- 0.00 17	0.2 0- 0.5 1	20. 23- 20. 38	
10	C - Carolina Bays	Jones Lake Bay	Carolina Bays, USA	34.682, - 78.5963	Coasta l Plain	Unconsolida ted lacustrine sediments	Soil Gas (in field)	H ₂ , N ₂ , CH ₄ , CO ₂ , O ₂	0.02 1- 0.08 15	NR NR NR NR	NR NR NR NR	NR NR NR NR		
11	C - Carolina Bays	Arthur Road Sandpit	Carolina Bays, USA	34.7871 , - 79.2267	Coasta l Plain	Unconsolida ted	Soil Gas	H ₂ , N ₂ , CH ₄ , CO ₂ ,	0.11	79. 28	0.07 35	1.2 1	19. 37	

						lacustrine sediments	(in field)	O ₂						
12	C - Carolina Bays	Jones Lake (Smaller Structure)	Carolina Bays, USA	34.693, -786005	Coastal Plain	Unconsolidated lacustrine sediments	Soil Gas (in field)	H ₂ , N ₂ , CH ₄ , CO ₂ , O ₂	0.07 19- 0.37	78. 11- 79. 61	0.01 94- 2.74 68	0.2 3- 1.3 8	16. 51- 20. 12	
13	D - Bourake bougou	Gassola	Gassola, Mali	13.194605, -6.242527	Sedimentary Basin	Unspecified soils/sediments	Soil Gas (in field)	H ₂ , N ₂ , CH ₄ , CO ₂ , O ₂ + Hydrocarbon Traces	0.00 1- 0.06	NR	NR	NR	NR	Prinzhofer <i>et al.</i> (2018)
14	E - Sao Francisco Basin	Campinas	São Francisco Basin, Brazil	-16.560083, -	Sedimentary Basin	Unspecified soils/sediments	Soil Gas (in field)	H ₂	0.02 21- 0.05 41	NR	NR	NR	NR	Prinzhofer <i>et al.</i> (2019)

				45.3436 67										
15	E - Sao Francisco Basin	Baru	São Francisco Basin, Brazil	- 16.5600 83, - 45.3436 67	Sedimentary Basin	Unspecified soils/sediments	Soil Gas (in field)	H ₂	0.00 1-1.2	NR	NR	NR	NR	Moretti <i>et al.</i> (2021a)
16	M - Moora	Moora: M1, M2, M3, M4, M5	North Perth Basin, Australia	- 30.5648 25, 115.962 6	Sedimentary Basin	Sediments	Soil Gas (in field)	H ₂ , CH ₄ , CO ₂ , O ₂	0- 0.00 96	NR	0-0.5	0- 0.3	20. 1- 21. 7	Frery <i>et al.</i> (2021)
17	M - Moora	Namban: N1	North Perth Basin, Australia	-30.371, 115.984	Sedimentary Basin	Sediments	Soil Gas (in field)	H ₂ , CH ₄ , CO ₂ , O ₂	0.00 05- 0.00 06	NR	0.2	0.1	21. 6- 21. 7	Frery <i>et al.</i> (2021)

18	M - Moora	Yallalie: Y1, Y2, Y3	North Perth Basin, Australia	-30.467, 115.776 5	Sedim entary Basin	Sediments	Soil Gas (in field)	H ₂ , CH ₄ , CO ₂ , O ₂	0- 0.00 04	NR	0.1- 0.2	0- 0.1	20. 6- 21. 9	Frery <i>et al.</i> (2021)
19	L – Amik Basin	Kurtbagi	Turkey	36.4018 , 36.0416	Ophioli te	Soil	Soil Gas (in field)	H ₂	38.4	NR	NR	NR	NR	Yuce <i>et al.</i> (2014)

Table A7 - 2 – Dry hydrogen seeps not associated with subcircular depression features. NR = not reported.

Seep #	Cluster Name	Site/Sample Name(s)	Location	Lat/Long	Geological Setting	Exposure /Surface Geology	Sample Method	Gases Present	% H₂	N₂ %	CH₄ %	CO₂ %	O₂ %	Key Reference(s)
20	F - Western Hajar Mountains	S 1 f 2 (1), S 1 f 2 (2)	Oman	23.61986 111, 57.11344 444	Ophiolitic Massif	Gabbro	Borehole Gas Samples (Vacutainers)	H ₂ , N ₂ , CH ₄ , CO ₂	0.00 8- 0.04 25	N R	0.00 81- 0.00 82	0	N R	Zgonnik et al. (2019)
21	F - Western Hajar Mountains	S 30 f 1, S 30 f 2	Oman	23.42416 667, 57.67205 556	Ophiolitic Massif	Ophiolitic (e.g. Peridotites)	Borehole Gas Samples (Vacutainers)	H ₂ , N ₂ , CH ₄ , CO ₂	0.00 2- 0.01 10	N R	0.00 24- 0.00 29	0.00 38- 0.00 58	N R	Zgonnik et al. (2019)

22	F - Western Hajar Mountains	S 46 f 1a, S 46 f 1b	Oman	23.39641 667, 57.38097 222	Ophiolitic Massif	Jasper and Carbonates	Borehole Gas Samples (Vacutainers)	H ₂ , N ₂ , CH ₄ , CO ₂	0.01 - 0.02 25	N R	0.00 11- 0.00 12	0.00 80- 0.01 16	N R
23	F - Western Hajar Mountains	S 48 f 1	Oman	23.39633 333, 57.38141 667	Ophiolitic Massif	Jasper and Carbonates	Borehole Gas Samples (Vacutainers)	H ₂ , N ₂ , CH ₄ , CO ₂	0.00 65	N R	0.00 12	0.01 15	N R
24	F - Western Hajar Mountains	S 49 f 2	Oman	23.27425 , 57.45791 667	Ophiolitic Massif	Shales	Borehole Gas Samples (Vacutainers)	H ₂ , N ₂ , CH ₄ , CO ₂	0.04 5	N R	0.00 49	0.02 19	N R
25	F - Western Hajar	S 50 f 1	Oman	23.27391 667,	Ophiolitic Massif	Shales	Borehole Gas Samples (Vacutainers)	H ₂ , N ₂ ,	0.06 25	N R	0 75	0.00	N R

	Mountains			57.45830556					CH ₄ , CO ₂						
26	F - Western Hajar Mountains	S 51 f 1, S 51 f 2	Oman	23.24105556, 57.42019444	Ophiolitic Massif	Marbles	Borehole Gas Samples (Vacutainers)	H ₂ , N ₂ , CH ₄ , CO ₂	0.00 2- 0.02 40	N R	0.00 15- 0.00 29	0.00 81- 0.01 02	N R		
27	F - Western Hajar Mountains	S 52 f 2	Oman	23.21208333, 57.39591667	Ophiolitic Massif	Shales	Borehole Gas Samples (Vacutainers)	H ₂ , N ₂ , CH ₄ , CO ₂	0.00 52	N R	0.00 14	0.02 02	N R		
28	F - Western Hajar Mountains	S 54 f 1, S 54 f 2, S 54 f 4	Oman	23.2110278, 57.3839722	Ophiolitic Massif	Shales	Borehole Gas Samples (Vacutainers)	H ₂ , N ₂ , CH ₄ , CO ₂	0.00 3- 0.34 00	N R	0- 0.00 36	0.00 75- 0.00 88	N R		

29	F	-	S 55 f 1,	Oman	23.17580 556, 57.41466 667	Ophiolitic Massif	Shales	Borehole Gas Samples (Vacutainers)	H ₂ , N ₂ , CH ₄ , CO ₂	0.00 3- 0.04	N R	0.00 88	0.01 54	N R	
30	F	-	S 61 f 1	Oman	22.882, 57.71163 889	Ophiolitic Massif	Jasper and Carbonates	Borehole Gas Samples (Vacutainers)	H ₂ , N ₂ , CH ₄ , CO ₂	0.00 6- 0.03 75	N R	0.00 27	0.01 67	N R	
31	G	-	K01, K02, K03, K05, K03, Ko6	Chimaera, Turkey	36.4314* , 30.4560*	Ophiolitic Massif	Ophiolitic	Pyrex Bottles (sealed with vacuum stop- cocks)	H ₂ , N ₂ , CH ₄ , CO ₂	7.46 - 11.3	2. 1- 4. 9	86.5 - 87.7 8	0.01 - 0.07	N R	Hosgor mez et al. (2008)
32	H	-	LFE-3, LFE-3	Zambales. Philippines	15.5718, 120.1513	Ophiolitic Massif	Ophiolitic	Evacuated Stainless Steel Containers	H ₂ , N ₂ , CH ₄ , CO ₂ ,	42.3 - 42.6	1. 5- 1. 8	54.8 - 55.3	<0.0 1- 0.03	N R	Abrajan o et al. (1988)

									O ₂						
33	H - Zambales	Nagasa	Zambales. Philippines	14.837, 120.1282	Ophiolitic Massif	Ophiolitic	Stainless Tubes Helium Valves)	Steel (w/ Proof	H ₂ , CH ₄ , CO ₂	58.5	1. 2	Not reported	<0.0 1	N R	Vacquand <i>et al.</i> (2018)

Table A7 - 3 – Hydrogen seeps where the emission style is as reduced gas seepages associated with bubbling waters. These are all found in ophiolitic settings. In most cases, hydrogen is thought to be as a product of serpentinization processes. * Indicates approximate location where lat/long is not provided in the literature. NR = not reported.

Seep #	Cluster Name	Site/Sample Name	Location	Lat/Long	Geological Setting	Exposure/Surface Geology	Surface Expression	Sample Method	Gases Present	% H ₂	N ₂ %	CH ₄ %	CO ₂ %	O ₂ %	Key Reference(s)
34	I - New Caledonia	Carénage 1, Carénage 2	New Caledonia	- 22.3048, 166.8409	Ophiolitic Massif	Ophiolitic (e.g. Peridotites)	Springs	Vacutainer	H ₂ , N ₂ , CH ₄ , CO ₂	32-47	50-25	13-68	0-15	NR	Deville and Prinzhofer (2016), Vacquand et al. (2018)
35	I - New Caledonia	Kaoris 1, Kaoris 2, Kaoris 3	New Caledonia	- 22.2994, 166.8618	Ophiolitic Massif	Ophiolitic (e.g. Peridotites)	Springs	Vacutainer	H ₂ , N ₂ , CH ₄ , CO ₂	26-1	55-29	11-26	0-11	NR	
36	F - Western	Magniyat	Oman	23.4061, -	Ophiolitic	Ophiolitic (e.g. Peridotites)	Springs	Stainless Steel Tubes	H ₂ , N ₂	87-3	9.8	2.9	0	NR	Vacquand et al. (2018)

	n Hajar Mountains			56.863 3	Massif	Peridotites)		(w/ Helium Proof Valves)	CH ₄ , CO ₂					0 1	
37	F - Western Hajar Mountains	Hawasina	Oman	23.683 3, 56.939 6	Ophiolitic Massif	Ophiolitic (e.g. Peridotites)	Springs	Stainless Steel Tubes (w/ Helium Proof Valves)	H ₂ , N ₂ , CH ₄ , CO ₂	85 .9	9.4	4.6	0 .0 1	N R	
38	F - Western Hajar Mountains	Bahla (2008, 2012)	Oman	22.992 2, 57.293 2	Ophiolitic Massif	Ophiolitic (e.g. Peridotites)	Springs	Stainless Steel Tubes (w/ Helium Proof Valves)	H ₂ , N ₂ , CH ₄ , CO ₂	85 .7	12- 12. 4	1.9 -	0 .0 1	N R	
39	F - Western Hajar Mountains	Kufeis	Oman	23.958 8, 56.44	Ophiolitic Massif	Ophiolitic (e.g. Peridotites)	Springs	Stainless Steel Tubes (w/ Helium Proof Valves)	H ₂ , N ₂ , CH ₄ , CO ₂	85 .4	14. 5	0.1	0 .0 1	N R	

40	F - Wester n Hajar Mounta ins	Haylan (2010, 2021-2a, 2012-6, 2021-8)	Oman	23.619 9, 57.113 2	Ophi olitic Massi f	Ophiolit ic (e.g. Peridoti tes)	Sprin gs	Stainless Steel Tubes (w/ Helium Proof Valves)	H ₂ , N ₂ , CH ₄ , CO ₂	75 - 79 .4	14. 2- 18. 1	4- 9.6 0 1	0 . 0 1	N R
41	F - Wester n Hajar Mounta ins	Barrage (Jizzi)	Oman	24.328 2, 56.130 7	Ophi olitic Massi f	Ophiolit ic (e.g. Peridoti tes)	Sprin gs	Stainless Steel Tubes (w/ Helium Proof Valves)	H ₂ , N ₂ , CH ₄ , CO ₂	75 .2 9 10	14. 9 0 1	0 . 0 1	N R	
42	F - Wester n Hajar Mounta ins	Halhal	Oman	23.717 2, 57.034	Ophi olitic Massi f	Ophiolit ic (e.g. Peridoti tes)	Sprin gs	Stainless Steel Tubes (w/ Helium Proof Valves)	H ₂ , N ₂ , CH ₄ , CO ₂	73 .4 8 5.8	20. 8 0 1	0 . 0 1	N R	
43	F - Wester n Hajar	Alkar	Oman	23.969 3,	Ophi olitic	Ophiolit ic (e.g.)	Sprin gs	Stainless Steel Tubes	H ₂ , N ₂ ,	68 .1 28. 5 3.3 0 . N R				

	Mountains			56.4219	Massif	Peridotites)		(w/ Helium Proof Valves)	CH ₄ , CO ₂				01		
44	F - Western Hajar Mountains	Huqain	Oman	23.5352, 57.3333	Ophiolitic Massif	Ophiolitic (e.g. Peridotites)	Springs	Stainless Steel Tubes (w/ Helium Proof Valves)	H ₂ , N ₂ , CH ₄ , CO ₂	65 .1	32. 4	2.5	0 .0 1	N R	
45	F - Western Hajar Mountains	Lauriers Roses	Oman	22.8956, 58.3946	Ophiolitic Massif	Ophiolitic (e.g. Peridotites)	Springs	Stainless Steel Tubes (w/ Helium Proof Valves)	H ₂ , N ₂ , CH ₄ , CO ₂	61	23. 2	15. 4	0 .0 1	N R	
46	F - Western Hajar Mountains	Abyiad (2010, 2010-29, 2010-30)	Oman	23.4285, 57.6683	Ophiolitic Massif	Ophiolitic (e.g. Peridotites)	Springs	Stainless Steel Tubes (w/ Helium Proof Valves)	H ₂ , N ₂ , CH ₄ , CO ₂	26 .9- 36 .1	57. 3- 59. 9	5.7 -15. 9	0 .0 1	N R	

47	F - Wester n Hajar Mounta ins	Bahla (1, 2, 3, 4, 5)	Oman	22.992 2, 57.293 2	Ophi olitic Massi f	Ophiolit ic (e.g. Peridoti tes)	Sprin gs	Glass Bottles (w/ teflon seals)	H ₂ , N ₂ , O ₂ , CH ₄	43 - 97	2- 43	0.9 - 2.2	N R	0. 1 - 1 3	Neal and Stanger (1983)
48	F - Wester n Hajar Mounta ins	Hawqayn (1, 2, 3)	Oman	23.545 7*, 57.341 1*	Ophi olitic Massi f	Ophiolit ic (e.g. Peridoti tes)	Sprin gs	Glass Bottles (w/ teflon seals)	H ₂ , N ₂ , O ₂ , CH ₄	39 - 48	39- 50	1.1 - 4.3	N R	8 - 1 0	
49	F - Wester n Hajar Mounta ins	Nizwa	Oman	22.937 3*, 57.333 5*	Ophi olitic Massi f	Ophiolit ic (e.g. Peridoti tes)	Sprin gs	Glass Bottles (w/ teflon seals)	H ₂ , N ₂ , CH ₄	95	1	4	N R	0	
50	F - Wester n Hajar	Huwayl Qufays	Oman	23.956 6,	Ophi olitic	Ophiolit ic (e.g.)	Sprin gs	Glass Bottles (w/ teflon seals)	H ₂ , N ₂ , CH ₄	99	1	0	N R	0	

	Mountains			56.437 1*	Massif	Peridotites)										
51	F - Western Hajar Mountains	B'lad	Oman	24.25*, 56.12*	Ophiolitic Massif	Ophiolitic (e.g. Peridotites)	Springs	Glass Bottles (w/teflon seals)	H ₂ , N ₂ , O ₂ , CH ₄	22	76	0	N R	1		
52	F - Western Hajar Mountains	S 30 (1), S 30 (2)	Oman	23.424 16667, 57.672 05556	Ophiolitic Massif	Ophiolitic (e.g. Peridotites)	Bubbling Springs	Glass Bell and Flow Chamber	H ₂ , N ₂ , O ₂ , CH ₄ , CO ₂	30 .3- 30 .7	60. 6- 61	7.5 - 7.6	0	1. 1		
53	F - Western Hajar Mountains	S 8 (1), S 8 (2)	Oman	23.618 05556, 57.107 80556	Ophiolitic Massif	Ophiolitic (e.g. Peridotites)	Bubbling Springs	Glass Bell and Flow Chamber	H ₂ , N ₂ , O ₂ , CH ₄ , CO ₂	70 - 71 .7	23- 24. 3	3.5	0	1. 7 - 2. 2		Zgonnik <i>et al.</i> (2019)

54	F - Western Hajar Mountains	S 39 (1), S 39 (2)	Oman	23.429 33333, 57.668 25	Ophiolitic Massif	Terrace	Bubbling Springs	Glass Bell and Chamber	H ₂ , N ₂ , O ₂ , CH ₄ , CO ₂	35 .1- 37 .3	52. 8- 54. 3	6.2 - 6.8	0	3. 1 - 4. 4	
55	F - Western Hajar Mountains	S 2-1	Oman	23.619 88889, 57.113 19444	Ophiolitic Massif	Gabbro	Bubbling Springs	Glass Bell and Chamber	H ₂ , N ₂ , O ₂ , CH ₄ , CO ₂	77	14. 2	8.8	0	0	
56	J - West USA	Barnes Spring (1, 5, 7), NS1, Camp Spring	Austin Creek, USA	38.620 7, - 123.13 39	Subduction Complex	Peridotite	Bubbling Springs	Beaker, then into pre-evacuated serum vials	H ₂ , N ₂ , CH ₄ , CO ₂	15 .7- 50 .9	36. 6- 63. 1	5.3 - 15. 8	0	N R	Morrill <i>et al.</i> (2013)
57	K - New Zealand	Poison Bay	Milford Sound, New	- 44.671 8,	Orogenic	Ultramafic, Mylonitic	Bubbling	Not Reported	H ₂ , N ₂ , O ₂ ,	56 .4	20. 2	16. 6	0 .7	6. 1	Wood, 1972

			Zealand	167.927		c Gneiss	Offshore		CH ₄ , CO ₂							
58	L - Amik Basin	Tahtakopru	Turkey	36.3835, 36.1636	Ophiolite	Ophiolitic (e.g. Peridotites)	Bubbling Springs	Inverted Funnel	H ₂	60.5	NR	NR	N R	N R		Yuce <i>et al.</i> (2014)
59	H - Zambales	LFE-1	Zambales, Philippines	15.6754*, 120.0827*	Ophiolitic Massif	Ophiolitic	Bubbling Springs	Evacuated Stainless Steel Containers	H ₂ , N ₂ , O ₂ , CH ₄ , CO ₂	8.4	60.6	13	0 .03	1 6.5		Abrajano <i>et al.</i> (1988)
60	H - Zambales	Mangatarem	Philippines	15.7033, 120.2825	Ophiolitic Massif	Ophiolitic (e.g. Peridotites)	Springs	Stainless Steel Tubes (w/ Helium Proof Valves)	H ₂ , N ₂ , CH ₄ , CO ₂	35.1	48	16.7	0 .01	N R		Vacquand <i>et al.</i> (2018)

Table A7 - 4 – Hydrogen seep rates. N corresponds to numbers in previous tables where applicable and N/A for those that are not site specific, but rather seepage rates over larger geological units.

N	Site/Sample Name	Seep Rate (m³/day)	Average Seep Rate (m³/day)	Average Seep Rate (g/day)	Seep Diameter (m)	Seep Radius (m)	Seep Radius (km)	Area (km²)	Average Flux (m³/day/km²)	Average Flux (g/m²/day)	Key Reference(s)
1	Elektrostal	30-50	40	3308	219	109	0.109	0.0375	800-1335	0.088	Larin et al. (2015)
5	Ozero Podovoye	3750-4800	4275	353542.5	1000	500	0.500	0.785	575-740	0.450	
6	Satellite Podovoye	40	40	3308	100	50	0.050	0.008	5093	0.421	
7	Verevskoye	21,000-27,000	24,000	1984800	1000	500	0.500	0.785	7,000,000-9,000,000	2.527	
8	Arthur Road Bay	1000–1370	1185	97999.5	782	391	0.391	0.48	2240–3060	0.204	

9	Smith Bay	750– 1000	875	72362.5	1205	602	0.602	1.14	660– 880	0.063	Zgonnik <i>et al.</i> (2015)
1 0	Jones Lake Bay	1120– 2740	1930	159611	2821	1410	1.410	6.25	180–440	0.026	
1 2	Jones Lake (Smaller Structure)	21–31	26	2150.2	94	47	0.047	0.00 7	3000–4400	0.307	
1 4	Capinas	80-102	85	7000	539	264	0.264	220	385	0.032	Moretti <i>et al.</i> (2021)
1 5	Baru	51-77	64	5300	460	230	0.230	166. 5	385	0.032	Moretti <i>et al.</i> (2021)
N / A	Peridotites	13505- 27195	20348	1682779.6	Not a circle	Not a circle	Not a circle	185	110	0.01	Zgonnik <i>et al.</i> (2019)

N / A	Proterozoic	29,700-	57750	4775925	Not a	Not a	Not a	66	875	0.072	
	Sediments	85,800			circle	circle	circle				

Appendix 8 – Logging data from the Harvey-2, Harvey-3 and Brumbys-1 cores

Table A8-1 – Fracture logging data from the Harvey-2 core.

Tray Number	Depth (m)	Lithology	Angle	Surface Roughness	Slickensines	Mineralised	Mineralisation Colour	Number Descriptor Total	Fracture Type	Comments	Photo Number	Column1
10	232.2	PS	0	0	0	1		1	0			
10	232.35	PS	0	0	0	1		1	0			
10	232.4	PS	0	0	0	1		1	0			
10	232.45	PS	0	0	0	1		1	0			
10	232.6	PS	0	0	0	1		1	0			
10	232.75	PS	0	0	0	1		1	0			
10	232.95	PS	3	0	0	1		4	1			
10	233.1	PS	3	0	0	1		4	2			
10	233.35	PS	0	0	0	1		1	0			
10	233.4	PS	0	0	0	1		1	0			
10	233.55	PS	0	0	0	1		1	0			
10	233.7	PS	0	0	0	1		1	0			
10	233.75	PS	0	0	0	1		1	0			
10	233.8	PS	0	0	0	1		1	0			
10	233.9	PS	0	0	0	1		1	0			
10	234.2	PS	0	0	0	1		1	0			
10	234.25	PS	3	1	1	1		6	2			
11	234.7	PS	3	1	1	1		6	3	Conjgate with fracture below.		
11	234.75	PS	3	1	1	1		6	3	Gradational change through to SST.		
11	234.85	PS	0	1	0	1		2	1			
11	235	SST	0	0	0	1		1	0			
11	235.2	SST	0	0	0	1		1	0			

11	235.6	SST	0	0	0	1		1	0			
11	236.05	SST	0	0	0	0	Green	0	0	Green concretion.		
11	236.25	SST	0	0	0	1		1	0			
11	236.7	SST	0	0	0	1		1	0	Gradational change through to PS.		
11	236.75	SST	0	0	0	1		1	0			
11	237.1	PS	0	0	0	1		1	0			
11	237.25	PS	0	0	0	1		1	0			
12	237.75	SST	0	0	0	1		1	0	SST = Grit (2-8mm clasts, pebbles), full section below until litho change.		
12	237.9	SST	0	0	0	1		1	0			
12	238.1	SST	0	0	0	1		1	0			
12	238.7	SST	1	0	0	1		2	0			
12	238.9	SST	0	0	0	1		1	0			
12	239	SST	0	0	0	1		1	0			
12	239.1	SST	1	0	0	1		2	0	Medium grained SST layer.		
12	239.2	SST	0	0	0	1		1	0			
12	239.55	SST	0	0	0	1		1	0			
12	239.8	PS	0	0	1	0	Purple	1	0			
12	239.85	PS	1	1	1	0	Purple	3	1			
12	239.9	PS	1	1	1	0	Purple	3	1	Less mineralisation than surrounding mineralised fractures		
12	239.92	PS	1	1	1	0	Purple	3	1	Less mineralisation than surrounding mineralised fractures		
12	239.95	PS	1	1	1	0	Purple	3	1			
12	239.97	PS	1	1	1	0	Purple	3	1			
12	240	PS	3	1	2	1		7	2			
12	240.15	PS	1	2	2	1		6	2			
12	240.2	PS	3	1	2	2		8	2			
13	240.45	PS	1	0	1	1		3	0			

13	240.6	PS	0	0	1	1		2	0			
13	240.65	PS	0	0	1	1		2	0			
13	240.7	PS	0	0	1	1		2	0			
13	240.85	PS	0	0	1	1		2	0			
13	241.3	PS	0	0	1	1		2	0			
13	241.5	PS	0	0	0	1		1	0	Sandy layer.		
13	241.9	SST	0	0	0	1		1	0			
13	241.95	SST	0	0	0	1		1	0			
13	242.05	SST	0	0	0	1		1	0			
13	242.2	SST	0	1	0	1		2	0			
13	242.6	SST	0	1	0	1		2	0			
13	242.7	SST	0	1	0	1		2	0			
14	243	SST	0	1	0	1		2	0			
14	243.2	SST	0	0	0	1		1	0			
14	243.35	SST	0	0	0	1		1	0			
14	243.4	SST	0	0	0	1		1	0			
14	243.5	SST	0	0	0	1		1	0			
14	243.55	SST	0	0	0	1		1	0			
14	243.7	SST	1	0	0	1		2	0			
14	243.85	SST	0	0	0	1		1	0			
14	244.2	SST	0	0	0	1		1	0			
14	244.5	SST	0	0	0	1		1	0			
14	244.8	SST	0	0	0	1		1	0			
14	244.85	SST	0	0	0	1		1	0			
14	244.9	SST	0	0	0	1		1	0			
14	245.5	PS	3	2	2	1		8	2			74

50	343.4	SST	0	0	0	1		1	0	SST = Grit (2-8mm clasts, pebbles), fines downwards		
50	343.45	SST	0	0	0	1		1	0			
50	343.9	SST	0	0	0	1		1	0			
50	343.96	SST	0	0	0	1		1	0			
50	344.6	SST	0	0	0	1		1	0	Finer sandstone.		
50	344.65	SST	1	0	0	1		2	0			
50	344.7	SST	0	0	0	1		1	0			
50	344.72	SST	0	0	0	1		1	0			
50	344.8	SST	0	0	0	1		1	0			
50	345.6	SST	0	0	0	1		1	0			
50	345.8	SST	0	0	0	1		1	0			
50	345.85	SST	0	0	0	1		1	0			
50	345.9	SST	0	0	0	1		1	0			
50	345.93	SST	0	0	0	1		1	0			
50	346	SST	0	0	0	1		1	0			
50	346.02	SST	0	0	0	1		1	0			
50	346.1	SST	0	0	0	1		1	0			
50	346.12	SST	0	0	0	1		1	0			
50	346.14	SST	0	0	0	1		1	0			
50	346.2	SST	0	0	0	1		1	0			
51	346.3	SST	0	1	0	1		2	0			
51	346.5	SST	0	1	0	1		2	0			
51	346.65	SST	0	0	0	1		1	0	Silt/sand layer.		
51	346.7	SST	0	1	0	1		2	0			
51	346.95	PS	0	1	0	1		2	0	Sandy		
51	347.1	PS	0	2	0	1		3	0	Sandy		
51	347.25	PS	0	2	0	1		3	0	Sandy		

51	347.5	SST	0	1	0	1		2	0			
51	347.6	SST	0	1	0	1		2	0			
51	347.9	SST	0	1	0	1		2	0			
51	348.48	SST	0	1	0	1		2	0			
51	348.7	SST	0	0	0	1		1	0			
51	348.8	SST	0	0	0	1		1	0			
51	348.84	SST	0	0	0	1		1	0			
51	348.86	SST	0	0	0	1		1	0			
51	348.87	SST	0	0	0	1		1	0			
52	349	SST	0	1	0	1		2	0			
52	349.2	SST	0	0	0	1		1	0			
52	349.24	SST	0	1	0	1		2	0			
52	349.3	SST	0	0	0	1		1	0			
52	349.35	SST	0	0	0	1		1	0	Bedding between SST and PS		
52	349.41	PS	0	0	0	1		1	0			
52	349.49	PS	0	0	0	1		1	0			
52	349.6	PS	1	2	0	1		4	1			
52	349.65	PS	0	1	0	0	Pale Yellow	1	0			
52	349.68	PS	1	0	1	1		3	1			
52	349.8	PS	1	1	1	1		4	1			
52	349.95	PS	1	2	0	1		4	1			
52	350	PS	1	2	0	1		4	1			
52	350.2	PS	0	0	0	1		1	0			
52	350.4	PS	0	0	0	1		1	0			
52	350.5	PS	0	0	0	1		1	0			
52	350.8	PS	0	1	0	1		2	0			
52	351	PS	1	0	0	1		2	0			

52	351.1	PS	0	1	0	1		2	0			
52	351.25	PS	0	1	0	1		2	0			
52	351.3	PS	0	1	0	1		2	0			
52	351.45	PS	0	0	0	1		1	0			
53	352.05	PS	0	0	0	1		1	0			
53	352.15	PS	0	0	0	1		1	0			
53	352.2	PS	0	0	0	1		1	0			
53	352.24	PS	0	0	0	1		1	0			
53	352.9	PS	0	1	0	1		2	1			
53	353.03	PS	0	0	0	1		1	0			
53	353.45	PS	0	0	0	1		1	0			
53	353.8	PS	0	0	0	1		1	0			
53	353.85	PS	0	0	0	1		1	0			
53	354.1	PS	0	0	0	1		1	0			
53	354.2	PS	0	0	0	1		1	0			
54	354.4	PS	3	1	1	1		6	1			
54	354.65	PS	0	0	0	1		1	0			
54	354.9	PS	0	0	0	1		1	0			
54	355	PS	0	1	0	1		2	0			
54	355.05	PS	0	1	0	1		2	0			
54	355.2	PS	3	2	1	1		7	2			
54	355.25	PS	0	1	0	1		2	0			
54	355.3	PS	0	1	0	1		2	0			
54	355.48	PS	0	1	0	1		2	0			
54	355.6	SST	0	0	0	1		1	0			
54	355.63	SST	0	0	0	1		1	0			
54	355.68	SST	0	0	0	1		1	0			

54	355.75	SST	0	0	0	1		1	0			
54	355.85	SST	0	0	0	1		1	0			
54	355.9	SST	0	0	0	1		1	0			
54	356.05	SST	0	0	0	1		1	0			
54	356.51	SST	0	1	0	1		2	0			
54	356.7	SST	0	0	0	1		1	0			
54	356.9	SST	0	0	0	1		1	0			
54	357.1	SST	0	0	0	1		1	0			89
90	451.4	PS	2	0	1	1		4	0			
90	451.5	PS	0	1	0	1		2	0			
90	451.57	PS	0	1	0	1		2	0			
90	451.65	PS	0	1	0	1		2	0			
90	452.5	PS	3	1	2	1		7	2			
90	452.9	PS	3	1	2	1		7	2			
90	453.02	PS	3	1	2	1		7	2			
90	453.3	SST	0	1	0	1		2	0			
90	453.65	SST	0	1	0	1		2	0			
90	454	SST	0	0	0	1		1	0			
90	454.03	SST	0	0	0	1		1	0			
91	454.45	SST	0	0	0	1		1	0			
91	454.75	SST	0	0	0	1		1	0			
91	454.9	SST	0	0	0	1		1	0	SST = Grit		
91	455.9	SST	0	0	0	1		1	0			
91	456.55	SST	0	0	0	1		1	0			
91	456.6	SST	0	0	0	1		1	0	SST = Cong		
92	457.45	SST	0	0	0	1		1	0			

92	458.1	SST	0	0	0	1		1	0			
92	458.4	SST	0	0	0	1		1	0			
92	458.75	SST	0	0	0	1		1	0			
92	459.35	SST	0	0	0	1		1	0			
92	459.45	SST	0	0	0	1		1	0			
92	459.6	SST	0	0	0	1		1	0			
92	459.7	SST	0	0	0	1		1	0			
93	460.3	SST	0	0	0	1		1	0			
93	461.25	SST	0	0	0	1		1	0			
93	461.6	SST	0	0	0	1		1	0			
93	461.8	SST	0	0	0	1		1	0			
93	462.1	SST	0	0	0	1		1	0			
93	462.35	SST	0	0	0	1		1	0			
93	462.75	PS	0	0	0	1		1	1	Clayey vertisol.		
93	462.85	PS	3	1	1	1		6	1			
94	462.95	PS	0	1	0	1		2	1			
94	463.02	PS	0	1	0	1		2	1			
94	463.08	PS	1	1	0	1		3	0			
94	463.15	PS	0	0	0	1		1	0			
94	463.35	PS	3	1	0	1		5	1			
94	463.7	SST	0	0	0	1		1	0			
94	463.8	SST	0	0	0	1		1	0			
94	463.95	PS	3	2	1	1		7	1			
94	464	PS	1	2	1	1		5	1			
94	464.05	PS	1	2	1	1		5	1			
94	464.25	PS	3	1	1	1		6	1			
94	464.27	PS	3	1	1	1		6	1			

94	464.6	PS	3	1	1	1		6	1			
94	464.65	PS	3	1	1	1		6	1			
94	465.05	PS	3	1	1	1		6	1			
94	465.1	PS	0	0	0	1		1	0			
94	465.3	PS	0	0	0	1		1	0			50
130	562.45	PS	0	0	0	1		1	0			
130	562.48	PS	1	0	0	1		2	0			
130	562.53	PS	0	0	0	1		1	0			
130	562.85	PS	0	0	0	1		1	0			
130	562.95	PS	0	0	0	1		1	0			
130	563.35	PS	0	0	0	1		1	0			
130	563.48	PS	0	0	0	1		1	0			
130	563.57	PS	0	0	0	1		1	0			
130	564.1	SST	1	0	0	1		2	0			
130	564.15	SST	1	0	0	1		2	0			
130	564.5	SST	0	0	0	1		1	0	Sandy PS		
130	564.8	SST	0	0	0	1		1	0			
131	565.4	PS	0	1	0	1		2	0			
131	565.48	PS	0	0	0	1		1	0			
131	565.55	SST	0	0	0	1		1	0			
131	565.95	PS	0	0	0	1		1	0			
131	566	PS	0	0	0	1		1	0			
131	566.05	PS	0	1	0	1		2	0			
131	566.25	PS	0	1	0	1		2	0			
131	466.4	PS	0	1	0	1		2	0			
131	466.45	PS	0	1	0	1		2	0			

131	466.5	SST	0	0	0	1		1	0			
131	466.8	SST	0	0	0	1		1	0			
131	567	SST	0	0	0	1		1	0			
131	567.5	PS	0	0	0	1		1	0			
131	567.95	PS	0	1	0	1		2	0			
131	568	PS	0	0	0	1		1	0			
131	568.03	PS	1	1	1	1		4	0			
132	568.2	PS	0	1	0	1		2	0	Sandy PS		
132	568.3	PS	0	0	0	1		1	0			
132	568.35	PS	1	0	0	1		2	0			
132	568.45	PS	1	0	0	1		2	0			
132	568.55	PS	0	0	0	1		1	0			
132	565.58	PS	0	0	0	1		1	0			
132	568.68	PS	0	0	0	1		1	0	Sandy PS		
132	569.1	PS	1	0	0	1		2	0			
132	569.2	PS	1	0	0	1		2	0			
132	569.45	PS	0	0	0	1		1	0			
132	569.47	PS	0	0	0	1		1	0			
132	599.6	PS	0	0	0	1		1	0			
132	569.63	SST	0	0	0	1		1	0			
132	569.9	SST	0	0	0	1		1	0			
133	573.5	SST	0	0	0	1		1	0			
134	573.6	SST	0	0	0	1		1	0			
134	574.1	SST	0	0	0	1		1	0			
134	574.55	SST	1	1	0	1		3	0			
134	574.66	PS	1	1	1	1		4	1			
134	574.67	PS	1	1	1	1		4	1			

134	574.73	PS	1	1	0	1		3	1			
134	574.8	PS	1	1	0	1		3	1			
134	474.9	PS	1	1	0	1		3	1			
134	574.97	PS	1	1	0	1		3	1			
134	575	PS	1	1	0	1		3	1			
134	575.01	PS	1	1	0	1		3	1			
134	575.04	PS	1	1	0	1		3	1			
134	575.1	PS	1	1	0	1		3	1			
134	575.13	PS	0	1	0	1		2	1			
134	575.15	PS	1	1	0	1		3	1			
134	575.21	PS	1	1	0	1		3	1			
134	575.24	PS	1	1	0	1		3	1			
134	575.29	PS	1	1	0	1		3	1			
134	575.32	PS	0	1	0	1		2	1			
134	575.33	PS	2	0	0	1		3	0			
134	575.35	PS	2	0	0	1		3	0			
134	575.5	PS	3	1	1	1		6	0			
134	575.53	PS	3	1	1	1		6	0			
134	575.58	PS	3	0	1	1		5	0			
134	575.63	PS	3	0	1	1		5	0			
134	575.68	PS	3	0	1	1		5	0			
134	575.7	PS	3	1	1	1		6	0			
134	575.75	PS	3	1	1	1		6	0			
134	575.83	PS	3	1	1	1		6	0			
134	575.9	PS	3	0	1	1		5	0			
134	575.92	PS	3	1	1	1		6	0			
134	576	PS	1	2	1	1		5	0			

134	576.03	PS	1	2	1	1		5	0			
134	576.1	PS	1	1	1	1		4	0			
134	576.14	PS	1	1	0	1		3	0			
134	576.2	PS	1	1	0	1		3	0			79
170	671.48	SST	0	0	0	1		1	0			
170	671.7	SST	0	0	0	1		1	0			
170	671.8	PS	0	1	0	1		2	0			
170	671.86	PS	0	1	0	1		2	0			
170	672.2	PS	0	1	1	0		2	1	Purple		
170	672.45	PS	0	1	1	1		3	0			
170	672.48	PS	0	1	1	1		3	0			
170	672.6	PS	0	1	0	1		2	0			
170	672.65	PS	0	1	0	1		2	0			
170	673	PS	2	1	1	1		5	0			
170	673.07	PS	0	1	1	1		3	0			
170	673.1	PS	0	1	1	1		3	0			
170	673.15	PS	0	1	1	1		3	0			
170	673.2	PS	0	1	1	1		3	0			
170	673.23	PS	0	1	1	1		3	0			
170	673.27	PS	0	1	1	1		3	0			
170	673.3	PS	1	1	1	1		4	0			
170	673.32	PS	3	2	0	1		6	2			
170	673.34	PS	3	2	0	1		6	2			
170	673.38	PS	1	0	1	1		3	0			
170	673.4	PS	0	1	1	1		3	0			
170	673.5	SST	0	0	0	1		1	0			

170	674	SST	1	0	0	1		2	0			
171	674.55	SST	0	0	0	1		1	0			
171	674.7	SST	0	0	0	1		1	0			
171	674.9	SST	0	0	0	1		1	0	GRIT (full length until next PS)		
171	675.15	SST	1	0	0	1		2	0			
171	675.5	SST	3	2	0	1		6	2			
171	675.85	SST	1	1	0	1		3	0	Deformation band (?) near.		
171	676	SST	0	1	0	1		2	0			
171	676.2	SST	0	0	0	1		1	0			
171	676.3	SST	1	1	0	1		3	0			
172	678.35	SST	1	0	0	1		2	0			
172	678.45	SST	0	0	0	1		1	0			
172	679.45	SST	0	0	0	1		1	0			
172	679.7	SST	1	0	0	1		2	0			
173	680	PS	1	0	0	1		2	0			
173	680.6	PS	0	1	1	1		3	0			
173	680.75	PS	1	0	2	1		4	1			
173	680.8	PS	1	0	2	1		4	1	Burrows		
173	680.9	PS	1	0	2	1		4	1			
173	680.95	PS	0	0	0	1		1	1			
173	681	PS	1	1	1	1		4	1			
173	681.5	SST	0	0	0	1		1	0			
173	682.4	SST	0	0	0	1		1	0			
174	682.85	SST	0	0	0	1		1	0			
174	683.05	SST	1	0	0	1		2	0			
174	683.15	PS	1	0	0	1		2	0			
174	683.25	PS	0	0	0	1		1	0			

174	683.75	SST	0	0	0	1		1	0			
174	683.9	SST	0	0	0	1		1	0			
174	684.3	PS	0	0	0	1		1	0			
174	684.5	SST	0	0	0	1		1	0			
174	684.85	SST	0	0	0	1		1	0	GRIT (full length until end of this sample section)		
174	685	SST	0	0	0	1		1	0			
174	685.05	SST	0	0	0	1		1	0			
174	685.1	SST	0	0	0	1		1	0			
174	685.3	SST	0	0	0	1		1	0			58
210	783.8	SST	0	0	0	1		1	0	Conglomerate/GRIT (until next PS)		
210	783.83	SST	0	0	0	1		1	0			
210	784.1	SST	0	0	0	1		1	0			
210	784.9	PS	0	0	0	1		1	0			
210	785.4	SST	0	0	0	1		1	0	Conglomerate/GRIT (until next PS)		
210	785.6	SST	1	0	0	1		2	0			
210	785.9	SST	0	0	0	1		1	0			
210	786.05	SST	3	0	0	1		4	0			
210	786.3	SST	0	0	0	1		1	0			
211	787	SST	1	0	0	1		2	0			
211	787.4	SST	1	0	0	1		2	0			
211	787.6	SST	0	0	0	1		1	0			
211	787.95	SST	0	0	0	1		1	0			
212	789.6	PS	0	1	0	1		2	0	Sandy PS.		
212	790.45	PS	0	1	0	1		2	0			
212	790.5	PS	3	0	1	1		5	1			
212	791.05	PS	3	2	1	1		7	2			

212	791.3	PS	1	1	0	1		3	1			
212	791.45	PS	0	0	0	1		1	0			
212	791.6	PS	1	1	1	1		4	0			
212	791.75	PS	1	1	1	1		4	0			
212	791.85	PS	1	1	1	1		4	0			
213	792	PS	1	1	0	1		3	0			
213	792.35	PS	1	1	0	1		3	0			
213	792.6	PS	1	1	0	1		3	0			
213	792.75	PS	1	1	0	1		3	0			
213	792.77	PS	0	1	0	1		2	0			
213	792.8	PS	0	1	0	1		2	0	Lots of little fractures.		
213	792.82	PS	1	1	0	1		3	0	Lots of little fractures.		
213	793.15	SST	1	0	0	1		2	0			
213	793.45	SST	0	0	0	1		1	0	SST/PS Boundary, Fault gouge?		
213	793.8	SST	1	2	0	1		4	2			
213	793.82	PS	1	1	0	1		3	2			
213	793.95	PS	1	2	0	1		4	1			
213	794.07	PS	0	2	0	1		3	0			
213	794.2	PS	1	2	0	1		4	0			
214	794.85	PS	0	0	0	1		1	0			
214	795.3	PS	0	0	0	1		1	0			
214	795.45	PS	0	0	0	1		1	0			
214	795.48	PS	1	1	1	1		4	1			
214	795.6	PS	0	0	0	1		1	0			
214	795.9	PS	0	0	0	1		1	0			
214	795.95	PS	0	0	0	1		1	0			
214	796.05	PS	0	0	0	1		1	0			

214	796.15	PS	0	0	0	1		1	0			
214	796.17	PS	0	0	0	1		1	0			
214	796.25	PS	1	0	0	1		2	0			
214	796.45	PS	2	0	0	1		3	0			
214	796.5	PS	0	0	0	1		1	0			
214	796.57	PS	0	1	0	1		2	0			
214	796.6	PS	0	1	0	1		2	0			
214	796.7	PS	1	0	0	1		2	0			
214	796.73	PS	0	0	0	1		1	0			
214	796.8	PS	0	0	1	1		2	0			
214	796.92	PS	0	0	0	1		1	0			
214	796.95	PS	0	0	0	1		1	0			
214	797	PS	2	1	0	1		4	0			
214	797.1	PS	0	2	0	1		3	0			
214	797.25	PS	0	0	0	1		1	0			59
250	894.5	PS	2	1	0	1		4	0			
250	894.55	PS	2	1	1	1		5	0			
250	894.6	PS	2	0	0	1		3	0			
250	894.7	PS	3	1	0	1		5	0			
250	894.8	PS	2	0	0	1		3	0			
250	894.85	PS	1	0	0	1		2	0			
250	894.9	PS	1	1	1	1		4	1			
250	894.92	PS	3	2	1	1		7	1			
250	895.05	PS	3	2	0	1		6	1	Moderate/strong drilling overprint.		
250	895.1	PS	3	1	0	1		5	1	Moderate/strong drilling overprint.		
250	895.15	PS	3	1	0	1		5	1	Moderate/strong drilling overprint.		

250	895.2	PS	1	1	0	1		3	1	Moderate/strong drilling overprint.		
250	895.7	PS	0	0	0	1		1	0			
250	895.75	PS	0	0	0	1		1	1			
250	895.77	PS	3	1	0	1		5	0			
250	895.85	PS	1	1	0	1		3	1			
250	895.9	PS	1	1	0	1		3	1			
250	896.05	PS	1	1	0	1		3	1			
250	896.07	PS	1	1	0	1		3	1			
250	896.1	PS	3	0	0	1		4	0			
250	896.35	PS	3	0	0	1		4	1			
250	896.37	PS	1	1	1	1		4	0			
250	896.53	PS	3	2	1	0	Brown	6	1			
250	896.7	PS	3	0	0	0	Brown	3	1			
250	896.95	PS	3	2	1	0	Brown	6	1			
251	897.4	PS	1	0	1	1		3	1			
251	897.45	PS	1	1	0	1		3	1			
251	897.48	PS	3	1	0	1		5	1			
251	897.53	PS	3	1	1	1		6	1			
251	897.6	PS	3	1	0	1		5	1			
251	897.65	PS	1	0	1	1		3	1			
251	898	PS	1	0	1	1		3	1			
251	898.03	PS	3	2	1	1		7	2			
251	898.45	PS	1	2	0	1		4	1			
251	899	PS	1	2	0	0	Purple/Rusty Yellow	3	1	Rock here is flaking.		
251	899.1	PS	1	0	0	1		2	1			
251	899.15	PS	1	0	0	1		2	1			
251	899.17	PS	1	1	0	1		3	1			

251	899.25	PS	1	0	0	1		2	1			
251	899.27	PS	0	2	0	1		3	1			
251	899.4	PS	3	0	0	1		4	1			
251	899.45	PS	1	0	0	1		2	1			
251	899.6	PS	1	2	0	0	Brown/Red/Rusty	3	2		#1 (3/3/23 @ 08:38)	
251	899.65	PS	1	1	0	1		3	1			
251	899.7	PS	2	1	2	1		6	0			
251	899.8	PS	1	0	2	1		4	1			
252	900.05	PS	1	1	0	1		3	0			
252	900.1	PS	1	0	0	1	Brown/Grey	2	1			
252	900.12	PS	1	2	0	0		3	1			
252	900.15	PS	2	0	0	1		3	0			
252	900.25	PS	3	1	0	1		5	0			
252	900.32	PS	3	0	0	0	Brown/Grey	3	1			
252	900.45	PS	1	2	1	0	Yellow	4	1			
252	900.65	PS	3	1	2	1		7	1			
252	900.67	PS	1	0	0	1		2	1			
252	900.7	PS	2	0	0	1		3	0			
252	900.72	PS	2	0	0	1		3	0			
252	900.75	PS	0	0	0	1		1	1			
252	900.77	PS	0	0	0	1		1	1			
252	900.9	PS	2	1	0	1		4	0			
252	900.95	PS	0	0	0	1		1	1			
252	900.97	PS	0	0	0	1		1	1			
252	901	PS	3	1	0	1		5	2			
252	901.5	PS	0	1	0	1		2	1			
252	901.6	PS	1	1	0	1		3	1			

252	901.7	PS	0	1	0	1		2	1			
252	902.35	SST	0	0	0	1		1	0			
253	902.68	SST	0	0	0	1		1	0			
253	903	SST	0	0	0	1		1	0			
253	903.3	SST	0	0	0	1		1	0			
253	903.55	SST	0	0	0	1		1	0			
253	903.75	SST	0	0	0	1		1	0			
253	904.05	SST	0	0	0	1		1	0			
253	904.35	SST	0	0	0	1		1	0			
253	904.55	SST	0	0	0	1		1	0			
254	905.95	SST	0	0	0	1		1	0			
254	906.9	SST	0	0	0	1		1	0			
254	907.1	SST	0	0	0	1		1	0			
254	907.35	SST	0	0	0	1		1	0			
254	907.99	SST	0	2	0	1		3	1	Clay layer in SST.		80
290	1007.25	PS	0	1	0	1		2	1			
290	1007.6	PS	1	0	0	1		2	1			
290	1007.65	PS	1	0	0	1		2	1			
290	1007.7	PS	0	1	2	1		4	1			
290	1007.75	PS	1	1	2	1		5	1			
290	1007.77	PS	2	1	2	1		6	1			
290	1007.8	PS	3	2	0	1		6	1			
290	1007.88	PS	3	0	0	1		4	1			
290	1008.5	PS	1	0	0	1		2	1			

290	1008.5 5	PS	0	0	0	1		1	1			
290	1008.5 8	PS	2	0	0	1		3	0			
290	1008.6 5	PS	1	0	0	1		2	1			
290	1009.1	PS	0	1	0	1		2	1			
290	1009.1 5	PS	0	2	0	1		3	0			
290	1009.4 5	PS	0	0	0	1		1	1			
290	1009.5 3	PS	0	0	0	1		1	1			
291	1009.7 5	PS	1	0	0	1		2	1			
291	1009.9	PS	0	0	0	1		1	1			
291	1010.0 7	PS	1	0	0	1		2	1			
291	1010.2	PS	1	1	0	1		3	1			
291	1010.2 5	PS	1	0	0	1		2	1			
291	1010.3	PS	3	2	0	1		6	1			
291	1010.3 2	PS	1	1	0	1		3	1	Shiny.		
291	1010.4	PS	1	0	0	1		2	1			
291	1010.4 5	PS	1	0	0	1		2	1			
291	1010.5	PS	0	0	2	1		3	1			
291	1010.5 5	PS	1	0	0	1		2	1			
291	1010.6	PS	1	0	0	1		2	1			
291	1010.6 2	PS	1	0	1	1		3	1			
291	1010.7	PS	0	1	0	1		2	1			
291	1010.8 5	PS	1	1	0	1		3	1			

291	1010.8 6	PS	1	2	0	1		4	1		
291	1010.9	PS	0	0	0	1		1	1		
291	1010.9 2	PS	0	0	0	1		1	1		
291	1010.9 8	PS	0	2	0	1		3	1		
291	1010.9 9	PS	0	2	0	1		3	1		
291	1011	PS	1	0	0	1		2	1		
291	1011.1	PS	0	0	0	1		1	1		
291	1011.1 1	PS	0	0	0	1		1	1		
291	1011.1 5	PS	0	1	0	1		2	1		
291	1011.1 7	PS	1	0	0	1		2	1		
291	1011.5 8	PS	0	1	0	1		2	1		
291	1011.7 5	PS	0	0	0	1		1	1		
291	1012.1	PS	0	1	0	1		2	1		
291	1012.2 5	PS	0	0	0	1		1	1	Boundary PS/SST	
292	1012.8 5	SST	0	0	0	1		1	0		
292	1013	SST	0	0	0	1		1	0		
292	1013.2	SST	0	0	0	1		1	0		
292	1013.6	SST	0	0	0	1		1	0		
292	1013.9	SST	0	0	0	1		1	0		
292	1014.2	SST	0	0	0	1		1	0		
292	1014.4	SST	0	0	0	1		1	0		
292	1015.1 5	SST	0	0	0	1		1	1	SST/PS Boundary - small PS layer	
293	1015.5 5	SST	0	0	0	1		1	0		

293	1016.1	SST	0	0	0	1		1	0			
293	1016.6	PS	3	0	1	1		5	1	PS/SST Boundary - small PS layer		
293	1016.8	SST	0	0	0	1		1	0			
293	1017.1	SST	0	0	0	1		1	0			
293	1017.7 5	SST	1	0	0	1		2	0			
293	1018	SST	0	0	0	1		1	0			
294	1018.2 5	SST	0	0	0	1		1	0	SST/PS Boundary		
294	1018.4 5	PS	1	0	0	1		2	1			
294	1018.6	PS	1	2	2	1		6	1			
294	1018.8	PS	1	1	2	1		5	1			
294	1018.9 5	PS	1	0	1	1		3	1			
294	1019	PS	1	0	1	1		3	1			
294	1019.6	SST	0	0	0	1		1	0			
294	1020.2 5	SST	0	0	0	1		1	0			
294	1020.4 7	SST	0	0	0	1		1	0			
294	1020.7	SST	0	0	0	1		1	0			
294	1020.9 5	SST	0	0	0	1		1	0			71
330	1121.3	SST	0	0	0	1		1	0			
330	1121.5 2	SST	0	0	0	1		1	0			
330	1121.7 2	SST	0	0	0	1		1	0			
330	1122.2	SST	0	0	0	1		1	0			
330	1122.4	PS	1	0	0	1		2	1			
330	1123.3	PS	0	0	0	1		1	0			

331	1124.3 5	PS	1	1	0	1		3	1		
331	1124.6 5	SST	0	0	0	1		1	0		
331	1125	SST	0	0	0	1		1	0		
331	1125.6 5	SST	0	0	0	1		1	0		
331	1125.8 7	SST	0	0	0	1		1	0		
331	1128.1	SST	0	0	0	1		1	0		
331	1128.5	SST	0	0	0	1		1	1		
332	1126.9 7	SST	0	0	0	1		1	0		
332	1127.3	SST	0	0	0	1		1	0		
332	1127.5	SST	0	0	0	1		1	0		
332	1127.9 8	PS	1	0	0	0	Grey/Purple	1	1	Polished shiny.	
332	1128.0 7	PS	1	1	0	1		3	1	PS/SST Boundary - not as poshied as above.	
332	1128.5	PS	1	1	1	1		4	1	Clay layer.	
332	1128.5 1	PS	1	1	1	1		4	1		
332	1128.5 3	PS	1	1	1	1		4	1		
332	1129.0 5	SST	0	0	0	1		1	0		
333	1129.6	SST	1	2	0	1		4	1		
333	1129.9 5	SST	0	0	0	1		1	0		
333	1130.5	PS	0	0	0	1		1	0		
333	1130.5 5	PS	1	0	0	1		2	1		
333	1130.7	PS	3	1	0	1		5	1		
333	1130.8	PS	0	1	0	1		2	1		
333	1131.2	PS	0	1	0	1		2	0		

333	1131.6	PS	0	1	0	1		2	0			
333	1131.6 2	PS	2	0	0	1		3	0			
333	1131.6 5	PS	0	1	0	1		2	0			
333	1131.7 2	PS	0	1	0	1		2	0			
334	1132.6 7	PS	0	0	0	1		1	0			
334	1132.9	PS	1	0	0	1		2	1			
334	1133.4 7	PS	0	1	0	1		2	0			
334	1133.6	PS	2	0	0	1		3	0			
334	1133.9	PS	0	1	0	1		2	0			
334	1134.4	PS	0	1	0	1		2	0			
334	1134.8	PS	1	1	1	1		4	1			
334	1134.8 5	PS	3	1	1	1		6	1			
334	1134.9	PS	3	1	1	1		6	1			
334	1135.1	PS	0	1	0	1		2	0			43
350	1177.9 5	PS	0	0	0	1		1	1			
350	1178.4	PS	0	0	0	1		1	0			
350	1178.5	PS	0	0	0	1		1	0			
350	1178.5 5	PS	0	0	0	1		1	1			
350	1178.8	PS	2	0	0	1		3	0			
350	1178.8 5	PS	0	0	0	1		1	0			
350	1178.9	PS	0	0	0	1		1	0			
350	1179.0 5	PS	0	0	0	1		1	0			
350	1179.3	PS	0	0	0	1		1	0			

350	1179.6 5	PS	1	1	0	1		3	1		
350	1179.8	SST	1	0	0	1		2	1	Bedding?	
350	1180.3 5	SST	0	0	0	1		1	0		
351	1180.9	SST	0	0	0	1		1	1	Bedding	
351	1180.9 7	SST	0	0	0	1		1	1		
351	1181.1	SST	0	0	0	1		1	0		
351	1181.6	SST	0	0	0	1		1	0		
351	1181.9	SST	1	1	0	1		3	1	SST/PS Boundary	
351	1182.2 5	PS	1	0	0	1		2	1		
351	1182.3	PS	0	1	0	1		2	1		
351	1182.3 5	PS	3	0	0	1		4	1		
351	1182.3 7	PS	0	1	0	1		2	1		
351	1182.3 8	PS	1	0	0	1		2	1		
351	1182.4 5	PS	0	0	0	1		1	1		
351	1183.0 3	PS	0	1	0	1		2	0		
351	1183.4 8	PS	0	1	0	1		2	0		
351	1183.5 5	PS	0	1	0	1		2	0		
351	1183.6	PS	0	1	0	1		2	0		
351	1183.6 5	PS	0	1	0	1		2	0		
352	1183.7 3	PS	0	0	0	1		1	1		
352	1184.0 2	SST	0	1	0	1		2	0		
352	1184.4 5	PS	0	0	0	1		1	1	Sandy	

352	1184.4 9	PS	0	0	0	1		1	1	Sandy		
352	1184.7	PS	0	1	0	1		2	0			
352	1185	PS	0	0	0	1		1	0			
352	1185.0 5	PS	1	1	0	1		3	1			
352	1186.0 4	SST	0	0	0	1		1	1			
352	1186.2	PS	3	0	0	1		4	1			
352	1186.2 5	PS	1	0	0	1		2	1			
352	1186.3	PS	1	0	0	1		2	1			
352	1186.4	PS	1	0	0	1		2	1			
352	1186.4 5	PS	1	0	0	1		2	1			
353	1186.5	PS	2	0	0	1		3	0			
353	1186.5 5	PS	1	1	0	1		3	1			
353	1186.5 8	PS	1	1	0	1		3	1			
353	1186.6 5	PS	0	0	0	1		1	0			
353	1187.1	PS	0	0	0	1		1	0			
353	1187.2	PS	0	0	0	1		1	0			
353	1187.3 5	PS	3	1	0	1		5	0			
353	1187.3 7	PS	0	0	0	1		1	0			
353	1187.4 7	PS	0	1	0	1		2	0			
353	1187.5 7	PS	0	1	0	1		2	0			
353	1187.9	SST	0	1	0	1		2	0			
353	1188.1	SST	0	1	0	1		2	0			
353	1188.8	SST	0	1	0	1		2	0			

354	1189.4 5	PS	0	1	0	1		2	0			
354	1190	SST	0	0	0	1		1	0			
354	1190.7	PS	1	0	0	1		2	1	SST/PS Boundary		
354	1191.0 5	PS	1	1	1	1		4	0			
354	1191.0 7	PS	1	1	0	1		3	0			
354	1191.1	PS	1	0	0	1		2	0			
354	1191.1 3	PS	1	1	0	1		3	0			
354	1191.3 5	PS	0	1	0	1		2	0			
354	1191.5 7	SST	0	0	0	1		1	1			
354	1191.9 9	SST	1	0	0	0		1	1			
354	1192.0 3	PS	1	1	0	0	Purple	2	1			
354	1192.0 5	PS	1	1	0	0	Purple	2	1			
354	1192.0 8	PS	3	2	0	1	Purple	6	0			
354	1192.1	SST	1	1	0	1		3	1	Bedding plane.		68
310	1063.9 2	SST	0	0	0	1		1	0	Bedding contact.		
310	1064.0 5	PS	0	0	0	1		1	0			
310	1064.2 5	PS	1	1	0	1		3	1			
310	1064.3	PS	1	0	2	1		4	1			
310	1064.6 5	PS	0	0	0	1		1	1			
310	1064.7 3	PS	0	0	0	1		1	0			
310	1064.8	PS	0	1	0	1		2	0			

310	1064.9 3	PS	0	0	0	1		1	1		
310	1065.3	PS	0	1	0	1		2	1	Bedding contact.	
310	1065.7	SST	0	1	0	1		2	0		
310	1066	SST	0	0	0	1		1	1		
311	1066.4 8	PS	0	1	0	1		2	0	Very sandy PS (for remainder of section)	
311	1066.8 5	PS	0	0	0	1		1	0		
311	1067.3 5	PS	0	0	0	1		1	1		
311	1067.9 9	PS	0	0	0	1		1	1		
311	1068.6 5	PS	0	1	0	1		2	0		
312	1069.5 5	PS	0	0	0	1		1	1		
312	1069.6 5	PS	0	0	0	1		1	1		
312	1070.0 7	PS	1	0	0	1		2	0		
312	1070.8	PS	1	1	1	1		4	1		
312	1070.9	PS	0	1	0	1		2	0		
312	1071.0 5	PS	0	1	0	1		2	0		
312	1071.1	PS	0	1	0	1		2	0		
312	1071.1 5	PS	0	0	0	1		1	0		
312	1071.1 7	PS	0	1	0	1		2	0		
312	1071.4	PS	0	1	0	1		2	0		
312	1071.4 5	PS	0	1	0	1		2	0		
312	1072	PS	0	1	0	1		2	0		
313	1072.3 5	PS	0	0	0	1		1	0		

313	1072.4 5	PS	0	1	0	1		2	1			
313	1072.6 5	PS	0	0	0	1		1	1			
313	1073.1	PS	0	1	0	1		2	0			
313	1073.1 7	PS	0	1	0	1		2	0			
313	1073.4 5	PS	0	0	0	1		1	1			
313	1073.4 9	PS	1	0	0	1		2	1	Bedding		
313	1074.4	PS	1	0	0	0	Green/Brown	1	1	Sandy, colouring evidence of fluid flow?		
313	1074.6	PS	0	1	0	1		2	0			
313	1074.7	PS	0	0	0	1		1	1			
314	1075.2 5	PS	1	0	0	1		2	1			
314	1075.3 7	PS	0	0	0	1		1	0			
314	1075.6 2	PS	1	1	1	1		4	1			
314	1075.6 5	PS	1	1	1	1		4	1			
314	1075.7	PS	0	0	0	1		1	0			
314	1076.2 5	PS	0	0	0	1		1	0			
314	1076.5 3	PS	0	1	0	1		2	1			
314	1076.7	PS	0	2	0	1		3	0			
314	1076.7 5	PS	0	2	0	1		3	0			
314	1077.4	PS	0	1	0	1		2	1			
314	1077.4 3	PS	1	1	0	1		3	1			
314	1077.7	PS	0	0	0	1		1	1			50
270	950.45	PS	2	1	0	1		4	0			

270	950.85	SST	0	0	0	1		1	0			
270	950.97	SST	0	0	0	1		1	0			
270	951.18	PS	1	1	0	1		3	1			
270	951.2	PS	1	1	0	1		3	1			
270	951.4	PS	2	1	0	1		4	1			
270	951.55	PS	1	0	0	1		2	1			
270	951.62	PS	1	0	0	1		2	0			
270	951.85	PS	0	1	0	1		2	0			
270	951.97	PS	0	0	0	1		1	1	Sandy/Conglomerate		
270	952.6	PS	0	1	0	1		2	1			
270	952.96	PS	0	0	0	1		1	0			
270	953.02	PS	0	0	0	1		1	0			
270	953.1	PS	0	0	0	1		1	0			
270	953.2	PS	0	0	0	1		1	0			
270	953.35	PS	0	0	0	1		1	0			
271	953.8	SST	0	0	0	1		1	0			
271	954.15	SST	0	1	0	1		2	0			
271	954.4	PS	1	0	0	1		2	1			
271	954.45 4	PS	1	0	0	1		2	0			
271	954.65	PS	0	0	0	1		1	0			
271	954.68	PS	1	0	0	1		2	0			
271	954.9	PS	0	0	0	1		1	0			
271	954.95	PS	0	0	0	1		1	0			
271	955.03	PS	0	0	0	1		1	0			
271	955.09	PS	0	0	0	1		1	0			
271	955.7	PS	0	0	0	1		1	0			
271	955.74	PS	0	0	0	1		1	0			

271	955.9	PS	1	0	0	1		2	1	Bedding		
271	956.15	PS	0	2	0	1		3	1	Bedding		
271	956.2	PS	0	2	0	1		3	1	Bedding		
271	956.23	PS	0	2	0	1		3	1	Bedding		
272	956.35	PS	0	1	0	1		2	1	Bedding		
272	956.42	PS	0	0	0	1		1	0			
272	956.55	PS	0	0	0	1		1	0			
272	956.8	PS	0	1	0	1		2	0			
272	956.82	PS	0	1	0	1		2	0			
272	956.83	PS	0	0	0	1		1	0			
272	957.08	PS	0	1	0	1		2	0	Sandy layer.		
272	957.55	PS	0	0	0	1		1	1	Sandy layer, Grit		
272	957.75	PS	0	1	0	1		2	1			
272	957.8	SST	0	0	0	1		1	1			
272	958	SST	1	0	0	1		2	0			
272	958.3	SST	0	0	0	1		1	0			
272	958.65	SST	3	1	0	1		5	2			
273	959.35	SST	3	1	0	1		5	2			
273	959.65	SST	0	0	0	1		1	1			
273	959.95	SST	1	1	1	1		4	1	Grit		
273	959.99	PS	1	0	0	1		2	0			
273	960.1	PS	1	0	0	1		2	0			
273	960.13	PS	1	1	0	1		3	0			
273	960.2	PS	1	1	0	1		3	0			
273	960.23	PS	0	0	0	1		1	0			
273	960.27	PS	1	1	0	1		3	0			
273	960.3	PS	2	0	0	1		3	0			

273	960.35	PS	1	0	0	1		2	1			
273	960.4	PS	0	1	0	1		2	0			
273	960.55	PS	3	1	0	1		5	1			
273	960.62	PS	1	1	0	1		3	1			
273	960.64	PS	1	1	0	1		3	1			
273	960.7	PS	1	1	0	1		3	1			
273	961.25	PS	0	0	0	1		1	1	PS w/ Grit		
273	961.45	PS	0	0	0	1		1	1	Bedding		
273	961.6	PS	1	1	0	1		3	1			
273	961.85	PS	0	0	0	1		1	1			
274	962	PS	3	1	0	1		5	2			
274	962.1	PS	1	0	0	1		2	1			
274	962.28	PS	1	1	0	1		3	1			
274	962.4	PS	1	1	0	1		3	1			
274	962.43	PS	0	1	0	1		2	1			
274	962.44	PS	2	0	0	1		3	0			
274	962.45	PS	3	2	0	1		6	2			
274	962.55	PS	1	1	0	1		3	0			
274	962.6	PS	2	0	0	1		3	0			
274	962.62	PS	3	2	0	1		6	2			
274	962.65	PS	1	2	0	1		4	2			
274	962.72	PS	1	0	0	1		2	1			
274	962.75	PS	1	0	0	1		2	1			
274	962.76	PS	1	0	0	1		2	1			
274	962.77	PS	0	0	0	1		1	1			
274	962.8	PS	0	0	0	1		1	0			
274	963	PS	2	0	0	1		3	0			

274	963.03	PS	1	1	0	1		3	1			
274	963.08	PS	0	1	0	1		2	1			
274	963.12	PS	1	1	0	1		3	1			
274	963.2	PS	1	2	0	1		4	1			
274	963.21	PS	0	2	0	1		3	1			
274	963.22	PS	0	2	0	1		3	1			
274	963.24	PS	1	1	0	1		3	1			
274	963.31	PS	0	1	0	1		2	1			
274	963.34	PS	0	1	0	1		2	1			
274	963.48	SST	1	0	0	1		2	1	Bedding		
274	963.51	SST	0	0	0	1		1	0			
274	963.57	SST	1	0	0	1		2	1			94
230	839.35	PS	1	1	0	1		3	1			
230	839.4	PS	2	0	0	1		3	0			
230	839.42	PS	1	0	0	1		2	1			
230	839.45	PS	1	0	0	1		2	1			
230	839.48	PS	2	0	0	1		3	0			
230	839.52	PS	2	0	0	1		3	0			
230	839.55	PS	1	1	0	1		3	1			
230	839.57	PS	3	1	0	1		5	0			
230	839.8	PS	1	0	0	1		2	0			
230	839.95	PS	3	0	0	1		4	1			
230	840.2	PS	3	0	0	1		4	1			
230	840.4	PS	1	0	0	1		2	1			
230	840.52	PS	3	2	0	1		6	2			
230	840.53	PS	3	1	0	0	Brown	4	2			

230	841.25	PS	1	0	0	1		2	1	Sandy layer.		
230	841.55	PS	1	0	0	1		2	1			
230	841.75	PS	3	1	0	1		5	0			
230	841.9	PS	1	1	0	1		3	1			
230	841.95	PS	0	2	0	1		3	1			
230	841.96	PS	0	0	0	1		1	0			
230	841.97	PS	2	0	0	1		3	0			
230	841.98	PS	2	0	0	1		3	0			
230	842	PS	3	2	1	1		7	1			
231	843.15	PS	1	1	0	1		3	1			
231	843.35	PS	0	0	0	1		1	1			
231	843.36	PS	3	0	0	1		4	0			
231	843.38	PS	3	0	0	1		4	0			
231	843.42	PS	3	0	0	1		4	0			
231	843.43	PS	2	0	0	1		3	0			
231	843.75	PS	1	1	0	1		3	0			
231	844.1	PS	1	1	0	1		3	0			
231	844.49	PS	1	1	0	1		3	0			
231	844.6	PS	3	1	1	0	Brown	5	2			
231	844.8	PS	1	0	0	1		2	1			
232	844.81	PS	2	1	1	0	Brown	4	2			
232	845.5	SST	0	0	0	1		1	0			
232	845.95	SST	0	0	0	1		1	0			
232	846.35	SST	0	0	0	1		1	0			
232	846.7	SST	1	0	0	1		2	1			
232	847	SST	1	0	0	1		2	1			
232	847.3	SST	1	0	0	1		2	1			

233	848.1	SST	1	0	0	1		2	1			
233	849	SST	1	0	0	1		2	1			
233	849.35	SST	0	0	0	1		1	1			
233	850.4	SST	0	0	0	1		1	0			
234	850.57	SST	0	0	0	1		1	1			
234	850.92	SST	0	0	0	1		1	1			
234	851.2	SST	0	0	0	1		1	1			
234	852.05	SST	0	0	0	1		1	1			
234	852.2	SST	0	0	0	1		1	1			
234	852.65	SST	0	0	0	1		1	1			
234	852.9	SST	0	0	0	1		1	1			52
190	727.35	SST	1	0	0	1		2	1			
190	727.4	SST	2	1	0	1		4	0	Silty		
190	727.52	SST	1	0	0	1		2	1	Silty		
190	727.55	SST	1	0	0	1		2	1	Silty		
190	727.56	SST	1	0	0	1		2	0			
190	727.75	SST	0	0	0	1		1	1			
190	728.1	SST	0	1	0	1		2	0			
190	728.75	SST	0	0	0	1		1	1			
190	728.9	SST	0	0	0	1		1	0			
190	729.2	SST	0	0	0	1		1	1			
190	729.3	SST	0	0	0	1		1	1			
190	729.7	SST	0	0	0	1		1	1			
191	729.95	SST	0	0	0	1		1	1			
191	730.15	SST	0	0	0	1		1	1			
191	730.3	SST	0	0	0	1		1	1			

191	730.35	SST	0	0	0	1		1	1			
191	730.6	SST	0	0	0	1		1	1			
191	730.72	SST	0	0	0	1		1	1			
191	730.85	SST	0	0	0	1		1	1			
191	731.02	SST	0	1	0	1		2	1			
191	732.15	SST	0	0	0	1		1	0	High bedding angle ~45 deg		
191	732.6	SST	3	2	0	1		6	2			
191	732.65	SST	3	2	0	1		6	0	Slip surface?	7/2/23 @ 10:11am	
192	732.7	SST	3	1	0	1		5	0			
192	732.72	PS	1	0	0	1		2	1			
192	732.85	PS	1	0	0	1		2	1			
192	733	PS	3	0	0	1		4	1			
192	734.35	PS	1	0	0	1		2	1	Boundary PS/SST		
192	735.15	SST	0	0	0	1		1	1			
192	735.4	SST	0	0	0	1		1	1			
193	735.9	SST	0	0	0	1		1	1			
193	736.1	SST	0	0	0	1		1	1			
193	736.25	SST	0	0	0	1		1	1			
193	736.28	SST	0	0	0	1		1	1			
193	736.6	SST	0	0	0	1		1	1			
193	737.95	SST	0	0	0	1		1	1			
193	737.3	SST	0	0	0	1		1	1			
193	737.6	SST	3	1	0	1		5	2			
193	737.9	SST	0	0	0	1		1	1			
193	738.2	PS	1	0	0	1		2	1	SST/PS Boundary		
194	738.65	PS	1	0	0	1		2	1			
194	738.82	PS	3	1	0	1		5	2			

194	738.85	PS	1	1	0	1		3	0			
194	739.05	PS	2	0	0	1		3	2		7/2/23 @ 10:30am	
194	739.1	PS	1	0	0	1		2	0			
194	739.18	PS	1	0	0	1		2	0			
194	739.19	PS	1	0	0	1		2	0			
194	739.3	PS	1	0	0	1		2	0			
194	739.4	PS	1	0	0	1		2	0			
194	739.5	PS	1	0	0	1		2	0			
194	739.52	PS	2	0	0	1		3	1			
194	739.6	PS	3	1	0	1		5	0			
194	740	PS	2	1	0	1		4	2		7/3/23 @ 10:25am	
194	740.03	PS	0	0	0	1		1	0			
194	740.15	PS	0	0	0	1		1	0			
194	740.3	PS	3	2	0	1		6	2			
194	740.48	PS	0	2	0	1		3	1			
194	740.6	PS	0	2	0	1		3	1			
194	740.8	PS	0	2	0	1		3	1			
194	740.95	PS	0	2	0	1		3	1			
194	741.22	PS	0	2	0	1		3	1			61
150	617.75	SST	1	0	0	1		2	1			
150	618.25	SST	0	0	0	1		1	0			
150	618.4	SST	0	0	0	1		1	0			
150	618.65	SST	0	0	0	1		1	0			
150	619	SST	0	0	0	1		1	1	Fracture split around clast		
150	619.52	SST	0	0	0	1		1	0			

150	619.75	SST	0	0	0	1		1	0			
151	620.22	SST	0	0	0	1		1	0			
151	620.38	SST	0	0	0	1		1	1			
151	620.5	SST	1	0	0	1		2	1		7/2/23 @ 10:46am	
151	620.55	PS	3	0	2	1		6	1			
151	620.6	PS	0	2	0	1		3	1			
151	620.85	PS	1	1	0	1		3	1			
151	620.88	PS	1	1	0	1		3	1			
151	620.95	PS	1	2	0	0	Green/White/ Yellow	3	1			
151	621.02	PS	1	1	0	1		3	0			
151	621.08	PS	1	1	0	1		3	0			
151	621.35	PS	1	2	0	1		4	1			
151	621.45	SST	0	0	0	1		1	0			
151	621.75	PS	1	1	2	1		5	1	Bedding		
151	621.98	SST	0	0	0	1		1	0			
151	622.07	SST	0	0	0	1		1	0			
151	622.4	SST	0	0	0	1		1	0			
151	622.45	SST	0	0	0	1		1	0			
152	623.3	SST	0	0	0	1		1	0	Grit		
152	623.67	SST	0	0	0	1		1	1			
152	623.8	SST	0	0	0	1		1	0			
152	623.9	SST	1	0	0	1		2	0			
152	624.3	SST	0	0	0	1		1	0			
152	624.53	SST	0	0	0	1		1	0			
152	624.64	SST	0	0	0	1		1	0			
152	624.8	SST	0	0	0	1		1	0			

153	625.2	SST	1	0	0	1		2	1			
153	625.23	SST	1	0	0	1		2	1	Boundary SST/PS		
153	625.3	PS	1	2	2	1		6	1			
153	625.33	PS	1	0	1	1		3	1			
153	625.39	PS	1	1	0	1		3	1			
153	625.6	PS	1	1	0	1		3	1			
153	625.9	PS	0	0	0	1		1	1			
153	626.3	PS	0	0	0	1		1	1			
153	626.57	PS	0	0	0	1		1	1			
153	627.3	PS	1	0	0	1		2	1	Sandy Grit/Cong. layer		
153	627.45	PS	3	0	0	1		4	0			
153	627.47	PS	2	0	0	1		2	0			
153	627.52	PS	1	0	0	1		2	0			
153	627.6	PS	3	0	0	1		4	0			
153	627.65	PS	3	0	0	1		4	0			
154	628	SST	0	0	0	1		1	0			
154	628.2	SST	0	0	0	1		1	0			
154	628.4	SST	0	0	0	1		1	0			
154	628.6	SST	0	0	0	1		1	0			
154	628.8	SST	0	0	0	1		1	0			
154	628.92	SST	0	0	0	1		1	0			
154	629.03	SST	0	0	0	1		1	0			
154	629.13	SST	0	0	0	1		1	0			
154	629.16	SST	0	0	0	1		1	0			
154	629.2	SST	0	0	0	1		1	0			
154	629.25	SST	0	1	0	1		2	1	SST/PS Boundary		
154	629.35	PS	1	1	0	1		3	1			

154	629.37	PS	1	1	0	1		3	1			
154	629.51	PS	1	1	0	1		3	1			
154	629.53	PS	2	0	2	1		5	1			
154	629.55	PS	3	2	2	1		8	1			
154	629.6	PS	0	0	0	1		1	1			
154	629.63	PS	0	0	0	1		1	0			
154	629.65	PS	0	0	0	1		1	0			
154	629.7	PS	0	0	0	1		1	0			
154	630.05	PS	0	0	0	1		1	0			
154	630.25	PS	0	0	0	1		1	0			
154	630.4	PS	0	0	0	1		1	0			70
110	506.62	PS	0	0	0	1		1	1	PS/SST Boundary		
110	506.7	SST	0	0	0	1		1	0			
110	506.95	SST	0	0	0	1		1	0			
110	507.05	SST	0	0	0	1		1	0			
110	507.25	SST	0	0	0	1		1	0			
110	507.8	SST	0	0	0	1		1	1			
110	508.1	SST	0	0	0	1		1	0	SST/PS Boundary		
110	508.3	SST	0	0	0	1		1	1			
110	508.6	PS	0	0	0	1		1	1			
110	508.95	PS	0	0	0	1		1	1	Sandy layer.		
111	509.5	PS	0	0	0	1		1	1			
111	509.9	PS	0	1	0	1		2	0			
111	509.92	PS	1	0	0	1		2	1			
111	509.98	PS	0	0	0	1		1	1			
111	510.03	PS	0	1	0	1		2	1			

111	510.04	PS	0	0	0	1		1	1			
111	510.1	PS	3	1	1	1		6	1			
111	510.12	PS	3	1	1	1		6	1			
111	510.45	PS	1	0	0	1		2	1			
111	510.47	PS	3	0	0	1		4	1			
111	510.5	PS	1	1	0	1		3	1			
111	510.55	PS	1	1	0	1		3	1			
111	510.57	PS	1	0	0	1		2	1			
111	510.6	PS	1	0	0	1		2	1			
111	510.61	PS	1	0	0	1		2	1			
111	510.65	PS	1	0	0	1		2	1			
111	510.7	PS	3	1	0	1		5	1			
111	510.75	PS	1	1	0	1		3	1			
111	510.77	PS	1	2	0	1		4	1			
111	510.78	PS	3	0	0	1		4	0			
111	510.79	PS	1	1	1	1		4	1			
111	510.82	PS	0	1	1	1		3	1			
111	510.85	PS	1	1	1	1		4	1			
111	510.88	PS	1	1	1	1		4	1			
111	511.45	PS	0	0	0	1		1	1			
111	511.7	PS	0	0	0	1		1	1			
111	512	PS	0	0	0	1		1	1			
112	512.3	PS	0	0	0	1		1	1			
112	513.2	PS	0	1	0	1		2	1			
112	513.3	PS	1	0	0	1		2	1			
112	514.2	SST	1	0	0	1		2	0		Sandy layer.	
112	514.65	PS	0	0	0	1		1	1			

113	514.97	SST	0	0	0	1		1	1			
113	515.35	SST	0	0	0	1		1	0			
113	515.4	SST	0	0	0	1		1	1	Bedding.		
113	515.8	SST	0	0	0	1		1	1			
113	516.45	SST	0	0	0	1		1	1			
113	517.2	SST	0	0	0	1		1	1			
114	517.8	SST	3	1	1	1		6	2	SST/PS Boundary		
114	517.87	PS	0	0	0	1		1	0			
114	518	PS	1	0	0	1		2	1			
114	518.04	PS	0	0	0	1		1	0			
114	518.1	PS	1	2	1	1		5	1			
114	518.12	PS	0	0	0	1		1	0			
114	518.35	PS	1	1	0	1		3	1			
114	518.36	PS	0	1	0	1		2	0			
114	518.37	PS	0	0	1	1		2	1			
114	518.39	PS	1	0	0	1		2	1			
114	518.4	PS	1	0	0	1		2	1			
114	518.45	PS	1	0	0	1		2	1			
114	518.47	PS	1	0	0	1		2	1			
114	518.52	PS	1	0	0	1		2	1			
114	518.85	PS	0	0	0	1		1	1			
114	519.02	PS	0	0	0	1		1	1			
114	519.4	PS	0	1	1	1		3	1			
114	519.92	PS	0	0	0	1		1	1			
114	520.3	PS	0	0	0	1		1	1			67
70	397.05	PS	0	0	0	1		1	1			

70	397.3	PS	0	0	0	1		1	1			
70	397.4	PS	0	0	0	1		1	1			
70	397.5	PS	0	0	0	1		1	1			
70	397.62	PS	0	0	0	1		1	1			
70	397.67	PS	0	0	0	1		1	1			
70	397.7	PS	0	0	0	1		1	1			
70	397.77	PS	0	0	0	1		1	1			
70	397.86	PS	0	0	0	1		1	1			
70	398.12	PS	0	0	0	1		1	1			
70	398.17	PS	0	0	0	1		1	1			
70	398.3	PS	0	0	0	1		1	1			
70	398.35	PS	2	0	0	1		3	1			
70	398.45	PS	0	0	0	1		1	1			
70	398.5	PS	1	0	0	1		2	1			
70	398.51	PS	1	0	0	1		2	1			
70	398.59	PS	1	0	0	1		2	1			
70	398.6	PS	3	0	0	1		4	1			
70	398.62	PS	1	0	0	1		2	1			
70	398.64	PS	1	0	0	1		2	1			
70	398.67	PS	1	0	0	1		2	1			
70	398.75	PS	3	0	0	1		4	0			
70	398.85	PS	1	0	0	1		2	1			
70	398.9	PS	3	0	0	1		4	0			
70	398.95	PS	0	0	0	1		1	1			
70	399.15	PS	1	0	0	1		2	1			
70	399.25	PS	1	0	0	1		2	1			
70	399.32	PS	0	0	0	1		1	1			

70	399.35	PS	1	0	0	1		2	1			
70	399.45	PS	1	0	0	1		2	1			
71	399.65	PS	2	0	0	1		3	1			
71	399.67	PS	0	1	0	1		2	1			
71	399.72	PS	0	0	0	1		1	1			
71	399.75	PS	0	0	0	1		1	1			
71	399.82	PS	0	0	0	1		1	1			
71	399.9	PS	0	0	0	1		1	1			
71	399.98	PS	0	0	0	1		1	1			
71	400.1	PS	0	0	0	1		1	1			
71	400.25	PS	0	0	0	1		1	1			
71	400.6	PS	0	0	0	1		1	1			
71	400.65	PS	3	0	0	1		4	1			
71	400.7	PS	1	0	0	1		2	1			
71	400.75	PS	0	0	0	1		1	1			
71	400.8	PS	0	0	0	1		1	1			
71	400.83	PS	0	0	0	1		1	1			
71	401.45	PS	1	0	0	1		2	1			
71	401.5	PS	0	0	0	1		1	1			
71	401.65	PS	0	0	0	1		1	1			
71	401.67	PS	0	0	0	1		1	1			
71	401.68	PS	0	0	0	1		1	1			
71	401.75	PS	0	0	0	1		1	1			
71	401.78	PS	0	0	0	1		1	1			
72	402.49	PS	0	0	0	1		1	1			
72	402.53	PS	0	0	0	1		1	1			
72	402.65	PS	0	0	0	1		1	1			

72	402.68	PS	1	0	0	1		2	1			
72	402.8	PS	1	0	0	1		2	1			
72	402.9	PS	2	0	0	1		3	1			
72	403.3	PS	1	0	0	1		2	1			
72	403.31	PS	2	0	0	1		3	1			
72	403.35	PS	1	0	0	1		2	1			
72	403.55	PS	1	0	0	1		2	1			
72	403.58	PS	0	0	0	1		1	1			
72	403.62	PS	0	0	0	1		1	0			
72	403.75	PS	1	0	0	1		2	1			
72	403.76	PS	0	0	0	1		1	1			
72	403.79	PS	1	0	0	1		2	1			
72	403.82	PS	1	0	0	1		2	1			
72	403.84	PS	3	0	0	1		4	1			
72	403.97	PS	0	0	0	1		1	1			
72	404	PS	1	0	0	1		2	1			
72	404.1	PS	1	0	0	1		2	1			
72	404.13	PS	3	0	0	1		4	1			
73	405.4	PS	1	0	0	1		2	1			
73	405.45	PS	1	0	0	1		2	1			
73	405.7	PS	0	1	0	1		2	1			
73	405.85	PS	0	0	0	1		1	1			
73	406.52	PS	0	1	0	1		2	1			
73	406.7	PS	0	0	0	1		1	1			
73	406.8	PS	0	1	0	1		2	1	PS/SST Boundary		
73	406.85	SST	0	1	0	1		2	1			
73	407.15	SST	0	0	0	1		1	1			

74	407.4	SST	1	0	0	1		2	1			
74	408	PS	0	0	0	1		1	1			
74	408.07	PS	0	0	0	1		1	1			
74	408.2	PS	1	1	1	1		4	1			
74	408.28	PS	1	0	0	1		2	1			
74	408.33	PS	1	0	1	1		3	1			
74	408.37	PS	1	0	0	1		2	1			
74	408.38	PS	0	0	0	1		1	1			
74	408.43	PS	0	0	0	1		1	1			
74	408.46	PS	0	0	0	1		1	1			
74	408.5	PS	1	0	0	1		2	1			
74	408.55	PS	0	0	0	1		1	1			
74	408.6	PS	0	0	0	1		1	1			
74	408.66	PS	0	0	0	1		1	1			
74	408.7	PS	3	1	0	1		5	1			
74	408.73	PS	1	0	0	1		2	1			
74	408.79	PS	0	0	0	1		1	1			
74	408.82	PS	0	0	0	1		1	1			
74	408.84	PS	0	0	0	1		1	1			
74	408.9	PS	1	0	0	1		2	1			
74	409.12	PS	1	0	0	1		2	1			
74	409.15	PS	2	0	1	1		4	1			
74	409.2	PS	1	0	0	1		2	1			
74	409.21	PS	0	0	0	1		1	1			
74	409.23	PS	1	0	0	1		2	1			
74	409.24	PS	0	0	0	1		1	1			
74	409.35	PS	0	0	0	1		1	1			

74	409.35	PS	1	1	0	1		3	1			
74	409.47	PS	1	1	0	1		3	1			111
30	286.73	SST	0	0	0	1		1	0			
30	286.94	SST	0	0	0	1		1	0			
30	287.12	SST	0	0	0	1		1	0			
30	287.46	SST	0	0	0	1		1	1			
30	287.97	SST	0	0	0	1		1	1		Grit	
30	288.4	PS	0	0	0	1		1	1		SST/PS Boundary	
30	288.42	PS	1	0	0	1		2	1			
30	288.95	PS	0	0	0	1		1	1		Bedding	
30	289.5	PS	0	0	0	1		1	1			
31	289.6	PS	1	0	0	1		2	1			
31	289.64	PS	1	0	0	1		2	1			
31	289.69	PS	0	0	0	1		1	1			
31	289.7	PS	0	0	0	1		1	1			
31	289.77	PS	1	0	0	1		2	1			
31	289.85	PS	1	0	0	1		2	1			
31	289.95	PS	0	0	0	1		1	1			
31	289.98	PS	1	0	0	1		2	1			
31	290.07	PS	1	1	0	1		3	1			
31	290.15	PS	1	1	0	1		3	1		Bedding	
31	290.25	PS	0	0	0	1		1	1			
31	290.45	PS	0	0	0	1		1	1			
31	290.82	PS	3	0	0	1		4	1			
31	290.85	PS	1	0	0	1		2	1			
31	290.95	PS	0	0	0	1		1	1			

31	291	PS	0	0	0	1		1	1			
31	291.23	PS	0	0	0	1		1	1			
31	291.41	PS	0	0	0	1		1	1			
31	291.43	PS	0	0	0	1		1	1			
31	291.47	PS	0	0	0	1		1	1			
31	291.52	PS	0	0	0	1		1	1			
31	291.6	PS	0	0	0	1		1	1			
31	291.63	PS	0	0	0	1		1	1			
31	291.65	PS	2	0	0	1		3	1			
31	291.96	SST	0	0	0	1		1	1	PS/SST Boundary		
31	292.1	SST	0	0	0	1		1	1			
31	292.16	SST	0	0	0	1		1	1			
31	292.45	SST	0	0	0	1		1	1			
31	292.47	SST	0	0	0	1		1	1			
32	292.75	SST	1	0	0	1		2	1			
32	293.4	SST	0	0	0	1		1	1			
32	293.5	SST	3	0	0	1		4	0			
32	293.55	SST	0	0	0	1		1	1			
32	293.6	SST	0	0	0	1		1	1			
32	294	SST	0	0	0	1		1	1	SST/PS Boundary		
32	294.01	PS	1	0	0	1		2	1			
32	294.15	PS	1	0	0	1		2	1			
32	294.22	PS	3	0	0	1		4	1			
32	294.35	PS	1	0	0	1		2	1			
32	294.36	PS	3	0	0	1		4	1			
32	294.38	PS	1	0	0	1		2	1			
32	294.4	PS	3	1	1	1		6	1			

32	294.42	PS	2	0	0	1		3	1			
32	294.5	PS	1	0	0	1		2	1			
32	294.5	PS	1	0	0	1		2	1			
32	294.51	PS	1	0	0	1		2	1			
32	294.57	PS	1	0	0	1		2	1			
32	294.8	PS	1	0	0	1		2	1			
32	294.83	PS	1	0	0	1		2	1			
32	294.92	PS	0	0	0	1		1	1			
32	294.95	PS	3	0	0	1		4	1			
32	294.98	PS	1	0	0	1		2	1			
32	295.06	PS	0	0	0	1		1	1			
32	295.18	PS	0	0	0	1		1	1			
33	295.53	PS	1	0	0	1		2	1			
33	295.6	PS	3	1	0	1		5	1			
33	295.8	PS	0	0	0	1		1	1			
33	295.97	PS	0	0	0	1		1	1			
33	296.1	PS	3	0	0	1		4	1			
33	296.2	PS	0	0	0	1		1	1			
33	296.24	PS	0	0	0	1		1	1			
33	296.52	PS	0	0	0	1		1	1			
33	296.53	PS	3	1	0	1		5	2	Deformation bands (?) nearby		
33	297.1	PS	0	0	0	1		1	1			
33	297.9	PS	0	0	0	1		1	1			
33	298	PS	0	0	0	1		1	1			
34	298.24	PS	0	0	0	1		1	0			
34	298.6	PS	1	0	0	1		2	1			
34	298.8	PS	0	0	0	1		1	1			

34	298.9	PS	0	0	0	1		1	1			
34	299.2	PS	0	0	0	1		1	1			
34	299.5	PS	0	0	0	1		1	1			
34	299.8	PS	0	0	0	1		1	1			
34	300.4	PS	0	0	0	1		1	1			
34	300.6	PS	0	0	0	1		1	1			
34	300.75	PS	3	2	0	1		6	2			
34	300.9	PS	2	2	0	1		5	2			
34	300.93	PS	0	0	0	1		1	1			
34	300.97	PS	0	0	0	1		1	1			
34	301	PS	0	0	0	1		1	1			
34	301.05	PS	0	0	0	1		1	1			90

Table A8-2 – Deformation logging data from the Harvey-2 core.

Tray Number	Tray Section	Lithology	Lithology (% of Total Tray Section)	Tray Start Depth (m)	Deformation Number (% of Total Tray Section)						Bedding (°)	Average Bedding (°)	Comments
					0	1	2	3	4	5			
1	A	PS	50	207.7	25		25						
1	A	SST	50			30	20						
1	B	SST	100			80			20		20-35	27.5	
1	C	SST	100			100							
2	A	SST	40	210.3			40						
2	A	PS	60			60							
2	B	PS	100				70		30				
2	C	PS	100					15	15	70			
3	A	PS	100	213				30		70			
3	B	PS	100				70	10		20			
3	C	PS	50			30		10	10				
3	C	SST	50			30	20						
4	A	SST	100	215.7	80					20			
4	B	SST	100		20	5				75			
4	C	SST	100		95	5							
5	A	PS	25	218.5				25					
5	A	SST	75		50								
5	B	SST	20			15		5			20	20	
5	B	PS	80		15	35		30					
5	C	PS	80			20	60						

13	B	PS	100		100								
13	C	SST	60		30	30							
13	C	PS	40		40								
14	A	SST	60	242.9		20	40						
14	A	PS	40			20		20					
14	B	SST	100		40	60							
14	C	SST	60			5	15	30					
14	C	SST	40			15			15				
15	A	PS	100	245.7	20	40							
15	B	PS	100			100							
15	C	PS	100			85			15				
16	A	PS	70	248.4	30	10	10	5	15				
16	A	SST	30		25				5				
16	B	SST	75		70		5						
16	B	PS	25		15	10							
16	C	PS	100		50	20	15	15					
17	A	PS	100	250.9			70	30					
17	B	PS	100			5	25	70					
17	C	PS	50			10	40						
17	C	SST	50		50								
18	A	SST	15	253.3	10			5					
18	A	PS	85		30	40	15						
18	B	PS	100		50	5							
18	C	PS	80			40	10	10					
18	C	SST	20		20								
19	A	PS	100	256.1	40		20	5	10	25			
19	B	PS	100			50	50						

19	C	PS	100		70	5				25			
20	A	PS	30	258.5	30								
20	A	SST	70		40	5			25				
20	B	SST	20						20		5	5	
20	B	PS	80			30	50						
20	C	PS	100			75	25						
21	A	PS	100	261.2	15			65	20				
21	B	PS	100		30	30	40						
21	C	PS	20				20						
21	C	SST	80		55	25							
22	A	SST	100	264	100								
22	B	SST	100		95	2	3				10	10	
22	C	SST	100		80	10		10					
23	A	SST	100	266.8	90		10		10				
23	B	SST	100		95			5			10-20	15	
23	C	SST	100		95	5							
24	A	SST	100	269.7	100						10-20	15	
24	B	SST	100		100								
24	C	SST	100		85				15				
25	A	SST	100	272.5		100							
25	B	SST	100			20	70	10					
25	C	SST	100						15	85			
26	A	SST	60	275.4			40		20				
26	A	PS	40			40							
26	B	PS	100		20	20	50	10					
26	C	PS	100			60	40						
27	A	PS	100	278.2		40	40	20					

27	B	PS	100				75	25					
27	C	PS	100				100						
28	A	PS	100	281		60	40						
28	B	PS	100		45	25	20						
28	C	PS	30		25		5						
28	C	SST	70			70							
29	A	PS	25	283.9		25							
29	A	SST	75			45	30						
29	B	PS	40				40				0	0	
29	B	SST	60			40		10	10				
29	C	SST	100			55	20	20	5				
30	A	SST	100	286.7		100							
30	B	SST	60			60					0-10	5	
30	B	PS	40			20	20						
30	C	PS	100			80	20						
31	A	PS	100	289.6			70	30					
31	B	PS	100				95			5			
31	C	PS	30			20	10				0-10	5	
31	C	SST	70			60	10						
32	A	SST	100	292.55	70		15			15	20	20	
32	B	SST	45				30			15			
32	B	PS	55			20	10	10		15			
32	C	PS	100		30		55	15					
33	A	PS	85	295.3	15	10	60						
33	A	SST	15				15				20	20	
33	B	SST	30			30							
33	B	PS	70		10	10	30	20					

33	C	PS	100		80	20							
34	A	PS	100	298.2	10	30	60						
34	B	PS	100		90	10							
34	C	PS	100		50	20	20	5	5				
35	A	PS	20	301.1			20						
35	A	SST	80			60	20						
35	B	SST	30			25			5				
35	B	PS	70					55	15				
35	C	PS	100			15	40	25	30				
36	A	PS	75	303.9	40		20	10	5				
36	A	SST	25			25							
36	B	SST	100		100						20	20	
36	C	SST	90		80	5			5				
36	C	PS	10			10							
37	A	PS	100	306.9	30	60		5	5				
37	B	PS	100		50	45			5		0-10	5	
37	C	PS	70		20	40	10						
37	C	SST	30		30								
38	A	SST	100	309.7		100					0-10	5	
38	B	SST	75			75							
38	B	PS	25		25								
38	C	PS	100		30		45	10	15				
39	A	PS	100	312.55	60		40						
39	B	PS	100		50	25	25						
39	C	PS	100				95	5					
40	A	PS	100	315.35	30	70							
40	B	PS	100		30		70						

40	C	PS	100		90	10							
41	A	SST	100	318.3	100								
41	B	SST	100		90	5			5				
41	C	SST	100		30		40		30				
42	A	SST	100	321			40	20	40				
42	B	SST	100			50		10	40				
42	C	SST	100		90			10					
43	A	SST	10	323.9			6		4				
43	A	PS	90		20	20	25	5					
43	B	PS	100		40	30	20		10				
43	C	PS	100		100								
44	A	PS	40	326.8	40								
44	A	SST	60		5		25	15	15				
44	B	SST	60				20	25	15				
44	B	PS	40			40							
44	C	PS	100		85		15						
45	A	SST	100	329.5	100								
45	B	SST	100		85	5			10		0-10	5	
45	C	SST	100		30	30		20	20				
46	A	SST	60	332.4	60								
46	A	PS	40				20	20					
46	B	PS	100		60		35		5				
46	C	PS	50		35		20						
46	C	SST	50			50							
47	A	SST	100	335.2		95			5		0-10	5	
47	B	SST	100			50	20		30				
47	C	SST	100				100						

48	A	SST	100	338			70		30				
48	B	SST	100				40	35	25				
48	C	SST	100			70	15	10	5				
49	A	SST	100	340.7		100							
49	B	SST	100			70			30				
49	C	SST	100			20	80						
50	A	SST	100	343.3	30		65	5					
50	B	SST	100			90			10		0-10	5	
50	C	SST	100			50	50						
51	A	SST	70	346.3	60		10				0	0	
51	A	PS	30		30								
51	B	PS	35		35								
51	B	SST	65			35	30				20	20	
51	C	sst	100		40	20			40				
52	A	SST	40	348.95		30	10						
52	A	PS	60				10	50					
52	B	PS	100		10		70	20					
52	C	PS	100		100								
53	A	PS	100	351.6	80	10			10				
53	B	PS	100		100								
53	C	PS	100		80	10	10						
54	A	PS	100	354.4	25	25	30	20					
54	B	SST	100		20	30	30	20					
54	C	SST	100		10	20	70						
55	A	SST	100	357.2			60	30	10				
55	B	SST	100				65	10	25				
55	C	SST	100				95	5					

56	A	SST	100	360	15		60	15	10				
56	B	SST	70				35	15	20				
56	B	PS	30			30							
56	C	PS	50			50							
56	C	SST	50			40	10						
57	A	SST	100	362.7		60	30	10					
57	B	SST	100		50		20		30				
57	B	SST	100				40	10	50				
58	A	SST	80	365.2			70		10				
58	A	PS	20					20					
58	B	PS	100			60	20	20					
58	C	PS	100		90		10						
59	A	PS	100	367.75	80		20						
59	B	PS	100		100								
59	C	PS	100		100								
60	A	PS	100	370.6	100								
60	B	SST	100		30		60	5	5				
60	C	SST	100				100						
61	A	SST	100	373.25			100						
61	B	SST	100			20	60		20				
61	C	SST	100		25	25	25		25				
62	A	SST	100	376.1		95		5					
62	B	SST	100		20		70	5	5		15	15	
62	C	SST	100			30	70						
63	A	SST	100	378.9		30	40		30				
63	B	SST	100			70		30					
63	B	SST	100					90	10				

64	A	SST	100	381.6			50	50					
64	B	SST	100				80	20					
64	C	PS	75			60	15						
64	C	SST	25			20	5						
65	A	SST	100	384.1		100							
65	B	SST	100				20	10		70			
65	C	SST	100							100			
66	A	SST	40	386.9		10	30						
66	A	PS	60			30			30				
66	B	PS	100			90	10						
66	C	PS	100			80	20						
67	A	PS	60	389.6	60								
67	A	SST	40					20	20				
67	B	SST	100			25	75				20	20	
67	C	SST	100				80		20				
68	A	SST	60	392.4			60						
68	A	PS	40			20	20						
68	B	PS	100				30	35	35				
68	C	PS	100						100				
69	A	PS	100	394.6			10	20	70				
69	B	PS	100		50	20	30						
69	C	PS	100			50	50						
70	A	PS	100	397			80	20					
70	B	PS	100				20	40	40				
70	C	PS	100				100						
71	A	PS	100	399.5		50	50						
71	B	PS	100				40	10	50				

71	C	PS	100				40	20	40				
72	A	PS	100	402.2			60		40				
72	B	PS	100				10	30	60				
72	C	PS	100				40	20	20	20			
73	A	PS	100	404.4							100		
73	B	PS	100		100								
73	C	PS	50		30	20							
73	C	SST	50		35	5			10				
74	A	SST	40	407.3		30		10					
74	A	PS	60					10	50				
74	B	PS	100				60	40					
74	C	PS	100				40	30	30				
75	A	PS	100	409.6	70			20	10				
75	B	PS	100		60	10	10	20					
75	C	PS	100		90			10					
76	A	PS	100	412.25		100							
76	B	PS	100			70		20	10				
76	C	PS	100			70		30					
77	A	PS	100	414.9		30	50	10	10				
77	B	PS	100			10	20	50	20				
77	C	PS	100		50	50							
78	A	PS	100	417.3	80	20							
78	B	PS	100		75	25							
78	C	SST	100		80			10	10				
79	A	SST	100	420.2	100								
79	B	SST	100		100								
79	C	SST	100		80			10	10				

80	A	PS	100	422.95	100								
80	B	PS	100		100								
80	C	PS	100		95			5					
81	A	PS	100	425.8	100								
81	B	PS	100		95			5					
81	C	PS	100		100								
82	A	SST	100	428.65	90		10						
82	B	SST	100				100						
82	C	SST	100				40	40	20				
83	A	SST	100	431.4			40	40	20				
83	B	SST	5						5				
83	B	PS	95		40	25	15	15					
83	C	PS	100		95			5					
84	A	PS	40	434.4	40								
84	A	SST	60		40			10	10				
84	B	SST	100		100								
84	C	SST	100		70		15		15				
85	A	SST	100	437.4			90		10				
85	B	SST	100		95				5		0-10	5	
85	C	SST	100			45	50		5				
86	A	SST	100	440.3	50			20	30				
86	B	SST	100		30	40			30				
86	C	SST	100				60	20	20				
87	A	SST	60	443		40	10		10				
87	A	PS	40		15	15	5	5					
87	B	PS	100		90			10					
87	C	PS	40		40								

87	C	SST	60		60								
88	A	SST	100	445.85	80		10	5	5				
88	B	SST	100				90		10				
88	C	SST	100				90		10				
89	A	SST	100	448			95		5				
89	B	SST	100				90		10				
89	C	SST	30				25		5				
89	C	PS	70		35			35					
90	A	PS	100	451.4	100								
90	B	PS	100		100								
90	C	SST	100		90	10							
91	A	SST	100	454.2	70	20			5				
91	B	SST	100			90		10					
91	C	SST	100			20	60	10	10				
92	A	SST	100	457.1			95		5				
92	B	SST	100				100						
92	C	SST	100				100						
93	A	SST	100	460	60		40						
93	B	SST	100			50	30	15	5		20	20	
93	C	SST	100		70		15	10	5				
94	A	PS	100	462.9	50		40	10					
94	B	PS	100		70			30					
94	C	PS	100		90			10					
95	A	SST	60	465.65	40			5	15				
95	A	PS	40		5			30	5				
95	B	PS	100			80		15	5				
95	C	PS	100		100								

96	A	PS	20	468.55	20						20	20	
96	A	SST	80		60			5	15				
96	B	SST	100		95				5				
96	C	SST	100				80	10	10				
97	A	SST	100	471.1			100						
97	B	SST	100				100						
97	C	SST	100		50		40	5	5				
98	A	SST	100	474.95	100								
98	B	SST	100		50	30	20						
98	C	SST	100		25		40	15	20				
99	A	SST	100	476.7		80	20						
99	B	SST	100				30			70			
99	C	PS	100		100								
100	A	PS	100	479.3	95			5					
100	B	PS	100		100								
100	C	PS	100		100								
101	A	SST	100	782.15		60		30	10				
101	B	SST	100		25			50	25				
101	C	PS	100				75		25				
102	A	SST	100	484.75	25	70			5				
102	B	SST	100			20	20	30	30				
102	C	PS	90		10	70	5	10	5				
102	C	SST	10		10								
103	A	SST	100	487.5	60	20	20				35	35	
103	B	SST	60			30	30				35	35	
103	B	PS	40			5		20	15				
103	C	PS	100			20	30	30	20		35	35	

104	A	PS	100	490	30			50		20			
104	B	PS	100		60	25	10		5				
104	C	PS	100					50	50				
105	A	PS	100	492.5	20		50		30		20-30	25	
105	B	SST	50		50								
105	B	PS	50		30	10		10					
105	C	PS	100		70	20		10					
106	A	SST	100	495.4	100								
106	B	SST	100		100								
106	C	SST	100		100						10-15	12.5	
107	A	SST	100	498.2	100								
107	B	SST	100		95				5				
107	C	SST	100		95		5						
108	A	SST	100	500.95	95			5			5-10	7.5	
108	B	PS	50		50								
108	B	SST	50		50								
108	C	SST	100		90				10				
109	A	SST	10	503.8					10		5	5	
109	A	PS	90			80		10					
109	B	PS	100		100								
109	C	PS	100		90	10							
110	A	SST	100	506.6	95			5					
110	B	SST	100		100								
110	C	PS	100		100								
111	A	PS	100	509.25	80		15	5					
111	B	PS	100			90	5	5					
111	C	PS	100		100								

112	A	PS	100	512.05	95			5					
112	B	PS	100		90		10				0-5	2.5	
112	C	PS	100		100								
113	A	PS	100	514.9	100								
113	B	PS	100		80	10		10					
113	C	PS	100			100							
114	A	SST	10	517.7		10							
114	A	PS	90		80			10					
114	B	PS	100		100								
114	C	PS	100		100								
115	A	PS	100	520.75	95				5				
115	B	PS	100		40			30	30				
115	C	PS	100			90		10					
116	A	PS	100	523.3		40	50	5	5				Tray is soft - different grey colour.
116	B	PS	100		100								
116	C	PS	100		95				5				
117	A	PS	100	526.1	90				10				
117	B	SST	100		95				5				
117	C	SST	100		10	30	55		5				
118	A	SST	100	528.85			100						
118	B	SST	100				100						
118	C	SST	100			30	70						
119	A	PS	100	531.8	75		10	10	5				
119	B	PS	100		90			10					
119	C	PS	60		60								
119	C	SST	40		20			20			20	20	
120	A	SST	100	534.6	95				5				

120	B	SST	100		15	40	25		20				
120	C	SST	100		50	35			15				
121	A	SST	100	537.4			95	5					
121	B	SST	100			60	20	10	10				
121	C	SST	100		95			5			10-15	12.5	
122	A	SST	25	540.3		25							
122	A	PS	75			65			10				
122	B	PS	100			60	20	10	10				
122	C	PS	100			90		10					
123	A	PS	100	543.2	70	30							
123	B	PS	100		95			5					
123	C	PS	100		70	30							
124	A	PS	100	546.05	100								
124	B	PS	100		95			5					
124	C	PS	100		90			10					
125	A	PS	100	548.6	100								
125	B	PS	80		80								
125	B	SST	20		20								
125	C	SST	100		100						5-10	7.5	
126	A	SST	50	551.6	45				5				
126	A	PS	50		10	20		30					
126	B	SST	100		95				5				
126	C	SST	100		95				5				
127	A	SST	100	554.3	60		25		15				
127	B	SST	100			50	10	10	30				
127	C	SST	100		35		45		20		5-10	7.5	
128	A	SST	100	557.05	100								

128	B	SST	100		20	65		5	10		20	20	
128	C	SST	100			100							
129	A	SST	100	559.85		90		10					
129	B	SST	100			55		40	5				
129	C	SST	100			30	35	35					
130	A	SST	100	562.4	90		5		5				
130	B	PS	30		30								
130	B	SST	70		60	10							
130	C	PS	30		30								
130	C	SST	70		70								
131	A	PS	70	565.25	65			5					
131	A	SST	30		30								
131	B	PS	30		30								
131	B	SST	70		70								
131	C	SST	20		15				5				
131	C	PS	80		75			5					
132	A	PS	100	568.1	95			5					
132	B	PS	70		70								
132	B	SST	30		25			5			0-5	2.5	
132	C	SST	100			40	40		20				
133	A	SST	100	570.8			90		10				
133	B	SST	100				50	30	20				
133	C	SST	100			40		20	40		5-10	7.5	
134	A	SST	100	573.55	85		10	5					
134	B	PS	100			90		10					
134	C	PS	100		50			50					
135	A	PS	100	576.4	50	50							

135	B	SST	100		100						0-20	10	
135	C	SST	100		100								SST looks like PS
136	A	SST	50	579.2	45			5					
136	A	PS	50		50								
136	B	SST	100		100								
136	C	SST	100			95			5		10-20	15	
137	A	SST	100	581.9			70		30				
137	B	SST	100			70	25		5				
137	C	SST	60			25	30		5				
137	C	PS	40			40					20	20	
138	A	PS	100	584.45	100								
138	B	PS	100		100								
138	C	PS	70		65			5					
138	C	SST	30		30								
139	A	PS	100	587.4	100								
139	B	PS	40		40								
139	B	SST	60		60								
139	C	SST	100		90			10					
140	A	SST	100	590.2	60	20	15		5		10-20	15	
140	B	SST	100			100							
140	C	SST	5				5						
140	C	SST	95			40	50			5			
141	A	SST	100	593.05		20	50	20	10				
141	B	SST	100				60	10	30				
141	C	SST	100			70	25		5				
142	A	PS	40	595.75	40								
142	A	SST	60		60								

142	B	SST	100			100							
142	C	SST	100			70			30		5-10	7.5	
143	A	SST	100	598.5			95		5				
143	B	SST	100				95		5				
143	C	SST	100				70	10	20				
144	A	SST	100	601.2	10	10	70	5	5				
144	B	SST	100				90		10				
144	C	SST	20				10	5	5				
144	C	PS	80			70		5	5				
145	A	PS	10	604			5	5					
145	A	SST	90		80	10							
145	B	SST	100		50	20	30						
145	C	SST	100			40	10		50				
146	A	SST	100	606.75	20		70		10				
146	B	SST	100		100						30	30	
146	C	SST	100		20	60	10		10		30	30	
147	A	SST	100	609.4			100				20-30	25	
147	B	SST	20		20								
147	B	PS	80		15	20	35	5	5				
147	C	PS	100					50	50				
148	A	PS	100	612.1			60	20	20				
148	B	PS	100				70	20	10				
148	C	PS	100		50		40		10				
149	A	PS	100	614.9	95			5			20-30	25	
149	B	SST	100		80		10	10					
149	C	SST	100		95			5					
150	A	SST	100	617.4	60			20	20				

150	B	SST	100			100							
150	C	SST	100			95			5				
151	A	SST	65	620		55		5	5				
151	A	PS	35		20			15					
151	B	PS	100		95			5					
151	C	SST	100		20	75			5		5-10	7.5	
152	A	SST	100	622.7			60		40				
152	B	SST	100				90		10				
152	C	SST	100				85		15				
153	A	SST	10	625.1		10			5				
153	A	PS	90		80				5				
153	B	PS	100		100								
153	C	PS	100		50			50					
154	A	PS	100	627.75	20	70		10					
154	B	SST	80			50	30						
154	B	PS	20			15			5				
154	C	PS	100		90			10					
155	A	PS	100	630.45		50		50					
155	B	PS	100		90			10			25	25	
155	C	SST	100		90	10							
156	A	SST	100	633.35		60			40				
156	B	SST	100			70		10	20				
156	C	SST	100			100							
157	A	SST	100	635.9	30	50	10		10				
157	B	SST	100			30	65		5				
157	C	SST	100				85		5				
158	A	SST	100	638.7		20	60	10	10				

158	B	PS	100		90			10					
158	C	PS	100		100								
159	A	PS	100	641.35	100								
159	B	PS	20		20								
159	B	SST	80		40	40					10	10	
159	C	SST	100				90	10					
160	A	SST	70	644.2			60	10					
160	A	PS	30			25		5					
160	B	PS	100		45	45		10					
160	C	PS	100		60	10	10	10	10				
161	A	PS	20	646.9	20						20	20	
161	A	SST	80		80								
161	B	SST	100			90			10				
161	C	SST	100		75		20		5				
162	A	SST	100	649.6	10	50	10	10	20				
162	B	SST	100			75		10	15				
162	C	SST	100				90		10				
163	A	SST	100	652.3		20	40	20	20				
163	B	SST	100		20		70		10				
163	C	SST	100		10		80		10				
164	A	SST	100	655.1	40		40	10	10				
164	B	SST	100			80	10		10				
164	C	SST	100			10	70		20				
165	A	SST	100	657.9		20	60		20				
165	B	SST	100				70	10	20				
165	C	SST	80		80								
165	C	PS	20			10		10					

166	A	PS	30	660.7	20			10			25-30	27.5	
166	A	SST	70			50	10		10				
166	B	SST	100				70		30				
166	C	SST	100		20		30		50				
167	A	SST	100	663.3	15	35	10		20				
167	B	SST	100			100					15-20	17.5	
167	C	SST	100			70		10	20				
168	A	SST	100	666				40	60				
168	B	SST	100		45	30		25	5		30-45	37.5	
168	C	SST	100		50			5	45				
169	A	SST	100	668.8	50	20		10	20				
169	B	SST	50		40			5	5				
169	B	PS	50			30		20					
169	C	SST	100			90		10					
170	A	SST	25	671.1	25								
170	A	PS	75		75								
170	B	PS	100		55	40			5				
170	C	PS	25		15			10					
170	C	SST	75		25	50					20	20	
171	A	SST	100	674.3	85		10		5				
171	B	SST	100				50	40	10				
171	C	SST	100			50	20	5	25				
172	A	SST	100	677							100		
172	B	SST	100				60				40	25	25
172	C	SST	85			75			10				
172	C	PS	15		15								
173	A	PS	100	679.85	95			5					

173	B	PS	50		35			15				
173	B	SST	50		45				5			
173	C	SST	100		85			5	10			
174	A	SST	75	682.55		65		10			20-30	25
174	A	PS	25		25							
174	B	SST	100		30	65			5			
174	C	SST	100			40	60				50	50
175	A	PS	100	685.4	60			20	20			
175	B	PS	100			80		10	10			
175	C	PS	80		40			20	20			
175	C	PS	20			10	5		5			
176	A	SST	100	688.2			10	20	70			
176	B	SST	100				10	10	80			
176	C	SST	100					20	80			
177	A	SST	100	690.8			60	30	10			
177	B	SST	100				50	20	30			
177	C	SST	100				70	10	20			
178	A	SST	100	693.35		15	80		5			
178	B	SST	100			100						
178	C	SST	100			80	10		10			
179	A	SST	100	696.25			50	20	30			
179	B	SST	40		25		15					
179	B	PS	60		55			5				
179	C	PS	60		60						20	20
179	C	SST	40		20	20						
180	A	SST	100	699.15	20	70		5	5		20	20
180	B	SST	100			60	30		10			

180	C	SST	100			70	10		20				
181	A	SST	100	701.8			80	20					
181	B	SST	100				95	5					
181	C	SST	100			60	30	10					
182	A	SST	100	704.55		85	10		5				
182	B	SST	20			20							
182	B	PS	80		80								
182	C	PS	10		5			5			5	5	
182	C	SST	90		90								
183	A	PS	100	707.3	100								
183	B	PS	15		15								
183	B	SST	85				85						
183	C	SST	40				40				10	10	
183	C	SST	60		60								
184	A	SST	100	710.2			90		10				
184	B	SST	100				90	5	5				
184	C	PS	100		100						15-20	17.5	
185	A	PS	100	713	100						20-25	22.5	
185	B	PS	100		100								
185	C	PS	100		100						20-25	22.5	
186	A	PS	100	715.9	95				5		30	30	
186	B	PS	100		95				5		30	30	
186	C	PS	20		20								
186	C	SST	80		65		10		5				
187	A	PS	100	718.9	80				20				
187	B	SST	100		100								
187	C	PS	100		95				5				

188	A	PS	100	721.6	90			10					
188	B	PS	100		100								
188	C	PS	100		90			10					
189	A	PS	100	724.4	90			10					
189	B	PS	70		40			30					
189	B	SST	30		30								
189	C	SST	100		100								
190	A	SST	100	727.1	70			30					
190	B	SST	100		20	60	20						
190	C	SST	100				95		5				
191	A	SST	100	729.95		50	50						
191	B	SST	100		100						45	45	
191	C	SST	100		90			5	5		35-45	40	
192	A	PS	100	732.7	95			5					
192	B	PS	100		100						20	20	
192	C	SST	100		60	30		5	5				
193	A	SST	100	735.5			95	5					
193	B	SST	100			100							
193	C	SST	60			55		5					
193	C	SST	40		40								
194	A	SST	30	738.3	30								
194	A	PS	70		50			20					
194	B	PS	100		60			40					
194	C	PS	100		90				10				
195	A	PS	100	741.25	25	25		25	25				
195	B	PS	100			30		50	20				
195	C	PS	100			10	30	50	10				

196	A	PS	100	744			60	20	20				
196	B	SST	100		90			5	5				
196	C	PS	60		60								
196	C	SST	40		40								
197	A	SST	100	746.8	100								
197	B	SST	40		40								
197	B	PS	60		50			5	5				
197	C	SST	100		90			5	5		25-30	27.5	Bedding is uncertain.
198	A	SST	100	749.6	50		50						
198	B	SST	100		100								
198	C	SST	100		85		10		5				
199	A	SST	100	752.45			100						
199	B	SST	10		10						15-20	17.5	
199	B	PS	90		85			5					
199	C	PS	100		100								
200	A	PS	100	755.4	100								PS in these few trays is very sandy.
200	B	PS	100		60	10		30					
200	C	PS	100		70	20		10					
201	A	PS	100	758.3	100								
201	B	PS	100		100								
201	C	PS	100		100								
202	A	PS	100	761.1	40		60						
202	B	PS	100		60		40						
202	C	PS	100		80	20							
203	A	PS	100	763.9	80	10		5	5				
203	B	PS	100		85		10		5				
203	C	PS	100		70	20			10				

204	A	PS	50	766.7	45				5			
204	A	SST	50		45				5		30	30
204	B	SST	100		75			5	20			
204	C	SST	100		90			5	5			
205	A	SST	100	769.5	70	30					20-25	22.5
205	B	SST	100				100					
205	C	SST	100		60	20	20					
206	A	SST	100	772.3	10	10	75	5				
206	B	SST	100		50	50						
206	C	SST	100			90			10			
207	A	SST	60	775.1		30	30					
207	A	PS	40				20	20				
207	B	PS	100		70	20		10				
207	C	PS	30		25							
207	C	SST	70		60	10						
208	A	SST	100	777.95	50	45			5			
208	B	SST	100			65	30		5			
208	C	SST	60				60					
208	C	PS	40		25		10		5			
209	A	SST	100	780.85	60		10	15	15			
209	B	PS	10						10			
209	B	SST	90		80			10				
209	C	SST	100		100							
210	A	SST	100	783.55	95			5				
210	B	SST	100		95			5				
210	C	SST	100		100							
211	A	SST	100	786.45	100							

211	B	SST	100		100								
211	C	SST	100		90			10			25	25	
212	A	SST	70	789.1	70								
212	A	PS	30		30								
212	B	PS	100		90			10					
212	C	PS	100		80			20					
213	A	PS	100	791.9	90				10		30	30	
213	B	SST	100		40	60							
213	C	SST	50			50					30	30	
213	C	PS	50		45				5				
214	A	PS	100	794.8	95				5				
214	B	PS	100		75	20				5			
214	C	PS	100		60	20			10	10			
215	A	SST	100	797.65	80	20					20	20	
215	B	SST	20				20						
215	B	PS	80		70				5	5			
215	C	PS	100		95				5				
216	A	PS	100	800.55		60			20	20			
216	B	PS	100		60	10			15	15			
216	C	PS	100		90	10							
217	A	PS	100	803.4	70	25				5			
217	B	PS	40		40								
217	B	SST	60			60							
217	C	SST	100			100							
218	A	SST	100	806.35		95				5			
218	B	SST	100			70	10	10	10				
218	C	SST	70				70				30	30	

218	C	PS	30				20		10				
219	A	PS	100	809.1			30	50	20				
219	B	PS	100					80	20				
219	C	PS	100		100								
220	A	PS	100	811.65	100								
220	B	PS	100		100								
220	C	PS	70		70								
220	C	SST	30					10	20		40	40	
221	A	SST	100	814.4	35	15	25	10	15				
221	B	PS	100		70			20	10		45	45	
221	C	PS	100		60	30		5	5				
222	A	PS	100	817	75	20		5	5				
222	B	PS	100		60	30		5	5				
222	C	PS	90		75	10			5				
222	C	SST	10					5	5				
223	A	SST	100	819.4	90			10			40	40	
223	B	SST	100		100								
223	C	SST	100		100								
224	A	SST	100	822.3	25	75					25-30	27.5	
224	B	SST	100		100								
224	C	SST	100		45	55							
225	A	SST	40	825.1		40							
225	A	PS	60		30			20	10				
225	B	PS	100		60	40							
225	C	PS	100		60	30		5	5				
226	A	SST	80	827.9	80								
226	A	PS	20		20								

226	B	SST	100		90		10					
226	C	SST	100		95			5				
227	A	SST	100	830.7	60	40						
227	B	SST	100			90			10			
227	C	SST	100			100						
228	A	SST	45	833.7		45					30	30
228	A	PS	55				20	20	15			
228	B	PS	100				90		10			
228	C	PS	20				15		5			
228	C	SST	80			60			20			
229	A	SST	100	836.45	100							
229	B	SST	30		30							
229	B	PS	70		70							
229	C	SST	30		25			5			40	40
229	C	PS	70		20		20	15	15			
230	A	PS	100	839.25	30		20	40	10			
230	B	PS	100		95				5			
230	C	PS	100		90			5	5		45	45
231	A	PS	100	842.1	80			20				
231	B	PS	100		90			10				
231	C	PS	100		100							
232	A	PS	30	844.8	30							
232	A	SST	70			70						
232	B	SST	100			100						
232	C	SST	100			100						
233	A	SST	100	847.6		100						
233	B	SST	100			60	20		20			

233	C	SST	100			40	50		10				
234	A	SST	100	850.5		30	70						
234	B	SST	100			40	60						
234	C	SST	100			50	50						
235	A	SST	70	853.3			60		10				
235	A	PS	30					15	15				
235	B	PS	100		10	10	30	35	10				
235	C	SST	100			100							
236	A	SST	100	855.7		20	80						Colour change -> related to edge of fault zone?
236	B	SST	100			70		15	15				
236	C	SST	100		20		10	35	35				
237	A	SST	100	858.2			30	35	35				
237	B	SST	100		30		50	10	10				
237	C	SST	100					50	50				
238	A	SST	100	860.5	100								
238	B	SST	100		100								
238	C	SST	100		100								
239	A	SST	100	863.4	100								
239	B	SST	100		95			5					
239	C	SST	100		100								
240	A	SST	40	866.25	40								
240	A	PS	60				10	30	20				
240	B	PS	70			20		30	20				
240	B	SST	30		30								
240	C	SST	100		100								
241	A	PS	70	869	70								

241	A	SST	30		25				5				
241	B	SST	60				60						
241	B	PS	40				40						
241	C	PS	60		55				5				
241	C	SST	40		35				5				
242	A	PS	100	870.8	65	10	20	5					
242	B	PS	100		100								
242	C	PS	100		100								
243	A	PS	100	874.6	95				5				
243	B	PS	100		70		20	5	5				
243	C	PS	100		100								
244	A	PS	100	877.7	100								
244	B	SST	100		100								
244	C	SST	100		100								
245	A	SST	100	880.55	100								
245	B	SST	100		100						15-20	17.5	
245	C	SST	100		90								
246	A	SST	100	883.3	100								
246	B	SST	100		100								
246	C	SST	100		100								
247	A	SST	100	886.25	100								
247	B	PS	100		95				5				
247	C	PS	50		50								
247	C	SST	50		50								
248	A	SST	100	889.05	90				10				
248	B	SST	100		100								
248	C	SST	100		100						25	25	

249	A	SST	90	891.85	90						30	30	
249	A	PS	10						10				
249	B	SST	40		40								
249	B	PS	60		40	20							
249	C	PS	100		50	20		15	15				
250	A	PS	100	894.5			40	40	20				
250	B	PS	100			20	40	30	10				
250	C	PS	100		80			15	5				
251	A	PS	100	897.3	70			25	5				
251	B	PS	100		80			5	15				
251	C	PS	100		25	25		25	25				
252	A	PS	100	900			40	40	20				
252	B	PS	100		60		20	10	10				
252	C	SST	100		100								
253	A	SST	100	902.6	100								
253	B	SST	100			100							
253	C	SST	100			90			10				10% of 4 - possible sample (coring) attempt?
254	A	SST	100	905.45		95			5				
254	B	SST	100			100							
254	C	SST	100			95			5				
255	A	SST	100	908.2		85		10	5				
255	B	SST	100			100					25-30	27.5	
255	C	SST	70			65							
255	C	PS	30			30			5				
256	A	PS	100	910.9	50		45		5				
256	B	SST	100		100								

256	C	SST	40		40								
256	C	PS	60		60								
257	A	PS	100	913.8	95			5					
257	B	SST	100		100								
257	C	PS	100		85			10	5		10-20	15	
258	A	PS	100	916.6	50	40			10				
258	B	PS	100		95				5				
258	C	PS	100				40	40	20				
259	A	PS	100	919.4			50	30	20				
259	B	PS	80			60		10	10				
259	B	SST	20		20								
259	C	SST	100		100								
260	A	SST	50	921.7	50								
260	A	PS	50		50								
260	B	PS	100		70	30					20	20	
260	C	PS	100		100								
261	A	PS	100	924.6	50	45		5					
261	B	PS	100		100						10	10	
261	C	PS	100		100								
262	A	PS	100	927.45	100								
262	B	PS	100		85		15						
262	C	PS	40		40								
262	C	SST	60		60								
263	A	SST	60	930.35	60								
263	A	PS	40		40								
263	B	SST	60		60								
263	B	PS	40			20		10	10				

263	C	PS	100		50		40	5	5				
264	A	PS	100	933.2	80	20							
264	B	PS	100		100								
264	C	PS	50		20		20	10					
264	C	SST	50		50								
265	A	SST	80	936.05		20							
265	A	PS	20					10	10				
265	B	PS	100			70		25	5				
265	C	PS	55		50								
265	C	SST	45		45								
266	A	SST	100	938.95	100								
266	B	PS	100		75	20		5					
266	C	PS	100		100								
267	A	PS	100	941.8	100								
267	B	SST	25		25								
267	B	PS	75		50	25							
267	C	SST	40		40								
267	C	PS	60		60								
268	A	PS	100	944.7	100								
268	B	PS	100		100								
268	C	PS	100		100						5-10	7.5	
269	A	SST	40	947.6	35			5					
269	A	PS	60		60								
269	B	PS	100		50	40		10					
269	C	PS	100		90	5			5				
270	A	PS	100	950.45	95				5				
270	B	PS	100		90	10							

270	C	PS	100		100								
271	A	SST	100	953.35	95								
271	B	PS	100		20	40		30	10				
271	C	PS	100		90			10					
272	A	PS	100	956.3	95				5				
272	B	PS	100		95				5				
272	C	PS	100		40	50		10					
273	A	PS	100	959.1	40		30	20	10				
273	B	PS	100			85		5	10				
273	C	PS	100		45	45		5	5				
274	A	PS	100	961.9	45	45		5	5				
274	B	PS	100			30	50	15	5				
274	C	PS	100		10	25	25	20	20				
275	A	SST	50	964.7	50								
275	A	PS	50		50								
275	B	SST	30		30								
275	B	PS	70			70							
275	C	PS	100			20	30	25	25				
276	A	PS	100	967.55			50	25	25				
276	B	PS	100				50	25	25				
276	C	PS	100				60	20	20				
277	A	PS	100	970.4		10	70	10	10				
277	B	PS	100		10	20	40	15	15				
277	C	PS	100			80		10	10				
278	A	PS	100	973.05		80		10	10				
278	B	PS	100			75		15	10				
278	C	PS	100			40	20	20	20				

279	A	PS	100	975.9		70		15	15				
279	B	PS	100			50	30	10	10				
279	C	PS	100			40	40	10	10				
280	A	PS	100	978.8			20	40	40				
280	B	PS	100			20	40	20	20				
280	C	PS	100			20	30	35	15				
281	A	PS	100	981.1	50	50							
281	B	PS	100		25	70		5					
281	C	PS	100		70		10	10	10				
282	A	PS	100	983.95		80	10	10					
282	B	PS	100			20	70	10					
282	C	PS	100				50	40	10				
283	A	PS	100	986.7			50	10	40				
283	B	PS	100				70	20	10				
283	C	SST	100		70	20		10			10	10	
284	A	PS	100	989.55		70	20	5	5				
284	B	PS	100		30	20	50						
284	C	PS	100		100								
285	A	SST	60	992.4	60								
285	A	PS	40		40								
285	B	PS	50		25	20			5				
285	B	SST	50		50								
285	C	SST	100		100								
286	A	SST	100	995.3	100								
286	B	SST	100		95			5					
286	C	PS	100		95			5					
287	A	PS	80		80								

287	A	SST	20	998.2	20								
287	B	SST	100		100								
287	C	SST	20		20								
287	C	PS	80		60			15	5				
288	A	PS	100	1001.1	80		15	5					
288	B	SST	100		95			5			10	10	
288	C	SST	50		45		5						
288	C	PS	50		50								
289	A	PS	100	1004	95			5					
289	B	PS	100		100								
289	C	PS	100		60		30	5	5				
290	A	PS	100	1006.95	70			30					
290	B	PS	100		85			15					
290	C	PS	100		85			5	10				
291	A	PS	100	1009.95		30	30	10	20				
291	B	PS	100		40	30		20	10				
291	C	PS	80		80								
291	C	SST	20				10		10				
292	A	SST	100	1012.4	60	40							
292	B	PS	100		100								
292	C	SST	100		100								
293	A	SST	100	1015.35	100								
293	B	SST	50		50								
293	B	PS	50		50								
293	C	SST	100		100								
294	A	PS	100	1018.2	50		30	10	10				
294	B	SST	100		100								

294	C	SST	100		100									
295	A	SST	100	1021.95	100									
295	B	SST	100		100									
295	C	SST	100		100									
296	A	SST	100	1023.8	100									
296	B	SST	20		20									
296	B	PS	80		75			5						
296	C	PS	100		80			15	5					
297	A	SST	100	1026.7	100									
297	B	SST	100		100						5-10	7.5		
297	C	SST	100		100									
298	A	SST	100	1029.6	100						10-20	15		
298	B	SST	100		100									
298	C	SST	50		50									
298	C	SST	50				40	5	5					
299	A	SST	100	1032.4	20	80								
299	B	SST	70		30	40								
299	B	PS	30		30									
299	C	PS	30		30									
299	C	SST	70		70									
300	A	SST	45	1035.3	45									
300	A	PS	55		10	35		5	5					
300	B	PS	100				50	20	30					
300	C	PS	100		30	40	20	5	5					
301	A	PS	100	1038	80			20						
301	B	PS	50		10		30	5	5					
301	B	SST	50		50									

301	C	SST	100		100								
302	A	SST	100	1040.75	100								
302	B	PS	60		60								
302	B	SST	40		40								
302	C	SST	100		100								
303	A	SST	50	1043.6	50								
303	A	PS	50		30		15	5	5				
303	B	PS	70		65			5					
303	B	SST	30		30								
303	C	SST	25		25								
303	C	SST	75		70				5				
304	A	PS	100	1046.45	100								
304	B	SST	80		80								
304	B	PS	20		20								
304	C	PS	100		100								
305	A	PS	100	1049.4	40	40		10	10				
305	B	PS	80			15	30	25	10				
305	B	SST	20		20								
305	C	PS	100		100								
306	A	SST	30	1052.2	30								
306	A	PS	70		60				10				
306	B	PS	60		60								
306	B	SST	40		40								
306	C	SST	60		60								
306	C	PS	40			30	10						
307	A	PS	100	1055.15	80			15	5				
307	B	PS	100		70			20	10				

307	C	PS	100		100								
308	A	PS	100	1058	100						15-20	17.5	
308	B	PS	100		95				5				
308	C	PS	100		100								
309	A	PS	40	1060.9	40								
309	A	SST	60		60								
309	B	SST	100			100							
309	C	SST	100		85			10	5				
310	A	SST	40	1063.65	40								
310	A	PS	60		50				10				
310	B	PS	100		100								
310	C	SST	100		100								Sandy PS.
311	A	PS	100	1066.3	100								
311	B	PS	100		100								
311	C	PS	100		100								
312	A	PS	100	1069.2	100								
312	B	PS	100		95			5					
312	C	PS	100		75			15	10				
313	A	PS	100	1072.1	70	30							
313	B	PS	100		95			5					
313	C	PS	100		100								
314	A	PS	100	1074.95	95								
314	B	PS	100		100								
314	C	PS	100		100								
315	A	PS	100	1077.9	85	10		5					
315	B	PS	100		40	40		15	5				
315	C	PS	100			70	30						

316	A	PS	100	1080.8	85			10	5				
316	B	PS	100		50	30		15	5				
316	C	PS	100		85			5	10				
317	A	PS	100	1083.75	50	30	15	5					
317	B	PS	100				80	10	10				
317	C	PS	100			20	60	10	10				
318	A	SST	100	1086.55	100						25	25	
318	B	SST	100		100								
318	C	SST	90		90								
318	C	PS	10		10								
319	A	PS	100	1089.35	65	25		5	5				
319	B	PS	100		95				5				
319	C	PS	25		20				5				
319	C	SST	75		75								
320	A	SST	20	1092.25	20								
320	A	PS	80		80								
320	B	PS	100		100								
320	C	SST	70		70								
320	C	PS	30		30								
321	A	PS	100	1095.15	100								
321	B	PS	100		90			5	5				
321	C	PS	100		95				5				
322	A	PS	60	1097.95	60								
322	A	SST	40		40								
322	B	PS	60		60								
322	B	SST	40		40								
322	C	SST	100		100								

323	A	SST	100	1100.85	100								
323	B	SST	100		100								
323	C	SST	50		50						20-30	25	
323	C	PS	50					10	40				
324	A	PS	75	1103.75	10		20	20	15				
324	A	SST	25		25								
324	B	SST	100		100								
324	C	SST	95		95								
324	C	PS	5					5					
325	A	PS	100	1106.5	100								
325	B	PS	100		85	15							
325	C	SST	90		90								
325	C	PS	10		10								
326	A	SST	100	1109.4	100								
326	B	SST	100		95			5			25	25	
326	C	SST	100		100								
327	A	SST	75	1112.25	75								
327	A	PS	25		25								
327	B	PS	100		100								
327	C	PS	100		50	30		10	10				
328	A	PS	100	1115.1	80	20							
328	B	PS	100		65	35							
328	C	PS	100		50	45		5					
329	A	PS	100	1118	90			10					
329	B	PS	85		65			20					
329	B	SST	15		15								
329	C	SST	100		100								

330	A	SST	100	1120.95	100								
330	B	SST	25		25								
330	B	PS	75		75								
330	C	PS	100		100								
331	A	PS	90	1123.8	90								
331	A	SST	10		10								
331	B	SST	100		100						20	20	
331	C	SST	100		100								
332	A	SST	100	1126.05	100								
332	B	SST	80		80								
332	B	PS	20		15			5					
332	C	SST	100		100								
333	A	SST	100	1129.55	100								
333	B	PS	100		90	10							
333	C	PS	100		100								
334	A	PS	100	1132.45	95			5					
334	B	PS	100		65	35							
334	C	PS	100		75	10		10	5				
335	A	PS	100	1135.25	50	40		5	5				
335	B	PS	100		90			5	5				
335	C	PS	100		80			15	5				
336	A	SST	100	1138.1	100								
336	B	SST	100		100						15-20	17.5	
336	C	SST	100		100								
337	A	PS	100	1140.85	45	20	15	15	5				
337	B	SST	100		100								
337	C	PS	100		65	15	15	5					

338	A	PS	100	1143.7	90			10					
338	B	PS	100		90	10							
338	C	PS	100		35		60	5					
339	A	PS	100	1146.6	100								
339	B	PS	100		100								
339	C	PS	100		95			5	5				
340	A	PS	100	1149.5	40	55		5					
340	B	PS	100		80	5		15					
340	C	PS	100		90			10					
341	A	PS	100	1152.45	100								
341	B	PS	100		50	40		10					
341	C	PS	100		60	10	25	5					
342	A	PS	80	1155.4	50	10	20						
342	A	SST	20		20								
342	B	SST	50		50								
342	B	PS	50		40				10		25	25	
342	C	SST	30		30								
342	C	PS	70		20	20	10	10	10				
343	A	PS	65	1158.2			30	20	15				
343	A	SST	35		15	20							
343	B	SST	100		100								
343	C	SST	100		85	10			5				
344	A	SST	100	1161.05	90		10						
344	B	SST	100		100								
344	C	SST	80		80								
344	C	PS	20				20						
345	A	PS	95	1163.95	50	15	15	20					

345	A	SST	5		5								
345	B	SST	95		55	40							
345	B	PS	5						5				
345	C	PS	100		70		20	5	5				
346	A	PS	100	1166.75		20	50	20	10				
346	B	PS	100			10	40	30	10				
346	C	PS	100		60	30		10					
347	A	PS	100	1169.5	60	30		10					
347	B	SST	65		65								
347	B	SST	35		25	15							
347	C	PS	100		95				5		10-15	12.5	
348	A	PS	100	1172.4	90			5	5				
348	B	PS	70		70								
348	B	SST	30		30								
348	C	PS	70		55	10		5					
348	C	SST	30		30								
349	A	SST	100	1175.3	60		30	5	5				
349	B	SST	35		35								
349	B	PS	65		55	10							
349	C	SST	35		35								
349	C	PS	65		15	15	25	10					
350	A	PS	100	1177.9	90			5	5				
350	B	PS	100		70	5			5				
350	C	SST	100		100								
351	A	SST	100	1180.8	90	10							
351	B	PS	100		50		50						
351	C	PS	100		90			5	5				

352	A	SST	65	1183.7	65						10	10	
352	A	PS	35		15			20					
352	B	PS	100		95				5				
352	C	SST	60		60								
352	C	PS	40				20		20				
353	A	SST	100	1186.5	70	10		10	10				
353	B	SST	70		70								
353	B	PS	30		30								
353	C	SST	100		100								
354	A	SST	100	1189.55	100								
354	B	SST	40		40								
354	B	PS	60		40			10	10				
354	C	PS	100		70		20	5	5				
355	A	PS	100	1192.25		30	50	15	5				
355	B	PS	100		65			25	10				
355	C	PS	100		100								
356	A	PS	100	1195		70	10	15	5				
356	B	PS	100		40	10	25	15	10				
356	C	PS	100		50		40	5	5				
357	A	PS	45	1198.7	15	25			5				
357	A	SST	55		55								
357	B	SST	70		65			5					
357	B	PS	30				25	5					
357	C	PS	100		70		25	5					
358	A	SST	40	1200.55	40								
358	A	PS	60			30		20	10				
358	B	PS	100		85			10	5				

358	C	PS	100		95				5				
359	A	PS	100	1203.3	90			5	5				
359	B	PS	100			20	60	10	10				
359	C	PS	100		20	20	30	20	10				
360	A	PS	85	1206.115	80			5					
360	B	SST	15		15								
360	B	SST	35		35			5					
360	B	PS	65		60								
360	C	SST	100		100								
361	A	SST	50	1209.05	50								
361	A	PS	50			10	30	5	5				
361	B	PS	100			30	50	10	10				
361	C	PS	100			40	50	10					
362	A	PS	100	1211.85	60		30	10					
362	B	PS	100			45	45	10					
362	C	PS	100			10	80		10				
363	A	PS	100	1214.7		60	30	5	5				
363	B	PS	100				60	20	20				
363	C	PS	70				40	15	15				
363	C	SST	30		30								
364	A	SST	100	1217.55	100								
364	B	SST	100		95			5					
364	C	SST	20		10			10					
364	C	PS	80				60	20					
365	A	PS	100	1220.25			30	20	50				
365	B	PS	60				40	10	10				
365	B	SST	40		40				5				

365	C	SST	100		95								
366	A	PS	80	1123	40		20	10	10				
366	A	SST	20		20								
366	B	SST	45		45								
366	B	PS	55				55						
366	C	PS	100				70	15	15				
367	A	PS	100	1225.75	55		25	10	10				
367	B	PS	70		70								
367	B	SST	30		25			5					
367	C	SST	100		80			20			25	25	
368	A	PS	100	1228.45	30			35	35				
368	B	PS	100		50		30	10	10				
368	C	PS	100		70		20	10					
369	A	PS	15	1231.25		10		5					
369	A	SST	85		85								
369	B	SST	100		100								
369	C	SST	100		70			30					
370	A	SST	100	1234		95			5				Core diameter and tray size change. Smaller diameter core.
370	B	SST	20		20								
370	B	PS	80		80								
370	C	PS	40		40								
370	C	SST	60		60								
370	D	SST	100		100								
371	A	SST	50	1237.75	50								
371	A	PS	50		45			5					Yalgorup
371	B	SST	100		100								Wonnerup

371	C	SST	100		100								
371	D	SST	100		100								
372	A	SST	100	1241.55	95			5					
372	B	SST	100		100								
372	C	SST	100		80		10	10					
372	D	SST	100		100								
373	A	SST	100	1245.1	100								
373	B	SST	100		95			5					
373	C	SST	100		100								
373	D	SST	100		100					5-10	7.5		
374	A	SST	100	1248.9	100								
374	B	SST	100		100								
374	C	SST	100		100								
374	D	SST	100		100								
375	A	SST	100	1252.8	100								
375	B	SST	100		100					10-15	12.5		
375	C	SST	100		100								
375	D	SST	100		95			5					
376	A	SST	100	1256.6	100								
376	B	SST	100		100								
376	C	SST	100		100					5-10	7.5		
376	D	SST	100		100								
377	A	SST	100	1260.3	95			5		5-10	7.5		
377	B	SST	100		100								
377	C	SST	100		100								
377	D	SST	100		100								
378	A	SST	100	1264.1	100								

378	B	SST	100		100								
378	C	SST	100		100								
378	D	SST	100		100								
379	A	SST	100	1267.95	100								
379	B	SST	100		100								
379	C	SST	100		100					5	5		
379	D	SST	100		100								
380	A	SST	100	1271.75	100								
380	B	SST	100		100								
380	C	SST	100		100								
380	D	SST	100		100								
381	A	SST	100	1275.55	80		10	10					
381	B	SST	100		100								
381	C	SST	100		50		50						
381	D	SST	100		90		10						
382	A	SST	100	1279.25	100								
382	B	SST	100		100								
382	C	SST	100		100								
382	D	SST	100		100								
383	A	SST	100	1282.95	100								
383	B	SST	100		95			5					
383	C	SST	100		100								
383	D	SST	100		90		10						
384	A	SST	100	1286.75	100								
384	B	SST	100		100								
384	C	SST	100		100								
384	D	SST	100		100								

385	A	SST	100	1290.65	100								
385	B	SST	100		100								
385	C	SST	100		100								
385	D	SST	100		100								
386	A	SST	100	1294.5	100								
386	B	SST	100		100								
386	C	SST	100		100								
386	D	SST	100		90	10							
387	A	SST	100	1298.4	20	35	35	10					
387	B	SST	100		100								
387	C	SST	100		90		10						
387	D	SST	100		60		40						
388	A	SST	100	1302.2	50	50							
388	B	SST	100		90		5	5					
388	C	SST	100		50		50						
388	D	SST	100		90		10						
389	A	SST	100	1306.25	90			10					
389	B	SST	100		95		5						
389	C	SST	100		80		20						
389	D	SST	100		40	15	40	5					
390	A	SST	100	1309.8	100								
390	B	SST	100		100								
390	C	SST	100		100								
390	D	SST	100		100								
391	A	SST	100	1313.6	100								
391	B	SST	100		100								
391	C	SST	100		95			5			0-5	2.5	

391	D	SST	100		100								
392	A	SST	100	1317.95	80		15		5				
392	B	SST	100		100								
392	C	SST	100		100								
392	D	SST	100		100								
393	A	SST	100	1321.3	100								
393	B	SST	100		100								
393	C	SST	100		100								
393	D	SST	100		100								
394	A	SST	100	1325.25	100						5	5	
394	B	SST	100		100								
394	C	SST	100		100								
394	D	SST	100		100								
395	A	SST	100	1329.15	100								
395	B	SST	100		100								
395	C	SST	100		100								
395	D	SST	100		100								
396	A	SST	100	1333.05	100								
396	B	SST	100		95				5				
396	C	SST	100		100								
396	D	SST	100		100								
397	A	SST	100	1336.9	100								
397	B	SST	100		100								
397	C	SST	100		100								
397	D	SST	100		95				5				
398	A	SST	100	1340.8	100								
398	B	SST	100		100								

398	C	SST	100		100								
398	D	SST	100		100								
399	A	SST	100	1344.6	100								
399	B	SST	100		100								
399	C	SST	100		95			5					
399	D	SST	100		95			5					
400	A	SST	100	1348.55	100								
400	B	SST	100		100								
400	C	SST	100		100								

Table A8-3 – Fracture logging data from the Harvey-3 core.

Tray Number	Tray Section	Depth (m)	Lithology	Angle	Surface Roughness	Slickenlines	Fracture Type	Mineralised	Mineralisation Colour	Number Descriptor Total	Comments
10	A	683.1	SST	1	0	0	0	1		2	
10	B	684.02	SST	0	0	0	0	1		1	
11	A	684.37	PS	0	0	0	0	1		1	
11	A	684.5	PS	2	0	0	0	1		3	
11	A	684.56	PS	1	0	0	0	1		2	
11	A	684.63	PS	0	0	0	0	1		1	
11	A	684.97	PS	1	0	0	0	1		2	
11	B	685.3	PS	3	0	0	0	1		4	
11	B	685.4	PS	2	0	0	0	1		3	
11	B	685.53	PS	1	0	0	0	1		2	
11	B	685.8	PS	0	0	0	0	1		1	
12	A	686.1	PS	1	0	0	0	1		2	
12	A	686.2	PS	1	0	0	0	1		2	
12	A	686.71	PS	0	0	0	0	1		1	
12	B	686.8	PS	1	0	0	0	1		2	
12	B	686.82	PS	3	0	0	0	1		4	
12	B	686.88	PS	1	1	0	0	1		3	
12	B	686.89	PS	1	0	0	0	1		2	
12	B	686.98	PS	2	0	0	0	1		3	
12	B	687	PS	1	0	0	0	1		2	
12	B	687.15	PS	1	0	0	0	1		2	
12	B	687.4	PS	1	0	0	0	1		2	

12	B	687.5	PS	2	0	0	0	1		3	
12	B	687.72	PS	1	0	0	0	1		2	
12	B	687.75	PS	1	0	0	0	1		2	
12	B	687.76	PS	1	0	0	0	1		2	
13	A	687.8	PS	1	0	0	0	1		2	
13	A	687.86	PS	0	0	0	0	1		1	
13	A	687.87	PS	0	0	0	0	1		1	
13	A	687.95	PS	0	0	0	0	1		1	
13	A	687.98	PS	1	0	0	0	1		2	
13	A	688.08	PS	0	0	0	0	1		1	
13	A	688.1	PS	1	0	0	0	1		2	
13	A	688.2	PS	1	0	0	0	1		2	
13	A	688.3	PS	2	0	0	0	1		3	
13	B	688.62	PS	1	0	0	0	1		2	
13	B	688.66	PS	0	0	0	0	1		1	
13	B	688.7	PS	1	0	0	0	1		2	
13	B	688.75	PS	0	0	0	0	1		1	
13	B	688.8	PS	2	0	0	0	1		3	
13	B	689.25	PS	0	0	0	0	1		1	
13	B	689.29	PS	0	0	0	0	1		1	
14	A	689.3	PS	3	0	0	0	1		4	
14	A	689.38	PS	1	0	0	0	1		2	
14	A	689.42	PS	3	0	0	0	1		4	
14	A	689.5	PS	0	0	0	0	1		1	
14	A	689.52	PS	0	0	0	0	1		1	
14	A	689.7	PS	1	0	0	0	1		2	
14	A	689.75	PS	1	0	0	0	1		2	

14	A	689.8	PS	1	0	0	0	1		2	
14	A	689.83	PS	0	0	0	0	1		1	
14	A	689.85	PS	1	0	0	0	1		2	
14	A	689.9	PS	2	0	0	0	1		3	
14	A	689.92	PS	1	0	0	0	1		2	
14	A	689.94	PS	0	0	0	0	1		1	
14	A	689.96	PS	0	0	0	0	1		1	
14	A	689.97	PS	0	0	0	0	1		1	
14	B	689.98	PS	1	0	0	0	1		2	
14	B	689.99	PS	0	0	0	0	1		1	
14	B	690	PS	0	0	0	0	1		1	
14	B	690.1	PS	1	0	0	0	1		2	
14	B	690.17	PS	1	0	0	0	1		2	
14	B	690.2	PS	0	0	0	0	1		1	
14	B	690.28	PS	0	0	0	0	1		1	
14	B	690.3	PS	1	0	0	0	1		2	
14	B	690.38	PS	0	0	0	0	1		1	
14	B	690.42	PS	1	0	0	0	1		2	
14	B	690.5	PS	2	0	0	0	1		3	
14	B	690.51	PS	1	0	0	0	1		2	
14	B	690.55	PS	0	0	0	0	1		1	
14	B	690.57	PS	1	0	0	0	1		2	
14	B	690.58	PS	1	0	0	0	1		2	
14	B	690.65	PS	0	0	0	0	1		1	
14	B	690.7	PS	1	0	0	0	1		2	
14	B	690.71	PS	1	0	0	0	1		2	
14	B	690.72	PS	1	0	0	0	1		2	

14	B	690.85	PS	2	0	0	0	1		3	
14	B	690.88	PS	1	0	0	0	1		2	
15	A	690.94	PS	1	0	0	0	1		2	
15	A	691	PS	1	0	0	0	1		2	
15	A	691.1	PS	0	0	0	0	1		1	
15	A	691.2	PS	1	0	0	0	1		2	
15	A	691.24	PS	1	0	0	0	1		2	
15	A	691.26	PS	1	0	0	0	1		2	
15	A	691.3	PS	1	0	0	0	1		2	
15	A	691.38	PS	1	0	0	0	1		2	
15	A	691.45	PS	1	0	0	0	1		2	
15	A	691.52	PS	1	0	0	0	1		2	
15	A	691.65	PS	1	0	0	0	1		2	
15	B	691.7	PS	1	1	1	0	1		4	
15	B	691.72	PS	1	1	1	0	1		4	
15	B	691.74	PS	0	1	1	0	1		3	
15	B	691.82	PS	0	0	0	0	1		1	
15	B	691.9	PS	0	0	0	0	1		1	
15	B	692.03	PS	1	2	0	0	1		4	
15	B	692.04	PS	0	0	0	0	1		1	
15	B	692.07	PS	0	0	0	0	1		1	
15	B	692.08	PS	0	0	0	0	1		1	
15	B	692.13	PS	0	0	0	0	1		1	
15	B	692.2	PS	0	0	0	0	1		1	
15	B	692.21	PS	1	0	0	0	1		2	
15	B	692.23	PS	1	0	0	0	1		2	
15	B	692.3	PS	1	0	1	0	1		3	

15	B	692.33	PS	1	0	0	0	1		2	
15	B	692.53	PS	1	0	0	0	1		2	
16	A	692.8	PS	0	0	0	0	1		1	
16	B	693.6	PS	0	0	0	0	1		1	
16	B	693.64	PS	1	0	0	0	1		2	
16	B	693.66	PS	1	0	0	0	1		2	
16	B	693.67	PS	1	0	0	0	1		2	
16	B	693.74	PS	0	0	0	0	1		1	
16	B	693.77	PS	1	0	0	0	1		2	
16	B	693.78	PS	1	0	1	0	1		3	
16	B	693.9	PS	0	0	0	0	1		1	
16	B	694	PS	1	0	0	0	1		2	
16	B	694.05	PS	1	0	0	0	1		2	
16	B	694.27	PS	0	0	0	0	1		1	
17	A	694.6	PS	2	0	0	0	1		3	
17	A	694.61	PS	2	0	0	0	1		3	
17	A	694.65	PS	1	0	0	0	1		2	
17	A	694.67	PS	3	0	0	0	1		4	
17	A	694.68	PS	1	0	0	0	1		2	
17	A	694.71	PS	2	0	2	0	1		5	
17	A	694.72	PS	0	0	0	0	1		1	
17	A	694.84	PS	1	0	0	0	1		2	
17	A	694.88	PS	1	0	0	0	1		2	
40	A	734.7	PS	1	0	0	0	1		2	
40	A	735	PS	1	0	0	0	1		2	
40	A	735.15	PS	1	0	0	0	1		2	
40	A	735.32	PS	1	0	0	0	1		2	

40	A	735.34	PS	0	0	0	0	1		1	
40	A	735.38	PS	3	0	1	0	1		5	
40	A	735.4	PS	1	0	0	0	1		2	
40	A	735.42	PS	0	0	0	0	1		1	
40	A	735.46	PS	0	0	0	0	1		1	
40	A	735.48	PS	1	0	0	0	1		2	
40	A	735.49	PS	1	1	1	0	1		4	
40	B	735.51	PS	1	0	0	0	1		2	
40	B	735.53	PS	0	0	0	0	1		1	
40	B	735.6	PS	1	0	0	0	1		2	
40	B	735.62	PS	1	0	0	0	1		2	
40	B	735.75	PS	0	0	0	0	1		1	
40	B	735.85	PS	2	0	0	0	1		3	
40	B	735.97	PS	1	0	0	0	1		2	
40	B	736.24	PS	0	0	0	0	1		1	
41	A	736.75	PS	0	0	0	0	1		1	
41	A	736.8	PS	0	0	0	0	1		1	
41	A	736.9	PS	0	0	0	0	1		1	
41	A	736.91	PS	2	0	0	0	1		3	
41	A	737.22	PS	1	0	1	0			2	
41	B	737.47	PS	1	0	0	0	1		2	
41	B	737.53	PS	0	0	0	0	1		1	
41	B	737.54	PS	3	0	0	0	1		4	
41	B	737.6	PS	0	0	0	0	1		1	
41	B	737.7	PS	2	0	0	0	1		3	
41	B	737.75	PS	1	0	0	0	1		2	
41	B	737.9	PS	3	0	0	0	1		4	

41	B	737.95	PS	1	0	0	0	1		2	
42	A	738.27	PS	1	0	0	0	1		2	
42	A	738.33	PS	0	0	0	0	1		1	
42	A	738.38	PS	0	0	0	0	1		1	
42	A	738.42	PS	0	0	0	0	1		1	
42	A	738.5	PS	0	0	0	0	1		1	
42	A	738.63	PS	1	0	0	0	1		2	
42	A	738.96	PS	0	0	0	0	1		1	
42	A	739.07	PS	0	0	0	0	1		1	
42	A	739.1	PS	1	0	0	0	1		2	
42	B	739.12	PS	1	0	0	0	1		2	
42	B	739.17	PS	1	0	0	0	1		2	
42	B	739.19	PS	1	0	0	0	1		2	
42	B	739.25	PS	1	0	0	0	1		2	
42	B	739.27	PS	2	0	0	0	1		3	
42	B	739.35	PS	1	0	0	0	1		2	
42	B	739.42	PS	0	0	0	0	1		1	
42	B	739.43	PS	0	0	0	0	1		1	
42	B	739.53	PS	0	0	0	0	1		1	
42	B	739.6	PS	1	0	0	0	1		2	
42	B	739.63	PS	1	0	0	0	1		2	
42	B	739.75	PS	1	0	0	0	1		2	
42	B	739.77	PS	1	0	0	0	1		2	
42	B	740	PS	3	0	1	0	1		5	
43	A	740.01	PS	1	1	1	0	1		4	
43	A	740.04	PS	3	0	1	0	1		5	
43	A	740.07	PS	2	0	0	0	1		3	

43	A	740.2	PS	1	1	1	0	1		4	
43	A	740.42	PS	1	0	0	0	1		2	
43	A	740.51	PS	1	0	0	0	1		2	
43	A	740.6	PS	1	0	0	0	1		2	
43	A	740.66	PS	1	0	0	0	1		2	
43	A	740.75	PS	0	0	0	0	1		1	
43	A	740.8	PS	3	0	1	0	1		5	
43	A	740.82	PS	1	0	1	0	1		3	
43	A	740.84	PS	0	0	0	0	1		1	
43	A	740.87	PS	2	0	0	0	1		3	
43	B	740.9	PS	2	0	0	0	1		3	
43	B	740.94	PS	1	0	0	0	1		2	
43	B	740.98	PS	1	0	0	0	1		2	
43	B	741	PS	1	0	0	0	1		2	
43	B	741.02	PS	0	0	0	0	1		1	
43	B	741.07	PS	3	0	0	0	1		4	
43	B	741.11	PS	0	0	0	0	1		1	
43	B	741.16	PS	1	0	1	0	1		3	
43	B	741.3	SST	0	0	0	0	1		1	
43	B	741.59	SST	1	0	0	0	1		2	
43	B	741.62	SST	0	0	0	0	1		1	
44	A	741.95	SST	0	0	0	0	1		1	
44	A	742.05	SST	1	0	0	0	1		2	
44	A	742.35	SST	0	0	0	0	1		1	
44	A	742.51	SST	0	0	0	0	1		1	
44	A	742.58	PS	1	0	1	0	1		3	
44	A	742.61	PS	1	0	1	0	1		3	

44	A	742.63	PS	2	1	1	0	1		5	
44	A	742.65	PS	1	0	0	0	1		2	
44	A	742.67	PS	1	2	1	0	1		5	
44	B	742.68	PS	1	0	0	0	1		2	
44	B	742.75	PS	2	0	0	0	1		3	
44	B	742.85	PS	1	2	0	0	1		4	
44	B	742.9	PS	1	0	0	0	1		2	
44	B	742.95	PS	0	0	0	0	1		1	
44	B	743	PS	1	2	1	0	1		5	
44	B	743.12	PS	1	1	1	0	1		4	
44	B	743.13	PS	0	0	0	0	1		1	
44	B	743.18	PS	1	0	1	0	1		3	
44	B	743.35	PS	1	1	1	0	1		4	
44	B	743.37	PS	3	1	0	0	1		5	
44	B	743.4	PS	1	0	0	0	1		2	
44	B	743.45	PS	1	1	1	0	1		4	
45	A	743.55	PS	1	0	0	0	1		2	
45	A	743.6	PS	1	0	0	0	1		2	
45	A	743.62	PS	1	0	0	0	1		2	
45	A	743.65	PS	1	0	0	0	1		2	
45	A	743.67	PS	1	0	0	0	1		2	
45	A	743.7	PS	1	0	0	0	1		2	
45	A	743.79	PS	1	0	0	0	1		2	
45	A	743.81	PS	1	0	0	0	1		2	
45	A	743.84	PS	1	0	0	0	1		2	
45	A	743.86	PS	1	0	0	0	1		2	
45	A	743.87	PS	1	0	0	0	1		2	

45	A	743.88	PS	1	0	0	0	1		2	
45	A	743.9	PS	0	0	0	0	1		1	
45	A	744.05	PS	0	0	0	0	1		1	
45	A	744.06	PS	0	0	0	0	1		1	
45	A	744.27	PS	0	0	0	0	1		1	
45	B	744.75	SST	0	0	0	0	1		1	
45	B	744.8	SST	1	0	0	0	1		2	
45	B	744.9	SST	0	0	0	0	1		1	
45	B	744.98	SST	0	0	0	0	1		1	
45	B	744.99	SST	1	0	0	0	1		2	
45	B	745.15	SST	0	0	0	0	1		1	
46	A	745.85	SST	0	0	0	0	1		1	
46	A	746.18	SST	1	0	0	0	1		2	
46	B	746.5	SST	0	0	0	0	1		1	
46	B	747.06	SST	0	0	0	0	1		1	
47	A	747.4	SST	0	0	0	0	1		1	
47	A	747.65	SST	0	0	0	0	1		1	
47	A	747.8	SST	1	0	0	0	1		2	
70	A	790.2	SST	0	0	0	0	1		1	
70	A	790.4	SST	0	0	0	0	1		1	
70	A	790.55	SST	0	0	0	0	1		1	
70	A	790.64	SST	0	0	0	0	1		1	
70	B	791.11	SST	0	0	0	0	1		1	
70	B	791.3	SST	0	0	0	0	1		1	
70	B	791.5	SST	0	0	0	0	1		1	
70	B	791.77	SST	0	0	0	0	1		1	
71	A	791.93	SST	1	0	0	0	1		2	

71	A	792.1	SST	1	0	0	0	1		2	
71	A	792.17	SST	0	0	0	0	1		1	
71	A	792.35	SST	1	0	0	0	1		2	
71	A	792.59	SST	0	0	0	0	1		1	
71	A	792.68	SST	1	0	0	0	1		2	
71	B	793.02	SST	1	0	0	0	1		2	
71	B	793.13	SST	1	0	0	0	1		2	
71	B	793.5	SST	0	0	0	0	1		1	
72	A	793.75	SST	0	0	0	0	1		1	
72	A	794.01	SST	0	0	0	0	1		1	
72	A	794.34	SST	1	0	0	0	1		2	
72	B	794.5	SST	0	0	0	0	1		1	
72	B	794.58	SST	1	0	0	0	1		2	
72	B	794.9	SST	0	0	0	0	1		1	
72	B	795.2	SST	0	0	0	0	1		1	
72	B	795.27	SST	1	0	0	0	1		2	
73	A	795.65	SST	0	0	0	0	1		1	
73	A	796.27	SST	0	0	0	0	1		1	
73	B	796.65	SST	3	0	0	0	1		4	
73	B	796.86	SST	0	0	0	0	1		1	
74	A	797.53	SST	1	0	0	0	1		2	
74	A	797.74	SST	0	0	0	0	1		1	
74	A	798.41	SST	0	0	0	0	1		1	
74	B	798.65	SST	0	0	0	0	1		1	
75	A	799.3	SST	0	0	0	0	1		1	
75	A	799.77	SST	1	0	0	0	1		2	
75	A	799.82	SST	1	0	0	0	1		2	

75	B	800.17	SST	1	0	0	0	1		2	
75	B	800.3	SST	1	0	0	0	1		2	
75	B	800.43	SST	1	0	0	0	1		2	
75	B	800.6	SST	0	0	0	0	1		1	
75	B	800.65	SST	0	0	0	0	1		1	
75	B	800.82	SST	0	0	0	0	1		1	
76	A	801.38	SST	0	0	0	0	1		1	
76	A	801.79	SST	0	0	0	0	1		1	
76	B	802	SST	0	0	0	0	1		1	
76	B	802.4	SST	1	0	0	0	1		2	
76	B	802.72	SST	0	0	0	0	1		1	
77	A	802.98	SST	0	0	0	0	1		1	
77	A	803.3	SST	1	0	0	0	1		2	
77	A	803.65	SST	0	0	0	0	1		1	
100	A	845.85	SST	1	0	0	0	1		2	
100	A	846.03	SST	0	0	0	0	1		1	
100	A	846.42	SST	1	0	0	0	1		2	
100	B	846.9	SST	0	0	0	0	1		1	
100	B	847.12	SST	0	0	0	0	1		1	
100	B	847.37	SST	1	0	0	0	1		2	
101	A	847.92	SST	0	0	0	0	1		1	
101	A	848.22	SST	1	0	0	0	1		2	
101	B	848.8	SST	1	0	0	0	1		2	
101	B	849.23	SST	1	0	0	0	1		2	
103	B	850.8	SST	0	0	0	0	1		1	No fractures in tray 102 section A

103	A	851.97	SST	0	0	0	0	1		1	
103	B	852.3	SST	0	0	0	0	1		1	
104	A	852.61	SST	3	0	0	0	1		4	
104	A	853.6	SST	1	0	0	0	1		2	
104	A	854	SST	1	0	0	0	1		2	
104	B	854.31	SST	0	0	0	0	1		1	
104	B	854.72	SST	0	0	0	0	1		1	
105	A	855.2	SST	0	0	0	0	1		1	
105	A	855.58	SST	0	0	0	0	1		1	
105	B	856.1	SST	0	0	0	0	1		1	
105	B	856.3	SST	0	0	0	0	1		1	
105	B	856.43	SST	1	0	0	0	1		2	
105	B	856.77	SST	0	0	0	0	1		1	
106	A	857.2	PS	0	0	0	0	1		1	Drill ripping at outside of core in boxes 106 and 107 - PS surface falling off
106	A	857.22	PS	1	0	0	0	1		2	
106	A	857.3	PS	1	0	0	0	1		2	
106	A	857.35	PS	1	0	0	0	1		2	
106	A	857.37	PS	1	0	0	0	1		2	
106	A	857.38	PS	1	0	0	0	1		2	
106	A	857.41	PS	1	0	0	0	1		2	
106	A	857.51	PS	1	0	0	0	1		2	
106	A	857.53	PS	1	0	1	0	1		3	

106	A	857.6	PS	1	0	0	0	1		2	
106	A	857.62	PS	1	1	0	0	1		3	
106	A	857.71	PS	0	0	0	0	1		1	
106	A	857.73	PS	0	0	0	0	1		1	
106	A	857.75	PS	1	0	0	0	1		2	
106	B	857.9	PS	1	0	0	0	1		2	
106	B	857.92	PS	3	1	1	0	0	Green/Brown/	5	
106	B	857.98	PS	0	0	0	0	1	Yellow	1	
106	B	858.01	PS	1	0	0	0	1		2	
106	B	858.1	PS	1	0	0	0	1		2	
106	B	858.15	PS	1	0	0	0	1		2	
106	B	858.16	PS	2	0	0	0	1		3	
106	B	858.17	PS	2	0	0	0	1		3	
106	B	858.35	PS	1	0	0	0	1		2	
106	B	858.36	PS	1	0	0	0	1		2	
106	B	858.38	PS	1	0	0	0	1		2	
106	B	858.53	PS	1	1	1	0	1		4	
107	A	858.68	PS	1	0	0	0	1		2	
107	A	858.69	PS	1	0	0	0	1		2	
107	A	858.72	PS	1	0	0	0	1		2	
107	A	858.75	PS	1	0	0	0	1		2	
107	A	858.8	PS	1	0	0	0	1		2	
107	A	858.83	PS	1	0	0	0	1		2	
107	A	858.86	PS	1	0	0	0	1		2	
107	A	858.9	PS	0	0	0	0	1		1	
107	A	859.31	PS	0	0	0	0	1		1	

107	A	859.32	PS	1	0	0	0	1		2	
107	A	859.33	PS	1	0	0	0	1		2	
107	A	859.34	PS	0	0	0	0	1		1	
107	A	859.35	PS	0	0	0	0	1		1	
130	A	900.73	SST	0	0	0	0	1		1	
130	A	900.8	SST	0	0	0	0	1		1	
130	A	901.42	SST	1	0	0	0	1		2	
130	B	901.9	SST	0	0	0	0	1		1	
130	B	902.35	SST	1	0	0	0	1		2	
131	A	902.7	SST	0	0	0	0	1		1	
131	A	903.25	SST	1	0	0	0	1		2	
131	B	903.8	SST	0	0	0	0	1		1	
131	B	903.9	SST	0	0	0	0	1		1	
131	B	904.23	SST	0	0	0	0	1		1	
132	A	904.71	SST	0	0	0	0	1		1	
132	A	905.02	SST	0	0	0	0	1		1	
132	B	905.48	SST	0	0	0	0	1		1	
132	B	906.15	SST	1	0	0	0	1		2	
133	A	906.65	SST	0	0	0	0	1		1	
133	A	907.1	SST	0	0	0	0	1		1	
133	B	907.85	SST	0	0	0	0	1		1	
134	A	908.75	SST	0	0	0	0	1		1	
134	A	908.95	SST	0	0	0	0	1		1	
134	B	909.87	SST	0	0	0	0	1		1	
134	B	909.9	SST	0	0	0	0	1		1	
135	A	910.48	SST	0	0	0	0	1		1	
135	B	912.2	SST	0	0	0	0	1		1	

135	B	912.22	SST	0	0	0	0	1		1	
136	A	912.62	SST	0	0	0	0	1		1	
136	B	913.82	SST	0	0	0	0	1		1	
137	A	913.95	PS	0	0	0	0	1		1	
137	A	913.96	PS	1	0	0	0	1		2	
137	A	914	PS	1	0	0	0	1		2	
137	A	914.03	PS	1	0	0	0	1		2	
137	A	914.05	PS	1	0	0	0	1		2	
137	A	914.07	PS	0	0	0	0	1		1	
137	A	914.14	PS	0	0	0	0	1		1	
137	A	914.19	PS	1	0	0	0	1		2	
137	A	914.22	PS	1	0	0	0	1		2	
137	A	914.25	PS	0	0	0	0	1		1	
137	A	914.26	PS	1	0	0	0	1		2	
137	A	914.3	PS	2	0	0	0	1		3	
137	A	914.4	PS	0	0	0	0	1		1	
137	A	914.48	PS	0	0	0	0	1		1	
137	A	914.53	PS	1	0	0	0	1		2	
137	A	914.54	PS	0	0	0	0	1		1	
137	A	914.6	PS	1	0	0	0	1		2	
137	A	914.65	PS	1	0	0	0	1		2	
137	A	914.7	PS	0	0	0	0	1		1	
160	A	957.55	SST	1	0	0	0	1		2	
160	A	958.2	SST	0	0	0	0	1		1	
160	B	958.85	SST	0	0	0	0	1		1	
160	B	959.41	SST	0	0	0	0	1		1	
161	A	960.24	SST	1	0	0	0	1		2	

161	B	961	SST	0	0	0	0	1		1	
162	A	961.6	SST	0	0	0	0	1		1	
162	B	962.62	SST	0	0	0	0	1		1	
162	B	963.07	SST	1	0	0	0	1		2	
163	A	963.65	SST	0	0	0	0	1		1	
163	A	964.11	SST	1	0	0	0	1		2	
163	B	964.7	SST	0	0	0	0	1		1	
163	B	964.79	SST	0	0	0	0	1		1	
163	B	964.97	SST	0	0	0	0	1		1	
164	A	965.6	SST	0	0	0	0	1		1	
164	A	965.93	SST	0	0	0	0	1		1	
164	A	966.23	SST	0	0	0	0	1		1	
164	B	966.6	SST	0	0	0	0	1		1	
164	B	966.84	SST	0	0	0	0	1		1	
165	A	967.5	SST	1	0	0	0	1		2	
165	B	968.25	PS	1	2	0	2	1		6	
165	B	968.35	PS	0	0	0	0	1		1	
165	B	968.38	PS	1	2	0	2	1		6	
165	B	968.4	PS	1	0	0	0	1		2	
165	B	968.42	PS	1	0	0	0	1		2	
165	B	968.5	PS	1	0	0	0	1		2	
165	B	968.51	PS	1	0	0	0	1		2	
165	B	968.53	PS	0	0	0	0	1		1	
165	B	968.54	PS	0	0	0	0	1		1	
165	B	968.58	PS	0	0	0	0	1		1	
165	B	968.59	PS	0	0	0	0	1		1	
165	B	968.64	PS	0	0	0	0	1		1	

165	B	968.76	PS	1	0	0	0	1		2	
165	B	968.77	PS	1	0	0	0	1		2	
165	B	968.79	PS	0	0	0	0	1		1	
165	B	968.81	PS	1	0	0	0	1		2	
165	B	968.9	PS	1	0	0	0	1		2	
165	B	968.97	PS	1	0	0	0	1		2	
165	B	968.98	PS	1	0	0	0	1		2	
165	B	968.99	PS	1	0	0	0	1		2	
165	B	969	PS	2	0	0	0	1		3	
165	B	969.03	PS	0	0	0	0	1		1	
165	B	969.07	PS	1	0	0	0	1		2	
165	B	969.1	PS	1	0	0	0	1		2	
166	A	969.17	PS	0	0	0	0	1		1	
166	A	969.25	PS	0	0	0	0	1		1	
166	A	969.27	PS	1	0	0	0	1		2	
166	A	969.3	SST	1	0	0	0	1		2	
166	A	969.65	SST	1	0	0	0	1		2	
166	B	970.15	SST	0	0	0	0	1		1	
166	B	970.49	SST	0	0	0	0	1		1	
166	B	970.52	SST	1	0	0	0	1		2	
166	B	970.6	SST	1	0	0	0	1		2	
166	B	970.61	SST	0	0	0	0	1		1	
166	B	971	SST	0	0	0	0	1		1	
167	A	971.44	SST	0	0	0	0	1		1	
167	A	971.77	SST	1	0	0	0	1		2	
191	A	1014.6	PS	1	1	1	1	1		5	
191	A	1014.9	PS	0	0	0	1	1		2	

191	A	1015.1	PS	0	0	0	1	1		2	
191	A	1015.4	PS	0	0	0	1	1		2	
191	B	1015.52	PS	0	0	0	0	1		1	
191	B	1016	PS	0	0	0	0	1		1	
191	B	1016.1	PS	0	0	0	0	1		1	
191	B	1016.2	PS	0	0	0	0	1		1	
191	B	1016.25	PS	0	0	0	0	1		1	
192	A	1016.31	PS	0	0	0	0	1		1	
192	A	1016.4	PS	0	0	0	0	1		1	
192	A	1016.6	PS	0	0	0	0	1		1	
192	A	1016.7	PS	0	0	0	0	1		1	
192	A	1017.1	PS	0	0	0	0	1		1	
192	B	1017.4	PS	0	0	0	0	1		1	
192	B	1017.8	PS	1	0	0	0	1		2	
192	B	1017.85	PS	0	0	0	1	1		2	
193	A	1018.37	PS	0	0	0	1	1		2	
193	A	1018.6	PS	0	2	2	2	1		7	
193	A	1018.85	PS	0	0	0	0	1		1	
193	A	1019.1	PS	0	0	0	0	1		1	
193	A	1019.2	PS	0	0	0	0	1		1	
193	B	1019.48	PS	0	0	0	0	1		1	
193	B	1019.8	PS	0	0	0	0	1		1	
193	B	1020	PS	0	0	0	0	1		1	
194	A	1020.2	PS	1	0	0	0	1		2	
194	A	1020.4	PS	0	0	0	0	1		1	
194	A	1020.7	PS	0	0	0	0	1		1	
194	A	1021.1	PS	1	0	0	0	1		2	

194	B	1021.48	PS	0	0	0	0	1		1	
194	B	1022.75	SST	0	0	0	0	1		1	
194	B	1023.2	SST	1	0	0	0	1		2	
194	B	1023.5	PS	0	0	0	0	1		1	
194	B	1023.53	PS	0	0	0	0	1		1	
194	B	1023.6	PS	0	0	0	0	1		1	
194	B	1023.7	PS	1	0	0	0	1		2	
194	B	1023.75	PS	1	0	0	0	1		2	
194	B	1023.8	PS	0	0	0	0	1		1	
194	B	1023.9	PS	1	0	0	0	1		2	
194	B	1023.95	PS	1	0	0	0	1		2	
195	A	1024	PS	1	0	0	0	1		2	
195	A	1024.02	PS	0	1	0	0	1		2	
195	A	1024.1	PS	0	0	0	0	1		1	
195	A	1024.2	PS	0	0	0	0	1		1	
195	A	1024.44	PS	0	0	0	0	1		1	
195	A	1022.65	PS	0	0	0	0	1		1	
195	A	1022.7	PS	0	0	0	0	1		1	
195	A	1022.75	PS	0	0	0	0	1		1	
195	A	1022.76	PS	0	0	0	0	1		1	
195	A	1022.77	PS	2	0	0	0	1		3	
195	A	1022.8	PS	0	0	0	0	1		1	
195	A	1022.81	PS	1	0	0	0	1		2	
195	A	1022.95	PS	0	0	0	0	0		0	
195	B	1025	PS	1	0	0	0	1		2	
195	B	1025.03	PS	0	0	0	0	1		1	
195	B	1025.04	PS	0	0	0	0	1		1	

195	B	1025.1	PS	0	0	0	0	1		1	
195	B	1025.2	PS	0	0	0	0	1		1	
195	B	1025.55	PS	0	0	0	0	1		1	
195	B	1025.62	PS	0	0	0	0	1		1	
195	B	1025.75	PS	0	0	0	0	1		1	
195	B	1025.8	PS	0	0	0	0	1		1	
195	B	1025.83	PS	0	0	0	0	1		1	
196	A	1025.84	PS	0	0	0	0	1		1	
196	A	1025.85	PS	2	0	0	0	1		3	
196	A	1025.87	PS	1	0	0	0	1		2	
196	A	1025.88	PS	1	0	0	0	1		2	
196	A	1025.9	PS	1	0	0	0	1		2	
196	A	1025.94	PS	1	0	0	0	1		2	
196	A	1026.05	PS	0	0	0	0	1		1	
196	A	1026.25	PS	0	0	0	0	1		1	
196	A	1026.35	PS	0	0	0	0	1		1	
196	A	1026.42	PS	0	0	0	0	1		1	
196	A	1026.47	PS	0	0	0	0	1		1	
196	A	1026.48	PS	1	0	0	0	1		2	
196	A	1026.51	PS	0	0	0	0	1		1	
196	A	1026.53	PS	1	0	0	0	1		2	
196	A	1026.56	PS	0	0	0	0	1		1	
196	A	1026.71	PS	0	0	0	0	1		1	
196	A	1026.72	PS	1	0	0	0	1		2	
196	A	1026.74	PS	1	0	0	0	1		2	
196	A	1026.75	PS	0	0	0	0	1		1	
196	A	1026.76	PS	3	0	0	0	1		4	

196	A	1026.79	PS	0	0	0	0	1		1	
196	B	1026.94	PS	0	0	0	0	1		1	
196	B	1027.3	PS	0	0	0	0	1		1	
196	B	1027.35	PS	1	0	0	0	1		2	
196	B	1027.37	PS	0	0	0	0	1		1	
196	B	1027.42	PS	0	0	0	0	1		1	
196	B	1027.45	PS	0	0	0	0	1		1	
196	B	1027.54	PS	0	0	0	0	1		1	
196	B	1027.95	PS	0	0	0	0	1		1	
196	B	1028.1	PS	0	0	0	0	1		1	
196	B	1028.12	PS	0	0	0	0	1		1	
196	B	1028.14	PS	0	0	0	0	1		1	
196	B	1028.4	PS	0	0	0	0	1		1	
196	B	1028.45	PS	0	0	0	0	1		1	
196	B	1028.57	PS	0	0	0	0	1		1	
220	A	1071.5	SST	0	0	0	0	1		1	
220	A	1071.8	SST	1	0	0	0	1		2	
220	A	1071.87	PS	0	0	0	0	1		1	
220	A	1072.15	PS	0	0	0	0	1		1	
220	A	1072.18	PS	0	0	0	0	1		1	
220	A	1072.19	PS	2	0	0	0	1		3	
220	A	1072.35	PS	3	0	0	0	1		4	
220	B	1072.4	PS	0	0	0	0	1		1	
220	B	1072.45	PS	0	0	0	0	1		1	
220	B	1072.55	PS	0	0	0	0	1		1	
220	B	1072.6	PS	0	0	0	0	1		1	
220	B	1072.75	PS	0	0	0	0	1		1	

220	B	1072.95	PS	1	0	0	0	1		2	
220	B	1073.05	PS	0	0	0	0	1		1	
221	A	1073.3	PS	2	0	0	0	1		3	
221	A	1073.4	PS	0	0	0	0	1		1	
221	A	1073.55	PS	0	0	0	0	1		1	
221	A	1073.65	PS	3	0	0	0	1		4	
221	A	1073.9	PS	1	0	0	0	1		2	
221	A	1073.95	PS	0	0	0	0	1		1	
221	A	1074.03	PS	0	0	0	0	1		1	
221	B	1074.42	PS	0	0	0	0	1		1	
221	B	1074.5	PS	0	0	0	0	1		1	
221	B	1074.58	PS	0	0	0	0	1		1	
221	B	1074.65	PS	0	0	0	0	1		1	
221	B	1074.97	PS	0	0	0	0	1		1	
222	A	1075.7	PS	0	0	0	0	1		1	
222	A	1076.05	PS	0	0	0	0	1		1	
222	A	1076.4	PS	0	0	0	0	1		1	
222	B	1076.82	PS	0	0	0	0	1		1	
223	A	1077	PS	2	1	0	0	1		4	
223	A	1077.12	PS	0	0	0	0	1		1	
223	A	1077.3	PS	0	0	0	0	1		1	
223	A	1077.3	PS	0	0	0	0	1		1	
223	A	1077.5	PS	0	0	0	0	1		1	
223	B	1077.85	PS	0	0	0	0	1		1	
223	B	1077.88	PS	0	0	0	0	1		1	
223	B	1078.05	PS	0	0	0	0	1		1	
224	A	1078.85	PS	0	0	0	0	1		1	

224	A	1079.05	PS	0	0	0	0	1		1	
224	B	1079.75	PS	0	0	0	0	1		1	
224	B	1080.3	SST	0	0	0	0	1		1	
225	A	1080.65	SST	3	0	0	0	1		4	
225	A	1081	PS	0	0	0	0	1		1	
225	B	1081.35	PS	0	0	0	0	1		1	
225	B	1081.75	SST	1	0	0	0	1		2	
226	A	1082.45	SST	0	0	0	0	1		1	
226	A	1082.52	PS	2	0	0	0	1		3	
226	B	1083.02	PS	0	0	0	0	1		1	
226	B	1083.45	SST	0	0	0	0	1		1	
226	B	1083.75	PS	0	0	0	0	1		1	
227	A	1084	PS	0	0	0	0	1		1	
227	A	1084.65	PS	0	0	0	0	1		1	
227	A	1084.7	PS	0	0	0	0	1		1	
250	A	1127.77	PS	0	0	0	0	1		1	
250	A	1127.79	PS	0	0	0	0	1		1	
250	A	1127.89	SST	0	0	0	0	1		1	
250	A	1128.1	SST	0	0	0	0	1		1	
250	B	1129.05	PS	0	0	0	0	1		1	
250	B	1129.2	PS	0	0	0	0	1		1	
250	B	1129.53	PS	1	0	0	0	1		2	
251	A	1129.7	PS	0	0	0	0	1		1	
251	A	1129.72	PS	0	0	0	0	1		1	
251	A	1130.3	PS	0	0	0	0	1		1	
251	B	1131.05	PS	0	0	0	0	1		1	
251	B	1131.3	PS	0	0	0	0	1		1	

251	B	1131.45	PS	0	0	0	0	1		1	
252	A	1132.25	SST	0	0	0	0	1		1	
252	B	1133.1	SST	0	0	0	0	1		1	
253	A	1133.55	SST	0	0	0	0	1		1	
253	A	1133.75	PS	1	0	0	0	1		2	
253	A	1133.78	PS	0	0	0	0	1		1	
253	A	1134.1	OS	1	0	0	0	1		2	
253	A	1134.2	PS	0	0	0	0	1		1	
253	A	1134.35	SST	0	0	0	0	1		1	
253	B	1134.8	PS	0	0	0	0	1		1	
253	B	1134.9	PS	0	0	0	0	1		1	
253	B	1134.98	PS	0	0	0	0	1		1	
253	B	1135.02	PS	0	0	0	0	1		1	
253	B	1135.1	PS	1	0	0	0	1		2	
254	A	1135.88	PS	0	0	0	0	1		1	
254	A	1135.9	PS	0	0	0	0	1		1	
254	A	1135.91	PS	0	0	0	0	1		1	
254	A	1135.95	PS	0	0	0	0	1		1	
254	A	1135.99	PS	0	0	0	0	1		1	
254	A	1136.03	PS	0	0	0	0	1		1	
254	A	1136.05	PS	0	0	0	0	1		1	
254	A	1136.09	PS	0	0	0	0	1		1	
254	B	1136.85	SST	0	0	0	0	1		1	
254	B	1137.15	SST	0	0	0	0	1		1	
254	B	1137.35	PS	0	0	0	0	1		1	
255	A	1137.4	PS	3	0	0	0	1		4	
255	A	1137.5	PS	0	0	0	0	1		1	

255	A	1137.57	PS	0	0	0	0	1		1	
255	A	1137.6	PS	0	0	0	0	1		1	
255	A	1137.92	PS	0	0	0	0	1		1	
255	B	1138.3	PS	0	0	0	0	1		1	
256	B	1138.33	PS	0	0	0	0	1		1	
256	A	1139.27	PS	0	0	0	0	1		1	
256	B	1141.03	PS	0	0	0	0	1		1	
257	B	1138.45	PS	0	0	0	0	1		1	
257	A	1139.3	PS	0	0	0	0	1		1	
257	A	1141.25	PS	0	0	0	0	1		1	
257	A	1141.27	PS	0	0	0	0	1		1	
257	A	1141.37	SST	1	0	0	0	1		2	
257	A	1141.8	PS	0	0	0	0	1		1	
257	A	1141.83	PS	0	0	0	0	1		1	
257	A	1141.88	PS	0	0	0	0	1		1	
257	A	1141.93	PS	0	0	0	0	1		1	
257	A	1141.95	PS	0	0	0	0	1		1	
257	A	1142	PS	0	0	0	0	1		1	
258	B	1138.49	PS	0	0	0	0	1		1	
258	A	1139.31	PS	0	0	0	0	1		1	
259	B	1138.55	PS	0	0	0	0	1		1	
259	A	1139.36	PS	0	0	0	0	1		1	
260	B	1138.75	PS	0	0	0	0	1		1	
260	A	1139.4	PS	0	0	0	0	1		1	
261	B	1138.8	PS	1	0	0	0	1		2	
261	A	1139.44	PS	0	0	0	0	1		1	
262	B	1138.82	PS	3	0	0	0	1		4	

262	A	1139.45	PS	0	0	0	0	1		1	
263	B	1138.9	PS	0	0	0	0	1		1	
263	A	1139.5	PS	0	0	0	0	1		1	
264	B	1139.1	PS	0	0	0	0	1		1	
264	A	1139.7	PS	0	0	0	0	1		1	
265	B	1139.11	PS	0	0	0	0	1		1	
265	A	1139.85	PS	1	0	0	0	1		2	
266	B	1139.12	PS	0	0	0	0	1		1	
266	A	1139.86	PS	2	0	0	0	1		3	
267	B	1139.14	PS	0	0	0	0	1		1	
267	A	1139.98	PS	0	0	0	0	1		1	
268	B	1139.15	PS	1	0	0	0	1		2	
268	A	1140	PS	2	0	0	0	1		3	
269	B	1139.16	PS	0	0	0	0	1		1	
269	A	1140.07	PS	0	0	0	0	1		1	
270	B	1139.17	PS	0	0	0	0	1		1	
270	A	1140.09	PS	0	0	0	0	1		1	
271	A	1140.15	PS	0	0	0	0	1		1	
272	B	1140.2	PS	2	0	0	0	1		3	
273	B	1140.25	PS	1	0	0	0	1		2	
274	B	1140.3	PS	0	0	0	0	1		1	
275	B	1141.01	PS	0	0	0	0	1		1	
280	A	1183.55	SST	0	0	0	0	1		1	
280	B	1184.6	SST	0	0	0	0	1		1	
280	B	1184.6	SST	0	0	0	0	1		1	
281	A	1185.25	SST	0	0	0	0	1		1	
281	A	1185.35	SST	0	0	0	0	1		1	

281	A	1185.4	PS	0	0	0	0	1		1	
281	A	1185.42	PS	0	0	0	0	1		1	
281	B	1186.35	PS	0	0	0	0	1		1	
281	B	1186.38	PS	0	0	0	0	1		1	
281	B	1186.41	PS	0	0	0	0	1		1	
281	B	1186.42	PS	0	0	0	0	1		1	
281	B	1186.44	PS	0	0	0	0	1		1	
281	B	1186.57	PS	0	0	0	0	1		1	
282	A	1187.2	SST	0	0	0	0	1		1	
282	A	1187.45	PS	0	0	0	0	1		1	
282	B	1185.55	SST	0	0	0	0	1		1	
283	A	1185.85	SST	0	0	0	0	1		1	
283	A	1189.3	SST	0	0	0	0	1		1	
283	B	1189.9	SST	0	0	0	0	1		1	
283	B	1190.3	SST	0	0	0	0	1		1	
284	A	1190.97	SST	0	0	0	0	1		1	
284	B	1192	SST	0	0	0	0	1		1	
284	B	1192.4	SST	0	0	0	0	1		1	
285	A	1192.8	SST	0	0	0	0	1		1	
285	A	1193.05	SST	0	0	0	0	1		1	
285	B	1193.6	SST	0	0	0	0	1		1	
285	B	1193.85	SST	0	0	0	0	1		1	
285	B	1194.1	SST	0	0	0	0	1		1	
286	A	1194.55	SST	0	0	0	0	1		1	
286	A	1194.05	SST	0	0	0	0	1		1	
286	B	1196	SST	0	0	0	0	1		1	
286	B	1196.6	SST	0	0	0	0	1		1	

286	B	1196.8	SST	0	0	0	0	1		1	
286	B	1196.9	SST	0	0	0	0	1		1	
310	A	1235.95	PS	0	0	0	0	1		1	
310	A	1240.1	PS	0	0	0	0	1		1	
310	A	1240.2	PS	0	0	0	0	1		1	
310	A	1240.25	PS	0	0	0	0	1		1	
310	B	1240.6	PS	2	2	0	0	1		5	
310	B	1240.7	PS	0	0	0	0	1		1	
310	B	1240.85	PS	0	0	0	0	1		1	
311	A	1241.4	SST	0	0	0	0	1		1	
311	A	1241.65	PS	0	0	0	0	1		1	
311	A	1241.75	PS	0	0	0	0	1		1	
311	A	1241.98	SST	0	0	0	0	1		1	
311	B	1242.5	SST	2	0	0	0	1		3	
311	B	1243.05	SST	0	0	0	0	1		1	
311	B	1243.2	PS	0	0	0	0	1		1	
311	B	1243.27	PS	0	0	0	0	1		1	
312	A	1243.31	PS	1	0	0	0	1		2	
312	A	1243.33	PS	0	0	0	0	1		1	
312	A	1243.37	PS	1	0	0	0	1		2	
312	A	1243.42	PS	2	0	0	0	1		3	
312	A	1243.55	PS	1	0	0	0	1		2	
312	A	1243.58	PS	1	0	0	0	1		2	
312	A	1243.6	PS	1	0	0	0	1		2	
312	A	1243.63	PS	0	0	0	0	1		1	
312	A	1243.64	PS	1	0	0	0	1		2	
312	A	1243.65	PS	0	0	0	0	1		1	

312	A	1243.67	PS	1	0	0	0	1		2	
312	A	1243.7	PS	3	0	1	0	1		5	
312	A	1243.8	PS	0	0	0	0	1		1	
312	A	1243.83	PS	0	0	0	0	1		1	
312	A	1243.88	PS	0	0	0	0	1		1	
312	A	1243.95	PS	1	0	0	0	1		2	
312	B	1243.98	PS	1	0	0	0	1		2	
312	B	1244.03	PS	0	0	0	0	1		1	
312	B	1244.8	PS	0	0	0	0	1		1	
312	B	1244.95	PS	0	0	0	0	1		1	
312	B	1244.97	PS	0	0	0	0	1		1	
312	B	1244.98	PS	1	0	0	0	1		2	
313	A	1245.14	PS	0	0	0	0	1		1	
313	A	1245.15	PS	0	0	0	0	1		1	
313	A	1245.5	PS	1	0	0	0	1		2	
313	A	1245.54	PS	0	0	0	0	1		1	
313	A	1245.56	PS	0	0	0	0	1		1	
313	A	1245.65	PS	1	0	0	0	1		2	
313	B	1246.09	PS	0	0	0	0	1		1	
313	B	1246.2	PS	1	0	0	0	1		2	
313	B	1246.22	PS	0	0	0	0	1		1	
313	B	1246.3	PS	0	0	0	0	1		1	
313	B	1246.56	PS	1	0	0	0	1		2	
313	B	1246.66	PS	0	0	0	0	1		1	
314	A	1247.15	PS	1	0	0	0	1		2	
314	A	1247.3	PS	2	0	0	0	1		3	
314	A	1247.4	PS	1	0	0	0	1		2	

314	A	1247.7	PS	2	0	0	0	1		3	
314	B	1248.05	PS	1	0	0	0	1		2	
314	B	1248.15	PS	1	0	0	0	1		2	
314	B	1248.19	PS	0	0	0	0	1		1	
314	B	1248.3	PS	0	0	0	0	1		1	
314	B	1248.39	PS	0	0	0	0	1		1	
314	B	1248.42	PS	1	0	0	0	1		2	
314	B	1248.44	PS	0	0	0	0	1		1	
314	B	1248.53	PS	0	0	0	0	1		1	
314	B	1248.8	PS	1	0	0	0	1		2	
315	A	1249.02	SST	0	0	0	0	1		1	
315	A	1249.2	SST	0	0	0	0	1		1	
315	A	1249.25	SST	0	0	0	0	1		1	
315	A	1249.35	SST	0	0	0	0	1		1	
315	A	1249.6	SST	0	0	0	0	1		1	
315	A	1249.82	SST	0	0	0	0	1		1	
315	B	1250.4	SST	0	0	0	0	1		1	
315	B	1250.7	SST	1	0	0	0	1		2	No fractures in tray 316 section A
316	B	1251.99	SST	0	0	0	0	1		1	No fractures in tray 316 section A
316	B	1252.3	SST	1	0	0	0	1		2	
316	B	1253.35	SST	1	0	0	0	1		2	
316	B	1252.7	PS	1	0	0	0	1		2	
316	B	1252.78	PS	0	0	0	0	1		1	

317	A	1252.9	PS	1	0	0	0	1		2	
317	A	1252.95	PS	1	0	0	0	1		2	
317	A	1253	PS	2	0	0	0	1		3	
317	A	1253.15	PS	0	0	0	0	1		1	
340	A	1297	PS	1	0	0	0	1		2	
340	A	1297.02	PS	1	0	0	0	1		2	
340	A	1297.1	PS	1	0	0	0	1		2	
340	A	1297.35	PS	0	0	0	0	1		1	
340	B	1297.6	PS	0	0	0	0	1		1	
340	B	1297.75	PS	0	0	0	0	1		1	
340	B	1297.9	PS	0	0	0	0	1		1	
341	A	1298.55	PS	1	0	0	0	1		2	
341	A	1295.63	PS	0	0	0	0	1		1	
341	A	1298.65	PS	0	0	0	0	1		1	
341	A	1298.67	PS	1	0	0	0	1		2	
341	A	1298.68	PS	0	0	0	0	1		1	
341	A	1298.71	PS	1	0	0	0	1		2	
341	A	1298.72	SST	1	0	0	0	1		2	
341	B	1299.8	SST	0	0	0	0	1		1	
342	A	1300.85	SST	0	0	0	0	1		1	
342	A	1300.92	SST	0	0	0	0	1		1	
342	B	1301.85	SST	0	0	0	0	1		1	
343	A	1302.25	PS	0	0	0	0	1		1	
343	A	1302.3	PS	0	0	0	0	1		1	
343	A	1302.32	PS	0	0	0	0	1		1	
343	A	1302.33	PS	3	0	0	0	1		4	
343	A	1302.4	PS	3	0	0	0	1		4	

343	A	1302.47	PS	1	0	0	0	1		2	
343	A	1302.5	PS	1	0	0	0	1		2	
343	A	1302.55	PS	1	0	0	0	1		2	
343	B	1302.9	PS	1	0	0	0	1		2	
343	B	1302.95	PS	2	0	0	0	1		3	
343	B	1302.97	PS	0	0	0	0	1		1	
343	B	1303.4	SST	0	0	0	0	1		1	
344	A	1304.1	SST	1	0	0	0	1		2	
344	B	1304.55	SST	0	0	0	0	1		1	
344	B	1304.85	SST	0	0	0	0	1		1	
344	B	1305	SST	1	0	0	0	1		2	
344	B	1305.15	SST	0	0	0	0	1		1	
344	B	1305.2	SST	3	0	0	0	1		4	
345	A	1305.7	SST	0	0	0	0	1		1	
345	A	1306.05	SST	1	0	0	0	1		2	
345	B	1306.2	SST	0	0	0	0	1		1	
345	B	1306.75	SST	0	0	0	0	1		1	
346	A	1307.25	SST	0	0	0	0	1		1	
346	A	1307.4	SST	2	0	0	0	1		3	
346	A	1307.6	SST	0	0	0	0	1		1	
346	B	1308.3	SST	2	0	0	0	1		3	
346	B	1308.4	SST	1	0	0	0	1		2	
346	B	1308.75	PS	1	0	0	0	1		2	
346	B	1308.76	PS	0	0	0	0	1		1	
347	A	1309.48	SST	0	0	0	0	1		1	
370	A	1352.6	PS	0	0	0	0	1		1	
370	A	1352.65	PS	1	0	0	0	1		2	

370	A	1352.75	PS	1	1	0	0	1		3	
370	A	1352.85	PS	1	1	0	0	1		3	
370	A	1352.86	PS	3	1	0	0	1		5	
370	A	1353	PS	1	1	0	0	1		3	
370	B	1353.55	PS	3	0	0	0	1		4	
370	B	1353.6	PS	1	1	0	0	1		3	
370	B	1353.64	PS	0	0	0	0	1		1	
370	B	1354	PS	0	0	0	0	1		1	
370	B	1354.05	PS	0	0	0	0	1		1	
370	B	1354.1	PS	0	0	0	0	1		1	
370	B	1354.12	PS	1	0	0	0	1		2	
370	B	1354.2	PS	1	0	0	0	1		2	
371	A	1354.27	PS	0	0	0	0	1		1	
371	A	1354.5	SST	1	0	0	0	1		2	
371	A	1354.82	SST	0	0	0	0	1		1	
371	A	1355.1	SST	1	0	0	0	1		2	Tray 371 B has no fractures
372	A	1356.7	SST	1	0	0	0	1		2	Tray 372 B has no fractures
373	A	1358.35	SST	0	0	0	0	1		1	
373	A	1358.55	PS	1	0	0	0	1		2	
373	A	1358.64	PS	1	0	0	0	1		2	
373	A	1358.65	PS	3	1	0	0	1		5	
373	B	1359.6	SST	0	0	0	0	1		1	
374	A	1360.4	SST	0	0	0	0	1		1	

374	A	1360.75	SST	0	0	0	0	1		1	
374	B	1361.4	SST	1	0	0	0	1		2	
374	B	1361.7	PS	1	0	0	0	1		2	
375	A	1362.25	SST	0	0	0	0	1		1	
375	B	1363.6	SST	0	0	0	0	1		1	
376	A	1364.05	SST	0	0	0	0	1		1	
376	A	1364.55	SST	0	0	0	0	1		1	
376	B	1364.63	SST	0	0	0	0	1		1	
376	B	1365.1	SST	1	0	0	0	1		2	
376	B	1365.47	SST	1	0	0	0	1		2	
377	A	1365.95	SST	0	0	0	0	1		1	
377	A	1366.5	SST	0	0	0	0	1		1	
377	A	1366.65	PS	0	0	0	0	1		1	
400	A	1409.05	PS	0	0	0	0	1		1	
400	A	1409.15	PS	0	0	0	0	1		1	
400	A	1409.25	SST	1	0	0	0	1		2	
400	A	1409.3	SST	1	0	0	0	1		2	
400	A	1409.7	SST	1	0	0	0	1		2	
400	B	1410.1	SST	1	0	0	0	1		2	
400	B	1410.25	SST	1	0	0	0	1		2	
401	A	1410.66	PS	1	0	0	0	1		2	
401	A	1410.67	PS	0	0	0	0	1		1	
401	A	1410.69	PS	1	0	0	0	1		2	
401	A	1410.75	PS	3	1	0	0	1		5	
401	A	1410.8	PS	0	0	0	0	1		1	
401	A	1410.95	PS	1	1	0	0	1		3	
401	A	1411	PS	1	1	0	0	1		3	

401	A	1411.02	PS	0	0	0	0	1		1	
401	A	1411.05	PS	1	1	0	0	1		3	
401	A	1411.15	PS	0	0	0	0	1		1	
401	A	1411.16	PS	1	1	0	0	1		3	
401	A	1411.2	PS	1	1	0	0	0	White/Cream	2	
401	B	1411.65	PS	0	0	0	0	1		1	
401	B	1411.65	PS	0	0	0	0	1		1	
401	B	1411.73	PS	1	0	0	0	1		2	
401	B	1411.9	PS	1	0	0	0	1		2	
401	B	1412.01	PS							0	
401	B	1212.25	PS	1	0	0	0	1		2	
401	B	1412.28	PS	1	0	0	0	1		2	
401	B	1412.3	PS	1	1	1	0	1		4	
401	B	1412.42	PS	1	1	1	0	1		4	
402	A	1213.45	SST	1	0	0	0	1		2	
402	B	1413.55	SST	0	0	0	0	1		1	
402	B	1413.55	SST	0	0	0	0	1		1	
402	B	1413.58	PS	0	0	0	0	1		1	
402	B	1413.78	PS	0	0	0	0	1		1	
403	A	1414.7	PS	1	0	0	0	1		2	
403	A	1414.93	PS	1	0	0	0	1		2	
403	A	1415.04	PS	1	0	0	0	1		2	
403	A	1415.15	PS	1	0	0	0	1		2	
403	A	1415.3	PS	1	1	1	0	1		4	
403	B	1415.35	PS	1	1	1	0	1		4	
403	B	1415.55	PS	0	0	0	0	1		1	

403	B	1415.65	PS	1	0	0	0	1		2	
403	B	1415.68	PS	0	0	0	0	1		1	
403	B	1415.75	PS	0	0	0	0	1		1	
403	B	1415.8	PS	1	1	0	0	1		3	
403	B	1416.2	PS	0	0	0	0	1		1	
404	A	1416.33	PS	1	0	0	0	1		2	
404	A	1416.5	PS	1	1	0	0	1		3	
404	A	1416.95	PS	1	1	0	0	1		3	
404	B	1417.3	PS	1	2	2	0	1		6	
404	B	1417.31	PS	2	0	1	0	1		4	WONNERUP
404	B	1417.45	PS	3	1	1	0	1		6	
404	B	1417.51	PS	1	0	0	0	1		2	
404	B	1417.7	PS	0	0	0	0	1		1	
404	B	1417.7	PS	0	0	0	0	1		1	
404	B	1417.75	PS	0	0	0	0	1		1	
404	B	1417.78	PS	0	0	0	0	1		1	
404	B	1417.82	PS	0	0	0	0	1		1	
404	B	1417.84	PS	1	0	0	0	1		2	
405	A	1418.2	SST	1	0	0	0	1		2	
405	A	1418.8	SST	0	0	0	0	1		1	
405	A	1418.85	SST	0	0	0	0	1		1	
405	B	1419.35	SST	1	0	0	0	1		2	
406	B	1421.13	SST	1	0	0	0	1		2	No fractures in tray 406 section A
406	B	1421.32	SST	1	0	0	0	1		2	
407	A	1422.14	SST	0	0	0	0	1		1	

429	C	1464.57	SST	0	0	0	0	1		1	Core now smaller in size and 4 boxes per tray
429	C	1464.77	SST	0	0	0	0	1		1	
429	C	1465.11	SST	0	0	0	0	1		1	
429	D	1465.7	SST	1	0	0	0	1		2	
429	D	1466.25	SST	1	0	0	0	1		2	
430	A	1466.45	SST	0	0	0	0	1		1	
430	A	1466.85	SST	0	0	0	0	1		1	
430	B	1467.3	SST	0	0	0	0	1		1	
430	B	1467.35	SST	0	0	0	0	1		1	
430	B	1467.4	SST	0	0	0	0	1		1	
430	B	1467.65	SST	0	0	0	0	1		1	
430	B	1467.98	SST	1	0	0	0	1		2	
430	C	1468.1	SST	0	0	0	0	1		1	
430	C	1468.64	SST	0	0	0	0	1		1	
430	C	1468.75	SST	0	0	0	0	1		1	
430	D	1469.37	SST	1	0	0	0	1		2	
430	D	1469.77	SST	0	0	0	0	1		1	
431	A	1470.17	SST	1	0	0	0	1		2	
431	A	1470.6	SST	1	0	0	0	1		2	No fractures in tray 431 section B
431	C	1472.19	SST	0	0	0	0	1		1	
431	C	1472.5	SST	0	0	0	0	1		1	

431	C	1472.72	SST	0	0	0	0	1		1	
431	C	1472.79	SST	0	0	0	0	1		1	
431	D	1472.95	SST	0	0	0	0	1		1	
431	D	1473.47	SST	0	0	0	0	1		1	
432	A	1474.29	SST	0	0	0	0	1		1	
432	A	1474.62	SST	0	0	0	0	1		1	
432	B	1475.16	SST	0	0	0	0	1		1	
432	C	1475.81	SST	0	0	0	0	1		1	
432	C	1476.47	SST	0	0	0	0	1		1	
432	D	1476.95	SST	1	0	0	0	1		2	
432	D	1477.4	SST	1	0	0	0	1		2	
433	A	1477.73	SST	0	0	0	0	1		1	
433	A	1478.52	SST	1	0	0	0	1		2	
444	C	1522.4	SST	0	0	0	0	1		1	No fractures in tray 444 section D
444	D	1524.76	SST	0	0	0	0	1		1	
445	A	1524.99	SST	0	0	0	0	1		1	
445	A	1525.3	SST	0	0	0	0	1		1	
445	B	1525.5	SST	1	0	0	0	1		2	
445	B	1525.95	SST	1	0	0	0	1		2	
445	C	1526.3	SST	1	0	0	0	1		2	
445	C	1526.7	SST	0	0	0	0	1		1	
445	D	1527.5	SST	0	0	0	0	1		1	
445	D	1527.7	SST	1	0	0	0	1		2	
445	D	1528.15	SST	0	0	0	0	1		1	
446	A	1528.5	SST	0	0	0	0	1		1	

446	B	1529.5	SST	0	0	0	0	1		1	
446	C	1530.3	SST	0	0	0	0	1		1	
446	C	1530.97	SST	0	0	0	0	1		1	
446	D	1531.53	SST	0	0	0	0	1		1	
447	A	1532.25	SST	0	0	0	0	1		1	
447	A	1533.05	SST	0	0	0	0	1		1	
447	B	1533.35	SST	0	0	0	0	1		1	
447	B	1533.36	SST	0	0	0	0	1		1	
447	C	1534.34	SST	1	0	0	0	1		2	
447	C	1534.72	SST	0	0	0	0	1		1	
447	D	1535.2	SST	0	0	0	0	1		1	
448	A	1536.7	SST	0	0	0	0	1		1	
448	A	1536.9	SST	0	0	0	0	1		1	

Table A8-4 – Deformation logging data from the Harvey-3 core.

Tray Number	Tray Section	Lithology	Lithology (% of Total Tray Section)	Tray Start Depth (m)	Deformation Number (% of Total Tray Section)						Bedding (°)	Average Bedding (°)	Comments
					0	1	2	3	4	5			
1	A	PS	100	668.4	20	40	15		25				
1	B	PS	45		35		5		5		0-5	5	
1	B	SST	55		50	5							
2	A	SST	100	670.1	20	60	20				5 - 10	7.5	
2	B	SST	100		50	45		5					
3	A	SST	15	671.9	15								
3	A	PS	85		25	5	10	15	20	10			
3	B	PS	100					70	30				
4	A	PS	100	673.4			30	50	20				
4	B	PS	100				50	25	25				
5	A	PS	100	675.05		30	20	40	10				
5	B	PS	5				5						
5	B	SST	95				50	25	20				
6	A	SST	100	676.75		60	20		20				
6	B	SST	100					30	70				
7	A	SST	50	678.3	40			10			15-20	17.5	
7	A	PS	50				5	40	5				
7	B	PS	25					20	5				
7	B	SST	75					25	50				
8	A	PS	10	679.9				10					

8	A	SST	90					90					
8	B	SST	100			10	10	40	40				
9	A	SST	40	681.3	15			15	10				
9	A	PS	60					10	50				
9	B	PS	30			30							
9	B	SST	70		55	5			10				
10	A	SST	100	682.8	60				40				
10	B	SST	90		90								
10	B	PS	10			10							
11	A	PS	100	684.4	45	45	10						
11	B	PS	100		50	40	10						
12	A	PS	100	686.1	40	10	10	10	30				
12	B	PS	100			70	20		10				
13	A	PS	100	687.8	30	30	30		10				
13	B	PS	100				50		50				
14	A	PS	100	689.3		10	25	50	15				
14	B	PS	100				80	10	10				
15	A	PS	100	690.9		15	35	25	25				
15	B	PS	100				90		10				
16	A	PS	100	692.6	100								
16	B	PS	100				20	40	40				
17	A	PS	100	694.3			30	40	30				
17	B	PS	100				80		20				
18	A	PS	100	695.85		50	50						
18	B	PS	100		80	20							
19	A	PS	100	697.7	100								
19	B	PS	100		90	10							

20	A	PS	100	699.6	30	60			10				
20	B	PS	100		60	40							
21	A	PS	65	701.5	10	65							
21	B	SST	35		35								
21	B	SST	70		70								
21	B	PS	30		10	20							
22	A	PS	100	703.4	90	10							
22	B	PS	100		95	5					0-5	5	
23	A	SST	45	705.3	45						0-5	5	
23	A	PS	55		25	30							
23	B	PS	10		10								
23	B	SST	90		80	10							
24	A	PS	30	707	25	5					0-5	5	
24	A	SST	70		70								
24	B	SST	90		90						0-5	5	
24	B	PS	10			5		5					
25	A	PS	15	708.8		15							
25	A	SST	85		85								
25	B	SST	20		20								
25	B	PS	80		30	25	25						
26	A	PS	100	710.6		50	30	5	15				
26	B	PS	100				90		10				
27	A	PS	100	712.4		10	85		5				
27	B	PS	100				80		20				
28	A	PS	100	714.25			60	30	10				
28	B	PS	100			50	10	40					
29	A	PS	100	716	10	70	20						

29	B	PS	100		40	40	20						
30	A	PS	100	717.9		40	20	20	20				
30	B	PS	100				50	25	25				
31	A	PS	100	719.5			80		20				
31	B	SST	10		10								
31	B	PS	90		70	15	5						
32	A	SST	20	721.3	20								
32	A	PS	80			35	35		10				
32	B	PS	100		15	85							
33	A	PS	100	722.9	55	40		5					
33	B	PS	100		25	60	10		5				
34	A	PS	100	724.7	70	15	15						
34	B	PS	100		30	30	40						
35	A	PS	100	726.6			80		20				
35	B	PS	100				20	45		35			
36	A	PS	100	728.1			20	60	20				
36	B	PS	100				60	30	10				
37	A	PS	100	729.4	30	30		20	20				
37	B	PS	100					70	30				
38	A	PS	100	731.5		20	70	10					
38	B	SST	25		15								
38	B	PS	75			65	10						
39	A	PS	100	732.8		70	25	5					
39	B	PS	100		70	20			10				
40	A	PS	100	734.6			10	70	20				
40	B	PS	100		50	45	5						
41	A	PS	100	736.6	60	40							

41	B	PS	100			30	30	30	10				
42	A	PS	100	738.2	30	45		25					
42	B	PS	100			20	50	25	5				
43	A	PS	100	740				90	10				
43	B	PS	40			10	30				5	5	
43	B	SST	60		50	10							
44	A	SST	85	741.8	85								
44	A	PS	15					15					
44	B	PS	100				50	40	10				
45	A	PS	50	743.5			30	10	10		0-5	5	
45	A	SST	50		40	5			5				
45	B	SST	100		70	30							
46	A	SST	100	745.25	90	10							
46	B	SST	100		100								
47	A	SST	100	747.2	100								
47	B	SST	100		100								
48	A	SST	100	749.1	95		5						
48	B	SST	100		80	5			15				
49	A	SST	100	750.9	100								
49	B	SST	100		100								
50	A	SST	100	752.8	80		15		5		5	5	
50	B	SST	50		50								
50	B	PS	50		50								
51	A	PS	5	754.7		5							
51	A	SST	95		90	5							
51	B	SST	100		50	20			30				
52	A	SST	100	756.5	75	10	15						

52	B	SST	100		70	30							
53	A	SST	100	758.5	50	50							
53	B	SST	100		100								
54	A	SST	100	760.4	90	10							
54	B	SST	100		85	15							
55	A	SST	100	762.35	90	10							
55	B	SST	100		90	10							
56	A	SST	100	764.1	90	10					0-20	10	
56	B	SST	5		5								
56	B	PS	95		85		5		5				
57	A	PS	70	766	55	15					5	5	
57	A	SST	30		30								
57	B	SST	100		90	10							
58	A	SST	100	767.9	35	30	30		5				
58	B	SST	100		60	20	20						
59	A	SST	100	769.75	100								
59	B	SST	100		90	10							
60	A	SST	100	771.1	55	20		25					
60	B	SST	100		80	20							
61	A	SST	100	773.4	100						5-10	7.5	SAMPLE
61	B	SST	45			45							
61	B	PS	55			5	50						
62	A	PS	100	775.4	50	45			5				
62	B	SST	40		40								
62	B	PS	60		60								
63	A	PS	100	777.05			60	30	10				
63	B	PS	100		30		40	20	10				SAMPLE

64	A	PS	100	778.9			50	30	20				
64	B	PS	100		15	30	40		15				
65	A	PS	100	780.6		20	20	30	30		30	30	
65	B	PS	10		10								
65	B	SST	90		65	10	10	5					
66	A	SST	100	782.6	30	70							
66	B	SST	100		70	15			15				
67	A	SST	100	784.5	85	15							
67	B	SST	100		80	20							
68	A	SST	100	786.4	90				10				
68	B	SST	100		90	10							
69	A	SST	100	788.2	80	20							
69	B	SST	100		60	40							
70	A	SST	100	790	30	30	40						
70	B	SST	100		45	45	10						
71	A	SST	100	791.9		55	45						
71	B	SST	100		95	5							
72	A	SST	100	793.6	100								
72	B	SST	100		75			5	20				
73	A	SST	100	795.5	20	40		10	30				
73	B	SST	100		90				10				
74	A	SST	100	797.25	90			5	5				
74	B	SST	100		90	5							
75	A	SST	100	799.05	80	10	10						
75	B	SST	100		80	10	5		5				
76	A	SST	100	801	90	10							
76	B	SST	100		85	10	5						

77	A	SST	100	802.9	100								
77	B	SST	100		95			5					
78	A	SST	100	804.8	100								
78	B	SST	100		100								
79	A	SST	100	806.75	100								
79	B	SST	100		95			5					
80	A	SST	100	808.6	100								
80	B	SST	100		100								
81	A	SST	100	810.55	100								
81	B	SST	100		100								
82	A	SST	100	812.4	100								
82	B	SST	100		100								
83	A	SST	100	814.3	100								
83	B	SST	100		100								
84	A	SST	100	816.2	90			5	5				
84	B	SST	60		60								
84	B	PS	40		20	20							
85	A	PS	100	818.9	70		30						
85	B	PS	100		85		15						
86	A	PS	100	819.9	30	30	30		10				
86	B	PS	100			40	40	20					
87	A	PS	100	821.8		20	60	10	10				
87	B	PS	65				65						
87	B	SST	35		35								
88	A	SST	20	823.7	20								
88	A	PS	80				50	15	15				
88	B	PS	100			40	30	15	15				

89	A	PS	100	825.5			20	40	40				
89	B	PS	60					30	30				
89	B	SST	40		40								
90	A	SST	100	827.25	100								
90	B	SST	100		95				5				
91	A	SST	100	829.1	100								
91	B	SST	100		100								
92	A	SST	100	831	100								
92	B	SST	100		100								
93	A	SST	100	832.9	50		50						
93	B	SST	100				10			90			
94	A	SST	100	834.8		100							
94	B	SST	100			90	10						
95	A	SST	100	836.7	80	20							
95	B	SST	100		80	20							
96	A	SST	100	838.5	90	10							
96	B	SST	100		40	60							
97	A	SST	100	840.4	50	10		30	10				
97	B	SST	100		100								
98	A	SST	100	842.1	25	50	25						
98	B	PS	80		40		30	10					
98	B	SST	20		20								
99	A	SST	100	843.9	100								
99	B	SST	100		70	20	10						
100	A	SST	100	845.6	100								
100	B	SST	100		95				5				
101	A	SST	100	847.5	90	10							

101	B	SST	100		85	15							
102	A	SST	100	849.4	80	15			5				
102	B	SST	100		95	5							
103	A	SST	100	851.2	95	5							
103	B	SST	100		95	5							
104	A	SST	100	853.1	85	15							
104	B	SST	100		100								
105	A	SST	100	855	100								
105	B	SST	100		95	5							
106	A	SST	25	856.95	25								
106	A	PS	75				25	25	25				
106	B	PS	100			30	30	20	20				
107	A	PS	100	858.65	40		40	10	10				
107	B	PS	100			50	20	20	10				
108	A	PS	100	860.3	60	20	20						
108	B	PS	100		30	40		30					
109	A	PS	40	862.3	20		20						
109	A	SST	60		60								
109	B	SST	100		100								
110	A	SST	100	864.2	90		10						
110	B	SST	100		100								
111	A	SST	100	866.1	100								
111	B	SST	100		100								
112	A	SST	100	868	10		30	30	30				FAULT
112	B	SST	100		90		10						
113	A	SST	100	869.6	100								
113	B	SST	100		40	30	25	5					

114	A	SST	100	871.4	100								
114	B	SST	100		60	40							
115	A	SST	100	873.3	50	50							
115	B	SST	100		40	60							
116	A	SST	100	875.1	80	20							
116	B	SST	100		80	10	10						
117	A	SST	100	877	60	40							
117	B	SST	100		10	80			10				
118	A	SST	100	878.9	15	65	10	10					
118	B	SST	100		80	20							
119	A	SST	100	880.7	40	60							
119	B	SST	100		100								
120	A	SST	100	882.45	100								
120	B	SST	100		100								
121	A	SST	70	884.35	65			5					
121	A	PS	30				20	5	5				
121	B	PS	100				50	25	25				
122	A	PS	100	885.9	60	35			5				
122	B	PS	100		70			30					
123	A	PS	100	887.75		60		20	20				
123	B	PS	20		15				5				
123	B	SST	80		80								
124	A	SST	100	889.55	100								
124	B	SST	100		100								
125	A	SST	100	891.35	100								
125	B	SST	100		100								
126	A	SST	100	893.2	100								

126	B	SST	100		95				5				
127	A	SST	100	895	100								
127	B	SST	100		100								
128	A	SST	100	896.8	95	5							
128	B	SST	100		100								
129	A	SST	100	898.8	95	5							
129	B	SST	100		70	20			10				
130	A	SST	100	900.7	95	5							
130	B	SST	100		100								
131	A	SST	100	902.6	100								
131	B	SST	100		95				5				
132	A	SST	100	904.4	100								
132	B	SST	100		100								
133	A	SST	100	906.35	95				5				
133	B	SST	100		100								
134	A	SST	100	908.25	100								
134	B	SST	100		95			5					
135	A	SST	100	910.2	100								
135	B	SST	100		95	5							
136	A	SST	100	912.1	100								
136	B	SST	100		90	10							
137	A	SST	5	913.9			5						
137	A	PS	95				80	5	10				
137	B	PS	100				60	20	20				
138	A	PS	60	915.8	20	20	20						
138	A	SST	40		40								
138	B	SST	100		100								

139	A	SST	100	917.7	95	5							
139	B	SST	100		95	5							
140	A	SST	100	919.7	100								
140	B	SST	100		100								
141	A	SST	100	921.6	95	5							
141	B	SST	100		95			5					
142	A	SST	100	923.7	100								
142	B	SST	100		100								
143	A	SST	100	925.95	90		10						
143	B	SST	100		100								
144	A	SST	100	927.45	90	10							
144	B	SST	100		95	5							
145	A	SST	100	929.3	100								
145	B	SST	100		30	70							
146	A	SST	100	931.1	100								
146	B	SST	60		60								
146	B	PS	40			30			10				
147	A	PS	100	933.1	60	30			10				
147	B	PS	100		100								
148	A	PS	100	934.9	100								
148	B	PS	100		90								
149	A	PS	100	936.55	100								
149	B	PS	100		100								
150	A	PS	100	938.45	100								
150	B	PS	100		100								
151	A	SST	30	940.1	30								
151	A	PS	70		60		10						

151	B	PS	100		90	10							
152	A	PS	100	942.3	75	25							
152	B	PS	70		60	10							
152	B	SST	30		30								
153	A	SST	100	944.25	100								
153	B	SST	100		95			5					
154	A	SST	100	946.15	100								
154	B	SST	100		100								
155	A	SST	100	948.1	100								
155	B	SST	100		100								
156	A	SST	100	949.85	100								
156	B	SST	100		50	50							
157	A	SST	100	951.8	100								
157	B	SST	100		40	60							
158	A	SST	100	953.7	100								
158	B	SST	100		40	60							
159	A	SST	100	955.75	30	70							
159	B	SST	100		90	10							
160	A	SST	100	957.5	100								
160	B	SST	100		70	30							
161	A	SST	100	959.5	100								
161	B	SST	100		100								
162	A	SST	100	961.4	95	5							
162	B	SST	100		80	20							
163	A	SST	100	963.35	90	5			5				
163	B	SST	100		90	10							
164	A	SST	100	965.3	90	10							

164	B	SST	100		85	15							
165	A	SST	100	967.2	65	35							
165	B	PS	100		50	45			5				
166	A	PS	100	969.15	75	15			10				
166	B	PS	100		80	10		10					
167	A	PS	100	971	100								
167	B	PS	10		10								
167	B	PS	90			80	10						
168	A	PS	100	972.95	50	20	20	5	5				
168	B	PS	100		10	50	20	10	10				
169	A	PS	100	974.8		65	30	5					
169	B	PS	100		95	5							
170	A	PS	100	976.75	60	35			5				
170	B	PS	100		50	10	30	10					
171	A	PS	100	978.6	90	10							
171	B	PS	60		50	5		5					
171	B	SST	40		40								
172	A	SST	100	980.55	100								
172	B	SST	100		90		10						
173	A	SST	100	982.5	100								
173	B	SST	100		90				10				
174	A	SST	30	984.25	20	10							
174	A	PS	70		65	5							
174	B	PS	30		10	5			15				
174	B	SST	70		70								
175	A	PS	10	986.15	5				5				
175	A	SST	90		90								

175	B	SST	100		100								
176	A	SST	100	987.95	100								
176	B	SST	100		100								
177	A	SST	100	989.9	100								
177	B	SST	100		100								
178	A	SST	100	991.75	100								
178	B	SST	100		100								
179	A	SST	100	993.5	100								
179	B	SST	100		100								
180	A	SST	100	995.45	70	30							
180	B	SST	100		85	15							
181	A	SST	100	997.35	100								
181	B	SST	100		65	35							
182	A	SST	100	999.25	90	10							
182	B	SST	100		40	60							
183	A	SST	100	1001.15	75	25							
183	B	SST	100		25	65			10				
184	A	SST	100	1003	100								
184	B	SST	100		100								
185	A	SST	100	1004.9	100								
185	B	SST	20		20								
185	B	PS	80		40	20	20						
186	A	PS	100	1006.8	90	10							
186	B	PS	100		100								
187	A	PS	100	1008.7	90	5	5						
187	B	PS	100		70	10	20						
188	A	PS	100	1010.6	60	30	10						

188	B	PS	100		80		20						
189	A	PS	100	1012.5	100								
189	B	PS	100		100								
190	A	PS	100	1014.5	95					5			
190	B	PS	100		95					5			
191	A	PS	100	1016.3	100								
191	B	PS	60		60								
191	B	SST	40		40						15	15	
192	A	SST	10	1018.25	10								
192	A	PS	90		90								
192	B	PS	100		100								
193	A	PS	100	1020.2	100								
193	B	PS	100		100								
194	A	PS	50	1022.05	50								
194	A	SST	50		50								
194	B	SST	35		35								
194	B	PS	65		50		15						
195	A	PS	100	1024	90		10						
195	B	PS	100		80		10			10			
196	A	PS	100	1025.8	50	30		10		10			
196	B	PS	100		50	20	20		10				
197	A	PS	100	1027.75	50	45				5			
197	B	PS	100		90	10							
198	A	PS	100	1029.65	80	10			10				
198	B	PS	100		100								
199	A	PS	100	1031.55	100								
199	B	PS	100		100								

200	A	PS	100	1033.5	100								
200	B	PS	55		55								
200	B	SST	45		10	30			5				
201	A	PS	100	1035.3	100								
201	B	PS	100		70	25			5				
202	A	PS	100	1037.3	100								
202	B	PS	100		95	5							
203	A	PS	70	1039.25	70								
203	A	SST	30		30								
203	B	SST	25		25								
203	B	PS	75		50	25							
204	A	PS	100	1041.5	95				5				
204	B	PS	100		40	50			10				Photo of PS slickenlines taken at this depth
205	A	PS	100	1043.1	80	20							
205	B	PS	100		80	15	5						
206	A	PS	100	1045	45	50	5						
206	B	PS	100		95		5						
207	A	PS	100	1046.65	70	30							
207	B	PS	100		20	80							
208	A	PS	60	1048.85	25	30	5						
208	A	SST	40		40								
208	B	SST	35		35								
208	B	PS	65		35	30							

209	A	PS	100	1050.8	100								
209	B	PS	90		90								
209	B	SST	10		10								
210	A	SST	95	1052.75	95								
210	A	PS	5					5					
210	B	SST	100		90	10							
211	A	SST	100	1054.6	100								
211	B	SST	90		90								
211	B	PS	10		5	5							
212	A	PS	100	1056.55	60	35		5					
212	B	PS	100		100								
213	A	SST	60	1058.5	60								
213	A	PS	40		40								
213	B	SST	30		30								
213	B	PS	70		10	60							
214	A	PS	100	1060.45	20	80							
214	B	PS	100				10	50	40				
215	A	PS	25	1062.3				25					
215	A	SST	75		75								
215	B	SST	100		100								
216	A	SST	25	1064	25								
216	A	PS	75			15	35	15	10				
216	B	PS	100		20	20	20	40					
217	A	PS	55	1065.9	25	25	5						
217	A	SST	45		45								
217	B	SST	100		50				50				SST 50% "4"

													Possibly fault gouge, with surroundi ng DZ
218	A	SST	35	1067.7	35								
218	A	PS	65		35	30							
218	B	PS	100		80		20						
219	A	PS	100	1069.65		50	10	20	20				
219	B	PS	60		30		15		15				
219	B	SST	40		40								
220	A	SST	35	1071.4	35								
220	A	PS	65		40	20		5					
220	A	SST	35		35								
220	B	PS	100		20	70	10						
221	A	PS	100	1073.3		50	45		5				
221	B	PS	80		30	50							
221	B	SST	20		20								
222	A	SST	50	1075.25	50								
222	A	PS	50		40	10							
222	B	PS	100		50	10	10	10	20				
223	A	SST	15	1076.95			15						
223	A	PS	85				30	30	25				
223	B	PS	100				80		20				
224	A	PS	70	1078.55	70								
224	A	SST	30		30								

224	B	SST	60		60						10-15	12.5	
224	B	PS	40		40								
225	A	SST	45	1080.4	35					10			
225	A	PS	55			10		40		5			
225	B	PS	30		30								
225	B	SST	70		70								
226	A	SST	40	1082	40								
226	A	PS	60		50	10							
226	B	SST	20		20								
226	B	PS	80		80								
227	A	SST	20	1083.9	20								
227	A	PS	80		70	5		5					
227	B	PS	100		90	10							
228	A	PS	60	1085.8	60								
228	A	SST	40		40								
228	B	SST	100		100								
229	A	SST	100	1087.75	100								
229	B	SST	30		30								
229	B	PS	70		10	35				25			
230	A	PS	10	1089.7	10								
230	A	SST	90		90								
230	B	SST	100		100								
231	A	SST	100	1091.5	100								
231	B	SST	70		70								
231	B	PS	30		30								
232	A	PS	100	1093.45	65	35							
232	B	PS	35		25	10							

232	B	SST	65		65								
233	A	SST	100		100								
233	B	SST	50	1095.3	50								
233	B	SST	50		10	30			10				
234	A	PS	70		50	20							
234	A	SST	30	1097.2	30								
234	B	SST	50				45			5			
234	B	PS	50			10	20	10	10				
235	A	PS	75	1099.05	50	25							
235	A	SST	25		25								
235	B	SST	85		85								
235	B	PS	15		15								
236	A	PS	85	1100.95	85								
236	A	SST	15		15								
236	B	SST	20		20								
236	B	PS	80		70	10							
237	A	SST	20	1102.9	20								
237	A	PS	80		70		10						
237	B	SST	35		35								
237	B	PS	65		40	25							
238	A	PS	100	1104.8	55	20			25				
238	B	PS	15		15								
238	B	SST	85		85								
239	A	SST	60	1106.7	60								
239	A	PS	40			30	5			5			
239	B	PS	100		95	5							
240	A	PS	20	1108.6	10	10							

240	A	SST	80		80								
240	B	PS	50		50								
240	B	SST	50		50								
241	A	SST	25	1110.4	25								
241	A	PS	75		75								
241	B	SST	40		40								
241	B	PS	60		60								
242	A	SST	100	1112.4	100								
242	B	SST	5		5								
242	B	PS	95		90			5					
243	A	PS	50	1114.3	50								
243	A	SST	50		50								
243	B	PS	80		75	5							
243	B	SST	20		20								
244	A	SST	5	1116.25	5								
244	A	PS	95		80	5	10						
244	B	SST	40		40								
244	B	PS	60		30	10		10	10				
245	A	PS	100	1118.15	90	10							
245	B	PS	100		95	5							
246	A	PS	100	1120.05	20	75			5				
246	B	PS	100			10	50	30	10				
247	A	PS	100	1122	10	60	30						
247	B	SST	20		20								
247	B	PS	80		80								
248	A	SST	10	1123.9	10								
248	A	PS	90		60	30							

248	B	PS	25			20	5						
248	B	SST	75		75								
249	A	PS	20	1125.85	20								
249	A	SST	80		80								
249	B	SST	40		40								
249	B	PS	60		60								
250	A	SST	20	1127.75	20								
250	A	PS	80		75	5							
250	B	PS	100		40	40	10	5	5				
251	A	PS	100	1129.6	85	10	5						
251	B	PS	100		95	5							
252	A	PS	40	1131.6	40								
252	A	SST	60		60								
252	B	SST	100		100								
253	A	SST	20	1133.5	20								
253	A	PS	80		60	20							
253	B	SST	5		5								
253	B	PS	95		35	40	10		10				
254	A	PS	100	1135.45	80		10		10				
254	B	PS	100		95	5							
255	A	PS	100	1137.4	85	5	5		5				
255	B	PS	100		30	50	20						
256	A	PS	100	1139.25	30	40	25		5				
256	B	PS	30			25			5				
256	B	SST	70		70								
257	A	SST	30	1141.15	30								
257	A	PS	70		20	50							

257	B	PS	100		20	80							
258	A	PS	80	1143	60	20							
258	A	SST	20		20								
258	B	PS	20			20							
258	B	SST	80		80								
259	A	SST	100	1144.95	100								
259	B	SST	100		90	10							
260	A	SST	60	1146.85	55		5						
260	A	PS	40		30	5				5			
260	B	PS	10			10							
260	B	SST	90		90								
261	A	SST	75	1148.75	75								
261	A	PS	25		25								
261	B	SST	90		90								
261	B	PS	10		10								
262	A	PS	100	1150.7	100								
262	B	PS	100		100								
263	A	PS	100	1152.65	30	30		20	20				
263	B	PS	100		70		10	10	10				
264	A	PS	100	1154.4	50	20		15	15				
264	B	PS	100		10	20	10	30	30				
265	A	PS	100	1156.25	25	15	10	25	25				
265	B	PS	100		60	40							
266	A	SST	40	1157.9	40								
266	A	PS	60		20	25			15				
266	B	PS	100		85	15							
267	A	PS	100	1159.8	30	65		5					

267	B	PS	100		50	40			10				
268	A	PS	100	1161.6	40	50			10				
268	B	PS	100		95			5					
269	A	PS	100	1163.45	30	50	5	10	5				
269	B	PS	100		25	20	10	20	25				
270	A	PS	100	1165.3	45	25		20	10				
270	B	PS	100		50	30	10	5	5				
271	A	SST	50	1167.1	50								
271	A	PS	50		50								
271	B	PS	100		100								
272	A	PS	100	1169	30	20	10	20	20				
272	B	PS	100				20	10	70				
273	A	PS	100	1170.5					100				
273	B	PS	100					50	50				
274	A	PS	100	1172			20	30	50				
274	B	PS	100				50	20	30				
275	A	PS	100	1173.7	50		40	5	5				
275	B	PS	60		60								
275	B	SST	40		40								
276	A	SST	100	1175.45	100								
276	B	SST	100		100								
277	A	SST	100	1177.2	100								
277	B	SST	100		100								
278	A	SST	100	1179.15	100								
278	B	SST	100		100								
279	A	SST	100	1181.1	100								
279	B	SST	100		100								

280	A	SST	100	1183	100								
280	B	SST	100		100								
281	A	SST	45	1184.95	45								
281	A	PS	55		55								
281	B	PS	70		70								
281	B	SST	30		30								
282	A	SST	100	1186.85	100								
282	B	SST	100		100								
283	A	SST	100	1188.65	100								
283	B	SST	100		100								
284	A	SST	100	1190.55	100								
284	B	SST	100		100								
285	A	SST	100	1192.45	95			5					
285	B	SST	100		100						10	10	
286	A	SST	100	1194.4	100						15	15	
286	B	SST	60		60								
286	B	PS	40		40								
287	A	PS	100	1196.35	95	5					10	10	
287	B	SST	30		30								
287	B	PS	70		65			5					
288	A	PS	100	1198.2		70	10	15	5				
288	B	PS	100			10	60	20	10				
289	A	PS	100	1200.1	30	30	20	10	10				
289	B	PS	100			80	20						
290	A	PS	100	1202	50	30	5	10	5				
290	B	PS	95				50	45					
290	B	SST	5		5								

291	A	SST	60	1203.85	60								
291	A	PS	40		35	5							
291	B	PS	100		30	30	5	5	30				
292	A	PS	95	1205.7	10	50		15	20				
292	A	SST	5		5								
292	B	SST	100		100								
293	A	SST	100	1207.4	100								
293	B	SST	100		100								
294	A	SST	60	1209.35	60								
294	A	PS	40		40								
294	B	PS	100		50	50							
295	A	SST	30	1211.3	30								
295	A	PS	70		60	5	5						
295	B	PS	30		30								
295	B	SST	70		70								
296	A	PS	100	1213.15	100								
296	B	PS	100		90	10							
297	A	PS	100	1215.05	10	50	30	5	5				
297	B	PS	100		80	20							
298	A	PS	100	1216.9	20	50	20		10				
298	B	PS	100		75	25							
299	A	PS	80	1218.8	60	20							
299	A	SST	20		20								
299	B	SST	70		70								
299	B	PS	30		20		5	5					
300	A	SST	100	1220.25	100								
300	B	SST	30		30								

300	B	PS	70		10	10	35	10	5				
301	A	PS	100	1222.6	20		60	10	10				
301	B	PS	100		100								
302	A	SST	100	1224.4	90	10							
302	B	PS	100		10	85		5					
303	A	PS	100	1226.2	65	30			5				
303	B	SST	100		100								
304	A	SST	30	1228.1	30								
304	A	PS	70		50				20				
304	B	PS	95		50	45							
304	B	SST	5		5								
305	A	SST	100	1229.85	100								
305	B	SST	20		20								
305	B	PS	80			80							
306	A	PS	100	1231.7	100								
306	B	PS	100		100								
307	A	PS	30	1233.65		30							
307	A	SST	70		70								
307	B	SST	100		100								
308	A	SST	50	1235.6	50								
308	A	PS	50				45		5				
308	B	PS	100		85		15						
309	A	PS	100	1237.55	95			5					
309	B	PS	100		95	5							
310	A	PS	100	1239.5	90	10							
310	B	PS	100		100								
311	A	SST	40	1241.3	40								

311	A	PS	60		60								
311	B	SST	90		10	30	30	15	5				
311	B	PS	10		10								
312	A	PS	100	1243.25		25	75						
312	B	PS	100		90	10							
313	A	PS	100	1245.1	85	15							
313	B	PS	100		80	20							
314	A	PS	100	1247.05	100								
314	B	PS	70		20	25	25						
314	B	SST	30		30								
315	A	SST	100	1249	100								
315	B	SST	100		100								
316	A	SST	100	1251	100								
316	B	PS	25			25							
316	B	SST	75		75								SAMPLE - No Core
317	A	PS	40	1252.85		40							
317	A	SST	60		60								
317	B	SST	100		100								
318	A	PS	55	1254.8	45		10						
318	A	SST	45			45							
318	B	SST	100		100								
319	A	SST	35	1256.75	35								
319	A	PS	65		60	5							
319	B	PS	100		80	10	10						
320	A	SST	100	1258.65	100								
320	B	SST	100		100								

321	A	SST	100	1260.55	50	40		5	5				
321	B	PS	50		20	30							
321	B	SST	50		50								
322	A	PS	100	1262.35	15	55		30					
322	B	PS	80		75				5				
322	B	SST	20		10	10							
323	A	SST	50	1264.3		40		10					
323	A	PS	50			40		10					
323	B	PS	80			70		10					
323	B	SST	20						20				
324	A	SST	100	1266.2		90			10				
324	B	SST	100			100							
325	A	SST	100	1268	100								
325	B	SST	100		100								
326	A	SST	25	1269.95	25								
326	A	PS	75		40	35							
326	B	PS	100			100							
327	A	PS	100	1271.9	50	50							
327	B	PS	100		70	30							
328	A	PS	100	1273.85	60	40							
328	B	PS	100		80	20							
329	A	PS	100	1273	80	20							
329	B	PS	100		95	5							
330	A	PS	100	1275.8	30	30	10	15	15				
330	B	PS	50			35	15						
330	B	PS	50		50								
331	A	SST	100	1279.5	100								

331	B	SST	100		100								
332	A	SST	30	1281.4	30								
332	A	PS	70		10	25		30	5				
332	B	PS	100		40	45	15						
333	A	PS	100	1283.25	50	50			5				
333	B	PS	100		75	20			5				
334	A	PS	20	1285.2				20					
334	A	SST	80		80								
334	B	SST	100		100								SAMPLE - No Core
335	A	SST	100	1287.5	100								
335	B	SST	70		70								
335	B	PS	30				30						
336	A	PS	100	1288.95	50	45			5				
336	B	PS	100		80	10	10						
337	A	PS	100	1290.9	95			5					
337	B	PS	100		100								
338	A	PS	100	1292.8	50	35		15					
338	B	PS	100		90	10							
339	A	PS	100	1294.7	95	5							
339	B	PS	100		90	10							
340	A	PS	100	1296.55	75	25							
340	B	PS	100		90	5		5					
341	A	PS	50	1298.3	25	25							
341	A	SST	50		50								
341	B	SST	100		100								
342	A	SST	100	1300.2	100								

342	B	SST	100		90				10				
343	A	SST	50	1301.9	50								
343	A	PS	50				10	15	25				
343	B	PS	30				5	15	10				
343	B	SST	70		40			10	20				
344	A	SST	100	1303.45	100								
344	B	SST	100		50	30		10	10				
345	A	SST	100	1305.2	100								
345	B	SST	100		100								
346	A	SST	100	1307.15	70	15		15					
346	B	SST	45		15	20		10					
346	B	PS	55		50	5							
347	A	PS	50	1309.1	50								
347	A	SST	50		50								
347	B	SST	100		100								
348	A	SST	100	1311	100								
348	B	SST	100		100								
349	A	SST	100	1312.85	100								
349	B	SST	100		100								
350	A	SST	75	1314.8	75								
350	A	PS	25			25							
350	B	PS	100		90	10							
351	A	PS	100	1316.7	95	5							
351	B	PS	100		95	5							
352	A	PS	100	1318.7	95	5							
352	B	SST	100		90			5	5				
353	A	SST	100	1320.65	100								

353	B	SST	50		50								
353	B	PS	50				30	10	10				
354	A	PS	100	1322.5		20	50	15	15				
354	B	PS	100		90	10							
355	A	PS	100	1324.35	80	15		5					
355	B	PS	100		75	15		10					
356	A	PS	100	1326.25	100								
356	B	PS	100		90	10							
357	A	SST	90	1328.2	90								
357	A	PS	10		10								
357	B	SST	100		100								
358	A	SST	100	1330	100								
358	B	SST	50		50								
358	B	PS	50		50								
359	A	PS	100	1331.85	30	65			5				
359	B	PS	100				95		5				
360	A	PS	100	1333.75		100							
360	B	PS	100			10	20	20	50				
361	A	PS	100	1335.65	80	5		10	5				
361	B	PS	25		15	10							
361	B	SST	75		70			5					
362	A	SST	100	1337.45	100								
362	B	SST	100		100								
363	A	SST	100	1339.4	100								
363	B	SST	80		80								
363	B	PS	20		10			10					
364	A	PS	100	1341.25	80	20							

364	B	PS	50		30	10	10						
364	B	SST	50		50								
365	A	SST	100	1343.15	100								
365	B	SST	100		100								
366	A	PS	20	1345.05	5		15						
366	A	SST	80		80								
366	B	PS	40		35		5						
366	B	SST	60		60								
367	A	PS	100	1346.8	50	40	10						
367	B	PS	100		85	15							
368	A	SST	100	1348.7	100								SAMPLE - No Core
368	B	SST	100		100								
369	A	SST	100	1350.6	100								
369	B	SST	65		65								
369	B	PS	35			20	10	5					
370	A	PS	100	1352.5	30	35		20	15				
370	B	SST	20		20								
370	B	PS	80			30	30	15	5				
371	A	PS	10	1354.25		10							
371	A	SST	90		90								
371	B	SST	100		100								
372	A	SST	100	1356.1	100								
372	B	SST	100		100								
373	A	SST	90	1358	90								
373	B	PS	10			10							
373	B	SST	100		100								

374	A	SST	100	1359.9	100								
374	B	SST	85		85								
374	B	PS	15		10	5							
375	A	SST	100	1361.75	100								
376	B	SST	100		100								
376	A	SST	100	1363.7	100								
376	B	SST	100		100								
377	A	SST	95	1365.6	95								
377	A	PS	5			5							
377	B	PS	100		70	20		10					
378	A	PS	55	1367.55	50		5						
378	A	SST	45		45								
378	B	SST	50		50								
378	B	PS	50		35	5	10						
379	A	PS	50	1369.5	50								
379	A	SST	50		50								
379	B	SST	100		100								
380	A	SST	100	1371.45	100								
380	B	SST	100		100								
381	A	SST	100	1373.35	95					5			
381	B	SST	100		100								
382	A	SST	100	1375.15	100								
382	B	SST	40		30		10						
382	B	PS	60					50	10				
383	A	PS	100	1377		20	50	20	10				
383	B	PS	50		50								
383	B	SST	50		25					25			

384	A	SST	40	1378.8	20				20				
384	A	PS	60		25	30			5				
384	B	SST	40		15			5	20				
384	B	PS	60		55			5					
385	A	PS	65	1380.7	55	10							
385	A	SST	35		35								
385	B	PS	50		10	35			5				
385	B	SST	50		50								
386	A	PS	100	1382.55	70	5		20	5				
386	B	PS	50		15		30		5				
386	B	SST	50		50								
387	A	SST	100	1384.5	100								
387	B	PS	75		35	35			5				
387	B	SST	25		25								
388	A	PS	65	1386.5	60			5					
388	A	SST	35		35								
388	B	SST	10				10						
388	B	PS	90		45	20	20		5				
389	A	PS	85	1388.35				80	5				
389	A	SST	15		15								
389	B	SST	20		20								
389	B	PS	80		65	15							
390	A	PS	95	1390.2	85	10							
390	A	SST	5		5								
390	B	SST	90		90								
390	B	PS	10		5	5							
391	A	SST	90	1392.1	90								

391	A	PS	10		10									
391	B	PS	100		90	5	5							
392	A	PS	5	1394		5								
392	A	SST	95		95									
392	B	SST	100		100									
393	A	SST	100	1395.95	100									SAMPLE - Not Much Core
393	B	SST	100		100									SAMPLE - Not Much Core
394	A	SST	100	1397.85	100									
394	B	SST	60		60									
394	B	PS	40		40									
395	A	SST	85	1399.75	85									
395	A	PS	15		15									
395	B	PS	100		50	45				5				
395	B	PS	100		100									
396	A	PS	100	1401.5	60	30				10				
397	A	PS	100	1403.35	95	5								
397	B	PS	100		40	55				5				
398	A	PS	100	1405.3	100									
398	B	PS	100		50	45				5				
399	A	PS	100	1407.1	10		60	20		10				
399	B	PS	100			60	30	5		5				
400	A	PS	55	1408.9	50				5					
400	A	SST	45		45									

400	B	SST	100		60	35		5					
401	A	PS	100	1410.65	30	30	30	10					
401	B	PS	100		90	5		5					
402	A	PS	10	1412.5	10								
402	A	SST	90		90								
402	B	PS	20		20								
402	B	SST	80		80								
403	A	SST	5	1414.45	5								
403	B	PS	95		90	5							
403	B	PS	100		80	20							
404	A	PS	100	1416.3	70			10	20				
404	B	PS	75		35	35		5					
404	B	SST	25		25								WONNER UP
405	A	SST	100	1418.1	100								
405	B	SST	100		100								
406	A	SST	100	1419.85	100								
406	B	SST	100		100								
407	A	SST	100	1421.7	100								
407	B	SST	100		100								
408	A	SST	100	1423.1	100								
408	B	PS	100		100								
409	A	PS	35	1425.4	35								
409	A	SST	65		65								
409	B	SST	100		100								
410	A	SST	100	1427.2	100								
410	B	SST	100		100								

411	A	SST	100	1429.15	100								
411	B	SST	100		100								
412	A	SST	100	1431.1	100								
412	B	SST	100		100								
413	A	SST	100	1433	100								
413	B	SST	100		100								
414	A	SST	100	1434.9	100								
414	B	SST	100		100								
415	A	SST	100	1436.8	100								
415	B	SST	100		100								
416	A	SST	100	1438.7	100								
416	B	SST	100		100								
417	A	SST	100	1440.7	100								
417	B	SST	100		100								
418	A	SST	100	1442.6	100								
418	B	SST	100		100								
419	A	SST	100	1444.6	100								
419	B	SST	100		100								
420	A	SST	100	1446.5	100								
420	B	SST	100		100								
421	A	SST	100	1448.4	100								
421	B	SST	100		100								
422	A	SST	100	1450.4	100								
422	B	SST	100		100								
423	A	SST	100	1452.3	100								
423	B	SST	100		100								
424	A	SST	100	1454.3	100								

424	B	SST	100		100								
425	A	SST	100	1456.2	100								
425	B	SST	100		100								
426	A	SST	100	1458.2	100								
426	B	SST	100							100			
427	A	SST	100	1460.1	100								
427	B	SST	100		100								
428	A	SST	100	1462.1	100								
429	A	SST	100	1462.7	100								
429	B	SST	100		100								
429	C	SST	100		100								
429	D	SST	100		100								
430	A	SST	100	1466.4	100								
430	B	SST	100		100								
430	C	SST	100		100								
430	D	SST	100		100								
431	A	SST	100	1470.1	100								
431	B	SST	100		100								
431	C	SST	100		100								
431	D	SST	100		100								
432	A	SST	100	1473.9	100								
432	B	SST	100		100								
432	C	SST	100		100								
432	D	SST	100		100								
433	A	SST	100	1477.7	100								

433	B	SST	100		100								
433	C	SST	100		100								
433	D	SST	100		100								
434	A	SST	100	1481.7	100								
434	B	SST	100		100								
434	C	SST	100		100								
434	D	SST	100		100								
435	A	SST	100	1485.5	100								
435	B	SST	100		100								
435	C	SST	100		100								
435	D	SST	100		100								
436	A	SST	100	1489.3	100								
436	B	SST	100		100								
436	C	SST	100		100								
436	D	SST	100		100								
437	A	SST	100	1493.1	100								
437	B	SST	100		100								
437	C	SST	100		100								
437	D	SST	100		100								
438	A	SST	100	1497	100								
438	B	SST	100		100								
438	C	SST	100		100								
438	D	SST	100		100								
439	A	SST	100	1500.9	100								
439	B	SST	100		100								
439	C	SST	100		100								
439	D	SST	100		100								

440	A	SST	100	1504.8	100								
440	B	SST	100		100								
440	C	SST	100		100								
440	D	SST	100		100								
441	A	SST	100	1508.7	100								
441	B	SST	100		100								
441	C	SST	100		100								
441	D	SST	100		100								
442	A	SST	100	1512.6	100								
442	B	SST	100		100								
442	C	SST	100		100								
442	D	SST	100		100								
443	A	SST	100	1516.5	100								
443	B	SST	100		100								
443	C	SST	100		100								
443	D	SST	100		100								
444	A	SST	100	1520.4	100								
444	B	SST	100		100								
444	C	SST	100		100								
444	D	SST	100		100								
445	A	SST	100	1524.3	100								
445	B	SST	100		100								
445	C	SST	100		100								
445	D	SST	100		100								
446	A	SST	100	1528.2	100								
446	B	SST	100		100								
446	C	SST	100		100								

446	D	SST	100		100									
447	A	SST	100	1532.2	100									
447	B	SST	100		100									
447	C	SST	100		100									
447	D	SST	100		100									
448	A	SST	100	1536.1	100									
448	B	SST	100		100									
448	C	SST	100		100									
448	D	SST	100		100									
449	A	SST	100	1539.9	90		10							
449	B	SST	100		100									
449	C	SST	100		100									
449	D	SST	100		100									
450	A	SST	100	1543.8	100									
450	B	SST	100		100									
450	C	SST	100		100									
450	D	SST	100		100									
451	A	SST	100	1547.7	100									
451	B	SST	100		100									
451	C	SST	100		100									

Table A8-5 – Deformation logging data from the Brumbys-1 core.

Tray Number	Tray Section	Lithology	Lithology (% of Total Tray Section)	Tray Start Depth (measured depth, m)	Deformation Number (% of Total Tray Section)					
					0	1	2	3	4	5
1	A	Soil	10	0						
1	A	Clay	90	0	90					
1	B	Clay	100	1	100					
1	C	Clay	60	2	50	10				
1	C	PCL	40	3		40				
2	A	PCL	100	3						100
2	B	PCL	100	3	100					
2	C	PCL	100	3						100
3	A	PCL	100	3.2		15	45	20	10	10
3	B	PCL	100	4.2			50	50		
3	C	PCL	100	4.5						100
4	A	PCL	100	4.8		70	15	5		10
4	B	PCL	100	5.8		80	20			
4	C	PCL	100	6.8		75	25			
5	A	PCL	100	7.8			50	50		
5	B	PCL	100	8.8		100				
5	C	PCL	100	9.8		100				
6	A	PCL	100	10.8			80	20		
6	B	PCL	100	11.8		30	70			
6	C	PCL	100	12.8		30	70			
7	A	PCL	100	13.8		50	50			
7	B	PCL	100	14.8		100				
7	C	PCL	100	15.8		80	20			

8	A	PCL	100	16.8		90		10		
8	B	PCL	100	17.8		100				
8	C	PCL	100	18.8		50	50			
9	A	PCL	100	19.8		80	10			
9	B	PCL	100	20.8		60	30	10		
9	C	PCL	100	21.8		10	50	30		
10	A	PCL	100	22.8		10	80	10		
10	B	PCL	100	23.8		80		20		
10	C	PCL	100	24.8		50		50		
11	A	PCL	100	25.8		20	70	10		
11	B	PCL	100	26.8		100				
11	C	PCL	100	27.8	10	80				10
12	A	PCL	100	28.8			100			
12	B	PCL	100	29.8		20	80			
12	C	PCL	100	30.8		20	70	10		
13	A	PCL	100	31.8			80	20		
13	B	PCL	100	32.8		30	40	30		
13	C	PCL	100	33.8			90	10		
14	A	PCL	100	34.8			70	30		
14	B	PCL	100	35.8		40	60			
14	C	PCL	100	36.8			20	80		
15	A	PCL	100	37.8		100				
15	B	PCL	100	38.8			100			
15	C	PCL	100	39.8		20		80		
16	A	PCL	100	40.8			80	20		
16	B	PCL	100	41.8		20	80			
16	C	PCL	100	42.8			100			

17	A	PCL	100	43.8			100			
17	B	PCL	100	44.8		30	70			
17	C	PCL	100	45.8			90	10		
18	A	PCL	100	46.8			10	90		
18	B	PCL	100	47.8			80	10		10
18	C	PCL	100	48.8			15	85		
19	A	PCL	100	49.8			80			20
19	B	PCL	100	50.8				80	20	
19	C	PCL	100	51.8			10	70	20	
20	A	PCL	100	52.8			90	10		
20	B	PCL	100	53.8		10	10	20	50	10
20	C	PCL	100	54.8			20	70	10	
21	A	PCL	100	55.8			15	75		10
21	B	PCL	100	56.8			60	40		
21	C	PCL	100	57.8		20	40	20		
22	A	PCL	100	58.8		10	80	10		
22	B	PCL	100	59.8			100			
22	C	PCL	100	60.8			70	30		
23	A	PCL	100	61.8			50	40	10	
23	B	PCL	100	62.8		80		10		10
23	C	PCL	100	63.8			50	50		
24	A	PCL	100	64.8		100				
24	B	PCL	100	65.8		70			30	
24	C	PCL	100	66.8		30	70			
25	A	PCL	100	67.8		80	20			
25	B	PCL	100	68.8		70	10		20	
25	C	PCL	100	69.8		40	60			

26	A	PCL	100	70.8		50	50			
26	B	PCL	100	71.8		100				
26	C	PCL	100	72.8		10	90			
27	A	PCL	100	73.8		15	85			10
27	B	PCL	100	74.8			100			
27	C	PCL	100	75.8			80	20		
28	A	PCL	100	76.8			90	10		
28	B	PCL	100	77.8			90	10		
28	C	PCL	100	78.8				60	40	
29	A	PCL	100	79.8			40	40	10	10
29	B	PCL	100	80.8			60	30		10
29	C	PCL	100	81.8			90			10
30	A	PCL	100	82.8			80	20		
30	B	PCL	100	83.8			90	10		
30	C	PCL	100	84.8			50	50		
31	A	PCL	100	85.8			30	70		
31	B	PCL	100	86.8			30	40	30	
31	C	PCL	100	87.8			40	60		
32	A	PCL	100	88.8		80		20		
32	B	PCL	100	89.8			10	30	40	20
32	C	PCL	100	90.8			10	90		
33	A	PCL	100	91.8			20	60	20	
33	B	PCL	100	92.8				100		
33	C	PCL	100	93.8			100			
34	A	PCL	100	94.8			10	55	20	15
34	B	PCL	100	95.8			10	75		15
34	C	PCL	100	96.8			65	20		15

35	A	PCL	100	97.8				30	70	
35	B	PCL	100	98.8					100	
35	C	PCL	100	99.8				10	90	
36	A	PCL	100	100.8				40	60	
36	B	PCL	100	101.8			20	50	30	
36	C	PCL	100	102.8				100		
37	A	PCL	100	103.8			90	10		
37	B	PCL	100	104.8			90	10		
37	C	PCL	100	105.8			75	25		
38	A	PCL	100	106.8			50	50		
38	B	PCL	100	107.8				100		
38	C	PCL	100	108.8			20	40	40	
39	A	PCL	100	109.8			70	30		
39	B	PCL	100	110.8			70	30		
39	C	PCL	100	111.8			30	70		
40	A	PCL	100	112.8			60	40		
40	B	PCL	100	113.8			80	20		
40	C	PCL	100	114.8			30	35	35	
41	A	PCL	100	115.8			10	70	20	
41	B	PCL	100	116.8			40	60		
41	C	PCL	100	117.8				100		
42	A	PCL	100	118.8			30	60		10
42	B	PCL	100	119.8			20	20	60	
42	C	PCL	100	120.8			50	30	10	10
43	A	Marl	100	121.8		100				
43	B	Marl	100	122.8		100				
43	C	Marl	100	123.8		20				80

44	A	Marl	100	124.8		90				10
44	B	Marl	100	125.8		95				5
44	C	Marl	100	126.8		100				